University of Venda
Creating Future Leaders



School of Environmental Sciences
Department of Mining and Environmental Geology

Investigation of the Geology, Structural Setting and Mineralisation of the Copper-Sulphide Deposits in the Musina Area, Limpopo Mobile Belt, South Africa

By
Ms. Mundalamo Humbulani Rejune
Student No. 9906682

A Thesis Submitted to the Department of Mining and Environmental Geology, School of Environmental Sciences, University of Venda, in fulfilment of the Requirements for the degree of Doctor of Philosophy of Environmental Sciences (Geology)

Promoter: Emeritus Professor Jason S. Ogola
School of Environmental Sciences, University of Venda

Co-Promoter: Professor Klaus W. Maas
Faculty of Environmental Engineering and Applied Informatics, University of Applied Sciences, Germany

August 2019

© University of Venda

DECLARATION

I, Mundalamo Humbulani Rejune, hereby declare that this thesis titled "Investigation of the Geology, Structural Setting and Mineralisation of the Copper-Sulphide Deposits in the Musina Area, Limpopo Mobile Belt, South Africa" submitted to the Department of Mining and Environmental Geology of the University of Venda has not been submitted before for any degree or examination at this or any other university and that it is my own work in design and execution, and that all materials have been duly acknowledged

---------- ----------

Student's signature Date

Ms. Humbulani R. Mundalamo

We, the Promoters, certify that this declaration is correct

---------- ----------

Promoter's Signature Date

Emeritus Professor Jason S. Ogola



---------- ----------

Co-Promoter's Signature Date

Professor Klaus W. Maas

© University of Venda

DEDICATION

To my lovely sons Mulweli and Sedzani, for their tolerance of my absence and busy life while carrying out this work at a time they needed me most and to my beloved parents the late Mrs. Tshisevhe Selinah Nemudzudzanyi and Mr. Tshililo Phineas Mundalamo for their inspiration, love and support.

© University of Venda

ACKNOWLEDGEMENTS

The work involved in the preparation and production of this thesis was so much that I alone would not have made it. Therefore, my heart pulsates with the thrill for tendering gratitude to those who helped me accomplish this work.

I am deeply indebted to my Promoter, Emeritus Professor Jason S. Ogola and my Co-promoter, Professor Klaus W. Maas without their critical advice, guidance, encouragement and patience the whole study would have been a failure. I wish also to sincerely thank them for creating time on assisting me throughout the research despite their many other academic work, professional and their family commitments.

I would like to express a word of gratitude for the support and unflagging help I have received from the following persons, Universities and Companies:

Professor van den Kerkhof, from Department of Applied Geology, Geoscience Institute, Göttingen University, Germany and Dr. Jeff B. Chaumba together with Ms. Julia, A. Cox and Christopher, J. Fleisher from Department of Geology, University of Georgia, Athens, United States of America for their great support on my laboratory work.

I gratefully acknowledge MINTEK; Société Générale de Surveillance (SGS) laboratories for mineralogical analysis I did at their laboratories; Southern Mapping Company for ASHTER data and training; Colleagues from Faculty of Environmental Engineering and Applied Informatics, University of Applied Sciences, Höxter, Germany led by Professor Maas K.W., for GIS and remote sensing training; and laboratory assistance I got from Department of Geology, University of Johannesburg.

My sincere gratitude goes to the Musina Municipality Farms and game reserve owners for allowing me to conduct my reach work and I also acknowledge the help I got from the Musina community members especially former workers of the Messina copper deposits for the grateful information I gathered and used in my research work.

I thank all the staff members from the Department of Mining and Environmental Geology. Special thanks to Dr. A.F. Dacosta, former Head of Department and Dr. M. Kataka, current Head

© University of Venda

of the Department who always understood my absence when conducting this work. I express my sincere thanks to Prof. J.O. Odiyo for his endless unflagging assistance and support throughout this period.

I acknowledge all the students who were part of the team during the entire research work, with my especial thanks to Tshitangano Mulamuleli, Ratshiedana Phathutshedzo, Nemasea Tshifhiwa, Mahamba Ronewa, Chauke Tiyani and Mudzanani Phambano.

This work would have not been accomplished without the financial support rendered by National Research Foundation, DAAD, and SANSA scholarships, Research and Innovation Directorate, University of Venda, I therefore, express my sincere gratitude for the grateful support.

My sincere thanks to my family, especially my Brother, Mr. H.S. Mundalamo and his late wife Mrs. N.E. Mundalamo for their support throughout my studies and my special thanks to Kokwani, Johana Mphephu Chauke who has been always there at home for my family during my absence. My sons Mulweli Mundalamo and Sedzani are sincerely acknowledged, as they understood the circumstances, I was in through the entire research work and became strong and patient at the time they needed my presence.

Above all, I acknowledge the almighty God for all the strength and blessings He anointed me with during the entire time of my life.

© University of Venda

ABSTRACT

The study focused on the geology, structural setting and mineralisation of copper-sulphide deposits in the Musina area, located in the Central Zone of the Limpopo Mobile Belt of South Africa. The Messina copper deposits are located in the eastern part of Limpopo Province near the border with Zimbambwe. The deposits stretch from northeastern to southwestern direction for about 15 km. Previous copper mining in the area took place at Artonvilla, Messina, Harper, Campbell and Lilly copper deposits. The current study, however, focused on two main deposits, Campbell and Artonvilla.

The origin, nature and mode of formation of the Cu-sulphide deposits in the Musina area have not been established with certainty. Two principal hypotheses on the origin of the Messina copper sulphide deposits have been proposed, viz; a magmatic-hydrothermal model, and meteoric waters model. Consequently, the mode of formation and mineralisation style of the Messina Cu-sulphide deposits remain contentious. Therefore, the main objective of the study was to investigate the nature and mode of formation of Cu-sulphide deposits in the Musina area.

Different research methods have been applied in the current study so as to unpack the contradictory positions on the genesis of the Messina copper deposits. This included fieldwork, remote sensing data acquisition, laboratory work, and data analysis and interpretation. Fieldwork involved soil geochemical survey as well as rock and ore sampling within the study area. A total of 295 soil samples, 33 rock specimens and 21 ore samples were collected for laboratory investigation.

Laboratory work consisted of a range of methods that included; geochemical analysis, petrographic and cathodoluminescence microscopy, ore mineralogy and ore microscopy, fluid inclusion geothermometry and isotope geochemistry. The work was done in different laboratories including: Mining and Environmental Geology Laboratory, Unviersity of Venda; Department of Geology Laboratory, University of Johannesburg; MINTEK Laboratory in Johannesburg; Société Générale de Surveillance Laboratory in Johannesburg, South Africa; Department of Applied Geology, Geoscience Institute, Göttingen University, Germany and Department of Geology, University of Georgia, Athens, United States of America. Remote

© University of Venda

sensing data was acquired from Southern Mapping Company, Johannesburg, South Africa. Interpretation of Remote sensing data was done at the University of Applied Sciences, Oswestfalen-Lippe, Germany.

Data analysis and interpretation of laboratory results involved the use of: Desktop ArcGIS 10.4.1 for geochemical data interpretation; ENVI 5.1 and ArcGIS 10.4.1 Softwares for remote sensing data; and Triplot version 4.1.2 software for ternary plot for compositional variation of rocks.

Soil geochemical survey revealed geochemical anomalies for Pb, Zn, Cu, As and Ni over the known copper deposits in the area as well as over six other areas that have not been associated with any sulphide mineralisation. Such new anomalous areas have been identified as target areas for future exploration of sulphide ore mineralisation.

Petrographic studies of the rocks confirmed the host rocks to be amphibolite-quartz granulite, biotite-garnet-quartz granulite, amphibolite, quartzite, hornblende gneiss, quartzo-feldspathic gneiss, potassium-feldspathic gneiss and cal-silicate gneiss. These rocks were subjected to hydrothermal alteration during ore mineralisation within the area. It was further noted that epidote alteration was quite intensive in ore samples, while in unmineralised rock samples it was less intensive. Remote sensing data interpretation revealed spatial distribution and intensity of epidote alteration within the study area and in places coincided either with the known copper deposits or structural features, thus led to the identification of target areas for future mineral exploration in the Musina area.

The current study established that the process of ore mineralisation in the Messina copper deposits took place in two distinct phases: first the formation of garnet, graphite, magnetite and hematite during regional metamorphism of the Limpopo Mobile Belt; and secondly, sulphide ore mineralisation resulting in the formation of copper ore comprising, veined, disseminated and brecciated ores. Sulphide ore mineralisation consisted mainly of pyrite, chalcopyrite, sphalerite, bornite, chalcocite and minor pyrrhotite and galena as well as traces of pentlandite, tennantite, mollybdenite, cobaltite and tetrahedrite. This confirms that the Messina copper deposits had complex sulphide ore mineralisation that is typical of hydrothermal mode of ore mineralisation from a magmatic source.

© University of Venda

The study further establishes the paragenitic sequence of ore mineralisation, comprising four stages: Stage I (Garnet- graphite – Fe oxides); stage II (Quartz- pyrite); stage III (Pyrite-sphalerite - chalcopyrite); and stage IV (Carbonates). Stage III represented the main stage of sulphide ore mineralisation in the area, while Stage IV comprising calcite, dolomite and ankarite marked the final stage of hydrothermal ore mineralisation.

Paragenetic sequence identified three generations of quartz; first generation being associated with garnet, graphite, magnetite and hematite, second generation with pyrite and third generation with pyrite, sphalerite and chalcopyrite. Previous studies, however, indicated that there was only one generation of quartz that formed at the temperature between 210^{o} to 150°C, but the current study established that the entrapment temperature of first generation quartz ranges from 315^{o} to 200°C; second generation quartz from 235^{o} to 135°C and third generation quartz from 240^{o} to 115°C. At the same time, sulphur isotope investigation of chalcopyrite-pyrite pair from Campbell deposit registered a temperature of 359°C. The study therefore concluded that the temperature of ore formation within the Messina copper deposits ranged between 359°C and 115°C.

The presence of halite and calcite as daughter minerals within the fluid inclusions was noted and this apparently is indicative of high salinity of fluid inclusions, which is considered as a product of direct exolution of crystalizing magma. Raman spectroscopy revealed the composition of gases in the fluid inclusions to be CH_4 and N_2 with 80% and 20% composition respectively, however, some inclusions were gas-poor. The presence of gases in the fluid inclusions is an indication that there was boiling at the time of entrapment. A narrow range of ^{34}S values of -0.5 to 0.5‰ obtained in this study further confirms the magmatic source of Sulphur as Sulphur from the host rock was found to have high $\delta^{34}S$ value of 8.2‰.

A genetic model for copper ore mineralisation within Musina area is proposed. The deposits are of polymetallic vein type that are genetically associated with porphyry copper deposits. According to this model, copper ore bodies were formed from hydrothermal fluids originating from magma and were epigenetic in nature. Geological structures in the area acted as conduits for hydrothermal fluids that resulted in the alteration of the host rocks and mineralisation of copper sulphide ore. Thus, the Messina coper deposits are of magmatic hydrothermal origin although the apparent location of a batholith is still unknown and the study recommends further

© University of Venda

research work on the location of the batholith that is presumed to have been the magmatic source. The study further recommend dating of later rocks as well as orebody s it is essential for understanding the process of ore formation in this area.

For further exploration, areas that have undergone “moderate” to “high” degree of epidote alteration and lie in close proximity to geological structures such as faults and thrust folds that could have acted as conduits for hydrothermal fluids and resulted in sulphide ore mineralisation and registered high geochemical anomalies for Pb, Zn, As and Ni should be targeted. In support of further mineral exploration within the study area, the study recommend a detailed geostatistical application for the purpose of delineating homogeneous areas based on the combination of lineaments, interpolated soil geochemical maps and thematic maps.

Keywords: Messina deposits, ore mineralisation, paragenetic sequence, genetic model

© University of Venda

University of Venda
Creating Future Leaders

TABLE OF CONTENT

Declaration i
Dedication ii
Acknowledgement iii
Abstract v
Table of Content ix
List of Figures xviii
List of Plates xxxi
List of Tables xxxiii
List of Abbreviations and Acronyms xxxv
List of Units and Symbols xxxviii
Glossary and Terminologies xxxix

CHAPTER 1: INTRODUCTION 1

1.1 Background 1
1.2 Study Area 2
1.2.1 Location 2
1.2.2 Climate 3
1.2.3 Topography and Drainage 3
1.2.4 Soil and Vegetation 5
1.2.5 Land-use 6
1.3 Problem Statement 7
1.4 Rationale 7
1.5 Research Questions 10
1.6 Hypothesis 10
1.7 Objectives 11
1.7.1 Main Objective 11
1.7.2 Specific Objectives 11
1.8 Thesis Structure 11

© University of Venda

University of Venda
Creating Future Leaders

CHAPTER 2: GEOLOGICAL SETTING AND GENETIC TYPES OF COPPER-SULPHIDE DEPOSITS 14

2.1 Magmatic Copper-sulphide Deposits 14
2.1.1 Copper-Nickel Sulphide (PGEs) Deposits 14
2.1.2 Porphyry Copper Deposits 16
2.1.3 Volcanogenic Massive Sulphide Deposits 19
2.1.4 Skarn Copper Deposits 20
2.1.5 Carbonatite Copper Deposits 20
2.2 Hydrothermal Deposits 23
2.3 Sediment-hosted Copper Deposits 26
2.4 Copper-sulphide Mineralisation within Metamorphic Terrain 29
2.4.1 Cape Fold Belt 30
2.4.2 Damara Fold Belt 31
2.4.3 Zambezi Belt 31
2.4.4 Mozambique Belt 32
2.4.5 Namaqua-Natal Belt 33
2.4.6 Limpopo Mobile Belt 33
2.4.6.1 Geological and Structural Setting 33
2.4.6.2 Copper-sulphide Mineralisation in Musina Area 37
2.4.6.3 Mining History of Musina Copper-sulphide Deposits 40

CHAPTER 3: METHODS 42

3.1 Preliminary Work 42
3.1.1 Desktop Study 42
3.1.2 Reconnaissance Survey 44
3.2 Fieldwork 44
3.2.1 Geochemical Soil Sampling 44
3.2.2 Rock Sampling 46
3.2.3 Ore Sampling 47
3.3 Laboratory Work 47

© University of Venda

University of Venda
Creating Future Leaders

3.3.1 Geochemical Analysis 47
3.3.2 Petrographic Microscopy 49
3.3.3 Cathodoluminescence Microscopy 49
3.3.4 Fluid Inclusion Geo-thermometry 50
3.3.5 Sulphur Isotope Geochemistry 50
3.4 Remote Sensing 51
3.5 Data Quality Management and Assurance 51

CHAPTER 4: GEOCHEMICAL SURVEY 53

4.1 Importance of Geochemical Survey 53
4.2 Geochemical Survey as an Exploration Tool 54
4.3 Pathfinder Elements for Copper 55
4.4 Laboratory Techniques 56
4.5 Methods for Data Analysis 58
4.5.1 Basic Statistical Methods 58
4.5.2 Geostatiscal Methods 60
4.5.2.1 Requirements for Geostatistics 60
4.5.2.2 Kriging Methods 62
4.5.2.3 Pre-processed Parameters for Development of Kriging Model 67
4.6 Geochemical Survey in the Musina Area 67
4.6.1 Specific Objectives 67
4.6.2 Data Preparation 68
4.6.3 Sample Preparation 70
4.6.4 Samples Analysis 71
4.6.4.1 Quality Control and Assurance 71
4.6.4.2 Soil Analysis 72
4.6.5 Data Analysis and Interpretation 74
4.6.5.1 Occurrence and distribution of metals in Soils 74
4.6.5.2 Interpolation of Geochemical Data 76
4.6.5.3 Analysis and Interpretation of Interpolated Soil Geochemical maps 82
4.7 Discussion 97

© University of Venda

University of Venda
Creating Future Leaders

CHAPTER 5: REMOTE SENSING STUDY 100

5.1 Fundamental of Remote Sensing 100
5.1.1 Principles of Remote Sensing 102
5.1.2 Remote Sensing Data Acquisition Process 104
5.1.3 Remote Sensing Instrumentation 106
5.1.3.1 Multispectral Sensors 107
5.1.3.2 Hyperspectral Sensors 110
5.1.4 Image Processing Software 111
5.1.5 Image Processing Techniques 111
5.1.5.1 Pre-processing Techniques 111
5.1.5.2 Image Enhancement Technique 115
5.1.5.3 Image Classification 116
5.1.6 Methods for Remote Sensing Data Analysis 117
5.1.6.1 Visual Interpretation 117
5.1.6.2 Digital interpretation 118
5.2 Application of Remote Sensing 120
5.3 History of Remote Sensing in Mineral Exploration 121
5.4 Remote Sensing Study of the Musina Area 122
5.4.1 Specific Objectives 123
5.4.2 Data Acquisition 124
5.4.3 ASTER Data Processing 124
5.4.3.1 Data Manipulation 124
5.4.3.2 Data Pre-Processing 125
5.4.3.3 Image Enhancement 126
5.4.3.4 Image Classification 129
5.4.4 ASTER Data Analysis 131
5.4.4.1 Visual Analysis 131
5.4.4.2 Digital Analysis 134
5.4.5 Data Quality Assurance (DQA) 138
5.4.6 Results and Interpretation 140

© University of Venda

University of Venda
Creating Future Leaders

5.4.6.1 Epidote Alteration within the Limpopo Mobile Belt 141
5.4.6.2 Geological Structures 146
5.4.6.3 Conceptual Model of Target Generation for Mineral Exploration within the Limpopo Mobile Belt 155
5.5 Discussion 162

CHAPTER 6: PETROGRAPHIC INVESTIGATION 165

6.1 Fundamentals and Importance of Petrology 165
6.2 Methods used for Petrological Analysis 166
6.3 Petrographic Study of the Messina Copper Deposits 168
6.3.1 Specific Objectives 168
6.3.2 Rocks of the Messina deposits 168
6.3.3 Sample Selection and Preparation 169
6.3.4 Petrographic Study 171
6.3.5. Whole Rock Geochemistry Analysis 182
6.3.5.1 Sample Preparation and Analysis 182
6.3.5.2 Results and Interpretation 184
6.3.6 Garnet Classification 188
6.3.6.1 Physical Characterization of Garnet 188
6.3.6.2 Sample Preparation and Analysis 189
6.3.6.3: Results and Interpretation 190
6.3.7 Mineral Alteration 193
6.4 Discussion 195

CHAPTER 7: ORE MINERALOGY AND ORE MICROSCOPY 198

7.1 Fundamentals of Ore Mineralogy and Ore-microscopy 198
7.1.1 Importance and Application 198
7.1.2 Properties of Ore Minerals 200
7.2 Methods for Ore Mineralogical Analysis 200
7.3 Ore Petrology and Ore-microscopy 201

© University of Venda

7.3.1 Specific Objectives 201
7.3.2 Ore Sample Preparation 201
7.3.3 Mineralogical Investigation 203
7.3.3.1 Mode of Occurrence 203
7.3.3.2 Industrial and Ore Minerals 210
7.4 Scanning Electron Microscopy 227
7.4.1 Sample Preparation and Analysis 228
7.4.2 Results and Interpretation 229
7.5 X-ray Diffractometry 232
7.5.1 Sample Preparation and Analysis 232
7.5.2 Results and Interpretation 233
7.6 X-ray Fluorescence Spectrometry 236
7.6.1 Sample Preparation and Analysis 236
7.6.2 Results and Interpretation 237
7.7 Monomineralic Analysis of Pyrite and Chalcopyrite 241
7.7.1 Sample Analysis 241
7.7.2 Results and Interpretation 241
7.8 Mineral Paragenesis 246
7.9 Discussion 251
7.9.1 Ore Types and Mode of Occurrence 252
7.9.2 Mineralisation 253
7.9.3 Mineral Assemblages and Paragenesis 256

CHAPTER 8: CATHODOLUMINESCENCE INVESTIGATION 259

8.1 Principles of Cathodoluminescence 259
8.2 Cathodoluminescence Instrumentation 263
8.3 Application of Cathodoluminescence 266
8.4 Cathodoluminescence Investigation of the Messina Copper Deposits 268
8.4.1 Objectives 268
8.4.2 Sample Selection 268
8.4.3 Sample Preparation 268

© University of Venda

University of Venda
Creating Future Leaders

8.4.4 Sample Analysis 270
8.4.5 Results and Interpretation 274
8.4.5.1 Quartz 274
8.4.5.2 Apatite 280
8.4.5.3 Prehnite 281
8.4.5.4 Calcite 282
8.5 Discussion 284

CHAPTER 9: FLUID INCLUSION INVESTIGATION 287

9.1 Types and Classification of Fluid Inclusions 287
9.2 Fundamentals of Fluid Inclusions 291
9.2.1 Assumptions of Fluid Inclusion Studies 291
9.2.2 Measurements in Fluid Inclusion Studies 292
9.2.3 Principles of Fluid Inclusion Analysis 292
9.3 Importance and Application of Fluid Inclusions 293
9.4 Methods for Fluid Inclusion Analysis 295
9.5 Fluid Inclusion Investigation of the Messina Copper Deposits 298
9.5.1 Fluid Inclusion Petrography 298
9.5.1.1 Sample Selection 298
9.5.1.2 Sample Preparation 298
9.5.1.3 Fluid Inclusion Analysis 300
9.5.1.4 Results and Interpretation 301
9.5.2 Microthermometry 308
9.5.2.1 Sample Selection 309
9.5.2.2 Sample Preparation and Analysis 309
9.5.2.3 Results and Interpretation 311
9.5.3 Raman Spectroscopy 323
9.5.3.1 Sample Selection and Analysis 323
6.5.3.2 Results and Interpretation 323
9.6 Discussion 326
9.6.1Occurrence and Types of Fluid Inclusion 327

© University of Venda

University of Venda
Creating Future Leaders

9.6.2 Microthermometry Analysis 328
9.6.3 Possible Sources and Evolution of Ore Forming Fluids 329

CHAPTER 10: SULPHUR ISOTOPE GEOCHEMISTRY 330

10.1 Fundamentals of Isotope Geochemistry 330
10.1.1 Types and Classification of Isotopes 330
10.1.2 Stable Isotope Fractionation 331
10.1.3 Reference Standards of Stable Isotopes 337
10.1.4 Methods of Stable Isotope Analysis and Instrumentation 338
10.2 Importance and Application of Stable Isotopes 341
10.3 Sulphur Isotopes Geochemistry 342
10.3.1 Fundamental Aspects of Suphur Isotopes 342
10.3.2 Standards and Analytical Methods 343
10.3.3 Sulphur Isotope Geo-thermometry 343
10.3.4 Processes that Result in the Fractionation of Sulphur Isotopes 345
10.3.5 Sulphur Isotopes in Various Geological Environments 345
10.4 Sulphur Isotopes Geochemistry Investigation of the Musina Copper Deposits 345
10.4.1 Objectives 345
10.4.2 Sample Selection 346
10.4.3 Sample Preparation 346
10.4.4 Sample Analysis 350
10.4.5 Results and interpretation 352
10.4.5.1 Campbell Copper Deposit δ^{34}S Values 352
10.4.5.2 Artonvilla Copper Deposit δ^{34}S Values 353
10.4.5.3 Comparison of δ^{34}S Values with other Previous Studies 354
10.4.5.4 Comparison of δ^{34}S Values within Artonvilla Sulphide Ore and country Rock Samples 356
10.4 5.5 Comparison of the Campbell and Artonvilla with the Mantle δ^{34}S Values 356
10.4.5.6 Sulphur Isotope Geo-thermometry of Musina Deposits 357
10.5 Discussion 360

© University of Venda

University of Venda
Creating Future Leaders

10.5.1 Possible Sources of Sulphur in Sulphide Ore Formation 360
10.5.2 Sources of Metals in Rocks and Ore Deposits 361
10.5.3 Geochemical Conditions and Mechanisms of Ore Formation 362
10.5.4 Sulphur Isotope Geothermometry of the Messina Copper Deposits 362

CHAPTER 11: GENESIS OF MESSINA COPPER-SULPHIDE DEPOSITS 365

11.1 Review of Previous Studies on Ore Genesis 365
11.2 Findings of the Current Study 367
11.3 Genetic Model of Messina Copper-Sulphide Deposits 372

CHAPTER 12: CONCLUSIONS AND FUTURE RESEARCH DIRECTIONS 378

12.1 Conclusions 378
12.2 Future Research Directions 381

REFERENCES 382

APPENDICES

© University of Venda

University of Venda
Creating Future Leaders

LIST OF FIGURES

Figure 1.1:	Geographical, topographical and geological location of the study area within the African continent	4
Figure 1.2:	A photographs showing topography of the study area	5
Figure 1.3:	Photographs showing most abundant soil and vegetation types within the study area	6
Figure 1.4:	Copper price since 1989 [USD/lb]	9
Figure 1.5:	Schematic representation of the thesis structure	13
Figure 2.1:	Figure 2.1: Arrangement of orebodies in copper – nickel sulphide deposits: (1) underlying rocks; (2) overlying rocks; (3) enclosing rocks; (a) hanging phenocrysts; (b) bottom ores; (c) brecciated ores; and (d) veins	16
Figure 2.2:	Formation of porphyry copper from magmatic source: A) Low grade Copper mineralisation; and B) Metal concentration and formation of secondary Chalcocite	18
Figure 2.3:	Geological map of Palabora alkaline carbonatite complex	22
Figure 2.4:	Mine levels of Macalder deposit with ore bodies localised along the troughs and anticlines of the folds and along the fault planes	25
Figure 2.5:	Distribution of mineralisation at Chingola B (based on copper grade boundaries) plotted onto the section geology: Mineralization is strongly related to the fault propagation folds and controlling thrusts, as well as basal detachments	28
Figure 2.6:	Simplified geological map showing the main crustal provinces in Southern Africa, including the main cratons and mobile belts	30
Figure 2.7:	The Limpopo Mobile Belt and its three distinct zones	31
Figure 2.8:	General geology in the vicinity of the Messina copper deposits	38
Figure 2.9:	Geological cross-section through the Frost and Grenfell shafts at Artonvilla mines	39
Figure 3.1:	Flow chart depicting the sequence of work undertaken during the study	43
Figure 3.2:	Photograph showing soil sampling procedure within the study area	45
Figure 3.3:	Rock and ore sampling within Artonvilla rock waste dump	46
Figure 4.1:	Simple illustration of basic principles and components of atomic absorption spectrometry equipment	57
Figure 4.2:	Flow chart indicating decision tree for kriging requirements)	63
Figure 4.3:	Ordinary Kriging with constant mean	64

© University of Venda

Figure 4.4:	Universal Kriging with the mean being a deterministic function	65
Figure 4.5:	Soil sampling points within the study area	69
Figure 4.6:	Preparation of soil samples. (a) Bench Vacutec Laboratory oven used for drying samples; (b) Retsch model RS 200 milling machine used for milling the samples; (c) Redwag model AS 220/*C/2* analytical weighing balance and (d) digestion of samples	71
Figure 4.7:	Calibration curves for Pb, Zn, Cu, As, Ni, Mo, Co, Cd, Mn and Cr.	73
Figure 4.8:	Photograph of a Perkin Elmer model AAnalyst 400 Atomic Absorption Spectrometer: (a) Burner compartment for protecting the flame; (b) Detector compartment; (c) Hallow cathode lamp compartment; (d) Blower and ventilation system; (e) sample holder; (f) Sample older compartment; (g) Output:Computer. (f) Output --- computer used to display the results	74
Figure 4.9:	Frequency diagrams of Cu for soil collected from (a) western (Campbell area) and (b) eastern (Artonvilla area) side of the study area	76
Figure 4.10:	The histograms of the original (always on the left) and the logtransformed values (on the right) of the soils from both Artonvilla and Campbell area	78
Figure 4.11	Semivariograms and covariance cloud of data sets showing clear trend (a) Trend for Campbell area soil data (b) Trend for Artonvilla area soil data	78
Figure 4.12:	Semivariograms of the datasets: (a) Semivariogram of Campbell soil; and (b)Artonvilla soil	79
Figure 4.13:	Scatter plots of datasets projecting similar parabolas.	81
Figure 4.14:	Lead prediction map showing distribution pattern and anomalous areas	84
Figure 4.15:	Zinc prediction map showing distribution pattern and anomalous areas	85
Figure 4.16:	Copper prediction map showing distribution pattern and anomalous areas	87
Figure 4.17:	Arsenic prediction map showing distribution pattern and anomalous areas	88
Figure 4.18:	Nickel prediction map showing distribution pattern and anomalous areas	89
Figure 4.19:	Lead prediction map showing distribution pattern and anomalies in the eastern part of the study area.	91
Figure 4.20:	Zn prediction map showing distribution pattern and anomalous areas in the eastern part of the study area	92
Figure 4.21:	Copper prediction map showing distribution pattern and anomalous areas In the eastern part of the study area	94

© University of Venda

Figure 4.22: Arsenic prediction map showing distribution pattern and anomalous areas in the eastern part of the study area. 85
Figure 4.23: Ni prediction map showing distribution pattern and anomalous areas in the eastern part of the study area 96
Figure 4.24: Identified target areas (TA) for future exploration in the study area 98

Figure 5.1: Overview on Fundamentals Basics and procedures of Remote Sensing 101
Figure 5.2: Spectral signature (response pattern) for vegetation, water, bare soil and altered rocks characteristics of a mineralised zone 103
Figure 5.3: Remote sensing processes (A) Energy source which is needed to illuminate or provide electromagnetic energy to the target of interest; (B) Atmospheric effects; (C) Interaction of energy with the target; (D) Satellite sensor where energy is recorded and measured; (E) Processing station where data is processed into an image form; (F) Interpretation and analysis of processed image; (G) Application of the information 105
Figure 5.4: Resampling and Interpolation of the image to obtain a new image in which all pixels are correctly positioned with (a) indicating an original map, (b) transformed image in map coordinated system, (c)grid overlaid image and (d) geocoded image after resampled and interpolated 114
Figure 5.5: Commonly used resampling methods used on (a) source image resampled using (b) nearest neighbour resampling, (c) cubic resampling, and (d) Bilinear interpolation methods 114
Figure 5.6: Layer staking of individual bands in the ENVI 5.1 software programme 125
Figure 5.7: Creation of epidote alteration band ratio image using Band Math Tool 127
Figure 5.8: Resulting band ratio image of epidote alteration: Epidote alteration is represented by light tone or white area 127
Figure 5.9: Creation of false colour composite image to enhance structural features using data manager window from ENVI 5.1 software programme 128
Figure 5.10: False colour composite image depicting enhanced structural features 129
Figure 5.11: Classification of false colour composite image using the K-Means algorithm 130
Figure 5.12: Classified epidote alteration band ratio image 131
Figure 5.13: A figure showing (a) Conversion of classified image from raster to vector (.evf file format), (b) conversion of .evf file format to shape files 133
Figure 5.14: Loading of data into ArchMap 133

© University of Venda

Figure 5.15: Isolated epidote and chlorite alteration 134
Figure 5.16: Data loading into the target detection wizard 135
Figure 5.17: Selection of target of interest 136
Figure 5.18: Spectral matching of epidote alteration 136
Figure 5.19: Selection of the preferred target detection method 137
Figure 5.20: Previewing of rule image 138
Figure 5.21: Validation using intercepted areas of digital and visual epidote alteration with visual epidote alteration 139
Figure 5.22: Association of epidote alteration from visual analysis and with known copper deposits using ground truthing method 140
Figure 5.23: Epidote alteration map within the Limpopo Mobile Belt 142
Figure 5.24: Close-up map of the epidote alteration within the vicinity of the Messina copper deposits 144
Figure 5.25: Generalized schematic representation of the concentric zonation of epidote alteration within the Messina copper deposits 145
Figure 5.26: Analysed enhanced image depicting structural features within the Limpopo Mobile Belt 147
Figure 5.27: Geological structural map showing folds and faults within the Limpopo Mobile Belt 148
Figure 5.28: Schematic illustration of the types of folding identified within the Limpopo Mobile Belt 149
Figure 5.29: Close up of the displacement at area D 151
Figure 5.30: Close up of the displacement at area E 152
Figure 5.31: Association map of epidote alteration and geological structures 154
Figure 5.32: Conceptual model (3D) showing Regions of interest (ROI) 157
Figure 5.33: Conceptual model for region of interest part 1 showing region of interest 1, 3, and 3 158
Figure 5.34: Conceptual model, region of interest part 2 showing region of interest 4, 5 and 6 159
Figure 5.35: Topographical map showing regions of interest for further mineral exploration within the Limpopo Mobile Belt 160
Figure 5.36: Exploration target areas of copper-sulphide mineralisation for further exploration within and around Musina area 161

Figure 6.1: Equipment used for thin sections preparations 170
Figure 6.2: Microscope used for petrographic study: (a) Olympus BX51 petrographic microscope attached to (b) Zeiss AxioCam ICc camera, at University of Venda. 171
Figure 6.3 Photomicrograph of grey gneiss displaying irregular stretched shaped quartz 172

© University of Venda

University of Venda
Creating Future Leaders

Figure 6.4: Photomicrograph of biotite-garnet-quartz granulite displaying occurrence of altered orthoclase with garnet grains 173
Figure 6.5: Photomicrograph of amphibolite displaying abundancy of hornblende grains altered by hydrothermal solutions 174
Figure 6.6: Photomicrograph of amphibolite with the presence of hornblende and plagioclase with few grains of pyroxene and epidote 174
Figure 6.7: Photomicrograph of quartzite with grains of magnetite within cryptocrystalline quartz 175
Figure 6.8: Photomicrograph of hornblende schist consisting of hornblende and plagioclase with few grains of pyroxene and epidote 176
Figure 6.9: Photomicrograph biotite schists with large grains of biotite, muscovite, quartz and amphibole 176
Figure 6.10: Photomicrograph of hornblende gneiss with grains of biotite interlocked in between hornblende and pyroxene grains 177
Figure 6.11: Photomicrograph of quartzo-feldspathic gneiss with plagioclase, quartz and minor content of biotite 178
Figure 6.12: Photomicrograph of k-feldspathic gneiss with abundant orthoclase and quartz and minor content of orthoclase and biotite 179
Figure 6.13: Photomicrograph of garnet–quartzo feldspathic gneiss displaying large grains of garnet 180
Figure 6.14: Photomicrograph of biotite-garnet gneiss displaying large grains of garnet and large occurrence of biotite 181
Figure 6.15: Photomicrograph of Cal-silicate genesis displaying cleavage of wollastonite , diopside (90 ^{o}C) amphibole 160 -120^{o}C 181
Figure 6.16: Equipment used for pellets preparation for XRF analysis 183
Figure 6.17: Photograph of S2 ranger XRF spectrometer used for major oxides and trace analysis. Touch control screen (b) sample chamber, (c) and (d) computer connected to a monitor 184
Figure 6.18: ACF classification of rocks 186
Figure 6.19: ACF ternary plot showing compositional variations of different rock types within the study area 187
Figure 6.20: Cameca SX-100 Electron microbe analyser connected to computer and monitors used for garnet analysis 190
Figure 6.21: Backscattered-electron image of garnet crystal from biotite-garnet gneiss rock showing selected points analysed 190
Figure 6.22: Photomicrographs of samples from both Campbell and Artonvilla copper deposit with plane polarized on the left and crossed polarized on the right side. (a) and (b) Quartz (Qtz) and Plagioclase (Pl) being replaced to albite; Plagioclase (Pl) and Quartz altered to sericite and cordierite altered to chlorites; (b) and (c) plagioclase (Pl) altered to

© University of Venda

University of Venda
Creating Future Leaders

zoisite(Zo) and epidote (Ep); and (d) and (e) alteration of biotite to chlorites 193

Figure 6.23: Photomicrographs of samples from both Campbell and Artonvilla copper deposit with plane polarized on the left and crossed polarized on the right side. (a) and (b) Chloritization of cordierite, biotite and perthite; and (d) and (e) revealing chloritization of garnet into anomalous blue chlorites 195

Figure: 7.1: Equipment for microscopic study: a) an Olympus BX51 petrographic microscope connected to (b) Olympus SC50 camera, (c) to the CPU and (d) monitor 203

Figure 7.2: Microphotographs of double polished thin sections (A and B) from Campbell copper deposit and polished surfaces C and D from Artonvilla and Campbell copper deposits respectively. (A) Chalcopyrite (Ccp) within micro-fractures forming extensional vein-type viewed under transmitted plane polarized light; and (B) under reflected crossed polarized light; (C) Stock-work vein-type of pyrite (Py) and (D) Euhedral, subhedral and anhedral pyrite (Py) and anhedral chalcopyrite (Ccp) within a quartz vein 205

Figure 7.3: Microphotographs of fine-grained disseminated sulphides within amphibolite (A); and disseminated pyrite (Py), chalcopyrite (Ccp) and bornite (Bn) within quartz vein with some calcite (B) from sample Atcal01and CPqtz03 from Artonvilla and Campbell copper deposits respectively 207

Figure 7.4: Microphotograph of minerals: pyrite (py) around the angular quartz (Qtz) and amphibolite breccias with alteration of amphibolite and deposition of chlorite 209

Figure 7.5: Photomicrographs of garnet (A) in plane polarized light; and (B) in crossed polarized light with potassium feldspar (Kfs) and chlorite (Chl); (C) highly fractured garnet (Grt) grains with micro-fractures filled with quartz; (D) quartz and pyrite (Py) deposited around and within microstructures in garnet (Grt) grains in reflected light 211

Figure 7.6: Microphotographs of Atcal01 (A, B. C, and D) in plane polarised reflected light and Cpqv01 (E and F) in plane and crossed polars of transmitted light from Artonvilla and Campbell copper deposits respectively. Flakes of graphite in association with sulphides such as pyrite (Py), sphalerite (Sp) and galena (Gn) and Chlorite (Chl), quartz, (Qtz) and amphibole (Amp) 214

Figure 7.7: Photomicrographs of Atcal01, Atavr12 and Cp01 ore samples showing: (A) plated light grey crystals of hematite (Hem) in places,

© University of Venda

University of Venda
Creating Future Leaders

replacing euhedral magnetite crystals (Mt); (B) tiny blades of hematite (Hem), replacing euhedral crystals of garnet (Grt); (C and D) allotriomophic pyrite (Py) being replaced by hematite (Hem), along the grain boundary and microfractures, whereas hematite is replaced by goethite; (E) pyrite crystals (Py) cut across grains of magnetite (Mt) 217

Figure. 7.8: Microphotograph illustrating: (A) sulphide mineralisation (pyrite (Py), sphalerite (Sp) and chalcopyrite (Ccp) within later formed quartz, in places, occurring between garnet grains (Grt); (B) later formed euhedral pyrite (Py) replaced by calcite 219

Figure 7.9: Microphotographs of ore samples from Artonvilla showing: (A) enclosed pyrite (Py) by chalcopyrite; (B) pyrite (Py) associated with chalcopyrite (Ccp) and hematite (Hem) where chalcopyrite (Ccp) is replacing pyrite (Py); (C) chalcopyrite (Ccp) replacing pyrite (Py); (D) chalcopyrite (Ccp) occurring as exsolution within sphalerite (Sp); (E) Early formed pyrite (Py) replaced by sphalerite (Sp); (F) Sphalerite (Sp) replacing chalcopyrite (Ccp); and (G) Later formed pyrite (Py) being replaced by sphalerite (Sp) and chalcopyrite (Ccp) 221

Figure 7.10: Photomicrograph of ore samples from Artonvilla copper deposit showing: (A) galena (Gn) with triangular pits, associated with anhedral pyrite (Py) and sphalerite (Sp) replacing pyrite (Py); (B) Galena (Gn) with graphite (Gr), tiny grains of pyrrhotite (Po), pyrite (Py) and chlorite 222

Figure 7.11: Photomicrographs showing: (A) internal reflection of malachite (Mal) and azurite (Az) occurring together with cuprite (Cup); (B) Replacement of euhedral pyrite (Py) by chalcopyrite (Ccp), malachite (Mal) and bornite (Bn) and chalcocite (Cc) along the margins of pyrite (Py); (C) Pyrite (Py) and chalcopyrite (Ccp) twinning with purplish-blue covellite (Cv) along the grain boundary; (D) Euhedral crystals of pyrite (Py) replaced by chalcopyrite (Ccp), covellite (Cv), bornite (Bn) and chalcocite (Cc); and (E) Total replacement of chalcopyrite (Ccp) by bornite (Bn) and pale blue chalcocite (Cc), replacement starting along the grain boundary 225

Figure 7.12: A photograph of Scanning electron microscope used for mineralogical analysis with (a) Electron column, (b) Sample chamber containing sample stage and back-scattered electron detector, (c) Electronics, (D) Energy dispersive spectrometer, and (e) Computer display with (f) joy stick 228

Figure 7.13 : Scanning Electron backscattered images of veined ore (A, B, C and D) and brecciated ore (E and F) samples showing (A) pyrite (Py) with inclusions of chalcopyrite (Ccp); (B) Infilling of sulphide mineralised

© University of Venda

University of Venda
Creating Future Leaders

solution within later formed quartz (Qtz) in-between garnets crystals; (C) high magnification of B with pyrite (Py) and chalcopyrite (Ccp) within Quartz (Qtz) 1 and 2; (D) chalcopyrite (Ccp), pyrite (Py), sphalerite (Sp) within later quartz (Qtz 3) occurring between (Grt) and quartz (Qtz 2) boundaries; (E) Chalcopyrite (Ccp) within chlorite (Chl) and quartz (Qtz) surrounding the brecciated epidote (Ep); and (F) Quartz with bornite (Bn) showing lighter colour than chalcopyrite (Ccp) within altered amphibole 231

Figure 7.14: SEM backscattered electron image of disseminated ore sample showing fine- grained of pentlandite with intergrowth of anhedral pyrite occurring as inclusion within the subhedral Ni-bearing pyrite forming around the quartz grain (Qtz 2) and at the boundary of the early formed quartz (Qtz 1) 232

Figure 7.15: A photograph of X-ray powdered diffraction spectrometer used for mineralogical analysis with (a) XRD goniometer that enhouse the sample, optics and detector; (b) XRD sample magazines with sample holder; and (c) Computer monitors for displaying the results 233

Figure 7.16: Distribution of elements within disseminated, veined and brecciated ores from Campbell and Artonvilla copper deposits (Note: Bar chart for Zn and Cu were plotted separately due to the high concentration) 240

Figure 7.17: Scatter plots for pyrite and chalcopyrite composition form Artonvilla and Campbell copper deposits compared to sulphide compositions from previously studied deposits: (A) wt% Ni and wt% Fe scatter plot of pyrite; (B) wt% Co and wt% Fe scatter plot of pyrite; (C) wt% Fe and wt% Cu scatter plot of chalcopyrite; and (D) wt% Cu and wt% Pb scatter plot of chalcopyrite 243

Figure:7.18: A) Fe- Ni-S ternary diagram showing pyrite (Py) elemental composition (wt%) from Artonvilla mine and high temperature mono-sulphide solid solution (mss) fields of Kullerud *et al.* (1969); (B) Fe-Cu-S ternary diagram at 300°C Fe-Cu-S system (Borton and Skinner, 1979) showing chalcopyrite (Ccp) elemental composition (wt%) from Campbell copper deposit. Different phases such as bornite (Bn), pyrite (py), pyrrhotite (Po), chalcocite (Cc), Chalcopyrite (Ccp), covellite (Cv) and intermediate solid solution (iss) are also indicated 245

Figure 7.19: Photomicrograph of sample CPQtz03 from Campbell copper deposit showing: (A) early formed quartz (Qtz 1) grains in crossed polars; and (B) crossed polars of the refracted light of later formed quartz (Qtz 2) grains with chalcopyrite (Ccp) within quartz 2 249

© University of Venda

Figure 8.1: Schematic illustration of interactions of an electron beam with a solid surface 260
Figure 8.2: Schematic illustration of energy levels in a band scheme for different crystal types: conductor with overlapping valence and conduction band, semiconductor with small inter-band and insulator with large band gap 261
Figure 8.3: Schematic representation of the processes that cause CL generation in minerals: (a) Defects within the band gap with electron traps; (b) De-localized electrons from valence band move to conduction band leaving holes in valence band; and (c) Trapped de-excited electrons emit this photons (CL) in the visible light range 262
Figure 8.4: Schematic cross-sectional view of (a) cathodoluminescence stages and (b) Cl microscope - HC5-LM 265
Figure 8.5: Nikon Super Coolscan 5000 ED 1.03 scanner used for scanning the thin-sections: (a) thin-section holder; (b) Scanner; (c) computer and monitor connected to the scanner 269
Figure 8.6: (a) *208*C High vacuum turbo carbon coater with; (b) Thickness monitor MTM-10; (c) Rotary-planetary-tilting stage with Metal evaporation accessory; and (d) Auxiliary power supply used for coating the thin-sections 270
Figure 8.7: Hot cathodoluminescence microscope HC3-LM stage used for the CL investigation: (a) Rotatory pump; (b) Diffusion pump; (c) Microscope; (d) Hot cathode; and (e) Computer and monitor 271
Figure 8.8: Early formed quartz (Qtz 1) in dark blue to violet CL being replaced by late formed quartz (Qtz 2) in dark red CL in sample CPdis01 from Campbell deposit 275
Figure 8.9: Early formed quartz in (a) bright blue CL replaced by late formed quartz in dark red CL and quartz showing no distinction between the two quartz types in (b) PL, (c) TL in sample ATavr12 from Artonvilla deposit 275
Figure 8.10: (a) Dark red-brown luminescence indicating late formed quartz replacing early formed quartz appeared black with apatite phenocryst that displayed blue luminescence (CL) and (b) in dark colour (PL). It is embedded within the altered rock materials and with quartz grains within and around the altered amphibole 276
Figure 8.11: (a) Early formed qtz (Qtz 1) replaced by late formed Qtz 2 with graphic intergrowth (Grpt) in Qtz 2 of sample CP01, and also viewed in (b) polarized light (PL); (C) transmitted light (TL) and (d) enlarged part of (a) from Campbell copper deposit 277

© University of Venda

Figure 8.12: Internal structure of highly fractured quartz (CL) showing infilling of micro-fractures by late formed quartz with large secondary fluid inclusions in sample AT02 from Artonvilla copper deposit 278
Figure 8.13: Zoned quartz indicating oscillatory zoning (Osz) in late formed sub-idiomorphic quartz crystals with early formed xenomorphic quartz crystals (Xnq) at the topwhich is displayed in CL, PL and TL in sample CP02 from Campbell 279
Figure 8.14: Zoned quartz displaying concentric zoning (Conz) indicated by stepped sub-idiomorphic crystals growth revealing different stages of crystal formation where the top most crystal is the older (early formed) and the bottom most crystal is the younger (late formed) crystals 279
Figure 8.15: Primary apatite (P-Apt) displayed by deep blue CL, with bright green rim indicating replacement in sample ATcal01 from Artonvilla copper deposit 280
Figure 8.16: Sample AT02 from Artonvilla: Strongly altered secondary apatite (S-Apt) displayed by yellowish to light greenish-pinkish CL with open fracture filled by chlorite 281
Figure 8.17 Prehnite crystals from sample CPqtz03 from Campbell copper deposit, displayed by bright green to yellowish green CL around and overgrowing on top of the idiomorphic black crystal of the host rock. Prehnite showed bright orange to yellow colours in plane polarized light surrounding white grey quartz. Prehnite in transmitted light showed brown to grey colour surrounding the light grey quartz 281
Figure 8.18: Late carbonate vein (calcite) in (a) bright red to orange CL cutting through earlier formed quartz and also cutting through (b and c) other earlier formed minerals such as altered amphiboles with quartz 2 in sample CPdis01 from Campbell copper deposit 282
Figure 8.19: Sub-hedral calcite (Sub-id) in bright red CL displaying sub-idiomorphic crystal shape with a distinct crystal boundary and xenomorphic calcite (Xnca) cutting the earlier formed minerals from AT01 of Artonvilla copper deposit 283
Figure 8.20: Influx of calcite displayed in bright red to orange CL cutting across altered rock materials and cutting through apatite in deep blue CL in sample ATcal01 from Artonvilla copper deposit 284

Figure 9.1: Sketches illustrating the common types of fluid inclusions at room temperature, classified based on the presence of phases within the fluid inclusion: L= aqueous fluid, V= vapour, LCO_2 = liquid CO_2 289
Figure 9.2: Sketch illustrating distinction among primary (p); pseudo-secondary (ps); secondary (s); and indeterminable (i) fluid inclusions 290

© University of Venda

University of Venda
Creating Future Leaders

Figure 9.3: P-T diagram showing changes occurring in a fluid inclusion as the rock is cooled and decompressed along an isochore and a phase boundary. Pt: entrapment pressure; T_t: entrapment temperature; T_h: homogenization temperature 291
Figure 9.4: Historical overview of the study of fluid inclusions 294
Figure 9.5: Photomicrograph of crisscrossing planes of fluid inclusions along microfractures of quartz vein in sample CPqtz03 from Campbell copper deposit. Trails of fluid inclusions indicating (a) transgranular, (b) intergranular and (c) intragranular textures 302
Figure 9.6: Photomicrographs of representative types of fluid inclusions in quartz crystals from disseminated, veined and brecciated ores from Campbell and Artonvilla copper deposits indicating different types of textures and relative age: (A) clustered and primary, (B) scattered and primary, (C) isolated and primary, (D) trails of fluid inclusions along fractures and secondary (E) along crystal growth zones and are primary inclusions 305
Figure 9.7: Fluid inclusions indicating different types of morphology: (A) Spherical; (B) irregular;(C) rectangular; and (D) necking-down of fluid inclusion only from Campbell deposit 306
Figure 9.8: Type II vapour-rich (V + L) fluid inclusion with large vapour phase with volume ≥ 60% exhibiting isolated texture and spherical shape. 306
Figure 9.9: Type III – High salinity + daughter minerals (L + V + D_{1+2}) fluid inclusions with (A) and (B) showing cubic daughter mineral (D_1); while (B) having a second daughter mineral (D_2) 307
Figure 9.10: Type IV – Gas-rich fluid inclusions from sample CPdis02 (A) along the crystal growth zones and AT02 (B) scattered and clustered within the crystal, with less liquid and vapour, while some had no visible bubbles 308
Figure 9.11: (a) Linkam THMS 600 heating-freezing microscope stage connected to (b) BH-2 standard petrographic microscope (c) TMS94 and LNP System Controllers (d) Nitrogen gas pump (e) CPU and (f) Monitor used for fluid inclusion study 311
Figure 9.12: Phase diagram for the Binary water-salt system (H2O-NaCL) indicating phase transition of fluid inclusion with -10 wt% salinity 312
Figure 9.13: Pie chart illustrating abundance of different types of fluid inclusions in terms of phase composition for Campbell copper deposit 313
Figure 9.14: Pie chart illustrating abundance of different types of fluid inclusions in terms of phase composition for Artonvilla copper deposit 313
Figure 9.15: Frequency histogram of the homogenization temperatures of samples from Campbell copper deposits 314

© University of Venda

University of Venda
Creating Future Leaders

Figure 9.16: Frequency histogram of the homogenization temperatures of samples from Artonvilla copper deposits 315
Figure 9.17: Bivariate plot illustrating $T_h/T_{m(ice)}$ graph for H_2O-NaCl and aqueous H_2O-NaCl + HL/CC fluid inclusion types for Campbell copper deposit 316
Figure 9.18: Bivariate plots illustrating $T_h/T_{m(ice)}$ graphs for H_2O-NaCl and aqueous H_2O-NaCl + HL/CC fluid inclusion types for Campbell and Artonvilla copper deposits 316
Figure 9.19: Bivariate plot illustrating salinity range of aqueous fluid inclusions, Type I – liquid-rich H_2O-NaCl, Type II - vapour-rich H_2O-NaCl and Type III- H_2O-NaCl-HL/CC from Campbell copper deposits 318
Figure 9.20: Bivariate plot illustrating salinity range of aqueous fluid inclusions, Type I – liquid-rich H2O-NaCl, Type II - vapour-rich H2O-NaCl and Type III- H2O-NaCl-HL/CC from Artonvilla copper deposits 318
Figure 9.21: Temperature-pressure graph showing representative isochores of aqueous inclusions from idiomorphic zoned quartz (brecciated ore) from Campbell copper deposit 321
Figure 9.22: Temperature-pressure graph showing representative isochores of aqueous inclusions from quartz with prehnite (veined ore) and isochores of quartz with aqueous carbonic fluid inclusions (disseminated ore) from Artonvilla copper deposit 321
Figure 9.23: Horiba Jobin Yvon LabRam HR800-UV Raman spectrometer, (a) Spectrometer running underneath top optic; (b) lasers behind main unit with citation laser of 488 nm used for determination of gas fluid composition; (c) Optic box with Olympus UC30 camera connected to a microscope (d) In-Gas detector and (e) silver control box 324
Figure 9.24: Raman spectra indicating relative wave numbers of gas fluid inclusions from three fluid inclusions of samples AT01 and AT02 325

Figure 10.1: Typical ranges of stable isotope ratios in geologic systems: (a) Sulphur; (b) oxygen 336
Figure 10.2: Schematic representation of a gas-source spectrometer used for stable isotope analysis. P denotes pumping system and V denotes variable volume 340
Figure 10.3: Schematic representation of the procedure followed for the production of gaseous SO_2 using vanadium pentoxide (V_2O_5) as a solid oxygen donor 349
Figure 10.4: An offline V_2O_5 combustion line with variable cryogenic temperature trap used for the production of pure SO_2 from sulphide minerals: (a) Combustion furnace; (b) water trap; (c) variable temperature trap; (d) sample collection port; (e) sample cold-finger and manometer 349

© University of Venda

University of Venda
Creating Future Leaders

Figure 10.5: Finnigan MAT 252 dual inlet mass spectrometer used for sulphur isotope analysis: (a) Sample inlet pot; (b) reference inlet pot; (c) ion source; (d) ion source control; (e) electromagnet; (f) ion collectors; (g) vacuum gauge; and (h) flight tube 350

Figure 10.6: Frequency plot of $\delta^{34}S$ values of pyrite, chalcopyrite, bornite from Campbell copper deposit and $\delta^{34}S$ values of pyrite, chalcopyrite and country rock (whole rock) from Artonvilla copper deposit 353

Figure 10.7: Frequency diagram showing a comparison of sulphur isotope values for sulphide minerals from both Campbell and Artonvilla copper deposits with sulphur isotope data of Mantos Brancos breccia pipes, Northern Chile and Ilkwang breccia pipe, South Korea 355

Figure 10.8: Comparison of the Campbell and Artonvilla copper deposits $\delta^{34}S$ values and the Mantle $\delta^{34}S$ values 359

Figure 11.1: Distribution of sulphide mineralisation and hydrothermal alteration within the Messina copper sulphide deposits 367

Figure 11.2: Genetic model of copper-sulphide mineralisation in the Musina area. Mineral deposits occured either along the fault planes or at the interaction of faults or faults and dykes with rock alteration along the weak zones 377

© University of Venda

University of Venda
Creating Future Leaders

LIST OF PLATES

Plate 6.1:	Photograph of amphibole-quartz granulite displaying coarse-grained texture with visible grains od biotite and garnet	172
Plate 6.2:	Photograph of biotite-garnet-quartz granulite displaying coarse-grained texture with visible grains of biotite and garnets	173
Plate 6.3:	Photograph of amphibolite displaying coarse-grained texture with visible hornblende grains	174
Plate 6.4:	Photograph of amphibolite composed highly of mafic minerals and some feldspar displaying weakly schistocity structure	174
Plate 6.5:	Photograph of quartzite displaying chloritization and cryptocrystalline texture	175
Plate 6.6:	Photograph of hornblende schist displaying schistocity due to amphibole platy structure with granular garnet grains	176
Plate 6.7:	Photograph of biotite schist displaying platy structure of biotite and muscovite with quartz grains	176
Plate 6.8:	Photograph of hornblende gneiss displaying coarse-grained texture with pyroxene and biotite grains	177
Plate 6.9:	Photograph of quartzo-feldspathic gneiss displaying medium to coarse-grain texture and gneissic bands	178
Plate 6.10:	Photograph of k-feldspathic gneiss displaying medium to coarse-granted texture and foliation	179
Plate 6.11:	Photograph of garnet quarto feldspathic gneiss displaying medium to coarse-grained texture and gneissic bands	180
Plate 6.12:	Photograph of biotite-garnet gneiss displaying medium coarse-grained texture and gneiss bands	181
Plate 6.13:	Photograph of calc-silicate gneiss displaying coarse-grained texture and foliation	181
Plate 6.14:	Large grains of garnet within host rock of sulphide mineralisation	189
Plate 7.1:	Sample CPqv01 (A) mineralised quartz vein within amphibolite from Campbell deposit: pyrite (Py); chalcopyrite (Ccp); bornite (Bn); and chalcocite (Cc). Sample ATavr11 (B) from Artonvilla deposit showing non-mineralised thin quartz vein within amphibolite schist	204
Plate 7.2:	Hand specimen showing disseminated sulphide mineralisation from Artonvilla and Campbell copper deposits. (A) Fine-grained chalcopyrite disseminated within amphibolite; and (B) Fine to medium-grained pyrite (Py) and chalcopyrite (Ccp) with minor bornite (Bn) and some calcite disseminated within quartz vein	206

© University of Venda

University of Venda
Creating Future Leaders

Plate 7.3: Hand specimen of brecciated ore samples of CP03 (A), CP05 (B) and CP01 (C) from Campbell, and Atbr01 from Artonvilla copper deposits: (A) sulphide mineralisation deposited as matrix around the brecciated quartz (Br qtz) grains; (B) sulphide mineralisation surrounds both the brecciated quartz (Br qtz) and amphibolite (Amp) fragments; (C) and (D) numerous breccias of both quartz and amphibolite fragments with minor sulphide mineralisation around the brecciated fragments 208

Plate 7.4: Garnet (Grt) and magnetite (Mt) minerals in quartz vein-amphibolite host rock from the Artonvilla copper deposit (A, B and C) 211

Plate 7.5: Ore specimens (Atcal01 and Cp03) with flakes of graphite (Gr) within amphibolite rock with calcite (Cal) vein from Artonvilla copper deposit (A), and within brecciated ore from Campbell copper deposit (B) 213

Plate 7.6: Occurrence of (A) large subhedral magnetite crystals (Mt) and hematite (Hem) with brownish to red colour within the quartz veined ore from Artonvilla copper deposit; (B) disseminated tiny magnetite crystals (Mt) within the amphibolite host rock of Campbell copper deposit 216

Plate 7.7: Hand specimen of sulphide secondary minerals: (A) malachite (Mal) in bright green colour after oxidation of chalcopyrite (Ccp) associated with hematite (Hem), cuprite (Cup) and azurite (Az); (B) Malachite (Mal) stains on chalcocite (Cc) with granular grains of chalcopyrite; (C) A grain of native copper surrounded by hematite (Hem) with tiny grains of pyrite and chalcopyrite (Ccp); and (D) Bornite (Bn) in pinkish colour occurring together with pyrite (Py), chalcopyrite (Ccp) and hematite (Hem) 224

Plate 7.8: A photograph showing calcite (Cal) vein cutting across amphibolite with disseminated sulphide mineralisation from Artonvilla copper deposit (Sample Atcal01) 251

© University of Venda

University of Venda
Creating Future Leaders

LIST OF TABLES

Table 2.1:	Base metal deposits of Damara Belt	32
Table 2.2:	Lithochronological units of the Central Zone	36
Table 4.1:	Summary of statistical parameters of concentration levels of metals within soil samples	75
Table 4.2:	Trend elimination of (a) soils from Campbell and (b) Artonvilla area	81
Table 4.3:	Mean heavy metal content in the major rock types in mg/kg	83
Table 5.1:	Characteristics of Multispectral and Hyperspectral sensors	109
Table 5.2:	Milestone in the history of remote sensing	123
Table 5.3:	Summary of the findings on association among texture, degree of alteration and geological structures	153
Table 6.1:	Summary of the main techniques employed for mineralogical and geochemical analysis of rocks	167
Table 6.2:	XRF results of major oxides (wt%) for rock specimens from both Campbell and Artonvilla copper deposits	185
Table 6.3	Composition of garnets grains in Mol% of end-members	191
Table 7.1:	Minerals from different ore types detected using X-ray Diffractometry	235
Table 7.2:	Distribution of elements within different ore types at Campbell and Artonvilla copper deposits	239
Table 7.3:	Chemical composition of pyrite and chalcopyrite	242
Table 7.4:	Paragenesis of the Campbell and Artonvilla copper-sulphide minerals	248
Table 8.1:	Differences between Cold-cathode and Hot-cathode cathodoluminescence	264
Table 8.2:	Important analytical parameters of CL microscopy	266
Table 8.3:	Campbell deposit minerals and their characteristics identified under cathodoluminescence	272
Table 8.4:	Artonvilla deposit minerals and their characteristics identified under cathodoluminescence	273
Table 9.1:	Overview of methods for studying inclusions	297
Table 9.2:	Quartz-sulphide ore samples from Campbell and Artonvilla deposits used for fluid inclusion studies	299
Table 9.3:	Characteristics of fluid inclusions identified in quartz associated with sulphide mineralisation within Campbell and Artonvilla copper deposits using optical microscopy method	304
Table 9.4:	Summary of fluid inclusion petrography and microthermometry data for measured fluid inclusions in quartz from veined,	

© University of Venda

	disseminated and brecciated ores of the Campbell and Artonvilla copper deposits	319
Table 9.5:	Entrapment temperature-pressure conditions of fluid inclusions of Messina copper deposits	322
Table 10.1:	Abundance of selected stable isotopes and reference standards used for measurement of isotope ratio	338
Table 10.2:	Sulphur isotope geo-thermometers	344
Table 10.3:	Description of samples from Campbell and Artonvilla copper deposits used for sulphur isotope geochemistry	347
Table 10.4:	$\delta^{34}S_{(VCDT)}$ data for Campbell and Artonvilla copper deposit samples	351

© University of Venda

LIST OF ABBREVIATIONS AND ACRONYMS

AAS	Atomic Absorption Spectrometer
SEM	Scanning Electron Microscope
ACE	Adaptive Coherence Estimator
ARTV	Artonvilla
ASTER	Advanced Spaceborne Thermal Emission and Reflection Radiometer
ATCOR	Atmospheric and Topographic Correction
ATR	Artonvilla rock specimen
AVIRIS	Airborne Visible/Infrared Imaging Spectrometer
CAMP	Campbell
CDF	Cumulative distribution function
CDT	Canyon Diablo Troilite
CEM	Constrained Energy Minimization
CFB	Cape Fold Belt
CL	Cathodoluminescence
CMZ	Central marginal zone
CZ	Central zone
DEM	Digital Elevation Model
DN	Digital Number
DQA	Data Quality Assurance
EDS	Energy dispersive spectroscopy
EMPA	Electron microprobe analyzer
EPMA	Electron probe microanalyzer
EOS	Earth Observation System
ERDAS ER	Earth Resources Data Analysis System, Earth Resources
ERTS	Earth Resources Technology Satellite
ETM	Enhanced Thermatic Mapper
FT-IR	Fourier Transform Infrared
GC	Gas chromatography
GC MS	Gas chromatography spectroscopy
GGT	Granitic greenstone terrain
GIS	Geographic Information System
GPS	Geographical Position System
HRV	High Resolution Visible sensors
IAEA	International Atomic Energy Commission
IAGC	International Association of Geochemistry
IC	Ion exchange chromatography
ICP MS	Inductively coupled plasma mass spectroscopy
ICP OES	Inductively coupled plasma-optical emission spectroscopy
IGCP	International Geological Correlation Programme
ISODATA	Iterative Self Organizing Data Analysis Techniques
IR	Infrared

© University of Venda

IRMS	Isotope dilution mass spectroscopy
IUGS	International Union of Geological Sciences
LBV	Local background value
LMB	Limpopo Mobile Belt
LOI	Loss of Ignition
LWIR	Long infrared
Ma	Million years
MF	Matched Filtering
MINTEK	Council for Mineral Technology
MIR	Mid infrared
MNF	Minimum Noise Fraction
MODTRAN	Moderate Resolution Atmosphere Transmission
MS	Mass spectroscopy
MSS	Multispectral Scanner
MT	Magnetotelluric
MTEF	Medium -Term Expenditure Framework
Mt	Million tons
MTMF	Mixture tuned matched filtering
MVT	Mississippi Valley Type
NASA	National Aeronautics and Space Administration
NMZ	Northern marginal zone
OCM	Optical cathodoluminescence microscopy.
OSP	Orthogonal Subspace Projection
PDB	Pee Dee Belemnite
PGEs	Platinum group elements
PL	Polarized light
RBV	Return Beam Vidicon
ROI	Regions of Interest
SACS	South African Committee of Stratigraphy
SARM	South African Reference Materials
SEM	Scanning Electron Microscopy
SEM-CL	Scanning electron microscopy cathodoluminescence
SMAC	Simulation of satellite in the Solar Spectrum
SMC	Southern Mapping Company
SMOW	Standard Mean Ocean Water
SMZ	Southern marginal zones
SPOT	Satellite Pour I ‘Observation de la Terra
SPOT PAN	Satellite Pour I ‘Observation de la Terra Panchromatic
SPOT XS	Satellite Pour I ‘Observation de la Terra Multispectral Sensor
SWIR	Shortwave infrared
TCIMF	Target Constrained Interference Minimized Filter
TDW	Target detecting wizard
TL	Transmitted light

© University of Venda

TM	Thematic Mapper
TEM	Transmission Electron Microscopy
USA	United States of America
USD/t	United State dollar per ton
USGS	United State Geological Survey
UV	Ultraviolet
Vis-IR	Visible Infrared
VMS	Volcanogenic massive sulphide
VNIR	Visible near infrared
VPDB	Vienna Pee Dee Belemnite
VSMOW	Viena Standard Mean Ocean Water
WDS	Wavelength dispersive spectroscopy
XRD	X-ray powder diffraction
XRF	X-ray fluorescence
XRPD	X-ray powdered diffraction
ZA	Zone A
ZAF	Atomic number, Absorption and Fluorescence corrections
ZB	Zone B
ZC	Zone C
ZD	Zone D

© University of Venda

LIST OF UNITS AND SYMBOLS

C	Degrees Celsius
δ	Delta –stable isotope ratio
g/t	Grams per ton
$\delta^{33}S$	Isotopic composition of sulphur isotopes
mg/kg	milligrams per kilograms
Ma	Million years
ppm	Parts per million
‰	Per mil
σn	Standard deviation
wt%	Weight percentage
T_m	Melting temperature
T_{mf}	Freezing temperature
T_h	Homogenization temperature
Tt	Entrapment temperature
Pt	Entrapment pressure
T_d	Decrepitating temperature

© University of Venda

GLOSSARY OF TERMINOLOGIES

Amygdale: Cavity in a rock or mineral that has been filled with later formed minerals

Analyte: An element that its concentration levels is to be measured in rocks, soil, plants and water

Ahedral: Textural term describing habit of shape of a mineral grain and it does not show a well-developed crystal form.

Anomalous areas/Anomalies: Geochemical anomalies, which area areas with high concentration levels of metals above the background values

Cathodoluminescence: An emission of visible (and UV) luminescence by a substance that is bombarded by electrons, where the cathode is the source of the electrons

Crystal zonation: Compositional variation of a crystal

Daughter minerals: Solid substances (mineral) within the fluid inclusion that possess its physical, chemical and its specific internal structure

Entrapment temperature: Temperature at the time of trapping (formation) of a fluid inclusion

Euhedral: Textural term describing habit of shape of a mineral grain that shows well-developed crystal form

Exsolution: Un-mixing of two solid solution phases from a solid solution state
Fluid inclusion: Small volume of fluid, trapped and closed in a solid mineral

Genetic model: Systematically arranged information that described the essential attributes of class of mineral deposits and these attributes are interrelated through some fundamental concept

Geochemical background values: Geochemical/natural background values that are natural abundance of an element in an environment i.e. soil, sediments, water and rocks.

Geochemical baseline: Natural spatial variation in the geochemistry of the earth's surface materials such as soil and sediments

Geochemical signatures: Chemical constituent within geological environment, i.e. rocks, soil, sediments and water.

Homogenization temperature: Temperature at which a fluid inclusion transforms from a heterogeneous phase to a homogeneous state

Hypothermal deposits: Deposited from hydrothermal fluids at high depth at high temperature and pressure.

Messina copper deposits: The four copper deposits i.e. Campbell, Harper, Messina, Artonvilla copper deposits.

Mineral association: Minerals that commonly occurred together in an ore deposit

© University of Venda

Musina: The name of town and municipality formally known as Messina.

Ore microscopy: Microscopic study of ore minerals

Ore mineralogy: A study of minerals that are of economic importance (ore minerals) and that form orebody

Paragenesis: Sequence in which minerals are formed within the ore deposit

Petrography: The descriptive study of rocks, minerals and mineral assemblages

Phenocryst: Large crystal that grow in a cooling magma

Primary sulphide minerals: Sulphide minerals that are formed during the original crystallization of the host rocks

Radioactive Isotopes: Unstable isotopes whose nuclei are unstable and disintegrate over time to form other isotopes

Regions of Interests: Possible prospecting areas for further copper sulphide mineralisation deduced through remote sensing outcomes

Secondary sulphide ore minerals: Sulphide minerals formed at a later stage through processes such as weathering and hydrothermal alteration

Stable isotopes: A non-radioactive chemical element that shows no tendency to undergo radioactive decomposition

Syngenetic: Mineral deposit which is formed at the same time with the rocks that enclose it

Target areas: Potential areas for mineral exploration that have been identified through prospecting and preliminary exploration, using geological, geophysical and geochemical techniques including remote sensing

Threshold: The upper limit of natural background is termed above which a value is considered anomalous

Xenoliths: A rock fragment picked up by a magma and reserved after the magma has solidifies

© University of Venda

CHAPTER 1

INTRODUCTION

Preamble

This chapter presents the overall picture of the study in terms of the background, and introduce the study area with respect to its geographical location, climate, topography, drainage and land use. The chapter further looks at statement of the problem, rationale, research questions, hypothesis and objectives of the study, and finally presents a summarized structure of the thesis.

1.1 Background

Copper deposits within metamorphic terrains are formed as a result of various processes. For example, metamorphic deposits within metamorphic belts are formed through a process of metamorphism with the participation of mineralised solutions like water, carbon dioxide, hydrogen sulphide, volatile compounds under intense temperature and pressure (Smirnov, 1976) in the form of either local or regional metamorphism. In local metamorphism, it can be in the form of autometamorphism, contact metamorphism and dynamic metamorphism along tectonic zones (Smirnov, 1976; Anthony and Ague, 2009; Van Reenen *et al.*, 2011). In the case of autometamorphism, the residual hydrothermal solutions are able to react with the igneous minerals, resulting in rock alteration and sometimes in the formation of economic minerals. Contact metamorphism is associated with igneous intrusions, the main agent being the heat supplied by igneous intrusion. This may result in metasomatic reaction of minerals, leading to deposition of economic minerals. Dynamic metamorphism is associated with epigenetic ores, developed along faults, with structures such as brecciation due to fault movements during and after mineralisation (Smirnov, 1976; Anthony and Ague, 2009; Van Reenen *et al.*, 2011).

Some copper deposits occurring within metamorphic belts are known to have been formed either long before or after metamorphism. For example, copper mineralisation within the Damara Belt had been formed long before metamorphism and metamorphism did not cause any remobilisation, relocation or concentration of ores within the belt (Martin, 1978), instead

© University of Venda

it was related to oceanic origin or subduction zones (Martin, 1978). On the other hand, the Messina copper deposits are known to have been formed long after the tectonic events, which resulted in the intense deformation and high grade metamorphism of the host rocks (Söhnge, 1945; Wilson, 1998).

The Messina copper deposits are located in the Musina area and are situated in the Central Zone (CZ) of the Limpopo Mobile Belt (LMB), South Africa. The deposits were discovered several hundred years ago, whereby the line of rich copper outcrops was originally discovered and exploited by the "Ancients", who were then later overran by the Bantu who took over the workings and produced copper artifacts. Later in 1903, Colonel John P. G. the founder of the Messina (Transvaal) Development Company Limited, was shown the workings and he prospected some of them (Van Graan, 1964). Modern mining started in 1906 when five mines were exploited (Van Graan, 1964). Decreasing copper prices, inflationary costs and reduced copper reserves, led to an increase in production costs that far outweighed the projected return and ultimately resulted in the decline of copper mining in Musina that led to the closure of the Messina copper mines in 1992 (Mundalamo and Ogola, 2012). At the time of closure of these Messina mines, there was also the political pressure on the then government, some of the previous mine workers believe that some of the mines were closed prematurely. Consequently, there is a possibility that some of these mines still had mineral resources for future exploration. Thus, Musina remains a potential area even for the discovery of new deposits.

This study therefore, focused on the geology, structural setting and mineralisation of copper-sulphide deposits in Musina area within the Limpopo Mobile Belt. Different research methods have been applied in the current study so as to unpack the contradictory issues on genesis in the Musina area.

1.2 Study Area

1.2.1 Location

The Messina copper deposits are situated within and around Musina town, which was formerly known as Messina. Geographically, Musina is the northern most town in Limpopo

© University of Venda

Province and it is situated about 10 km south of the Limpopo River which marks the border between South Africa and Zimbabwe. The town is about 200 km north of Polokwane city. The study area lies between Latitude 22°15′00″ ; 22°26′00″ and longitude 29°54′00″; 30°10′00″ (Fig. 1.1). Geologically, the Musina area is within the Central marginal zone (CMZ) located between the Northern and Southern marginal zones (SMZ) of the Limpopo Mobile Belt, which is flanked by the Zimbabwean and the Kaapvaal Cratons (Fig. 1.1).

1.2.2 Climate

The Musina area experiences a hot semi-arid climate with hot temperatures dominating the year. The average midday temperatures for Musina are 23.9°C in winter and 32.1°C in summer. Daily average temperature can be much higher, particularly in summer when it can be up to 45°C. The Musina area receives about 246 mm of rainfall per year, maximum rainfall in January (55 mm). The winter months are generally dry without any rain (Nel and Nel, 2009; www.saexplorer.co.za/South Africa/climate/Musinaclimate.asp).

1.2.3 Topography and Drainage

Musina is mainly characterized by flat to gentle terrain of Soutpansberg Mountains. A range of mountains stretch from Tropic of Capricorn towards Beit Bridge, the border post across the Limpopo River. The area is fairly flat in the northern and south-eastern side, but undulating hills and rocky outcrops are typical on the eastern and western side (Fig. 1.2). A number of hills occur in the area, for example, the Viskop hill that occupies the western part (Fig. 1.2).

The Musina area lies within the Limpopo Basin and the study area falls within the Sand River catchment (Fig. 1.1). The tributaries on the northern side of the Sand River catchment flow towards the south-eastern direction. The drainage pattern of streams is dendritic, forming a tree-like pattern. Most of the streams for example, the Soutsloot River, flow in a southern direction towards the Sand River that receives a high-water discharge during summer and low or no discharge during winter. Consequently, the river is non-perennial in nature (Zengeya *et al*., 2011).

© University of Venda

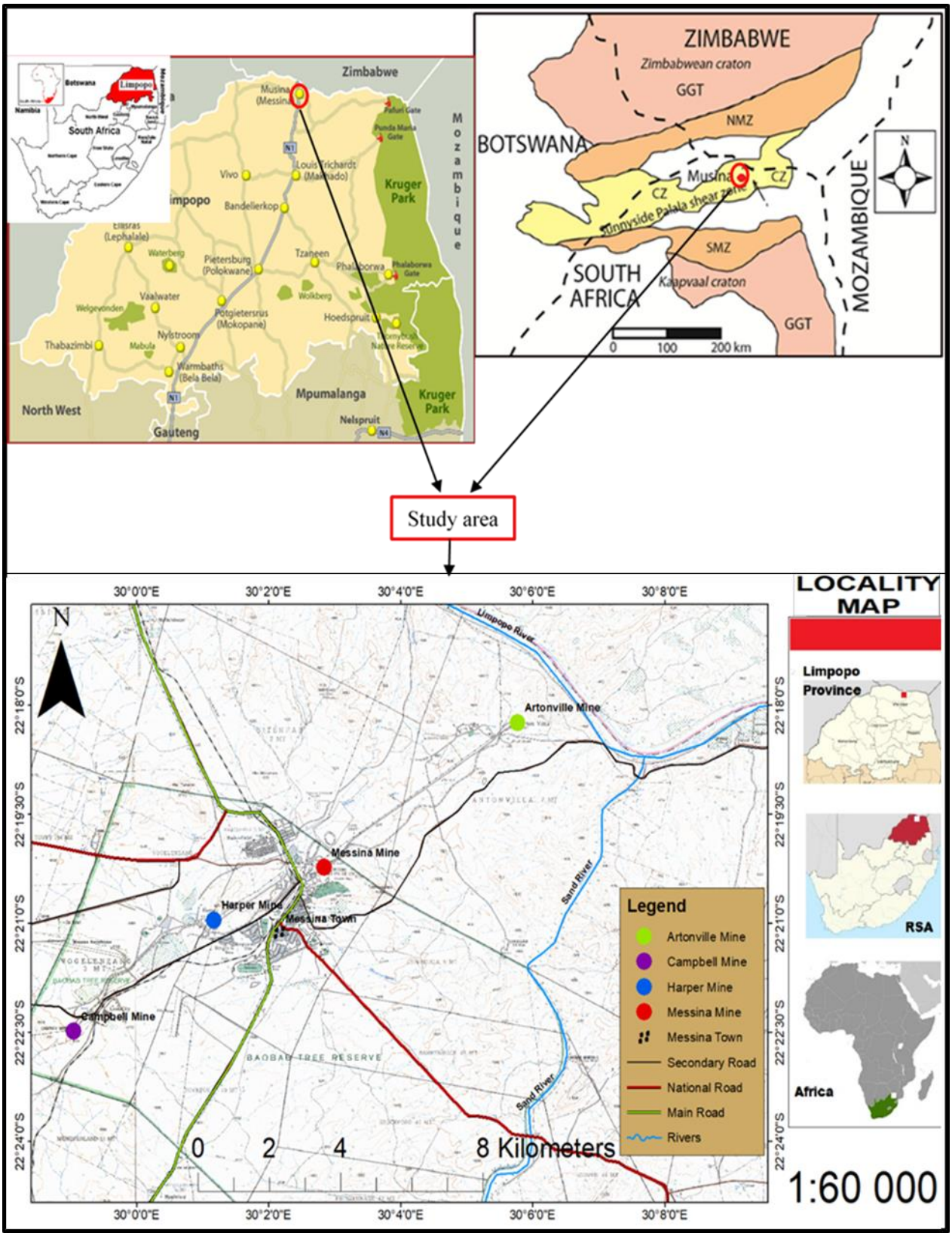


Figure 1.1: Geographical, topographical and geological location of the study area within the African continent. Abbreviations: GGT- Granitic greenstone terrain, NMZ- Northern marginal zone, CZ- Central zone, SMZ- Southern marginal zone (www.places.co.za/maps/Limpopo; Chaumba *et al*.,2016; ArchGIS).

© University of Venda



Figure 1.2: Photographs showing topography of the study area.

1.2.4 Soil and Vegetation

A Large variety of soils occurs in the area; however, sandy and loamy soils are the most common ones derived from the gneiss, quartzite and sandstone within the area. Most areas contain high proportions of red iron-rich soils associated with the undulating hills of rocks such as diabase, gabbro, basalt, shale, siltstone and mudstones and dolerite, and these areas are mostly used for agricultural purposes. The soils near the streams are mainly sandy soils and mostly densely vegetated by low-shrubs, Marula, Mopani and thorn trees. In some areas baobab trees are widely scattered (Fig. 1.3).

The study area is mostly covered by vegetation that belongs to the Musina Mopane Bushveld that is found on sandy, loamy to rocky soils. For example, *Acacia nigrescens* (Knobthorn), *Kirkia acuminata* (White seringa), *Acacia tortilis* (Umbrella thorn) and *Adansonia digitata* (Baobab) (Nel and Nel, 2009). The Limpopo Ridge Bushveld vegetation [e.g. *S. birrea* (Marula), *C. mopane* (Mopane), *C. glandulosa* (Tall common corkwood)] flanked the Mopane Bushveld and is mainly along the Limpopo and Sand Rivers (Nel and Nel, 2009).

© University of Venda

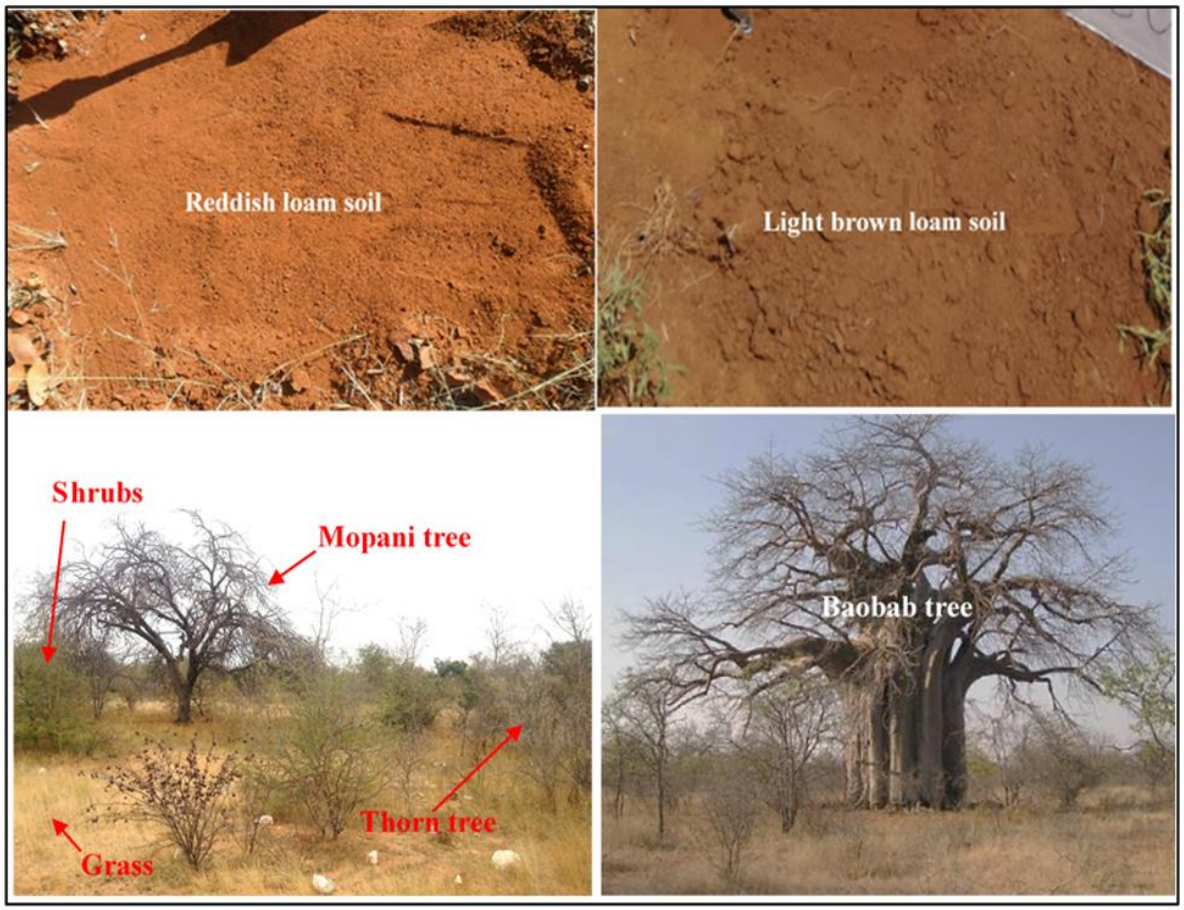


Figure 1.3: Photographs showing most abundant soil and vegetation types within the study area.

1.2.5 Land-use

The study area is used for activities such as subsistence/commercial farming, residential use, commercial use, industrial use, conservation sites and mining. Musina town owes its existence to the region's abundant mineral wealth, which includes iron ore, graphite, coal, magnetite, diamond, asbestos and copper. Active mining includes; Venetia diamond mining and Vele Colliery coal mining. The terrain around Musina town supports low-shrub and thorny tree vegetation which is used for animal grazing, and undoubtedly the main attraction for holiday makers, hence the establishment of many game lodges offering safaris, both photographic and hunting. There are a number of natural reserves that include Musina Nature Reserve, characterized by its abundance of the oddly-shaped baobab trees, and the Limpopo Valley National Park incorporating the archaeological site of Mapungubwe. Other points of interest include the massive Matakwe granite rock at the Musina Experimental Farm, and the Dingola Execution Rocks historically used by Musina chiefs for punishment of wrong-doers.

© University of Venda

The settlement is mainly around the town comprising medium to low class households, while several villages are scattered outside the town and these belong to farm workers.

1.3 Problem Statement

The origin, nature and mode of formation of the Cu-sulphide deposits in the Musina area have not been established with certainty. Two principal models have been suggested: Magmatic-hydrothermal model (Jacobsen, 1974, Jacobsen and McCarthy, 1976; Jacobsen *et al.*, 1976), and convective flows of largely meteoric waters model formed at temperatures of 150 - 214°C which is lower than temperatures of magmatic-hydrothermal origin (Sawkins, 1977; Sawkins and Rye, 1979). Consequently, the mode of formation and mineralisation style of Cu-sulphide deposits remain contentious.

1.4 Rationale

Previous studies suggested that there was structural and lithological control on Cu-sulphide mineralisation of the Messina deposits (Brandl, 1981; Wilson, 1998). Ore formation processes appeared to have been associated with rock alteration and formation of breccia pipes. The breccia pipes are assumed to have been formed through hydrothermal solutions and gases under high pressure at the time of ore formation. However, the origin of the breccia pipes, according to previous studies, poses more questions than answers (Van Graan, 1964). Jacobsen (1974), Jacobsen and McCathy (1976) and Jacobsen *et al.* (1976), propose a magmatic hydrothermal origin, while Sawkins (1977) and Sawkins and Rye (1979) propose that the mineralisation may have been a result of convective flows of largely meteoric waters. Following Söhnge (1945), both models invoke Karoo Age Group (300 -145Ma) as the source of copper, while Bahnemann (1986) noted that both models overlook the Soutpansberg Group rocks (2000 – 1800 Ma) some of which are known to be rich in copper (Wilson, 1998).

Consequently, without adequate data, the mode of formation remains controversial. In most of the mobile belts of Southern Africa, ore deposits are located within the rocks that had undergone medium to high grade metamorphism. The most problematic question is whether mineralisation resulted due to metamorphism process. Such questions should be answered

© University of Venda

through detailed study of ore deposits, metamorphic petrology, isotopes, and geochemistry of the rocks associated with the ore deposits.

When Colonel John P. G. from Transvaal Development Company Limited took over the prospecting of copper which was exploited in the past, he discovered several blind ore bodies and prospected some of them. It is possible that there may be undiscovered blind orebodies of economic value within the Musina area. The current study therefore, incorporated remote sensing technique and geochemical survey as exploration tools for identifying targets areas.

Geochemical signatures are important for both mineral exploration and environmental management. The South African Government is in the process of developing geochemical maps of the whole country and the Council for Geoscience has already embarked on this exercise, however, geochemical baseline study has not been conducted in the Musina area. Geochemical baseline study has proved to be a powerful tool for mineral exploration. For example, geochemical signatures may reveal the occurrence of geochemical aureoles or haloes that are indicative of either weathered or buried ore bodies. Some countries like the former Soviet Union had successfully applied geochemical baseline study to discover a number of buried deposits.

The remotely sensed data can be analysed and interpreted to provide valuable information with regards to mineral exploration. Their ability to cover large area, map inaccessible areas, map the geological features including minor structures, as well as increased understanding of the information derived from the data has facilitated the use of remote sensing in mineral exploration (Thenkabail, 2015). However, remotely sensed data have not been studied within and around the Musina copper deposits. Consequently, both geochemical survey and remote sensing techniques were used in this study.

In addition to the historic study that included the concept of supercontinents, continental drift and plate tectonics, the metamorphic belts are of interest as there still remains a number of difficult questions concerning the origin and the characteristics of these belts (Wynne-Edwards, 1978; Cornell, *et al.,* 2006; Kramers *et. al.,* 2006; Newton, *et al.,* 2006; Booth, 2011). There are enough sulphide mineralisation within or which had survived the metamorphic processes and it has been ascertained that mineral deposits can occur and

© University of Venda

survive all stages of metamorphism. The textural and mineralogical effects have been studied in most of these belts (Wynne-Edwards, 1978; Kramers *et. al*., 2006; Booth, 2011), but the most crucial problem in exploration is to predict their settings and distribution, which are major factors that play a major role in the genesis of ore deposits.

In South Africa, much work has been focusing on gold and diamond, and less focused on base metals mainly within the un-metamorphosed geological environments and less attention on mobile belts. It has been postulated that exploration in highly metamorphosed terrains is highly expensive as the areas are complex, thus there is less of exploration work conducted within these geologic terrains (Cornell *et al.*, 2006; Kramers *et. al*., 2006; Booth, 2011). Consequently, there is a need to conduct further work in metamorphosed terrains so as to ascertain their potential for ore mineralisation.

The price of copper in the world market has decreased from 1989 to 2004 with an average of 0.98 USD/Ib (2 155.88 USD/t), but this was followed by sharp increase from 2004 to 2018 with an average price of 2.85 USD/Ib (6 268.05 USD/t) (Fig. 1.4) (www.macrotrends.net/1476/copper-prices-historical-chart-data and www.infomine.com/investment/metal-prices/copper/5-year/). This reflects high demand of copper during this period. Consequently, exploration of copper has also gained momentum over the cited period.



Figure 1.4: Copper price since 1989 [], Note: 2.72 USD/Ib = 5, 987.09 USD/t, ratio 1 USD/lb: 2, 201. 14 USD/t, (www.infomine.com/investment/metal-prices/copper/5-year).

© University of Venda

1.5 Research Questions

- Which geochemical signatures act as indicators for copper-sulphide mineralisation?
- Were there any structural and lithological controls on mineralisation?
- What was the nature of sulphide mineralisation?
- What was the source material for ore formation?
- What were the physical and chemical conditions of ore formation?

1.6 Hypothesis

The above research questions include and involve hypothesis relating to mineralisation style of copper within the mobile belts. For any mineral deposits, factors such as pathfinders, environment of formation, structures, lithology, mode of formation, source of mineralised solution, temperature and pressure conditions, and mineralisation in space and time are of importance in deciphering the genesis of the deposits. Consequently, the study is based on the following hypothesis:

- Copper mineralisation is generally associated with sulphide base metals such as Pb, Zn, As, Au, Co, Mo;
- Copper sulphide deposits generally occur in different geological environments that include magmatic, hydrothermal, sedimentary hosted strati-form and metamorphic;
- Most copper deposits are structurally controlled by faults and folds. In some cases copper ore bodies are also lithologically controlled;
- The mineralisation style of copper deposits occur in form of disseminated, veined and brecciated orebodies; and
- Copper deposits are of either epithermal, mesothermal and hypothermal origin with the source of mineralised solution being of magmatic, meteoric and mixed origin.

© University of Venda

1.7 Objectives

1.7.1 Main Objective

The main objective of the study was to investigate the origin, nature and mode of formation of Cu-sulphide deposits in the Musina area, thus establish the physical and chemical conditions of copper-sulphide ore.

1.7.2 Specific Objectives

Specific objectives were to:

- Determine the geochemistry of soils within the Musina area;
- Investigate the structural features and petrological characteristics of the rocks hosting Cu-sulphide mineralisation;
- Study the mineralogical and characteristics of ore and gangue minerals through ore-mineralogy and ore-microscopy, and cathodoluminescence study;
- Undertake fluid inclusion studies on mineralised samples for determination of physical and chemical conditions of ore formation; and
- Undertake isotopic geochemistry for the determination of the possible source of mineralised solution and temperature of ore formation.

1.8 Thesis Structure

The thesis is presented in twelve chapters (Fig. 1.5). Chapter 1 is an introduction to the thesis. It covers the description of the study area in terms of its location, climate, topography and drainage, soil and vegetation, and land-use. It further provides insight on problem statement, rationale, research questions, hypothesis and objectives of the study. Chapter 2 is literature review on the geological setting and genetic types of copper-sulphide deposits.

Chapter 3 provided the methods and procedures that have been applied in the entire research work. Each method was clearly explained in detail as individual chapters whereby principles, sample preparation and analysis, interpretation of results, and discussion and were fully covered.

© University of Venda

Chapter 4 dealt with soils geochemical survey within and around Messina copper deposits for determination of geochemical signatures that may be associated with the copper-sulphide mineralisation as well as developing target areas for further exploration purpose. Chapter 5 focused on mineral alteration and structural investigation, using remote sensing technique. The geological and mineralogical interpretation of the study area were dealt with in Chapter 6 (Petrography), Chapter 7 (Ore mineralogy and ore-microscopy), and Chapter 8 (Cathodoluminescence investigation), wherein rock and ore forming mineral characterization, mineral association and assemblages; and CL minerals characterization in terms of their textures, internal structures, different generations and interrelations were covered (Fig. 1.5).

Chapter 9 covers fluid inclusion study of such minerals as quartz and carbonates. It involves identification of primary fluids in minerals, their composition and geothermometry. Chapter 10 (Sulphur Isotope Geochemistry) focused on sulphur isotope composition of the sulphide mineralisation and rocks associated with the deposits so as to identify possible sources of sulphur during ore formation; and determination of temperature of ore formation. Chapter 11 looked at the genesis of the Messina copper deposits and its genetic model while Chapter 12 is the concluding chapter that covers the main findings of the study and spells out future research direction in the study area (Fig. 1.5).

© University of Venda

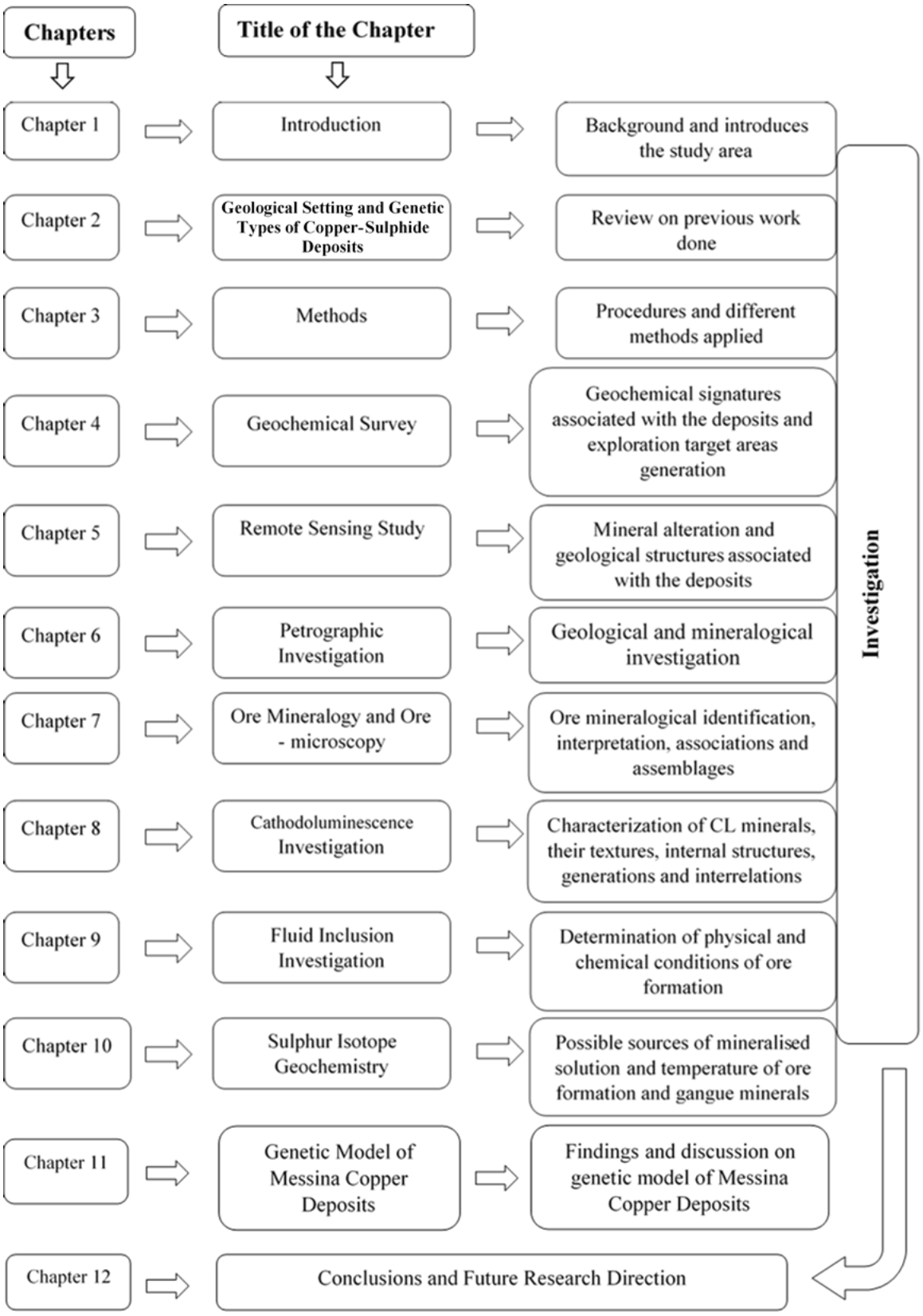


Figure 1.5: Schematic representation of the thesis structure.

© University of Venda

CHAPTER 2

GEOLOGICAL SETTING AND GENETIC TYPES OF COPPER-SULPHIDE DEPOSITS

Preamble

This chapter present a review of the genetic types of copper-sulphide mineralisation in different geological environments that are either magmatic in origin or in association with igneous intrusions, and the sediment-hosted stratiform copper mineralisation. It further discuss the geological setting and mineralisation of the Limpopo Mobile Belt as well as the history of the copper mining within the Musina area. The occurrence of copper deposit in a particular geological setting is important in understanding the nature of the deposit, however, it is not enough to understand the physical and chemical conditions under which ore mineralisation took place.

2.1 Magmatic Copper-sulphide Deposits

Magmatic copper sulphide deposits are mineral concentrations in mafic and ultramafic rocks derived from immiscible sulphide liquids. Among the magmatic copper deposits are:

- Copper-Nickel (PGEs) deposits;
- Porphyry copper deposits associated with igneous intrusions;
- Volcanogenic massive sulphide deposits;
- Skarn copper deposits; and
- Carbonatite copper deposits.

2.1.1 Copper-Nickel Sulphide (PGEs) Deposits

The copper-nickel sulphide deposits are deposits of magmatic segregation formations of ultramafic and mafic rocks. Typical examples of this type of ore deposits are the Norilsky deposits in Krasnoyarsky, the Mocha-Tundra and Pachenga deposits of the Kola Peninsula and the Voronezh anteclise all in Russia, and the Sudbury and the Lynn Lake and Mystery Lake deposits in Canada, the Alaska and Stillwater deposits in the United States of America

© University of Venda

(USA) and the Bushveld Complex of South Africa within which Copper-Nickel-Platinum of a segregation origin are formed. According to Smirnov (1976), these deposits form on platforms that are tectonically re-activated linked with hypabyssal intrusions of gabbro and are predominantly localised in association with fully differentiated massifs of these rocks. The deposits of Copper and Nickel (PGEs) consist of (a) copper associated minerals: pyrrhotite and chalcopyrite as primary minerals, and bornite, chalcocite covellite, violarite, cubanite and digenite as secondary minerals; (b) Nickel associated minerals: pentlandite, violarite, millerite, bravoite, polydymite, and parkerite; and (c) Cobalt mineral: Cobaltite. Associated minerals include pyrite, titanomagnetite, ilmenite, marcasite, sphalerite, molybdenite, and galena. The non-ore minerals include garnet, pyroxene, epidote, serpentine, actinolite, talc, chlorite and carbonates.

The Bushveld Igneous Complex is a large layered igneous intrusion that had been tilted and eroded and now outcrops around what appears to be the edge of a great geological basin. In the Bushveld Complex, Ni, Cu, and Pt mineralisation is developed at two levels of the ultramafic rocks of the Lower Zone, namely; a zone of mineralisation within the Volspruit pyroxenite subzone and mineralisation associated with the chromitite layers of the Drummondlea harzburgite-chromitite subzone as noted by Hulbert and von Gruenewaldt (1982). These researchers postulated that separation of an immiscible sulphide liquid was brought about by a drop in temperature of the magma, possibly caused by the emplacement of less primitive, cooler magma that mixed with the residual, crystallizing, lower zone magma.

Smirnov (1976) and Misra (2000) noted that in terms of their morphological features, ore bodies can be divided into four groups: (a) hanging sheet deposits of disseminated ore; (b) sheet and lenticular bodies of massive ore or streaky disseminated ore; c) lenses and irregular bodies of contact breccia; and d) veins. He further noted that the geological position of these ore bodies is determined by two principal causes: (a) the force of gravity, which brings about gravitational separation of the sulphide melt; and (b) tectonic stresses, which force this melt wholly or in part along the parted elements of the geological structure, thus layered zones of tectonic crushing control the localization of bedded, veined and breccia ores (Fig. 2.1).

© University of Venda

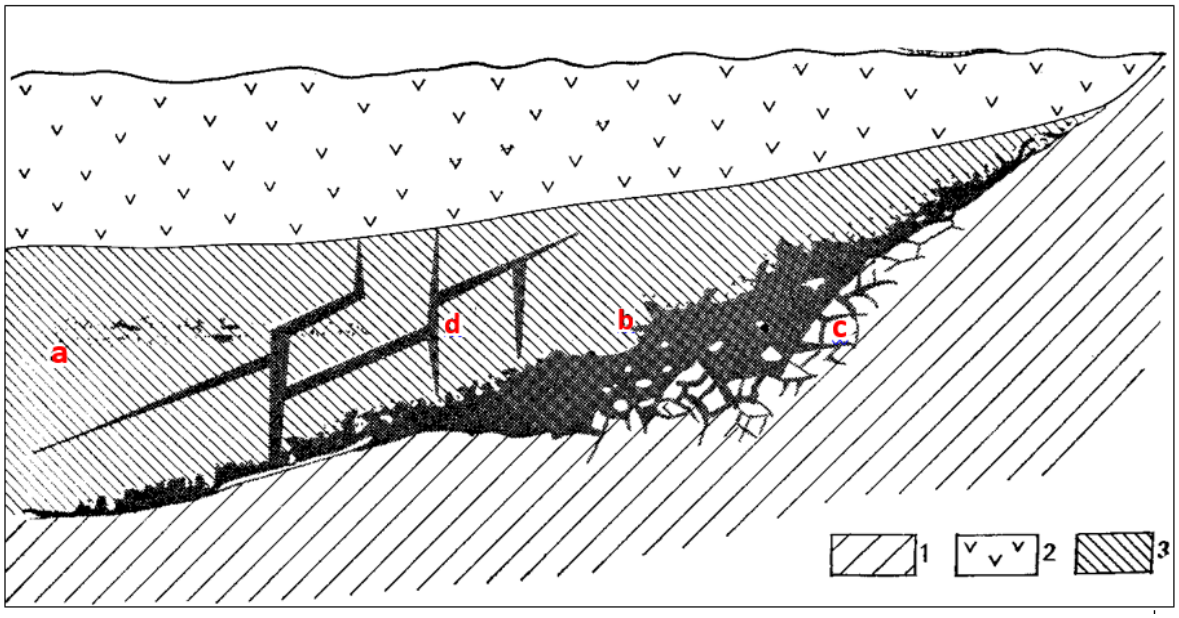


Figure 2.1: Arrangement of orebodies in copper – nickel sulphide deposits: (1) underlying rocks; (2) overlying rocks; (3) enclosing rocks; (a) hanging phenocrysts; (b) bottom ores; (c) brecciated ores; and (d) veins (Smirnov, 1976).

2.1.2 Porphyry Copper Deposits

Porphyry copper deposits are copper orebodies that are formed from hydrothermal fluids originating from magma. Initial formation of porphyry copper deposit associated with magma results in low-grade mineralisation (0.3%-0.9%) next to the solidifying magma and in chemically reactive wall rocks like limestone (Fig. 2.2). The upper chamber of the magma is where the hydrothermal fluids collect and mineralizing the surrounding rocks, leading to formation of copper and other sulphide minerals. Some deposits may be richer in gold rather than copper, thus they are considered as gold deposits. Others don't contain gold, but a part from copper, are molybdenum rich,

The process of porphyry copper formation has been proposed as follows (https://www.911metallurgist.com/blog/geology-of-porphyry-copper-deposits:

- Crystallizing magma releases water and gas at high pressure;
- Pressure further increased by increase in volume as feldspar crystals take more space than when molten;
- High pressure steam (water, CO_2, H_2S, salt) rupture within the intrusion;

© University of Venda

- Metals (copper, molybdenum, gold) transported initially in steam as chlorine complexes (CuCl);
- Steam (600^{o}C) gradually condenses to salty metal-rich brines which make their way outwards and upwards;
- Metals deposited as fluids cool (350^{o}-250^{o}C); Cu and Mo first, then Zn and Pb.

Porphyries often form in and around the magma chambers that feed volcanoes. During the process of ore mineralisation, the hydrothermal fluids alter the host rock, thus such minerals as biotite, amphibole, pyroxene are altered to chlorite, actinolite, epidote and calcite, hence the host rock attains a greenish tinge colour that is due to prophylactic alteration process (hppt://sprottglobal.com/natural.resource-investing/investment-university/cited noted that as the rock-forming minerals are altered to potassiun feldspar, chances of ore mineralisation are much higher. Potassic alteration (Sericitisation) is thus important for the exploration of copper porphyry mineralisation.

A typical type of porphyry copper deposits is the Chuquicamata porphyry copper deposit in Chile that is related to the Precordilleran fault system. The faults border the deposit to the west and east. The Chuquicamata deposit occurs in the Chuquicamata Intrusive Complex and is concentrated in a zone of pervasive quartz-sericite alteration that grades eastward into overprints a K-feldspar-biotite alteration zone. Potassic alteration gives way to a zone of chlorite-magnetite-specularite (-epidote) alteration in the easternmost part of the deposit (Ossandon *et al.*, 2001). The deposit consists of supergene and hypogene ores, the former being formed through meteoritic waters circulating with associated oxidation and chemical weathering, and thus the descending waters oxidized the primary hypogene sulphide ores (John, 2010). Ore reserves at the Chuquicamata porphyry copper deposit is 16,000,000,000 tons.

© University of Venda

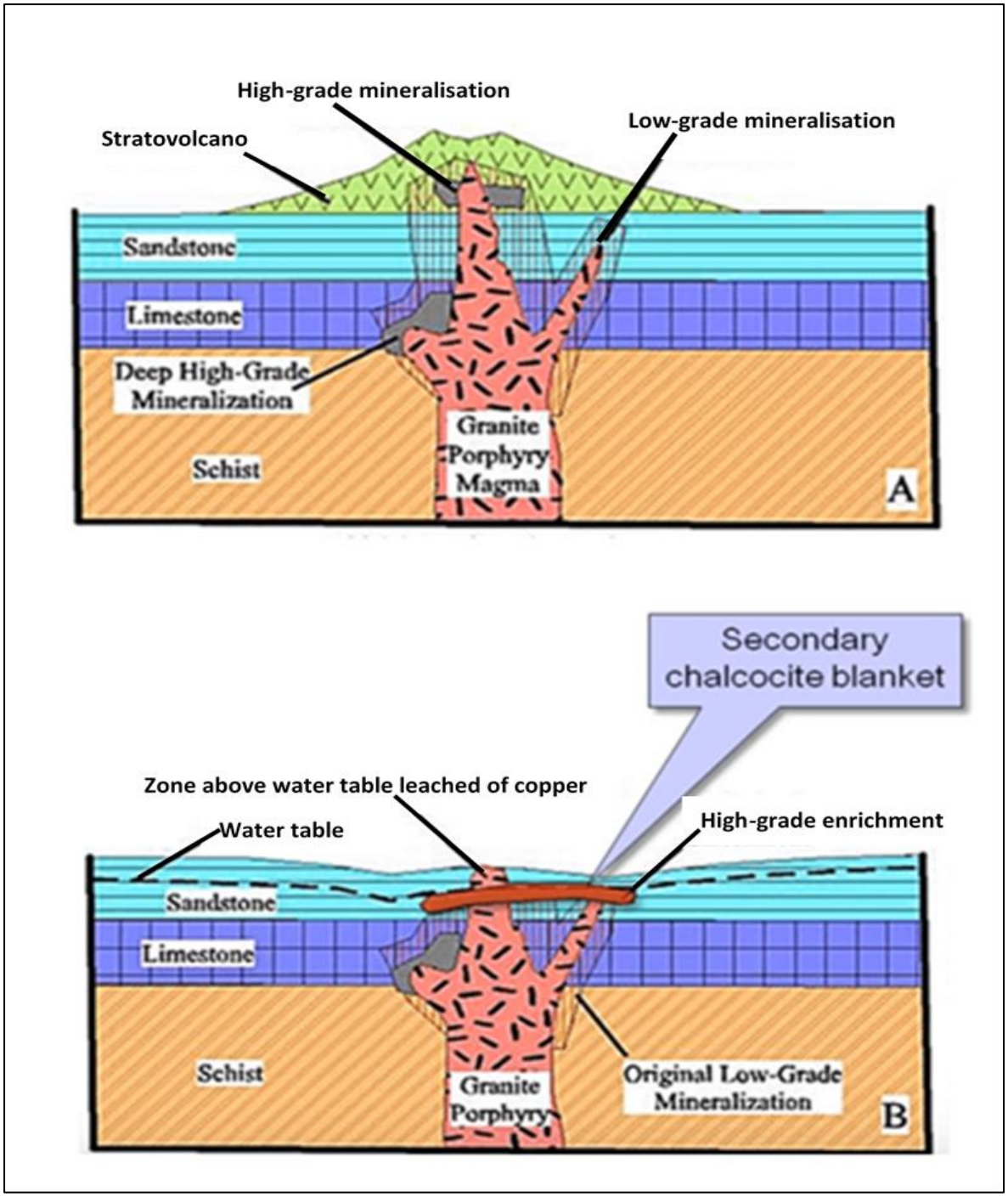


Figure 2.2: Formation of porphyry copper from magmatic source: A) Low grade Copper mineralisation; and B) Metal concentration and formation of secondary Chalcocite (https://www.911metallurgist.com/blog/geology-of-porphyry-copper-deposits.

© University of Venda

2.1.3 Volcanogenic Massive Sulphide Deposits

Volcanogenic massive sulphide (VMS) deposits are important sources of copper, zinc, lead, gold, and silver. They form at or near the seafloor where circulating hydrothermal fluids driven by magmatic heat are quenched through mixing with bottom waters or pore waters in near-seafloor lithologies (Shanks III and Koski, 2010). Massive sulphide lenses vary widely in shape and size and may be podlike or sheetlike. They are generally stratiform and may occur as multiple lenses. These are deposits associated with hydrothermal events in submarine environments (Colin-Garcia *et al.*, 2016).

Volcanogenic massive sulphide deposits are predominantly stratiform accumulations of sulphide minerals that precipitate from hydrothermal fluids on or below the seafloor in a wide range of ancient and modern geological settings. In modern oceans they are synonymous with sulphurous plumes called black smokers. According to Colin-Garcia *et al.* (2016), the source of metal and sulphur in VMS deposits is a combination of incompatible elements which are leached from the volcanic pile in the sub-seafloor hydrothermal alteration zone by hydrothermal circulation that is driven via heat in the crust, often related to deep-seated gabbro intrusions. Consequently, the transport of metals occurs via convection of hydrothermal fluids, the heat for this supplied by the magma chamber which sits below the volcanic edifice. Cool ocean water is drawn into the hydrothermal zone and is heated by the volcanic rock and is then expelled into the ocean, the process enriching the hydrothermal fluid in sulphur and metal ions.

According to Tourtelot and Vine (1976) copper deposits occur in sedimentary and volcanogenic rocks within a wide variety of geologic environments where there may be little or no evidence of hydrothermal alteration. Some deposits may be hypogene and have a deep-seated source for the ore fluids, but because of rapid cooling and dilution during syngenetic deposition on the ocean floor, the resulting deposits are not associated with hydrothermal alteration. Many of these deposits are formed at or near major tectonic features on the Earth's crust, including plate boundaries, rift valleys, and island arcs.

© University of Venda

2.1.4 Skarn Copper Deposits

Skarns are major sources of copper-sulphide minerals. The deposits occur in varying geological environments ranging from Precambrian to late Tertiary. Misra (2000) notes that most of the deposits are young and are related to magmatic-hydrothermal activity associated with dioritic and granitic belts. Skarns are rich in Ca, Fe, Mg, Al and Mn and the associated ore deposits are formed through metasomatic processes when the intrusive comes into contact with the carbonate rocks and the magmatic fluids attack the latter.

Occurrence of skarn deposits in shales (Shimazaki, 1982), quartzites (Atkison and Einaudi, 1978), and igneous rocks (Einaudi *et al.*, 1981; Harris and Einaudi, 1982) have been reported. According to Einaudi and Burt (1982), the sequence of skarn ore mineralisation is Cu>Fe>Zn>Pb>W. Calcic copper skarns are characterised by (Einaudi *et al.*, 1981; Meinert, 1992):

a) close spatial association with felsic porphyry –textured stocks with hydrothermal alteration;
b) relatively oxidised mineral assemblage comprising andradite, diopsitic pyroxene, magnetite and hematite;
c) high garnet-pyroxene ratios; and
d) moderate to high sulphide content.

Misra (2000) noted that the skarn is commonly zoned, with massive garnet near the pluton while wollastonite occurs near the carbonate contact. At the contact of skarn and the carbonate rock is a reaction zone where sulphide ore minerals (pyrite, chalcopyrite, bornite, sphalerite, tennantite) form either in the endo-contact or exo-contact. Burt (1977) noted the change from andradite-chalcopyrite to bornite-wollastonite with a decrease in the Fe-Cu rati in the Fe-rich oxidizing fluids that alter wollastonite to andradite resulting in the precipitation of bornite instead of chalcopyrite.

2.1.5 Carbonatite Copper Deposits

Carbonatites are endogenous accumulations of calcite, dolomite and other carbonates closely associated spatially and genetically with complex ultramafic-alkali intrusions (Smirnov,

© University of Venda

University of Venda
Creating Future Leaders

1976), although some are of volcanic origin as the case with the Ol Doinyo Langai volcano in Tanzania. They are rich in carbonate rocks (>50%). In some places, they form ring dykes as the case with Palaborwa carbonatite. Nearly all carbonatites are associated with tectonic structure, commonly with the rift systems as is the case with the Great Rift system of East Africa. Their formation is attributed to either direct generation by low degree partial melts in the mantle and melt differentiation, or liquid immiscibility between a carbonate melt and a silicate melt or extreme crystal fractionation (Bell, 1994). Carbonatites occur in form of plugs within zoned alkalic intrusive complexes, or as dikes, sills, breccias, and veins. Carbonatite complexes are associated with mineralisation of copper, iron, titanium, phosphorus, niobium, uranium, thorium, barium, fluorine, zirconium and even PGEs and gold. Most deposits are enriched in Th, U, Ti, Zn, Nb, Y, Mo, Cu, V, P, Mn, S, La, Ce, Sm, Eu, Pb, Zr, and Ba.

One of the classic carbonatite copper deposits of the world is the Palabora carbonatite complex in South Africa. The geology of the carbonatite was well established by Russel *et al.* I954 (Fig. 2.3) and later modified by Lombaard *et al.* in1964. The alkaline carbonatitic massif is a bicentered ring complex that has been intruded into Archean granite as a vertical pipe (Fig. 2.3). The complex is cut by a swarm of northeast-striking, parallel vertical diabase dikes of Karoo age. The complex itself had been dated at 2060 Ma (Holmes and Cahen, 1957). Small plugs of syenite run through the main complex to the east and west. The complex is flanked by an incomplete outermost ring of syenite which has been interpreted as fenite (Shand, 1931).

The Palabora carbonatite is a ring complex, comprising idealized sequence of units inward (Russell *et al.,* 1954; Lombaard *et al.*, l964; Heinrich, 1966; Verwoerd, 1966): Older Granite (country rock); Fenite; Syenite; and Feldspathic pyroxenite with carbonatite within the southern center. Vertical radial dikes of banded, older carbonatite cut all outer-zone rocks. The older carbonatite forms an elliptical, vertical plug central to the phoscorite mass and also appears as vertical arcuate sills with intervening screens of phoscorite and pyroxenite. It is characterised by a white medium- to very coarse-grained rock with a pronounced vertical to steeply dipping foliation. Strings of magnetite grains form foliation and banding within the older carbonatite (Lombaard *et al.*, l964; Verwoerd, 1966). The younger carbonatite has been divided into older banded and younger Transgressive. Emplacement of the younger carbonatite was controlled by two intersecting sets of fractures, N. 70^{o} W and N 70^{o} E, whose main juncture lies just east of the centre of the older carbonatite pipe and forms the focus of

© University of Venda

the copper mineralization and the vertical subparallel dikes of younger carbonatite cut older carbonatite phoscorite and pyroxenite (Heinrich, 1970).

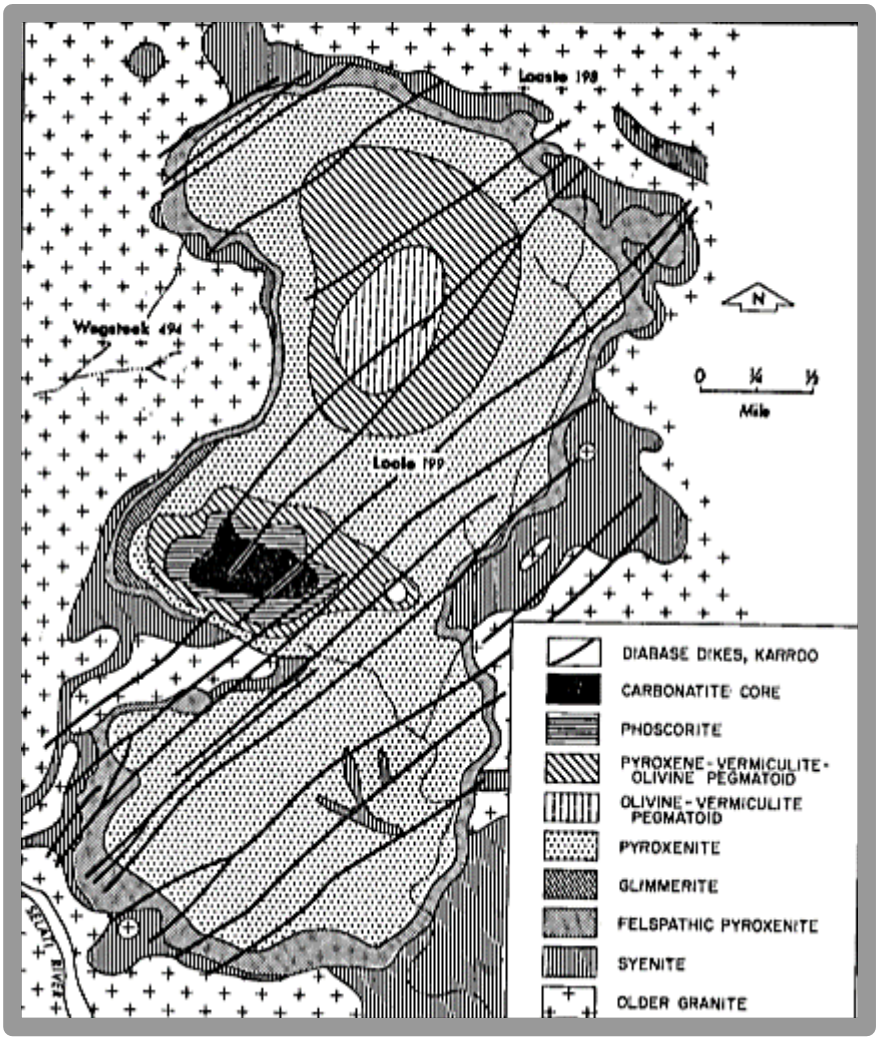


Figure 2.3: Geological map of Palabora alkaline carbonatite complex (Russell *et al.*, 1954).

The vertical copper ore body is elliptical and is centered on the intersection of the two sets of younger carbonatite dikes and the bulk of the mineralization was controlled by a subparallel set of post-younger carbonatite fractures that trend N 85^{o} W to west (Heinrich, 1970). Copper mineralization occurs in both carbonatites and in some of the phoscorite. Chalcopyrite is the most abundant ore mineral followed by bornite. Apparently, there was a single stage of mineralization, but the deposit was mineralogically zoned, with chalcopyrite predominating over bomite in the central part of the deposit ("core ore") mainly in younger carbonatite. Bornite is generally more abundant in the outer, lower temperature zone. The main ore minerals are; chalcopyrite, bornite, chalcocite, valleriite, cubanite, and pyrrhotite (minor).

© University of Venda

The exploration program delineated 315 million tons of ore, averaging 0.68% Cu. In addition to Cu, there is by-product magnetite, sulphuric acid, vermiculite and apatite.

2.2 Hydrothermal Deposits

Hydrothermal mineral deposits are those deposits that are formed as a result of hot mineralised fluids that concentrate, transport and deposit valuable ore minerals at suitable geological environments (Park and MacDiarmid, 1975; Misra, 2000; Pirajno, 2012). Deposits of this nature are products of hydrothermal solutions that are rich in brines with ore minerals in complex form. Sodium-calcium chloride brines are the most common transporting agents of sulphide and oxide minerals, although it is water that is believed to be the main solvent for mineral salts and gases (Park and MacDiarmid, 1975; Misra, 2000; Pirajno, 2012).

It was Steno in 1669 who noted that ores are a product from vapours ascending through fissures; and Henkel in 1725 and Zimmermann in 1746 acknowledged the importance of hydrothermal solutions or vapours of deep-seated origin that contained dissolved rock materials and they recognised the products of ore deposition by metasomatism (Park and MacDiarmid, 1975). It was not until 1749 that von Oppel made distinction between veins and bedded deposits with veins being cross-cutting features of secondary, open-fissure origin, while bedded deposits are conformably interbedded with the stratified sediments (Park and MacDiarmid, 1975).

Lindgren in his classification of hydrothermal deposits in 1907, 1913, 1922 and 1933, identified deposits at great depths and high temperatures between 300-500^{o}C to be hypothermal; those formed at intermediate depths and between 200-300^{o}C as mesothermal; and those formed at shallow depths and relatively low temperatures of 50-200^{o}C as epithermal (Park and MacDiarmid, 1975). Today, it is more or less accepted that magma is not the only source of hydrothermal fluids that result into formation of ore deposits. The mineral-bearing metamorphic fluids can also act in the same way as fluids of magmatic origin (Park and MacDiarmid, 1975). Smirnov (1976) had noted that meteoric water of free circulation can penetrate deep into the interior of the crust in appropriate hydrogeological conditions, thus become heated and mineralised and acquire the properties of hydrothermal

© University of Venda

solutions. The genesis of ore deposits, however, remains controversial even for those deposits that have been studied in detail.

Hydrothermal solutions are generally derived from magmatic intrusions that have excess sulphur over ore metals, this is required for efficient ore mineral precipitation (Seo *et al.*, 2009). According to these researchers, sulphur, copper and gold are highly enriched in vapour-like magmatic fluids, implying that such low-salinity fluids are the key agent for the formation of porphyry copper and epithermal deposits. The role of sulphur in the formation of such deposits as porphyry copper, skarn and polymetallic vein deposits is crucial (Hedenquest *et al.*, 1993).

Generally, porphyry copper or disseminated copper deposits are considered to be of hydrothermal origin. Examples include several disseminated copper deposits in the Miami district of Arizona in the USA, Chuquicamata porphyry copper deposit in Chile (Smirnov, 1976). For the polymetallic veins, mineralisation occurs within faults and folds, in the case of the latter, ore bodies are localised along the troughs and anticlines of the folds (Ogola, 1987). This type of mineralisation is often characterised by pinching and swelling resulting in boudinage structure and in some cases, with stockworks and apophyses (Fig. 2.4). The ore bodies are often disseminated, veined and brecciated. Such orebodies can stretch for long distances of up to two or three kilometres long as is the case of gold-bearing quartz veins of the Berezovo deposit in the Urals, while others can be much longer like the Mother Lode of California that stretches for 200 km (Smirnov, 1976).

The orebodies of hydrothermal origin generally lie in rocks that have undergone hydrothermal alteration during ore formation (Smirnov, 1976). Consequently, they are bordered by aureoles of disseminated mineralisation that die outwards. In such cases, there is no distinct contact between the orebody and the host rock, hence the contact of the two is established through geochemical sampling and assaying, based on the cut-off grade (Smirnov, 1976).

© University of Venda

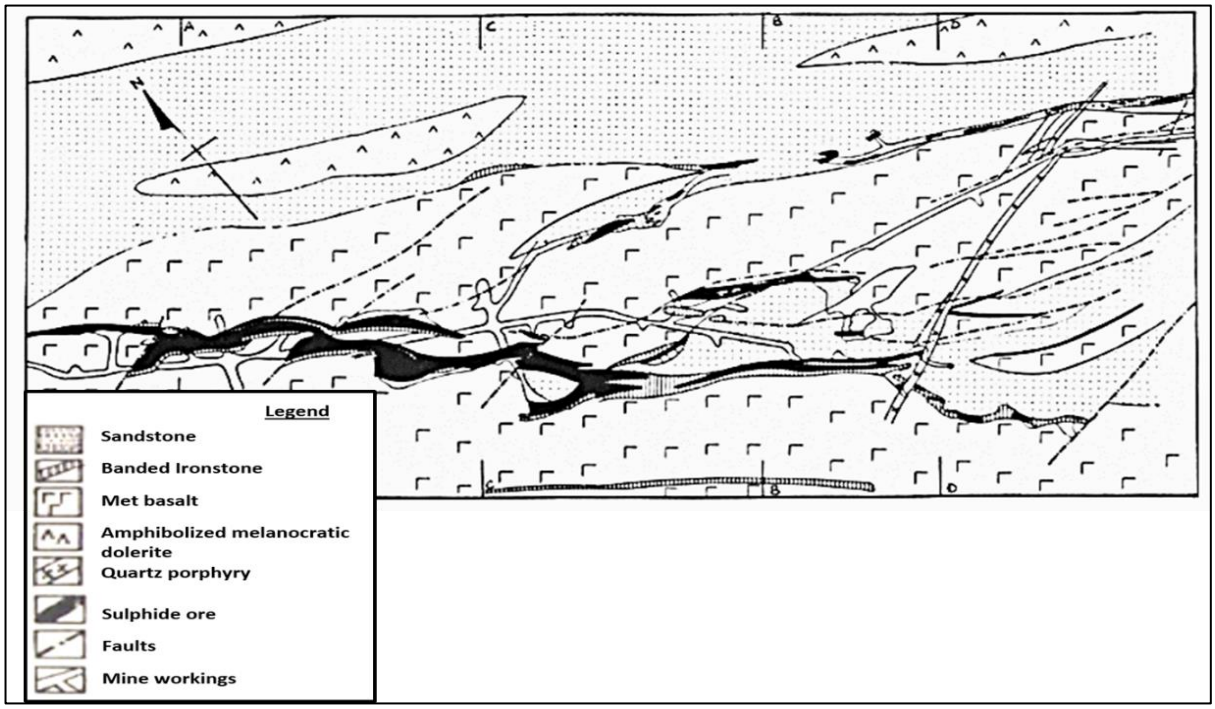


Figure 2.4: Mine levels of Macalder deposit with ore bodies localised along the troughs and anticlines of the folds and along the fault planes [compiled by Allum (1954) and Errington, (1963)].

Examples of copper mineral deposits formed by hydrothermal processes include (Misra, 2000):

- Stratiform and strata-bound base metal sulphide deposits: a) volcanic associated Cu-Zn-Pb massive sulphide deposits represented by the Nevada and Buthurst districts, Canada; Kuroko district, Japan; and Sulitjelma district, Norway; b) sediment-hosted stratiform Cu deposits represented by the Zambian-Katanga sediment-hosted stratiform copper mineralisation; Kupferschefer, Germany-Poland; and White Pine, USA.

- Porphyry deposits associated with felsic intrusions: Porphyry copper deposits represented by the Valley Copper, Canada; Bingham and Morenci, USA; Panguna, Papua New Guinea; Atlas ,Philippines; El Salvador and Chuquicamata, Chile.

- Contact metasomatic deposits associated with felsic intrusions: Copper skarn deposits represented by the Car Fork Utah, USA; Cerro de Pasco, Peru (Cu-Zn-Pb-Ag).

© University of Venda

The Macalder copper-sulphide deposit located on the northern margin of the intensively dislocated and metamorphosed volcanogenic-sedimentary rocks within a tectonic zone in the Migori Greenstone Belt of western Kenya is a typical hydrothermal copper-sulphide deposit (Ogola, 1987). Sulphide bodies occur as sheets, veins, and lenses which were emplaced at the contact of metabasalts, banded iron formation and sandstone and also at the hinges and along the fault planes within these rocks (Fig. 2.4). According to Ogola (1987), the location of the Macalder ore bodies was determined by the nature and position of the sheared zones, faults and rock fissures, which created passageways and enabling geological environments for hydrothermal fluids and ore localisation. He further noted that the Macalder deposit occurs at the intersection of several faults that postdate ore mineralisation.

2.3 Sediment-hosted Copper Deposits

This type of copper deposits contribute 20% - 25% of the world's Cu production and is only second to porphyry Cu *http://www.nr.gov.nl.ca/nr/mines/prospector/ matty_mitchell/Virtual/Metallic%20Mineral%20Deposits%20of%20NL,%20Part%203,%20Sedimentary-Hosted.pdf*). The origin of this type of copper mineralisation is still controversial. Some researchers attribute their origin to metals leaching from sediments as water is expelled by compaction, fluids migrate along porous horizons and faults to basin margins, and metals are deposited where reduced sulphur is encountered. In this scenario, mineralisation is continuous within beds or may follow old channels, in some places the mineralisation may cut beds. Mineralisation of these types of deposits include chalcocite and bornite with lesser native copper, chalcopyrite, galena, hematite and pyrite and may contain significant silver, cobalt, uranium, gold and platinum group metals.

According to Cox *et al.* (2007), sediment-hosted copper deposits are formed by fluid mixing in permeable sedimentary and rarely in volcanic rocks. Two fluids are involved: an oxidized brine carrying copper as a chloride complex, and a reduced fluid, commonly formed in the presence of anaerobic sulphate-reducing bacteria. Accordingly, for a sediment-hosted copper deposit to form, four conditions are required (Cox *et al.*, 2007):

- There must be an oxidized source rock. This rock must be hematite stable and must contain ferromagnesian minerals or mafic rock fragments from which copper can be

© University of Venda

leached. In Zambia erosion of an early-formed porphyry copper deposit is thought to have contributed copper to the source rock (Wakefield, 1978). Typical source rocks are continental red sandstone, shale, conglomerate, and subaerial volcanic rocks. Marine volcanic rocks are unsuitable as source rocks because they have not degassed their volatile components. Contained reduced sulphur in marine volcanics precludes the formation of a hematite-stable environment. Leaching of copper from the source rock at moderately low pH may be described by equation 2.1 (Cox *et al.*, 2007):

$$Cu_2O + 6Cl^- + 2H^+ = 2CuCl_3^{2-} + H_2O \qquad \text{Equation 2.1}$$

- There must be a source of brine to mobilize copper. Evaporites are commonly interbedded with red beds and act as brine sources, but any sedimentary environment in which evaporation exceeds rainfall will produce brines. Brines may also form by evaporation of sea water where connection with the open sea is restricted as in rift valleys. The brines are generally rich in sodium because other cations like potassium, calcium, and magnesium, are removed during formation of clays, sulphates, and carbonates. Davidson (1966) directed attention to the coincidence of evaporite deposits with Phanerozoic stratabound sediment-hosted copper deposits in many parts of the world and proposed that brine derived from evaporites was the transporting medium for copper and other metals.

- There must be a source of reduced fluid to precipitate copper and form a deposit. Reduced fluids can be derived from organic-rich shales and carbonate rocks, from pockets of liquid or gaseous hydrocarbons in the host sediments or from any sedimentary fluid in equilibrium with pyrite. In equation 2.1 copper-rich brine contacts organic material and produces native copper (Cox *et al.*, 2007):

$$2CuCl_3^{2-} + 4H_2O + C = 2CuO + CO_2 + 8H^+ + 6\,Cl \qquad \text{Equation 2.2}$$

- There must be conditions favourable for fluid mixing. Prelithification permeability in shale provides bedding-parallel sites for fluid mixing. Fluid pressures derived from sediment compaction is an important factor in fluid mixing, and deposits are most commonly situated at basin margins where mixing is most likely to take place.

© University of Venda

Faulting or folding may produce a hydraulic head that causes one fluid to invade the site of another (Cox *et al.*, 2007).

Zambian-Katanga sediment-hosted stratiform copper mineralisation

The Zambian-Katanga copper belt is a classic example of the sediment-hosted stratiform copper mineralization, although the genesis of copper within this belt remains controversial. The Lower Orebody consists of copper only, hosted at the top of the Lower Arkose unit and the base of the overlying Lower Shale and the Upper Orebody has both copper and cobalt, hosted mostly within the Feldspathic Arenite unit (McGowan *et al.*, 2003). In the Lower Orebody, sulphides tend to be concentrated within arenites or coarser-grained layers within shale units, suggesting that host-rock porosity and possibly permeability played a role in ore formation. In the Upper Orebody, ore zones are preferentially developed in proximity to fault-propagation fold structures and controlling thrusts, as well as basal detachments and where there is no evidence of thrust-fold development within the Katangan sequence, such as in the Block A Open Pit, mineralisation at the level of the Upper Orebody is absent (Fig. 2.5). This apparently is confirming structural control on ore mineralisation of these deposits. Hydrothermal alteration minerals include dolomite, phlogophite, sericite, rutile, quartz, tourmaline, and chlorite.

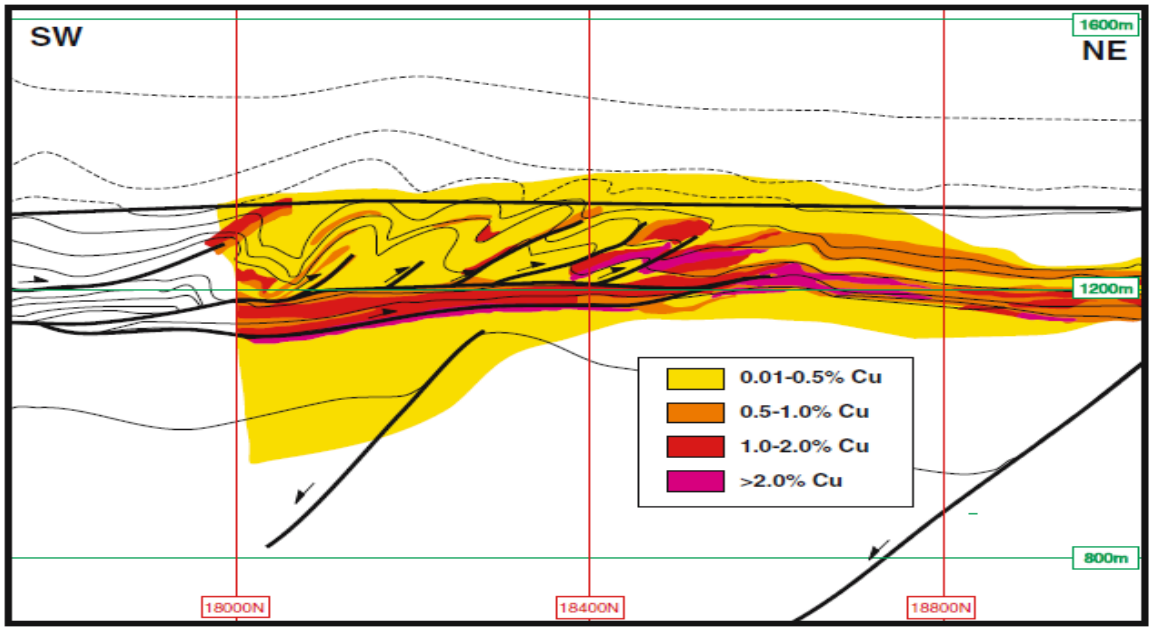


Figure 2.5: Distribution of mineralisation at Chingola B (based on copper grade boundaries) plotted onto the section geology: Mineralization is strongly related to the fault propagation folds and controlling thrusts, as well as basal detachments (McGowan *et al.*, 2003).

© University of Venda

McGowan *et al.* (2003) further noted that quartz veins from the mine sequence show halite-saturated fluid inclusions, ranging from 31 to 38 wt% equivalent NaCl, with homogenisation temperatures (Th_{tot}) ranging between 140 and 180°C and diagenetic pyrites in the Lower Orebody show distinct, relatively low $\delta^{34}S$, ranging from -1 to -17 and whereas arenite and shale-hosted copper and cobalt sulphides reveal distinctly $\delta^{34}S$ from -1 to +12 and for the Lower Orebody, and +5 to +18 for the Upper Orebody. There is also a clear distinction between the $\delta^{34}S$ mean of +12.1±3.3 (n=65) for the Upper Orebody compared with +5.2±3.6 (n=23) for the Lower Orebody (McGowan *et al.*, 2003). This study concluded that the mineralogy, hydrothermal alteration, and stable isotope data support models consistent with the thermochemical reduction of a sulphate- (and metal) enriched hydrothermal fluid. Early studies concluded that the ore bodies formed from marine waters in nearshore lagoonal environments (Mendelsohn, 1961; Garlick and Fleischer, 1972); although others suggested an epigenetic hydrothermal origin, with the ore derived from an unexposed magmatic source. Annels (1974, 1984, 1989) considered that ore formation was due to hydrothermal fluids ascending faults and mineralizing relatively unconsolidated sediment; a view supported by the studies of Sweeney *et al.* (1986).

2.4 Copper-sulphide Mineralisation within Metamorphic Terrain

Copper-sulphide mineralisation is known to occur within ancient high-grade metamorphic rocks associated with regional metamorphism. Typical examples of this type of ore mineralisation is found in Afghanistan with low-sulphide gold-quartz veins, which form in clusters in the northern part of the country in Badakhshan Province and also within the mobile belts of Africa that include the Cape Fold, Damara, Mozambique, Manaqua-Natal, Zambezi and Limpopo Belts (Fig. 2.6). The occurrence of copper-sulphide mineralisation within the mobile metamorphic belts, however, does not necessarily signify direct relationship to ore genesis. Copper-sulphide mineralisation within these mobile belts is briefly discussed below, but with more detailed geological and structural setting of the Limpopo Mobile Belt.

© University of Venda

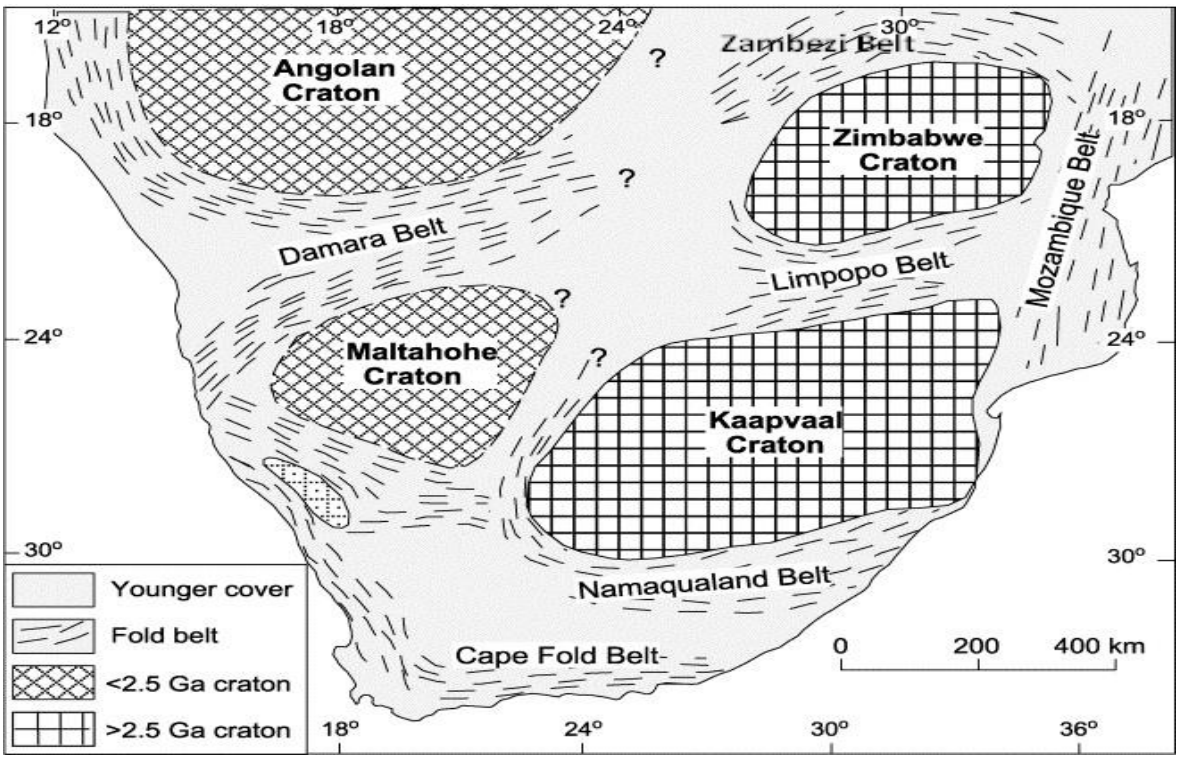


Figure 2.6: Simplified geological map showing the main crustal provinces in Southern Africa, including the main cratons and mobile belts (Anhaeusser, 1990).

2.4.1 Cape Fold Belt

The Cape Fold Belt (CFB) consists mainly of the Cape Fold Mountains which are 450 Ma in age and where folding occurred during the Carboniferous and Permian periods (Theron, 1969). The Cape orogeny affected the sandstones, shales of the Cape Supergroup and older pre-Cape rocks and younger Karoo Supergroup (Theron, 1969; Newton *et al.*, 2006; Tankard *et al.*, 2009). Previous and recent studies confirmed the northwest to north trending folds, thrusting and low greenschist grade metamorphism (Theron, 1969; Hiller and Snowden, 1983; Fagereng, 2012).

In the Cape Fold Belt of South Africa, minor copper occurrence is associated with molybdenum and tin-copper bearing quartz veins in the Cape granite suite and in the low-grade ore bodies of disseminated sulphides. Uranium deposits within the sedimentary rocks of the Beaufort Group are known to be associated with the molybdenum, copper and arsenic. (Nxumalo, 2013; Cole and Wipplinger 2001).

© University of Venda

2.4.2 Damara Fold Belt

The Damara Belt is a well exposed belt between the Congo and Kalahari Cratons in Namibia and it is of Pan African orogeny and of medium grade metamorphism in the southeastern part and high grade regional metamorphism to the north-west of the Belt (Norman and Whitfield, 2006). According to Katongo *et al*. (2004), the axial zone of the belt contains turbidites, basalts, and alpine-type ultramafic bodies, which represent an oceanic assemblage metamorphism.

In the Damara Fold Belt, copper mineralisation is mainly within the quartzitic sandstone, conglomerate, and occasionally in carbonate rocks associated with minor faults (Martin, 1978). The copper was postulated to have been formed by denudation of pre-Damara basement. Copper mineralisation was also formed within the dolomites and dolomitic limestone which were thought to have been deposited by basin-wide circulation of saline thermal water (Martin, 1978). The mineralisation within the Damara Fold Belt had not been caused by metamorphism, thus metamorphism has not caused any re-mobilisation, relocation or concentration of ores within the belt (Martin, 1978). It was postulated that the sediments might have lost their permeability during a deformation process that took place at low temperature before the low to medium grade of metamorphism was reached. Consequently, the mineralisation style of the Damara Fold Belt was related to oceanic origin or subduction zones (Martin, 1978). Foster *et al*. (2001) points out that the Damara Belt hosts a number of small and medium-size base-metal deposits, the largest of which are indicated in Table 2.1 below.

2.4.3 Zambezi Belt

The Zambezi Belt falls within the complex geology and multiplicity of tectono-thermal events that are enclosed by Kasai, Zimbabwe, Kaapvaal and Tanzania cratons (Hanson *et al*., 1998).

The Zambezi Belt hosts one of the major copper producing copper belts in the world that is highly mineralized with copper and cobalt. It is a strata-bound type of mineralisation within arenites, shales and carbonate rocks of the Katanga mine series group (McGowan *et al*.,

© University of Venda

2003). Copper resources have also been identified in the thrust zones. Deposits of this belt include Mkushi, Kitwe, Ndola, Mufulira, Luanshya, Chingola, Chililabombwe, Luiswisi, Lome and Nchanga (McGowan *et al*., 2003).

The origin of these deposits has been hotly debated for more than six decades, as the processes that generated ore mineralisation are poorly understood, in particular, the relationships between tectonics, fluid circulation, and ore deposition. What is apparent with these deposits is that high grade regional metamorphism might have not been responsible for ore mineralisation. New field and isotopic data for the Nchanga deposits indicated that the bulk of the mineralisation was hosted by shale-capped feldspathic arenites and arkoses that have undergone recrystallization and hydrothermal alteration within a host-rock package controlled by low-angle thrust faults (McGowan *et al*., 2003). A new epigenetic model was suggested for the formation of the spectacular Nchanga orebodies that involved the introduction of metal and sulphate-bearing hydrothermal fluids into quartzo-feldspathic units during basin inversion, with sulphide derived from thermochemical reduction of the sulphate near the site of deposition (McGowan *et al*., 2003).

Table 2.1: Base metal deposits of Damara Belt (Foster *et al*., 2001)

Deposit	**Type, Grade**	**Tonnage**	**Contained metals**
Tsumeb	Mississippi Valley type (MVT)	25000 000	Cu, Pb, Zn, Sb, V, As, Ag, Ge, G
Otjihase	Volcanogenic massive sulphide	17000000 2.0%	Cu 340 000 t Cu
Matchless	Volcanogenic massive sulphide	2 500 000 2.5%	Cu 1.5%, Zn, Ag 8 g/t 100 000t Cu + Zn
Oamites	Sedimentary Cu	8 000 000 1.2%	Cu +Ag 96 000 t Cu

2.4.4 Mozambique Belt

The Mozambique belt wraps the eastern part of the Zimbabwean Craton in Mozamique. It extends from east Antactica through East Africa up to the Arabian-Nubian Shield. It belongs

© University of Venda

to the Pan African Orogeny and is of medium to high grade metamorphism formed through the continental collisions (Cutten *et al.*, 2004).

The search for mineralisation in this Belt has not been successful because of several reasons such as, geological complexity (high-grade metamorphism, multi-phase deformation) and often remoteness of the terrain has contributed to the perception that the Mozambique Belt is of low potential and is difficult to explore (Forster *et al*., 2001). Nevertheless, different types of ore deposits such as disseminated low- to moderate-grade copper occurrences (Mozambique and Tanzania), massive copper and zinc–copper (eastern Zambia), hydrothermal alteration (Mozambique and southern Tanzania), late and post-tectonic mineralized granitoids and pegmatites have been reported (Forster *et al*., 2001).

2.4.5 Namaqua-Natal Belt

The Namaqua-Natal Belt wraps around the southern margin of the Kalahari Craton. It was formed during the mid-Proterozoic period (Kröner, 1978; Norman and Whitfield, 2006). Economically, the belt is mainly rich in copper mineralisation within the Okiep copper district on the western part of the belt. The copper mineralisation is hosted in mafic to intermediate rocks of the Koperberg Suite (Cornradie and Schoch, 1986). Metamorphism in this belt varies from greenschist to granulite facies. It is characterized by mineralized dioritic bodies hosted by large-scale folds that refolded the granite gneiss succession (Bevelander, 1994). Sulphide mineralisation occurs mainly as disseminations within diorite, formed through immiscibility and from late magmatically derived hydrothermal fluids (Wilson, 1998). The copper ore is dominated by pyrrhotite with less chalcopyrite and pentlandite. Clifford *et al*. (1995) recognized two types of mineralisation, namely: syngenetic and Hoit's type (remobilized).

2.4.6 Limpopo Mobile Belt

2.4.6.1 Geological and Structural Setting

The Limpopo Mobile Belt is a metamorphic belt of the early Proterozoic period (2000 Ma) which is between the Zimbabwean and Kaapvaal Cratons and it is separated from the cratons

© University of Venda

by two major thrust zones, the Limpopo thrust zone in the north and the Hout River Shear Zone in the South (Mason, 1973; Coward *et al*., 1976; Kramers *et. al*., 2006; Chinoda *et al*., 2009).

It has been interpreted as an Archaean collisional orogeny, comprising the North Marginal Zone (NMZ), Central Zone (CZ) and Southern Marginal Zone (SMZ) (Mason, 1973; Coward *et al*., 1976; Kramers *et. al*., 2006; Chinoda *et al*., 2009). The CZ is separated from the marginal zones by the dextral triangle shear zone to the north and the sinistral Palala shear zone to the south (Fig. 2.7). Deformation occurred at the CZ of high grade metamorphism (Chinoda *et al*., 2009).

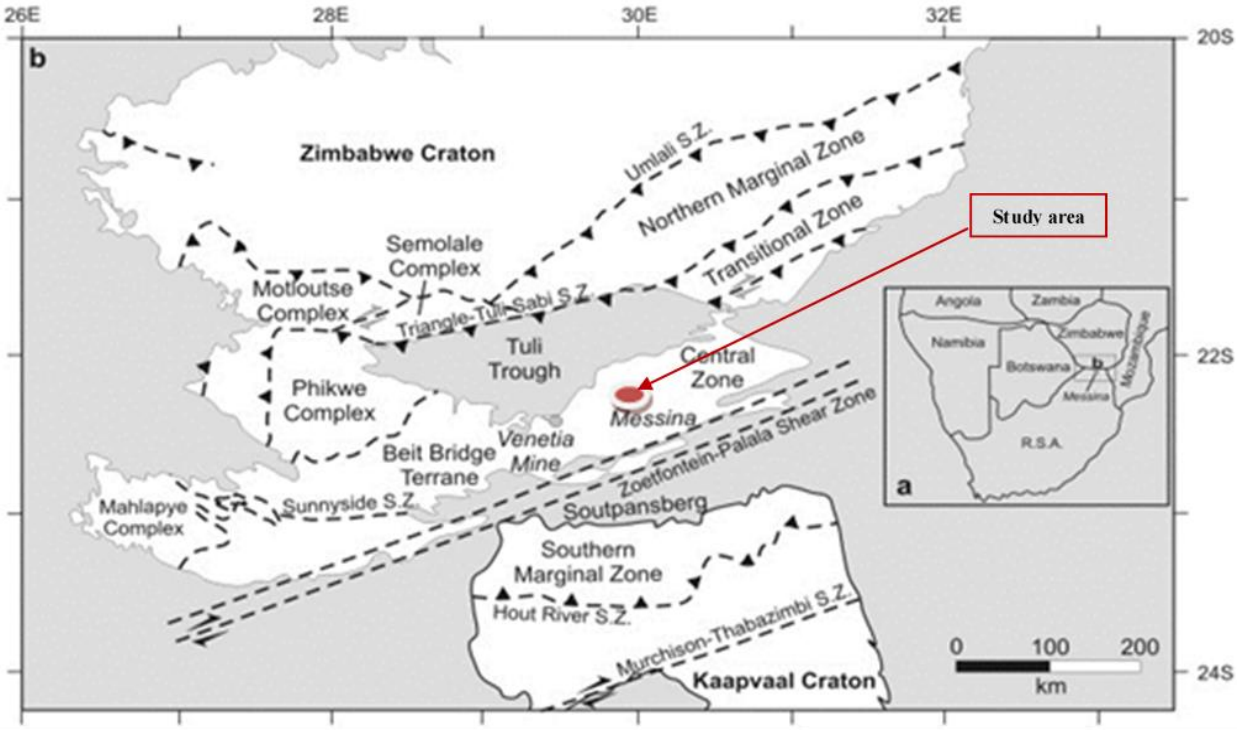


Figure 2.7: The Limpopo Mobile Belt and its three distinct zones (Rigby *et al*., 2011).

Northern Marginal Zone

The Limpopo Mobile Belt is a zone of complexly deformed Archaean gneiss units and rocks of high metamorphic grade. The NMZ is separated from the CZ by the Triangle Shear Zone, an approximately 20 km wide, shallowly south-dipping, dextral strike-slip feature dated at 2000 Ma (Kramers *et al*., 2011). The boundary between the NMZ and the Zimbabwe Craton has been defined as the orthopyroxene-in-iso-grad in felsic rocks (Kramers *et al*., 2011). The

© University of Venda

NMZ is dominated by granulite facies orthogneisses ranging in composition from quartz-diorite to trondhjemite, tonalite and granodiorite. These rock types were referred to as charnockite enderbite gneisses by Ridley (1992), who argued that they are magmatic rocks that crystallized under granulite facies conditions. The NMZ is mostly dominated by orthogranulites which accounts for over 90% of the surface area (Ridley, 1992).

Southern Marginal Zone

The SMZ is composed of the granulite facies of high-grade supracrustal gneisses of mafic, ultramafic and metapelitic composition known as Bandelierkop Complex that are tectonically mixed with the Goudplaats-Hout River gneiss comprising tonalitic grey gneiss (Van Reenen *et al*., 1990). The rock types forming the SMZ are interpreted to be the high-grade metamorphic equivalent of the adjacent granitoid-assemblage of the northern Kaapvaal Craton (Van Reenen *et al.,* 1990), which is similar to that of the NMZ and the Zimbabwe Craton.

Khoza *et al.* (2011) addressed several issues including the uncertainty of the nature of the geometry of the shear zones separating the cratonic units, and investigated the exotic terrain status of the Limpopo Belt, particularly for the CZ and pointed out that questions still remain regarding the timing of the metamorphic events (particularly in the SMZ), orientation and rate of plate movement in the Archaean period. The study based on all available data including new Magnetotelluric (MT) data, suggested that horizontal collisional movement is the most plausible of all the models that have been presented thus far (Khoza *et al*., 2011).

Central Zone

The dominant rocks in the CZ are of high-grade metamorphosed gneiss occurring in different forms: leuco-gneiss, quartz-feldspathic gneiss and granitic gneiss, and other rock types include: amphibolites, pyroxene granulite, metaquartzite, calc-silicate, magnetic iron formation and minor meta-sedimentary and marble, forming the Beit Bridge Complex (SACS, 1980; Bahnemann, 1986). The CZ has seven major lithological units arranged chronologically (Table 2.2).

© University of Venda

Table 2.2: Lithochronological units of the Central Zone (Kramers *et al*., 2006)

Unit	**Lithology**	**Age (Ga)**	**Interpretation**
7. Granitic melt patches	Granatic patches	2.0-2.01	Anatectic melts
6. Gumbu Group	Marble, calc-silicate rocks, minor metapelite and meta-greywacke	2.0-2.2	Mainly platform sediments
5. Tshipise and Venetia Gneisses (younger grey-gneiss and Zoetfontein gneiss)	Tonalitic and granatoids gneiss	2.45-2.52	Intrusive in Mount Dowe and Malala Drift suite
4. Quartz-Feldsparthic gneiss (Beit Bridge Complex) Alldayds and Verbaardgneiss	Interlayered Qtz-Fsp gneiss, Charnockitic gneiss, Tonalitic gneiss	2.56-2.68	Mainly anatecic melts Intruded in Beit Bridge, Complex
3. Messina Suite	Interlayered mafic rocks	3.15	Intruded as sills
2. Mount Dowe group and Malala drift suite	Quartzite, magnetite quartzite, metapelite, calc-silicate rock	3.3-3.15	Platform sediments
1. Sand River Gneiss	Banded tonalitic gneiss	3.2-3.4	Basement to meta-sediments

While various models are able to explain the geological features within the Limpopo Belt, there is no synthesis that can account for all the features within the belt (Kramers *et al*., 2006). Another obstacle is that, in the CZ the structures and metamorphic features have not been reliably discriminated as both were intense, thus there is no clear explanation of the way in which continental tectonics worked in the Archaean and early Proterozoic eras (Kramers *et al*., 2006).

The SMZ is absent in the western part and there is no clear zonation between the NMZ and CZ. The SMZ hosts the enderbitic gneiss with strongly developed E-W to ENE-WSW

© University of Venda

striking fabrics (Du Toit *et al.*, 1983), while the rocks of the NMZ strongly pronounced the ENE-WSW striking fabrics (Rollison and Blekinsop, 1995).

The CZ occupies the largest area within the belt with rocks of high grade metamorphism showing no uniform structural grain. The E-W and NE striking and closed structures are prominent and also show no uniform structural grain (Mason, 1973). Lithologicaly, South African Committee of Stratigraphy (SACS, 1980) divided the Beitbridge Complex into Mount Dowe, Malala Drift and Gumbu Group. However, owing to tectonism and metamorphism, it is still not clear if the boundaries between these units are stratigraphically controlled or tectonic in nature, consequently, all the units were grouped together as the Beitbridge Complex (Brandl, 2001). Krammer *et al*. (2006) pointed out that owing to the great structural complexity and widely prevailing high-grade metamorphism, stratigraphic relationship between the units in most cases cannot be readily defined.

Like the other metamorphic belts of the world, the Limpopo Mobile Belt is not highly mineralized, nevertheless it has a few deposits such as the Gumbu graphite deposit (CZ), small gold workings (SMZ), Pikwe nickel deposits (CZ-Botswana) and Messina copper deposits (CZ) (Wakefield, 1976; Gallon, 1986). The Renco deposit is an important gold producer in the NMZ of Zimbambwe (Kisters *et al.*, 1998; Blenkinsop *et al.*, 2004).

2.4.6.2 Copper-sulphide Mineralisation in Musina Area

The Messina deposits are located within the Central Zone of the Limpopo mobile belt. According to Söhnge (1945), Watkeys (1979), Bahnemann (1986) and Chamba *et al.* (2016), the granodioritic and tonalitic orthogneisses form the basement rocks in the area, being overlain by metasediments and leucogneisses, garnetiferous schists, amphibole and pyroxene granulite, metaquartzites, calc-silicates and iron formation, forming a structurally complex suite of lithologies resulting from multiple folding and metamorphic crystallization (Figs. 2.8 and 2.9).

© University of Venda

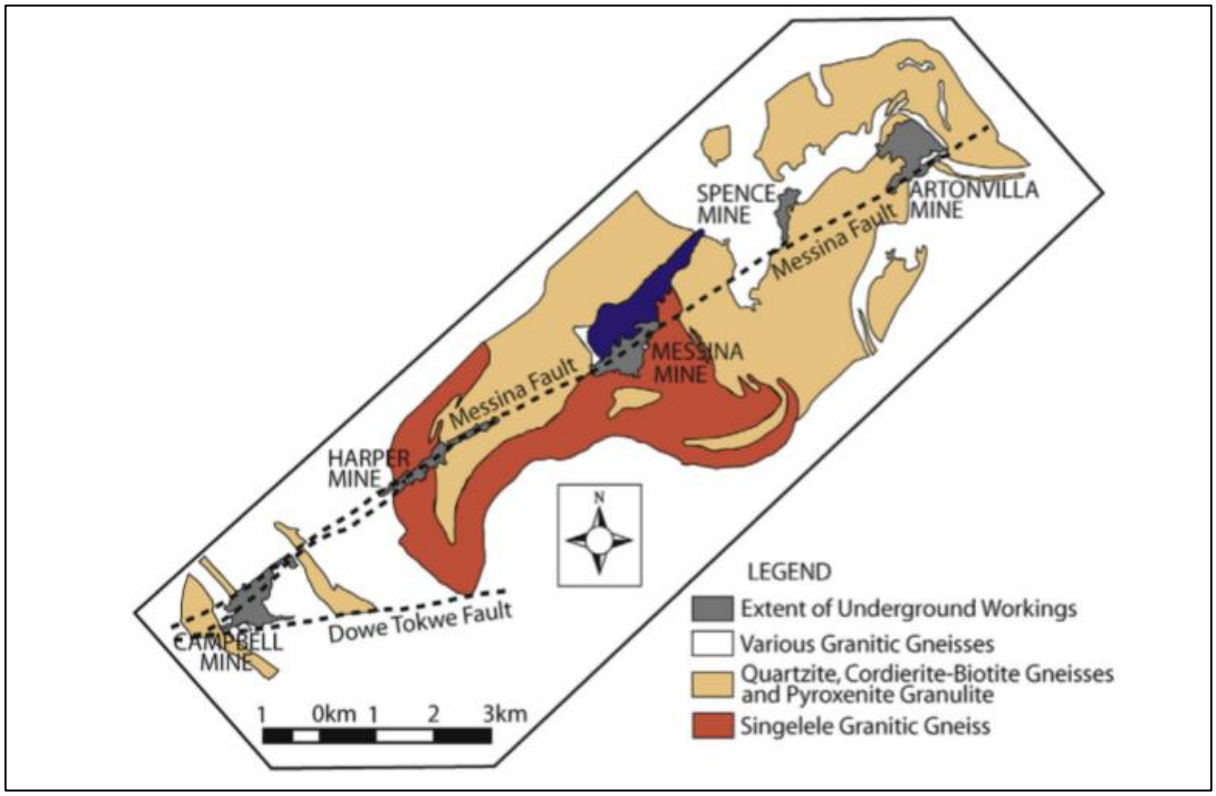


Figure 2.8: General geology in the vicinity of the Messina copper deposits (Bahnemann, 1986; Chaumba et al., 2016).

The Singelele granitic gneiss that has been dated at 2647 Ma (Zeh *et al.*, 2007) occur within the vicinity of Messina copper deposits (Fig. 2.8). Earlier, Söhnge (1945) noted that the Messina copper-sulphide mineralisation lies along or close to the northeast striking Messina fault and is hosted in the meta-quartzites, amphibolites, biotite-hornblende gneisses and rocks associated with Mount Dowe Formation of the Beitbridge Complex.

Bahnemann (1972) had noted that the basement rocks consisted of pyroxene tonalities, overlain by complexly folded metasediments, while the rocks in contact with the orebodies had been metamorphosed to granulite and amphibolite facies.

Jacobsen and McCarthy (1976) had noted that lower-grade metamorphism associated with mineralisation resulted in prophylitic hydrothermal alteration. Contact metamorphism is generally a common feature with hydrothermal ore mineralisationn. A similar case had been noted at the Macalder copper deposit in Kenya, where for instance, copper sulphide mineralisation was accompanied with intense chloritization (Ogola, 1987).

© University of Venda

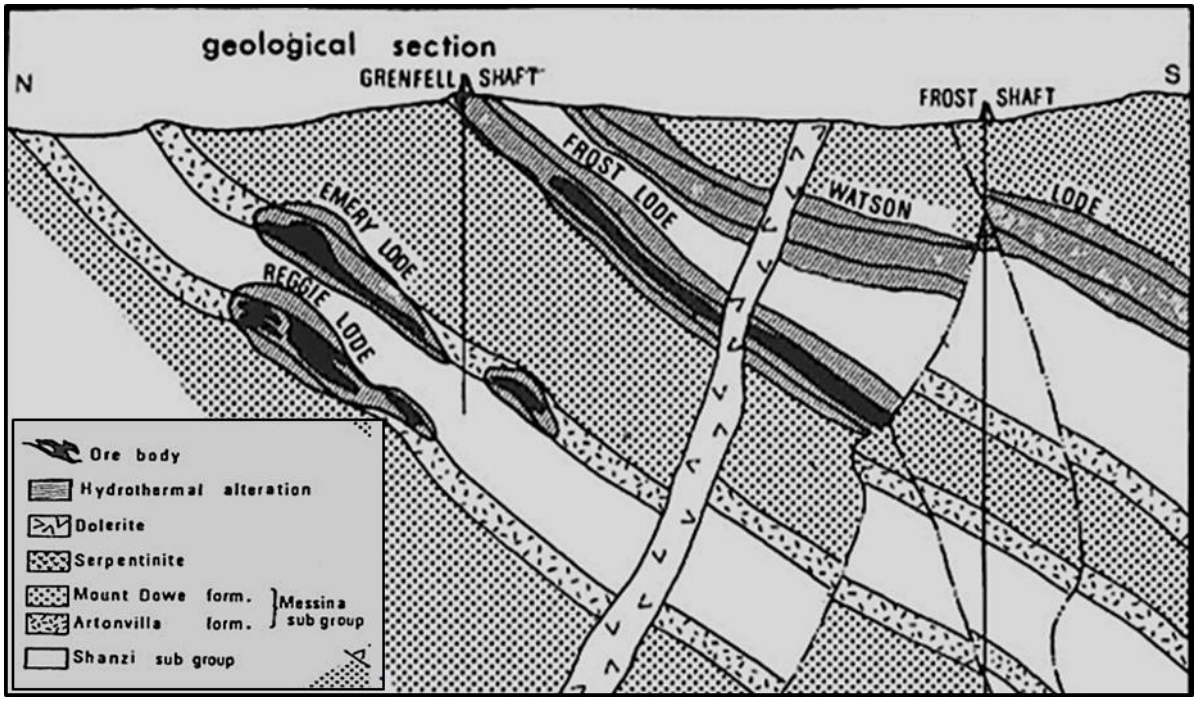


Figure 2.9: Geological cross-section through the Frost and Grenfell shafts at Artonvilla mines (Jacobsen and McCarthy, 1976).

The Messina suite includes intrusive rocks of ultramafic and anorthositic to gabbroic composition that occur as layers or lenses in the supracrustal succession (Brandl, 1981). These intrusive rocks of late Karoo age occur close to and within the mine area (Figs. 2.8 and 2.9). Cox *et al.* (1965) had referred to these intrusive rocks as the Nuanetsi Igneous Complex and were considered by other researchers to be the intrusive event that introduced the copper mineralisation (Jacobsen, 1967; Jacobsen and McCarthy, 1975 and 1976).

Radiometric age dating of these rocks gave 3 150 Ma (Barton *et al.*, 1979a). These apparently, were earlier intrusive rocks. The ultramafic intrusive rocks that apparently were of post-Karoo in age and that are associated with ore mineralisation occurred much later. Dating of later intrusive rocks as well as orebody is essential for understanding the processes of ore formation in this area.

The deposits are known to have been formed long after the tectonic events which resulted in the intense deformation and high grade metamorphism of the host rocks (Söhnge, 1945; Wilson, 1998). The origin of the Messina copper-sulphide deposits remains contentious. Some researchers attribute their formation to hydrothermal replacement ores, forming pipe-

© University of Venda

like breccia bodies exhibiting collapse features and associated mineral fractures and fissures (Jacobsen, 1974; Jacobsen and McCarthy, 1976; Jacobsen et al., 1976), while others support the meteoric source of hydrothermal source (Sawkins, 1977; Sawkins and Rye, 1979). Jacobsen (1974) noted that the orebodies had been structurally controlled mainly by wrench fault systems. Cairncross (1991), however, noted that shapes of the individual orebodies were influenced by the fold structures, fracturing and the nature of the lithologies.

Copper-sulphide mineralisation within the Messina deposits occurred as chalcopyrite, bornite and chalcocite. Jacobsen and McCarthy (1976) noted sulphide changes which display a zonation from an outer pyrite zone, through chalcopyrite and bornite to chalcocite and occasionally to native copper in the core. Jacobsen and McCarthy (1976) concluded that at the Artonvilla deposit, there was a single hydrothermal fluid that was introduced into the Archaean rocks, eroding the structural traps at a temperature in excess of 650^{o}C and passed through the rocks down to a temperature gradient of 400^{o}C at the outer extremity, resulting in well-developed zonation. They equilibrated the central parts of the orebody at temperature range of 140^{o}C to 280^{o}C.

It was noted that host rock alteration followed zonation of the sulphides by an increase in hydration of silicate minerals, leaching of quartz and development of albite, zoisite and epidote leading to the complete destruction of the host rock (Cairncross, 1991).The Messina copper deposits consisted of breccia pipes, disseminated and veined ores. The main copper deposits were at Artonvilla, Messina, Harper, Spence and Campbell deposits.

2.4.6.3 Mining History of Musina Copper-sulphide Deposits

The line of rich copper outcrops was originally discovered several hundred years ago and exploited by the "Ancients." Later, those people were overran by the Bantu who took over the workings and produced copper artifacts. In 1903, Colonel John P. Gremfell, the founder of the Messina (Transvaal) Development Company Limited, was shown the workings and was sufficiently impressed to prospect some of them (Van Graan, 1964). Modern exploitation began in 1906 and a number of mines were operated around the area. They started to produce about 14,000 tons of ore per annum. Ore reserves by 1960 were given at 6, 374, 570 tons at 1.61% copper (Pelletier, 1964).

© University of Venda

The operated five mines in the area, from east to west, were Artonvilla, Messina, Harper, Spence and Campbell deposits (Pelletier, 1964). They are located at a distance of about 5 km from each other along the Messina fault. The oldest mine in the area is the Messina mine and the latest to be mined was the Artonvilla deposit (Pelletier, 1964; Wilson, 1998).

In 1992, the last mine, Messina-No. 5 shaft stopped production and was closed down. This ended about 88 years of copper mining in the region. At the time of closure, the mines had produced a total of 42 Mt of ore and 0.75 Mt of copper (Wilson, 1998). There is no clear evidence as to why the mines were closed. Some members from the nearest settlement (Lost City) gave the information that the mines were closed after former President, Nelson Mandela, was released from prison in 1991, thus the closure of the mines was political. If this was the case, then the Messina deposits have the potential for future exploitation.

© University of Venda

CHAPTER 3

METHODS

Preamble

This chapter discusses the steps, procedures and briefly outlined the different methods applied throughout the research work. The study was divided into four main phases to ensure that the research work was efficiently and effectively executed. The four phases were categorized into: Preliminary work which involved desktop study and reconnaissance survey (Phase 1); Fieldwork (Phase 2); Laboratory work, data acquisition, data analysis and interpretation as well as discussion (Phase 3); Conclusions and future research directions (Phase 4) (Fig. 3.1).

Phase 1 was a preparatory stage, while Phase 2, which was fieldwork, focused on soil geochemical survey, rock and ore specimen sampling. Phase 3 that include laboratory work that consisted of sample preparation and analysis for different purposes such as geochemical, petrographic, ore microscopy, cathodoluminescence, fluid inclusion, and isotopic studies. At this phase, data acquisition, analysis and interpretation were conducted ending with discussion. The last phase include conclusions and future research direction (Phase 4). Further in this chapter, a brief explanation of the methods (Geochemical, Remote sensing, petrographic, ore microscopy, cathodoluminescence, fluid inclusion, and isotopic studies) used was done while the detailed explanation of each method is given in the respective chapters.

3.1 Preliminary Work

3.1.1 Desktop Study

Desktop study involved preparatory work that was executed in order to gather materials and information relevant to the work. This included literature review comprising books, technical reports and journals. Satellite images, aerial photographs and different types of maps such as topographical maps (1:50, 000) and geological maps (1:50, 000) were reviewed.

© University of Venda

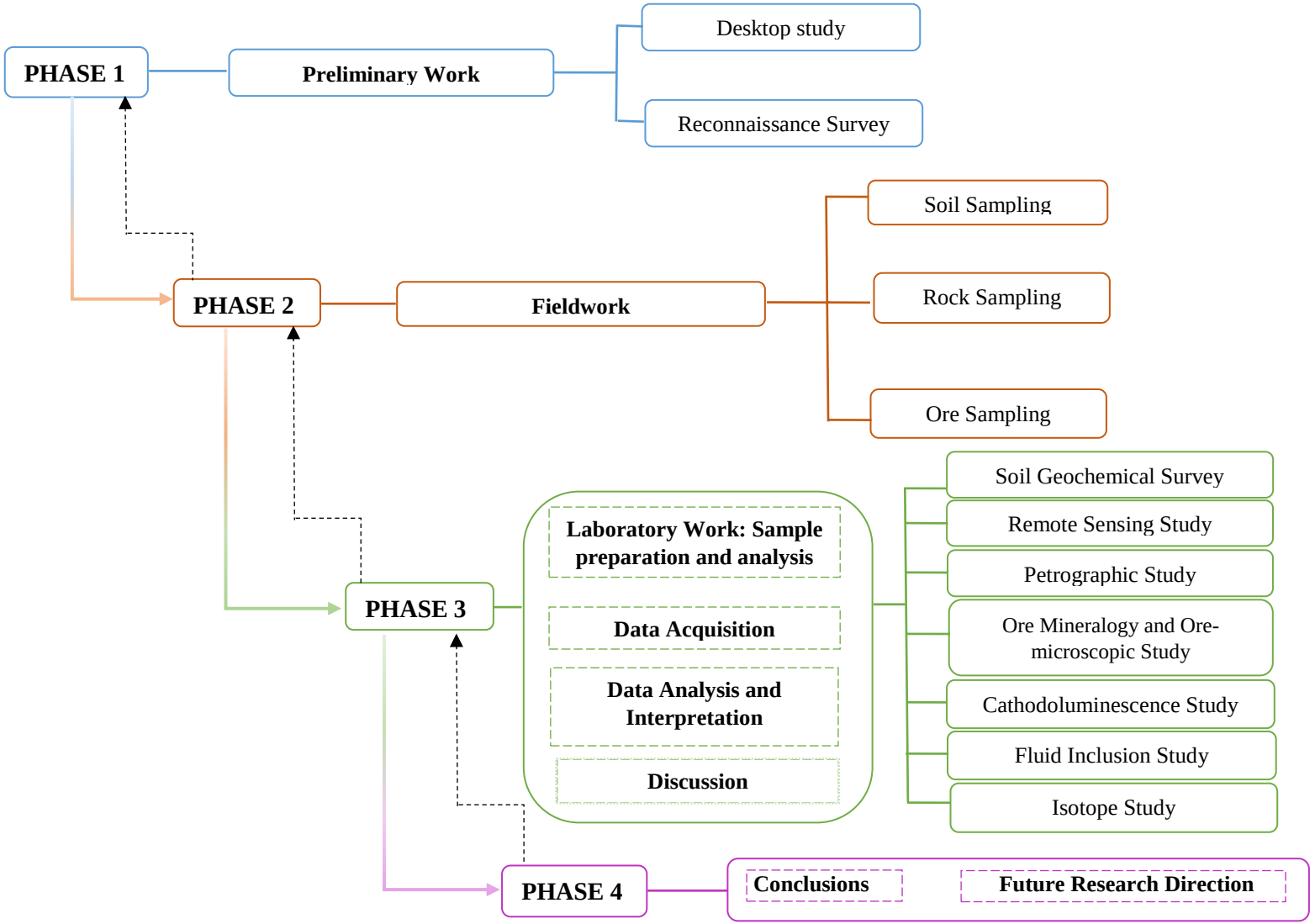


Figure 3.1: Flow chart depicting the sequence of work undertaken during the study.

© University of Venda

Furthermore, information regarding the types of software that could be used to process and interpret the data was also reviewed during this stage.

3.1.2 Reconnaissance Survey

Reconnaissance survey was a second stage in phase 1. This stage was conducted prior to embarking on fieldwork. It is necessary to conduct reconnaissance survey in order to get an overview and to familiarise oneself with the study area. Musina is an area that consists mainly of private farmlands and game reserves and it is also bordering Zimbabwe. Consequently, it was important at this stage to seek permission from a number of stake-holders before carrying out actual fieldwork, thus the local municipality, boarder security, farm owners and local communities were consulted. During this stage, the geological setting and physiography; topography; drainage pattern; soil and vegetation types; and land-use were investigated.

3.2 Fieldwork

Phase 2 involved fieldwork which entailed geochemical survey comprising soil sampling, rock and ore sampling within the study area. This phase was divided into two main stages, viz: soil, rocks and ore sampling on the western side of the Musina town (stage 1) and soil, rocks, and ore sampling on the eastern side of Musina town (stage 2). The work was carried out from February to November 2012, from June – November 2013 and March – July 2014.

3.2.1 Geochemical Soil Sampling

Soil sampling was conducted using systematic sampling method along designed traverses across the general strike of lithologies, covering about 60 km^2 (12 km x 5 km) of the entire study area. Profiles were sited at an interval of 500 m and sampling interval of 500 m. Following a sampling procedure set by the International Union of Geological Sciences (IUGS)/ International Association of Geochemistry (IAGC) Task Group on Geochemical Baselines (2015), Harris (2007) and Landon (1984), about 2 kg of soil sample was collected from the B-horizon at a depth of about 10 -15 cm using hand shovel (Fig. 3.2). This horizon is likely to host any weathered material from the mineralised rocks. The collected soil

© University of Venda

samples were put in the sample bags and labelled accordingly. The sample bags were properly sealed to avoid cross-contamination.



Figure 3.2: Photographs showing soil sampling procedure in the field.

Although systemic sampling method was adopted along specific profiles for soil sampling, it was difficult to apply this method in some areas due to settlement, roads, private farms and game reserves that were not accessible. In such cases, random sampling was adopted. Areas such as the top northeastern and bottom southwestern sides were not sampled, as the area comprised of game reserves and private farmlands.

At the point of sampling Garmin etrex 30x Geographical Position System (GPS) was used for determination of co-ordinates and elevation readings, which were then recorded in a note-book together with physical characteristics such as soil type, colour, texture and vegetation types of the area around the sampling points (Appendices 3AI and 3AII). After collection of

© University of Venda

each sample, the dug area was rehabilitated (Fig. 3.2). From the western side (Campbell) and eastern side (Artonvilla) of the study area, 102 and 193 soil samples were collected respectively giving a total of 295 samples collected from the entire study area.

3.2.2 Rock Sampling

During this stage, host rocks associated with ore mineralisation were collected randomly from the waste rock dumps of the Campbell and Artonvilla mines (Fig. 3.3) as mining stopped and closed in 1992 and it was not possible to sample mineralised rock insitu. An attempt to collect mineralised samples from Council for Geoscience that is the custodian of previous mineral collections and from other sources failed.



Figure 3.3: Waste rock dump at Artonvilla mine.

A total of 33 fresh rock specimens were collected from both mines with 14 from Campbell and 19 from Artonvilla (Appendix 3BI and 3BII). Collected samples were used for thin-section preparation for petrographic study and for geochemistry investigation, and some of the specimen were used for sulphur isoptope geochemistry study. When undertaking sampling, specimen description was done focusing on the physical properties of rocks, including colour, competency, texture, structure, and sulphide mineralisation and these data were then summarised (Appendix 3BI and 3BII).

© University of Venda

3.2.3 Ore Sampling

Ore samples were collected from the waste rock dumps at Campbell and Artonvilla (Fig. 3.3) copper mines, since the mines have ceased operations. About 2 kg of fresh ore samples that are mineralised were collected randomly from the waste rock dump. At this stage, a total of 21 ore samples were collected whereby 13 and 8 ore samples (Appendix 3CI and 3CII) were from Campbell and Artonvilla mines respectively. The ore samples were characterised using physical properties that included colour, texture, structures, mineralogy in terms of types of minerals and content of sulphide mineralisation within each sample (Appendix 3CI and 3CII). All samples were then numbered and packaged accordingly and ready for polished ore sample preparation for the purpose of ore mineralogy and ore microscopy study and other samples were ready for milling so as to be used for XRF and XRD analysis in chapter 7, while other samples were used for the preparation of double polished thin sections for the purpose of both Cathodoluminescence and fluid inclusion study in chapter 8 and 9 respectively.

3.3 Laboratory Work

Laboratory work comprised a range of methods including geochemical analysis, petrographic and cathodoluminescence microscopy, ore mineralogy and ore microscopy, fluid inclusion geothermometry and isotope geochemistry.

3.3.1 Geochemical Analysis

Geochemical analysis involved several laboratory techniques including; Atomic absorption spectrometry (AAS), X-ray fluorescence spectrometry (XRF), X-ray Diffractometry (XRF) and Scanning electron microscopy (SEM). Flame Atomic absorption spectroscopy was used for the determination of the concentration levels of Pb, Zn, Cu, As, Mo, Ni, Cd, Co, Cr and Mn in soils and ore samples so as to determine the occurrence and distribution of metals within the samples, elements associated with copper and to generate target areas for further exploration purposes.

© University of Venda

The Atomic absorption spectrometry technique assess the concentration of an analyte in a sample. It requires standards with known analyte content to establish the relation between the measured absorbance and the analyte concentration. The wavelength is specific to a particular electron transition in a particular element thus each wavelength corresponds to only one element, and the width of an absorption line is only of the order of a few picometers (pm), which gives the technique its elemental selectivity (Ferreira *et al.,* 2018; Skoog *et al.,* 2007). The details on the preparation of samples and principles for this method was fully discussed in geochemical survey in Chapter 4.

XRF spectroscopy method was used for the determination of both major oxides and trace elements within rocks and ore samples of the Messina copper deposits. The analysis of major and trace elements in geological materials by X-ray fluorescence spectrometry is made possible when atoms interact with radiation (Watson, 1996; Ichikawa *et al.,* 2019). The details of this method is explained in petrological investigation (Chapter 6) and also in ore mineralogy and ore microscopy (Chapter 7).

A primary use of the X-ray diffraction technique is the identification and characterization of compounds based on their diffraction pattern (Potts, 1987; Dinnebier and Friese, 2018). In this study, XRD spectrometry was used for the determination of the mineral composition of the ore samples so as to identify different minerals occurring in Messina copper ores. This method was applied in ore mineralogy and ore microscopy, wherein its principles, and procedure are explained.

Scanning electron microscopy (SEM) was used do to determine the surface topography or morphology and composition of the ore samples with a better resolution of less than one nanometer. This is achieved when electron microscope produces an image of a sample through scanning the surface of the sample by a beam of electrons which then interact with atoms and then the various signals that contain information about the sample are produced (Butterfield *et al.,* 2017; Mignot, 2018).

© University of Venda

3.3.2 Petrographic Microscopy

Petrographic microscopy is one of the most useful methods applied in geological research. This method is widely used for different purposes such as characterization of rocks and minerals. It involves geochemical analysis that entails mineralogical and elemental investigation of rocks so as to infer the rocks formation processes. Petrographic microscopy uses optical microscopy to identify rock forming minerals in thin sections. The microscope uses transmitted light that is refracted through the thin section for rock forming minerals identification. For ore minerals identification, the ore microscope is used and it uses incident light ray that is reflected back from the polished surface sample for ore minerals identification (Craig and Vaughan, 1994; Wenk and Bulakh, 2008).

In this study, dual petrographic microscope that uses both transmitted and reflected light was used to characterize and identify both rock forming and ore minerals, so as to characterize different rock types and ore minerals forming the Musina copper orebodies. This was important in understanding the geological setting of the host rocks and mineralisation style of the Messina copper deposits.

3.3.3 Cathodoluminescence Microscopy

Cathodoluminescence (CL) is one of the geoscience field with most common luminescence phenomena that is used both in a purely descriptive way to detect and distinguish different minerals or mineral generations, zonation of crystals, textural relationships among minerals, and brittle deformation of mineral grains (van den Kerkhof, 2003; Rusk, 2012; Frelinger *et al.*, 2013; Agangi *et al.*, 2016). In this study, Cathodoluminescence (CL) study of CL minerals was undertaken such as quartz and calcite associated with Campbell and Artonvilla ore mineralisation so as to characterize the Cathodoluminescence in terms of their generation, crystal zonation and micro-textural relationship. This was done so as to interpret the mineral forming processes and to decipher the genesis of the deposits.

Detailed explanation on this method together with detailed work on cathodoluminescence study of the Campbell and Artonvilla minerals that are associated with mineralisation was discussed in Chapter 8.

© University of Venda

3.3.4 Fluid Inclusion Geo-thermometry

Fluid inclusion studies have over the last 30 years evolved into one of the fundamental tools for understanding the genesis of hydrothermal ore deposits (Wilkinson, 2000). Fluid inclusions are tiny remnants of bubbles of liquid, gas and 'daughter' minerals of the exact fluid from which the host mineral and its associated ore minerals were derived from. Fluid inclusions provide information about the fluid mineral composition, temperature and pressure at which the hydrothermal deposit formed (Ogola, 1985; Misra, 2000; Wilkinson, 2000; Van den Kerkhof and Hein 2001; Santosh and Omori, 2008; Xu et al., 2016; Li, *et al.,* 2018).

In this study, fluid inclusion petrography, geothermometry and geochemistry was performed, using BH-2 Olympus standard petrographic microscope, Linkam THMS 600 heating and freezing stage, and Horiba Jobin Yvon LabRam HR800-UV Raman spectrometer respectively. Details of these techniques are discussed in Chapter 9. These techniques were used for the determination of occurrence and distribution, temperature, pressure, and composition of fluid inclusions so as to unpack the genetic processes of the Messina copper deposits.

3.3.5 Sulphur Isotope Geochemistry

Isotope geochemistry is a discipline of geology based upon the study of relative and absolute concentration levels of the elements and their isotopes in the earth. The variation in concentration levels of the isotopes reveals the information about ore genesis (Sharp, 2007; Allègre, 2008; Liu, 2016). Both stable and unstable isotopes have been applied in the deciphering of ore processes and ore genesis. Unstable isotopes decay over time while stable isotope's concentration remains constant for a long period of time. The understanding of the origin and evolution of sulphide minerals is revealed from variations of the isotopic composition of sulphide minerals and related compounds such as sulphate minerals or aqueous sulphate species (Cloutier *et al.,* 2015; Lode *et al.,* 2017). Consequently, the sulphur stable isotopes were investigated for the purposes of interpretation of ore forming processes hence deciphering ore genesis. Sulphur isotopes ($\delta^{32}S$ and $\delta^{34}S$) were used as the Messina copper ore deposits are associated with sulphide mineralisation that contains sulphur.

© University of Venda

A study on sulphur isotope geochemistry of the Campbell and Artonvilla copper deposits was undertaken in Chapter 10, wherein the method and application is discussed in detail.

3.4 Remote Sensing

Besides laboratory techniques, remote sensing technique was also used in the study. The use of remote sensing data increases the efficiency of field work, especially in areas with difficult access or where geologic fieldwork is expensive or hazardous (Kariuki *et al*., 2004; Zumsprekel and Prinz, 2000; Ngcofe, 2010;; Reif *et al*., 2011; Ali, 2017). In this study, ASTER imageries were used for mineral alteration and structural investigation associated with the Messina copper-sulphide mineralisation. The method was used for ore mineralisation within Musina area and its srroundings.

ASTER imageries were processed using ENVI 5.1 and ArcGIS 10.4.1 computer software programmes. Band combination for data manipulation, band rationing for image enhancement, unsupervised classification technique, both visual and digital analysis, and ground-truthing were done. Visual analysis was done to identify the mineral alteration distribution, identification of geological structures and correlating of mineral alteration and lineaments using ASTER and Digital Elevation Model (DEM).

Detailed information on fundamentals and principles of remote sensing, data acquisition, processing and analysis, results and interpretation as well as discussion of the outcome is discussed in Chapter 5.

3.5 Data Quality Management and Assurance

According to Ballinger and Shugar (2011), quality assurance plans and quality control programmes are the key components of all analytical protocols in all areas of data analysis including geochemical, environmental, pharmaceutical and forensic. Quality assurance plans and quality control programmes mandate that every laboratory follow a set of well-defined guidelines so as to achieve analytical results at a high degree of accuracy (Ballinger and Shugar, 2011). Consequently, in this study, quality control measures were taken seriously during sampling and sample handling, preparation and analysis. Calibration of the equipment

© University of Venda

was always taken into consideration, reference standards were used and analysed, blanks, analytical precision and sample analysis were executed in triplicate and the mean value was used. Validation and ground-truthing methods were also used to ensure quality. Quality control and assurance were fully explained for each technique in the respective chapters.

© University of Venda

CHAPTER 4

GEOCHEMICAL SURVEY

Preamble

This chapter deals with the determination of concentration levels of metals in soil within and around the Messina copper deposits. The chapter gives a review on the following: importance of geochemical survey in mineral exploration; the use of geochemical survey as a tool in mineral exploration; pathfinder elements for copper; laboratory techniques generally used for soil analysis; and methods used for data analysis and interpretation. After a review, the chapter presents the geochemical survey of the Musina, incorporating the following: specific objectives; soil sampling; sample preparation and analysis; quality control and assurance; data analysis and interpretation; and discussion.

4.1 Importance of Geochemical Survey

Geochemical survey is a common method used for mineral exploration and plays a relatively crucial role in this regard. It involves generation of concentration values that helps in discovering buried deposits. Large amounts of chemical substances in the environment mainly from both natural and anthropogenic sources have caused enrichment of some elements or metals above the geochemical background concentrations within soils, sediments, and water. This often results into geochemical anomalies of such elements or metals and this has become an essential part of geochemical and environmental research.

Geochemical survey has been widely used both regionally and locally. Regionally, it has been referred to as geochemical baseline survey. The first application of the concept of geochemical baseline survey to geochemistry was during geochemical prospecting purposes where the role was to provide information on the distribution of the chemical elements. Thereafter the term ‘geochemical baseline survey was officially introduced in the year 1993 in the context of the International Geological Correlation Programme (IGCP project). This was done in order to create a global reference network for national regional geochemical datasets and as international background data for environmental legislation. Geochemical

© University of Venda

baseline refers to the variation in the concentration of elements in superficial environment (Darnley *et al.*, 1995; Salminen and Tarvainen, 1997; Salminen and Gregorauskiene, 2000).

Locally, geochemical survey has been widely applied for chemical analysis of systematically collected samples such as rocks, soil, stream sediments, water and plants so as to determine the distribution of elements within an area for the purpose of locating geochemical anomalies. Geochemical background has been defined in many different ways (Levinson, 1980; Beus and Grigorian, 1977; Rose *et al.*, 1979). The most common definition is the natural abundance of an element in a particular environmental compartment such as soil, sediment or rock with reference to a particular area or dataset. It is usually expressed as a single value showing the threshold between anomalous and background concentrations. Some authors use different terms instead of geochemical background and some few examples include; natural background, ambient background and preindustrial background (Reimann and Garret, 2005); and others include: anthropogenic background, area background, naturally occurring background, and pedogeochemical background (Gałuszka, 2007); Gałuszka and Migaszewski, 2011).

In many developing countries, geochemical mapping is now an integral part of strategic systematic geoscience surveys aiming to produce geochemical data (Plant *et al.*, 1996) with South Africa being one of the countries. These geochemical data can be used for several applications such as mineral exploration, environmental management, environmental legislations, epidemiological studies, improving the efficiency of agriculture, and supporting land-use planning because they give the basis of sources of heavy metals, which can be either natural or anthropogenic (Halder, 2018; Li, 2014; Kelepertzis, 2013; Antibachi, 2012; Severson and Tidball, 1979).

4.2 Geochemical Survey as an Exploration Tool

Pedo- or soil geochemical surveying technique is one of the most widely used methods for exploration of hidden ore bodies, for example, for determination of targets for geochemical exploration (Sadeghi, *et al.*, 2015; Randive, 2012, Megan *et al.*, 2002). Where the parent rock is mineralized, some kind of chemical dispersion is always found in the residual soil that results from weathering of the bedrock. The residual soil surveys are most commonly applied in the areas of deep soil cover where the outcrops are scanty and weathering is intense. Any

© University of Venda

metal can disperse and show anomaly in the soil, however, immobile elements such as Pb, Mo, Pt, As, Cu, Cr show more pronounced anomalies (Randive, 2012; Podlešáková, *et al.*, 1999).

The geochemical survey data are also useful in the determination of pathfinder elements that can be used in mineral exploration to effectively narrow down the study area for many different types of ore deposits. For example, recently, Martin *et al.* (2016) used geochemical data for baseline geochemical soil survey in Southern New Zealand. Almasi *et al.* (2017) conducted a study on geochemical soil survey for gold exploration in gold deposits in Saqez-Sardasht Goldfield, Iran. Several regional, national and continental-scale geochemical soil surveys have been conducted in several parts of the world (Martin *et al.*, 2016), which include Africa (Chon and Hwang, 2007; South Africa (Sadeghi *et al.*, 2015; Ogola *et al.*, 2011).

Target generations for ore deposits in conjunction with baseline geochemical survey is one of the area where South Africa is concentrating on in terms of exploration. Most work is done under the Medium -Term Expenditure Framework (MTEF) project conducted by Council for Geoscience (CGS) of South Africa. This is done so as to stimulate investment in exploration/mining in South Africa by providing new high quality geochemical data and maps as well as mineral prospectively maps (maps showing areas of mineral potential). For example, several authors have published articles on this matter (Bensid, *et al.*, 2016; Billay, 2016; Carranza *et al.*, 2015; Ndlalose *et al.*, 2015).

4.3 Pathfinder Elements for Copper

A pathfinder element is an element that gives clues into the possible presence, and location of a specific type of mineralisation. Pathfinder elements can be used in mineral exploration to effectively narrow down the study area for many different types of ore deposits. Environmental compartments such as soils, rocks or sediments are either geochemically tested or visually inspected for clues into the distance and direction of the explored deposit. Most commonly, pathfinder elements are used in the search for gold, diamond, copper and nickel deposits, Platinum Group Metals (PGM), porphyry copper deposits, massive sulphide deposits, and tungsten deposits (Toovey, 2011).

© University of Venda

Copper is a chalcophile (high affinity for sulphur) element and is genetically associated with other Sulphur metals such as nickel, lead, zinc, arsenic, cobalt, cadmium, gold. Yet, because the presence of copper deposits at Musina area are known and proven to be existent, possibility of finding the copper associative elements in environmental compartments is pronounced and the finding of these elements in the study area will undoubtedly confirm the relationship between copper and those elements.

4.4 Laboratory Techniques

Preferred methods of analysis for geological materials (rocks, soils and sediments) have been used in several research activities such as Atomic Absorption Spectrometry (AAS), X-ray Diffraction Spectrometry (XRD), Induced Coupled Plasma Atomic Emission Spectrometry (ICP AES), X-Ray Fluorescence Spectrometry (XRF), Induced Coupled Plasma Maas Spectrometry (ICP MS). Imamalipour and Mousavi, 2017; Farber *et al*., 2016; Toulkeridis *et al.*, 2015; Mundalamo and Ogola, 2012; Ogola and Mundalamo, 2011; Mokhtari *et al.*, 2009). The work done by Geological Survey of Finland in partnership with State Company "Mineral", from Russia on Geochemical Atlas of Northern Europe in 2009, also clearly indicated different sample media, how they were prepared, which analytical method was used and which elements were analysed by each method (Salminen, 2009). In this study, AAS method was used for the determination of the concentration levels for soils because analyse elements even at less than 10 ppm and possibly in ppb. It easy to use, high precision, inexpensive technique and readily available (Potts, 1987).

Atomic Absorption Spectrometry

AAS is a technique for determining the concentrations of a particular element in a sample. It is a standard laboratory analytical technique in which trace elements in solution are measured in elemental form in a flame (Potts, 1987). When small numbers of samples for few elements are analysed, AAS is more appropriate than other analytical techniques such as XRF and ICP MS.

The technique makes use of absorption spectrometry to measure the concentration of an analyte in a sample. It requires standards with known element content to establish the relationship between the measured absorbance and the metal concentration and relies

© University of Venda

therefore on Lambert-Beer's Law. The electrons of the atoms in the atomizer can be promoted to higher orbitals for a short period of time by absorbing a defined quantity of energy (radiation of a given wavelength). The amount of wavelength is specific to a particular electron transition in a particular element thus each wavelength corresponds to only one element, and the width of an absorption line is only of the order of a few picometers, which gives the technique its elemental selectivity (Skoog *et al.*, 2007).

Since samples are usually liquids or solids, the sample atoms or ions must be vaporized in a flame or graphite furnace. The mirrors (labelled M Fig. 4.1) are rotated to measure original and the absorbed light characteristics. The path that is deflected away from the flame (labelled as unaltered energy path, Fig. 4.1) measures the unaffected light intensity. The path that goes through the flame (labelled as absorbed energy path) measures the intensity of the light after it has passed through a burner containing the co-injected dissolved sample and then detected. Finally, the concentrations are determined from a working curve after calibrating the instrument with standards of known concentration (Worden, 2005).

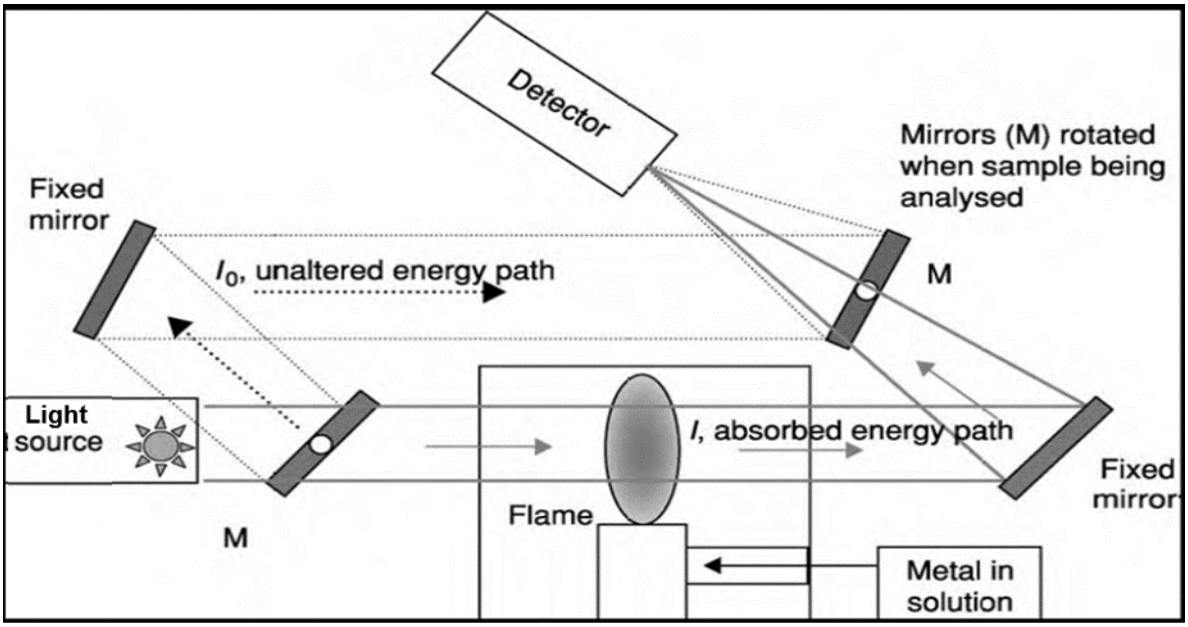


Figure 4.1: Simple illustration of basic principles and components of atomic absorption spectrometry equipment (Worden, 2005).

© University of Venda

4.5 Methods for Data Analysis

Several methods have been used for data analysis and interpretation for concentration levels of various elements for the development of geochemical maps, which could be used either for exploration purpose or environmental management and epidemiological studies. These methods include: basic statistical and geostatistical methods such as determination of maximum, minimum, mean and standard deviation values; percentile statistics (Sheppard *et al.*, 2009); Principal component analysis; box plots; histogram plots (Sheppard *et al.*, 2009; Michael, 2008; Unwin, 2008; Unwin *et al.*, 2008). Correlation coefficient factor method (Yaylali-abanuz and Tüysüz, 2011; Seyoum, 2006; Rollinson, 1993); Cumulative distribution function plots (Khalil *et al.*, 2013; Olea, 2008), Interpolation maps using kriging methods (Zuo and Wang, 2016; Sheppard *et al.*, 2009; Peters, 2008; Olea, 2008; Burrough and McDonnell, 1998; Burrough, 1986). In this study basic statistical methods were used such as maximum, minimum, mean and standard deviation values and histogram plots; and geostatistical method such as kriging for interpolating maps.

4.5.1 Basic Statistical Methods

Multi-elemental data from geochemical survey can be analysed using standard or basic statistical method to express the characteristics of each element. This is achieved through determination of frequency distribution, maximum, minimum, range, median, mode and mean of the sample population that helps in deducing the background, threshold and anomalous values (Habibzadeh, 2017).

Range

Range refers to the difference between the largest and smallest observed values of each sample. The range is determined using equation 4.1.

Range (r) = Max. Observed – Min. Observed value Equation 4.1

Mean

Mean is determined by summing the observed values of the samples and dividing by total number of the samples (Equation 4.2).

© University of Venda

Mean $(m) = \sum(x_1 + x_2 \ldots + _n) / n$ Equation 4.2

Whereby; Σ = means sum across the values

x = observed value of each sample

n = total number of samples

Variance

Variance describes the relationship between the distribution of a set of numbers and their average value, i.e. it measures how far a set of random numbers are spread out from their average value.

Standard deviation

Standard deviation (σn) is defined as the standard deviation error of each sample. Determination of standard deviation is deduced by using equation 4.3.

Standard Deviation $(\boldsymbol{\sigma_n}) = \sqrt{\frac{\boldsymbol{\Sigma(x-m)^2}}{\boldsymbol{n-1}}}$ Equation 4.3

Whereby; $\sum$ = sum across the values

x = observed value of each sample

n = total number of samples

m = mean

Local background value

Local background value (LBV) is defined as value above the sum of standard deviation and mean. Determination of the parameter is deduced using equation 4.4:

Local background value (LBV) = $\boldsymbol{m + \sigma}$ Equation 4.4

Whereby; m = mean

σ = standard deviation

Histogram plots

Histograms are a type of bar plot for numeric data that group the data into bins. It is used to plot the frequency of score occurrences in a continuous data set that has been divided into classes, called bins (Oles, 2008).

© University of Venda

Cumulative distribution function plots

Cumulative distribution function (CDF) plots are plots that shows the empirical cumulative distribution function of the data set and are used to determine or compare the distribution of different sets of given data (Oles, 2008).

4.5.2 Geostatiscal Methods

4.5.2.1 Requirements for Geostatistics

In geostatistic, interpolation of data is one of the important requirement for data analysis. In spite that Kriging is one of the most common geostatiscal method used and that it has been used successfully mainly in soil science (Burrough, 1991), interpolation in Kriging still remains important, thus need to be tested.

There are three requirements that have to be fulfilled to run a Kriging method properly and these include; Normal distribution, Stationarity and Autocorrelation of data (Smith *et al.*, 2018).

Normal Distribution

One of the requirements for Kriging method is for the datasets to be normally distributed. This is so because if data are not normally distributed, probability mapping which is one of the Kriging operations is not possible. Prediction mapping would be possible, but the quality and reliability are substantially higher with normally distributed data (Peters, 2008). According to Deutsch and Journel (1997); Isaak and Srivastava, (1989), Hohn, (1988) and de Wijs (1951), normal distribution is a mathematical base for the proper use of descriptive statistics, which include; variance, mean, mode, median etc. Normal distribution is usually conditioned by variogram, which is a basis for kriging mapping. When datasets are not normally distributed, various transformations such as logarithmical transformation, box-cox power transformation etc. are to be applied so as to fit in the Gaussian bell curve (Zelenika *et. al.*, 2011).

© University of Venda

Stationarity

The basic prerequisite of geostatistics is stationarity (Cressie, 1986; Smith *et al.*, 2018). If a stochastic variable is not stationary, a continuity of the mean values would not be existing and with that no spatial homogeneity either. This means for Kriging, all the samples have to come from the same probability distribution (Smith *et al.*, 2018).

It is common in geostatistics to assume stationarity if the intrinsic hypothesis is fulfilled. Mathematically, the intrinsic hypothesis says that the expected value of the increment is supposed to be zero as shown in equation 4.5 (Burrough, 1986).

$$E[Z(x) - Z(x+h)] = m(x) \stackrel{!}{=} 0 \qquad \text{Equation 4.5}$$

The second part of intrinsic hypothesis describes the variance as illustrated by equation 4.6.

$$\frac{1}{2}VAR[Z(x+h) - Z(x)] = \frac{1}{2}E[(Z(x) - Z(x+h))^2] = \gamma(h) \qquad \text{Equation 4.6}$$

This implies that if the intrinsic hypothesis is fulfilled then a spatial trend is not existing (equation 4.5) and the variance is not dependent on the location of the variables but on the distance (equation 4.6). The $\gamma(h)$ describes the variogram. This implies that to describe the spatial correlation the variogram has to be known (Burrough, 1986). The intrinsic hypothesis can be approved graphically by considering the empiric semivariograms (Peters, 2008).

If the prerequisites of geostatisctis are not fulfilled, different mathematical models exist to eliminate a trend, thus making Kriging possible (Peters, 2008). For example, ArcGIS 10.1 provides the possibility to eliminate a trend during the Kriging interpolation by choosing the right parameters.

© University of Venda

Autocorrelation

Another important prerequisite for Kriging is autocorrelation within the dataset. Spatial auto-correlation means that neighbouring variables have similar values that bring out local clusters (Peters, 2008). Autocorrelation can be approved by the Mc-Moran-Coefficient or graphically by the theoretical semivariograms where autocorrelation can be assumed if the nugget variance is smaller than the still (Burrough and McDonnell, 1998).

Consequently, these requirements needed for kriging method are crucial as they help in decision making whether spatial data is suitable for a kriging interpolation or not. Hence, the decision tree for kriging method can be developed (Fig. 4.2) if its requirements are fulfilled, thus kriging is possible. If the data is not normally distributed, transformations are possible to produce normal distribution (Fig. 4.2). If the data is not stationary, it depends on how strong the trend is. A minor trend can still be eliminated during the kriging estimation. If one of the requirements of normal distribution, stationarity or autocorrelation is not fulfilled and cannot be generated through mathematical procedure a deterministic method (Fig. 4.2) has to be chosen instead of a kriging method.

4.5.2.2 Kriging Methods

Kriging is a generic term used to describe a set of interpolation methods such as Ordinary, Simple, Universal, Indicator, Probability, Disjunctive, Block and Empirical Bayesian Kriging of which all are used for different purposes. The method is ideal in cases where there was irregular sampling method, whereas determinative is ideal in cases where location of samples is regular. To apply kriging statistical method requires that the dataset should be normally distributed, should have stationarity and autocorrelation (Smith *et al*., 2018), as was the case in this study. Hence having spatial maps was not ideal in this case.

Ordinary Kriging

Ordinary Kriging is a Kriging method that is used for data that seems to have a trend, thus when dataset is stationary, autocorrelated and normally distributed (Fig. 4.1). It is successful if the variables are fairly homogeneous with a constant mean within a local search radius

© University of Venda

(Peters, 2008) but less successful if sudden boundaries are existing (Burrough and McDonnell, 1998).

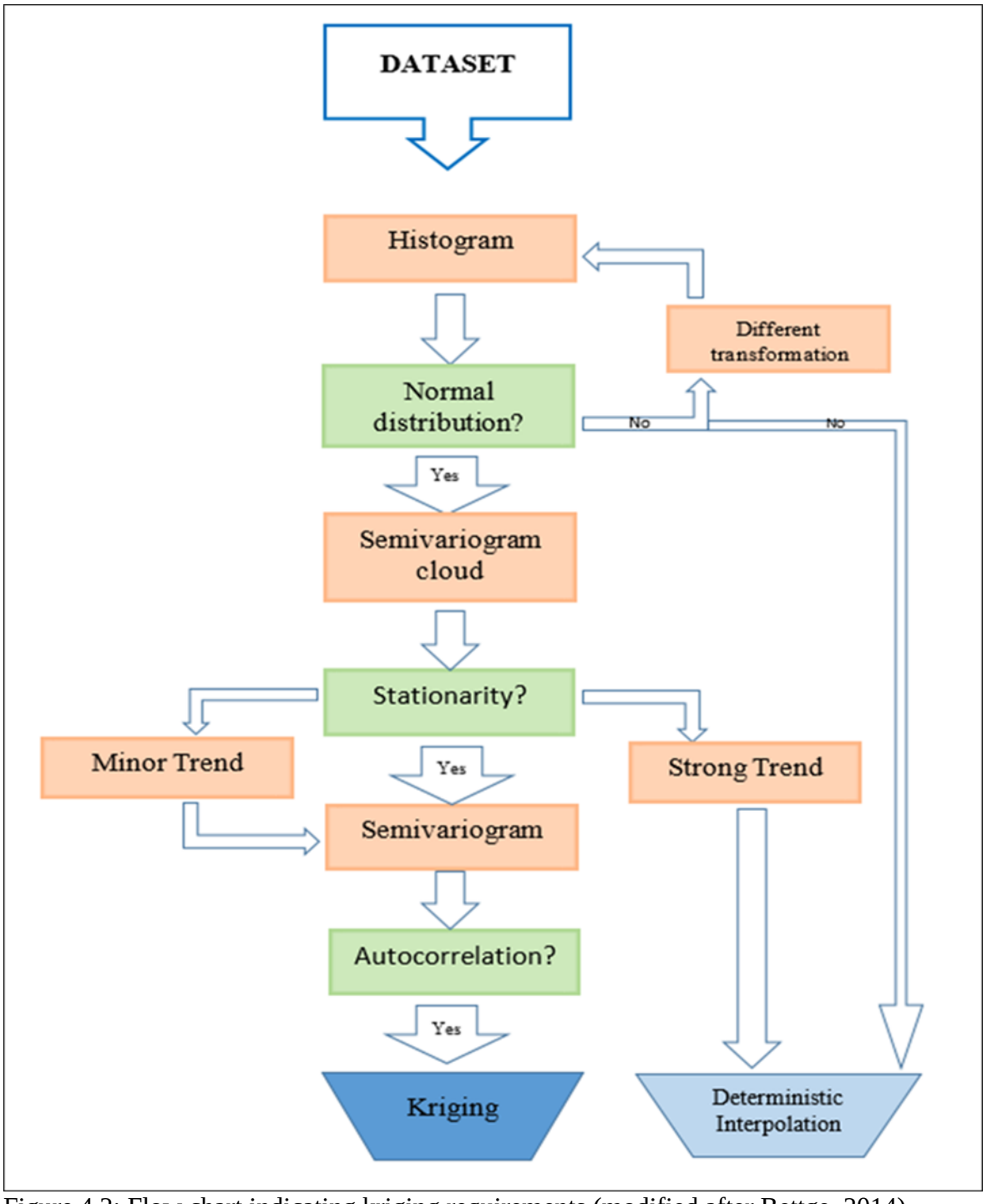


Figure 4.2: Flow chart indicating kriging requirements (modified after Bettge, 2014).

© University of Venda

Mathematically, ordinary Kriging assumes a model shown in equation 4.7. Where Z(s) is the observed data set, μ is unknown constant mean and ε(s) is an error (Bohling, 2005; Peters, 2008; www.desktop.arcgis.com/understanding-ordinary-kriging.htm).

$$Z(s) = \mu + \varepsilon(s)$$

Equation 4.7

The Ordinary Kriging can use either semivariograms or covarians, which are mathematical forms that are used to express autocorrelation. This method uses transformations and removes trends and allow measurement error [ε(**s**)] (Bohling, 2005; Peters, 2008; www.desktop.arcgis.com/understanding-ordinary-kriging.htm. It assumes a constant mathematical expectation (μ) within a local search radius with μ being an unknown constant (Fig. 4.3), one of the main concern in ordinary Kriging is whether the assumption of constant mean (μ) is reasonable. The mathematical expectation has to be estimated. Some geostatistical softwares such as ArcGIS are able to eliminate a minor trend semiautomatically in the forefront of an Ordinary Kriging (Peters, 2008; Bohling, 2005). www.desktop.arcgis.com/understanding-ordinary-kriging.htm.

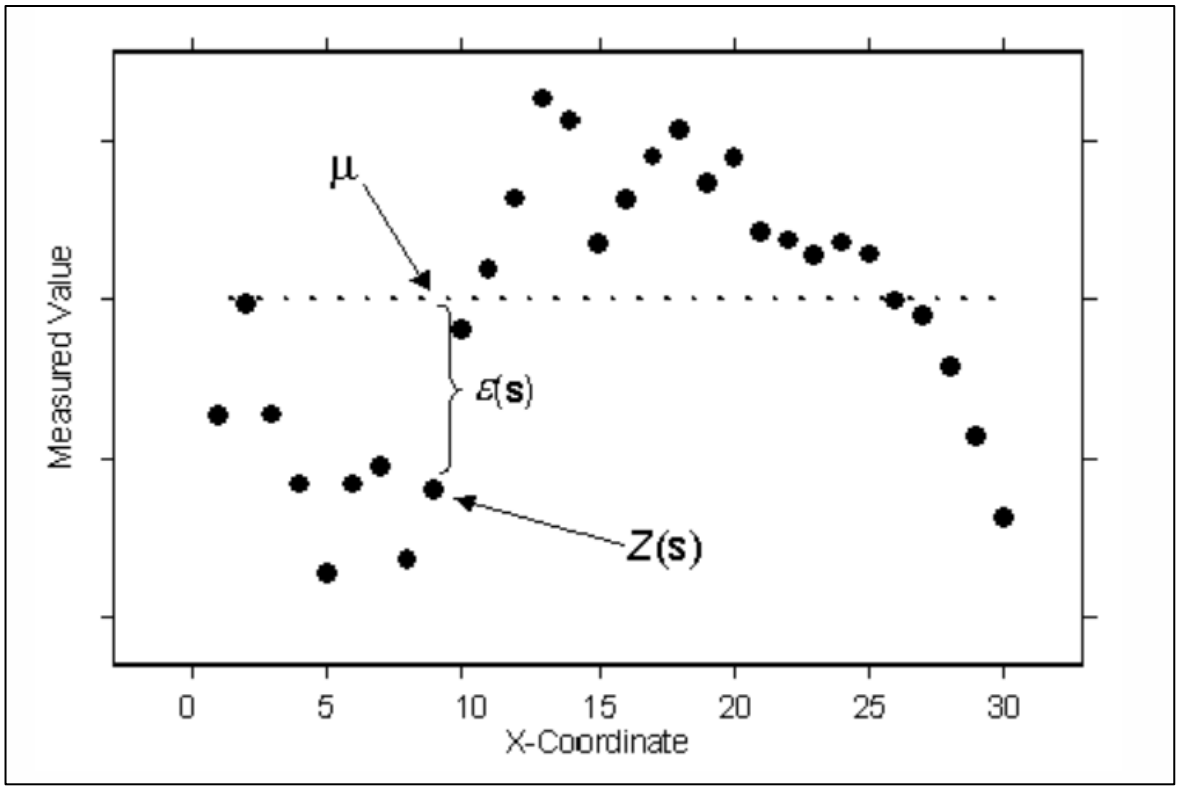


Figure 4.3: Ordinary Kriging with constant mean (www.desktop.arcgis.com/understanding-ordinary-kriging.htm).

© University of Venda

Universal Kriging

Universal Kriging is used if a significant trend exists. The mean is not a constant but a deterministic function of the spatial reference (Peters, 2008). Mathematically it assumes a model as shown in equation 4.8 (www.desktop.arcgis.com/understanding-ordinary-kriging.htm).

$$Z(s) = \mu(s) + \varepsilon(s)$$

Equation 4.8

Where, μ(s) is a deterministic function and second-order polynomial trend (long dashed line) (Equation 4.8) (Fig. 4.4). By subtracting the second- order polynomial [μ(s)] from the original data [Z(s)], the error ε(s) is obtained which is assumed to be random (Equation 4.8). Consequently, the autocorrelation is then modeled from the random error [ε(s)]. This implies that instead of assuming the errors [ε(s)] independently, the errors are modelled so as to be autocorrelated.

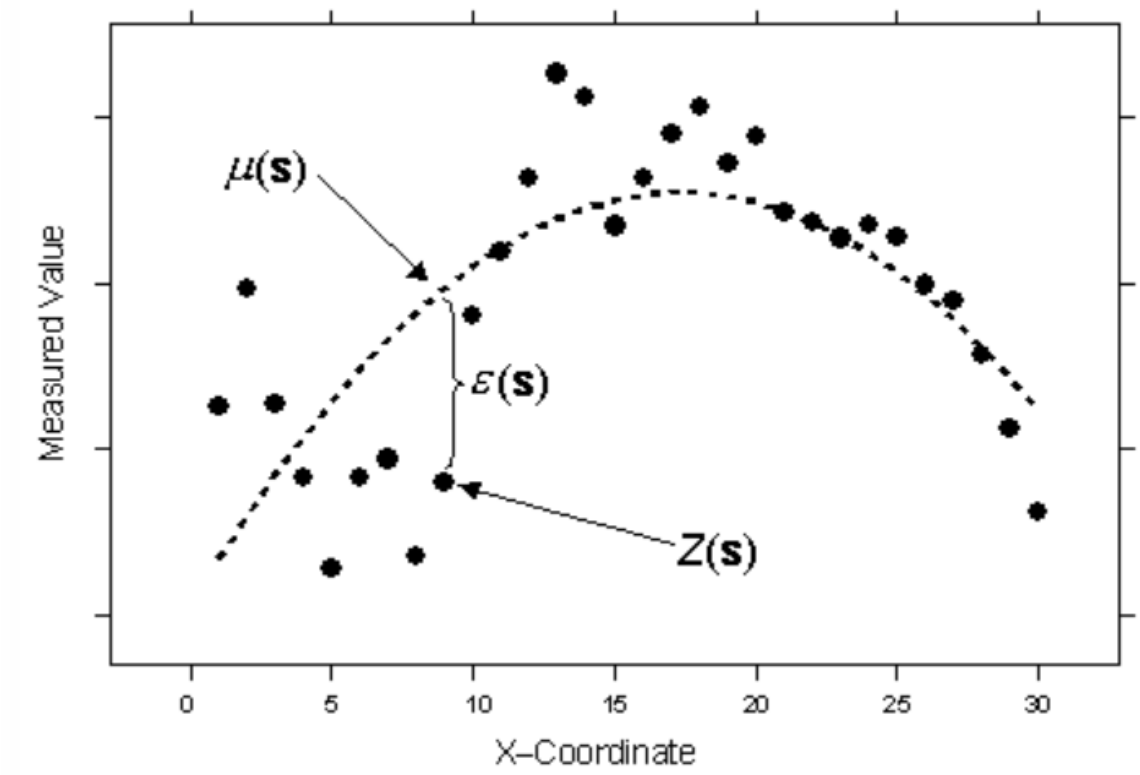


Figure 4.4: Universal Kriging with the mean being a deterministic function (www.desktop.arcgis.com/understanding-ordinary-kriging.htm).

© University of Venda

Universal Kriging eliminates the spatial trend by a polynomial function and interpolating with Ordinary Kriging afterwards (Peters, 2008). Similarly, as ordinary Kriging, Universal Kriging can use either semivariograms or covariances, transformations and allow for measurement error (www.desktop.arcgis.com/understanding-ordinary-kriging.htm).

Simple Kriging

Contrary to Ordinary Kriging where the mean has to be constant in the local neighborhood of each estimation point, simple Kriging is used if the mean is constant all over the study area (Peters, 2008).

Indicator Kriging

Indicator Kriging allocates the values 1 or 0 to the investigated attributes. Afterwards these values are interpolated just as for ordinary Kriging. Consequently, this method can estimate even boundaries of nominal values. It can also be used as a probability method for numeric variables. All values of the dataset above a certain threshold can be allocated as 1 while all other values as 0. The results can be interpreted as probability to be above this threshold value (Longley *et al.*, 2011; Rivoirard, 1994).

Probability Kriging

Probability Kriging puts out probabilities for exceeding certain threshold values. Unlike above discussed methods, Probability Kriging does not generate surfaces with interpolated values for every estimation point. It generates maps which display the probability to what extend (in %) a certain value is exceeded (Mukhopadhyay et al., 2017; Martin and Simpson, 2005; Rivoirard, 1994; Burrough, 1991).

The Geostatistical Wizard of ArcGIS 10.1 lists Probability Kriging as an independent method but it is also possible to choose probability as an Output Surface Type for any other Kriging method except Empirical Bayesian Kriging (Mukhopadhyay, 2017; Martin, 2005; Rivoirard, 1994; Burrough, 1991).

© University of Venda

Disjunctive Kriging

Disjunctive Kriging is an independent method to create probabilities. In contrast to Probability Kriging where all the three requirements for geostatistics have to be fulfilled. It is used if data is not normally distributed (Martin, 2005; Ortiz *et al.*, 2005; Rivoirard, 1994; Burrough ,1991).

Empirical Bayesian Kriging

For all the Kriging methods mentioned above, a lot of parameters such as trend elimination; construction of semivariogram; and neighborhood search have to be specified. Empirical Bayesian Kriging relieves the user of the choice of these parameters by automatic calculations. However, much time is required to create the interpolated maps (Martin, 2005; Ortiz *et al.*, 2005).

4.5.2.3 Pre-processed Parameters for Development of Kriging Model

Several processes or parameters such as trend elimination, semi-variograms construction and neighborhood searching are involved in creating an interpolated map using kriging. Before the use of Geostatistical Analyst tool in ArcGIS, it needs to be enabled through performing trend elimination, constructing semi-variograms and search neighborhood.

4.6 Geochemical Survey in the Musina Area

4.6.1 Specific Objectives

The specific objective of the study was to conduct soil sampling and analysis in order to ascertain the following:

- Concentration levels and dispersion of elements in soils within the study area;
- Determination of metals associated with copper sulphide mineralisation; and
- To establish anomalous areas of elements to support further exploration work within the study area.

© University of Venda

4.6.2 Data Preparation

For geochemical survey, soil samples were collected and all the necessary data such as physical characteristics of samples together with coordinates of sample location were recorded as explained in section 3.2 of Chapter 3 (Appendix 3A). During this stage, coherent notation of coordinates was done and this was achieved through converting coordinates in degrees, minutes and seconds to decimal degrees using equation 4.9 (www.desktop.arcgis.com/en/arcmap/10.3/guide)

Decimal degrees = degrees + (minutes/60) + (seconds/3600	Equation 4.9

The datasets in chapter 3 contain the actual spatial data but not in metadata standard form which is one of the requirement for data to be used in ArcGIS. Metadata are used to describe data in a structured way (Rühle, 2012).

To define the Metadata Standards helps in the interoperability, compatibility, reusability, transparency and integration ability (Hein, 2011) when analysing the data. The standard defined by EN ISO 19115 that supplies a comprehensive set of metadata elements is wildly used in geospatial metadata services (Walker and Rackham, 2010). Consequently, this standard was chosen to design a concept for geospatial metadata in this study (EN ISO 19115, 2014).

According to ISO 19115 (2014), the use of metadata facilitates the user to discover, access, retrieve data and to determine whether this data is useful to them. The advantage in Metadata for the producers is the improvement in the organization and the management of the production, storage, updating and reuse of the data. Following previous metadata created by ISO 19115 (2014), the hierarchical metadata structure in this study was developed (Appendix 4A).

Topographical map of 1:50 000 scale was used as a base map. The decimal degrees coordinates readings for both soils and sediments sampling points were used to plot the sampling points on the 1:50 000 scale topographical map using Desktop ArcGIS 10.4.1 software to produce sampling point maps (Fig. 4.5).

© University of Venda

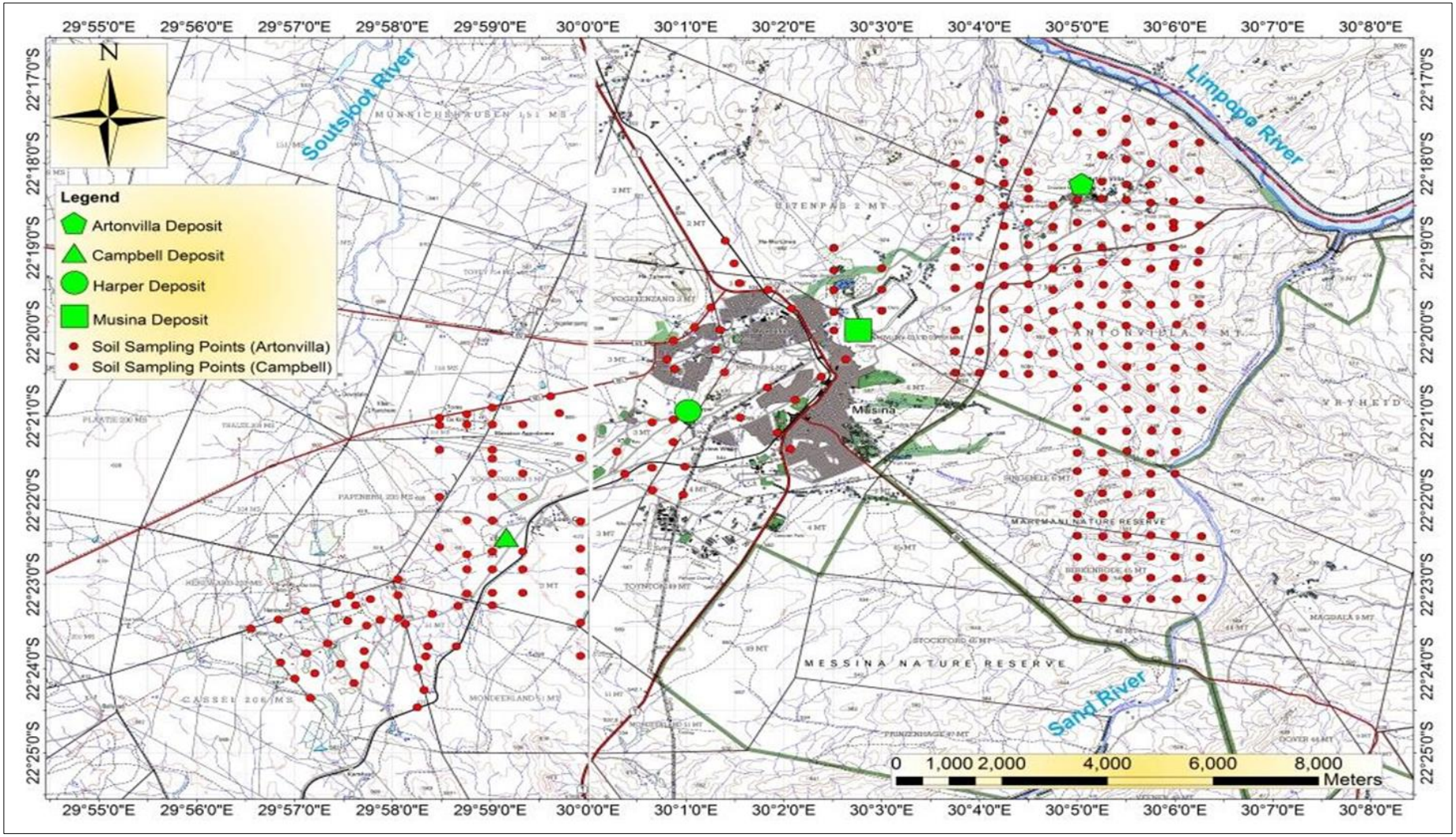


Figure 4.5: Soil sampling points within the study area.

© University of Venda

4.6.3 Sample Preparation

Drying and quartering of samples

Soil samples were air-dried, and riffle quartered to homogenise the material. The air-dried samples were further dried using the Bench Vacutec laboratory oven (Fig. 4.6a) at 110°C for about 10 hours to remove moisture. The prepared samples were removed from the oven and cooled for about 6 hours to room temperature of about 25°C and placed in paper bags, ready for milling.

Milling of Samples

The oven dried samples were transferred into a milling pot and placed in Stainless steel RJM Ring Mill which was used for milling the samples into powder form (Fig. 4.6b). For AAS analysis, it is necessary to mill and digest samples before they can be analysed. The samples were milled to at least 80% less than 75 µ in size in order to ensure homogeneity and total dissolving of the grains. During milling of samples, cleaning of the milling pot was done after each sample was milled, using pure and clean milky quartz to avoid cross contamination between any two samples. Milled samples were then transferred to clean paper sample bags and labeled accordingly.

Weighing of samples

A Redwag model AS 220/C/2 analytical weighing balance (Fig. 4.6c) was used to precisely weigh 5 grams of each sample and transferring it into a clean sterilized 250 ml decomposition beaker. All the samples were moistened with few drops of deionized water to avoid sputtering. Five grams of the two approved Certified Reference Material samples acquired from the Council of Mineral Technology of South Africa (MINTEK) were also weighed.

Digesting of Samples

A 15 ml of an aqua-regia (1 part of HNO_3 : 3 parts of HCl) was added to the weighed samples to dissolve the metal elements. The solution was mixed thoroughly and digested to a volume of about 5 ml on hotplate in a fume cupboard (Fig. 4.6d) for an hour. Samples were then cooled and transferred to clean sterilized 100 ml volumetric flasks and left to cool for an hour. Deionized water was used to fill the volumetric flask up to the 100 ml mark (Fig. 4.6e), thus ready for analysis.

© University of Venda

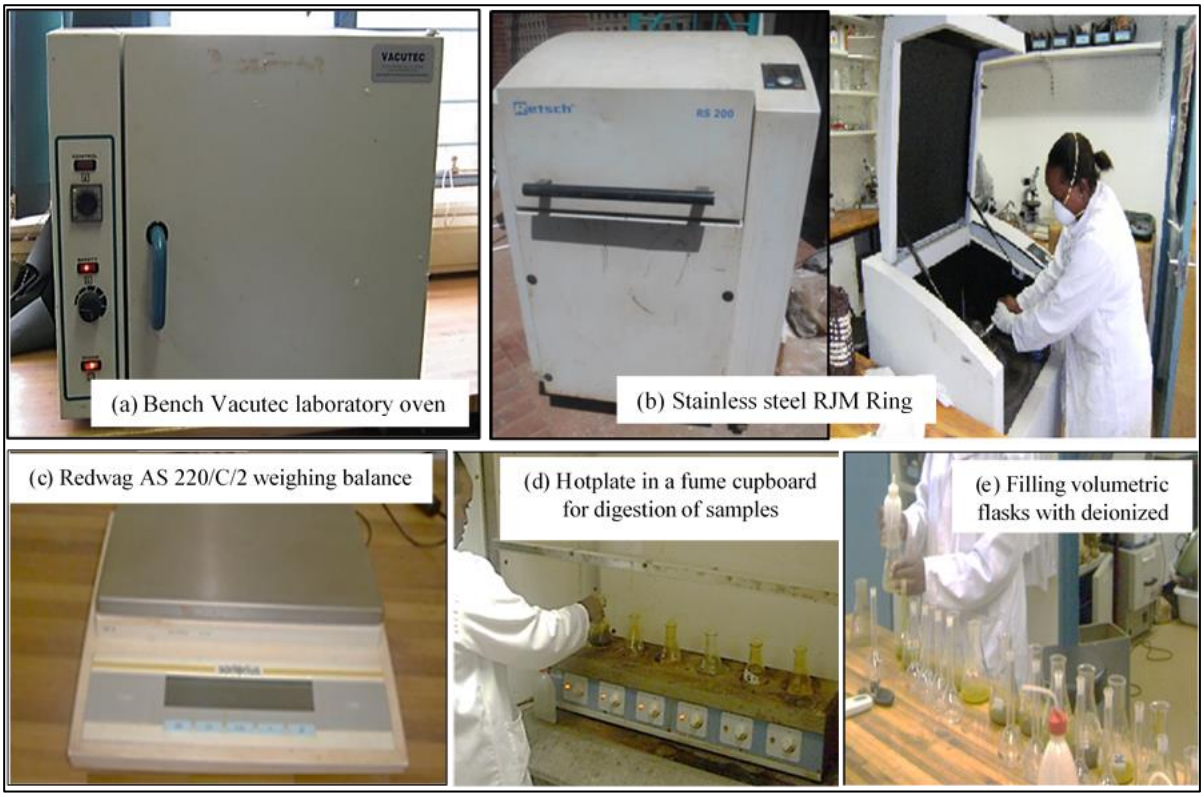


Figure 4.6: Preparation of soil samples. (a) Bench Vacutec Laboratory oven used for drying samples; (b) Retsch model RS 200 milling machine used for milling the samples; (c) Redwag model AS 220/*C/2* analytical weighing balance and (d) digestion of samples.

4.6.4 Samples Analysis

4.6.4.1 Quality Control and Assurance

According to Ballinger and Shugar (2011), quality assurance plans and quality control programmes are the key components of all analytical protocols in all areas of analysis including geochemical, environmental, pharmaceutical and forensic among others. Quality assurance plans and quality control programmes mandate that every laboratory follows a set of well-defined guidelines so as to achieve analytical results at a high degree of accuracy (Ballinger and Shugar, 2011). Consequently, in this study quality control was assured through determination of the calibration curves; and through using reference samples, blanks and triplicates and execute analytical precision. For the analyzed samples, the average values were obtained and recorded (Appendices 4BI and 4BII).

© University of Venda

Calibration curves

Calibration standards were prepared by adding a ratio of 1:4 of known volume of sediment solution (100 ppm) and de-ionised water in a 100 ml standard volumetric flask up to a mark for obtaining working standard solutions of 0.5 ppm, 1.0 ppm, 2.0 ppm, 5.0 ppm, 10 ppm, 20 ppm and 40 ppm of each element. The artifact of known accuracy was traceable continuously on a measurement system when calibrating the measuring instrument and the calibration curves were determined. The calibration curves for the elements to be analysed were deduced through analysis of MINTEK standard references samples for Pb, Zn, Cu, As, Ni, Mo, Co, Cd, Mn and Cr. (Fig. 4.7) prior to determination of concentration of each element.

Reference samples and analytical precision

Certified Reference Material sample SARM 52 from MINTEK was analysed to determine analytical errors and duplicate measurements were conducted for 10% of the analysed soil samples to monitor the chemical analyses for soil.

4.6.4.2 Soil Analysis

All digested sample solutions were analysed for elements using Perkin Elmer model AAnalyst 400 AAS (Fig 4.8) at the Department of Mining and Environmental Geology laboratory, School of Environmental Sciences, University of Venda. The analysis was conducted for the determination of the concentration levels of Pb, Zn, Cu, As, Ni, Mo, Co, Cd, Mn and Cr from soil samples and the concentration levels were recorded (Appendix 4BI and 4BII. The de-ionized water was used as a blank sample and also analysed at the same time with the other samples to assess the quality of the results obtained.

© University of Venda

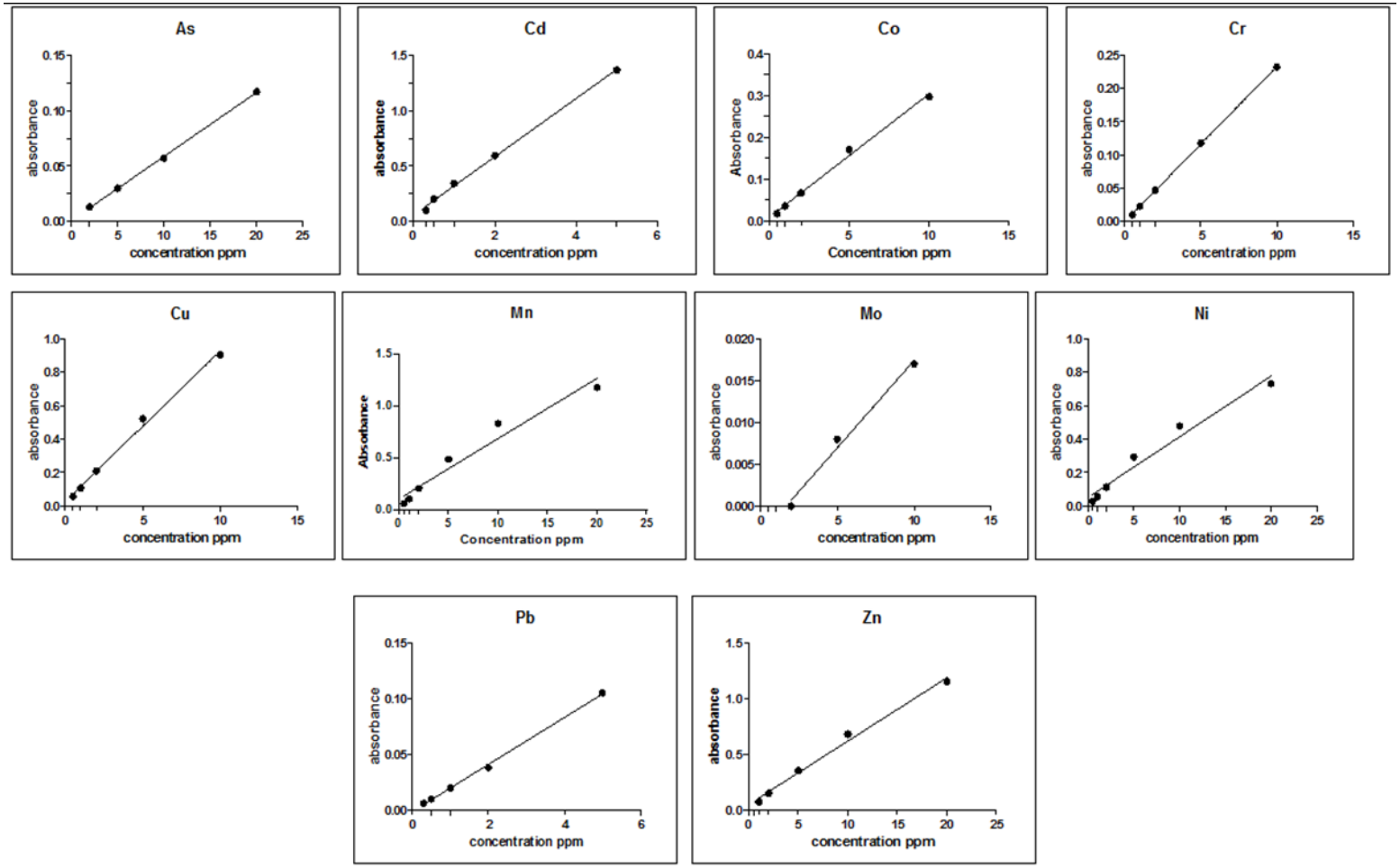


Figure 4.7: Calibration curves for Pb, Zn, Cu, As, Ni, Mo, Co, Cd, Mn and Cr.

© University of Venda

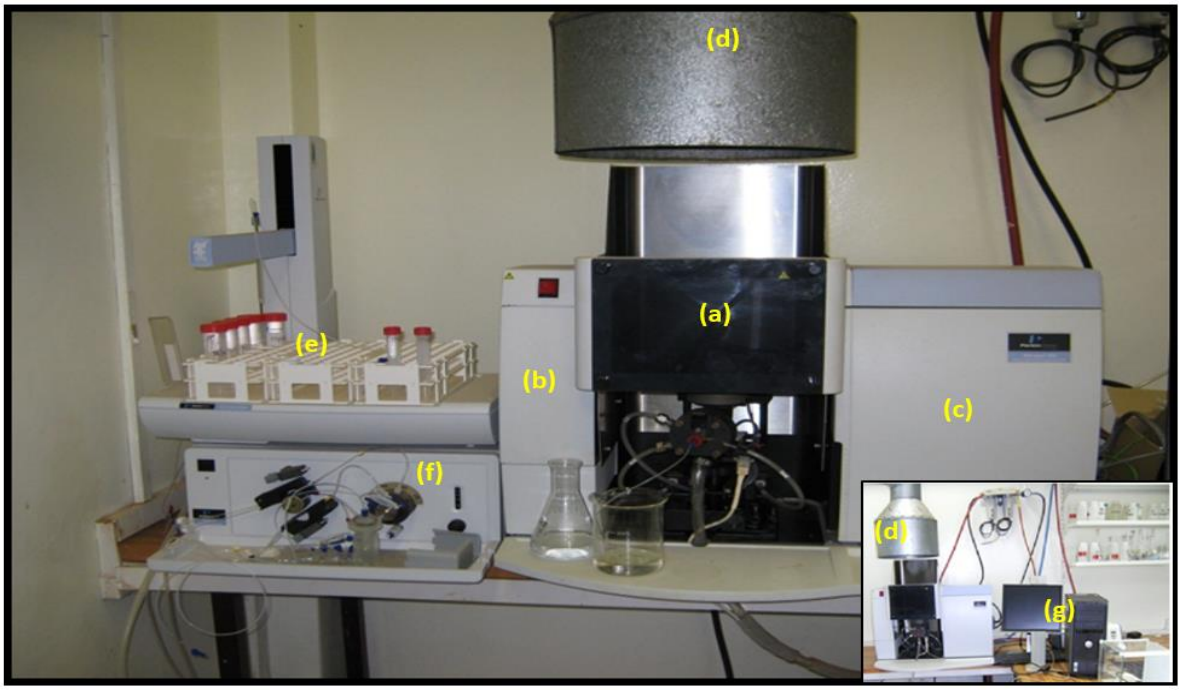


Figure 4.8: Photograph of a Perkin Elmer model AAnalyst 400 Atomic Absorption Spectrometer: (a) Burner compartment for protecting the flame; (b) Detector compartment; (c) Hallow cathode lamp compartment; (d) Blower and ventilation system; (e) sample holder; (f) Sample older compartment; (g) Output:Computer. (f) Output --- computer used to display the results.

4.6.5 Data Analysis and Interpretation

Concentration values from soil samples were used to execute data analysis and interpretation of the occurrence and distribution of the metals within the study area and also used for determination of the metals associated with copper sulphide mineralisation in the area. Concentration data was also used for the determination of anomalous areas for the development of exploration target areas within the study area.

4.6.5.1 Occurrence and distribution of metals in Soils

The concentration levels of Pb, Zn, Cu, As, Ni, Mo, Co, Cd, Mn and Cr in soils from Campbell and Artonvilla areas (Appendix 4B and 4C and Table 4.1) were used to evaluate the amount and distribution patterns using basic statistics of the metal concentration levels (Table 4.1) and also using Frequency diagrams (Fig. 4.9 and Appendix 4C).

© University of Venda

Table 4.1: Summary of statistical parameters of concentration levels of metals within soil samples

Area	Statistics	As	Cd	Co	Cr	Cu	Mn	Ni	Pb	Zn
Campbell soil n=102	**Min**	3.5	<5	3.5	12.8	7.8	6	8.8	3.5	3.5
	Max	20	<5	17	109.8	1580.2	351.6	260.8	30.8	141
	Mean	8.70	<5	8.33	45.45	61.9	172.18	27.70	6.86	11.60
	Median	8	<5	7.8	39.2	19.8	165	23.4	6.2	4.6
	SD	4.16		3.15	20.96	198.74	72.64	26.50	3.55	15.75
Artonvilla soil n=193	**Min.**	5	0	3	3	5	3	10	4	1
	Max.	215	0.753	59	202	1321	1009	100	25	82
	Median	61	0.196	14	36	28	188	36	12	20
	Mean	59.1	0.195	15.97	42.	50.57	186.93	61.3	12.67	22.2
	SD	43.6	0.126	8.4	27.96	114.67	114.58	117.	4.14	12.8

From basic statistics (Table 4.1) and histograms (Fig. 4.9 and Appendix 4C), it was established that As, Co and Cd showed low content within soils with cadmium content of <5 ppm values in Campbell soil. The low values of Co and Cd could be attributed to the fact that they are generally found in trace quantities in sulphide minerals (Table 4.1 and Appendix 4C).

On the other hand, manganese and nickel had high values with maximum value of 351 ppm and mean value of 172 ppm from western side of the study area while the eastern side of the study area, registered maximum value of 1009 ppm and mean value of 186 ppm. High values of Mn could be attributed to have come from the rocks within the study area (Table 4.1 and Appendix 4C).

Copper had highest maximum value of 1580 ppm with a mean value of 61 ppm while the eastern side of the study area had maximum value of 1321 ppm and mean value of 50 pp (Table 4.1, Fig. 4.9 and Appendix 4C). High occurrence of Cu could be due to the presence of copper deposits within the study area.

Nickel showed maximum value of 200 ppm with mean value of 27 ppm at Campbell area at the eastern side of the study area (Artonvilla area), Ni, registered maximum value of 100 ppm with mean value of 61.3 ppm (Table 4.1 and Appendix 4C). High values of Nickel could be

© University of Venda

attributed to the presence of pentlandite mineral, which is one of the sulphide minerals identified within the study area that was confirmed through the study of ore mineralogy and ore microscopy.

Pb, Zn and As indicated maximum values of 30 ppm, 141 ppm and 20 ppm within and around the Campbell area respectively while at Artonvilla area the Pb, Zn, and Cu indicated maximum values of 25 ppm, 82 ppm, and 215ppm (Table 4.1 and Appendix 4C). The occurrence of these metals could be attributed to the fact that they are copper sulphide metals.

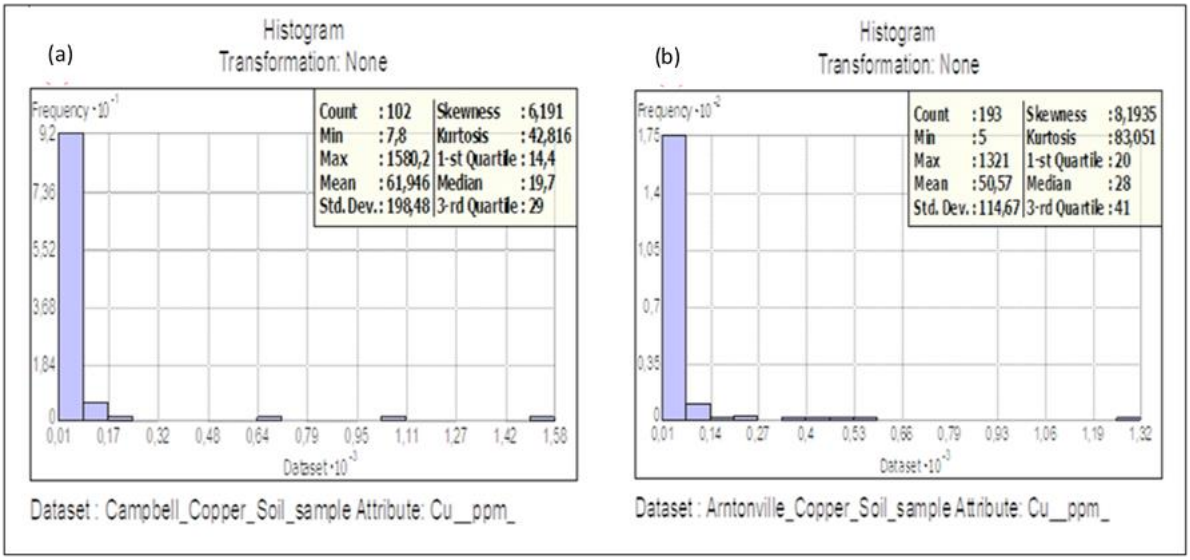


Figure 4.9: Frequency diagrams of Cu for soil collected from (a) western (Campbell area) and (b) eastern (Artonvilla area) side of the study area.

4.6.5.2 Interpolation of Geochemical Data

Interpolation of data is a crucial step in developing the geochemical maps for further exploration purposes. Different interpolation methods are available but because of the fact that the Messina copper deposits are situated along the Messina fault zone, running from the northeast to the southwest, a spatial coherence can be assumed, thus, Kriging is most applicable method in this study. In spite of the fact that a spatial coherence can be assumed and Kriging has been used successfully in soil science (Burrough, 1991; Zhang *et al.*, 2017; Wang and Zuo, 2018; Liu *et al*., 2019), the requirements of a Kriging interpolation still have to be tested. Consequently, the three processes; normal distribution, stationarity, and

© University of Venda

autocorrelation that are requirements to run a Kriging method properly have to be processed as discussed above in section 4.5.2.1.

Following the decision tree flow chart (Fig. 4.2), the data was subjected to all the processes necessary for decision making on using Kriging or not and an example of copper datasets were used to present these processes. Consequently, these requirements needed for kriging method are crucial as they help in decision making whether spatial data is suitable for a kriging interpolation or not. Hence, the flow chart for kriging method can be developed that helps with decision-making (Fig. 4.2) and if all the requirements are fulfilled, then kriging is possible.

Normalizing Distribution of Data

To normalize the datasets, logarithmical transformation of data was done using logtransformation within the geostatistical wizard, which can also be achieved by adding a logtransformed column within ArcGIS. All the datasets (concentrations values of soil) were normalized by executing logarithmic transformation.

For example, Cu was used to present the logarithmical transformation of data (Fig. 4.10). In this figure, the histograms of the original (always on the left) and the logtransformed values (always on the right) are presented in order to offer a proper comparison. The abscissas on the left histograms show the copper values of the datasets while the abscissas on the right histograms show these values as logtransformed. The rest of the metals histograms are shown in Appendix C.

Stationarity of datasets

After logarithmic transformation of dataset, data sets need to be stationary (Fig. 4.2). For datasets to be stationary, an empiric semivariograms should be deduced. In this study, Semivariogram/Covariance Cloud tool in ArcGIS was used which produced pairs of points with a dissimilarity above the semivarigram (blue points in Figure 4.11). The points were then selected and lines produced on a map (blue lines in Figure 4.11) with lines pointing at one direction, for example, towards Musina town and the centre of the former copper mine areas (Fig.4.11), implying that a trend can be assumed and stationarity is highly improbable.

© University of Venda

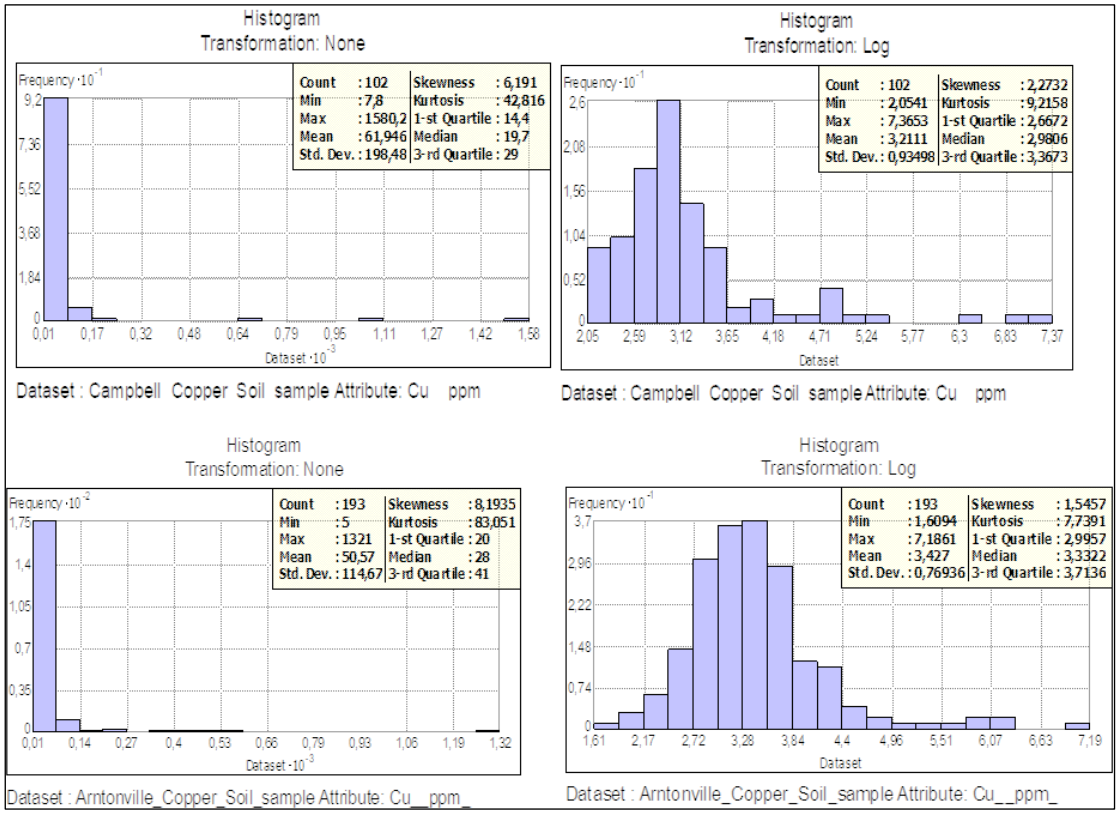


Figure 4.10: The histograms of the original (always on the left) and the logtransformed values (on the right) of the soils from both Artonvilla and Campbell area.

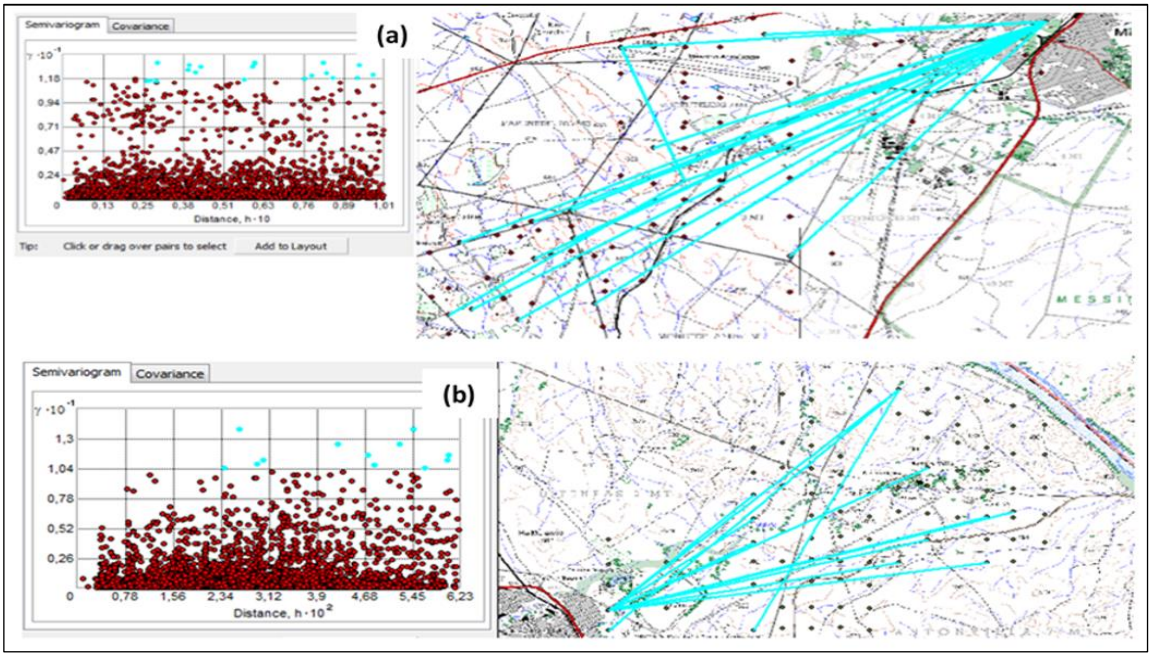


Figure: 4.11: Semivariograms and covarience cloud of datasets showing clear trend (a) Trend for Campbell area soil data, (b) Trend for Artonvilla area soil data.

© University of Venda

If the datasets are not stationary, to fulfill the decision tree requirements (Fig.4.2), different mathematical models exist to eliminate a trend, thus making Kriging possible (Peters, 2008). In ArcGIS 10.1, eliminating trend during Kriging interpolation is done by choosing parameters such as choosing order of the trend removal, Kernel function, advanced mode for Neighborhood type, predicted coordinate and weights, but this depends on the choice of Kriging methods to be used (see section on choice of Kriging method below).

Autocorrelation

For data to be spatially autocorrelated, theoretical semivariograms were constructed (Fig. 4.12) so as to assume autocorrelation of the data. The autocorrelation was confirmed because a clear nugget variance was seen which is smaller than the still for all the datasets as described by Burrough and McDonnell (1998).

For this study, all the four datasets fulfilled the requirements of autocorrelation as indicated by the decision tree flow chart (Fig. 4.2). However, further processing of data is needed as a minor trend was detected after logarithmic transformation of datasets which needs to be eliminated. Eliminating of trend was done through choosing the right Kriging method so as to set the right parameters.

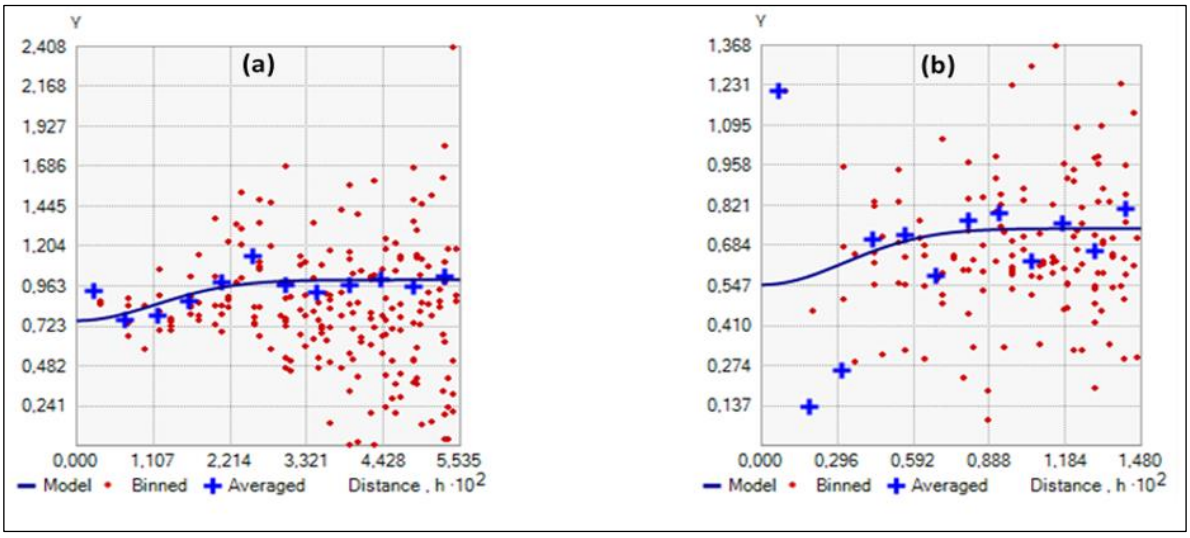


Figure 4.12: Semivariograms of the datasets: (a) Semivariogram of Campbell soil; and (b)Artonvilla soil.

© University of Venda

Choosing of the Kriging Method

The choice of the Kriging method was based on the outcome of the processed data (Decision making flow chart, Fig. 4.2) and also based on the purpose of the study which was to develop the interpolated maps that indicate anomalies within and around Musina area so as to generate the exploration targets for further exploration work. In this case, the probability methods (Probability Kriging and Disjunctive Kriging methods; section 4.5.2.2) were not suitable. Neither is the Indicator Kriging method, because the interpolated values are numeric copper contents and not nominal fields. As already deduced, autocorrelation exists and normal distribution can be produced by a logarithmical transformation while stationarity requires further processing, thus Simple Kriging method at this stage was not appropriate.

The decision between Ordinary and Universal Kriging methods depended on how significant the trend is and, finally, the quality of the results. Pre-testing these two methods, it was deduced that the Universal Kriging Method seems more disordered than the Ordinary Kriging. Experience has shown that the extent of confusion increases during the process of setting the method properties.

Furthermore, the Root-Mean-Square-Error (RMSE) is always an essential factor for the quality of an interpolation, thus for the Ordinary Kriging it is just 80% of the Root-Mean-Square-Error of the Universal Kriging. For these reasons, the Ordinary Kriging was chosen for further interpolation.

Bayesian Kriging method sets most of the Kriging parameters by itself, thus the user won't have an overview on how the results were achieved. Consequently, Bayesian Kriging can be used as a second alternative method to verify the results.

Further Interpolation using Ordinary Kriging Method

When executing stationarity, a trend was found for all the datasets and needs to be eliminated. To eliminate the trend, further analysis of the trend was to be done using Ordinary Kriging method chosen for this study. Using the Trend Analysis tool from ArcGIS, it was revealed that all the datasets project similar parabolas through the scatter plots (Fig. 4.13). As the parabolic projection was revealed, trend elimination was done using Kernel function in

© University of Venda

ArcGIS, which was then changed to fit the surface as good as possible while the advanced mode was activated to change the values manually.

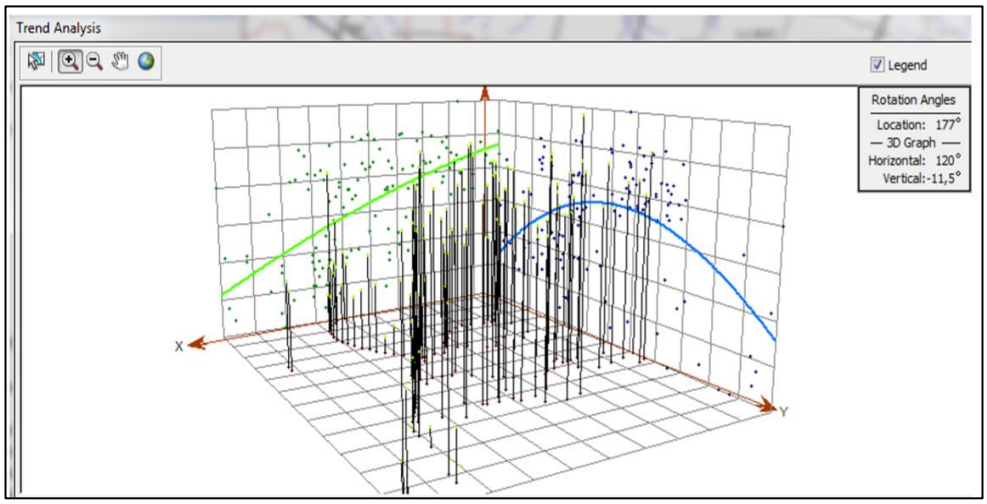


Figure 4.13: Scatter plots of datasets projecting similar parabolas.

The neighbourhood type was set to standard and all the values of parameters of trend elimination analysis were set right with the Root Mean Square Error (RMSE) at the top of the parameters Table 4.14).

Table 4.2: Trend elimination of (a) soils from Campbell and (b) Artonvilla areas

(a)	
Trend	[western_soil_KO...
General Properties	
Exploratory Trend S...	
Order of polynomial	2
Kernel Function	Constant
Goodness of Fit	0,779011
Optimize Model	☑
Advanced mode	True
Advanced Properties	
Neighborhood type	Standard
Maximum neighbors	1000
Minimum neighbors	10
Sector type	○ 1 Sector
Angle	30
Major semiaxis	0,03314383
Minor semiaxis	0,032
Anisotropy factor	1,035745
Bandwidth	0,03314383 ☑
Use Spatial Conditio...	False
Spatial Condition Nu...	
Predicted Value	
X	29,99319
Y	-22,36042
Value	2,948932
Weights (50 neighbors)	

RMSE: 0,7741452

(b)	
Trend	[eastern_soil$_Fe...
General Properties	
Exploratory Trend S...	
Order of polynomial	2
Kernel Function	Constant
Goodness of Fit	0,8003002
Optimize Model	☑
Advanced mode	True
Advanced Properties	
Neighborhood type	Standard
Maximum neighbors	1000
Minimum neighbors	10
Sector type	⊕ 4 Sectors
Angle	40
Major semiaxis	0,0294
Minor semiaxis	0,02933886
Anisotropy factor	1,002084
Bandwidth	0,02107109 ☑
Use Spatial Conditio...	True
Spatial Condition Nu...	37,64592 ☑
Predicted Value	
X	30,073
Y	-22,31556
Value	3,361249
Weights (85 neighbors)	

RMSE: 0,7862085

© University of Venda

4.6.5.3 Analysis and Interpretation of Interpolated Soil Geochemical maps

Major sulphide metals identified in soil included Pb, Zn, Cu, As, and Ni and these metals were used for further geochemical data analysis using ordinary Kriging method. These metals were used in order to determine their distribution pattern and geochemical anomalies within the study area. Of great interest was to investigate any link between the anomalous areas and the known copper-sulphide deposits in the area. Consequently, the prediction geochemical maps together with their prediction standard error maps for Pb, Zn, Cu, As and Ni from Campbell and Artonvilla areas were developed and interpreted (Figs. 4.14 - 4.23).

The standard error of all the maps indicated high precision because the standard error values were much smaller than the values and the range of the input data as stated in www.desktop.arcgis.com/en/arcmap/latest/extensions/geostatistical-analyst/.

The anomalous areas were determined in relation to local background values (LBV) deduced using Equation 4.4 and taking into consideration areas with high precision (areas with low standard errors).

For the classification of anomalous areas, concentration values above the LBV were considered to be anomalous, but also considering the Clarke values of the rocks associated with the study area. Consequently, for an area to be anomalous, the concentration values should be higher not only to LBV but also higher than the Clarke values of the local rocks.

As discussed in petrology and previous studies, the study area comprised gneissic rocks such as granitoid gneiss, quartzofeldsparthic gneiss, calc-silicate gneiss; carbonate rocks, amphibolites and meta-sedimentary rocks such as meta-quartzites being quartz rich sandstones, thus, generally the rocks within the study area originated from metamorphosed granitic rocks, mafic rocks and sedimentary rocks such as limestone and sandstone. Consequently, the Clarke values (Table 4.3) of heavy metals within the mafic, granitic, limestone and sandstone were compared with the concentration levels (local background values) of sulphide metals within the study area.

© University of Venda

Table 4.3: Mean heavy metal content in the major rock types in mg/kg (Kraukopf, 1967; Rose et al., 1979 and Alloway, 1995)

Heavy metals	Igneous rocks			Sedimentary rocks	
	Ultramafic (mg/kg)	Mafic (mg/kg)	Granitic (mg/kg)	Limestone (mg/kg)	Sandstone (mg/kg)
Pb	14	3	24	5.7	10
Zn Cu	58 42	100 90	52 13	20 5.5	30 30
As	1	1.5	1.5	1	1
Ni	2000	150	0.5	7	9

Soil geochemical maps in the western part of the study area (Campbell area)

Lead (Pb)

The concentration of lead values ranged from 6.5 to 7.9 ppm over the Harper and Campbell copper deposits while Messina copper deposit area had high concentration values that ranged from 10.2 to 30.5 ppm and found to be higher than the local background value of 10 ppm, which was classified as anomalous area. The high values of Pb within the Messina copper deposit area could be attributed to the fact that mineral processing for all the mined materials from the mines were mainly processed in this area, consequently the high occurrence of Pb. Two lead anomalous areas within the high precision areas (Fig.4.14b) were identified; one was associated with the Messina copper deposit while the second one was an isolated anomaly found towards the southern part of the Campbell area (Fig. 4.14a).

Zinc (Zn)

All the three copper deposits revealed anomalous values of zinc ranging from 28 ppm to 141 ppm with one anomalous area that was not considered as it was situated outside the precision area with respect to prediction standard error map (Fig.4.15a).

© University of Venda

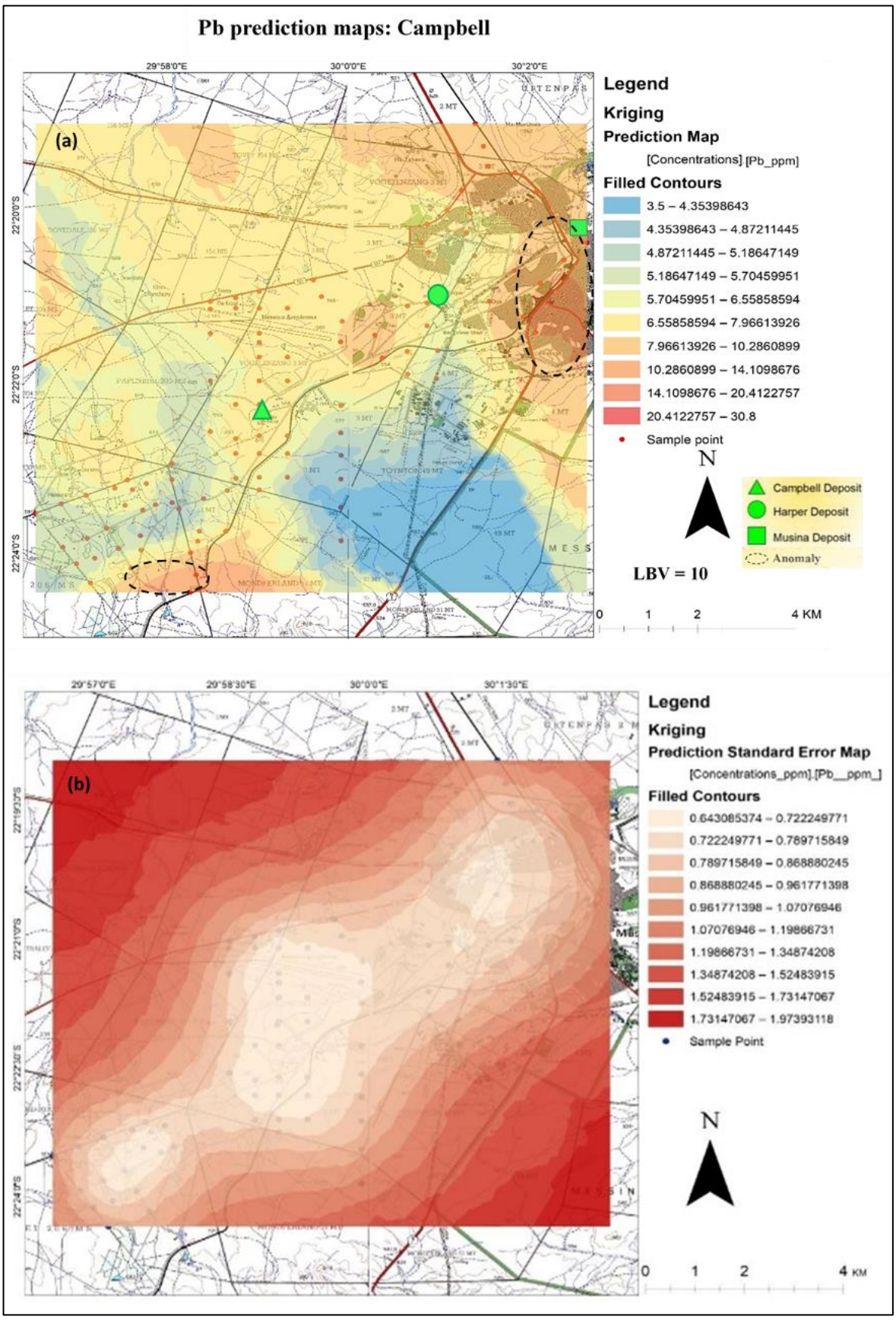


Figure 4.14: Lead prediction map showing distribution pattern and anomalous areas at Campbell area.

© University of Venda

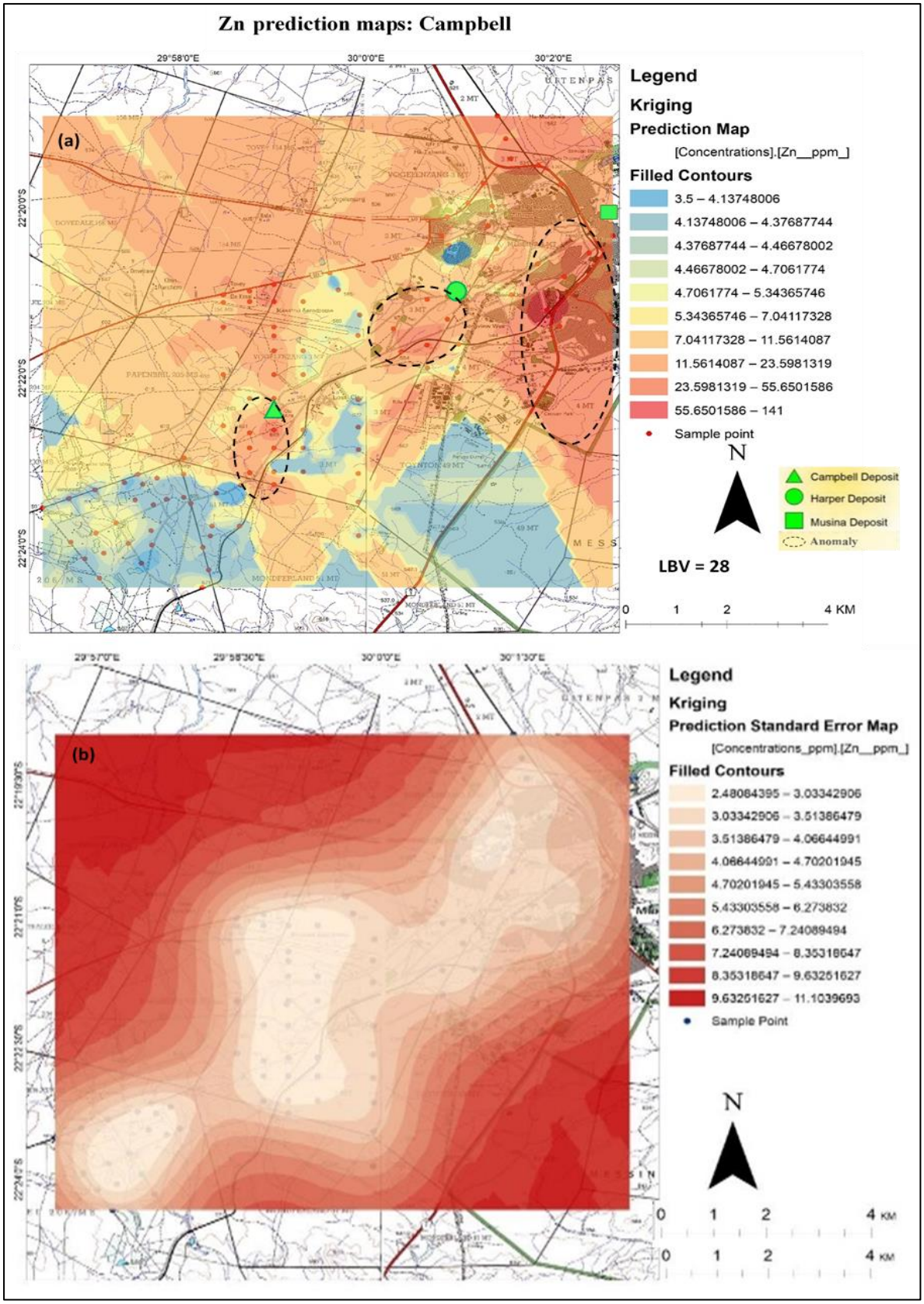


Figure 4.15: Zinc prediction map showing distribution pattern and anomalous areas at Campbell area.

© University of Venda

Copper (Cu)

Copper revealed a clear link between the occurrence of Cu anomalous values and the three copper deposits at Messina, Harper and Campbell (Fig. 4.16a) that falls within the high precision areas with low prediction error values (Fig. 4.16b). The copper anomalous values ranged from 261 to 1500 ppm with the southern part and northern part of the Campbell and Messina copper deposits registering a range from 26.9 to 94.4 ppm respectively.

Arsenic (As)

Arsenic revealed low concentration values with highest concentration levels of 15.9 ppm, which was just above the local background value (LBV) of 13 ppm (Fig. 4.17a). Two anomalous areas were revealed and were located within the areas with high precision as revealed by the error map (Fig. 4.17b). One of the anomaly occurred towards the southwestern part of the Campbell copper deposit while the second one occurred towards the northern part of the Campbell copper deposit. The concentration values within the copper deposits revealed values lower than the background values.

Nickel (Ni)

Two anomalous areas were identified; the first anomaly was located towards the southern part of Campbell copper deposit that registered the highest concentration levels that ranged from 92 to 152 ppm. The second anomaly was found located towards the northern part of the Campbell copper deposit with highest concentration levels that ranged from 39.8 to 58.7 ppm (Fig. 4.18a). One of the anomaly was situated towards the northern side of Harper deposit (Fig. 4.18a), but towards the area with low level of confidence in terms of standard error map (Fig. 4.18b), thus it was not considered in this case. Both Messina and Campbell copper deposits had Ni concentration values that ranged from 23.2 to 29.2 ppm while the Harper deposit registered lower concentration values that ranged from 8.8 to 18.7 ppm. All these values were below the LBV of 36 pp (Fig. 4.18a).

© University of Venda

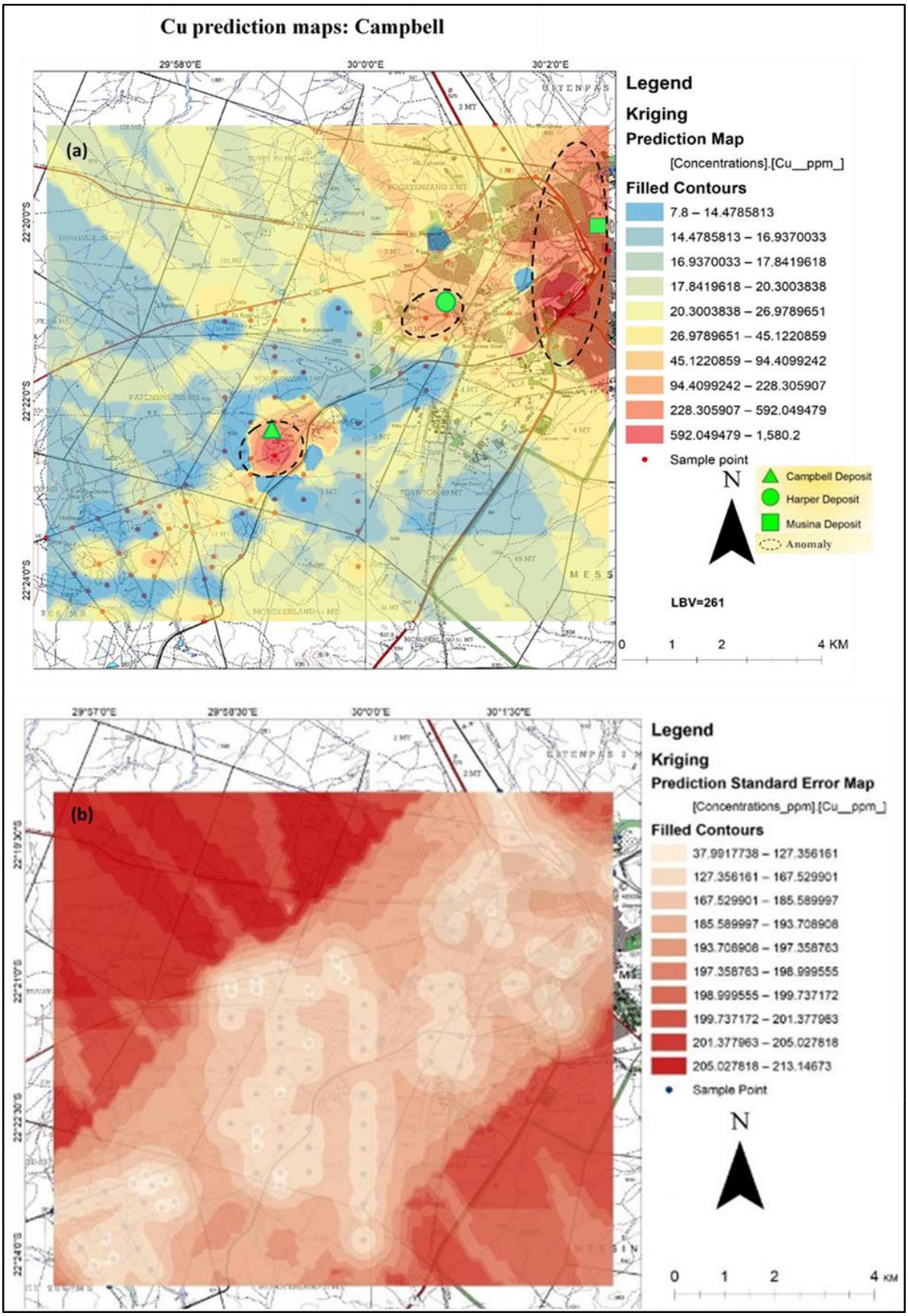


Figure 4.16: Copper prediction map showing distribution pattern and anomalous areas at Campbell area.

© University of Venda

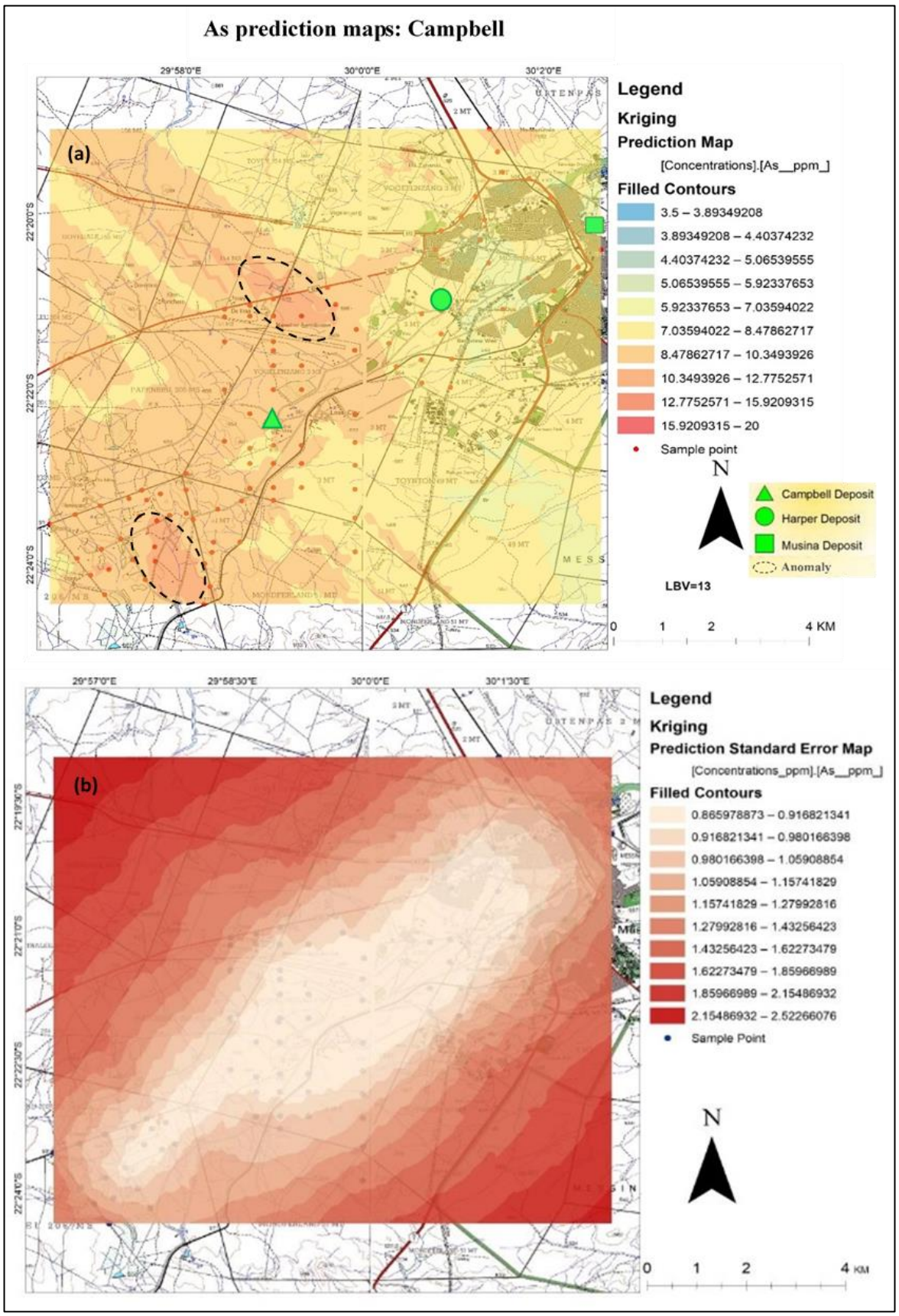


Figure 4.17: Arsenic prediction map showing distribution pattern and anomalous areas at Campbell area.

© University of Venda

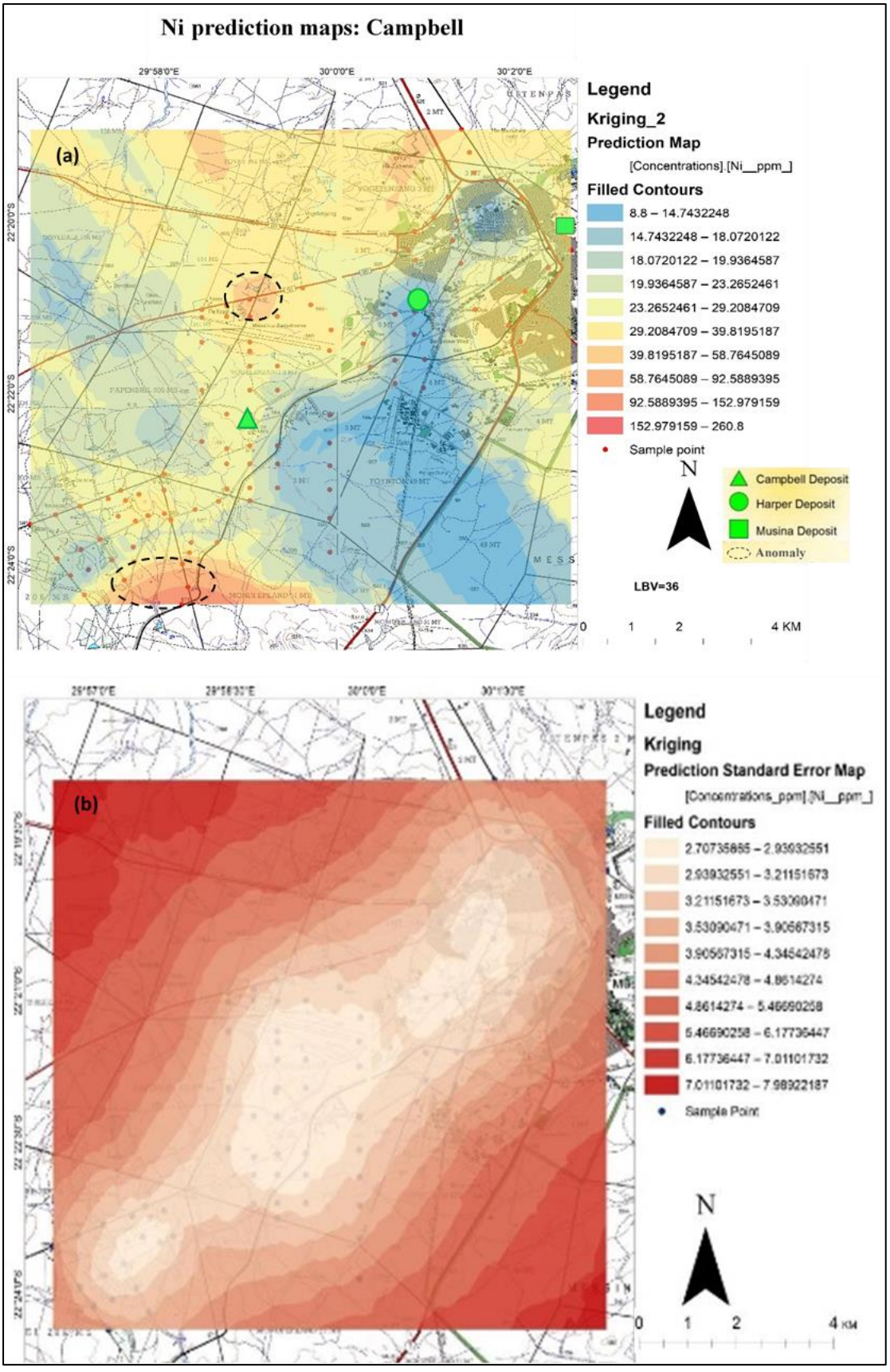


Figure 4.18: Nickel prediction map showing distribution pattern and anomalous areas at Campbell area.

© University of Venda

Generally, in the western part of the study area, it was deduced that the sulphide metals such as Pb, Zn, Cu, As and Ni registered high concentration levels over the known copper deposits, however, new areas were also identified. Most of these metals revealed anomalous areas that registered concentration values that were higher than the local background values and located at high level of precision in terms of the predictive standard error maps.

Soil geochemical maps of the eastern part of the study area (Artonvilla area)

Lead (Pb)

Lead anomaly over the known copper deposit occurred within the Messina copper deposit, which registered concentration levels of 17.7-20.8 ppm, higher than the local background value of 17.4 ppm. Four other anomalies that ranged from 20.8 to 25 ppm were identified and they were not associated with the known deposits (Fig.4.19a). The two anomalies were found towards the northern part of the study area, whereas the other two formed segmentation stretching down towards the southern part of the study area (Fig. 4.19a). The anomaly on the western side of Artonvilla was near less precision areas with respect to error map.

Zinc (Zn)

The concentration levels of zinc over the Messina and Artonvilla copper deposits registered concentrations from 30.2 to 37. 7 ppm, which was found to be less than the local background value of 52.6 ppm, however, an anomaly was located to the northeastern side of the Artonvilla copper deposited with values ranging from 48.1 to 62.3 ppm that was above the LBV of 52.6 ppm. One anomaly located at the northeastern side of the Artonvilla copper deposited was identified and was not associated with any known deposit. This anomaly registered the highest zinc concentration level that ranged from 48.1 to 62.3 ppm, which is above the LBV of 52.6 ppm. Two other areas registered high zinc concentrations but not higher than the LBV value (Fig. 4.20a). The two areas were located towards southern and southeastern side of the Artonvilla copper deposit and falls within the high precision areas with respect to error map (Fig. 4.20b).

© University of Venda

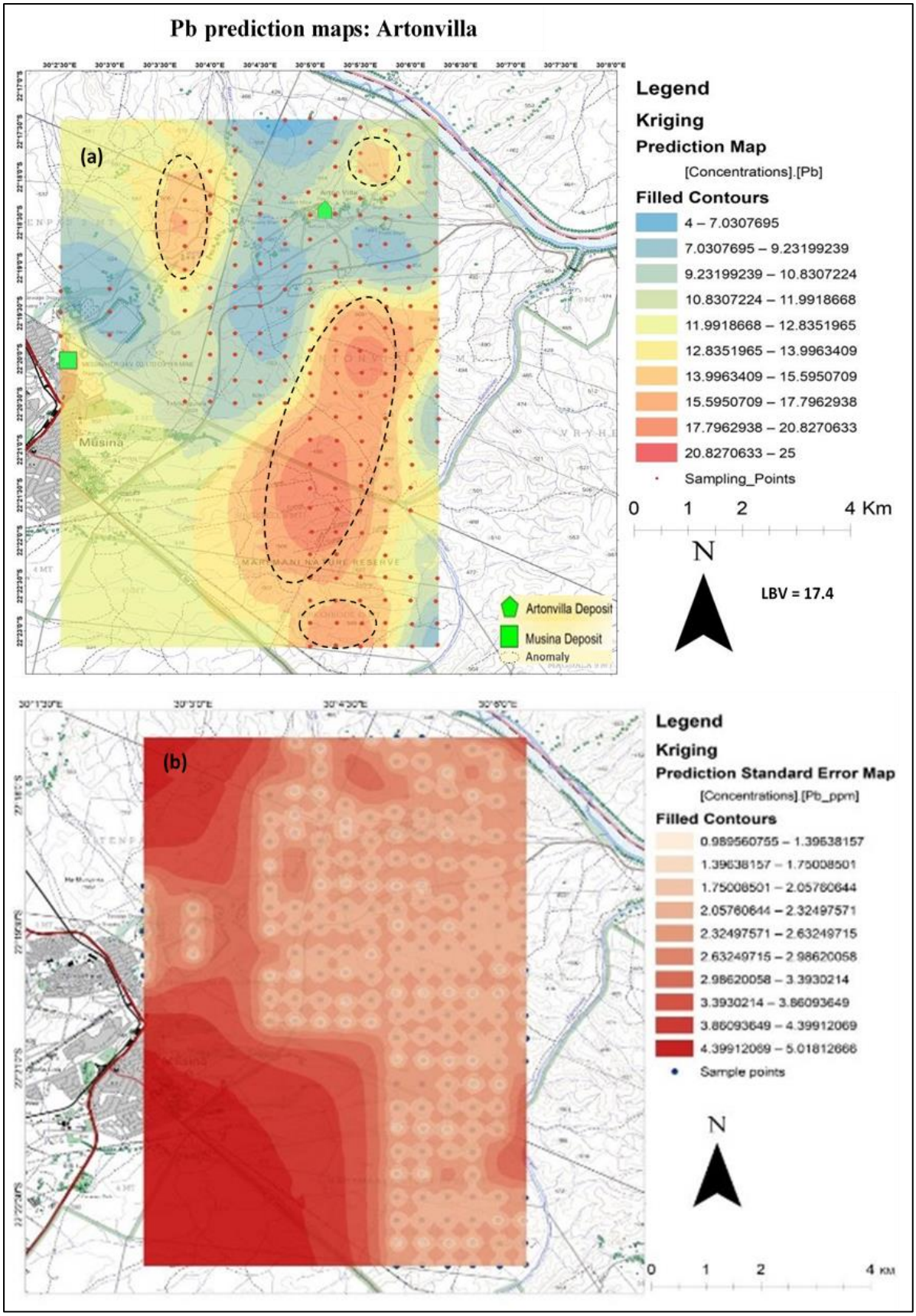


Figure 4.19: Lead prediction map showing distribution pattern and anomalies at Artonvilla area.

© University of Venda

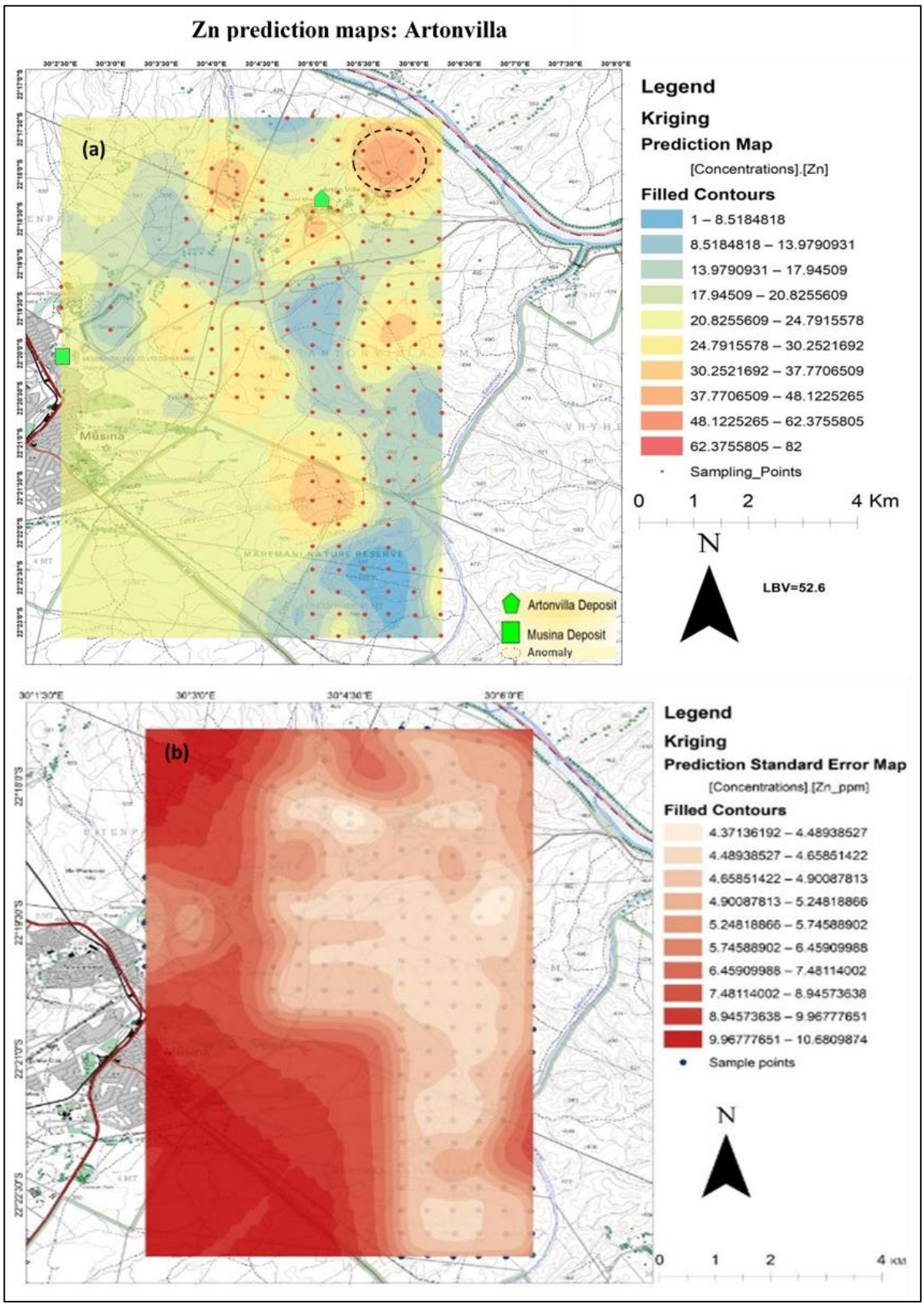


Figure 4.20: Zn prediction map showing distribution pattern and anomalous areas at Artonvilla area.

© University of Venda

Copper (Cu)

Copper registered anomalous concentration levels over the Messina copper deposits with the highest concentration levels of copper that ranged from 581 ppm to 1321 ppm, which was found to be higher than the local background value of 165.3 ppm. Around Artonvilla deposit high concentration levels of Cu (64.6 – 124.2 ppm) were registered but were lower than the LBV (Fig. 4.21a). The copper anomaly within the Messina deposit showed a dispersion towards the southeastern side of the deposit with a decrease in metal values away from the deposit.

Arsenic (As)

The distribution of arsenic in the eastern side of the study area indicated high values around the Messina and Artonvilla copper deposits (Fig.4.22a). However, there was an increase of values towards the northwestern part of the area (Fig.4 22a), although this was beyond the high precision area with respect to the error map (Fig. 4.22b).

Nickel (Ni)

Nickel registered anomalous values over the Artonvilla deposit and also to the northeast and southern part of the deposit (Fig. 4.23a). The anomaly to the northeastern part of the deposit was quite prominent with high values ranging from 473 to 1000 ppm. The other anomalies to the southern part of Artonvilla copper deposit had relatively lower values of up to 229 ppm (Fig.4.23a). These anomalies fall within the high precision areas of the prediction standard error map (Fig.4.23b).

© University of Venda

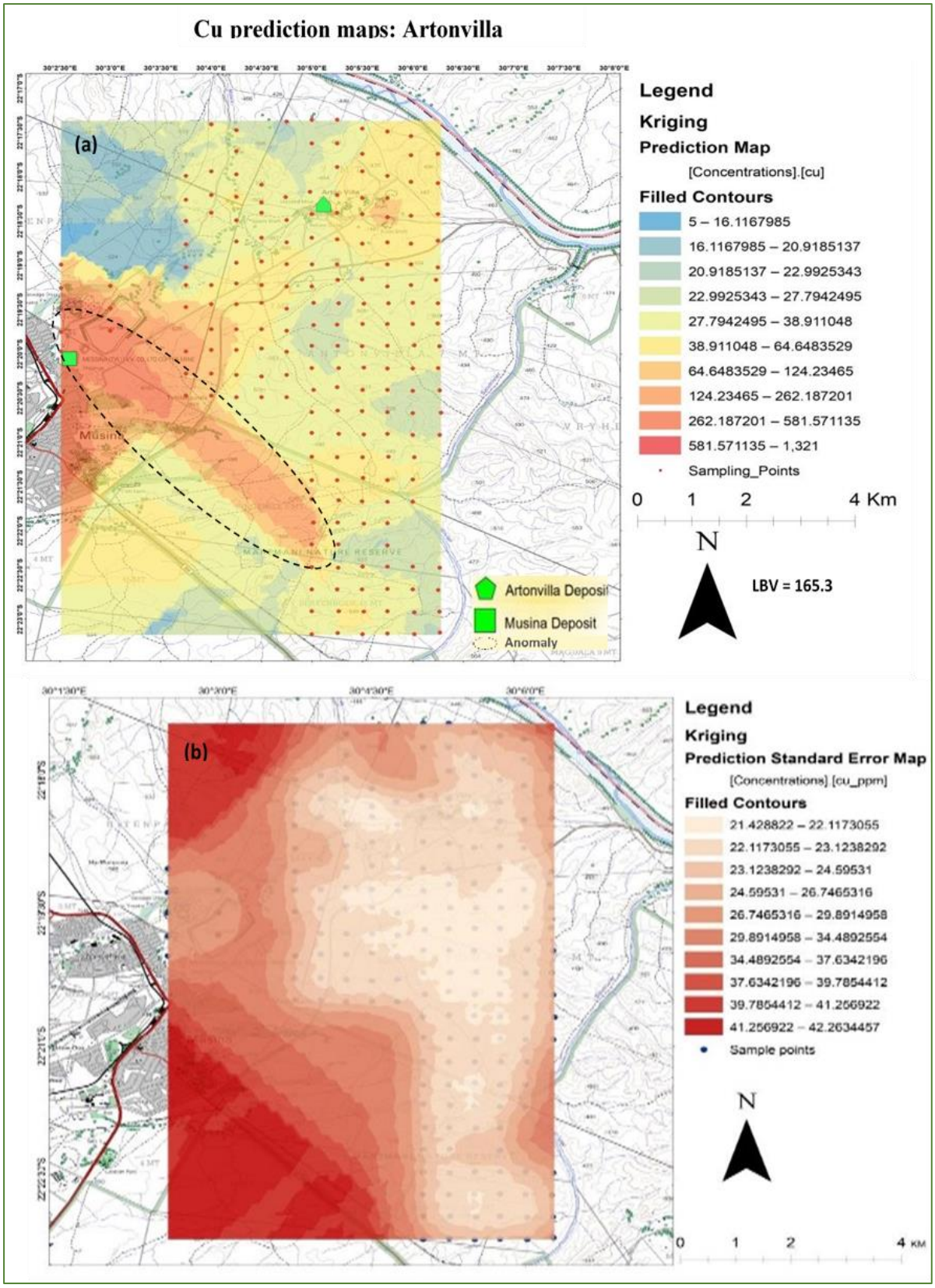


Figure 4.21: Copper prediction map showing distribution pattern and anomalous areas at Artonvilla area.

© University of Venda

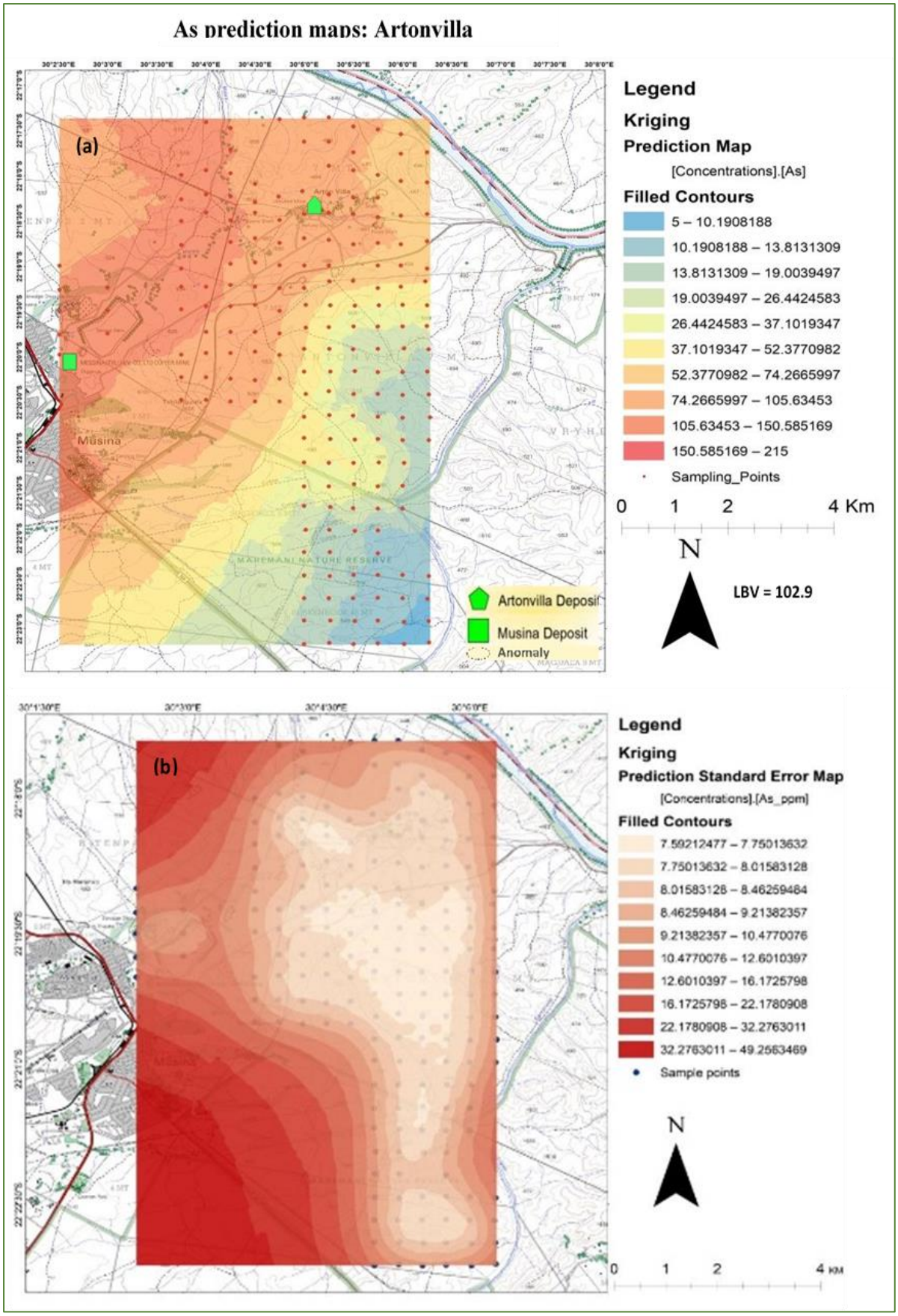


Figure 4.22: Arsenic prediction map showing distribution pattern and anomalous areas at Artonvilla area.

© University of Venda

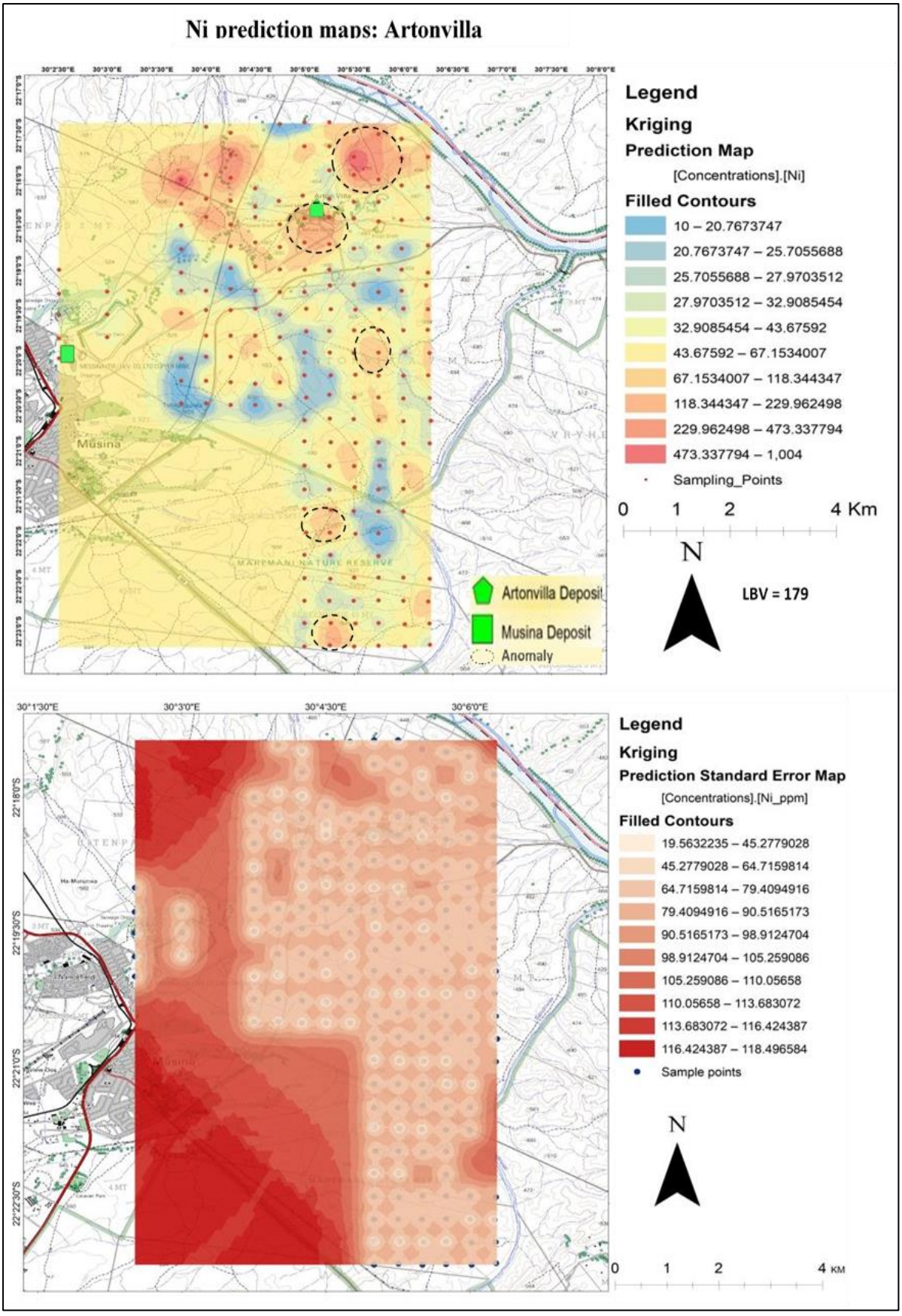


Figure 4.23: Ni prediction map showing distribution pattern and anomalous areas at Artonvilla area.

© University of Venda

Based on these findings, the study revealed a total of 5 anomalous areas within the study area (Fig, 4.24). These anomalous areas were referred to as Target areas (TA): Target area 1 was situated to the southern part of Campbell copper deposit while TA 2 was situated towards the northeastern part of Artonvilla copper deposit with TA 3 situated towards the southern part of Artonvilla deposit. Target area 4 was located further south from the Artonvilla copper deposit while TA 5 was situated towards the western part of Messina copper deposit.

From the target areas (Fig. 4.24), it was observed that Ni occurred in all the target areas with Pb also occurring in all the target areas with the exception of TA 5. Arsenic was in target area on the western side of the study area with Zn found only in TA 2 on the eastern part of the study area. The overall deduction was that Pb, Zn, As and Ni were the sulphide elements with anomalous concentration levels within the study area.

The Campbell and Harper copper deposits revealed anomalous concentration of Zn and Cu while Artonvilla revealed anomalous concentration levels of As and Ni. Messina copper deposits revealed anomalous concentration levels of Pb, Cu and As. Consequently, the Messina copper sulphide deposits revealed anomalous concentration levels of Pb, Zn, Cu As and Ni of which all were also revealed within the target areas with the exception of copper.

4.7 Discussion

Soil geochemical survey is a powerful tool for mineral exploration of buried ore bodies. The method is generally applied to determine whether or not the soil contains elevated values of metals, for example, in the case of base metals exploration such metals as Pb, Zn, Cu, As, Ni. can act as precursors of ore mineralisation in the studied area. To determine whether or not soil contains valuable metals, it is necessary to determine the natural abundance of the metal/element in soil. This is referred to as the geochemical background value of the metal/element in soil. Any values above the background value can be considered as anomalous values. Generally, the weathering of mineralized rocks or ore bodies result in chemical dispersion of the ore minerals that are re-deposited in residual soil, thus soil geochemical survey is commonly applied in areas of deep soil cover, where the outcrops are scanty and weathering is intensive. Randive (2012) and Podlešáková *et al.* (1999) noted that any metal can disperse and show in the soil, however, immobile elements like Pb, Cu, As, Mo, Pt and Cr show more pronounced anomalies.

© University of Venda

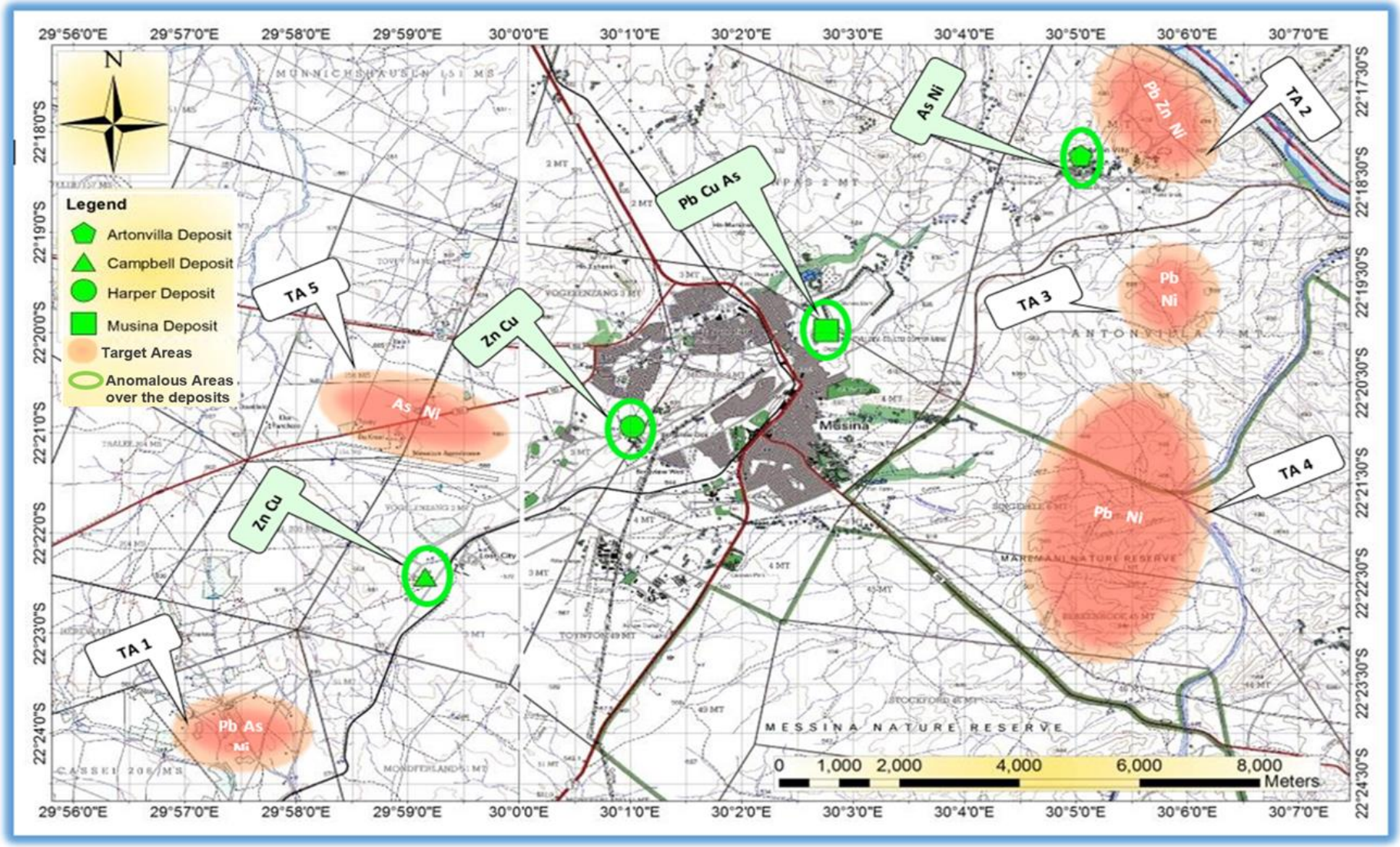


Figure 4.24: Identified target areas (TA) for future exploration in the study area.

© University of Venda

In the current study, soil geochemical survey was undertaken in order to ascertain the occurrence, concentration levels and dispersion of sulphide minerals, namely; Pb, Zn, Cu, As and Ni in soil within the study area. This was done in order to identify new, currently unknown ore mineralisation in the area. The study involved: soil sampling in both the western and eastern sides of Messina copper deposit; sample preparation; sample analysis, using atomic absorption spectrometry; and data analysis, using Ordinary Kriging method.

Data analysis revealed a number of metal anomalies, for example, Pb, Zn, Cu, As and Ni over the known copper deposits at Campbell, Harper, Messina and Artonvilla as well as over five other areas that have not been associated with any sulphide mineralisation. Such new anomalous areas have been identified as target areas for future exploration of sulphide ore mineralisation.

The identified target areas include the following (Fig. 4.24): TA 1 at the southern part of Campbell copper deposit for Pb, As and Ni; TA 2 and 3 towards northeastern and southeastern side of Artonvilla copper deposit for Pb, Zn and Ni; TA 4 situated further south of the Artonvilla deposits with Pb and Ni anomalies and TA 5 located towards the western side of Harper deposit and northern part of Campbell deposit with As and Ni anomalies.

The potential for sulphide ore mineralisation in the Musina area and it's environs is quite high, thus there is need to continue with further exploration in the region. Copper anomalies were only identified over known deposits and this could be due to the fact that the background values of Cu were high due to the exposure of copper within the known copper deposits as compared to Cu levels within the area of unknown copper deposits.

© University of Venda

CHAPTER 5

REMOTE SENSING STUDY

Preamble

This chapter focuses on the study of remote sensing within the study area for the purpose of identifying structural features that are associated with the Messina copper deposits as well as to establish hydrothermally altered minerals in the area. The chapter, firstly, introduce fundamental principles of remote sensing, data acquisition, instrumentation, softwares, techniques and methods of analysis, application of remote sensing; and history of remote sensing for mineral exploration. Secondly, the chapter gives details on the data acquisition, processing, analysis and interpretation of the geological structures and mineral alteration within and around the Messina copper deposits. This study was done in order to depict the association of the mineral alteration and geological structures so as to identify potential areas as exploration target sites for ore mineralisation.

5.1 Fundamentals of Remote Sensing

Remote sensing has been defined in many different ways, for example, Lintz and Simonett (1976) defined remote sensing as the acquisition of physical data of an object without any any contact. According to Gregory (1979) remote sensing denotes the aerospace practices of measuring the ultraviolet, visible, infrared and microwave radiations emitted and reflected from the surface of the Earth and from the atmosphere. Sabins (1999) on the other hand defined remote sensing as the science of acquiring, processing and interpreting images acquired from aircraft and satellites. Sabins (1999) and Torres (2016) further defined remote sensing as the practice of deriving information about the Earth's mineral composition and structural features, using images acquired from an overhead perspective by means of electromagnetic radiation in one or more regions of the electromagnetic spectrum, reflected or emitted from the Earth's surface. For the application of remote sensing investigation, one has to be conversant with its fundamental basics and procedures of remote sensing, for example, fundamental principles, data acquisition, processes, instrumentation, processing techniques, different methods of analysis and different softwares used in remote sensing (Fig. 5.1).

© University of Venda

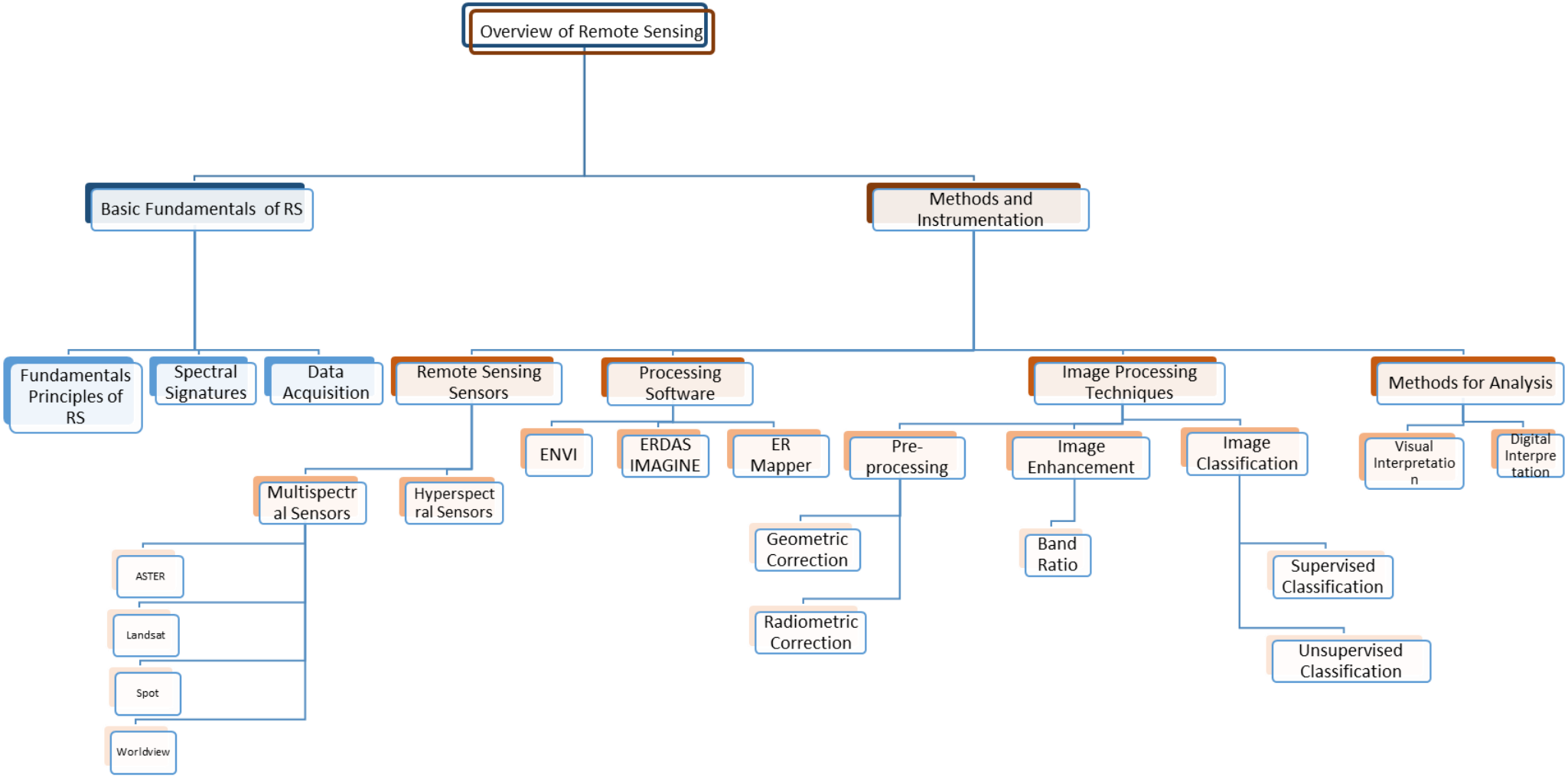


Figure 5.1: Overview on fundamentals and procedures of remote Sensing.

© University of Venda

5.1.1 Principles of Remote Sensing

Remote sensing is based on the principles of spectroscopy which is simply the measurement of light as a function of wavelength reflected or emitted from materials (Asadzadeh and de Souza Filho, 2015). As a results, in order for remote sensing to detect and discriminate between objects, it requires the detection and recording of radiant energy reflected or emitted by objects or surface features (Aggarwal, 2003). Electron magnetic radiation is classified by wavelength into radio and microwave (1000 μm to 1 m), infrared (700 nm – 1 mm), visible (400 to 700 nm), ultraviolet (10 to 380 nm), Xrays and gamma rays (0.01 to 10 nm). Different objects or surface features reflect different amount of energy in different bands of the electromagnetic spectrum, since materials absorb and reflected incident light at wavelength dependent fashion. The amount of energy reflected depends on the properties of the material, for example, their physical and chemical or mineralogical characteristics. These properties determine which wavelength band within the electromagnetic spectrum gets reflected, absorbed or transmitted and at what levels, thereby defining the spectral signatures (the ratio of reflected energy to incident energy as a function of wavelength) of each object (Aggarwal, 2003).

Spectral signatures are the reflectance and unique absorption properties of an object attributed to the fact that every natural and artificial object reflects and emits electromagnetic radiation over a range of wavelength in its own characteristic manner, according to its physical and chemical properties (Aggarwal, 2003). For example, minerals, rocks and hydrocarbons exhibit diagnostic absorption features in either the visible –near infrared (VNIR) (0.4 – 1.0μm), shortwave infrared (SWIR) (1.0 – 2.0 μm), mid infrared (MIR) (3 -5 μm), and/or longwave infrared (LWIR) (8 – 14 μm) wavelength ranges (Asadzadeh and de Souza, 2015).

According to Aggarwal (2003) and (Hauff, 2005), the spectral signature is responsible for the colour tone of an object in a satellite image and as a result it is used to distinguish between features. For example, in a true colour composite image, the colour of vegetation appears green because the plant pigment in the leaves (chlorophyll) strongly absorbs radiation in the red and blue wavelengths, but reflects the green wavelength band. Water appears blue or blue-green because longer visible wavelengths and near infrared radiation is absorbed more than the visible wavelengths (Fig. 5.2).

© University of Venda

Spectral signature curves are used to effectively detect and discriminate between objects using their spectral signatures**.** These curves show distinctive reflectance and emittance properties of certain type of objects and their conditions. Consequently, the spectral signature curves facilitate the determination of which bands are most useful for discriminating between certain features (University of Cincinnati, 2016). For example, when trying to discriminate between healthy and unhealthy vegetation, it is particularly useful to look at the infrared band of the electromagnetic spectrum. This is so because as the internal structure of the healthy leaves acts as a diffuse reflector of VNIR wavelengths meaning that the higher the reflectance in the infrared band, the healthier the vegetation (Aggarwal, 2003).

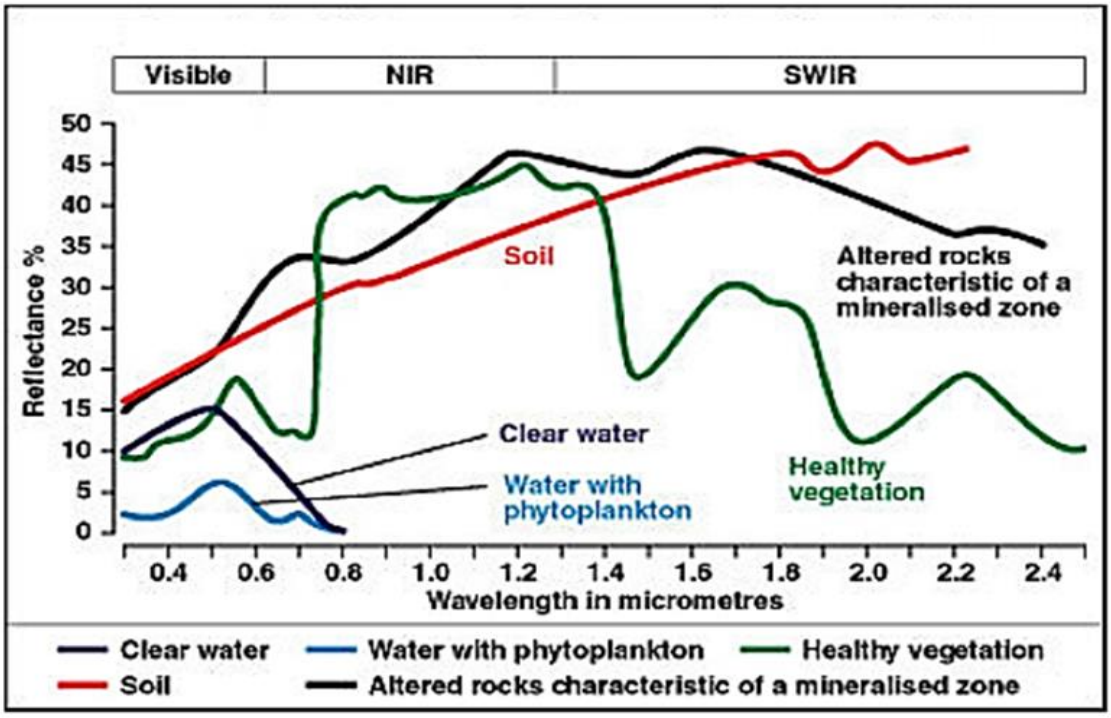


Figure 5.2: Spectral signature (response pattern) for vegetation, water, bare soil and altered rocks characteristics of a mineralised zone (Hauff, 2005).

There are several properties that influence the spectral signature of minerals *viz*; crystal structure, molecular substitution, chemical composition and water content. These properties influence the spectral signature of minerals because they determine the manner in which minerals absorb and reflect radiations which then produce characteristic reflectance spectra that can be used to discriminate between minerals (Clark, 1999; Aggarwal, 2003).

© University of Venda

5.1.2 Remote Sensing Data Acquisition Process

Remote sensing data acquisition process involves several elements, for example, energy source, atmosphere, target, sensor, processing, interpretation and analysis.

Energy source/illumination

The first requirement for data acquisition is the energy source [Fig. 5.3(A)] which is needed to illuminate or provide electromagnetic energy to the target of interest. Most of the multispectral sensors such as Advanced Spaceborne Thermal Emission and Reflection Radiometer (ASTER) use the electromagnetic energy provided by the sun (natural energy) and these are referred to as passive sensors because they rely on natural illumination of the target of interest (Aggarwal, 2003). However, there are some sensors that provide their own electromagnetic energy, and these are referred to as active sensors because they rely on artificial illumination of the target of interest (Aggarwal, 2003).

Radiation and the atmosphere

When energy travels from the source to the target, it comes into contact with and interacts with the atmosphere as it passes through and causes scattering, absorption and refraction of the electromagnetic energy and this causes errors in the amount of energy measured by the sensors. These interactions are collectively referred to as atmospheric effects [Fig. 5.3 (B)] and they interfere with the remote sensing process and must be corrected before undertaking any analysis of the data collected (Aggarwal, 2003).

Interaction of energy with the target

Once the energy makes its way to the target through the atmosphere, it interacts with the target, then depending on the properties of the target and the wavelength of the incident energy, specific wavelength within the incident energy will be absorbed or transmitted and some will be reflected back to the satellite sensor (Aggarwal, 2003). The energy that is reflected back to the sensor is representative of the properties of the target, as it will be missing certain wavelength bands that have been absorbed by the target of interest [Fig. 5.3(C)]. The reflected energy is characterised as the spectral response pattern of the target (Clarke Labs, 2008).

© University of Venda

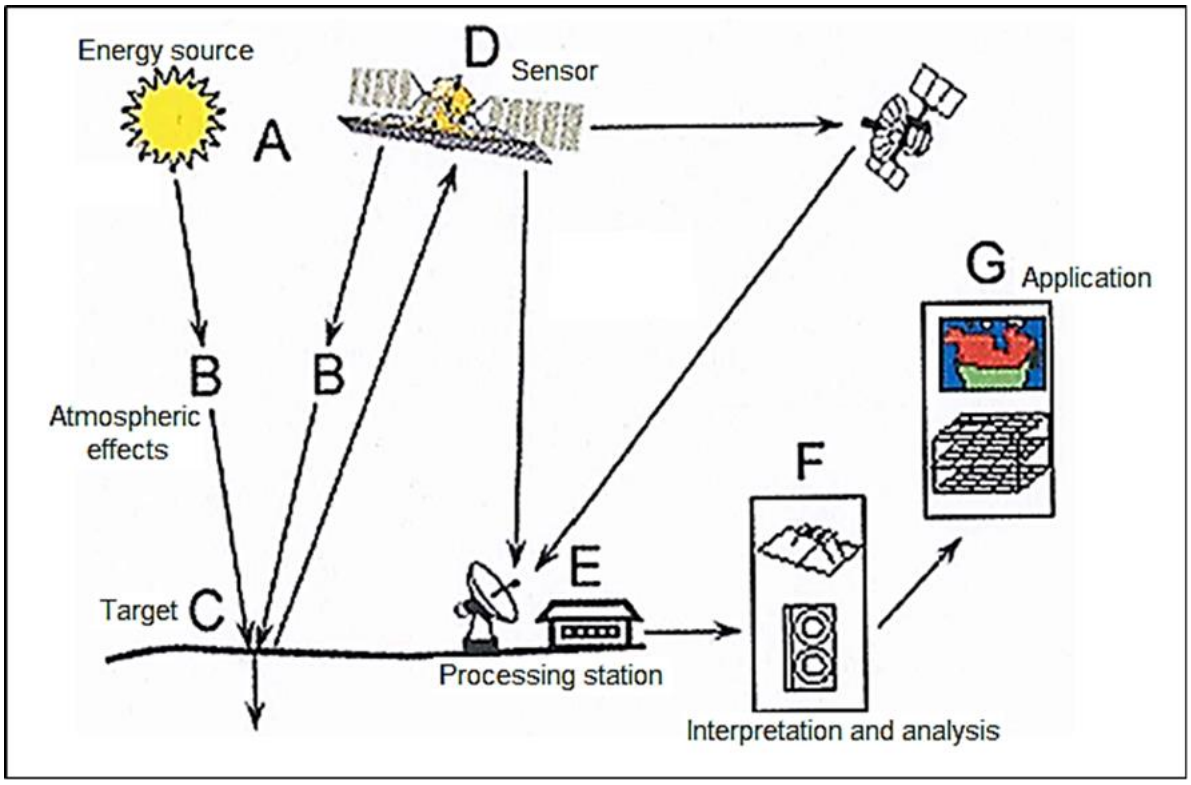


Figure 5.3: Remote sensing processes (A) Energy source which is needed to illuminate or provide electromagnetic energy to the target of interest; (B) Atmospheric effects; (C) Interaction of energy with the target; (D) Satellite sensor where energy is recorded and measured; (E) Processing station where data is processed into an image form; (F) Interpretation and analysis of processed image; (G) Application of the information (Aggarwal, 2003).

Recording of the energy by the sensor

After the energy has been reflected from the target, it then travels back through the atmosphere to the satellite sensor, where it is measured and recorded. During scanning of the targeted view, the sensor moves from western to eastern direction and also from northern to southern direction. Together this movement allows the sensor to collect, measure and record the reflected energy, thus providing the means of composing a raster image of the target of interest [Fig. 5.3 (D)] (Clarke Labs, 2008).

Processing

The energy recorded by the sensor is then transmitted in electronic form (raster data), to a receiving and processing station where the data will be processed into an image [Fig.5.3 (E)]

© University of Venda

(Government of Canada, 2015). Processing of the data entails correction of the atmospheric effects and errors (Government of Canada, 2015).

Interpretation and analysis

The processed image is then interpreted [Fig. 5.3(F)] to extract information about the target of interest. Interpretation includes two techniques, viz; visual interpretation and digital interpretation, and these are discussed below.

Application

The final element in the data acquisition process is the application [Fig. 5.3(G)] of the information that has been extracted from the imagery about the target of interest (Government of Canada, 2015). For the purpose of this study, the extracted information is the relationship among the Messina copper deposits, the mineral alteration and the geological structures found within and around these deposits. This information is used to develop target generation for mineral exploration as well as to infer the mineralisation style within the study area.

5.1.3 Remote Sensing Instrumentation

Satellite imageries are area acquired using either air-born or space-born sensors. For example, air-born sensors such as Hyperspectral and space-born sensors such as multispectral sensors like Landsat, ASTER, Worldview and SPOT imageries. Satellite imageries are acquired using variety of space-borne sensors where each sensor has unique specification that provides unique information about the Earth's surface. Two main characteristics that guide the choice of which sensor to use include; spatial resolution and spectral resolution.

Spatial resolution refers to a capability of the sensor to discriminate the smallest object on the ground of different sizes (Joseph, 2005), thus the smaller the spatial resolution the better as this allows the sensor to record minute details and discriminate between two closely spaced objects (Clark Labs, 2008). Spectral resolution refers to the number and width of the spectral bands that the satellite sensor detects, thus the higher the number of bands the sensor can record at small band widths, the better it detects and differentiates between similar spectral signatures (Clark Labs, 2008). The spatial and spectral resolution issues also affect the cost during data acquisition, thus also an important factor to consider when choosing a particular

© University of Venda

sensor for a project (Clark Labs, 2008). Satellite sensors are divided into two categories based on their spectral resolution, i.e. Multispectral and Hyperspectral sensors (Table 5.1).

5.1.3.1 Multispectral Sensors

Multispectral sensors are sensors that measure and record electromagnetic radiation reflected from the Earth's surface in several wavelength bands along the electromagnetic spectrum (Government of Canada, 2013). Multispectral sensors are characterised by 3 to 20 different band measurements in each pixel they produce, and these bands include the VNIR, SWIR and LWIR (Centre for Remote Imaging, Sensing and Processing, 2001). Images produced by these sensors, require knowledge of the spectral reflectance signatures of the target in the image. In this case, the spectral information content of the image was used in the interpretation of the image (Centre for Remote Imaging, Sensing and Processing, 2001).

Among the various multispectral sensors available, only a few are used for mineral exploration, namely; Worldview-2, ASTER, Landsat 7+ETM, Satellite Pour I 'Observation de la Terra (SPOT) multispectral scanner, SPOT panchromatic, and Landsat 4.5 Thematic Mapper (TM) (Table 5.1).

Landsat 4.5 Thematic mapper (TM) and Landsat 7 Enhanced TM+

Combination of Landsat Thematic Mapper (TM) Landsat 7 enhanced TM+ bands provide information about landscape and regolith materials for use in geological mapping. Landsat strength are generally seen to be its regular acquisition schedule, long term data archive and relatively rich spectral information (but richer than for hyperspectral data). Limitation of Landsat data is that it is only a moderate –resolution image source (30 m multispectral, 120 m thermal infrared) and the fixed acquisition schedule makes it sometimes difficult to acquire imageries (Gillan, 2013; Government of South Australia, 2014).

SPOT Multispectral Scanner (XS) and SPOT Panchromatic (PAN)

Satellite Pour l'Observation de la Terre (SPOT) is the European earth observing satellite system and its data are visible and near-infrared radiance data obtained from High Resolution

© University of Venda

Visible (HRV) sensors carried on the SPOT-1, -2 and -3 satellites. SPOT acquires image in multispectral scanner and panchromatic modes, which acquires image at spatial resolution of 20 m and 10 m respectively. Both sensors cover 60 km by 60 km of terrain (Table 5.1) Sabins, 1999).

SPOT images are useful in mineral exploration because they have high ground resolution at 10 m and 20 m (Table 5.1) which proves to be effective when mapping a large scale (Rousselot and Weber, 1987). SPOT images considerably improve the identification of secondary structural features that may be significant for mineral exploration (Rousselot and Weber, 1987). Its limitation is that its spectral resolution only measures and records reflected radiation along 8 bands. This greatly impedes their application in mineral exploration, as they cannot effectively discriminate between different types of mineral alteration (Sabins, 1999).

ASTER

The Advanced Spaceborne Thermal Emission and Reflection Radiometer (ASTER) is an advanced multispectral imager that was launched on board of NASA's Terra spacecraft in December 1999. ASTER covers a wide spectral region with 14 bands, ranging from the visible to the thermal infrared wavelength band, with high special spectral and radiometric resolution (Abrahams and Hook, 2006; Duda *et al*., 2015). The spatial resolution varies with the wavelength for instances, 15 m in the VNIR, 30 m in the SWIR and 60 m in the thermal TIR. Each image covers an area of 60 km x 60 km (Abrams and Hook, 2006; Duda *et al.*, 2015).

The high number of bands in ASTER increases the spatial resolution of the images and it also has the best spatial and radiometric resolution currently available. ASTER is good for mineral exploration as there is a standardized processing methodology to transform the raw data into 17 geoscience products that reflect mineral abundance derived from the VNIR and SWIR bands (Government of South Australia, 2014; Duda *et al.,* 2015). Consequently, ASTER images were used in this study to delineate the spatial relationship between Messina copper sulphide deposits, mineral alteration and the geological structures within and around the study area

© University of Venda

Table 5.1: Characteristics of Multispectral and Hyperspectral sensors (www.satimagingcorp.com/satellite-sensors/worldview-3/; Sabins, 1999)

Characteristics	Multispectral sensors						Hyperspectral sensors
	Landsat 4.5 Thematic mapper (TM)	**Landsat 7 Enhanced TM**	**SPOT multispectral scanner (XS)**	**Spot panchromatic (PAN)**	**ASTER**	**Worldview-2 and Worldview-3**	**AVIRIS hyperspectral**
Spectral region							
Visible and reflected IR	0.45 -2.35 µm	0.45 - 2.35 µm	0.50 - 0.89 µm	-	0.52–2.43 µm	0.4 – 0.9 µm 0.4 – 0.7 µm	0.4 – 2.50 µm
Panchromatic	-	0.52 - 0.90 µm	-	051-0.73 µm	-	0.45 -0.8 µm 0.45 – 0.8 µm	
Thermal IR	10.5 - 12.5 µm	-	-	-	8.125-11.65 µm	-	
Spectral bands	7	8	3	1	14	1pan +8mult 8 , 12 CAVIS	200
Terrain coverage							
East to west	185 km	185 km	60 km	60 km	60 km	Swath width of 16.4 km at nadir/ nadir: 13.1 km	10.5 km cross track
North to South	170 km	170 km	60 km	60 km	60 km		
Ground resolution cell							
Visible and reflected IR	30 by 30 m	30 by 30 m	20 by 20 m	-	15 - 30 m	Multispectral: 1.84 m GSD at nadir, 2.08 m GSD at 20° off-nadir	20 m
Panchromatic	-	15 by 15 m	-	10 by 10 m	-	0.46 m GSD at nadir, 0.52 m GSD at 20° off-nadir Nadir: 0.31 m GSD at Nadir 0.34 m at 20° Off-Nadi	Panchromatic
Thermal IR	120 by 120 m	60 by 60 m	-	-	90	-	

© University of Venda

WorldView-2 and Worldview3

The WorldView2 satellite was launched in October 2009 from Vandenburg Air Force Base in California. It is a high-resolution satellite with 8 – multispectral imaging bands. It runs in the 770 km high sun –synchronous orbit and collects both Panchromatic and Multispectral imageries simultaneously at 0.46 m and 1.84 m respectively, but it is available commercially as 0.5 m imagery. Each sensor is focused narrowly on a specific range of the electromagnetic spectrum that is sensitive to a specific feature on the ground. The sensors are designed to improve the segmentation and classification of land and aquatic features beyond any other spaced-based remote sensing platform. WorldView-2 satellite has geolocation accuracy specification of 6.5 m, with predicted performance in the range of 4.6 to 10.7 m, excluding terrain and off –nadir effects (Zhang Ruisi *et al.,* 2011; DigitalGlobe Core Imagery Products Guide, 2015) (Table 5.1). Zhang Ruisi *et al.* (2011) demonstrated that besides, ASTER, WorldView-2 is also effective in the interpretation of geological structures such as bedding planes, faults and folds as well as for large scale geological mapping. WorldView-3 satellite was launched in 13 August 2014 with high spectral resolution, with 8 bands in VNIR and additional 8 bands in SWIR (Bei *et al.,* 2017). In this study, ASTER was chosen over WorldView because WorldView does not have the standardized methodology to transform the raw data into mineral abundance.

5.1.3.2 Hyperspectral Sensors

Hyperspectral sensors are special types of multispectral sensors that are generally composed of about 100 to 200 bands of relatively narrow bandwidths of 5-10 nm (Sabins, 1999; Borzov, 2016; www.csr.utexas.edu/projects/rs/hrs/hyper.html). They have high spectral resolution as compared to normal multispectral sensors. Thus makes them particularly useful in mineral exploration because they are able to discriminate between minerals with closely related spectral signatures (Sabins, 1999; Borzov, 2016).

Hyperspectral sensor that is currently operational and commercially available is the Airborne Visible Infrared Imaging spectrometer (AVIRIS). The images produced by this sensor are 10.5 km wide and several km long (Sabins, 1999; Borzov, 2016; www.csr.utexas.edu/projects/rs/hrs/hyper.html).

© University of Venda

Hyperspectral sensors are limited to airborne platforms and this severely limits the amount of terrain coverage, thus increasing the cost of data acquisition (Sabins, 1999). For this sensor the post-processing techniques are so complex and labour intensive as there is more information due to large number of spectral bands available. Consequently, multispectral sensor was used in this study, instead of hyperspectral sensors.

5.1.4 Image Processing Software

Image processing is a process that uses digital remote sensing data that can be interpreted by computer programs that manipulate the data recorded in pixel to yield information about specific subjects (Schwengerdt, 1983). Image processing is done using a variety of good image processing systems such as Earth Resources Data Analysis System, Earth Resources (ERDAS ER) Mapper, EASI/PACE, Environment for Visualizing Images (ENVI), ERDAS Imagine, GRASS GIS, IDRISI. The choice of which computer program to use is governed by the cost of the program as well as the level of computer processing skills required by each program (Schwengerdt, 1983).

5.1.5 Image Processing Techniques

Remotely sensed data which are collected and measured by satellite sensors are subjected to different types of errors due to four main factors; imaging characteristics of the sensor, stability and orbit characteristics of the satellite, surface characteristics, motion of the earth, atmospheric effects (Joseph, 2005). These factors yield errors such as geometric and radiometric distortions in the data which can lead to the cascading errors in the interpretation of the data. Consequently, these errors must be corrected by using digital processing techniques which are; pre-processing, enhancement and classification and this must be done before analysis (Schowengerdt, 1983).

5.1.5.1 Pre-processing Techniques

This involves initial processing stage of the raw data to calibrate the image radiometry, correct geometric distortions and remove noise, with the goal of creating data that depicts a

© University of Venda

true representation of the original scene and facilitate further manipulation and analysis of the data (Schowengerdt, 1983).

Radiometric corrections

These are done in order to adjust digital values for hazy atmospheric effects. They are performed in order to remove radiometric errors which are undesired spatial or temporal variations in the image brightness that are not associated with the variations in the image surface. If these errors are not corrected they limit one's ability to quantitatively process and analyses the satellite image (Joseph, 2005). Radiometric errors are classified into three type namely; radiance calibration, topographic corrections, and atmospheric corrections.

Radiance calibration: This is performed when an image has vignetting property which is showing darker colour at the corners of the image while the centre of the image is lighter. With the respect of ASTER images, this is performed using image processing software such as ERDAS Imagine, or ENVI (ER mapper) by scaling the ASTER sensor signal to 8-bit data (Kalinowski and Oliver, 2004).

Topographic correction: This is performed to correct radiometric error which is due to modification of illumination conditions by the topography. The two commonly used methods of topographic correction method are the lambertian behavior and non-lambertian effects methods (Vicente-Serrano *et al.*, 2008).

Atmospheric corrections: These are models that are executed in order to correct radiometric errors caused by atmospheric processes such as absorption and scattering of incident and reflected radiations from the target. The atmospheric correction methods range from simple method which is based on information in the image such as dark object subtraction-based method to complex methods such as Simplified Method of the Atmospheric Corrections (SMAC), Moderate Resolution Atmosphere Transmission (MODTRAN) and Atmospheric and Topographic Correction (ATCOR) that stimulate the atmosphere/light interactions between the sun and surface-sensor trajectories (Vicente-Serrano *et al.*, 2008).

In this study, the simple models based on dark object subtraction were considered, focusing on the dark pixel correction method which assumes that some areas of the image have near-zero reflectance (Vicente-Serrano *et al.*, 2008). Based on this assumption, a minimum value

© University of Venda

for each data set is subtracted from the data to account for scattering conditions and other effects of the atmosphere. This method can be undertaken by any image processing software using the following algorithm formula l1-RMIN (R1, l1), where RMIN gives the minimum value for a particular band, R1 specifies the region of interest, and l1 specifies the input band (Kalinowski and Oliver, 2004)

Geometric distortion corrections

This is done in order to correct the distortions that are due to errors in the satellite's positioning on its obit, Earth's rotation and Earth's curvature and relief (Cambell and Wynne, 2011). This is done by converting the digital image to real world co-ordinates, using ground control points as well as georeferencing and geocoding, which can be carried out, using any commercially available image processing software (Cambell and Wynne, 2011).

Georeferencing: This is the first step in geometric corrections. It involves the calculation of the appropriate transformation from image to terrain coordinates. This is achieved by selecting an appropriate projection that is geographically referenced to the real world and then by selecting a set of ground control points that can be used to align the satellite image to the reference image. Thereafter, the transformation is defined and computation of the positions of the reference point in the image coordinates (Government of Canada, 2015).

Geocoding: This is the second step in geometric corrections. This involves resampling the image to obtain a new image in which all pixels are correctly positioned within the terrain coordinate system (Fig. 5.4). in this step, the original image is transformed in a coordinated map system, then overlaid with grid so as to resample and interpolate to get the geocoded image (Fig. 5.4). There are three commonly used methods for resampling; Nearest neighbourhood, Bilinear interpolation, and Cubic convolution methods (Richards, 2013).

In the Nearest neighbourhood method (Fig.5.5b), the digital values of the image pixel are assigned to the nearest base map coordinate, for example, the base map grid values correspond to actual measured values. The disadvantage of this method is that the value assigned to the grid point of the base map won't be representative of the measured value; however, the method is the fastest and cheapest for resampling (Richards, 2013).

© University of Venda

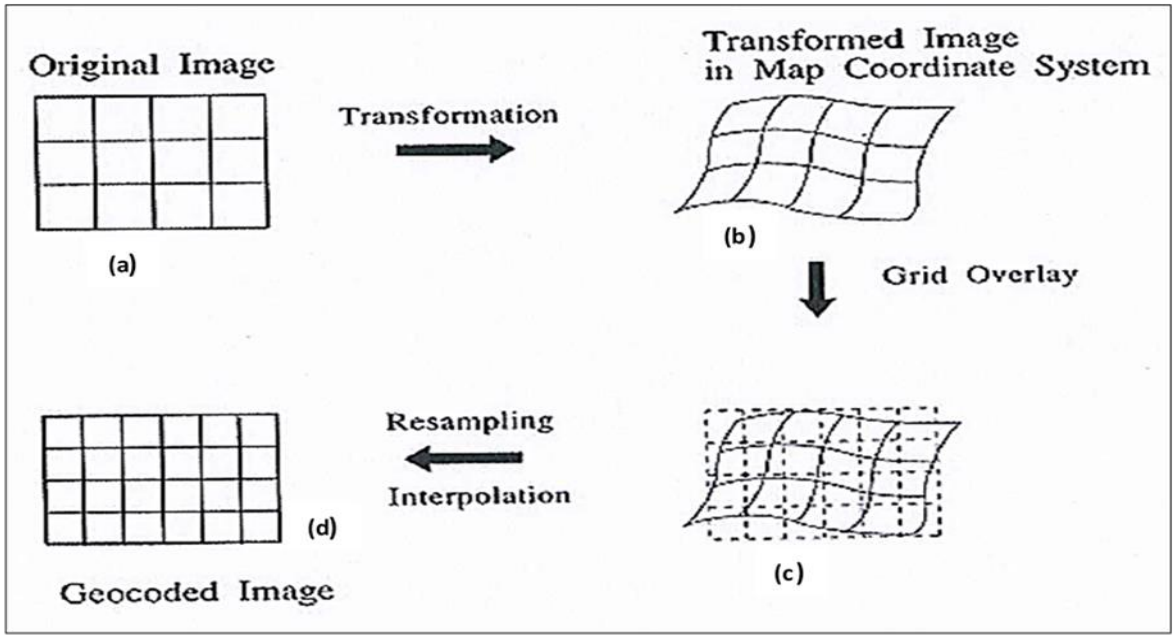


Figure 5.4: Resampling and Interpolation of the image to obtain a new image in which all pixels are correctly positioned with (a) indicating an original map, (b) transformed image in map coordinated system, (c)grid overlaid image and (d) geocoded image after resampled and interpolated (Devaraj and Shah, 2014).

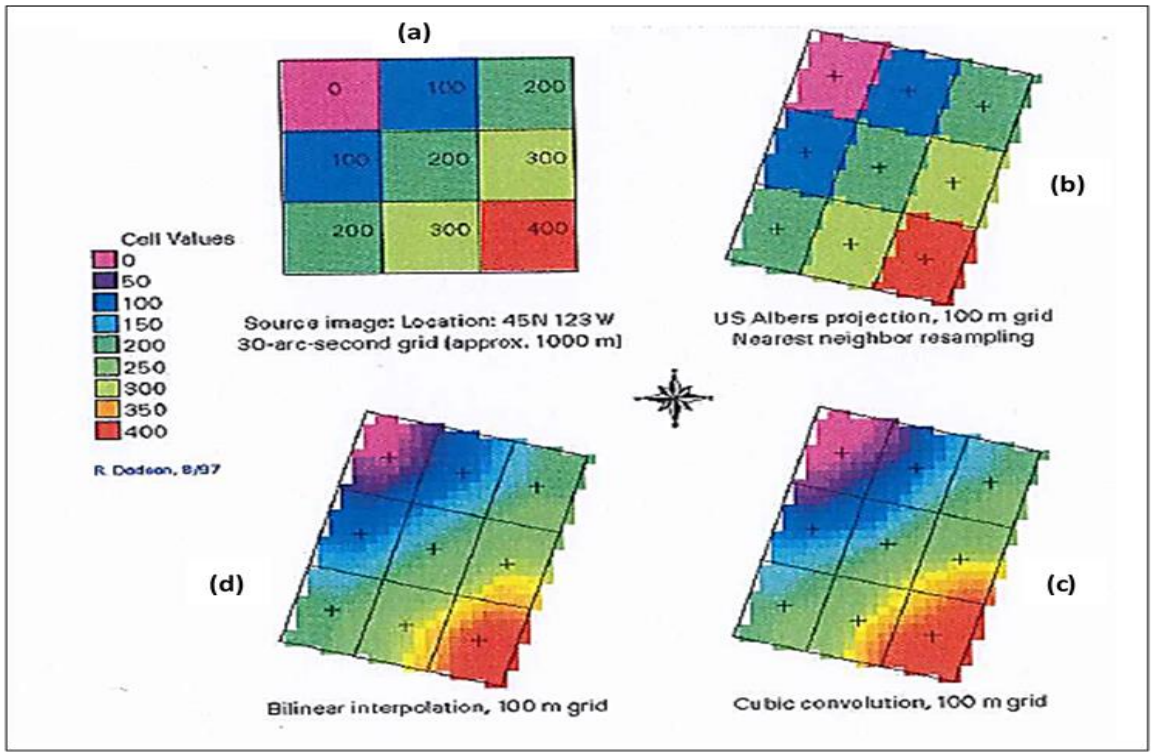


Figure 5.5: Commonly used resampling methods used on (a) source image resampled using (b) nearest neighbour resampling, (c) cubic resampling, and (d) Bilinear interpolation methods (Dodson and Santa, 1998).

© University of Venda

In the cubic convolution method (Fig. 5.5c), resampling goes even further as to calculate a distance weighted average of a block of sixteen from the original image which surrounds the new output pixel location (Philpot, 2001). This method produces a smoother image than the bilinear interpolation method, however, it also suffers from the greatest loss in radiometric information since the value assigned to the grid pixel represents a weighted average of the sixteen nearest points (Dodson and Santa, 1998).

Bilinear interpolation (Fig. 5.5d), involves taking a weighted average of four image pixel closest to the grid coordinate and obtaining the value for grid coordinate by linear interpolation. When the image pixel is farther away from the grid coordinate, the less effect it will have on the values assigned to the coordinate. As a result of this, the output image produced by this resampling method will produce a smoother and less blocky appearance than one created by the nearest neighbourhood method. The disadvantage of this method is that it causes loss of radiometric information since the value assigned to the grid pixel represents a weighted average of the four nearest points (Philpot, 2001).

5.1.5.2 Image Enhancement Technique

Image enhancement is the process that improves the interpretability of information in satellite images and providing better input for other automated image processing techniques (Maini and Saggarwal, 2010). It is used to modify the attributes of the image to make it more suitable for a given task. The most commonly used techniques for image enhancement include; contrast enhancement, density slicing, frequency filtering, and band rationing (Schowengerdt, 1983).

Band Rationing

This is an image enhancement technique whereby the pixel in one band of an image is divided by pixel from a corresponding second band (University of Leicester, 2007). The advantage of this method is its ability to enhance the spectral signatures of altered rocks such as alunite, clay, iron oxides which are valuable indicators of possible presence of ore deposits (Sabins, 1999). To identify this kind of surface effect, the image maybe enhanced by rationing bands 4 and 2. This will allow the geologist to easily identify the spectral signatures of the alteration

© University of Venda

minerals such as malachite, azurite, thereby successfully identifying the presence of possible copper mineral deposits (Kalinowski and Oliver, 2004). The choice of which band ratios are to be used largely depends on a mineral to be enhanced (Appendices 5A and 5B). This method was used in this study.

Histogram and filtering techniques

Histogram equalization is a technique for adjusting the image contrast whereby the it plots the frequency where the intensity values of the original image are plotted. The grey levels are modified pixel by pixel with the same transformation applied to each pixel Filtering techniques acomprised of sets of digital processing functions used to enhance the appearance of an image. In this process the specific features are highlighted or suppressed (Kriti and Rishi, 2017).

5.1.5.3 Image Classification

Image classification is a digital processing technique that is used to extract information of interest from the digital image, thereby facilitating further analysis and interpretation of the image. It categorizes pixels in the image into specific mineral classes based on the reflectance properties of the pixels (Cui *et al*., 2016). There are three main image classification techniques, viz; unsupervised, supervised, and object-based classification. The most commonly used techniques are unsupervised and supervised classification and these techniques are computer algorithms such as K-means and Iterative Self-Organizing Data Analysis (ISODATA) to group pixels and image (Cui *et al.*, 2016).

Unsupervised classification

This is a pixel-based image classification technique, where the grouping of pixel in the imagery is solely carried out by software analysis without user guidance (Weih and Riggan, 2010). The user can specify which algorithm to use and the desired number of output classes they require, but otherwise the user does not aid in the classification process, although the user must have knowledge of the area being classified, because when the grouping of the pixel is done, the classes have to be related to actual features on the ground (eXtension, 2013).

© University of Venda

Supervised classification

This is also a pixel-based image classification technique, however, in supervised classification; the user guides the computer through the classification process (Weih and Riggan, 2007). In this technique, the user selects sample pixel in the image that are representative of specific classes and then directs the image processing software to use the sample pixel as reference for the classification of all other pixel in the image (eXtension, 2013). These sample pixels are called training sites and are selected based on the knowledge of the user about the area (Aronoff, 2005). The user may also set the restrictions often based on the spectral characteristics of the training sites such as brightness or strength of reflection in a specific spectral band (eXtension, 2013).

Object-based classification

This is an object-based classification technique that classifies images based on information from a set of similar pixel called objects (Weih and Riggan, 2007). These objects are groups of pixel that are similar to one another based on a measure of their spectral properties, for example, colour, size, shape, texture (Liu and Xia, 2010). The classification is achieved by splitting the image into unclassified 'object primitives' based on the shape, colour and pixel topology, using segmentation process (Liu and Xia, 2010).

5.1.6 Methods for Remote Sensing Data Analysis

Data analysis is the process of extracting valuable information from digital with the purpose of drawing conclusions about the information extracted (Joseph, 2005). In remote sensing, this process mainly involves two techniques; visual interpretation and digital interpretation. These techniques can be used either independently or in combination (Joseph, 2005).

5.1.6.1 Visual Interpretation

This is a technique that extracts information from the digital image on the image's physical characteristics that can be seen by the human eye and these characteristics include; tone, texture, shadow, shape, size, association (Joseph. 2005). It is a simple and straight forward

© University of Venda

technique, but its shortcomings are the fact that the interpretation depends solely on human sight which becomes a problem because human eyes and their processing counterpart such as the human brain have a finite number of colour tones that they can recognize. Hence, the full advantage of the high radiometric resolution images cannot be used during visual interpretation (Joseph. 2005). Visual interpretation tends to be qualitative rather than quantitative (Joseph, 2005), and shall not be considered in this study.

5.1.6.2 Digital interpretation

This is an interpretation that is carried out by computer-based image processing software (Asadzadeh and de Souza Filho, 2015). This type of interpretation facilitates quantitative analysis because it makes full use of the spectral information present in the imagery and avoids bias (Joseph, 2005). This technique can be grouped into two categories; knowledge-based, and data driven approaches, based on the following: their date of emergence (conventional or advanced); type of data they are applied to, multispectral vs. hyperspectral; and the need for training data, supervised or unsupervised (Asadzadeh and Souza Filho, 2015).

Knowledge-based approach

This approach incorporates the user's knowledge about the spectral behaviour of the target to extract meaningful information from the individual spectrum without reliance on reference data. Among the commonly used knowledge-based techniques are the band calculation (band ratios), feature mapping, expert system, spectral deconvolution, wavelet analysis, and scattering theory (Asadzadeh and de Souza Filho, 2015).

Data driven methods

These methods are an alternative spectral analysis approach in which only the digital imagery and some additional reference data are needed. In this approach, there is no need for user knowledge to extract information from the imagery, rather it uses reference data also called training classes to extract information (Asadzadeh and de Souza Filho, 2015). Common techniques used in the data driven approach may include similarly-based group, least squares-based group, training based group, geostatic-based group, partial unmixing group, full

© University of Venda

unmixing group (Asadzadeh and de Souza Filho, 2015). For the purpose of this study, only the partial unmixing group techniques are discussed.

Partial Unmixing algorithms/Techniques: This aims to isolate spectral features of interest from each pixel, by assuming that each pixel vector measures the response of more than one single underlying material, as a result partial unmixing algorithms detect spectral signatures that match the known target in each pixel (Asadzadeh and de Souza Filho, 2015).

Partial unmixing algorithms vary from matched filtering (MF), constrained energy minimization (CEM), orthogonal subspace projection (OSP) (Harsanyi and Chein, 1994), and adaptive coherence estimator (ACE), to target-constrained interference-minimized filter (TCIMF) (Ren and Chang, 2000), and mixture tuned matched filtering (MTMF) (Boardman and Kruse, 2011).

In the OSP detector, the subspace of the background basis functions is removed from the analysed pixel, leaving only the part related to the known end-member (Harsanyi and Chein, 1994). In MF, the response of the target signature is maximized and the response of the background subspace is minimized by a likelihood ratio, thus matching the signature. The CEM utilizes a finite impulse response filter to pass through the target signature, while minimizing its output energy resulting from the composite background. Mathematically though, the MF is a mean centred version of the CEM (Chang, 2003).

The Target-constrained interference-minimized filter (TCIMF) can minimize the effects caused by interference. It designs a finite-impulse-response filter that specifies targets of interest in such a way that the desired targets and undesired targets will be passed through and rejected by the filter, respectively; the filter output energy resulting from unknown signal sources is also minimized. More precisely, the TCIMF accomplishes three tasks simultaneously: detection of the desired targets, elimination of the undesired targets, and minimization of interfering effects (Ren and Chang, 2000).

The ACE detector is based on the generalized likelihood ratio and thus is invariant to relative scaling of the test data. In the MTMF, beside the MF, an “infeasibility” image is also calculated for each target signature and then the predominant material and its abundance is determined, using the combined criteria of high MF and low infeasibility scores (Boardman and Kruse, 2011).

© University of Venda

In essence, these detectors carry out a partial unmixing and their output is a single score (abundance of the target) per pixel, which bear some resemblance to similarity measures group techniques. These methods are not yet comparatively studied for geologic applications. However, based on the current case study, it seems they yield acceptable results for the smaller bright target with the exception of the MF and the ACE. These methods are only able to detect the strongest signals, but for the pervasive darker signal, they yield poor results while the CEM has confusion in discriminating between the targets. The performance of these detectors is found to broadly improve using clustering or feature extraction techniques (Boardman and Kruse, 2011). As a result, the only feasible target detection algorithm that can be used for mineral exploration is the TCIMF algorithm.

There is no pre-defined way of choosing which method is better for interpretation and analysis as there are numerous factors to consider when choosing a particular method, for instance, a particular mineral that is being explored, the surface condition in the study area, the type of data used are considered. As a result, the choice of which method to use is mainly dependent on best practice of exploring for a particular mineral in a particular area.

In areas that do not have previous remote sensing based mineral exploration, the lack of best practice knowledge presents a problem, however, it is always a good starting point to use procedures and techniques that have been used in previous studies with the same criteria. Based on this fact, this study will consider a two-fold analysis using a combination of band calculation techniques and target detection algorithms, in particular the TCIMF algorithm. These techniques have been selected for their relative simplicity and computational tractability.

5.2 Application of Remote Sensing

Remote sensing data can be applicable in many different ways such as in (a) mapping or monitoring of Earth resources, (b) retrieval of bio-geo-physical parameters used in models to predict changes in geosphere and biosphere, (c) management and decision making (Ray, 2004). Remote sensing applications have been applied in several fields that showed that it is highly useful. Its application has been in agriculture, water resources, forest and ecosystem, disaster management, infrastructure development, atmospheric and oceanic sciences and geology especially in mineral exploration (Ray, 2004).

© University of Venda

For example, in agriculture, forestry and land cover, remote sensing can be used for crop identification, assessment, acreage estimation, soil moisture, drought monitoring, land-use cover mapping, and forest fire detection (Ray, 2004; Ray *et al*., 2005). In water resources, it can be used for water quality monitoring, mapping surface water bodies, snow and flood mapping (Ray, 2004; Manson *et al.,* 2014). In marine resources and coastal studies, remote sensing can be used for phytoplankton estimation, sea surface temperature, wetland mapping and oil slicks (Ray, 2004; Giri *et al.,* 2013). In mineral exploration, it can be used for structural, rock and mineral mapping (Ray, 2004; van der Meer *et al.,* 2012; Ncgofe *et al.,* 2013; Salati *et al.,* 2014).

Technology of remote sensing is continuously improving. This is so because new types of platforms, advanced sensors, modern data analysis approaches are making remote sensing more and more amenable to use for societal benefits (Ray, 2004).

5.3 History of Remote Sensing in Mineral Exploration

According to Torres (2016), satellite remote sensing images have been used for mineral exploration since the launch of the Landsat program in 1972. This was possible by the pioneering work of John Hunt and Ronald Lyon in the early 70's, who paved the way for interpretation of spectral data. Their work established a link between observed variations in reflectance/emittance spectra data and chemical and physical properties of minerals. Their work also demonstrated the potential use of satellite remote sensing images in mineral exploration (Asadzadeh and de Souza Filho, 2015).

The ASTER sensor obtains high resolution (15 to 90 square meters per pixel) images of the Earth in 14 different wavelength bands of the electromagnetic spectrum, ranging from visible to thermal infrared light (Torres, 2016). This was a great improvement from the sensors that came before it, like the Landsat Multispectral Scanner (MSS) and Return Beam Vidicon (RBV) that were only able to acquire low resolution images of the Earth. With the MSS sensor having only 80 Square meter ground resolution in four spectral bands ranging from visible to near infrared, and the RBV having 80 square meter ground resolution in three bands in the visible spectrum (U.S. Geological Survey, 2013).

© University of Venda

The introduction of advanced sensors like the ASTER, revolutionised the application of remote sensing in mineral exploration and these improved capabilities such as; Increased number of bands; dedicated channels for geological applications; increased sensitivity of the detectors; reduced footprint of the pixel; improved geometry; ability to digitally filter out vegetation interference; and improved Radar imaging to penetrate the clouds and penetrate the ground (Cambell and Wynne, 2011).

The introduction of these new capabilities paved the way for more geological information to be extracted from the satellite images, such as; major faults and other geological structures; paleo-drainage systems; alteration signature of hydrothermal minerals; vegetation stress related to metals and hydrocarbon seepage; ocean oil seepage; surface structural geology below jungle canopies; concealed structures beneath dry sand dunes; mineralogy, and many more (Abrams and Hook, 2006).

Some of the important events that have transpired throughout the history of remote sensing have been summarised, in order to emphasize their contribution to the application of remote sensing in mineral exploration (Table 5.2).

5.4 Remote Sensing Study of the Musina Area

According to Söhnge (1946), epidote is an accessory mineral above the 300 m elevation of the Messina copper deposits, but it becomes an increasingly important alteration mineral with depth. Consequently, epidote is closely associated with copper mineralisation within the Messina copper deposits, thus it is a good indicator of copper sulphide mineralisation within the study area. In this study, epidote alteration and its intensity was investigated so as to ascertain its association with sulphide mineralisation in the area.

Geological structures are important features that act as conduits for mineralisation especially for hydrothermal deposits, thus in exploration geological structures are important indicators of ore mineralisation as they play a major role in ore localization. Consequently, rock alteration and geological structures can be used as a tool for target generation in mineral exploration. More so, these features can be identified by the use of remote sensing techniques.

© University of Venda

Table 5.2: Milestone in the history of remote sensing (Aggarwal, 2003; www.digitalglobe.com/)

Events throughout History	Year
Launch Landsat-1 [Earth Resources Technology Satellite (ERTS-1)]: MSS Sensor	1972
Rapid Advances in Digital Image Processing	1972
Launch of Landsat -4: New Generation of Landsat Sensors: TM	1982
French Commercial Earth Observation Satellite SPOT	1986
Development High Resolution Space borne Systems First Commercial Developments in Remote Sensing	1990
Towards Cheap One-Goal Satellite Missions	1998
Launch EOS: National Aeronautics and Space Administration ((NASA) Earth Observing Mission	1999
Launch of ASTER, very high spatial resolution sensor system	1999
Launch of WorldView-1	2007
Launch of GeoEye-1	2008
Launch of WorldView-2	2009
Launch of WorldView-3	2014
Sport 7	2014
Launch of WorldView-4	2016

5.4.1 Specific Objectives

In this study, remote sensing technique was applied in the study area and its environs in order to:

- Identify areas of epidote alteration;
- Identify geological structures such as faults, folding and any other lineaments that might have influence on localisation of mineralisation;
- To ascertain any relationship between ore mineralisation, rock alteration, geological structures and soil geochemistry anomalies so as to depict target generation for mineral exploration purpose and;
- Assist in developing a genetic model for copper sulphide mineralisation in the Musina area.

© University of Venda

5.4.2 Data Acquisition

Data were acquired from data clearing-houses, for example, ASTER Level 1B and Digital Elevation Model data were purchased from a company called Southern Mapping Company (SMC), located in Johannesburg, South Africa.

A search of the available archives showed the availability of ASTER satellite imagery that was acquired on the 2nd of October 2003. ASTER Level 1B data is bought free from any atmospheric and radiometric distortions and doesn't require the need for data pre-processing. This was considered the most economic and most logical step for acquiring the required remotely sensed data, taking into consideration the highly sophisticated equipment and overly complex processes involved in the acquisition of remotely sensed data.

The necessary software programs required in the effective processing and interpretation of the data, were also acquired during this phase. This included the acquisition of ENVI 5.1 and ArcGIS 10.4.1 Softwares.

5.4.3 ASTER Data Processing

ASTER data processing was done to convert the raw data into meaningful information that could be used for further processing and analysis. This phase comprised of distinctive processes such as data manipulation, data pre-processing, image enhancement and image classification. ASTER data processing was done at a regional scale which is part of the Limpopo Mobile Belt (LMB) as clear trend for mineral alteration and geological structures can be clearly visible in a large scale.

5.4.3.1 Data Manipulation

The acquired data were in the form of individual monochromatic bands for example, VNIR bands SWIR bands. These bands were not effective for structural and mineralogical delineation, as a result these individual bands needed to be combined to form one dataset that could then be used to identify the spectral signature of the alteration minerals of interest and to identify the geological structural features.

© University of Venda

The process of combining the individual monochromatic bands was undertaken, using the layer staking tool, found in the ENVI 5.1 software programme. This was accomplished by loading all 14 bands of the ASTER Level 1B data into the programme, then converting the original format of the data i.e. .dat file format, to ENVI file format i.e. .hdf. This was done to ensure that when the individual bands were combined, they could retain their spectral information such as the wavelength value represented by each pixel. Once the data had been saved in the correct format, the individual bands of data were then combined together, using the layer stacking tool, to form the required dataset (Fig. 5.6). The nearest neighbour resampling method was used during the layer staking to ensure that all the pixels in the bands were reordered in an appropriate manner and to ensure that the radiometric integrity of the data remained intact.

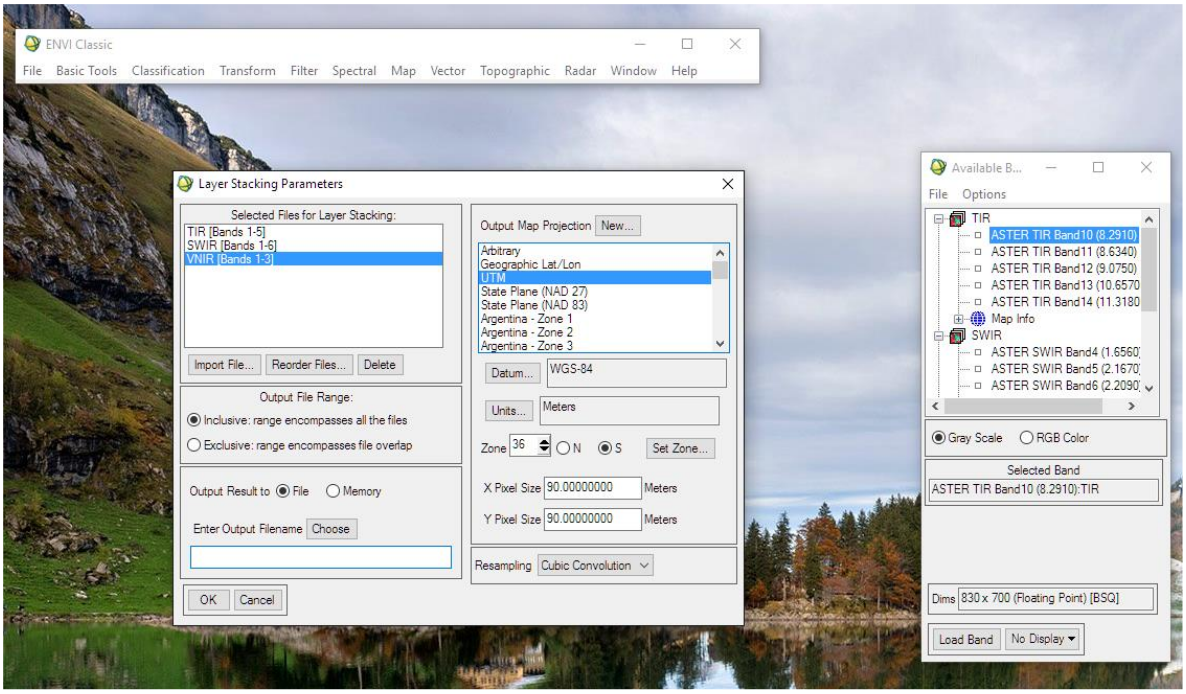


Figure 5.6: Layer staking of individual bands in the ENVI 5.1 software programme.

5.4.3.2 Data Pre-Processing

According to Government of Canada (2015), data pre-processing is undertaken in order to remove distortions inherent (i.e. radiometric and geometric distortions) and to enhance the quality of the raw data as to facilitate better interpretation of the data. Due to the nature of

© University of Venda

the ASTER level 1B data, there was no need to undertake pre-processing to remove geometric and radiometric distortions as the data has been corrected for geometric and radiometric distortions (Abrams and Hook, 2006).

5.4.3.3 Image Enhancement

This was done by using band rationing and composite images. These images enabled the identification of epidote alteration and enhanced the visibility and identification of the geological structures.

Band rationing

Following the Environmental Systems Research Institute (2012), band rationing was used to produce a band ratio image that was used to enhance the contrast between epidote alteration and the host rock. This was accomplished by using the Band Math Tool in ENVI 5.1 to input the mathematical expression required to create the band ratio image for enhancing epidote alteration [i.e. (B6 + B9) / (B7 + B8)]. The mathematical expression explicitly tells the software which band needs to be divided by the other. In order to enhance the visibility of epidote alteration, band 6 and 9 needed to be added together then divided by the sum total of band 7 and 8 (Fig. 5.7). The resulting band ratio image, viz; epidote alteration image was then saved to facilitate further analysis (Fig. 5.8).

© University of Venda

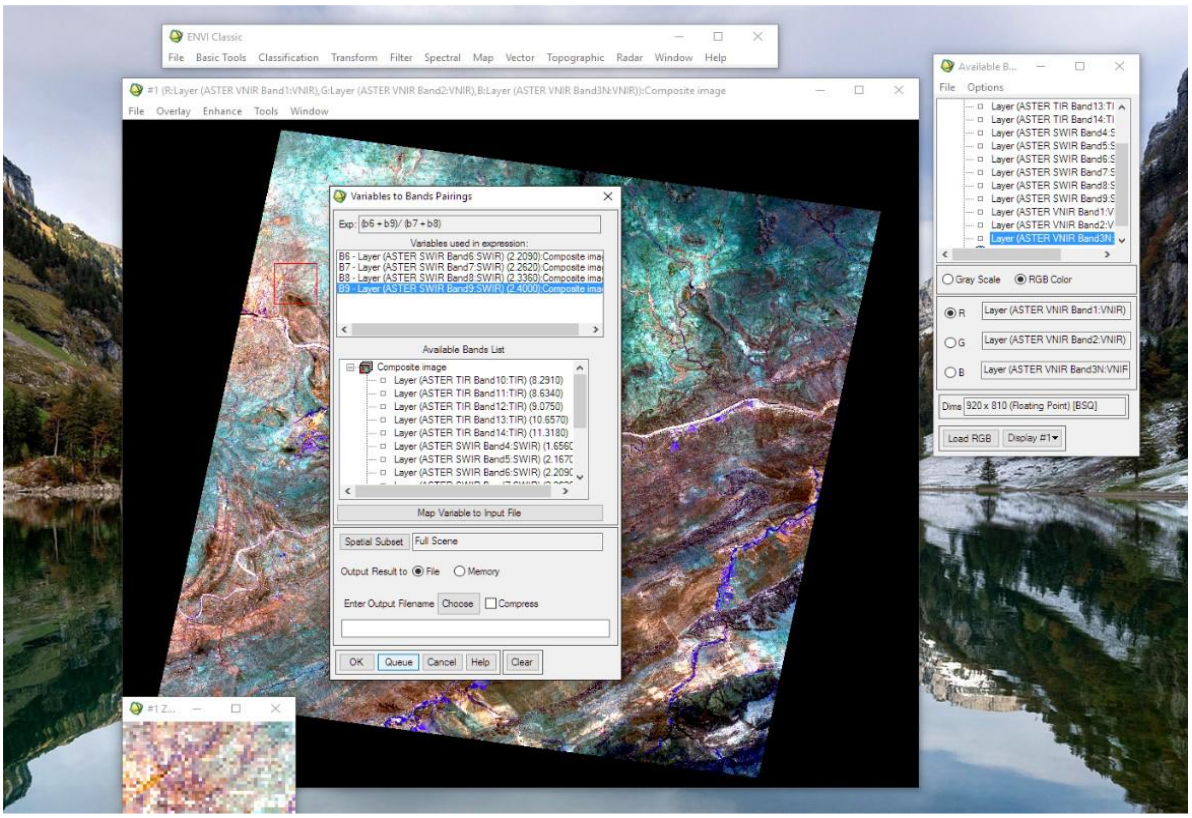


Figure 5.7: Creation of epidote alteration band ratio image using Band Math Tool.

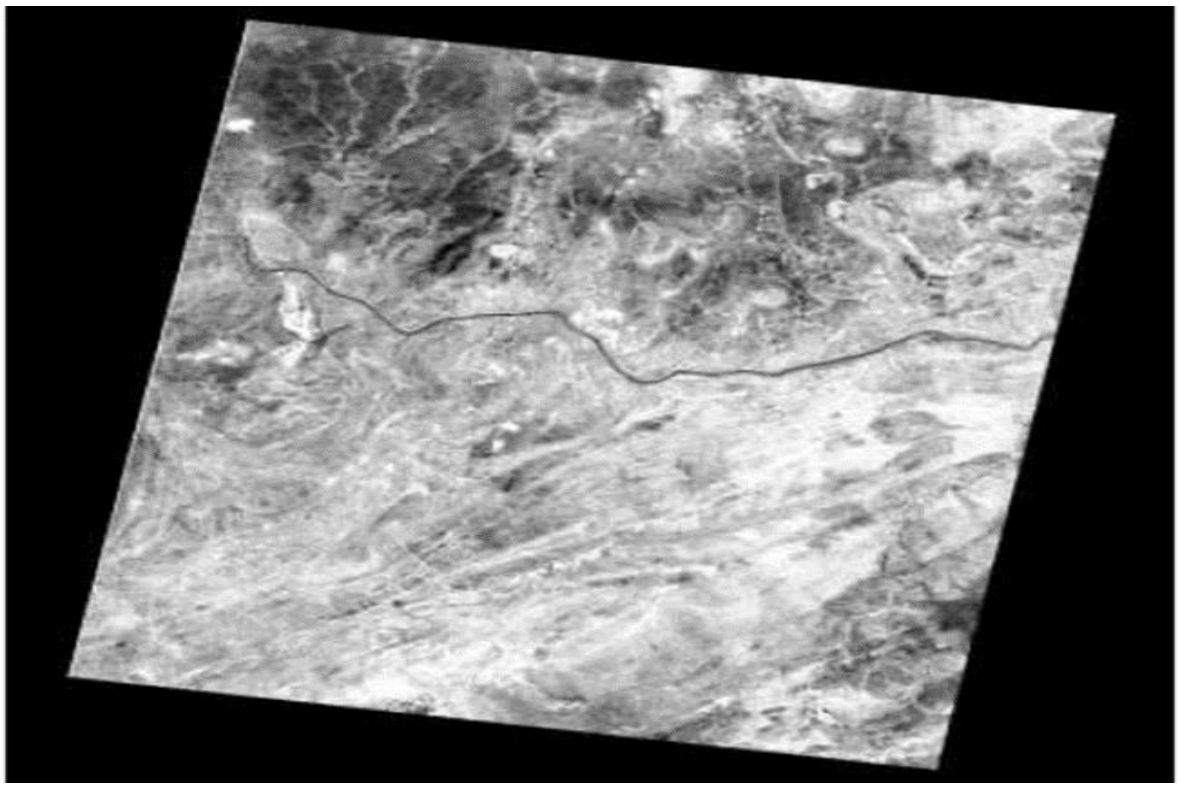


Figure 5.8: Resulting band ratio image of epidote alteration: Epidote alteration is represented by light tone or white area.

© University of Venda

Composite images

These are images that are made from the combination of multiple images merged into a single surface. These images provide a means by which certain objects in a satellite image can be detected in a much easier manner than when they are viewed on monochromatic images. As a result, a false colour composite image was used to enhance the structural features within the study area. The false colour composite image was created by representing a combination of visible colour bands and short wave bands in three primary colours; red, blue, green. This was accomplished by using the data manager window present in ENVI 5.1 to present band 7, 4 and 2 from the layer stacked ASTER level 1-B dataset as the primary colours red, green and blue respectively (Fig. 5.9). The resulting false colour composite image was then saved in .tiff format, to facilitate further analysis (Fig. 5.10).

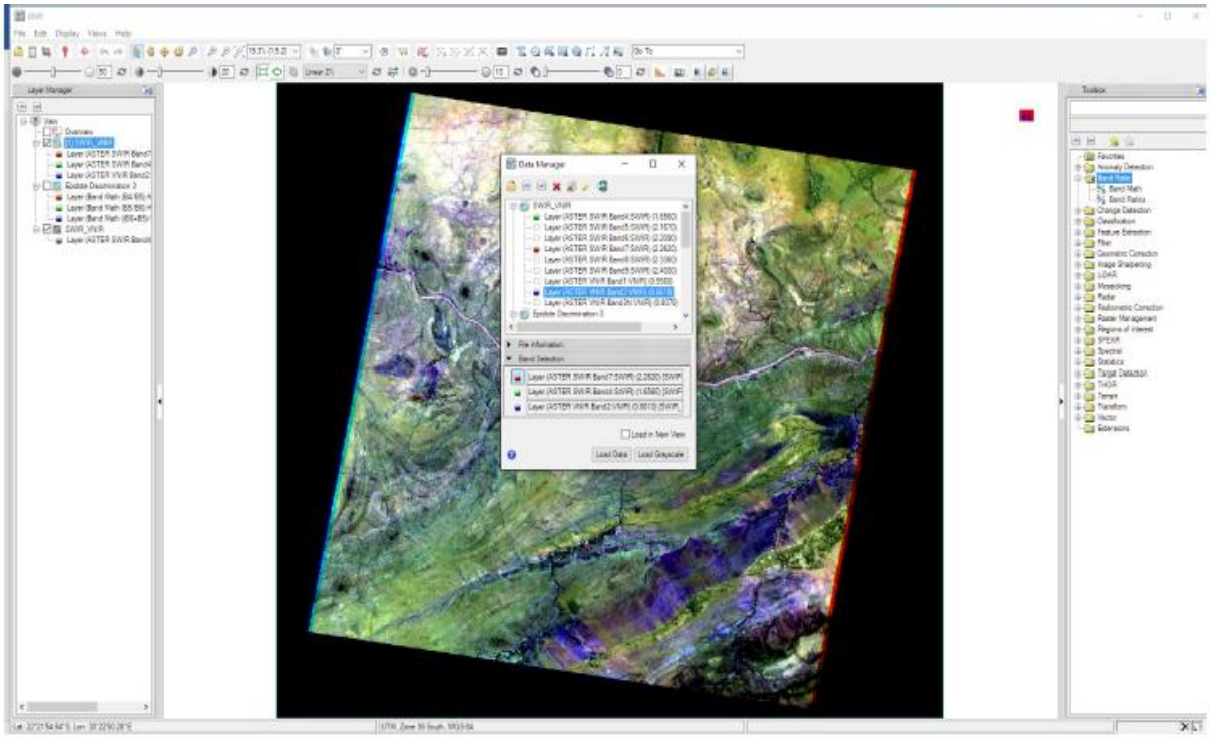


Figure 5.9: Creation of false colour composite image to enhance structural features using data manager window from ENVI 5.1 software programme.

© University of Venda

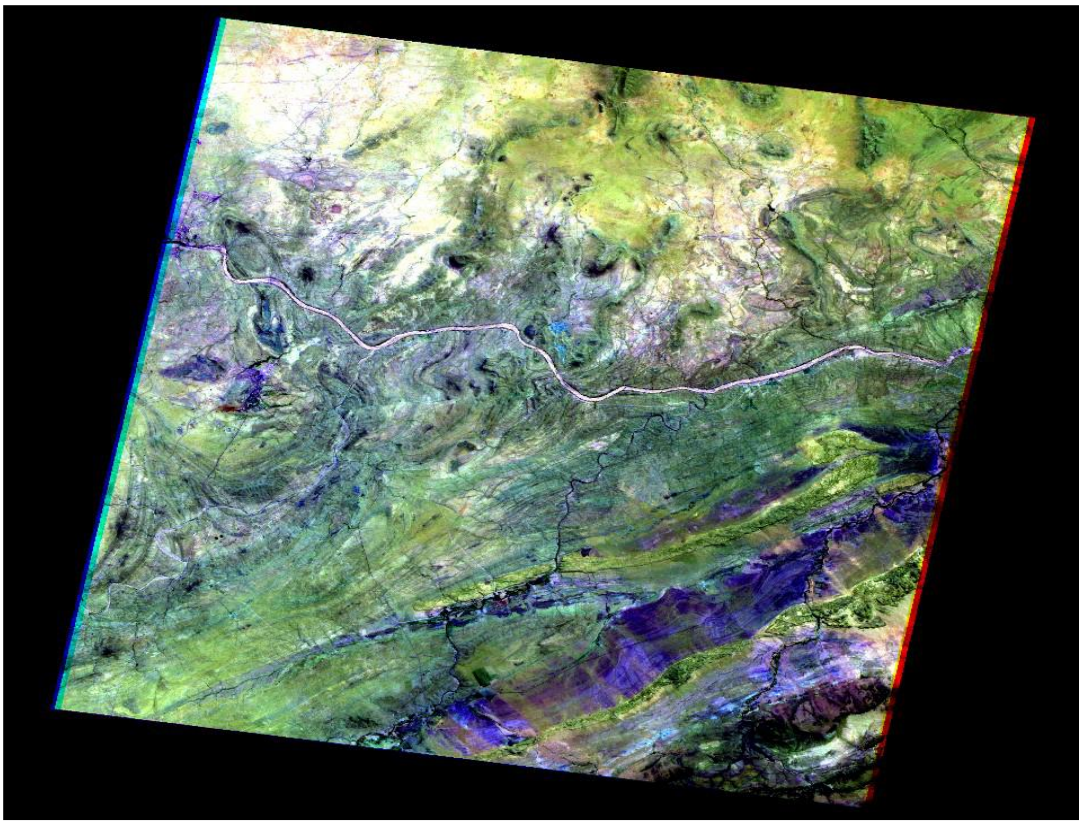


Figure 5.10: False colour composite image depicting enhanced structural features.

5.4.3.4 Image Classification

Image classification was done to automatically categorize all the pixels in the epidote alteration band ratio image into specific mineral classes or themes, based on their digital number (DN values), so as to ascertain the group of pixels that represent the epidote alteration with a high degree of confidence. This was done to ensure that the results acquired during analysis and interpretation of the image were as accurate as possible. Image classification was undertaken using the k-means algorithm method of the unsupervised classification technique.

The k-means algorithm method of the unsupervised approach attempts to group the pixel in an image into a series of related groups with the same spectral signature, however, the meaning of the spectral groups representing different features is unknown to the analyst. The analyst has to then try to associate a specific spectral signature with that of each group to identify what that particular group represents.

© University of Venda

In order to undertake the classification, the epidote alteration band ratio image was loaded onto the ENVI 5.1 software program and was classified using the k-means algorithm found under the unsupervised classification tool. In order to run the k- means algorithm, a series of parameters needed to be specified for example, parameters such as the number of classes required from the classification, the class maximum standard deviation. These parameters were left in their default state as they did not influence the classification in a significant manner except that of the number of classes required from the classification, which was set to 5, so that the program could efficiently and effectively differentiate between the host rock and the epidote alteration (Fig. 5.11). This is because the higher the number of classes required from the classification the more stringent the program becomes when grouping a set of pixels into different classes. However, the higher the number of required classes the longer the classification, thus as a compromise between speed and efficiency/accuracy the number of classes required from the classification were set as 5. The resulting classified Image was then saved in .tiff format to facilitate further analysis (Fig. 5.12).

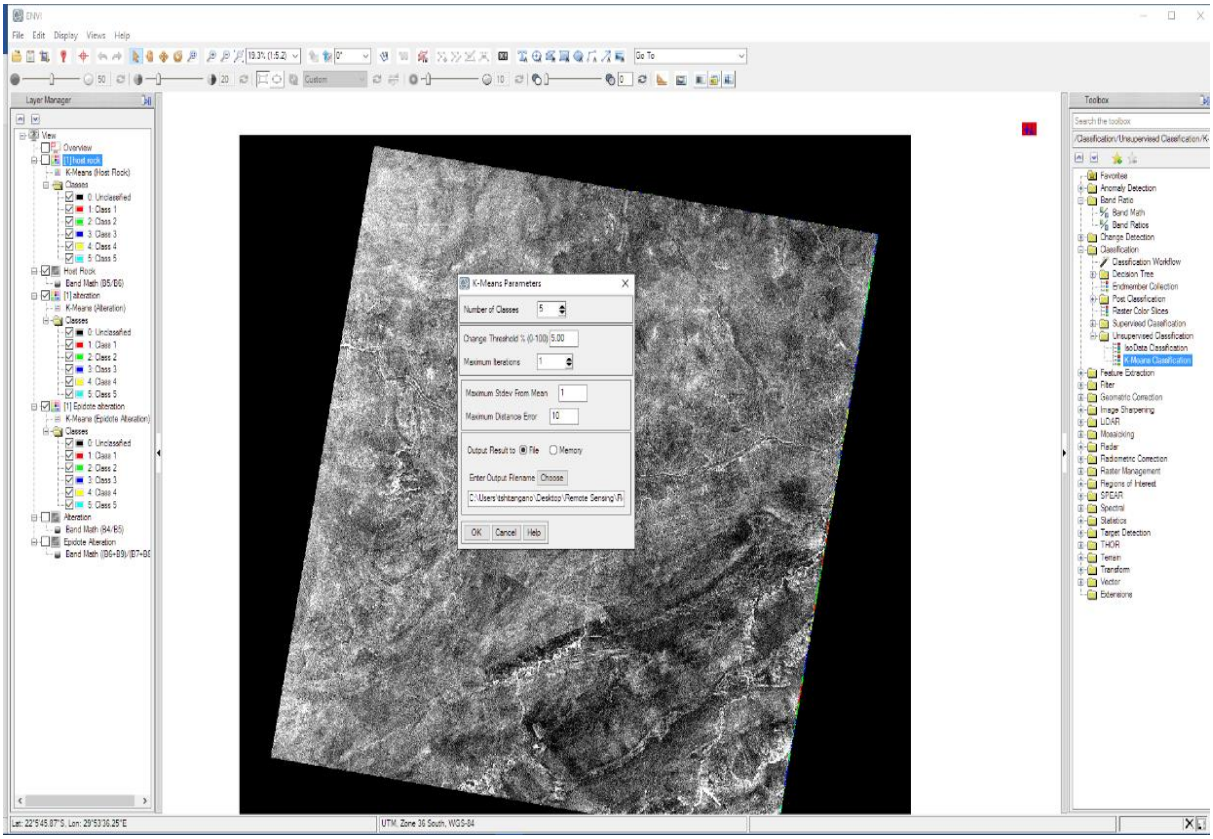


Figure 5.11: Classification of false colour composite image using the K-Means algorithm.

© University of Venda

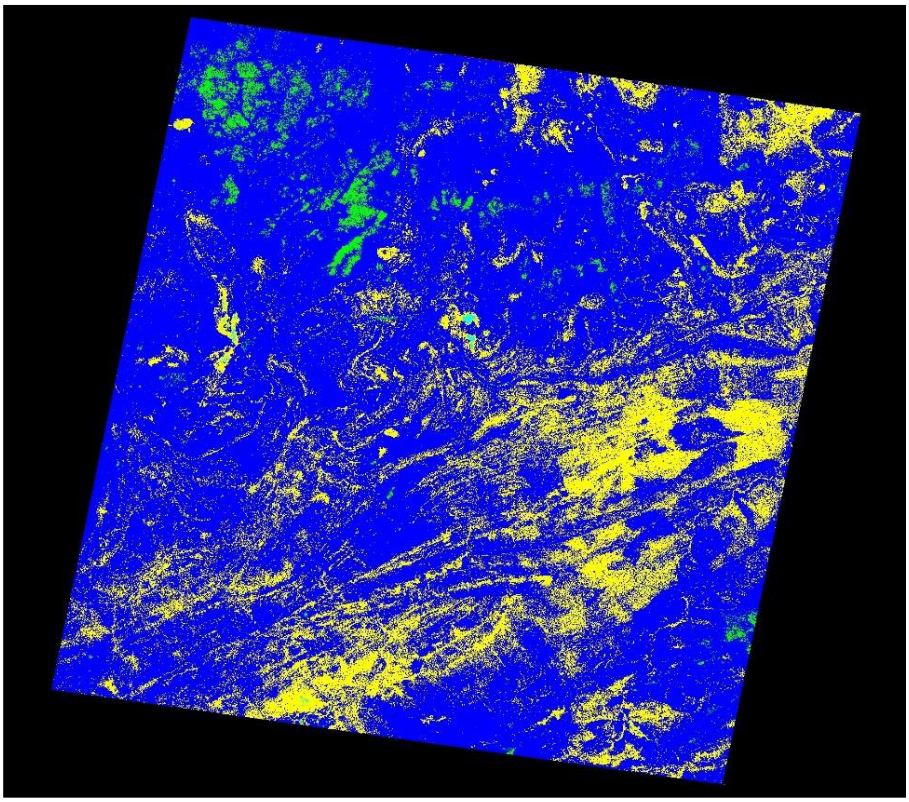


Figure 5.12: Classified epidote alteration band ratio image.

5.4.4 ASTER Data Analysis

Data analysis is the process of extracting valuable information from the digital image. This process was undertaken to identify and extract the class that represented epidote alteration from the classified epidote alteration band ratio image as well as to evaluate the structural control on the epidote alteration within the Musina area. Data analysis was undertaken using two primary methods; visual analysis and digital analysis.

5.4.4.1 Visual Analysis

Visual analysis was characterized by trying to associate specific spectral signatures with that of each class in the classified epidote band ratio image, thus, this method was used for isolating the class that represented epidote alteration. This was accomplished, by comparing the classified data to reference data in the form of the original epidote alteration band ratio imagery.

© University of Venda

To achieve this, the classified image was converted to shapefile format to facilitate visual analysis using the ArcGIS 10.4.1 software programme. This was done by using the "Raster to Vector" tool present in the ENVI 5.1 software programme. This tool converted the classified image to .evf file format (Fig. 5.13a) and to shapefile format using the "evf to shapefile" tool (Fig. 5.13b).

Once the classified image had been converted to shapefile format, it was then loaded onto the ArcMap programme present in the ArcGIS 10.4.1 software, along with the reference data required to identify the epidote alteration class (i.e. epidote band ratio image) (Fig 5.14).

Determination of class that represented epidote alteration was done by overlaying the classified image on top of the reference data and the transparency of the classified image was increased to 60%. This was done because the epidote alteration in the reference image appeared brighter than the surrounding areas and thus it was readily visible, to a point where it allowed the correlation of a specific class to the bright areas in the reference image.

Consequently, the bright areas in the reference data were associated with a specific class in the classified image and this allowed the identification of the class that represented the epidote alteration as well as chlorite alteration as the two alteration uses the same band ratios.

© University of Venda

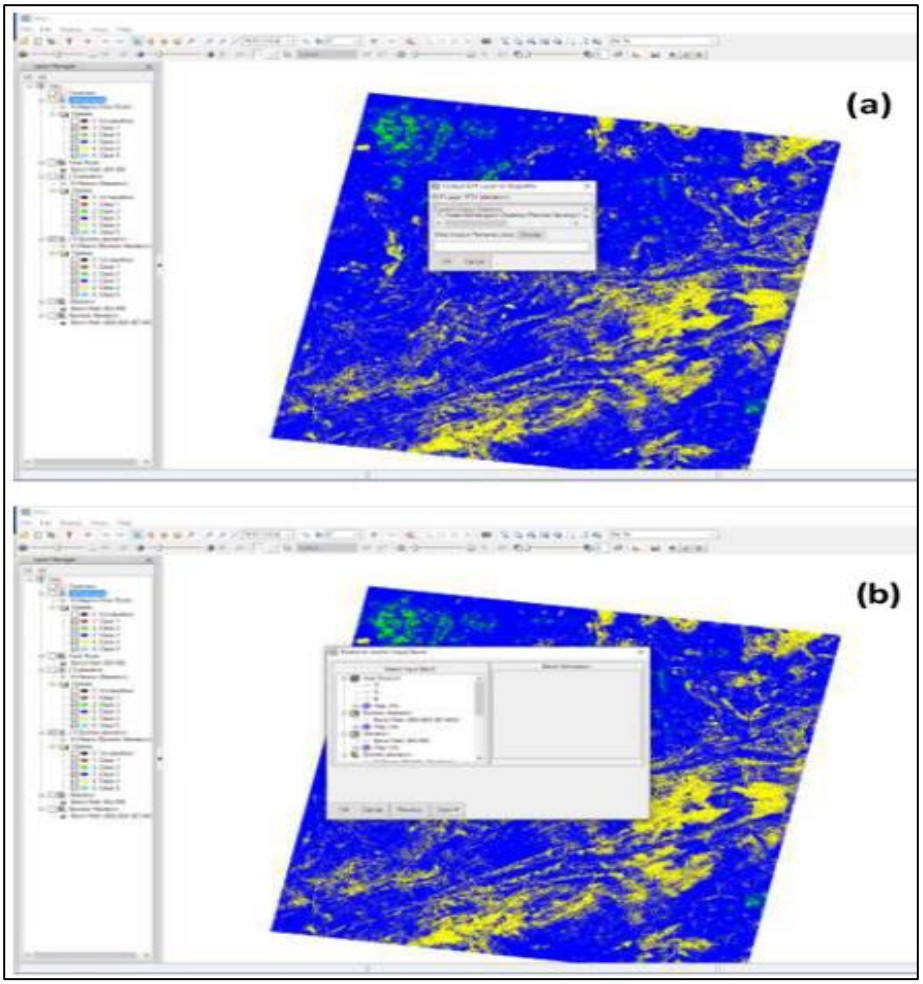


Figure 5.13: A figure showing (a) Conversion of classified image from raster to vector (.evf file format), (b) conversion of .evf file format to shape files.

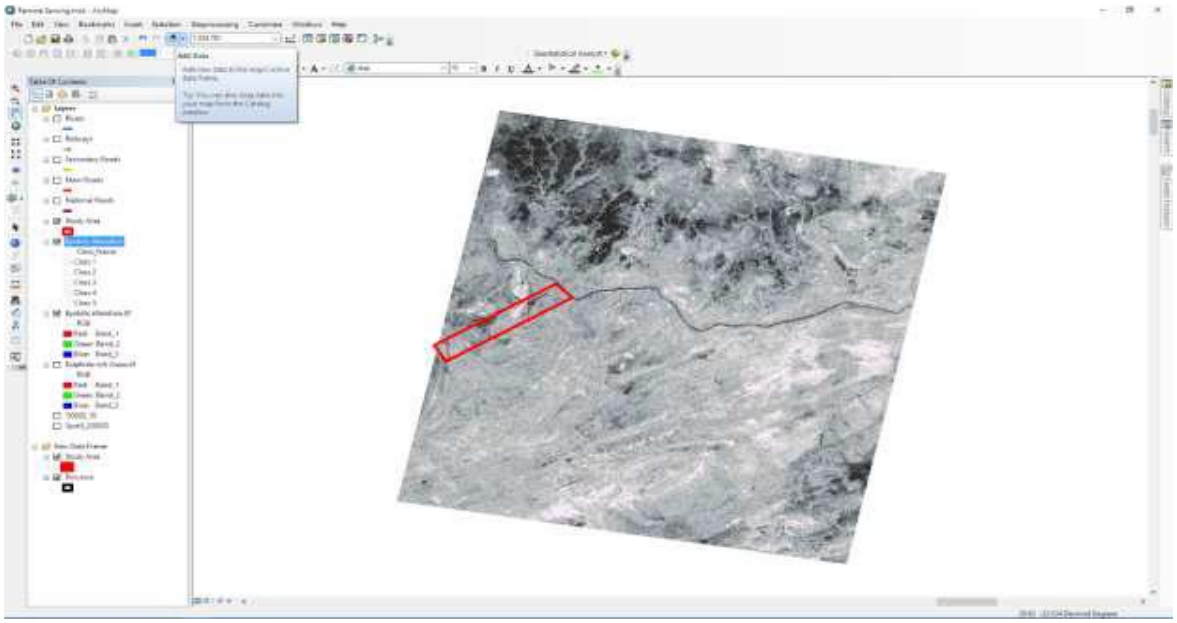


Figure 5.14: Loading of data into ArchMap.

© University of Venda

Once the class that represented epidote alteration was located, all other classes were removed and the epidote and chlorite alteration (same band rationing as epidote) classes were extracted to facilitate further analysis and interpretation (Fig. 5.15).

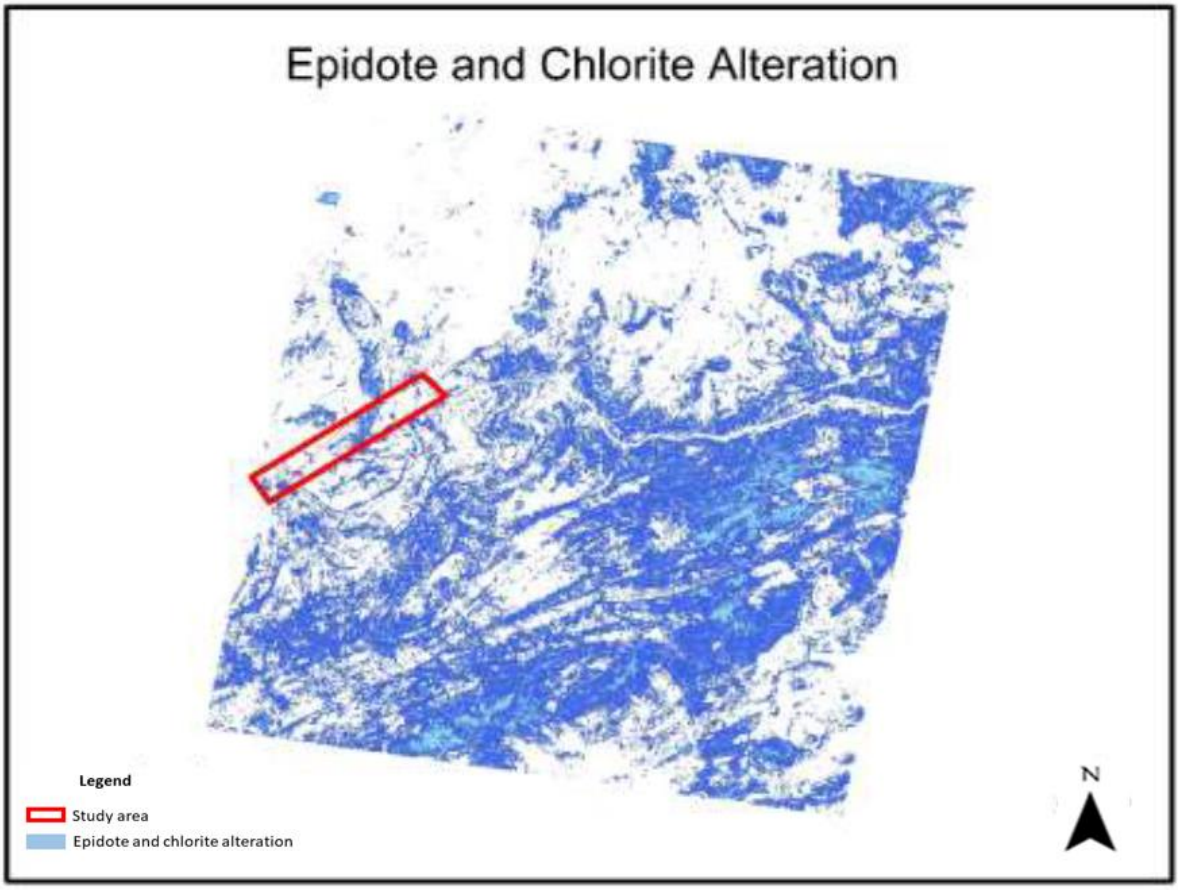


Figure 5.15: Isolated epidote and chlorite alteration within the Limpopo Mobile Belt.

5.4.4.2 Digital Analysis

Both knowledge based, and data driven approaches were used during digital analysis. For the knowledge-based approach, band ratio technique was used while for the data driven approach, the partial unmixing algorithm technique (i.e. TCIMF) was used.

During this method, spectral matching was done for validating the results obtained from the visual analysis. This was achieved by using TCIMF technique, which detected and isolated the spectral signature of epidote alteration associated with the Messina copper sulphide deposits. Target detecting wizard (TDW) tool was used following several steps such as; (1) Input/output File Selection, (2) Atmospheric Correction, (3) Select Target Spectra, (4) Select Non-Target Spectra, (5) Apply MNF (Minimum Noise Fraction) Transformation, (6) Select

© University of Venda

Target Detection Methods, (7) Load Rule Images and Preview Results, (8) Filter Targets, (9) Export Results and (10) View Statistics and Report.

During this stage, (1) loading of layered stacked ASTER level 1-B data set created during data manipulation was done (Fig. 5.16), and (2) atmospheric corrections was not done as the data was free from the atmospheric distortions.

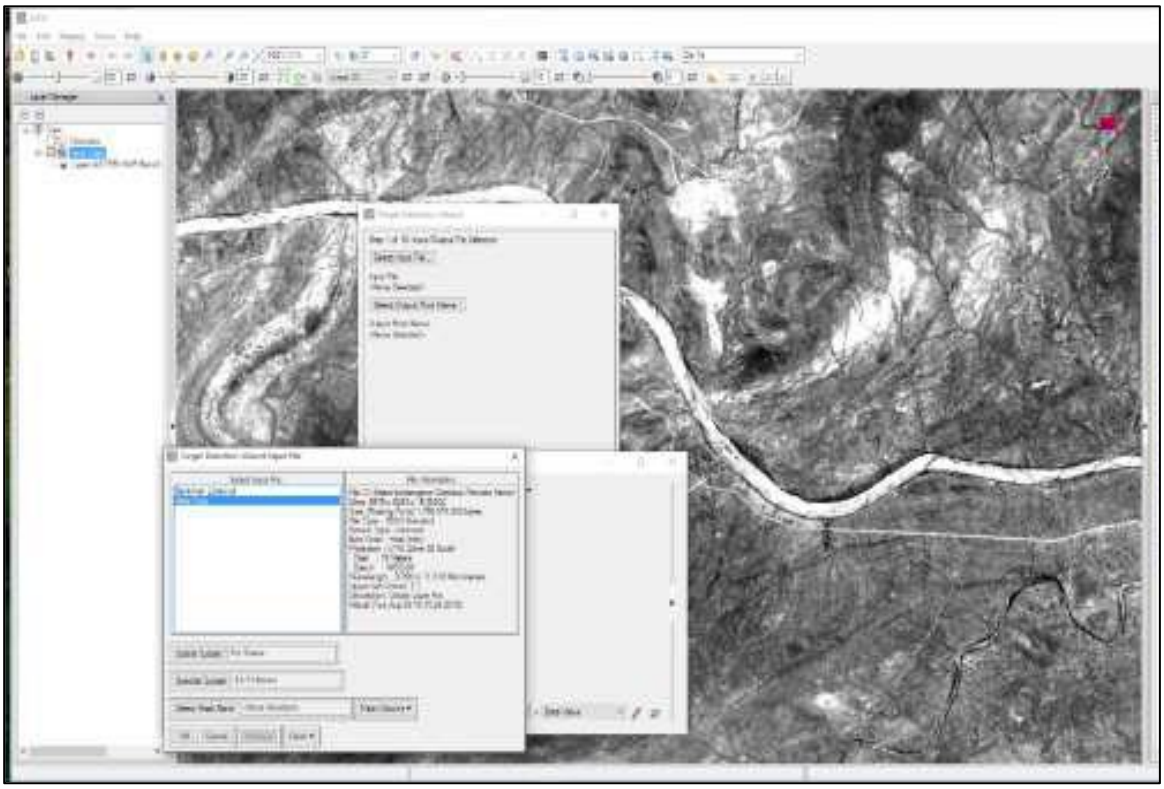


Figure 5.16: Data loading into the target detection wizard.

The next step (3 and 4) was to import the spectral signature of epidote from the ENVI spectral library (Fig. 5.17) obtained from cathodoluminescence study and then compared to various spectral signatures in the ENVI spectral library until the match was found (Fig. 5.18). The collected spectral signature was imported into the Envi software system. This was achieved by taking spectral signature from cathodoluminescence study.

The collected spectral signature was then compared with well known spectral signatures that have been collected by USGS (United States Geological Survey). This was undertaken to ensure that the collected spectral signature was a true and correct representation of the spectral signature of epidote. The comparison of the collected spectral signature and the well-known epidote spectral signatures was done as indicated in Figure 5.18.

© University of Venda

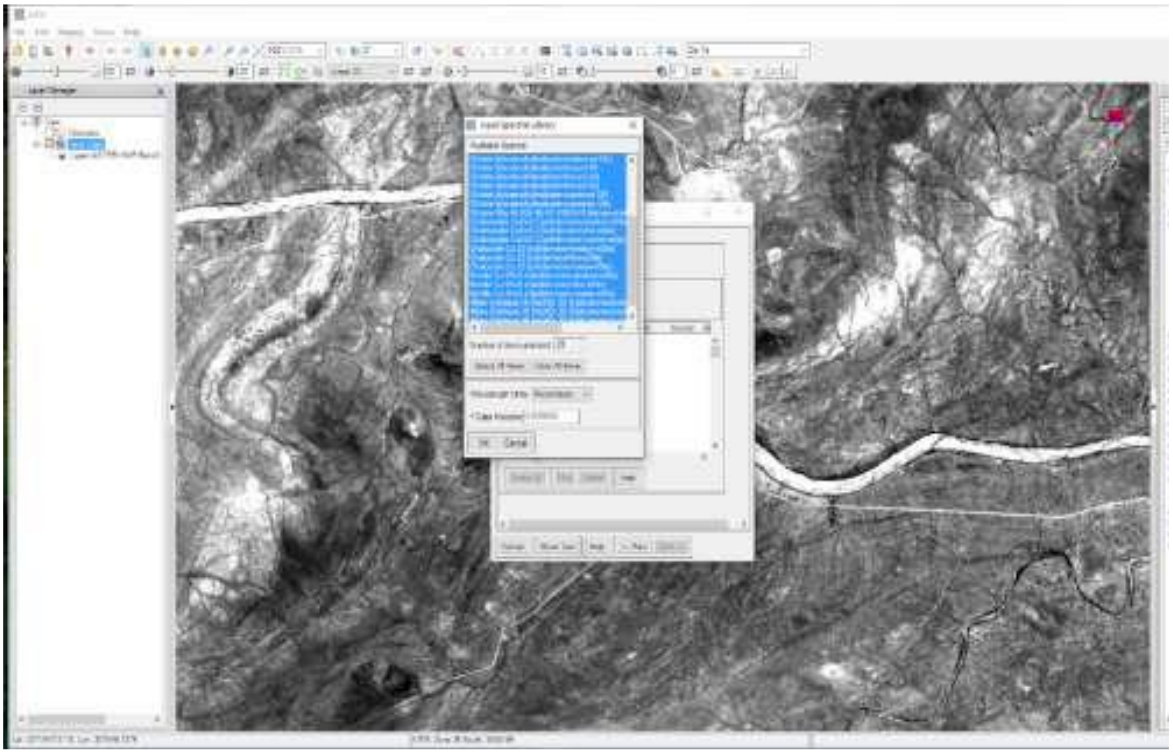


Figure 5.17: Selection of target of interest.

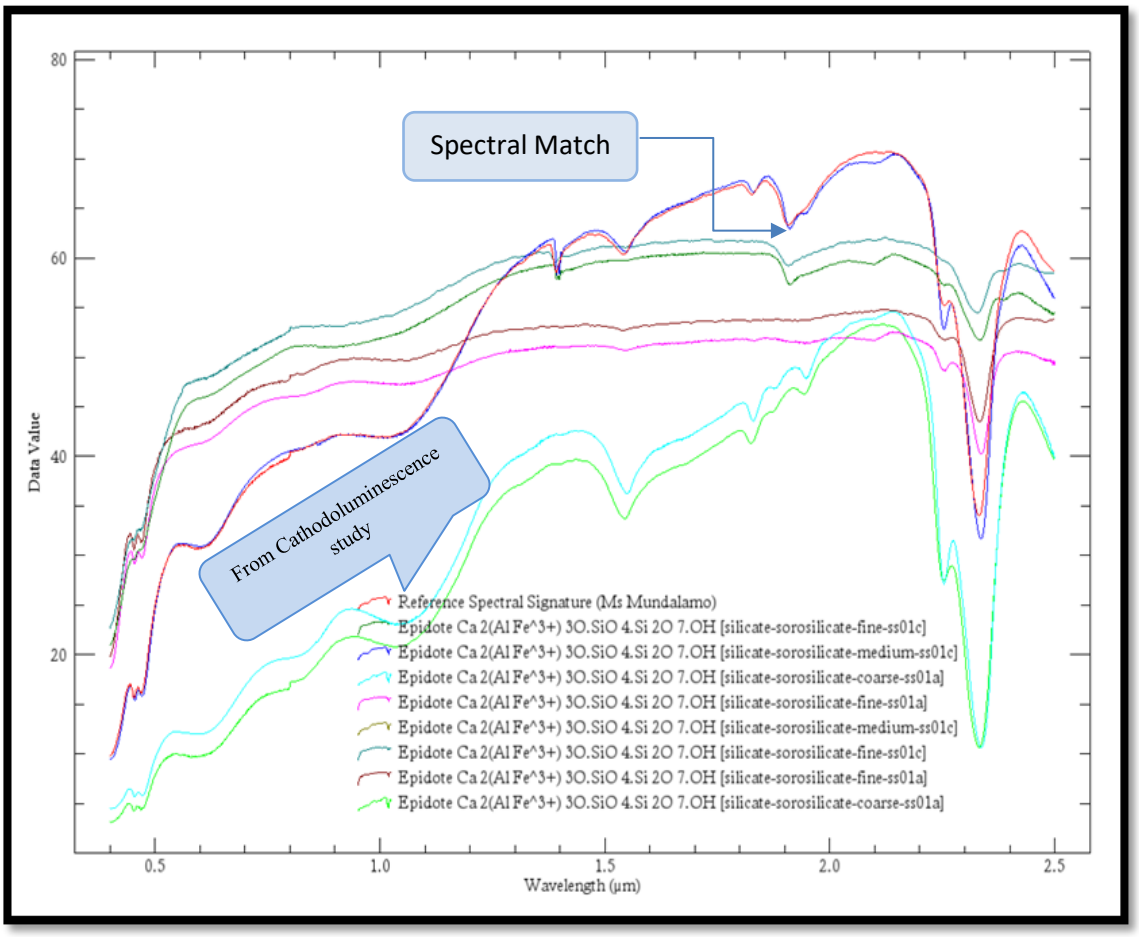


Figure 5.18: Spectral matching of epidote alteration.

© University of Venda

The next step was (5) to apply Minimum Noise Fraction (MNF) transformation to maximize the efficiency in detecting the desired target signatures by reducing the noise present in the data. Selecting and running the preferred target detecting method (i.e. CIMF) was done (Fig. 5.19), wherein the image was scanned and compared to the target spectra selected from the spectral signatures present in each pixel within the image and the rule image was produced which depicts the area where the target spectral have been positively correlated to the spectral signatures in the image. Loading of rule image and previewing of results (7) was done (Fig. 5.20). The results were then filtered (8) to eliminate the none target spectra in the image and exported (9) as shape file for further analysis.

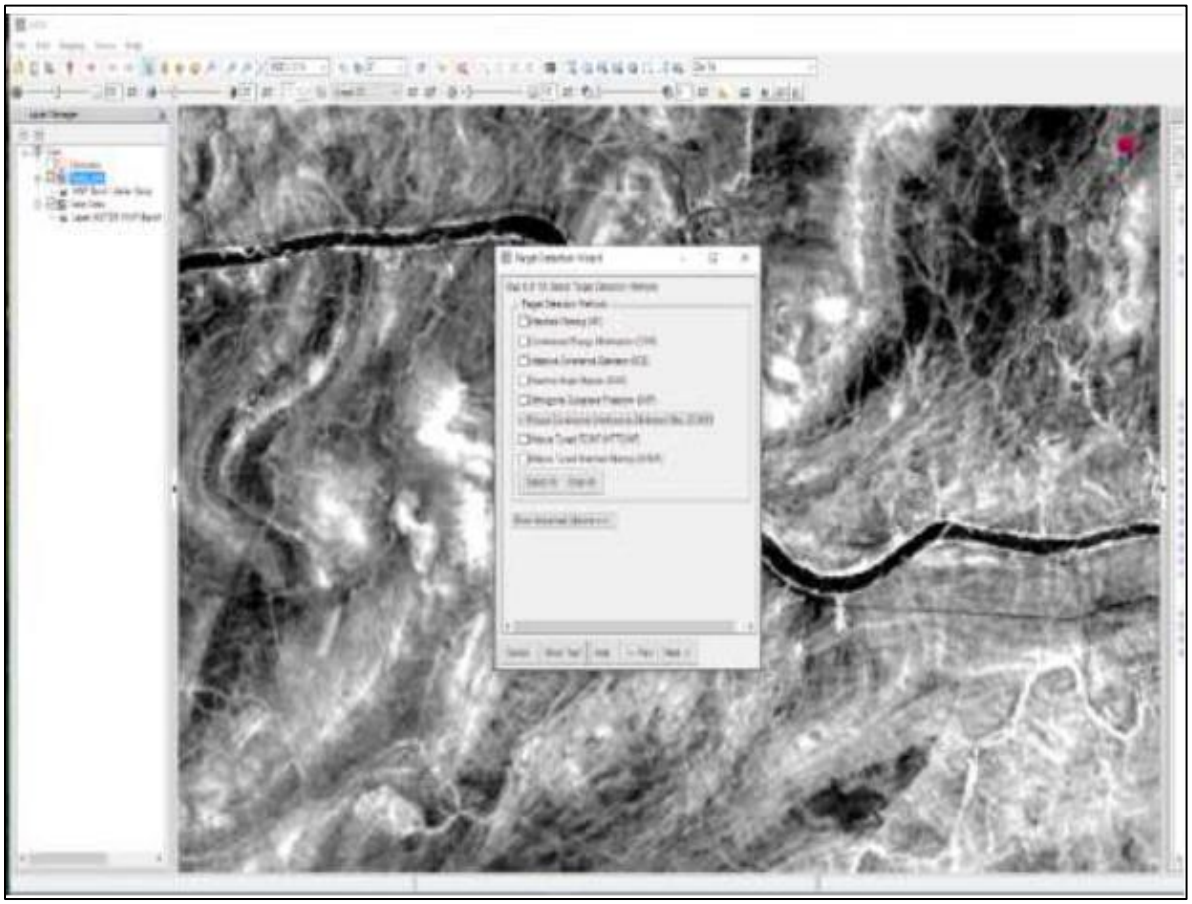


Figure 5.19: Selection of the preferred target detection method.

© University of Venda

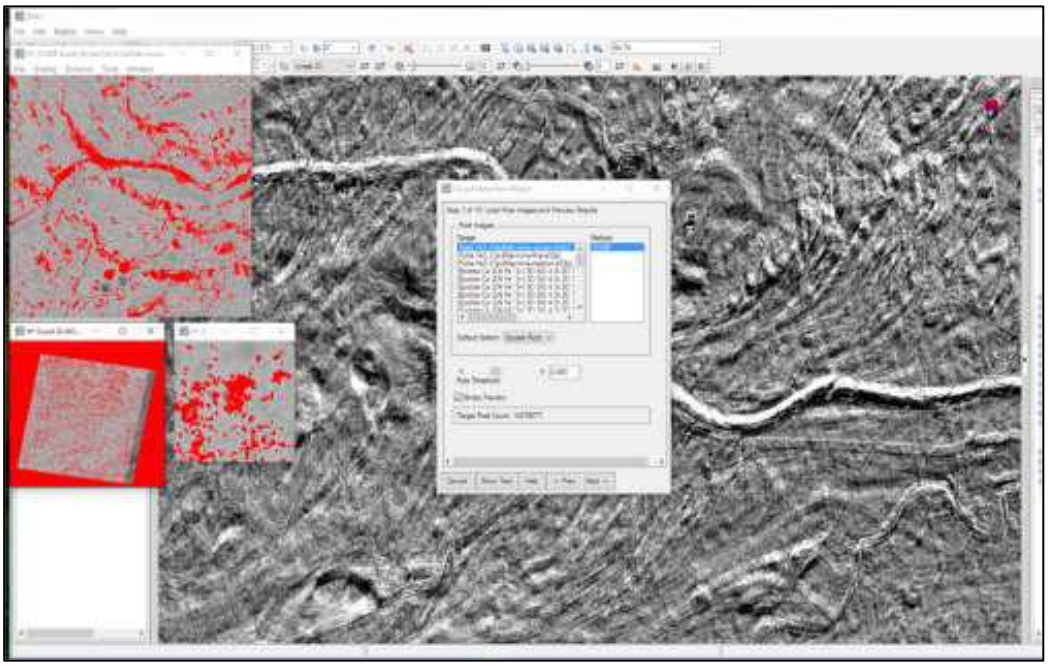


Figure 5.20: Previewing of rule image.

Classification of epidote intensity was done by defining the intensity of alteration into different classes, using TCMIF technique. This method classified the intensity of alteration based on the pixel size or number. The system defines the correlation into minimum of 2 pixel that were correlating to give a correlation coefficient of 1:1 that indicates 100% correlation. In this case the intensity were classified into three main ranges that is 0.8 – 1 (high intensity); 0.4 – 0,8 (medium intensity); 0.2 – 0.4 (low intensity) and below 0.2 (no correlation).

5.4.5 Data Quality Assurance (DQA)

Data Quality Assurance is the process that assures the quality of data through verifying its validity, reliability, precision, integrity and timeliness (Oxford University, 2016). In this study, DQA was done using validation and ground truthing methods.

Validation Method

This method used the results from digital analysis to verify the quality of the results obtained from the visual analysis. The result from digital analysis was overlaid on top of the results obtained from visual analysis. To validate the results, a layer with area where the two data

© University of Venda

sets intercept was created and then compared with area of the epidote alteration obtained from visual analysis (Fig. 5.21). The correlation percentage of 90.5% was deduced by dividing the area of epidote layer by area of epidote from visual analysis, which strengthen the quality of the results.

Ground Truthing

Ground truthing is the process of verifying results obtained from satellite image analysis through direct observation of the phenomenon on the ground (Oxford University, 2016). In this study, this method was done by associating the position of the known Messina copper deposits (comprised epidote alteration) with the epidote alteration obtained through visual analysis (Fig. 5.22).

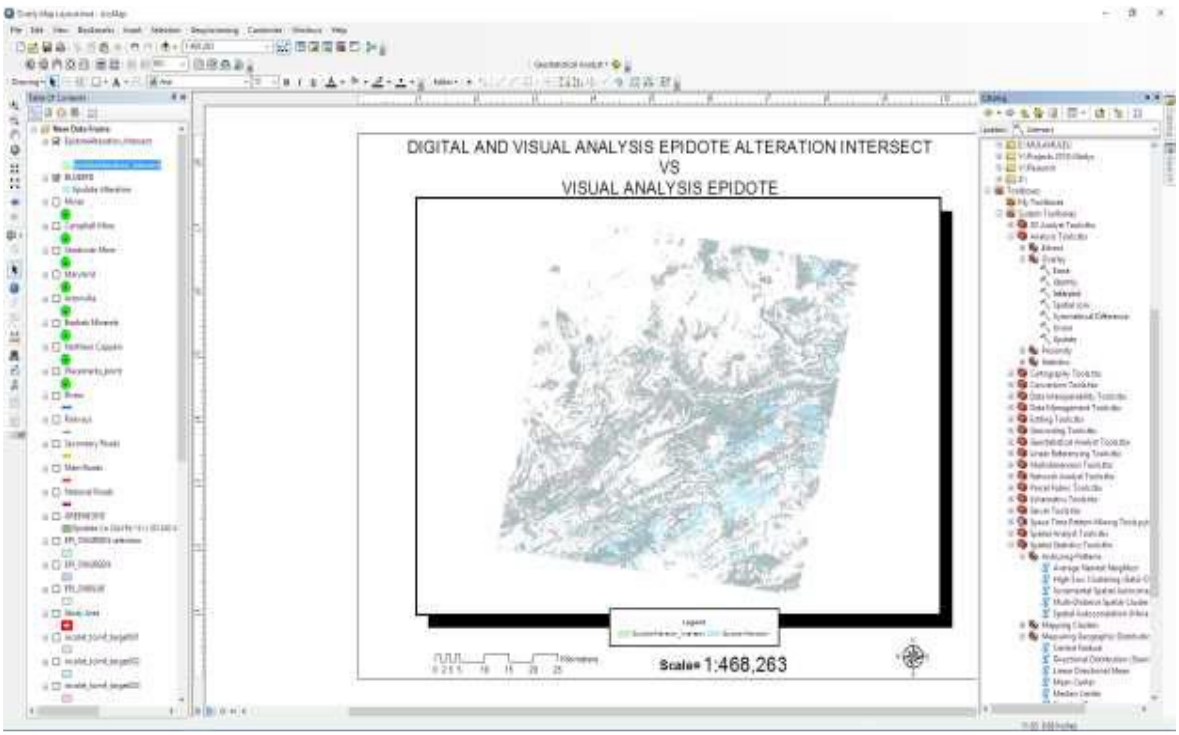


Figure 5.21: Validation using intercepted areas of digital and visual epidote alteration with visual epidote alteration.

© University of Venda

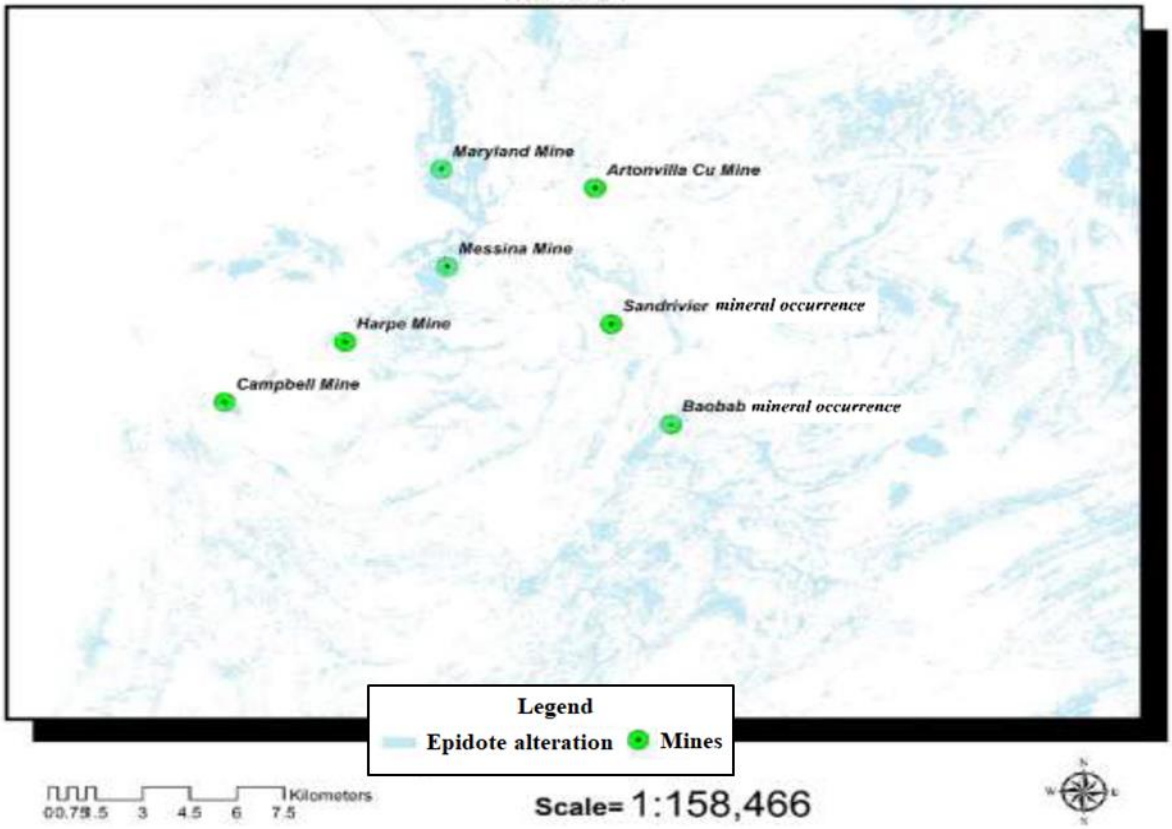


Figure 5.22: Association of epidote alteration from visual analysis and with known copper deposits using ground truthing method.

5.4.6 Results and Interpretation

The results obtained from the analysis and interpretation of multispectral ASTER data were used to undertake detailed analysis and interpretation of the mineral alteration and geological structures. The results were also used to provide a detailed spatial correlation between the mineral alteration of interest and the geological structures within the study area. Lastly, a conceptual model depicting the relationship between the mineral alteration of interest and the geological structures within the area as well as the geochemistry of soils and sediments was deduced which allowed inferences to be made with regard to the potential areas, which could yield significant amount of copper mineralisation to justify further exploration work.

© University of Venda

5.4.6.1 Epidote Alteration within the Limpopo Mobile Belt

The distribution of mineral alteration was extracted as discussed in section 5.4.4 whereby ASTER data was analysed using visual and digital analysis. From the extracted epidote alteration, ground truthing was undertaken whereby verification of the obtained epidote alteration from satellite image analysis was done through direct observation of the epidote alteration on the ground and associating the position of the known Messina copper deposits with the epidote alteration obtained through visual analysis (Fig. 5.22). The associated mines included Artonvilla, Messina, Harper, Campbell Maryland mines as well as Sand River and Baobab mineral occurrences. The mines were found to be situated within the intensive epidote alteration zones, while Sand River mineral occurrence sitting in an area with low epidote intensity (Fig. 5.22). The Maryland mine and Baobab mineral occurrence were situated on high epidote intensity zones (Fig. 5.22). Consequently, the epidote alteration was found to be associated with copper mineralisation within the Limpopo Mobile Belt (LMB) with high intensity of alteration occurring within the known mineral deposits (Fig. 5.22).

The position of epidote alteration within the region was isolated from the surrounding rocks and minerals using various image processing techniques such as visual and digital analysis as previously discussed. The extracted epidote alteration layer that was used in this study, was an amalgamation of the epidote alteration extracted from visual analysis and the epidote alteration extracted from the digital analysis. The amalgamation was done using the intercept tool present in ArcMap, to display areas where the two datasets intercepted each other. This was done in order to ascertain a higher degree of data quality. The epidote alteration layer that was extracted from the interception was converted to raster data. This enabled the production of an epidote alteration map depicting the various degrees of alteration throughout the region (Fig. 5.23).

Various degrees of epidote alteration was found to be concentrated at different locations within the Limpopo Mobile Belt. Consequently, the distribution of epidote alteration was grouped into four main epidote alteration zones, namely, ZA, ZB, ZC and ZD (Fig. 5.23).

© University of Venda

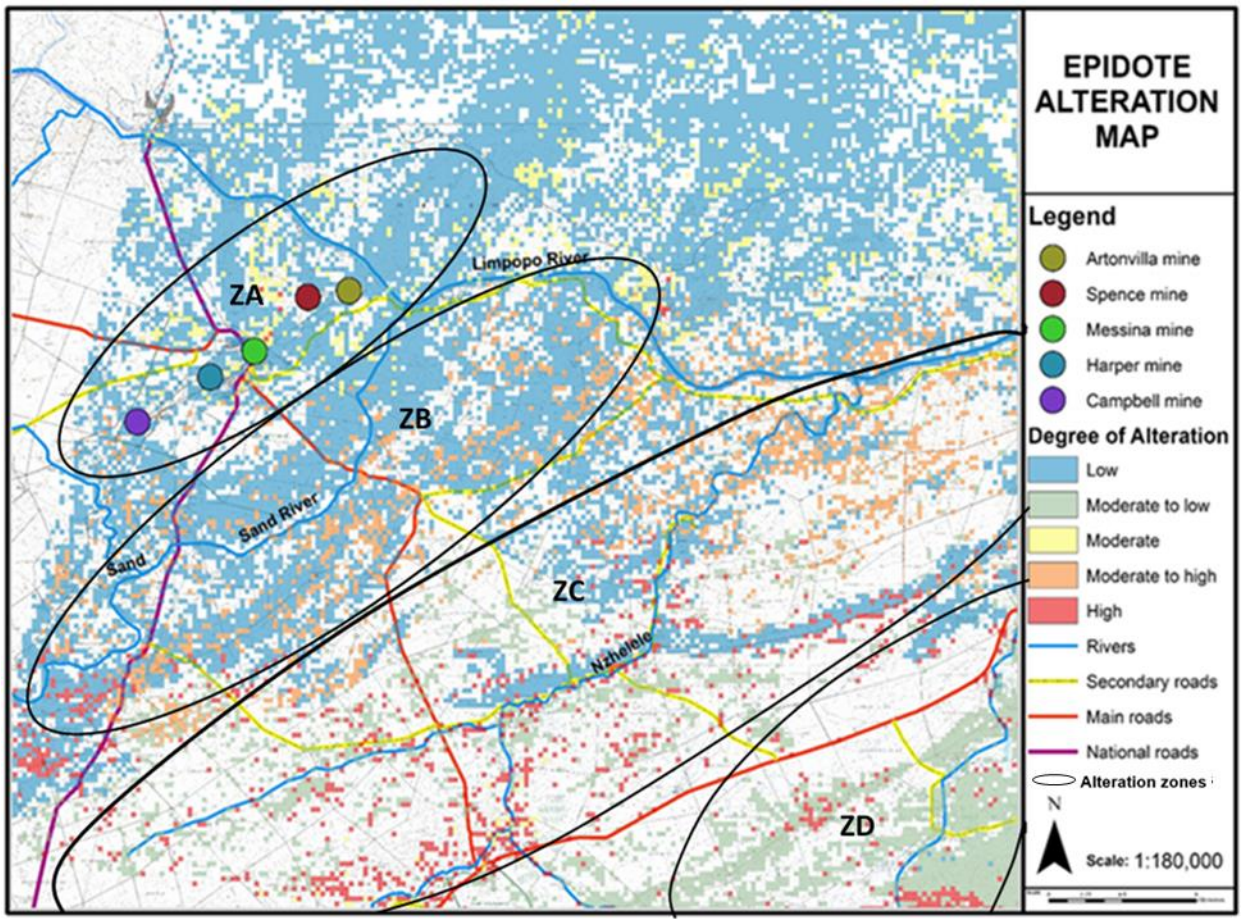


Figure 5.23: Epidote alteration map within the Limpopo Mobile Belt.

Zone ZA epidote alteration occurred within the vicinity of Musina town and the Messina copper deposits and was found to be fairly large and concentrated as compared to the alteration in other parts of the area. The zone was characterised by mainly concentrated low (blue) alteration with moderate (yellow) epidote alteration mainly within the vicinity of the Messina copper deposits. The low degree alteration had no discernible shape but was scattered all over the region. Although no discernible shape was identified, a linear trend was revealed with a north-eastern to south-western trend and this was so for all the four identified zones (Fig. 5.23).

Zone ZB epidote alteration was found to be distributed on the southern side of the Messina copper deposits and covered the Sand River. This Zone strikes on the southwestern to north-eastern direction. The alteration was fairly large and concentrated towards the south-western part of the zone (Fig. 5.23). This zone was characterised by a significant amount of both low (blue) and moderate to high (orange) degree of epidote alteration. Patches of moderate to low

© University of Venda

(greenish) and high (red) degree alteration also occurred towards the lower part of the zone (Fig 5.26).

Zone ZC epidote alteration occurred further south of the region, covering the Nchelele river basin up to the Limpopo River to the north-eastern margin (Fig. 5.23). The zone was characterised by a significant amount of high (red) epidote alteration as compared to other alteration zones in the region. The zone was also characterised by minor patches of low (blue), moderate to low (green) and moderate to high (orange) epidote alteration (Fig. 5.23).

Zone ZD epidote alteration occurred on the southern margin of the region and it covered the Nwanedi River (Fig. 5.23). The alteration zone was characterised by a large amount of moderate to low (green) epidote alteration with minor amounts of high (red) epidote alteration especially to the southwestern margin of the zone (Fig. 5.23).

Generally, epidote alteration within the Central zone of the LMB had more or less a northeastern - southwestern trend. Apart from Zone A (ZA) that runs along the Musina fault zone, the rest of the alteration zones seem to have occurred along the river basin, following the Sand River, Nzhelele and Nwanedi River basins. Noting that the river profiles are often associated with fault zones, it is therefore, imperative to note that the intensity of epidote alteration within region was linked to faulting. Thus, the fault planes acted as conduits for the out-coming fluids that were responsible for rock alteration just at the time of copper – sulphide mineralisation within the LMB.

Epidote alteration associated with the Messina copper sulphide deposits

From the epidote alteration map (Fig. 5.23), a close-up map within the Messina copper deposits was created (Fig. 5.24). Upon assessing the close up epidote alteration map (Fig. 5.24), it was observed that there were various degrees of epidote alteration within the study area that ranged from low to high throughout the study area with Messina copper deposits being characterised by “moderate” to “high” degree of epidote alteration (Fig. 5.24).

The Messina mine displayed the highest degree of epidote alteration in the area. It was characterised by moderate degree of epidote alteration (yellow) with patches of high degree alteration (red). The high degree of alteration was encapsulated by moderate degree alteration, which was in turn encapsulated by low degree alteration (blue) on the outer flanks of the deposit. In terms of aerial distribution, the Messina copper deposit also displayed the

© University of Venda

largest aerial distribution of moderate degree alteration (yellow) as well as the largest aerial distribution of high degree alteration as compared to other deposits (Fig. 5.24).

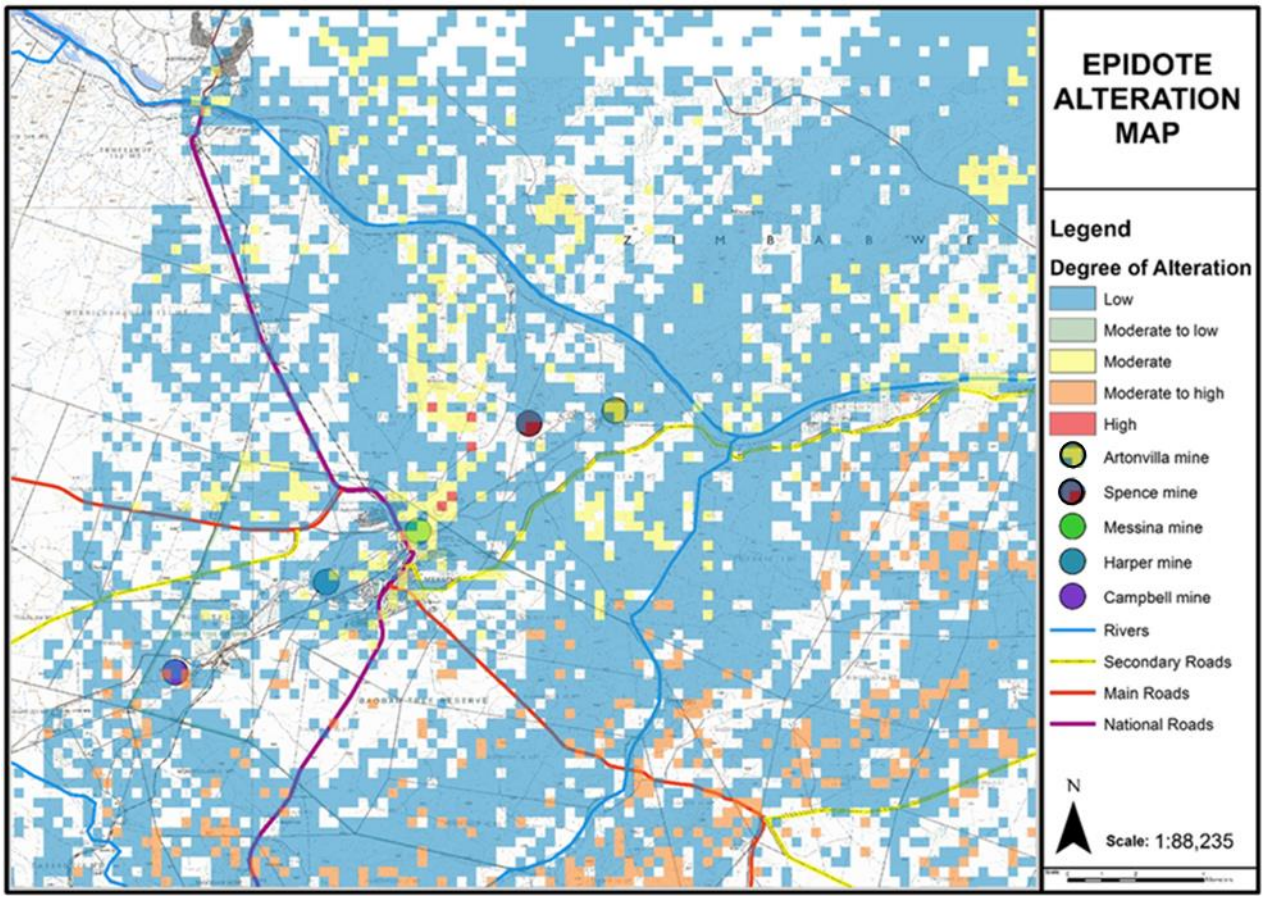


Figure 5.24: Close-up map of the epidote alteration within the vicinity of the Messina copper deposits.

Campbell copper deposit displayed the second highest degree of epidote alteration in the area. This deposit was characterised by moderate to high degree (orange) of epidote alteration. The moderate to high degree of epidote alteration was encapsulated by a low (blue) degree of epidote alteration. In terms of aerial distribution, the moderate to high degree of epidote alteration present in the Campbell deposit was characterised as being fairly small as compared to the epidote alteration at the Messina deposit (Figs. 5.23 and 5.24).

Artonvilla copper deposit displayed the third highest degree of epidote alteration. It was characterised by moderate (yellow) degree of epidote alteration that was encapsulated by a low (blue) degree of epidote alteration. In terms of aerial distribution, the moderate degree of epidote alteration present at the Artonvilla deposit was small (Figs. 5.23 and 5.24).

© University of Venda

The Harper deposit, located within the vicinity of the Harper Mine, displayed the same degree of epidote alteration as that displayed at the Artonvilla deposit. The Harper deposit was characterised by the same moderate (yellow) degree of epidote alteration, encapsulated by the same low (blue) degree of epidote alteration as observed at the Artonvilla deposit. Although in terms of aerial distribution, the moderate degree of epidote alteration located at the Harper deposit was significantly smaller as compared to that observed at the Artonvilla deposit (Figs. 5.23 and 5.24).

The Spence deposit came in last place with the lowest degree of epidote alteration with a small moderate (yellow) degree of epidote alteration on the outer flanks of the deposit (Figs. 5.23 and 5.24).

In summary, epidote alteration map revealed a discernible relationship between the Messina copper deposits and the epidote alteration within the Musina area. It was revealed that the Messina copper deposits in the study area were associated with moderate to high degree of epidote alteration that was encapsulated by a low degree of epidote alteration on the outer flanks of the deposits. This created concentric zones of various degrees of epidote alteration, with high alteration in the centre decreasing to a lower degree of alteration on the outer flanks of the deposits (Fig. 5.25). The epidote alteration map also revealed that the Messina deposit had the highest degree of epidote alteration in terms of both areal distribution and degree of alteration.

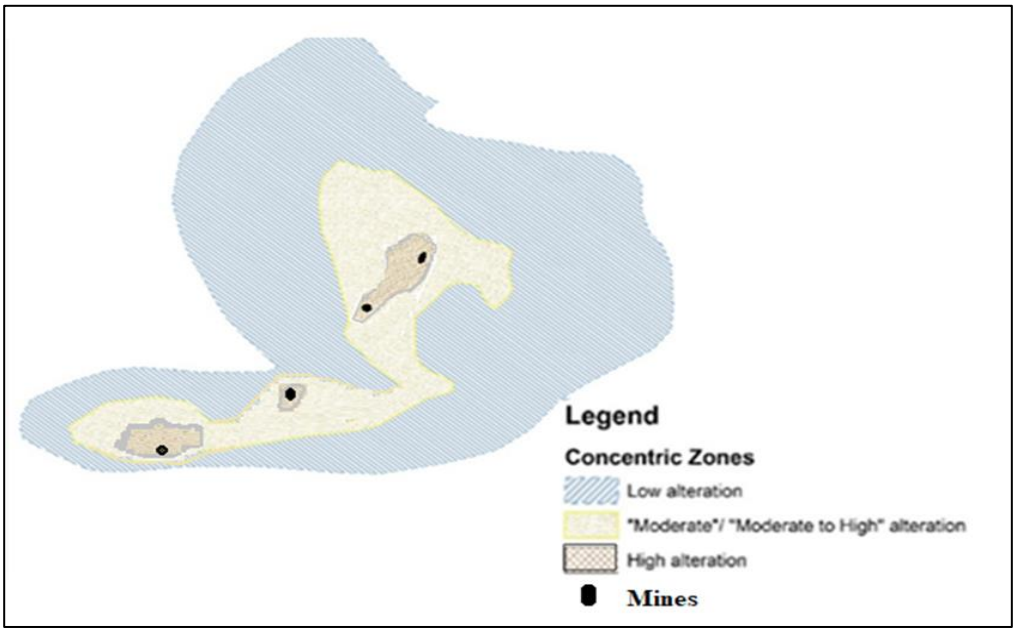


Figure 5.25: Generalized schematic representation of the concentric zonation of epidote alteration within the Messina copper deposits.

© University of Venda

5.4.6.2 Geological Structures

Geological structures such as folding and faulting were identified from a band composite image created during the processing of the ASTER data such that the enhanced geological structural image was revealed (Figs 5.10; 5.26 and 5.27). The image was analysed using various visual interpretation elements such as shape, colour, site and texture.

Folding

Upon assessment of the enhanced geological structures image, it was noted that the LMB was characterised by different structural features (Figs. 5.26 and 5.27). Areas labelled A and B were characterised by a coarser texture as compared to area labelled C which had a fine or smooth texture. It was also noted that there was a difference in colour between the coarse-textured and the fine-textured areas. The coarse-textured areas were characterised by dark green colour, with patches of dark purple to blue colour in some areas, while the fine-textured areas were characterised by light green colour (Figs. 5.26 and 5.27).

The coarse-textured areas were also found to be highly extensive, striking to the northeastern direction. Area A revealed a meandering shape, which occurred along Sand River, close to Musina town (Figs. 5.26 and 5.27). Area A depicts thrust folding with anticline and syncline folds especially along Sand River both in the western part and towards Limpopo River where it covers both Spence and Artonvilla deposits (Figs. 5.27). A major thrust fold in the western part took place over the Campbell deposit (Fig. 5.27).

Area B is characterised by two linear features, with the northern feature runs from the eastern side of Nzhelele River and extends northeast wards parallel to the Limpopo River. The structure thins towards the southwestern direction, but bulges to the northeastern direction (Fig. 5.27). The southern feature of Area B (dark purple to blue colour) runs in the same trend as the above, cutting through Nwanedi River towards Limpopo River. Both features display undulating structures towards the northeastern part and minor folding at the central section.

Consequently, it was revealed that there was a linear relationship between the texture of an area and its shape, whereby the coarser the texture of an area, the more the meandering shape is displayed. This could imply that the coarse-textured areas might have been subjected to various degrees of compressive stress, which resulted in the deformation of the rocks, thus causing the surface of the rocks to reflect light differently as compared to the fine textured areas (Area C).

© University of Venda

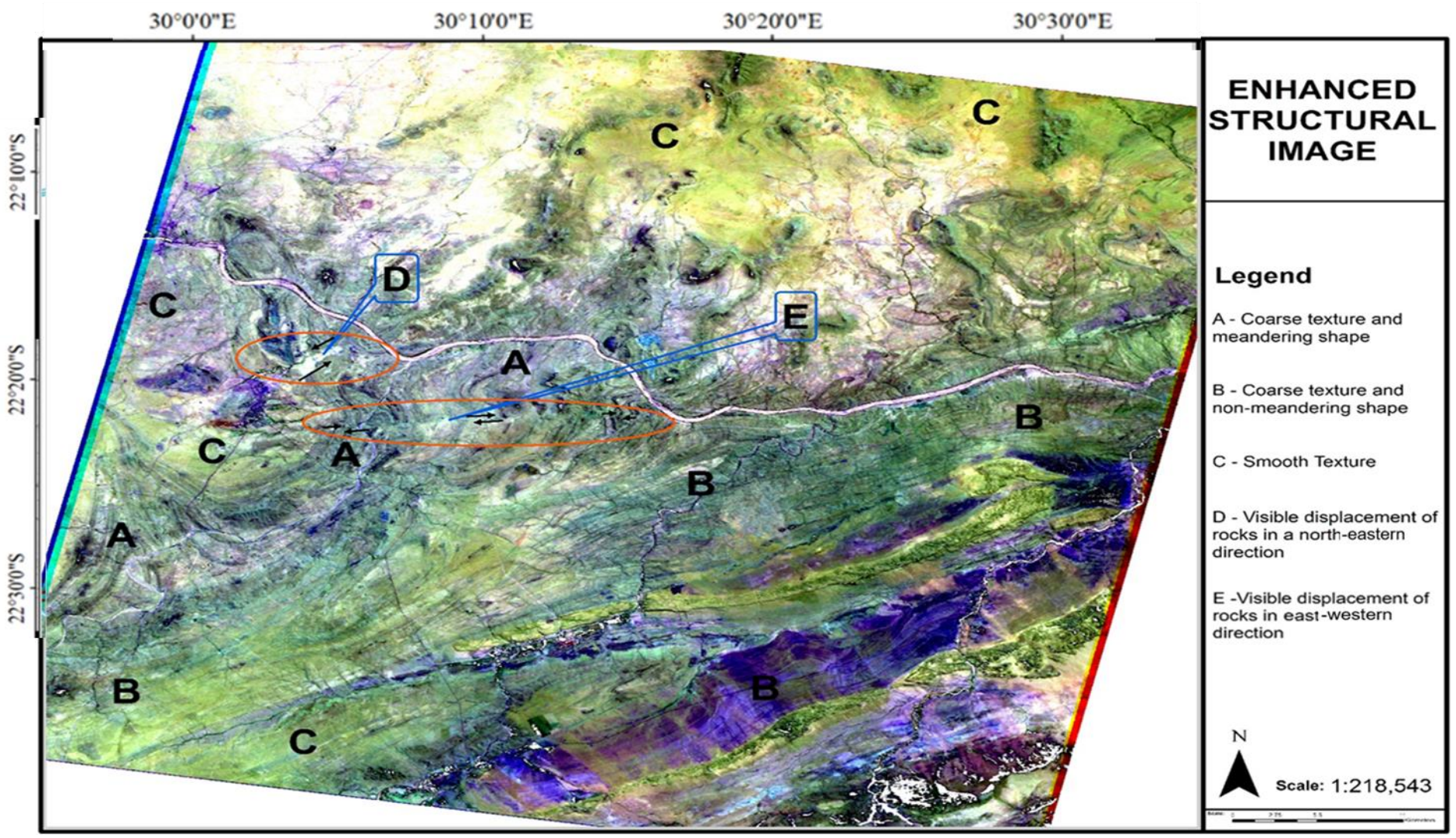


Figure 5.26: Analysed enhanced image depicting structural features within the Limpopo Mobile Belt.

© University of Venda

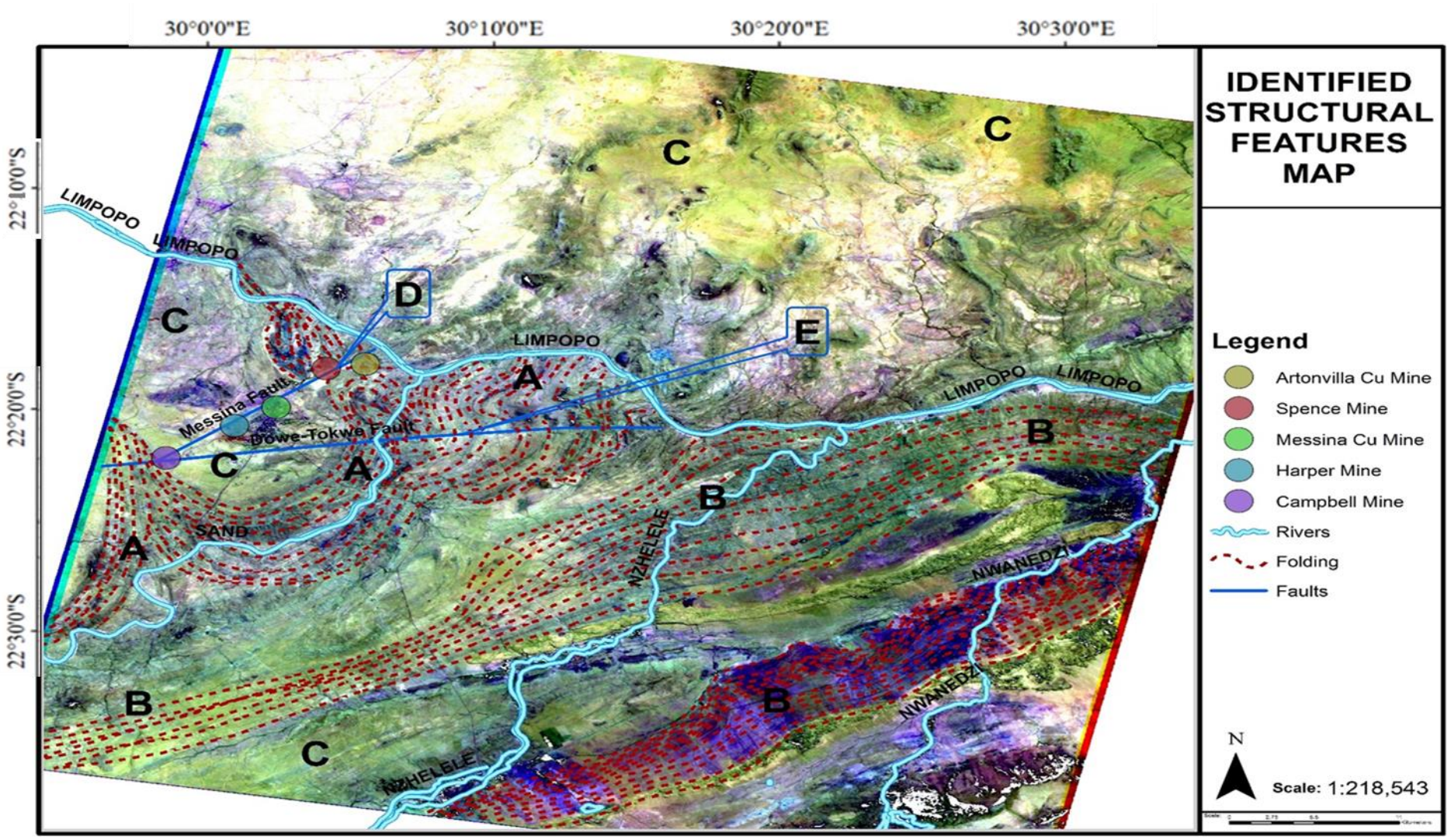


Figure 5.27: Geological structural map showing folds and faults within the Limpopo Mobile Belt.

© University of Venda

Area A revealed thrust folding consisting of anticline and syncline folds as it had a meandering shape. This also implied that it underwent a higher degree of compressive stress as compared to Area B that revealed horizontal or gentle step-like dipping sequence (folds) which was indicative of monocline folding as it lacked the meandering shape, and this implied that it underwent a lower degree of compressive stress (Fig. 5.26; 5.27 and 5.28) (Ramsay and Huber, 1987).

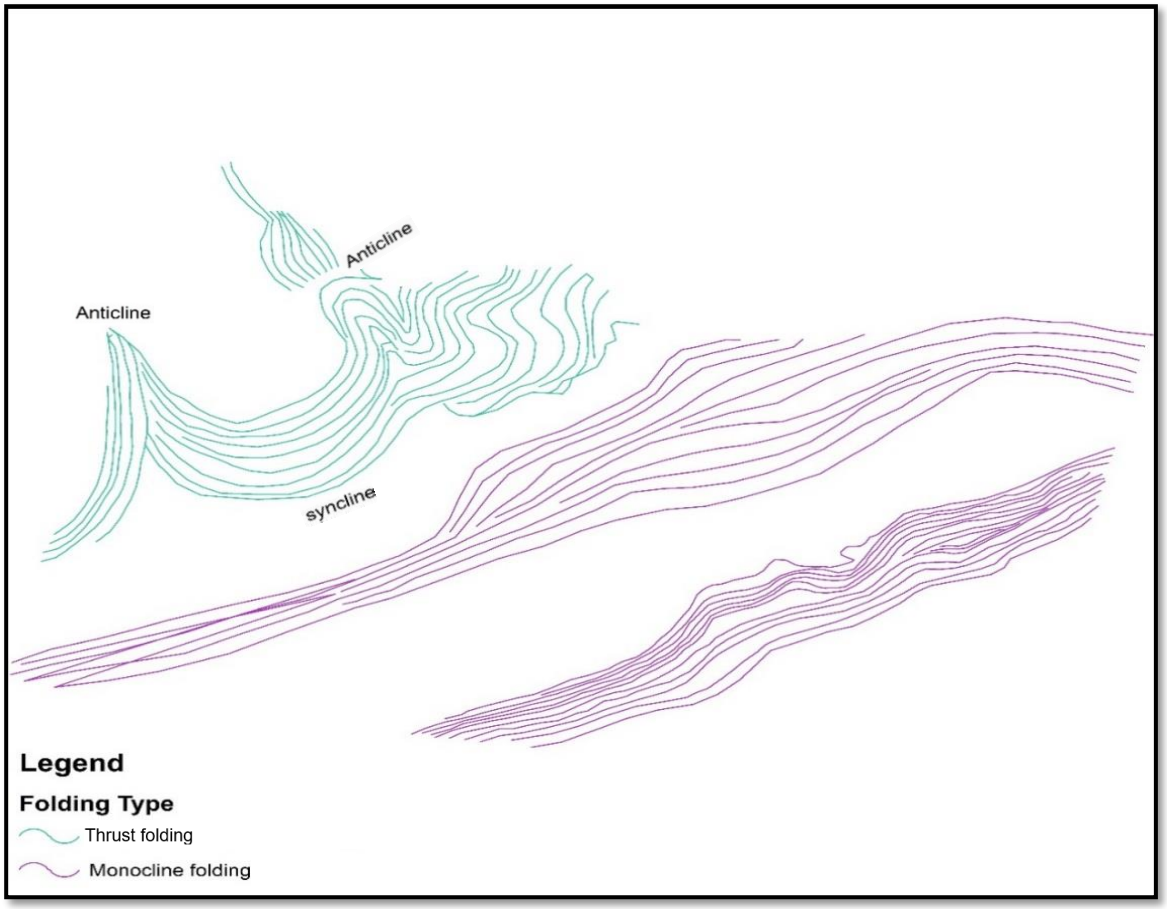


Figure 5.28: Schematic illustration of the types of folding identified within the Limpopo Mobile Belt.

Faulting

Continued assessment of the enhanced structural image revealed areas that were characterised by sudden displacement of the rocks (Area D and E) (Figs. 5.26; 5.27; 5.29 and 5.30). This displacement occurred along a specific linear trend. Area D, located on the north side of Musina town near Spence and Artonvilla mine, displayed a linear displacement of the

© University of Venda

rocks in a northeastern, southwestern direction cutting across the anticlines folds of the thrust folding (Figs. 5.26; 5.27 and 5.29). The linear trend ran through Musina town and perfectly aligned with the Musina copper sulphide deposits (Fig. 5.27). As a result, it was noted that the linear trend observed had to be the Messina Fault, as that the Musina copper sulphide deposits are located along the ENE trending of the Messina Fault (Söhnge, 1946; Pelletier, 1964; Mundalamo and Ogola, 2012).

Area E, located on the eastern side of Musina town, displayed a linear displacement within the rocks in an eastwestern direction (Figs. 5.26; 5.27 and 5.30). As the trend extended, it intersected with the displacement identified at Area D (Fig. 5.27). Based on the linear shape, strike direction and the association with the Messina Fault (Area D), Area E was said to be the Dowe-Tokwe Fault (Chinoda, *et al.*, 2009).

The Messina and the Dowe-Tokwe Fault were the only major faults that could be identified within the region. Their identification was made possible due to the fact that they displaced rocks along folded areas which made them easily discernible. The faults could not be traced in areas which were not folded, which suggested that the faults must have been healed with infilling material such as unconsolidated sediments, which resulted in the disappearance of the fault lines (Ramsay and Huber, 1987).

© University of Venda

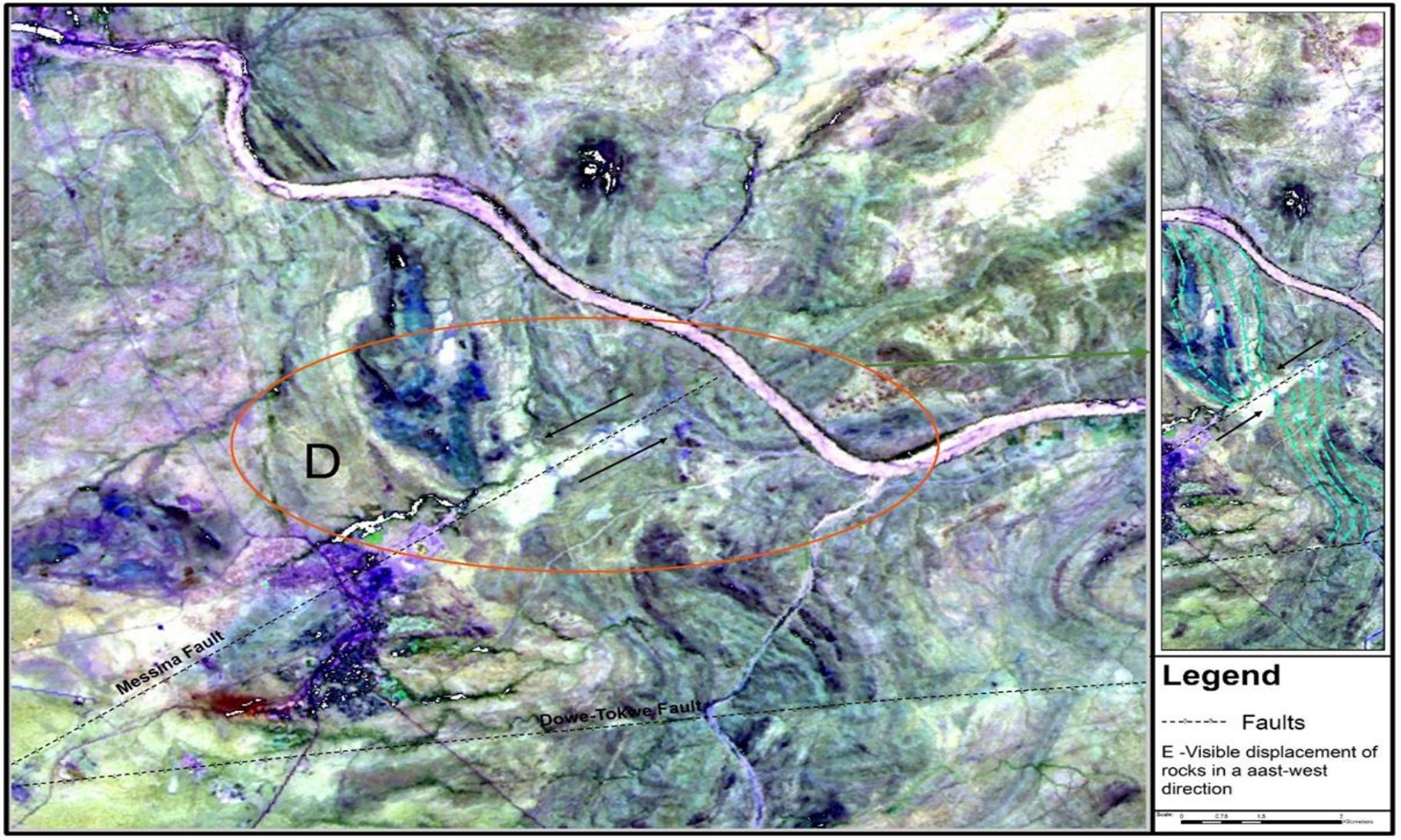


Figure 5.29: Close up of the displacement at area D.

© University of Venda

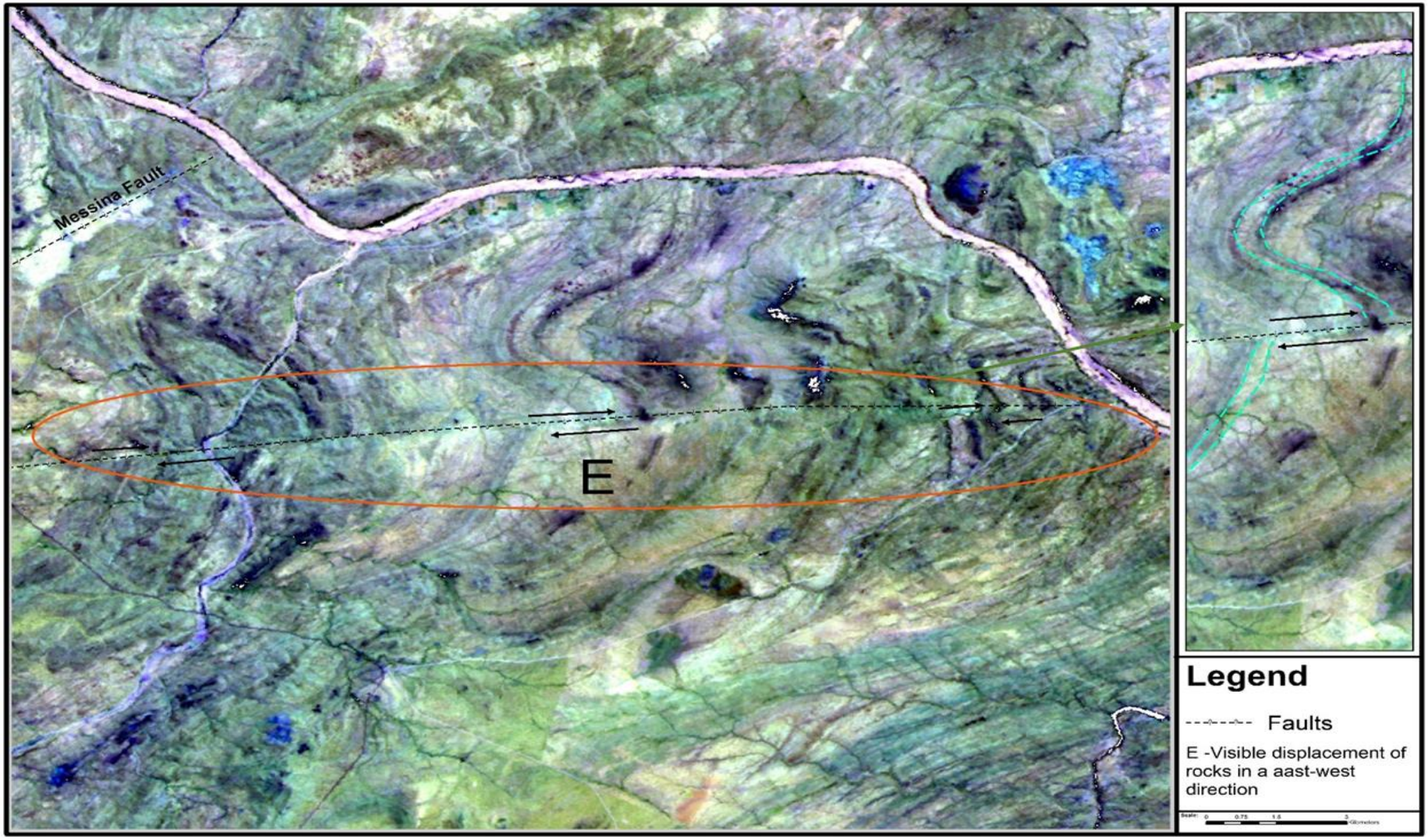


Figure 5.30: Close up of the displacement at area E.

© University of Venda

The identified geological structures were overlaid with the epidote alteration (Fig. 5.31). From Figure 5.31, it was noted that smooth-textured areas (Area C) were associated with either lack of epidote alteration or low degree of alteration and the area was not associated with any geological structures. Coarse-textured areas (Area A and B), occurred were degree of alteration was ranging from low to high and this area was associated with folding. Moderate to high degree of alteration within the coarse-textured areas (Area D and E) was associated with faults. Evidence from the association map suggested that the epidote alteration was confined to the areas that were characterised by coarse texture or linear displacement i.e. folding and faulting areas (Fig. 5.31 and Table 5.3).

Table 5.3: Summary of the findings on association among texture, degree of alteration and geological structures

Texture	**Degree of Alteration**	**Geological Structures**	**Area**
Smooth texture	Lack of epidote alteration to low degree alteration.	Not associated with any geological structures	Area C
Coarse texture	Low to high	Associated with various types of folding	Area A and B
	Moderate to high	Associated with Linear displacement (Faults)	Area D and E

© University of Venda

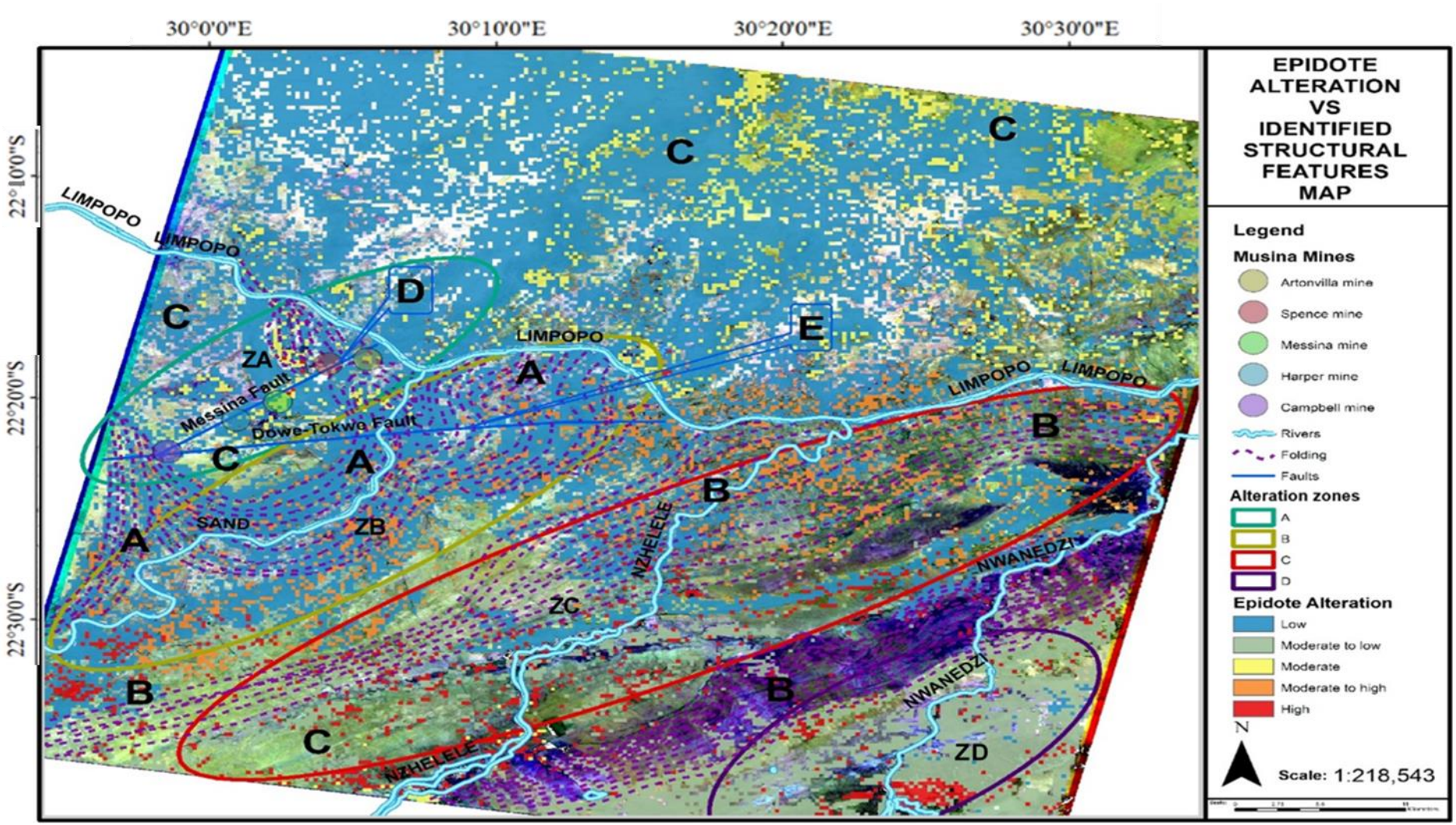


Figure 5.31: Association map of epidote alteration and geological structures.

© University of Venda

5.4.6.3 Conceptual Model of Target Generation for Mineral Exploration within the Limpopo Mobile Belt

In order to unequivocally justify the use of remote sensing in exploration of copper-sulphide mineralisation within the musina area and its environs and regionally within the Limpopo Mobile Belt, a conceptual model showing regions of interests for exploration of copper-sulphide mineralisation was developed. The conceptual model was created using Arc-scene, a 3D modelling software programme found in ArcGIS, by extracting a DEM from the ASTER Image and using it as a reference base height to provide 3D relief (topography) of the area. The epidote alteration data was then overlaid on top of the reference base height in order to model the behaviour of the epidote in the region of interest (Fig. 5.32).

Upon visual analysis of the conceptual model, it was noted that the epidote alteration generally occurred near high elevation and decreased with elevation and this was evidenced by the red and orange coloured mountain peaks in the model. The high elevation peaks were confined to areas classified as folding areas during structural identification while areas that lacked folding were relatively flat (Fig. 5.31). This suggested that the folded areas with large peaks had undergone high degree of compressive stress which resulted in the overturning as well as in the development of a large number of fractures. The fractures may have acted as conduits which enabled the hydrothermal fluid to move more easily within these areas, which could have been the reason for the epidote alteration appearing as more concentrated as compared to areas that underwent a lower degree of compressive stress and had less fractures to allow the movement and crystallization of hydrothermal fluids.

One important finding that was made possible by the 3D model was that, it clearly displayed the degree to which the epidote alteration was confined to the geological structures. It was also possible to see that the degree of epidote alteration associated with the Messina copper deposits was “moderate” to “high” (Figs. 5.32 and 5.33) as indicated by the yellow, orange and red colours that occurred in close proximity to the copper deposits. As a result, it can be concluded that potential areas that can yield high degree of copper-sulphide mineralisation had undergone “moderate” to “high” epidote alteration. This implied that any area coloured by yellow, orange or red in the conceptual model (Figs. 5.32, 5.33 and 5.34) provided a potential area of interest for further exploration work.

The conceptual model enabled the identification of six regions of interest (ROI) that could yield significant copper-sulphide mineralisation and should be given priority for further

© University of Venda

exploration in the Musina area and its environs and regionally within the Limpopo Mobile Belt. These areas or regions of interest were considered to be the most feasible areas to conduct exploration because they exhibited the same conditions as those observed at the Messina copper deposits. For example, ROI 1 exhibited the same conditions as those observed at the Messina deposit. This is because ROI 1 was characterised by "moderate" degree of epidote alteration that was expansive as that of the Messina deposit. The area was also structurally bound, occurring within the anticline of folding Area A and it occurred in close proximity to the Dowe-Tokwe Fault (Fig. 5.33).

ROI 5 exhibited the same conditions as those observed at the Campbell deposit. This is because ROI 5 was characterised by "moderate to high" degree of alteration as that of the Campbell deposit. However, the alteration displayed by ROI 5 was larger in area than that of the Campbell area (Fig. 5.33). This could be indicative of higher level of hydrothermal alteration and perhaps a higher degree of copper-sulphide mineralisation. ROI 5 was also structurally bound, thus localisation of copper orebodies at Campbell is also attributed to the role played by both the Messina and Dowe Tokwe faults.

It stands to reason, that if the copper-sulphide mineralisation within the Musina area was structurally controlled, as is suggested by the conditions present at all the five copper deposits, then the conditions displayed at ROI 1, ROI 5 and all other regions of interest may be indicative of areas that may yield significant copper-sulphide mineralisation (Figs. 5.32; 5.33 and 5.34). The six identified ROI were also plotted on the topographical map (Fig. 5.35).

Generation of mineral exploration targets has been and still one of the key tasks of any mineral exploration company or indeed of any country, looking to define regions of interests, which could attract investors. In this study, target generation was achieved through the association of regions of interest determined from epidote alteration and geological features using remote sensing data (Figs. 5.32; 5.33; 5.34 and 5.35) with anomalous areas achieved through soil geochemistry study in Chapter 4 (Fig. 4.21). The anomalous areas and areas of regions of interests were plotted together in a topographical map in order to deduce the association between them (Fig. 5.36). It was noted that out of the six anomalous areas determined through soil geochemistry and six regions of interests from remote sensing, three anomalous areas (TA 3, TA4 and TA 5) were associated with two regions of interests (ROI 1 and ROI 2). This gives such areas high probability of sulphide mineralisation in the study area (TA 3, TA4 and TA 5 in Figure 4.21).

© University of Venda

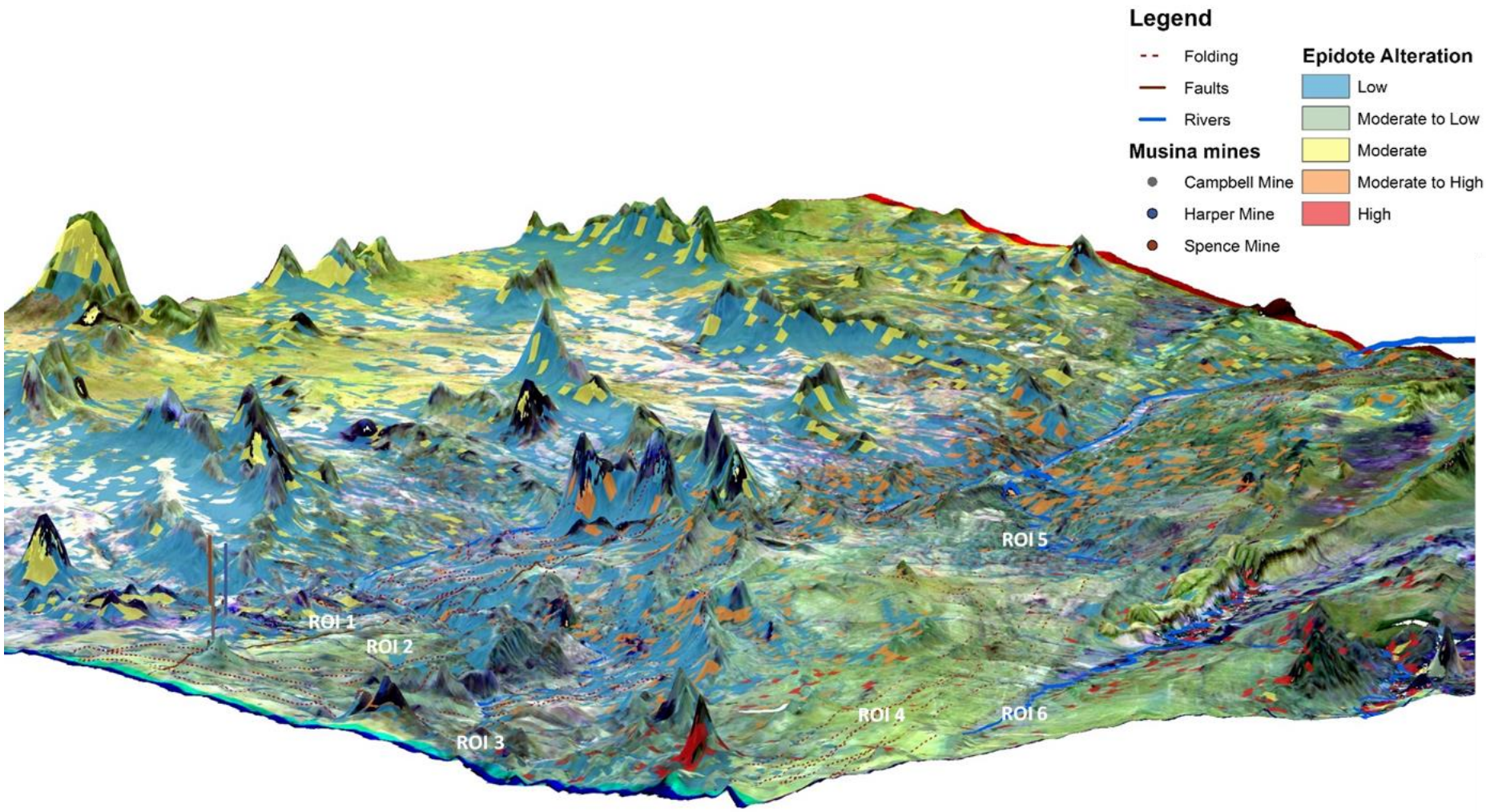


Figure 5.32: Conceptual model (3D) showing Regions of interest (ROI).

© University of Venda

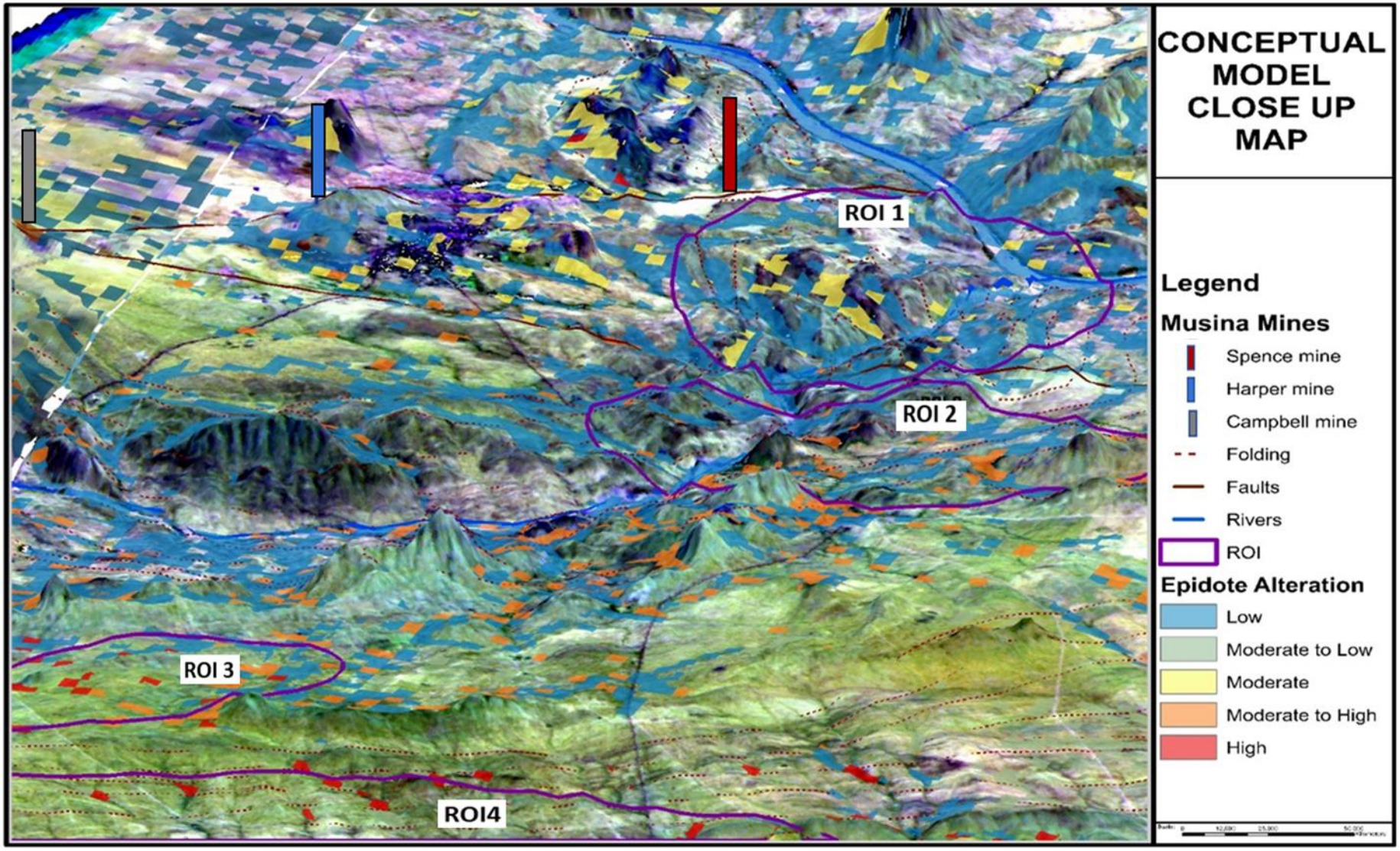


Figure 5.33: Conceptual model for region of interest part 1 showing region of interest 1, 3, and 3.

© University of Venda

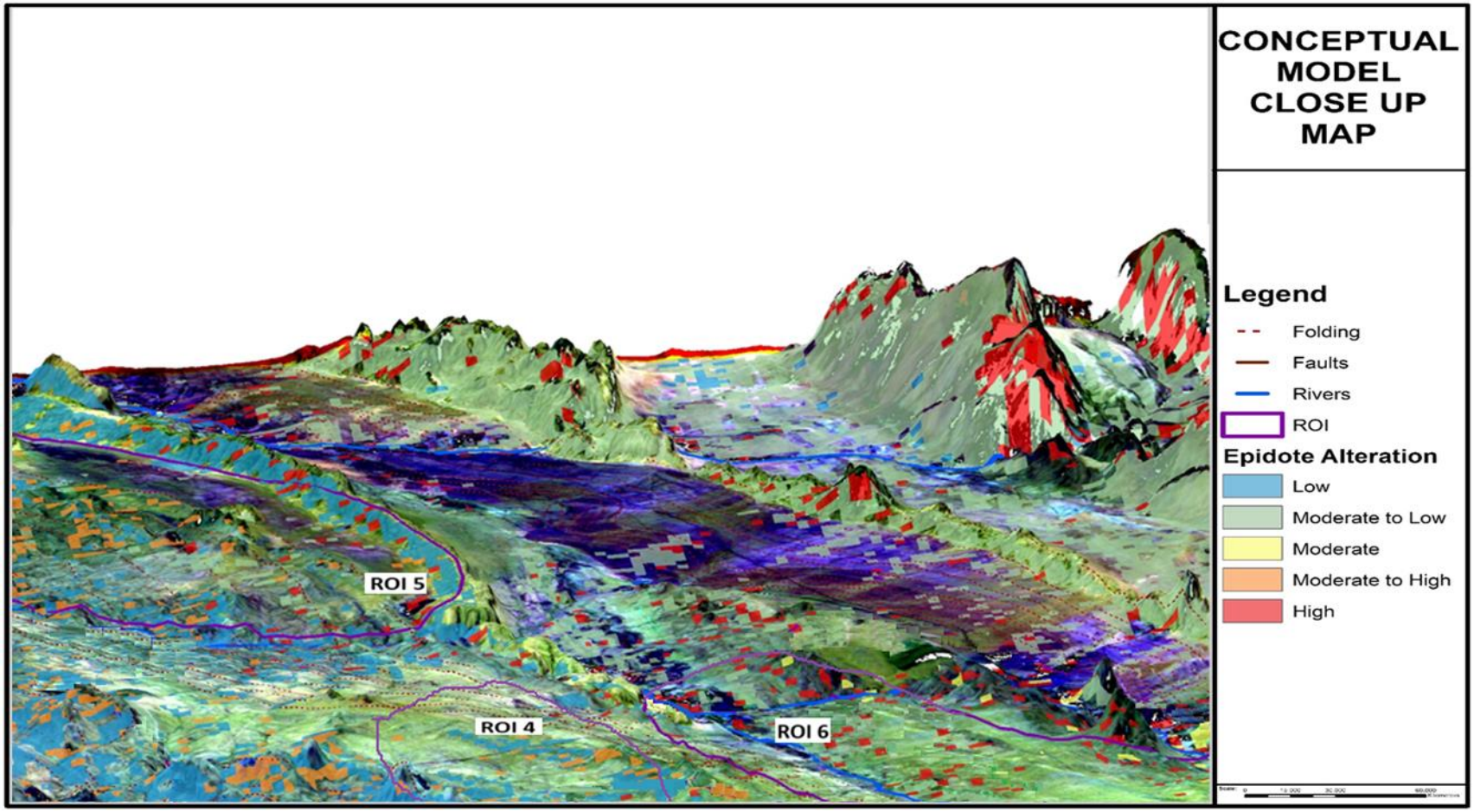


Figure 5.34: Conceptual model, region of interest part 2 showing region of interest 4, 5 and 6.

© University of Venda

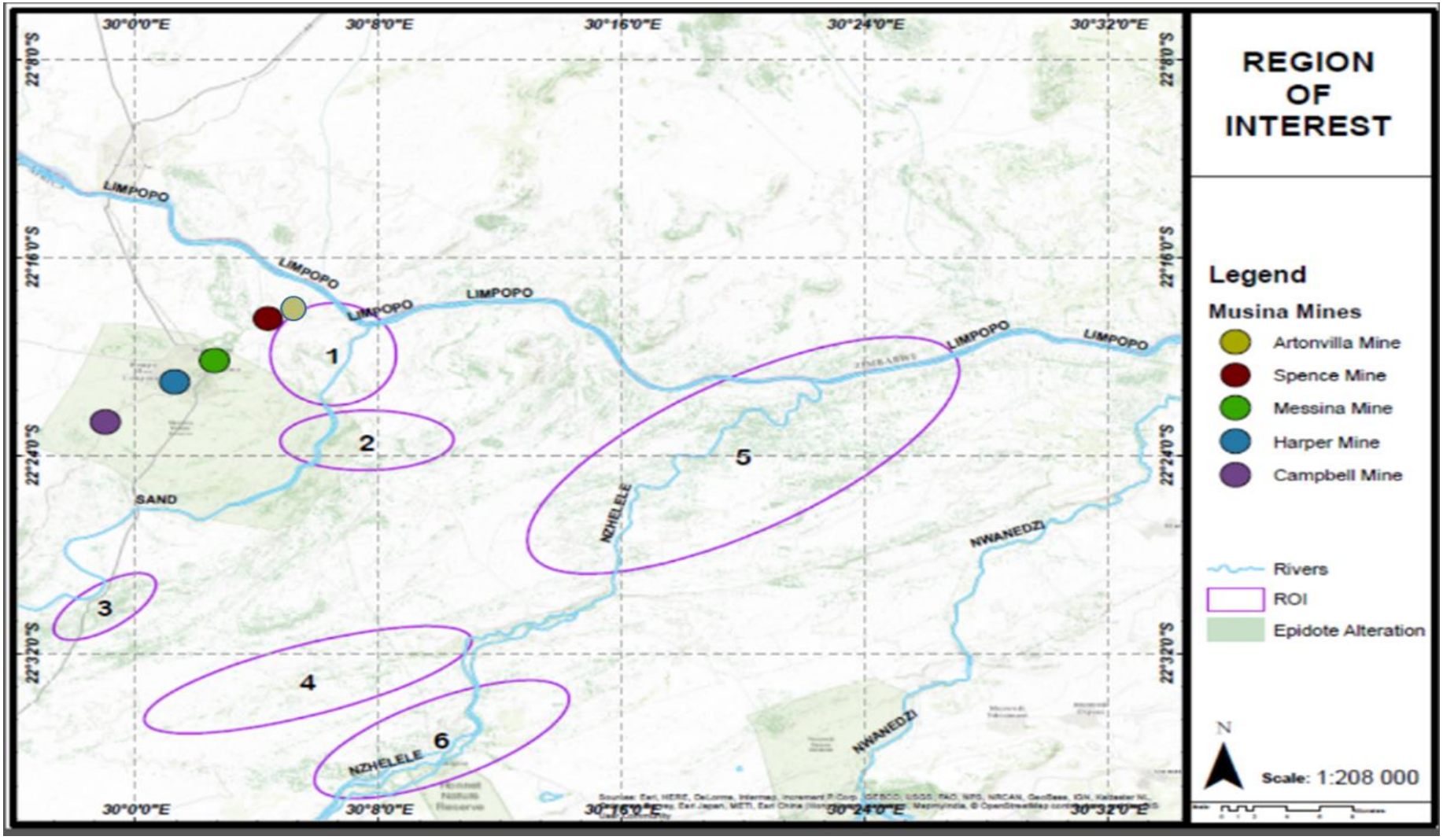


Figure 5.35: Topographical map showing regions of interest for further mineral exploration within the Limpopo Mobile Belt.

© University of Venda

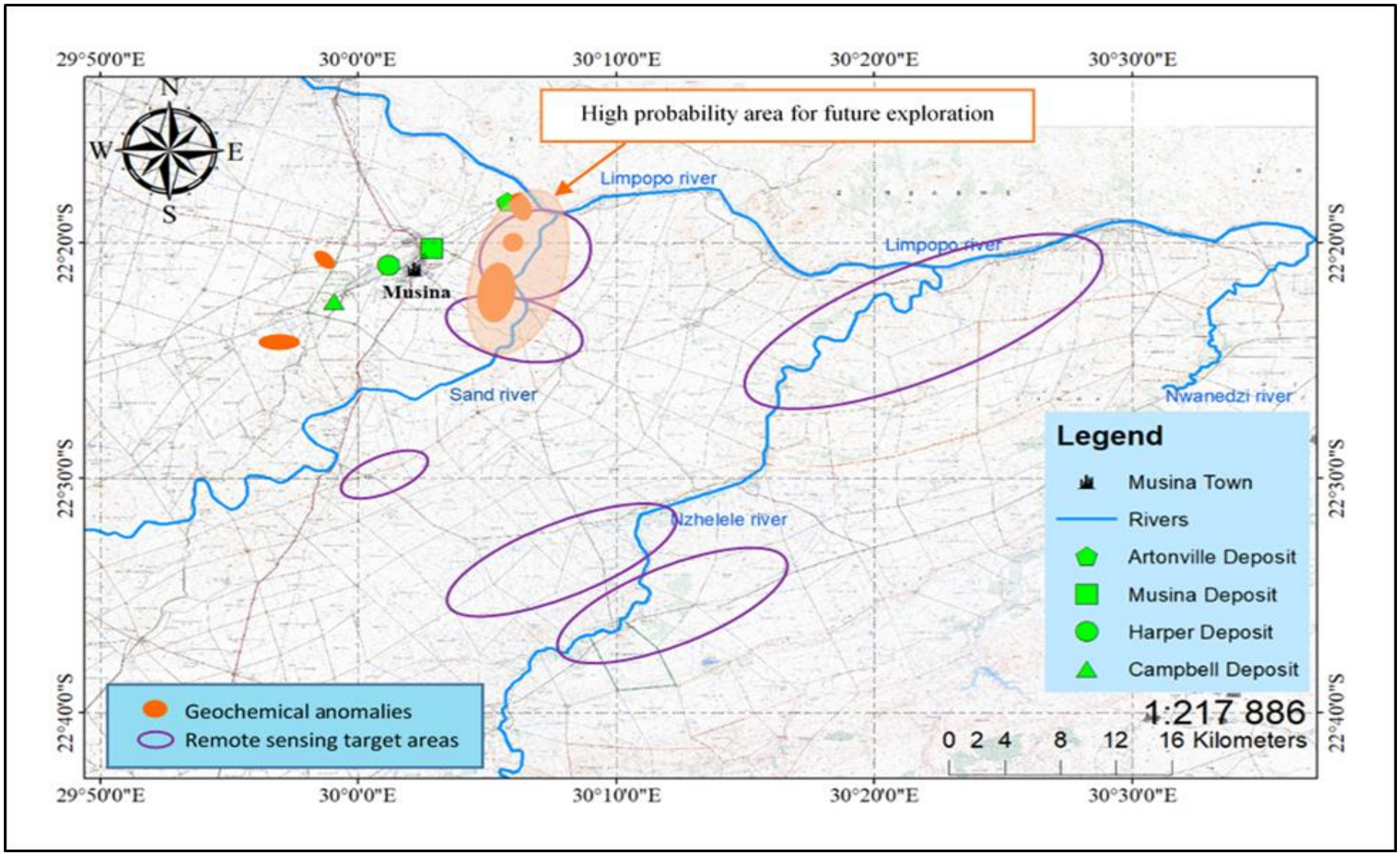


Figure 5.36: Exploration target areas of copper-sulphide mineralisation for further exploration within and around Musina area.

© University of Venda

5.5 Discussion

Remote sensing study set out to investigate whether the Messina copper-sulphide mineralisation was structurally controlled through determination of epidote alteration and geological structures such as faults and folding. This was also done so as to identify exploration target areas for future mineral exploration.

The investigation was made possible by identifying a hydrothermal alteration mineral epidote and it was revealed that it is possible to detect and isolate hydrothermal mineral alterations using remote sensing techniques. This enabled the study to identify the spatial relationship between the Messina copper-sulphide deposits and the epidote alteration within the study area. The study depicted zones of "low", "moderate" to "high" degree of epidote alteration within the LMB and this coincided either with the known copper deposits or structural features (Fig. 5.31). The spatial distribution and intensity of epidote alteration was confirmed to have been influenced by the geological structures in the area.

Taking a holistic view of the findings within the copper deposits, the study confirmed that the Messina copper-sulphide deposits created concentric zones of various degrees of epidote alteration with low degree alteration occurring on the outer flanks of the deposits with increasing degree of alteration towards the centre of the deposit (Fig. 5.28). This was in line with what was reported by Jacobsen *et al.* (1976), who stated that the Musina copper sulphide mineralisation was characterised by intense hydrothermal alteration that occurred in distinct concentric zones. The findings suggested that presence of copper mineralisation, within the study area, was irrefutably linked to the presence of "moderate" to "high" degree of epidote alteration. This spatial relationship was supported by the fact that, the mine which had the largest aerial distribution of "moderate" to "high" degree of alteration (i.e. Messina Mine) also had the largest copper ore reserves and was historically the last mine to close according to Mundalamo and Ogola (2012). It was also supported by the fact that, the majority of "Moderate" degree of alteration occurred near the Limpopo River and it was suggested by Hanisch (1974) that the BaLemba people used to mine copper lodes near the Limpopo River prior to European settlement in the area.

The spatial relationship between the Messina copper-sulphide mineralisation and the epidote alteration, provided the required mechanism to study the structural control on the Musina

© University of Venda

copper sulphide mineralisation as well as providing vital information for early stage exploration work.

The study also revealed that the epidote alteration within the study area could be grouped into zones based on the intensity, shape and trend of the alteration. The most interesting finding, was that all the identified epidote alteration zones that is Zone A, B, C and D were all trending in the same north-eastern direction and more or less in line with the general trend of the geological structures in the region (Fig. 5.23 and 5.31). Consequently, the geological structures in the region acted as the conduit for hydrothermal fluids that resulted in the host rock alteration and the mineralisation of copper-sulphide ore. The main known geological structures are the Messina and Dowe-Tokwe faults, however the current study through remote sensing has revealed the spatial distribution of intense epidote alteration over the known river basin, thus depicting possible structural control of these rivers by faults. Further to this, the study identified the occurrence of thrust folds that are likely to be target areas for copper-sulphide mineralisation. Similarly, the study conducted by Drew (2006) indicated that the copper mineralisation in the Central Europe was controlled by wrench fault at the site of ore deposition, which provided carapace development and fracturing for focusing of hydrothermal fluid flow which resulted in the copper sulphide mineralisation.

The findings of the study implied that significant copper mineralisation within the Musina area could be found mainly in areas that were highly fractured, to provide the necessary focusing of hydrothermal fluid to result in significant copper mineralisation. The degree of fracturing that is required to satisfy this condition on a regional scale and produce significant copper deposits could have only resulted from a geological event that created geological structures. Thus, it could be undoubtedly stated, that the spatial position of the copper deposits/mineralisation within the Musina area was structurally controlled.

Upon evaluation of the conceptual model the study suggested that for further exploration, areas that have undergone “moderate” to “high” degree of epidote alteration and lie in close proximity to geological structures that could have provided the required fracturing that acted as conduit for hydrothermal fluid which could have resulted in the production of significant copper deposits should be targeted. Areas such as the synclines and anticlines of the folding are potential areas of interest as these areas have undergone extreme compressive stress during deformation and contain the most fractures as compared to other parts of the folding. This is also evident when looking at the degree of alteration encountered at the trough and

© University of Venda

crest of the syncline and anticline fold. These areas were characterised by "moderate to high" degree of epidote alteration (Fig. 5.31).

The study also suggested that early stage exploration should not focus on the epidote alteration and the geological structures in isolation but rather should take a holistic view, also taking into account the local geology of the area. Due to the nature of how the copper deposits formed in the past, it was suggested that exploration should target more brittle geological units (geological units that deform easily to form fractures). Within the Musina area these would be the metamorphic rocks such as the quartzite because they contain large amounts of brittle minerals i.e. quartz (Nelson, 2015). This was further supported by the work of van Graan (1964), who reported that the metamorphosed sediments such as meta-quartzite, quartz-magnetite rocks, granulite and biotite-garnet-corderite gneisses in the study area had been subject to plastic deformation under conditions of high temperature and differential pressure, which resulted in this suite of rocks being characterised by complex folded structures. This proved that geological units that were more brittle could be structurally bound and thus yield significant amounts of copper mineralisation. Thus, areas that are characterised by "moderate" to "high" degree of epidote alteration are structurally bound and occur within metamorphic units (or any other brittle geological unit) are the best areas of interest for early stage exploration (Fig. 5.31, 5.32 5.33 and 5.34).

With regard to exploration target generation, association of remote sensing findings with the baseline geochemistry findings was done so as to locate the area of interests. This association revealed three main exploration target areas (TA2, TA3 and TA5) whereby the alteration zones, geological structures together with the anomalous area from baseline geochemistry were found to have same spatial position or distribution. Consequently, the conceptual model of target generation for mineral exploration was revealed that can be used for early exploration purposes.

The study proved that remotely sensed data could significantly contribute to early stage exploration work in the Musina area or within the LMB. It was also ultimately substantiated that remote sensing could lead to a cost-effective way of identifying areas that could yield significant copper mineralisation. In this study, geochemical baseline study further supported the remote sensing study thus revealing exploration target areas that are useful for early stage of mineral exploration.

© University of Venda

CHAPTER 6

PETROGRAPHIC INVESTIGATION

Preamble

The chapter focuses on the petrological study of different rock types associated with the Campbell (CAMP) and Artonvilla (ARTV) copper deposits. This involves petrography and petrochemistry, whereby petrography deals with the description of rocks through studying both their physical and optical properties, while petrochemistry is concerned with the chemical interrelationships within different rock types. The study entails the use of microscopic techniques such as; Petrographic microscopy (using transmitted light), X-ray fluorescence spectrometry (XRF) and Electron microprobe analyzer (EMPA). This was undertaken so as to ascertain the mineralogical and chemical composition, structure, texture, mineral alteration of the rocks associated with the Messina copper deposits. The chapter encompasses; fundamentals of petrography (application and importance), microscopic techniques, sample preparation and analysis; petrographic study of textural, mineralogical, and mineral alteration investigation; geochemical classification of garnet, and discussion.

6.1 Fundamentals and Importance of Petrology

Petrology is one of the geology discipline that deals with the study of rocks, their occurrences, composition, origin and evolution i.e. focuses primarily on the rock formation and or petrogenesis. Petrological description includes definition of the unit in which the rock occurred, its attitude and structure, its mineralogy and chemical composition, and conclusions regarding its origin. Petrological study is closely related to mineralogy, mineral chemistry and geochemistry of rocks (Halder and Tišljar, 2014; Harvey *et al.*, 2006).

Petrology is an important branch of geology therefore its importance and application have been widely recognized within the earth science discipline. It is strongly connected to various aspects of geology such as mineralogy and geochemistry. Consequently, petrology is important and mostly applicable in qualitative analysis such as mineralogical analysis of rocks, structural features within the rocks, geochemical analysis (chemical composition), spatial relationship between grains, mineral formation and processes. Petrology is also most important in quantitative analysis which includes; textural analysis (grain sizes and shapes)

© University of Venda

and grain size distribution and all these applications are done so as to understand the origin of the rocks (Halder and Tišljar, 2014; Harvey *et al.*, 2006; Li Wang 1995).

Textural analysis, grain size distribution and their spatial relationship within the rocks are important in the recognition and classification of rocks, fundamental factors in the understanding of processes of the rock formation (genesis). Information such as amount and types of mineral present in a rock (mineralogical analysis) are important and applicable in the classification of rocks through determination of mineral constituents and chemical composition of the rocks so as to know and distinguish minerals and also for resolving the origin of the rocks, including the understanding of mineral genesis. Mineral chemistry or geochemistry of rocks is one of the important analysis in petrology for the purpose of understanding the complex chemical reactions and processes that lead to crystallization, or convention of minerals and rocks (Halder and Tišljar, 2014; Harvey *et al.*, 2006; Li Wang 1995).

6.2 Methods used for Petrological Analysis

Petrological analysis involves several methodologies such as mineralogical, petrographic, and geochemical analysis that involves the identification and determination of minerals, textures, structures and chemical composition of rocks for better understanding of the origin of the rocks and these uses several techniques such as optical microscopy, Scanning electron microscopy, X-ray diffractometry, X-ray fluorescence spectroscopy, Atomic absorption spectrometry (Table 6.1).

Various methods for mineralogical and chemical analysis of rocks include optical microscopy and analytical techniques. Although petrographic study is one of the traditional method used in the identification of minerals, abundance, liberation, their textures, physical and structural features using transmitted petrographic microscopy, it still remains as one of the aspects used in modern days because its combination with mineralogical and chemical study can be particularly illuminating. Modern petrographic microscope these days have both transmitted and reflected lights so as to relate the gangue and opaque minerals at the same time. Development in automation of SEM- based techniques, computerised XRD processing and

© University of Venda

identification and imaging softwares has impacted on the improvement of this field (Schouwstra and Smit, 2011).

Table 6.1: Summary of the main techniques employed for mineralogical and geochemical analysis of rocks (Worden, 2005; Blatt *et. al*, 2006)

Technique	Method	Output type	Samples type
Microscopic	Optical microscopy	Mineral composition, and texture of rocks	Solid (rock, mineral, sediment, soil)
	Scanning electron microscopy (SEM)	Point mineral composition	Solid (rock, mineral, sediment, soil)
X-ray	X-ray electron probe microbe analysis (EMPA)	Point mineral composition	Solid, solid organic and fluids trapped in solids
	X-ray fluorescence (XRF)	Rock composition	Solid (rock, mineral, sediment, soil, filtrate) fluid organic
	X-ray diffraction (XRD)	Mineralogy	Solid (rock, mineral, sediment, soil, filtrate) and solid organic
Spectroscopic	Atomic absorption spectroscopy (AAS)	Solution composition	Artificially dissolved solid, water and fluids trapped in solid
	Inductively coupled plasma-optical emission spectroscopy (ICP OES)	Solution composition	Artificially dissolved solid, water and fluids trapped in solid
Chromatography	Gas chromatography (GC)	Gas composition	Water, organic fluids, gas and fluids trapped in solids
	Ion exchange chromatography (IC)	Aqueous liquid composition	Artificially dissolved solid, water and fluids trapped in solids
Mass spectroscopy	Mass spectroscopy (MS)	Composition and isotope content	Artificially dissolved solids, water, solids (rock, mineral, soil, filtrate) solid organic, gas and fluid
	Isotope dilution mass spectroscopy (IRMS)	Isotope ratio	Dissolved solids, water, fluids trapped in solids and solid organic, gas and fluid
	Inductively coupled plasma mass spectroscopy (ICP MS)	Composition	Artificially dissolved solids, water, fluids in solids and solid organic, gas and fluid
	Gas chromatography spectroscopy (GC MS)	Composition	Water, organic fluids, gas and fluids in solids

© University of Venda

The methods for determining the chemical compositions of rocks and minerals are diverse, ranging from traditional wet chemical quantitative analysis to modern spectroscopic and mass spectroscopic techniques (Harver *et al.*, 2006). For example, XRF, AAS (Table 6.1). In this study, petrographic, mineralogical and geochemical techniques were applied.

6.3 Petrographic Study of the Messina Copper Deposits

6.3.1 Specific Objectives

Petrological study of the Messina copper sulphide deposits (Campbell and Artonvilla deposits) was done in order to determine the following:

- Textural and grain size analysis of the rocks;
- Determination of mineral composition of the rocks;
- Geochemical characterization of different rock types: and
- Mineral alteration processes.

6.3.2 Rocks of the Messina deposits

The current study focuses on those rocks that are associated with copper-sulphide mineralisation in the Musina area. These included the following rock types:

- Granulites: These are rocks that had been subjected to high grade metamorphism that formed under intense temperature and pressure. In the study area, these rocks were formed during the regional metamorphism of the Limpopo mobile belt and they consist of the following rock types: amphibolite-quartz granulite; and biotite-garnet-quartz granulite
- Amphibolite: Rocks formed by moderate temperature and pressure. The rock contains mainly amphibole especially hornblende. Sometimes amphibole fofrms as a retrograde transformation of granulite to amphibolite facies.
- Quartzite: A nonfoliated metamorphic rock composed entirely of quartz, formed from sandstone and with cryptocrystalline texture;
- Hornblende schist and biotite schist: Foliated medium grade metamorphic rocks formed from mudstone, shale or igneous rocks composed of micas and other platy minerals with either abundance of hornblende or biotite.

© University of Venda

- Gneisses: Rocks of metamorphic origin, formed under high temperature and pressure, derived either from igneous or sedimentary rocks. In the study area, the following gneiss rock types were identified; Hornblende gneiss, quartzo-feldspathic gneiss, potassium-feldspathic gneiss, and calc-silicate gneiss.

In this study, petrographic description of these rocks was undertaken with a view to determine their relationship with ore mineralisation in the area, especially the effect on rock alteration. The study involved determination of physical characteristics of the different rock types within the study areas. It further involved both the textural and mineralogical investigation of the rocks and the mineral alteration processes that occurred within the different rock types.

6.3.3 Sample Selection and Preparation

Representative rock specimens associated with the deposits collected during fieldwork were selected for petrological studies. From a total of 33 rock specimen (14 and 19 rock specimens from Campbell and Artonvilla copper deposits respectively), 25 rock specimens (11 and 14 from Campbell and Artonvilla deposits respectively) were selected as representative samples for thin sections preparation and study.

Preparation of thin sections was done at the Department of Mining and Environmental Geology, University of Venda and also at MINTEK, Johannesburg. The specimens were subjected to a series of steps consisting of sectioning (cutting and trimming), bonding, cutting of bonded samples, grinding, lapping, and polishing, following thin section preparation procedure by Craig and Vaughan (1994).

Cutting: The large rock specimen were cut to smaller sizes using a diamond saw (Fig. 6.1A). Specimen were cut into rectangular blocks of approximately 50 x 80 mm size.

© University of Venda

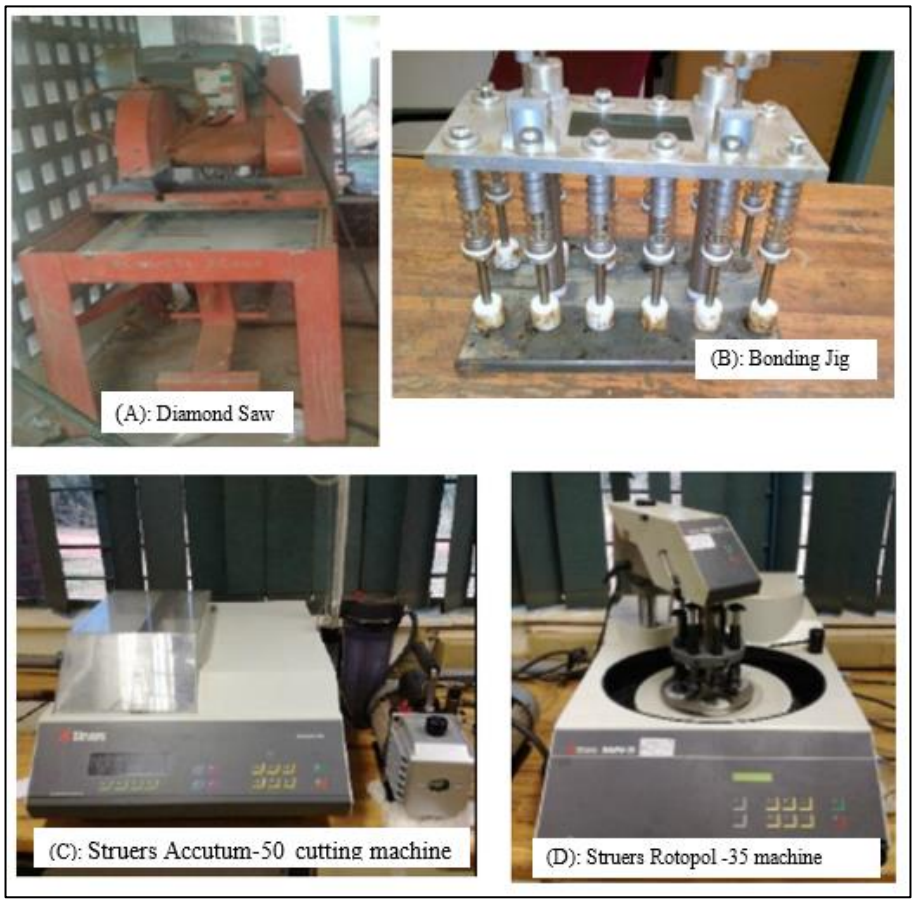


Figure 6.1: Equipment used for thin sections preparations.

Trimming: The rectangular blocks were trimmed to 30 x 40 mm size, using Struers Accutum-50 machine (Fig. 6.1C) and they were polished using silicon carbide grit in sequence of 120, 220, 400 and 800 grit sizes until they were smooth for bonding process. The polished samples were cleaned by using deionised water and dried in a Vacutec drying oven. They were cooled to room temperature after being dried for 15 minutes at a temperature of 85°C before bonding.

Bonding: An epoxy solution which is a bonding solution was prepared by mixing hardener and resin using ratio of 2:15 (2 parts hardener and 15 parts resin). Samples were bonded on frosted glass slides using epoxy. The samples were placed on a bonding jig (Fig 6.1B) for a period of 24 hours for effective bonding.

Grinding: The bonded samples were firstly cut to reduce the thickness from 40 mm to 10 mm using Struers Accutum-50 cutting machine (Fig. 6.1C). Cutting process took approximately

© University of Venda

8 to 20 minutes. The samples were then grinded to 50 micrometers for approximately 30 minutes. The instrument was programmed to grind and stop the process automatically.

Polishing: Grinded samples were placed onto a RotoPol-35 polishing machine (Fig. 6.1D) and polished using the polishing disk for approximately two hours. The sample thickness was checked using a micrometre gangue to confirm the required thickness of approximately 30 µm or less for petrographic studies. The thin sections were clearly labelled, cleaned using deionized water, dried and ready for petrographic analysis.

6.3.4 Petrographic Study

Petrologic study involved both macroscopic and microscopic investigation of rock specimens and thin sections. A total of 25 thin sections were studied under the Olympus BX51 dual Petrographic microscope which uses both transmitted and reflected lights for identification of both gangue and ore minerals at the same time. The microscope was attached to Zeiss AxioCam ICc camera and computer for the ease of capturing photomicrographs (Fig.6.2). The study was undertaken at the Department of Mining and Environmental Geology, University of Venda, Department of Geology, University of Johannesburg, and at MINTEK.

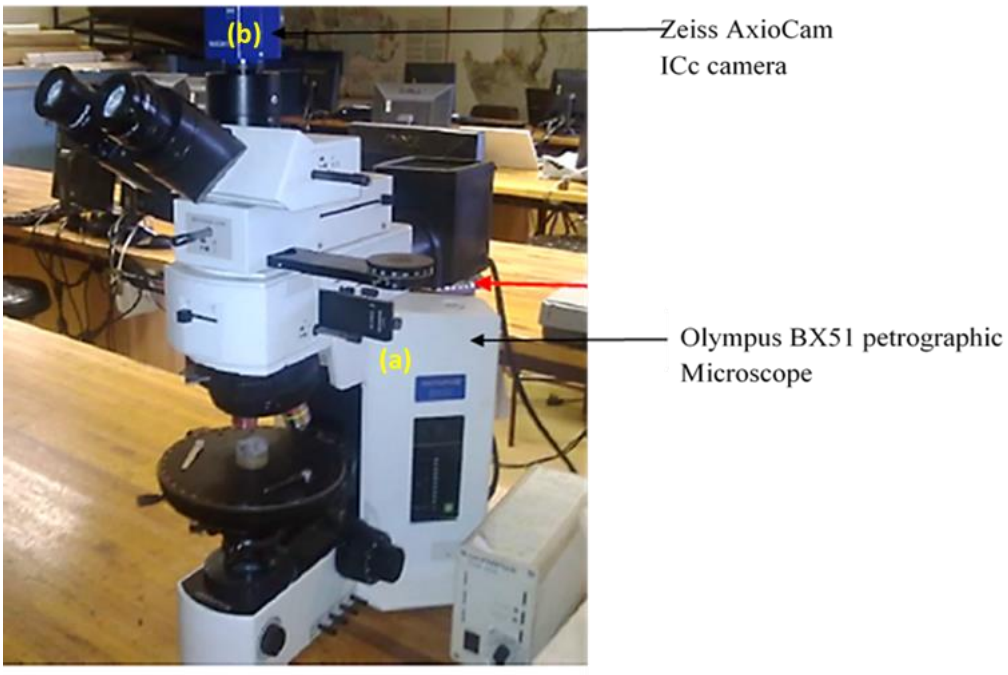


Figure 6.2: Microscope used for petrographic study: (a) Olympus BX51 petrographic microscope attached to (b) Zeiss AxioCam ICc camera, at University of Venda.

© University of Venda

Rock petrology focused on the study of major minerals, minor minerals, accessory minerals and their texture. During this study, the mineral grain size and mineral alteration were also investigated as indicated below. In cases where opaque minerals were identified, mainly ore minerals, polished ore surfaces were prepared for microscopic study (Chapter 7).

Amphibolite-quartz granulite (CPR 05)

The rock sample (CPR 05) was dominated by hornblende, quartz and feldspars with medium to course-grain texture. Biotite occurred as an accessory mineral. The rock was greyish to black in colour (Plate 6.1). In thin section, hornblende was the dominant mineral with some alteration, apparently due to hydrothermal alteration during ore mineralisation. The thin section revealed quartz and some minor feldspar and biotite (Fig. 6.3). Hornblende was apparently, altered to biotite.



Plate 6.1: Photograph of amphibolite-quartz granulite displaying coarse-grained texture with visible grains of biotite and lot occurrence of quartz.

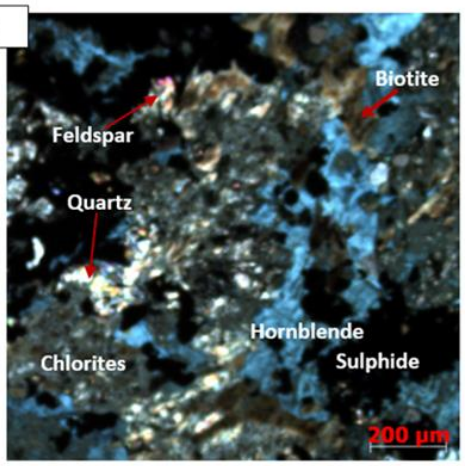


Figure 6.3: Photomicrograph of amphibolite-quartz granulite displaying occurrence of altered hornblende with chlorites and occurrence of quartz with minor feldspars.

Biotite-garnet-quartz granulite (CPR 06)

The specimen (CPR 06) was rich in biotite, garnet and quartz minerals. In places, feldspars and epidote were interlocked within biotite grains as accessory minerals. The rock was coarse grained in texture with grain size ranging from 5 mm to 2 cm (Plate 6.2).

© University of Venda

In thin section, biotite with perfect cleavage dominated the rock. The course-grained texture of orthoclase and quartz were embedded within biotite. Twinning was characteristic of orthoclase. The garnet was disseminated throughout the rock specimen (Fig. 6.4).



Plate 6.2: Photograph of Biotite-garnet-quartz granulite displaying coarse-grained texture with visible grains of biotite and garnet.

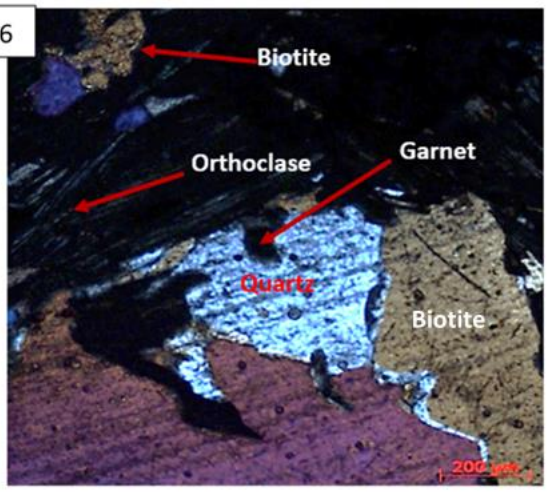


Figure 6.4: Photomicrograph of Biotite - garnet-quartz granulite displaying occurrence of altered orthoclase with garnet grains.

Amphibolite (CPR 04)

The rock sample (CPR 04) contained hornblende as the major mineral and feldspars and quartz as accessory minerals. The rock was black in colour and with medium to coarse grained texture (Plate 6.3). In thin section, the grains ranged from 10 microns to 2 mm. Hornblende grains were altered to biotite. The presence of sulphide mineralisation was displayed by black colour both on plane polarised and cross polarised light and was seen to alter the early formed hornblende. Few plagioclase, quartz and biotite were also present. (Fig. 6.5).

In some places, for example, within Artonvilla copper deposit, amphibolite (Plate 6.4) was massive, coarse textured and dark in colour due to the high presence of mafic minerals mainly amphibole. The minor content of felsic minerals such as feldspar was identified with little occurrence of quartz and weakly foliation (schistose) structure (Pate 6.4).

© University of Venda

In thin section, hornblende made up most of the rock's composition and showed a perfect cleavage. Plagioclase was white and showed a moderate relief with twinning property. Few grains of pyroxene and epidote were identified (Fig. 6.6).

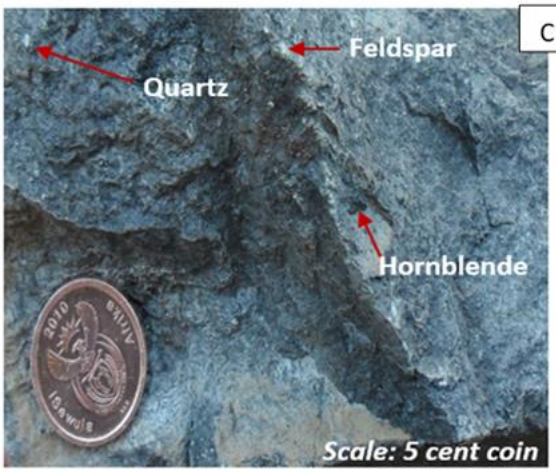


Plate 6.3: Photograph of amphibolite displaying coarse-grained texture with visible hornblende grains.

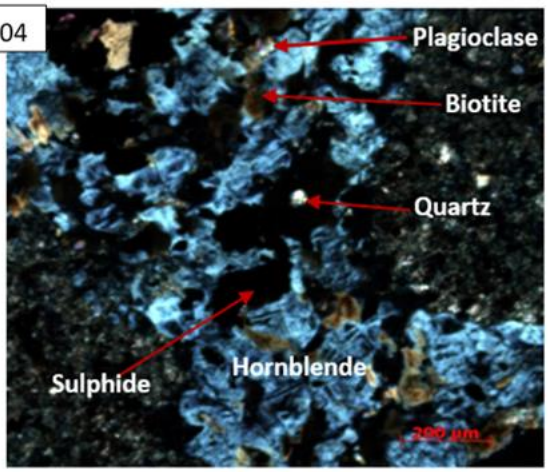


Figure 6.5: Photomicrograph of amphibolite displaying abundancy of hornblende grains altered by hydrothermal solution.

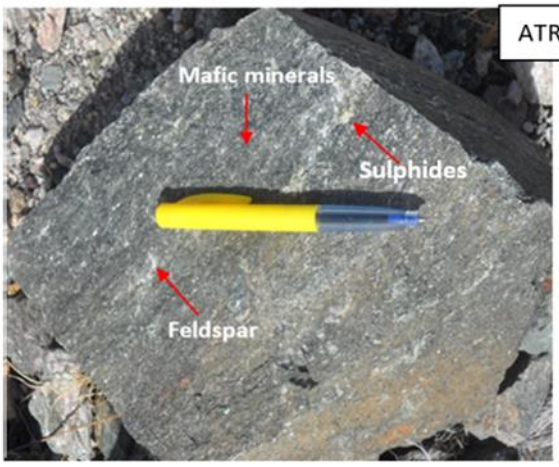


Plate 6.4: Photograph of Amphibolite composed highly of mafic minerals and some feldspar and displaying weakly schistocity structure.

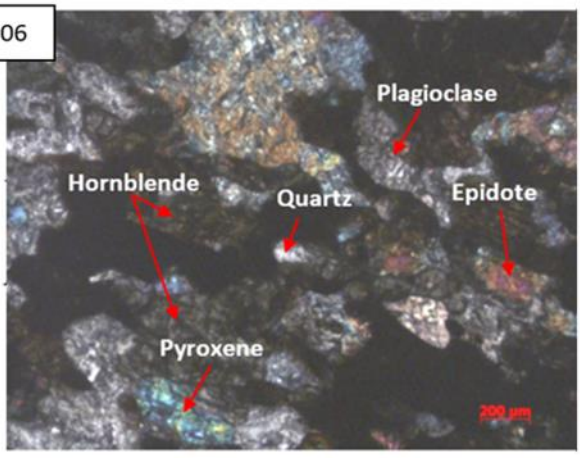


Figure: 6.6: Photomicrograph of amphibolite with the presence of hornblende and plagioclase with few grains of pyroxene and epidote.

© University of Venda

Quartzite (CPR 02)

The rock sample (CPR 02) contained coarse grains of quartz of up to 2 mm as the dominant mineral displaying cryptocrystalline texture and minor content of feldspars. The rock was light green in colour due to some presence of chlorites. (Plate 6.5).

In thin section, the rock was found to contain quartz with tiny grains displaying cryptocrystalline texture. Plagioclase feldspars showed twining and magnetic apperered black. Biotite was brownish in colour with tabular shape and the plates were trapped between quartz grains (Fig. 6.7).

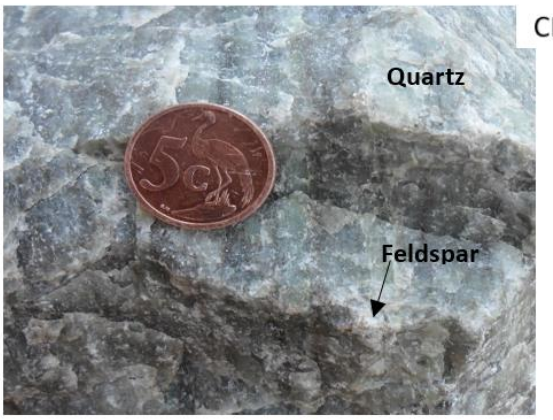


Plate 6.5: Photograph of quartzite displaying chloritization and cryptocrystalline texture.

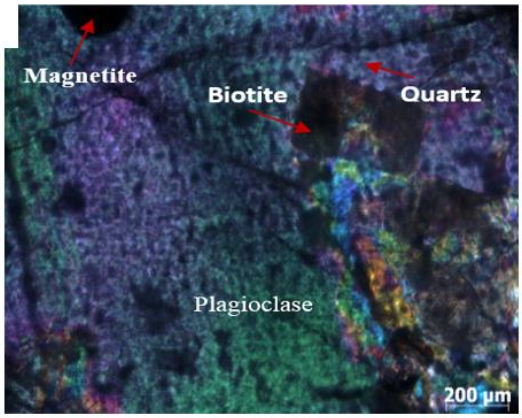


Figure 6.7: Photograph of quartzite with grains of magnetite within cryptocrystalline quartz.

Hornblende schist (ATR 07)

The rock sample (ATR 07) was dark green in colour. It was dominated by platy green amphiboles displaying schistocity structure. Few grains of garnets were also present, and occurred in granular form with red colour and vitreous lustre (Plate 6.6). In thin section, hornblende grains displayed perfect cleavage in two directions with medium to high relief. In places, hornblende was altered to chlorite which displayed brownish green dirty-like colour. Anhedral dark grey grains of garnets with high relief were identified. Epidote displayed bright colours with strong relief and high interference colours (Fig. 6. 8).

© University of Venda

Biotite schist (ATR 08)

Macroscopically, the rock (ATR 08) displayed coarse texture with grains of mica flakes in a preferred orientation. The rock was dominated by interleaved quartz and biotite, as well as minor amounts of hornblende. It had a tendency to split into layers and displayed weakly foliated structure (Plate 6.7).

Microscopically, large crystal of biotite and quartz surrounded by inner zone of deeper feldspars with weak twinning. Biotite displayed large brown crystal with high relief and subhedral shape, quartz displayed large clear crystal with low relief and granular shape while amphiboles were characterised by high order of interference colours, moderate relief and euhedral shape as well as thick black fractures (Fig. 6.9).



Plate 6.6: Photograph of Hornblende schist displaying schistocity due to amphibole platy structure with granular garnet grains.

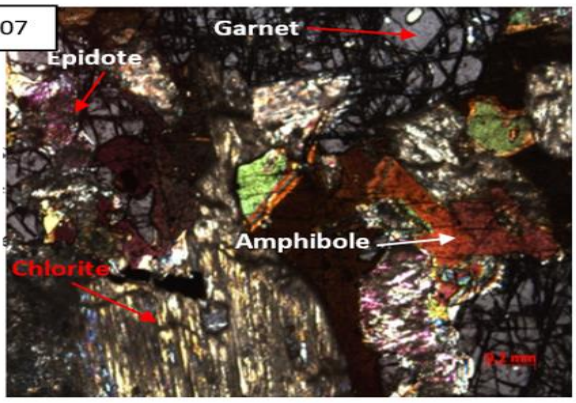


Figure 6.8: Photomicrograph of Hornblende schist consisting of hornblende and plagioclase with few grains of pyroxene and epidote.

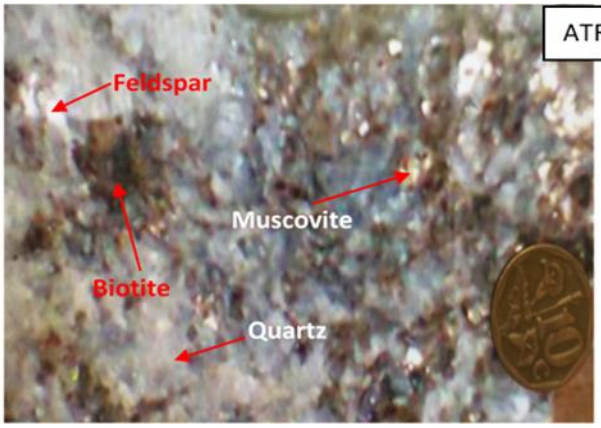


Plate 6.7: Photograph of biotite schist displaying platy structure of biotite and muscovite with quartz grains

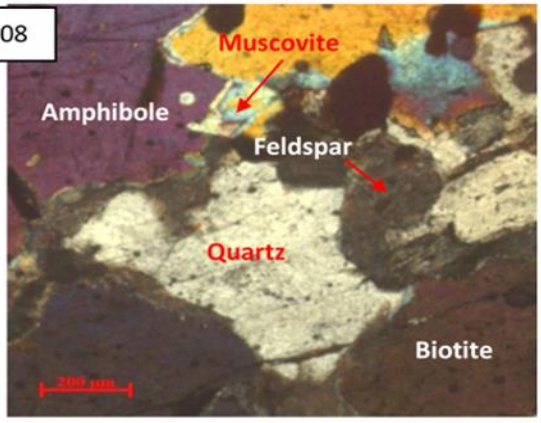


Figure 6.9: Photomicrograph of biotite schist with large grain of biotite, muscovite, quartz and amphibolite.

© University of Venda

Hornblende gneiss (CPR 03)

The rock sample (CPR 03) was shiny and black in colour. It was rich in hornblende with some pyroxenes with minor biotite, quartz and feldspars. It was medium to coarse grained with grains ranging from 10 μm to 2 mm (Plate 6.8).

In thin section, it displayed large crystals of hornblende, pyroxene and biotite. The quartz and feldspar minerals in small quantity occurred interlocked between the mafic mineral. The hornblende showed cleavage in two directions of that intersect at 60º and 120º and displayed euhedral prismatic shape while pyroxene showed two directions at 90º with biotite displaying a basal cleavage (Fig. 6.10).



Plate 6.8: Photograph of hornblende gneiss displaying coarse grained texture with visible pyroxenes and biotite grains.

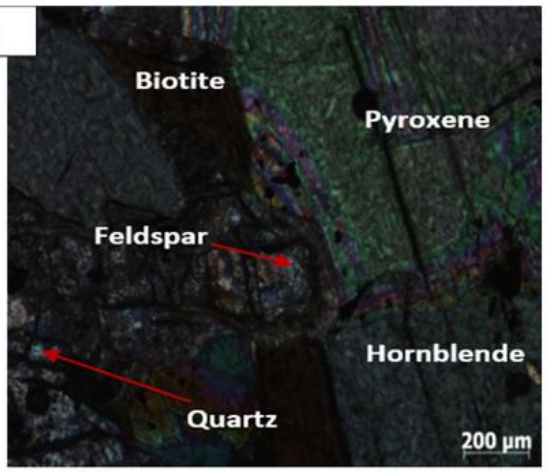


Figure 6.10: Photomicrograph of hornblende gneiss with grains of biotite interlocked in between the hornblende and pyroxene grains.

Quartzo-feldspathic gneiss (CPR01/CPR 07/ATR03)

The rocks quartzo-feldspathic gneiss (*(CPR 07)/ /CPR01 /ATR03)* were found to be rich in feldspars and quartz. Specimens showed amphiboles and garnet as minor minerals. The feldspars and quartz were foliated while the dark minerals of amphibole occurred as large granules. The grains were medium to course and with sizes ranging from 2 mm to 5 mm (Plate 6.9).

© University of Venda

The thin section revealed abundance of quartz, plagioclase of subhedral shape with fine to medium in texture and grain size ranging from 10 μm – 2 mm. The amphiboles were interlocked between the quartz and feldspars crystals with grain sizes ranging from 5 mm to 2 cm. The small grains of garnet were scattered within the rock specimen (Fig. 6.11).

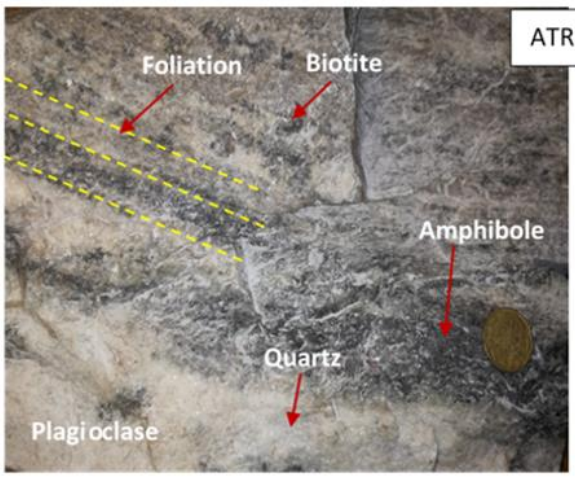


Plate 6.9: Photograph of Quartzo-feldspathic gneiss displaying medium to coarse grained texture and gneissic bends.

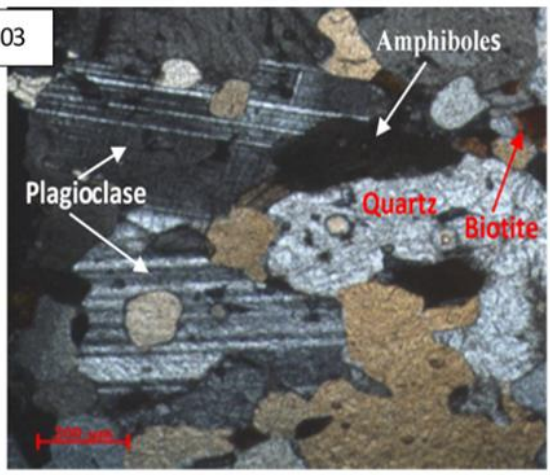


Figure 6.11: Photomicrograph of Quartzo-feldspathic gneiss with plagioclase, quartz and minor content of biotite.

Potassic feldspathic gneiss (CPR 08/(ATR 02)

The specimens (CPR 08/ATR 02) comprised of K-feldspars and quartz as major minerals and amphibole, and minor occurrence of amphibole and biotite. The rocks had medium to large bended layers of which some were rich in feldspars and quartz while some were rich in mafic minerals such as amphibole and biotite. The rocks sample were highly bended with layers of thickness ranging from 0.5 cm – 2.0 cm forming a chevron shape (Plate 6.10).

The specimens displayed subhedral orthoclase and euhedral and anhedral quartz as the dominant minerals under petrographic microscope. There were minor accessory minerals such as biotite and hornblende. The texture was coarse with large grain size of orthoclase and quartz of 5 mm – 2 cm in size (Fig. 6.12).

© University of Venda

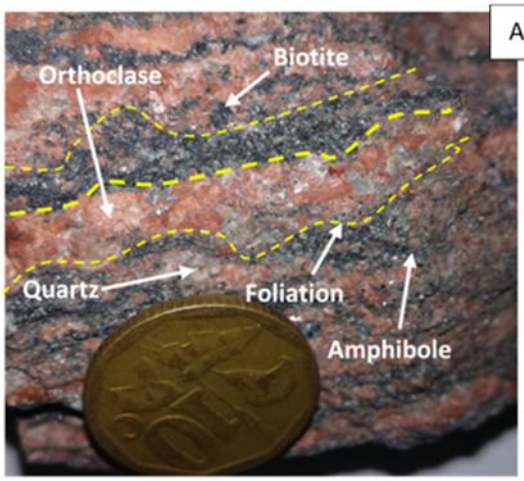


Plate 6.10: Photograph of K feldspathic gneiss displaying medium to coarse grained texture and foliation.

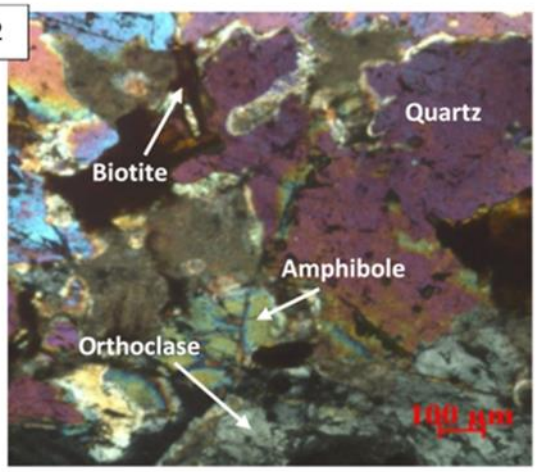


Figure: 6.12: Photomicrograph of K feldspathic gneiss with abundant orthoclase and quartz, and minor content of amphibole and biotite.

Garnet-quartzo-feldsphathic gneiss (ATR 04)

Rock specimen (ATR 04) was generally white in colour with pink due to occurrence of garnet. It was dominated by alternating layers of white feldspathic minerals that were in matrix with quartz grains and garnets. The garnets occurred in a massive granular form, with coarse grain texture. The rock showed well gneissic texture displayed by a distinct foliation formed by alternating layers of quartz-feldspar and garnets. It displayed a medium to coarse texture, with grain sizes (Plate 6.11).

The thin section was dominated by interlocked crystals of feldspars, quartz and garnets. Garnet displayed a pinkish to dark brown colour. It was clearly identified by its lack of pleochroisim and high relief. The garnet crystals revealed subhedral shape with crystal sizes ranging from 2 - 5 mm. Plagioclase displayed twinning and perfect cleavage while microcline displayed cross cutting twins. Quartz exhibits anhedral grain shape. Minor content of biotite was also identified displaying brown colour. The overall texture of the rock was medium to coarse (Fig. 6.13).

© University of Venda

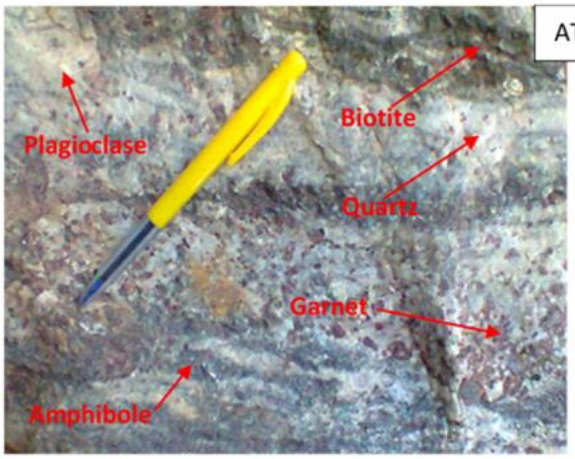


Plate 6.11: Photograph of Garnet quartzo-feldspathic gneiss displaying medium to coarse grained texture and gneissic bends.

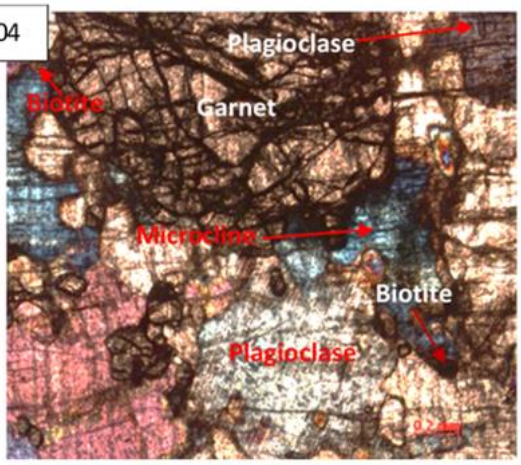


Figure 6.13: Photomicrograph of Garnet quartzo-feldspathic gneiss displaying large grains of garnet.

Biotite-garnet gneiss (ATR 05)

Rock specimen (ATR 05) displayed coarse texture and generally white with greyish and reddish colour due to the presence of mafic minerals and garnet respectively. It displayed a gneissic bends with felsic layer included by lots of garnet grains of grain sizes ranging from 2 mm to 5 mm. The mafic layer was dominated by biotite grains with minor content of amphibole grains. Garnet grains were light pink in colour, occurring in a granular form and displayed a vitreous lustre. Biotite crystals were brown in colour with perfect cleavage (Plate 6.12).

In thin section, the rock was dominated by biotite, garnets and quartz. Minor content of plagioclase and amphibole grains were also identified. Garnets displayed light brown colour and showed no pleochiosm with fractured structure. The garnet crystals revealed a subhedral shape, with grain size ranging from sizes 2mm - 5 mm. Elongated, tabular biotites which were brown in colour displayed perfect cleavage and pleochroism. The thin section displayed anhedral grains of quartz that were colourless, with low relief as well as minor content of plagioclase displaying twinning and higher relief than that of quartz (Fig. 6.14).

© University of Venda

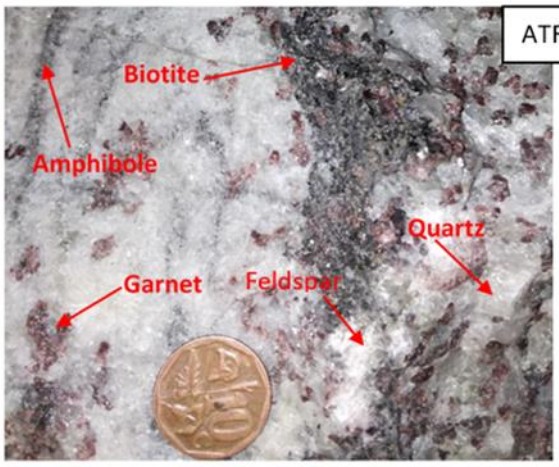


Plate 6.12: Photograph of Biotite garnet gneiss displaying medium coarse-grained texture and gneissic bends.

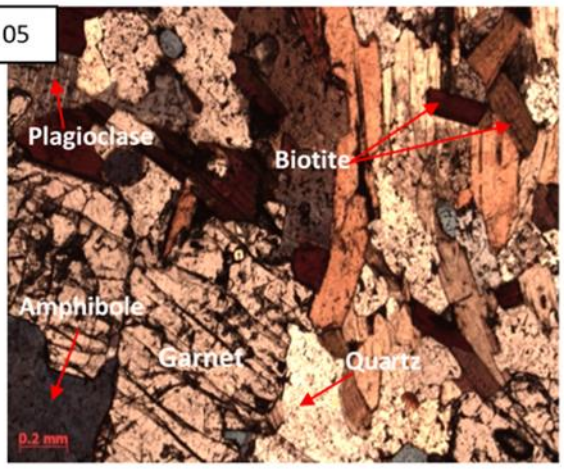


Figure 6.14 Photomicrograph of Biotite garnet gneiss displaying large grains of garnet with large occurrence of biotite.

Calc- silicate gneiss (ATR 01)

In hand specimen cal-silicate gneiss (ATR 01) displayed medium to coarse-grained texture with foliation indicated by folded alternating layers of mafic and felsic minerals. Minor occurrence of calcite was identified by its perfect cleavage and its effervescence property (Plate 6.13).

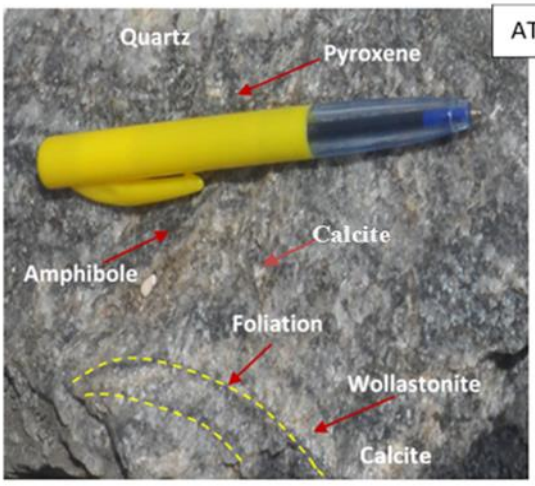


Plate 6.13: Photograph of Calc-silicate gneiss displaying medium to coarse grained texture and foliation.

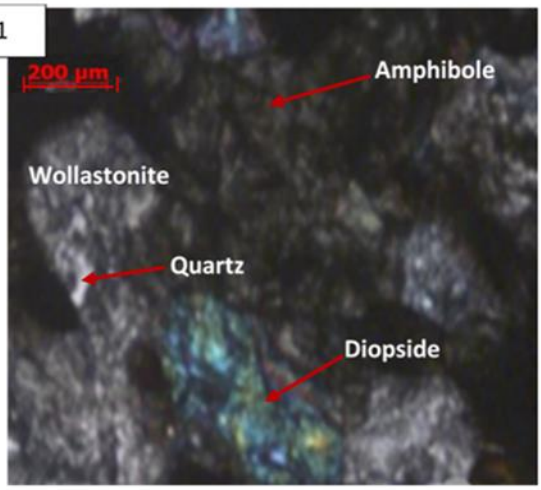


Figure 6.15: Photomicrograph of Calc-silicate gneiss displaying cleavages of wollastonite, diopside (90°) and amphibole (60°/120°).

© University of Venda

In thin section, the cal-silicate gneiss displayed anhedral shape of wollastonite that was of moderate to high relief and displayed first order interference colours with its 90° perfect cleavage. Diopside displayed its 90° cleavage, while amphibole revealed its 60° and 120° cleavage. Quartz grains were also identified mainly within the linear structure of wollastonite (Fig. 6.15).

Macroscopic and optical characterization of rock specimen from Campbell and Artonvilla copper deposits in this study revealed different types of rocks associated with the deposits that included; amphibolite quartz granulite, biotite-garnet-quartz granulite, Amphibolite, Quartzite, hornblende schist, biotite schist, hornblende gneiss, quartzo-feldspathic gneiss, k-quartzo-feldspathic gneiss, calc-silicate gneiss. In few cases, hornblende quartz granulite, pegmatite, and marble rocks were identified. At this stage, the identification was based on colour, textural and grain size analysis, structures and mineralogical characterization were used for the identification of different rock types as shown in Appendix 6.A.

6.3.5. Whole Rock Geochemistry Analysis

6.3.5.1 Sample Preparation and Analysis

From a total of 25 rock specimens used for thin sections, (11 and 14 from Campbell and Artonvilla deposits respectively), 17 representative specimens were selected for whole rock geochemistry preparation and analysis.

Pellets were prepared for whole rock geochemistry. Samples were dried overnight in the Vacutec drying oven (Fig 6.16A) at 30°C to release any moisture before milling so as to avoid the jamming of the milling pots due to moisture from the samples. Samples were hammered into smaller particles using a sledge hammer and were milled using the Retsch RS 200 milling machine (Fig. 6.16B) on manual operation mode for five minutes to particle size of about 75 μm. About 10 g of each milled samples was weighed and pressed in an aluminium cups on a bed of approximately 2.5 g of boric acid. A manual compressor (Fig. 6.16C) was then used to apply a pressure of about 40 tons for about 1 minute to create pellets (Fig. 6.16D).

© University of Venda



Figure 6.16: Equipment used for pellets preparation for XRF analysis.

Prior analysis, a set of 5 reference standards purchased from Mintek which include; SARM 1, SARM 2, SARM 3, SARM 42 and SARM 52) were used to calibrate the S2 Ranger XRF spectrometer. Prepared pellets were analysed using S2 ranger XRF spectrometer (Fig. 4.17) fron the Department of Mining and Environmental Geiology, University of Venda.

The samples were analysed for the determination of both major oxides and trace elements. The pellets were inserted to the sample holder and during analysis the sample is subjected to X-rays fluorescence which is directly excited by beam of X-rays from X-ray tube. The X-rays are then detected by X-flax thereafter the energy is produces in the form of an intensity versas energy spectrum.

© University of Venda

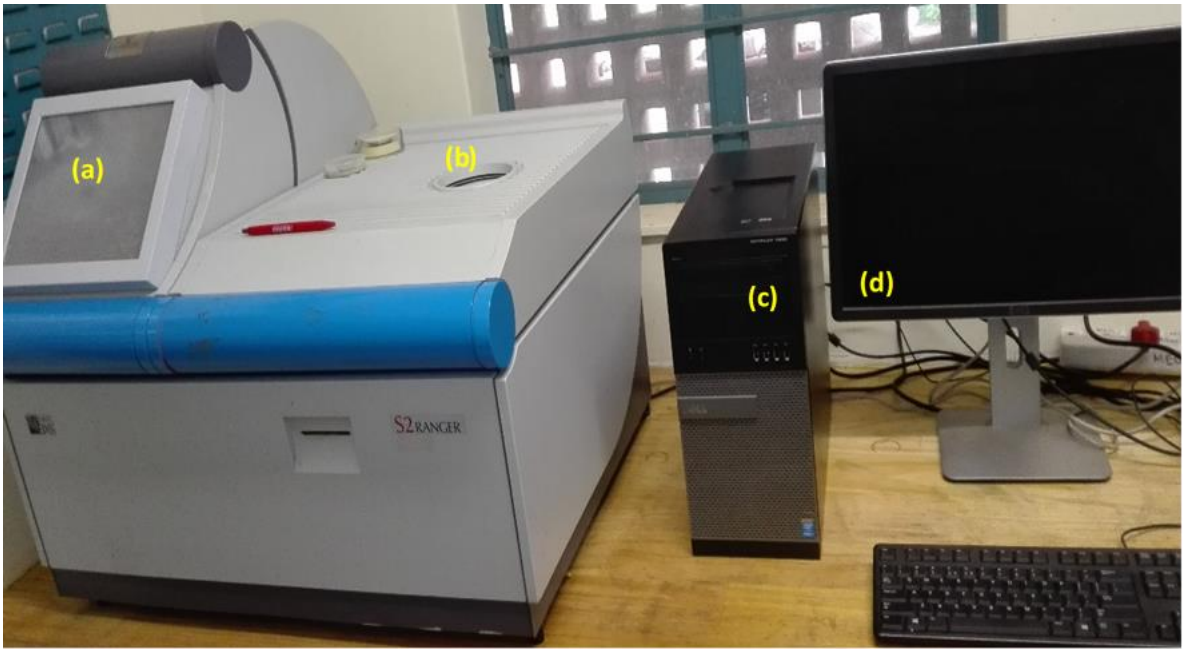


Figure 6.17: Photograph of S2 ranger XRF spectrometer used for major oxides and trace analysis. Touch control screen (b) sample chamber, (c) and (d) computer connected to a monitor.

6.3.5.2 Results and Interpretation

Whole rock geochemistry analysis was conducted to establish the elemental geochemistry of different rock types, i.e. to determine the concentrations of major elements of rock samples within the study area. From the analysis, the major oxides concentrations were summarised in Table 6.2. Loss of Ignition (LOI) (Table 6.2) refers to the mass loss of a combustion residue, whenever it is heated to high temperature, whereas H_2O refers to the amount of water lost during the analysis of the rock samples.

Major oxides analysis

Major oxides are important in petrology. They are useful mainly in the classification of igneous and metamorphic rocks and in understanding the conditions under which metamorphic rocks were formed. The ACF diagram was used in classification of the metamorphic rocks.

© University of Venda

Table 6.2: XRF results of major oxides (wt%) for rock specimens from both Campbell and Artonvilla copper deposits

Sample ID	**Plate**	**Specimen Name**	**Oxides**													
			SiO_2	TiO_2	Al_2O_3	Fe_2O_3	MnO	MgO	CaO	Na_2O	K_2O	P_2O_5	Cr_2O_3	LOL	Total	H_2O^-
Camp/A24 - CPR05	6.1	Amphibolite-Quartz granulite	50,05	3,67	12,40	13,23	0,217	5,28	8,62	2,51	2,15	0,690	0,024	0,47	99,30	0,64
Camp/A18 - CPR06	6.2	Biotite-Garnet-Quartz granulite	66,86	0,09	17,27	1,54	0,016	0,45	2,50	9,63	0,03	0,063	<0.001	1,41	99,84	0,16
Camp/A07 - CPR04	6.3	Amphibolite	49.1	0.82	15.05	10.3	0.25	9.68	9.54	2.6	1.62	0.05	<0.001	0.99	99.9	0.15
AVR01-ATR01	6.3	Calc-Silicate gneiss	74.20	0.06	13.75	0.62	0.009	0.14	0.62	2.88	7.10	0.062	<0.001	0.32	99.75	0.17
AVR13 - ATR06	6.4	Amphibolite	50.56	0.78	14.74	9.8	0.16	7.13	10.25	3.12	0.49	0.19	0.10	1.00	98.48	0.28
Camp04 - CPR02	6.5	Quartzite	81.50	1.95	6.41	2.69	0.027	0.05	5.19	0.06	0.41	0.314	0.012	0.97	99.58	0.48
AVR13a- ATR07	6.6	Hornblende Schist	48.8	0.96	14.06	12.46	0.18	6.89	11.53	1.58	0.31	0.10	0.10	1.78	98.78	0.28
AVR15 - ATR08	6.7	Biotite Schist	69,93	0,82	13,17	3,40	0,024	3,28	1,45	2,57	4,33	0,032	<0.001	0,69	99,68	0,150
Camp/A17 - CPR03	6.8	Hornblende gneiss	74,26	0,39	3,67	10,94	0,102	8,78	0,59	0,29	0,91	0,006	<0.001	-0,10	99,85	0,18
AVR20 - ATR03	6.9	Quartzo-feldspathic gneiss	60,16	0,92	16,70	10,20	0,164	4,04	2,87	2,37	1,87	0,020	0,066	0,41	99,80	0,24
Camp03- CPR01	6.9	Qtz-felds. gneiss (Grey gneiss)	71.96	0.26	14.51	1.80	0.034	0.42	1.72	3.29	4.99	0.051	<0.001	0.67	99.70	0.28
Camp05 - CPR07	6.9	Quartzo-Feldspathic gneiss	73.17	0.05	14.46	1.05	0.139	<0.01	1.10	4.59	4.64	0.106	0.002	0.25	99.55	0.31
Camp02 - CPR08	6.10	K-Quartzo-Feldspathic gneiss	96.26	0.12	1.38	0.85	0.007	0.06	0.13	0.34	0.43	0.007	0.011	0.14	99.73	0.15
AVR08 - ATR02	6.10	K-feldspathic gneiss	49,78	1,15	18,03	15,26	0,102	4,22	0,93	5,59	1,18	0,119	0,056	3,40	99,81	0,32
ATN01 - ATR04	6.11	Garnet-quartzo-feldspathic gneiss	76.09	0.07	13.32	1.83	0.069	0.23	3.58	3.47	0.71	0.013	<0.001	0.34	99.71	0.20
ATN03 - ATR05	6.12	Biotite-Garnet gneiss	60.96	0.70	21.77	7.68	0.136	3.88	0.57	0.60	3.01	0.025	0.051	0.38	99.76	0.27
AVR25 - ATR09	-	Amphibole-quartz granulite	53.43	3.32	12.78	14.87	0.206	3.10	4.29	2.42	2.40	0.966	<0.001	1.99	99.77	1.00

© University of Venda

The ACF diagramme plots three components representing minerals of metamorphic rocks. The interpretation of the classification was done following West (2003) (Fig. 6.18) where metamorphic rocks are classified into pelitic, quartzo-feldspathic, basic, and calcareous rocks depending on the amount of aluminium oxide, calcium oxide and iron and magnesium oxides.

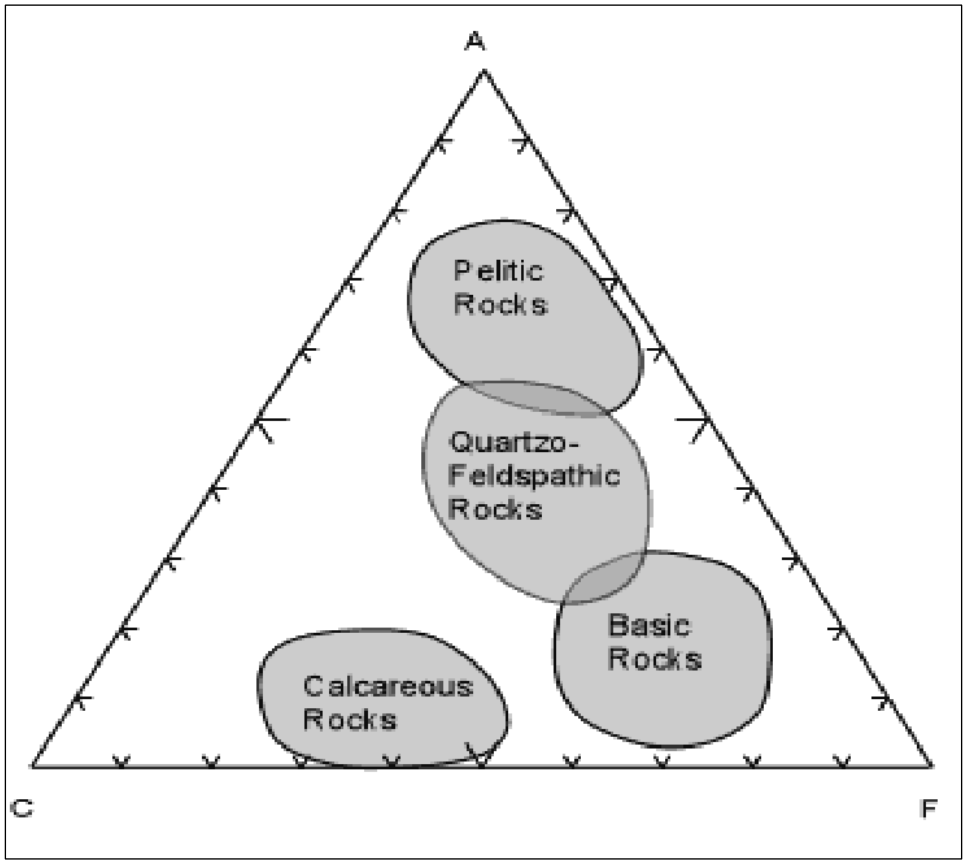


Figure 6.18: ACF classification of rocks (West, 2003).

The ACF diagram plots the following components: A= Al_2O_3; C= CaO and, and F= FeO +MgO. These components are deduced through determination of molecular proportions of all components, and then normalized. Example of how the components were calculated was done using specimen number Camp03 (plate 6.1) as illustrated in appendix 6B. The ACF ternary plot showing compositional variations of analysed rocks was constructed using Triplot version 4.1.2 software was used to construct the ternary diagram (Fig. 6.19). The ACF ternary diagram showed variations of A, C, and F of all the analysed samples from both Campbell and Artonvilla mines (Fig. 6.19).

Biotite-garnet gneiss, quartzo-feldspathic gneiss and k-feldspathic gneiss showed to be of a pelitic origin and highly composed of aluminous minerals. Amphibole-quartz granulite,

© University of Venda

quartzo-feldspathic gneiss (grey gneiss) and biotite gneiss were found to be within the quartzo-feldspathic rock types that are highly composed of quartz and feldspar minerals. Also within the quartzo-feldspathic region are k-feldspathic gneiss.

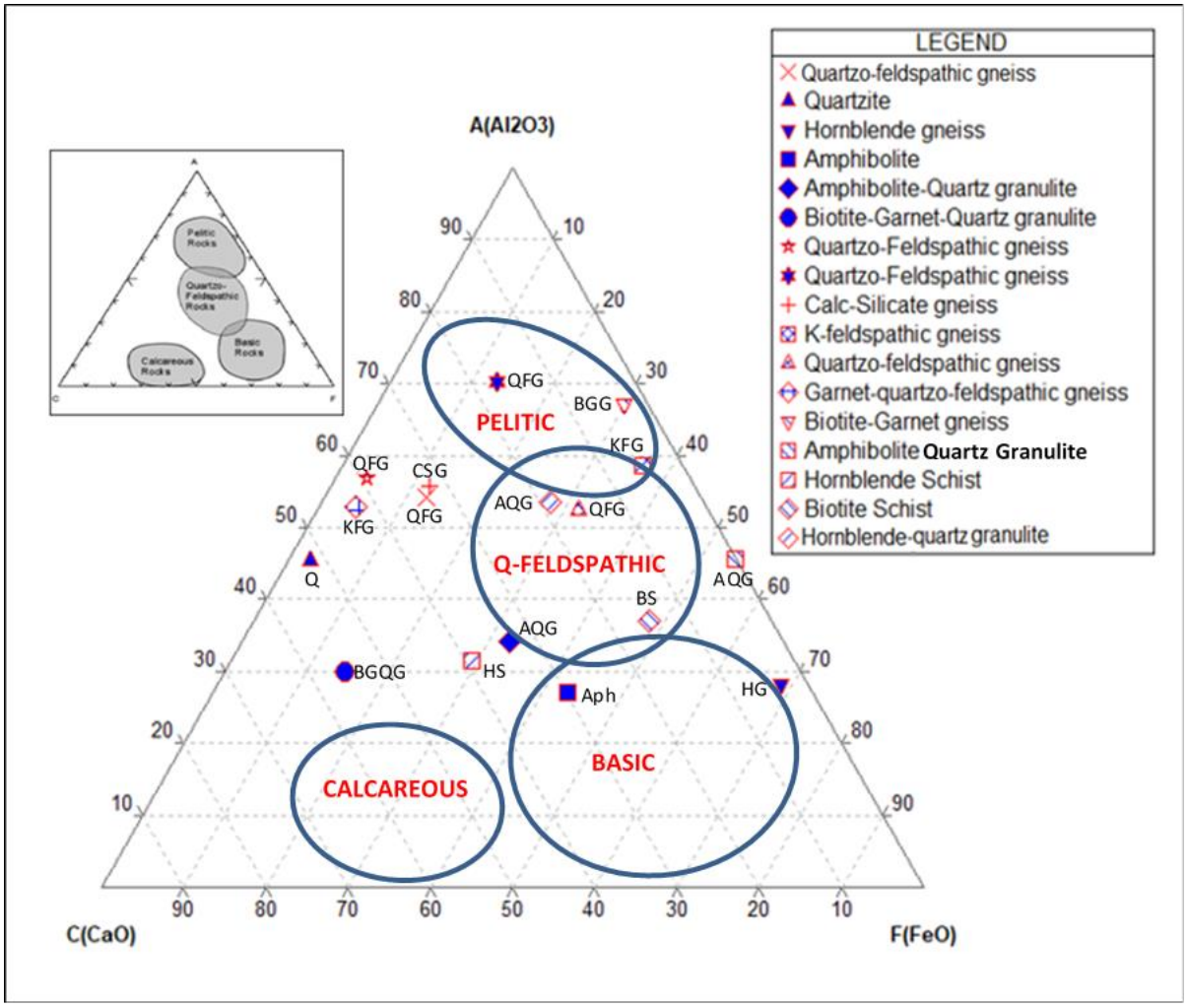


Figure 6.19: ACF ternary plot showing compositional variations of different rock types within the study area.

Hornblende gneiss and amphibolite were of basic origin that is highly composed of a mafic mineral such as hornblende. Hornblende schist plotted in between the quartzo-feldspathic rocks and basic rocks. While biotite-garnet-quartz granulite plotted in between the quartzo-feldspathic rocks and the calcareous rocks. Other rock types, for example, k-feldspathic gneiss, quartz feldspathic gneiss, cal-feldspathic gneiss and quartzite were found to occur outside the ACF classified groups of rocks. Consequently, the ACF ternary diagram revealed that the rocks within the study area were mainly of quartzo-felspathic gneiss group,

© University of Venda

6.3.6 Garnet Classification

Garnet is the general name for a group of complex silicate minerals with similar crystalline structures and diverse chemical compositions (Olson, 2000). The general chemical formula of the garnet group is $A_3B_2(SiO_4)_3$, where "A" can be calcium, magnesium, ferrous iron, or manganese, and "B" can be aluminum, chromium, ferric iron, or rarely, titanium (Olson, 2000). Garnet occurs in many rock types but especially common in some metamorphic rocks like schist and amphibolite. Garnets are rarely of pure composition; pyrope, almadine and spessernite belong to the pyralspite group whereas uvarovite, grossular and andradite belong to the ugrandite series (Price and Walsh, 2005).

Garnet is an important mineral both geologically and economically. Geologically they are used to identify type of geological terrain as garnet is metamorphic mineral. Garnet is used in mining exploration as an indicator to help locate diamond deposits and in many mineral deposits, they are important in linking Paragenesis sequence (Evans *et. al.,* 2006). Garnet as an industrial mineral has been used for several purposes such as gemstone, as a filtration medium in water purification systems, as optical lens grinding and plate-glass grinding, it has been slowly replacing silica sand in the blast cleaning market (Harris, 2000; Olson, 2000).

Garnet has been encountered in several rock samples in this study. For example, rocks such as quartzo-feldspathic gneiss, biotite-garnet-quartz granulite, and marble revealed occurrences of garnet. Geochemical analysis of these garnets was done so as to classify the type of garnet within the Musina area.

6.3.6.1 Physical Characterization of Garnet

Physical characteristics and occurrence: Garnet was found mainly within the granulite gneiss rocks such as hornblende granulite, garnet gneiss, quartzo-feldspathic gneiss at Campbell and Artonvilla deposits, but highly dominated at Artonvilla deposit. Formation of garnets within the host rock, however, is associated with regional metamorphism of the Limpopo mobile belt. Several hand specimens exhibited large grains of garnet, For example, Plates 6.2, 6.7, 6.11 and 6.12. Some of the host rocks of copper mineralisation, revealed occurrence of such garnets (Plate 6.14 and plate 7.4). Crystal of garnet of up to 10 mm in diameter (Plate 6.14 and plate 7.4) were identified. The garnet grains revealed red to brownish colour that occurred as

© University of Venda

octahedral to subhedral crystals with vitreous lustre and hardness greater than 7 in the Moh's scale of hardness.

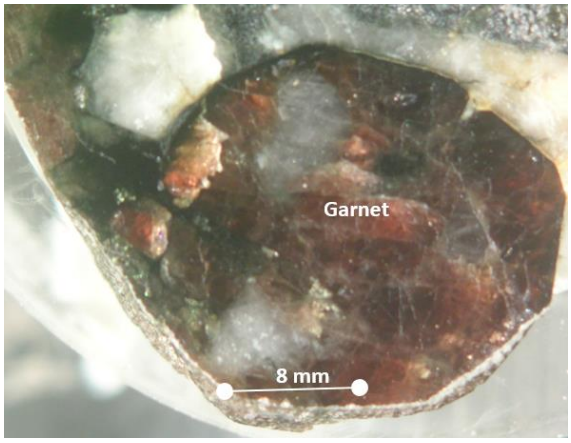


Plate 6.14: Large grains of garnet within host rock of sulphide mineralisation.

Microscopically, the garnet exhibited large grains with sizes up to 10 mm. The garnets were microscopically distinguished by their fractures and high relief under plane polarized light and its isotropism property under crossed polarization light. Garnet was altered resulting into chlorites which were anomalous blue and this indicates iron rich chlorites (Figs. 6.16, 6.17 and 7.5) as compared to magnesium rich chlorites which are indicated by greenish brown colour.

6.3.6.2 Sample Preparation and Analysis

A total of six rock sprcimen associated with both deposits (garnet gneiss, quartzo-feldspathic gneiss, hornblende granulite) were used for garnet analysis. Polished samples were prepared at MINTEK, Johannesburg; at the Department of Geology, University of Johannesburg; and at the Department of Mining and Environmental Geology, University of Venda. The specimens were subjected to a series of steps consisting of sectioning, impregnation and encapsulation, grinding, lapping, and polishing. Cameca SX-100 Electron microbe analyser (Fig. 6.20) was used to analyse seven prepared polished sections at the Department of Geology, University of Johannesburg. Various grains of garnets within the polished sections were selected for analysis. The selection of the point within the garnet grain was done at the centre and or at the margins of the grain because some of the grains showed dark (centre) and lighter (margins) sections in a single grain (Fig. 6.21).

© University of Venda

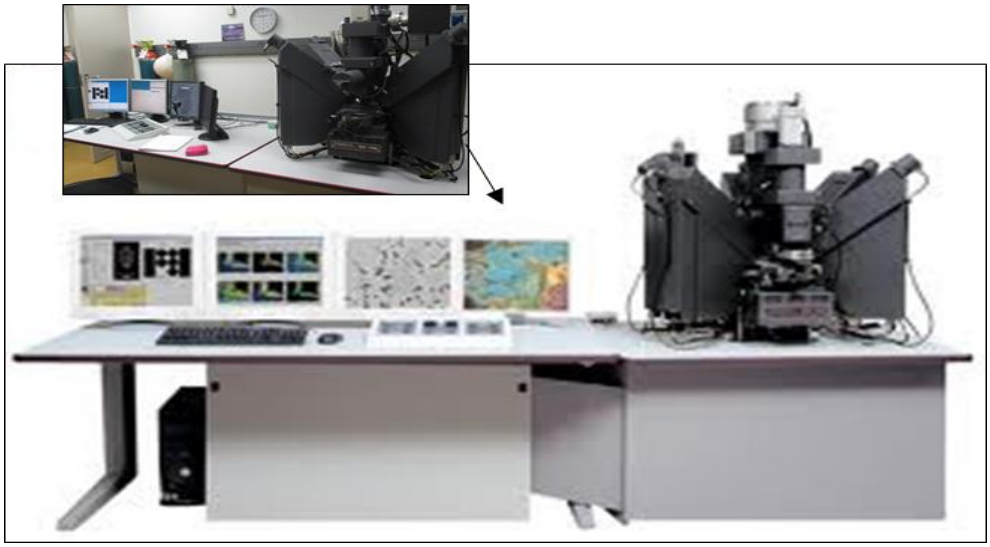


Figure 6.20: Cameca SX-100 Electron microbe analyser connected to computer and monitors used for garnet analysis.

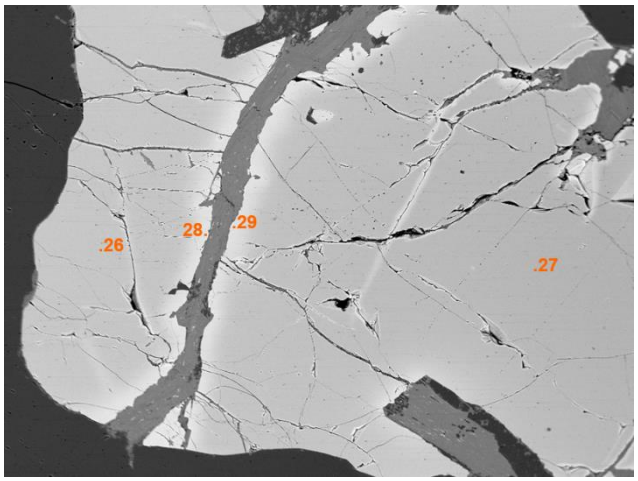


Figure 6.21: Backscattered-electron image of garnet crystal from biotite-garnet gneiss rock showing selected points analysed.

6.3.6.3: Results and Interpretation

The results from the analysis included major oxides given in weight percentages and the number of catioans in terms of 24 oxygen atoms (Appendix 6B). The chemical compositions of the garnets were deduced by calculating the molecular percentage end members from the cations (Table 6.3) (Appendix 6B) following Jianjun, (2009) procedure whereby equation 1 and 2 derived from Deer *et al.*, (1992) were used.

© University of Venda

Table 6.3: Composition of garnet grains in Mol% of end-members

Point analysed	SUM	Grosular (Ca)	Almadine (Fe)	Pyrope (Mg)	Spessartine (Mn)	Total
M1-p7	6	10	66	22	2	100
M1-p8	6	9	67	22	2	100
M1-p9	6	9	67	22	2	100
M1-p11 rep	6	6	66	23	2	100
M1-p12 rep	6	9	68	21	2	100
M1-p13	6	8	66	23	2	100
M1-p14	6	5	66	23	2	100
M1-p15	6	9	67	23	2	100
M1-p16	6	9	67	22	2	100
M2 p1	6	7	60	32	1	100
M2-zoned dark p2	6	5	54	40	1	100
M2 zoned light p3	6	5	71	22	2	100
M2-grain 2 p4	6	5	51	43	1	100
M2-grain3 p5	6	5	51	42	1	100
M3 a1 p1	6	8	68	22	2	100
M3 a1 p2	6	10	67	22	2	100
M3 a1 p3	6	9	65	25	2	100
M3 a2 p4	6	9	70	20	1	100
M3 a2 p5	6	9	62	28	1	100
M3 a2 p6	6	9	62	28	1	100
M3 a2 p7	6	9	62	28	1	100
M3 a2 p8	6	9	62	28	1	100
M3 a2 p9	6	9	62	28	1	100
M4 a1 p10	6	17	63	20	1	100
M4 a1 p11	6	17	62	20	1	100
M4 a1 p12	6	17	63	20	1	100
M4 a1 p13	6	16	63	20	1	100
M4 a1 p14	6	17	63	20	1	100
M4 a1 p15	6	17	63	20	1	100
M4 a2 p16	6	17	64	19	1	100
M4 a2 p17	6	17	64	19	1	100
M4 a2 p18	6	17	63	19	1	100
M4 a2 p19	6	17	63	19	1	100
M5 a1 p20	6	3	60	34	2	100
M5 a1 p21	6	3	77	15	5	100
M5 a2 p22	6	3	71	18	8	100
M5 a2 p23	6	3	73	16	8	100
M5 a2 p24	6	3	74	16	7	100
M5 a2 p25	6	3	72	17	8	100
M5 a3 p26	6	4	57	37	2	100
M5 a3 p27	6	5	57	36	2	100
M5 a3 p28	6	4	72	19	4	100
M5 a3 p29	6	4	71	21	4	100
M6 a1 p30	6	25	54	20	1	100
M6 a1 p31	6	21	55	23	1	100
M6 a1 p32	6	20	57	20	3	100
M6 a1 p33	6	22	54	23	1	100
M6 a1 p34	6	25	54	20	1	100
M6 a2 p35	6	25	54	20	1	100
M6 a2 p36	6	23	55	21	1	100
M6 a2 p37	6	24	56	18	2	100
M6 a2 p38	6	20	57	20	2	100
M6 a2 p39	6	20	58	20	2	100
M7 a1 p40	6	10	57	30	3	100
M7 a1 p41	6	10	58	29	3	100
M7 a2 p42	6	7	65	24	3	100
M7 a2 p43	6	8	64	25	3	100
M7 a2 p44	6	8	59	30	3	100
M7 a2 p45	6	7	60	30	3	100
M7 a2 p46	6	8	68	21	4	100
M7 a3 p47	6	8	59	30	3	100
M7 a3 p48	6	6	60	31	3	100
M7 a3 p49	6	10	59	29	3	100

© University of Venda

According to Deer *et al.,* (1992) the general formula of garnet is $A_3B_2(SiO_4)_3$ whereby A can be $Fe^{2+,}$ Mg^{2+}, Mn $^{2+}$ or Ca and B can be Al, Fe^{3+}. The ideal chemical formulae of garnet is (Mg, Fe^{2+}, Mn, Ca) (Al, $Fe^{3+,}$ Cr) (Si, Al)$_3O_{12}$. The end members are Mg_3Al_2 pyrope; $Fe_3^{2+}Al_2$ almadndine; Mn_3Al_2 spessartine; Ca_3Al_2 grossular; $Ca_3Fe_2^{3+}$ andradite and Ca_3Cr_2 uvarovite.

The following formulas where used to calculate the molecular proportions in percentages of end members of the garnets (Table 6.3).

For site A: A/Σ (Mg, $Fe^{2+,}$ Mn, Ca)* 100

where, A can be Mg, Fe^{2+}, Mn or Ca Equation 6.1

For site B: A/Σ (Al, Fe^{3+}, Cr) * 100

where B can be Al, $Fe^{3+,}$ Cr. Equation 6.2

All the samples revealed highest percentage of FeO wich ranged from 23.72 to 34.69, MgO 3.84 to 11.40, CaO ranging from 0.96 to 9.19 and MnO 0.26 to 3.52. The lowest percentages were of Cr_2O_3 ranging from 0.00 to 0.18, Nao ranging from 0.00 to 0.02 and TiO_2 with almost zero percentage.

From the results (Table 6.3), it was revealed that all the garnet grains from the different polished samples had high molecular percentage end members of almandine and pyrope ranging from 51 to 77 and 15 to 43 % respectively. They also contained minor content of grossular ranging from 3 to 10 % and spessartine in all garnet grains except those of sample M4 and M6 where the chemical composition of grossular revealed grossular $_{17\text{-}25}$ (Table 6.3).

The average chemical compositions of the garnet grains in sample M1, M2, M3, M4, M5, M6 and M7 were; Alm $_{67}$ Prp $_{22}$ Grs $_9$ Sps $_2$; Alm $_{58}$ Prp $_{36}$ Grs $_5$ Sps $_1$; Alm $_{64}$ Prp $_{26}$ Grs $_9$ Sps $_2$; Alm $_{63}$ Prp $_{20}$ Grs $_{17}$ Sps$_1$; Alm $_{68}$ Prp $_{23}$ Grs $_3$ Sps $_5$; Alm $_{55}$ Prp $_{21}$ Grs $_{23}$ Sps $_2$ and Alm $_{61}$ Prp $_{28}$ Grs $_8$ Sps $_3$ respectively. Consequently, it was concluded that the garnets were of almandine type of garnet with varying composition of pyrope, grossular and spessartine.

© University of Venda

6.3.7 Mineral Alteration

Investigation of mineral alteration was done because in petrology, mineral alteration is one of the key factor that is useful in the interpretation of genesis of mineralisation in a specific deposit. Thin sections of quartzo-felspathic gneiss and amphibolite rocks that were associated with copper sulphide mineralisation at Campbell and Artonvilla deposits were used for the interpretation of wall rock alteration (Figs. 6.22 and 6.23).

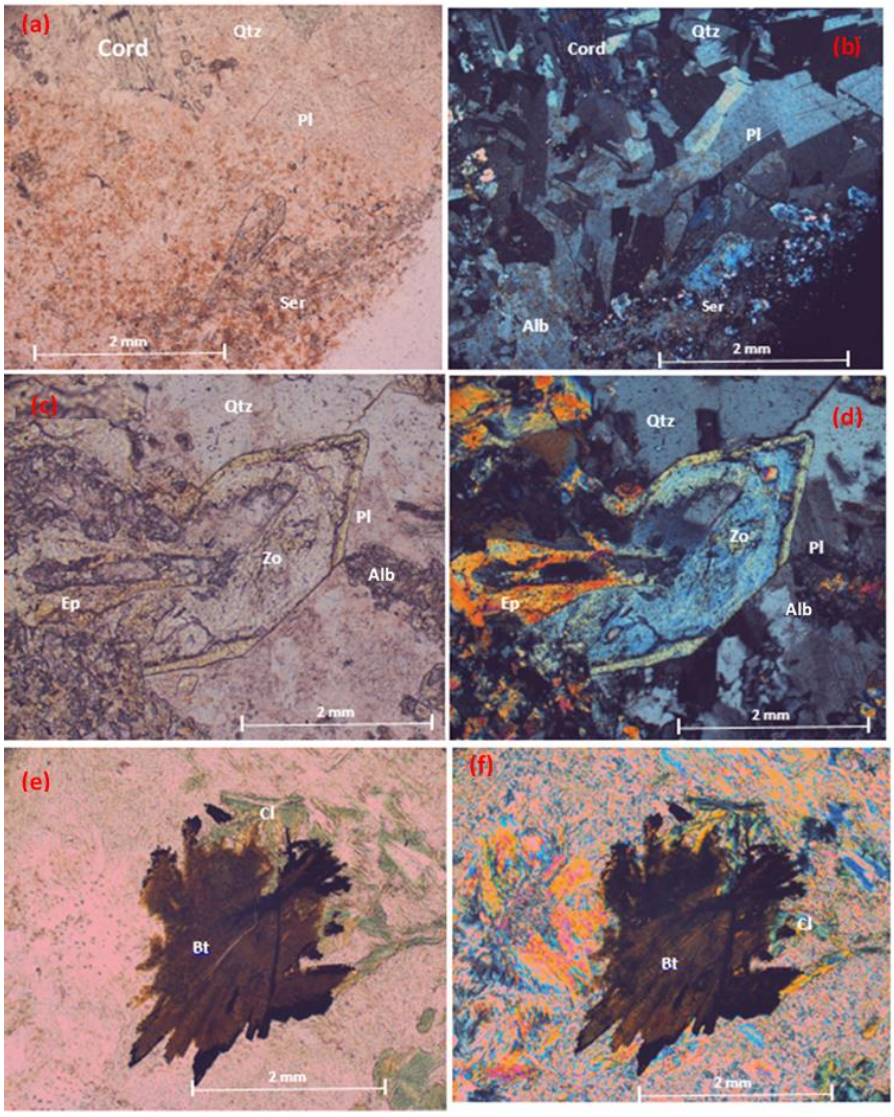


Figure: 6.22: Photomicrographs of rocks from both Campbell and Artonvilla copper deposit with plane polarized on the left and crossed polarized on the right side. (a) and (b) Quartz (Qtz) and Plagioclase (Pl) being replaced to albite; Plagioclase (Pl) and cordierite altered to chlorite; (c) plagioclase (Pl) altered to zoisite (Zo) and epidote (Ep); and (d) and (e) alteration of biotite to chlorite.

© University of Venda

Mineral such plagioclase and quartz were seen to be altered to form sericite. Plagioclase crystal showed its twinning with other parts of the crystal revealed alteration and twinning was not clear at this point (Fig. 6.22). This phenomenon of large grains of plagioclase and quartz being altered to sericite was clearly seen in thin sections from rocks associated with both Campbell and Artonvilla. For example, specimen biotite-garnet quartz granulite and biotite-garnet gneiss from Campbell and Artonvilla copper deposits respectively revealed this alteration (Figs. 6.22a and b). Cordierite was seen to be altered to chlorites. In plane polarized light it was identified by its light whitish green colour. Albite was identified with its alternating twinning that appeared crossing each other but this phenomenon was not clearly visible because the crystal displayed highly altered part of the crystal (Figs. 6.22a and b).

In Figure 6.22c and d, replacement of plagioclase and quartz was identified on the left edge of the thin section that was gradually forming albite revealing alternating patterns of twinning. Altered plagioclase was revealed intense alteration whereby it was altered to form zoisite identified by its high interference colours (orange to brownish in colour). In places zoisite was trimmed by epidote and on most of the thin sections epidote was mostly seen together with zoisite. This phenomenon was seen mostly in host rocks that were highly mineralised.

Chloritization was a common phenomenon in most of the host rocks as displayed in Figure 6.27e and f. in this micrograph, biotite revealed chloritization process in greenish dirty chlorites. Chloritization was revealed by alteration of garnet into anomalous bluish colour of chlorites (Figs. 6.23 a and b) which is an indication of Fe rich as opposed to mg rich greenish chlorites. This process of chloritization was also revealed in Figures 6.23 a,b,c and d, whereby cordierite, biotite, perthite and garnet were altered to chlorites.

The mineral assemblages at both Campbell and Artonvilla copper deposits were found to be quartz, plagioclase, chlorites which are consistance with sericitic alteration. While alteration of plagioclase , quartz, perthite to albite conform with albatization stage of alteration. Further alteration of albite was seen to to be alterd to zoisite and epidote. Consequently the study revealed sericitic and albatization alteration process with further intense alteration of albite to epidote and zoisite.

© University of Venda

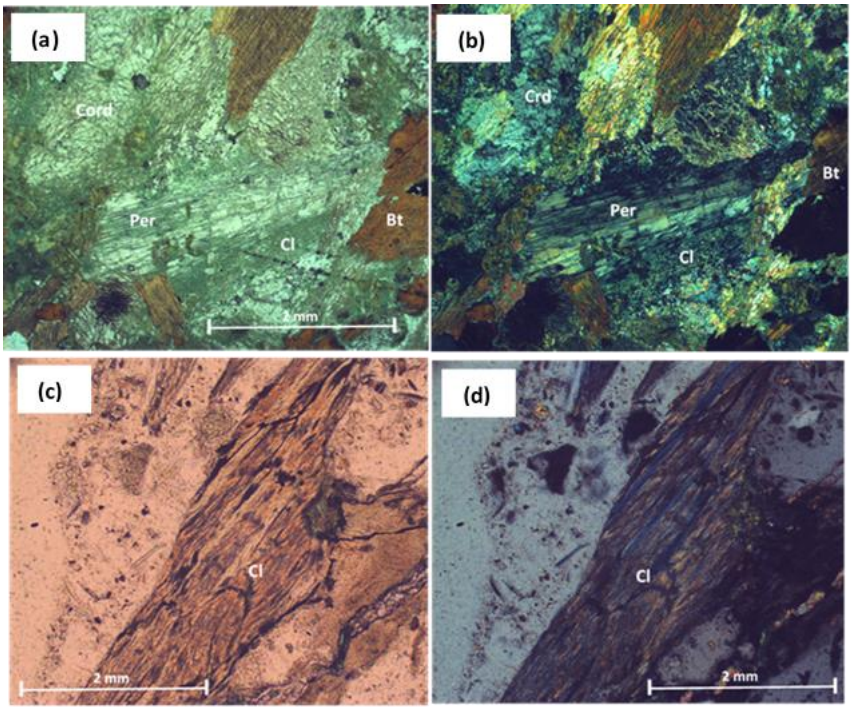


Figure: 6.23: Photomicrographs of thin sections of amphibolite and hornblende gneiss from Campbell and Artonvilla deposits: (a) and (b) Chloritization of cordierite, biotite and perthite; and (c) and (d) revealing chloritization of garnet into anomalous blue chlorites.

6.4 Discussion

The study of rocks within and around the area is one of the most important investigation in understating the type of geological environment of a specific deposits occurred. Classification of rock types is one of the crucial aspects as it gives a clear indication whether the environment is of metamorphic or sedimentary or even igneous in nature. The classification of rocks can be achieved through both physical and chemical investigation of the rocks, whereby geochemical analysis can be of importance in classifying rocks in terms of their chemical composition using ternary diagrammes and which will then help in the classification of the rocks in terms of grade of metamorphism.

In the current study, physical, and optical characterization of the rocks within the study area revealed different types of metamorphic rocks that are of pelitic origin, quartoz-feldspathetic and basic composition and few with calcareous composition. The dominant rocks in the study area were found to be high-grade metamorphosed rocks namely; amphibolite quartz granulite, biotite-garnet-quartz granulite, Amphibolite, quartzite, hornblende schist, biotite schist, hornblende gneiss, quartzo-feldspathic gneiss, k-quartzo-feldspathic gneiss, calc-silicate

© University of Venda

gneiss. Minor occurrence of hornblende quartz granulite, pegmatite, and marble rocks were identified.

Major oxides values within the rocks revealed different types of metamorphic rocks such as metamorphic rocks of politic origin, granulite gneissic rocks, basic metamorphic rocks and few calcareous rocks such as calc-silicate rock. Consequently, the study was dominated by rocks of granulite and amphibolite facies.

The investigation of garnet is of importance both geologically and economically. Geologicall, garnet suggest the type of geological environment in which a deposit was formed. It is also important as it helps when deducing the paragenesis of mineralisation of a deposit. This is so because garnet is a metamorphic mineral that is usually formed in high temperature (Wenk and Bulakh, 2004). The occurrence of garnets in most of the rock samples within the study area confirms the high grate metamorphism.

Different types of garnets have different importance depending on their physical and chemical characteristics both geologically and economically. According to Nesse (2012) almandine rich garnets in mica schist are influenced by the temperature, pressure and related conditions at the time of growth and can be used to determine the temperature, pressure and other conditions by which their host rocks were formed and also unpack the alteration process that could have happen. For example, almandine is altered to blue chlorites (Spear, 2017). Economically, almandine garnets are used in the manufacturing of sand paper, in sand blasting and as a filtration medium and it is replacing silica because of health effect of silica in human health (Evans *et. al.*, 2006).

From the encountered rocks, it was noted that most of the rocks comprised garnet mineral. The garnet grains where found to be up to 10 mm in grain size. Determination of molecular percentages of the oxides analysed, revealed chemical composition of the Musina garnet, which was found to be almandine.

Mineral alteration has been used as one of the criteria to investigate the genesis of the mineralisation and also can be used as a tool in mineral exploration. In this study, mineral alteration of the Messina copper deposits were associated with sericite and albatization alteration, which was further intensely altered into zoisite and epidote. This alteration is consistent with hydrothermal origin of the deposit. The outcome of this alteration is also consistence with work done by and Jacobsen (1976) and Jacobsen *et al.* 1(976). In this study

© University of Venda

University of Venda
Creating Future Leaders

the alteration were investigated in mineralised and un-mineralised rocks and it was noted that albite was intense within the ore samples than in unmineralised rocks, thus, epidote occurrence was abundant in ore samples because epidote is an alteration product of albite.

© University of Venda

CHAPTER 7

ORE MINERALOGY AND ORE MICROSCOPY

Preamble

This chapter presents the study of ore minerals in different copper-sulphide ore samples from Campbell (CAMP) and Artonvilla (ARTV) copper deposits, using ore microscopic techniques such as; Reflected ore microscopy, Scanning electron microscopy (SEM), X-ray diffraction (XRD) and X-ray fluorescence (XRF) spectrometry. This was undertaken so as to ascertain the mineral composition and association, mineral assemblages and paragenesis of minerals within the two deposits for better understanding of the genesis of the Messina copper-sulphide deposits. The chapter includes; fundamentals of ore mineralogy and ore microscopy (application, importance and properties of ore minerals), ore-microscopy, laboratory investigation, paragenesis, results and interpretation, and discussion.

7.1 Fundamentals of Ore Mineralogy and Ore-microscopy

Ore mineralogy is one of the scientific discipline and a branch of ore geology/economic geology that deals with the study of ore minerals, while ore-microscopy is an investigation of ore minerals under the microscope. An ore is a metalliferous mineral or aggregate of metalliferous minerals which are more or less mixed with gangue minerals and are profitable or of economic value. Therefore, ore mineralogy and ore-microscopy is a study of ore minerals and their optical properties.

7.1.1 Importance and Application

Ore mineralogy and ore-microscopy is an essential branch of economic geology; consequently, its importance and application becomes widely recognised. It is most important in mineral identification, study of ore textures, mineral association and assemblages (Paragenesis), in order to understand the processes of ore formation and genesis of mineral deposits.

© University of Venda

For mineral identification, physical, chemical and optical properties are investigated. Physical properties such as colour, macro-textures/structures, hardness, luster are identified by using hand specimen and field observation. Chemical properties of minerals are established through chemical analysis, whereas optical properties such as reflectance, bireflectance, internal reflection, isotropism and anisotropism are identified through ore microscopy.

Ore-microscopy involves not only identification of individual mineral grains, but commonly used for the interpretation of ore mineral textures which are useful for deciphering ore genesis, for example, providing evidence on ore deposition processes, and post-depositional processes such as metamorphism, deformation, annealing or meteoric weathering of the ore. Textural analysis of ore is also important in mineral beneficiation, for example, equigranular textured ore is fairly easy for liberation as compared to graphic or interlocked textured ore.

Mineral association and assemblages is usually revealed through the identification of individual grains, macro and micro-textural relation, morphology and grain boundary relation which unpack the paragenesis and conditions at which the minerals were formed leading to deciphering of ore genesis.

Chemical determination or chemistry of ore is an important factor in the study of ore minerals. This is achieved through a number of ancillary techniques such as X-ray powdered diffraction (XRPD) spectroscopy, scanning electron microscopy (SEM) and X-ray fluorescence (XRF) technique and these are commonly used in conjunction with reflected light microscopy (ore-microscopy) for the purpose of obtaining more detailed information on the chemical composition of the mineral phases. For example, XRPD is used for the identification of mineral phases, thus revealing the chemical composition of such phases, while SEM further gives the content of such elements within each mineral phase. The XRF gives the content of both major elements and trace elements within the ore which are important in the interpretation of the origin of the fluids from which the minerals were formed. For example, sulphide deposit that is formed from different fluids are likely to record corresponding differences in their trace element composition (Keays *et al.,* 1982; Plant, 1986; Gray and Russell, 1977) and also used in the determination of grade distribution, beneficiation and metal extraction (Misra, 2000).

© University of Venda

7.1.2 Properties of Ore Minerals

Mineral identification and characterization involves a number of properties such as physical, optical and chemical characterization of mineral phases. Physical properties of minerals include those properties that can be identified using naked eyes; properties such as luster, colour, cleavage and fracture.

Mineral identification includes both qualitative and quantitative properties. Qualitative properties of minerals fall under four categories: optical properties; properties dependent on hardness (polishing hardness and scratch hardness); properties dependent on structure and morphology of phases (crystal form and habit, cleavage and parting, twinning) and textures in association with two or more mineral phases (grain boundary relationship) (Bernahardt, 1987 and 1990; Craig and Vaughan, 1994).

Qualitative optical properties involve colour, reflectance, bireflectance, reflectance pleochroism, anisotropism, isotropism, and internal reflection, whereas quantitative optical property of ore minerals refers to reflectance and absolute hardness measurements of mineral grains.

Chemical characterization or geochemical characterization is an important study of mineral deposits because chemical processes result in the precipitation of minerals. Consequently, the geochemical characterization of mineral deposits helps in the understanding of ore genesis, mineral deposit classification, mineral exploration, mineral processing and geo-environmental studies (Carranza, 2012).

Analysis and interpretation of major and trace elements, rare-earth elements, isotopes, fluid inclusion micro-thermometry can be used to unpack the genesis of ore deposits (Loftus-Hills and Solomon, 1967; Ghosh, 1972; Hurai *et al.*, 2002; Carranza, 2011; Carranza, 2012; Liu *et al.*, 2018).

7.2 Methods for Ore Mineralogical Analysis

There are a number of methods or techniques that are used for ore mineralogical analysis. Specific techniques are chosen based on the objectives of the research and the characteristics of the samples to be analysed. The most common methods used for the characterization of minerals include; petrographic examination and spectroscopic analysis of mineral phases as

© University of Venda

explained in section 6. 2 (Table 6.1). Scanning electron microscopy (SEM), X-ray diffraction (XRD) powdered method and X-ray fluorescence (XRF) spectroscopy were used in conjunction with ore-microscopy for the study of ore minerals at the two study areas.

7.3 Ore Petrology and Ore-microscopy

7.3.1 Specific Objectives

In this study, ore mineralogy and ore-microscopy of the Musina copper-sulphide deposits (Artonvilla and Campbell deposits) was done in order to determine the following:

- mode of occurrence of the copper-sulphide minerals;
- mineral composition of the ore;
- mineral phases, their micro-structures and compositional variation, using scanning electron microscopy;
- mineral phases and their chemical composition, using X-ray powdered diffraction spectrometry;
- geochemical characterization of different ore types, using X-ray Fluorescence Spectrometry; and
- mineral association and assemblages so as to establis the paragenesis of the ore minerals.

7.3.2 Ore Sample Preparation

From the 21 ore samples collected from the two deposits, a total of 18 ore samples were selected for ore mineralogy and ore microscopy (Appendix 3D1 and 3DII). Eighteen polished ore surfaces were prepared, 10 from Campbell and 8 from Artonvilla deposits.

Preparation of polished surface samples was done at MINTEK, Johannesburg; at the Department of Geology, University of Johannesburg; and at the Department of Mining and Environmental Geology, University of Venda. The specimens were subjected to a series of steps consisting of sectioning, impregnation and encapsulation, grinding, lapping, and polishing in accordance with guidelines given by Craig and Vaughan (1994).

© University of Venda

Sectioning: Sectioning was achieved using Petrotrim Saw machine. Samples were cut into rectangular blocks of approximately 2.5 × 3 cm. It was performed in order to obtain a manageable size specimen from the parent material, and to reduce the thickness of the specimen so as to reduce the grinding time and to expose the surface of the ore minerals.

Encapsulation: The blocks were thoroughly washed and dried in the oven for about 30 minutes. The specimen was then placed in a flexible container coated with a thin film of mold release agent. Impregnation was done through mixing epoxy solution at resin to hardener ratio of 2:15 (2 parts hardener and 15 of resin) and poured on and around the sample to immerse it completely in the epoxy. This was left overnight for epoxy to harden and thereafter the epoxy was removed from the mold.

Grinding/Lapping: Lapping was performed using the precision lapping machine to remove deformation induced in sectioning and make the surface flat. Lapping was done using successively finer grained abrasives in solvent on a horizontal rotary grinding wheel of the lapping machine. In transition from a coarse to the next fine grit size, for example, 120, 400 and 800, 1000, 1200 grit size, the ground surface was thoroughly cleaned to remove the loose abrasives and fine particles of sample produced during coarse grinding. A finely ground surface was achieved.

Polishing: Polishing of a specimen was done using a RotoPol-35 polishing machine to remove the final deformation induced by the grinding process. Polishing was accomplished by abrading the surface using fine abrasives progressively decreasing from 120 to 1000 grit sizes. The specimens were monitored and checked whether to continue polishing or stop, until a smooth, flat and scratch-free surface was obtained. The polished sections were then cleaned with deionized water, air dried, ready for microscopic study.

Double polished thin sections were also used in ore-microscopy. The advantage of the doubly polished thin sections was that both rock forming and ore minerals could be identified from the same thin section. A total of 12 doubly polished thin sections were prepared at Société Générale de Surveillance (SGS) Laboratory in Johannesburg, South Africa and at the Department of Applied Geology, Geoscience Institute, Göttingen University, Germany as fully explained in Fluid Inclusion Chapter, Section 9.5.1.2.

© University of Venda

7.3.3 Mineralogical Investigation

Both macro- and microscopic investigation of the ore samples were done so as to determine the physical and optical properties of ore minerals within different types of ore specimens. The microscopic study of the ore minerals was conducted at MINTEK and University of Venda using Olympus BX51 petrographic microscope, with an Olympus SC50 and Zeiss AxioCam ICc1 camera attached to the computer (Fig. 7.1).

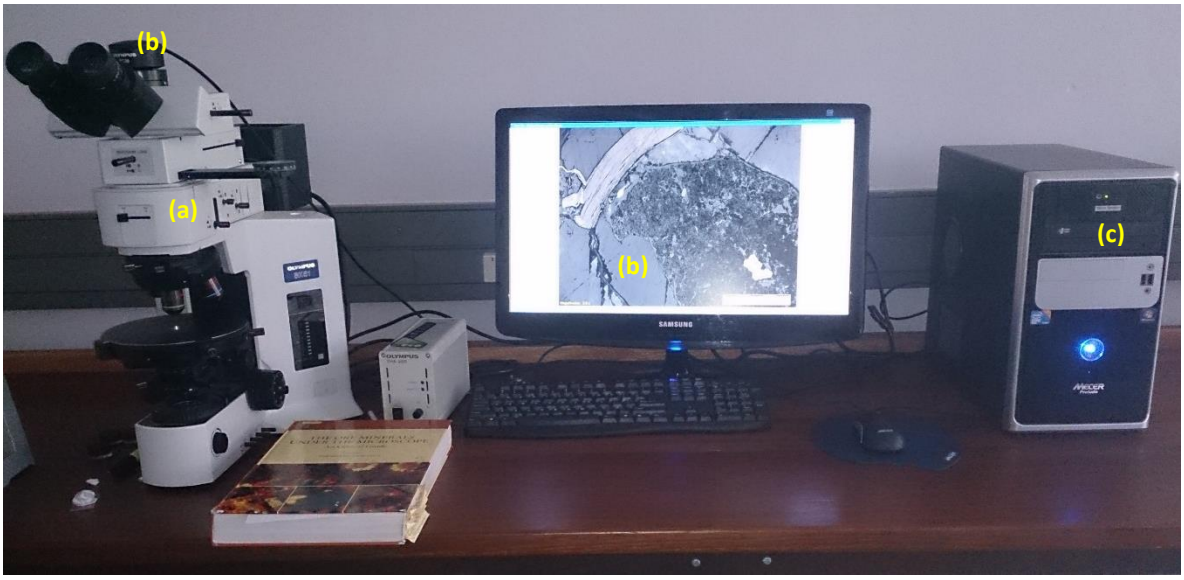


Figure 7.1: Equipment for microscopic study: a) an Olympus BX51 petrographic microscope connected to (b) Olympus SC50 camera, (c) to the CPU and (d) monitor.

The analysis was done focussing on the mode of occurrence of minerals and identification and characterization of different types of ore and industrial minerals within the ore samples from both Campbell and Artonvilla copper deposits.

7.3.3.1 Mode of Occurrence

Mode of occurrence refers to the pattern of distribution of ore minerals in a host rock which could be subtle (invisible to the naked eye) or quite pronounced (visible), for example, veined, massive, brecciated, stockwork (stringers), strata-bound (Evans and Moon, 2006; Misra, 2000). Three main mode of ore occurrence were identified; veined, disseminated and brecciated ores (Plates 7.1 – 7.3 and Figs. 7.2 – 7.4).

Veined ore

Veined ores are defined as a discrete hypogene masses mostly hosted within a planar channel, load or conduit which may be either shear zone, fissures or fractures, fault zone or lithological contact, bed or unit and commonly discordant to the host rock. They fall under regularly shaped orebodies such as tabular ore shaped types and sometimes they are referred to as loads and mostly pinch and swell during the deposition (Evans and Moon, 2006; Misra, 2000; Peters, 1993).

Several specimens revealed veined ore within Campbell and Artonvilla copper deposits, for example, specimens CPqv01, CPqtz03, CPA4, CP02 and Cp05 from Campbell deposit and specimens ATavr12, AT02 and ATavr11 from Artonvilla deposit.

Hand specimen revealed that sulphide mineralisation occurred within quartz veins. Along the quartz vein, mineralisation cuts across the host rock. The veins had variable thickness that ranged from few mm to few cm (Plate. 7.1). In some cases, an elongated thin quartz vein without ore mineralisation was identified (Plate 7.1B).

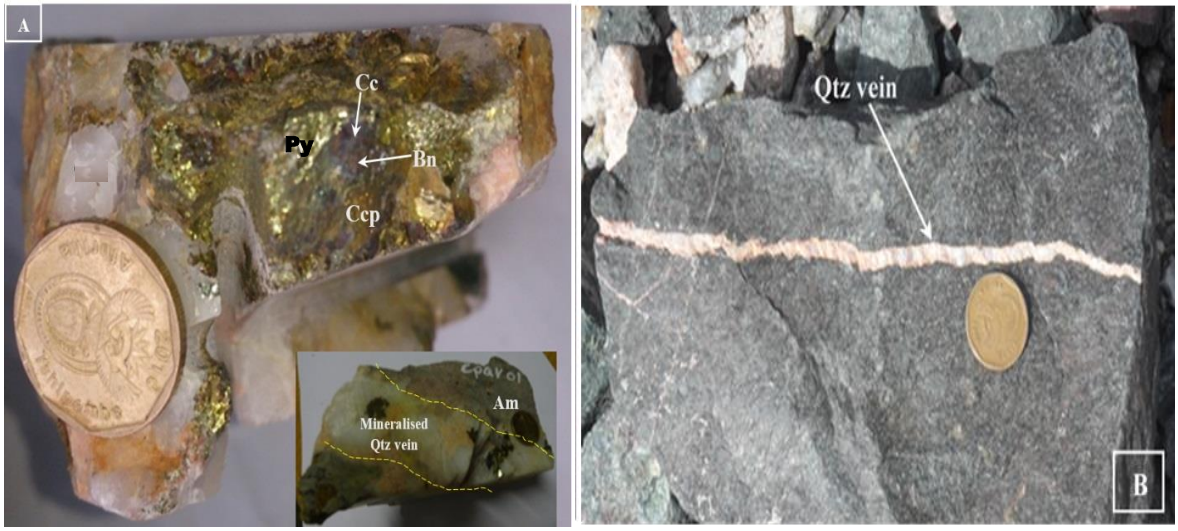


Plate 7.1: Sample CPqv01 (A) mineralised quartz vein within amphibolite from Campbell deposit: pyrite (Py); chalcopyrite (Ccp); bornite (Bn); and chalcocite (Cc). Sample ATavr11 (B) from Artonvilla deposit showing non-mineralised thin quartz vein within amphibolite schist.

Microscopically, mineralisation was seen along extensional veins with chalcopyrite and pyrite filling quartz fractures in sample CPqv01 (Fig. 7.2A and B). Ore sample Cpqv01 revealed high content of sulphide mineralisation, mainly chalcopyrite and pyrite occurring either as veinlets disseminated mineralisation, exhibiting fine to coarse- grained texture (Fig.7.2A and B). The vein-type chalcopyrite had inclusions of the host rock (amphibolite) (Fig. 7.2A and B).

In some cases, mineralisation occurred within stockwork forming stringers around the fractured garnets Cp01 (Fig.6.2C). Within the quartz vein, the anhedral chalcopyrite, and euhedral, subhedral and anhedral pyrite occurred also forming vein-type morphology with grain size up to 400 µm (Fig. 7.2D).

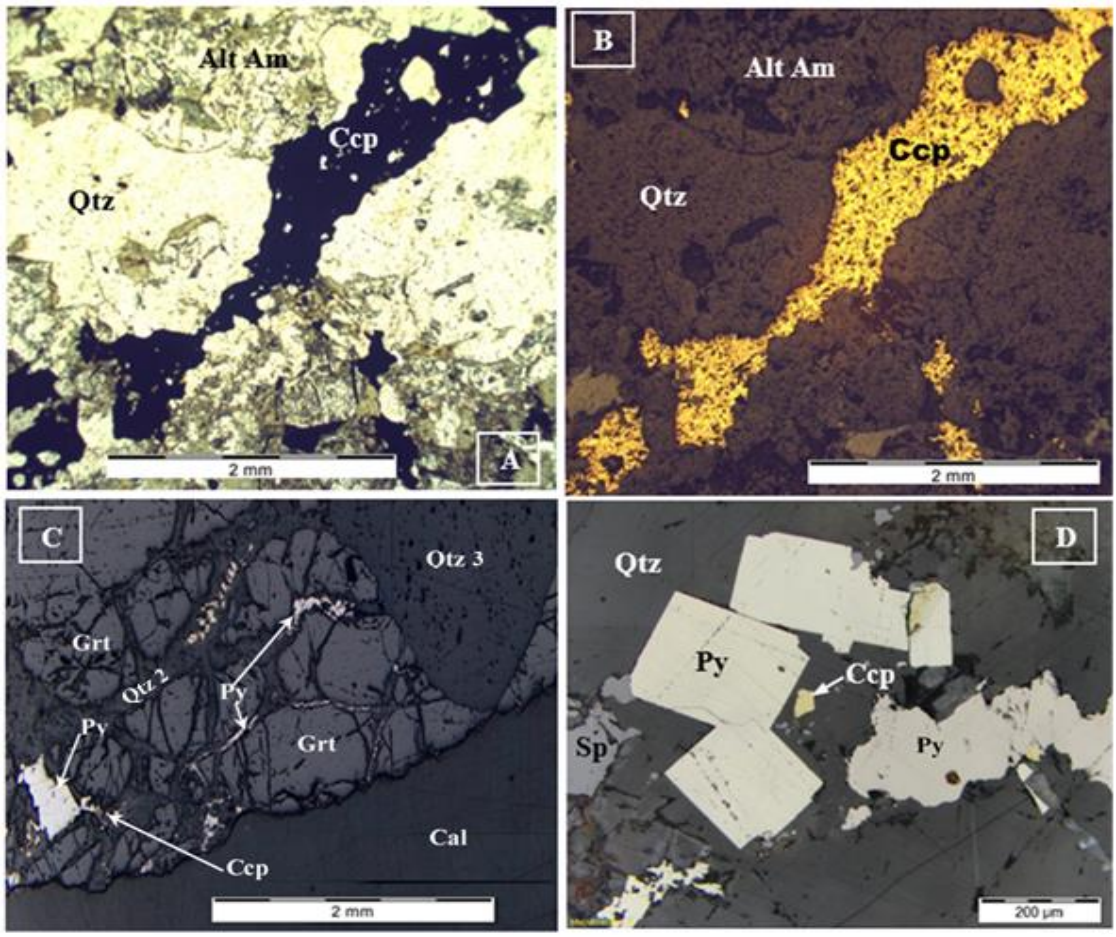


Figure 7.2: Microphotographs of double polished thin sections (A and B) from Campbell copper deposit and polished surfaces C and D from Artonvilla and Campbell copper deposits respectively. (A) Chalcopyrite (Ccp) within microfractures forming extensional vein-type viewed under transmitted plane polarized light; and (B) under reflected crossed polarized

© University of Venda

light; (C) Stockwork vein-type of pyrite (Py) and (D) Euhedral, subhedral and anhedral pyrite (Py) and anhedral chalcopyrite (Ccp) within a quartz vein.

Disseminated ore

In disseminated ore, mineralisation is usually characterized by fine grains that are scattered or dispersed within the host rock (Misra, 2000, Allaby, 2008). Disseminated sulphide mineralisation of the Campbell and Artonvilla copper deposits were evidenced in samples CPqtzv03 and Atcal01 respectively occurring within the quartz vein.

In hand specimen, two types of disseminated were identified: large amount of fine- grained sulphide minerals, mainly pyrite and chalcopyrite, distributed within amphibolite (Plate 7.2A); while the second type was dissemination of fine to medium-grained pyrite and chalcopyrite with minor bornite and some calcite within quartz vein (Plate 7. 2B).

Microscopically, dissemination of tiny grains of sulphide minerals were identified as anhedral chalcopyrite replacing pyrite and in some places, chalcopyrite was replaced by bornite (Fig. 7.3 A and B).

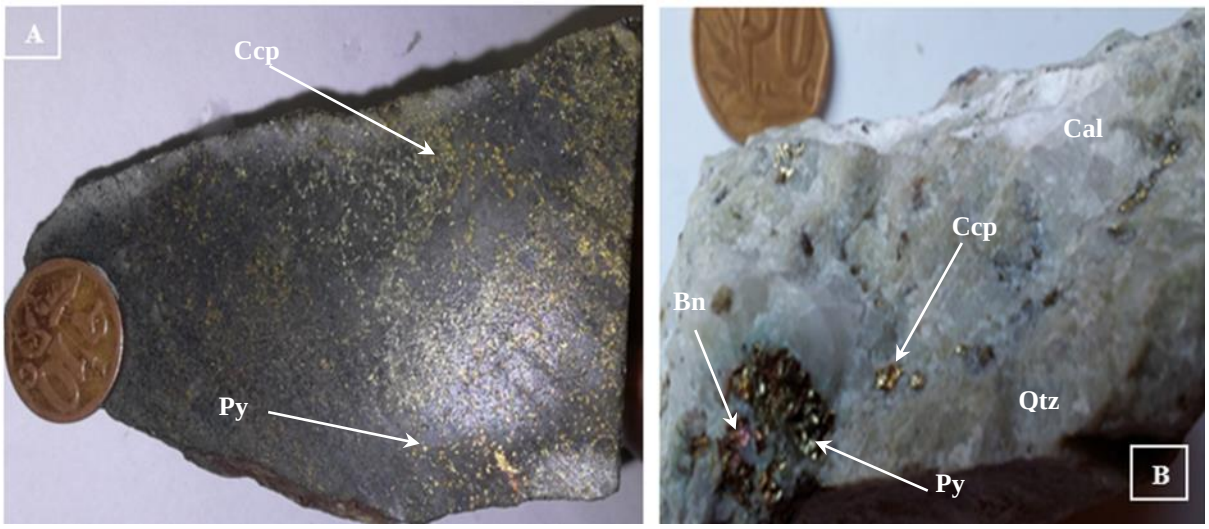


Plate 7.2: Hand specimen showing disseminated sulphide mineralisation from Artonvilla and Campbell copper deposits. (A) Fine-grained chalcopyrite disseminated within amphibolite; and (B) Fine to medium-grained pyrite (Py) and chalcopyrite (Ccp) with minor bornite (Bn) and some calcite disseminated within quartz vein.

© University of Venda

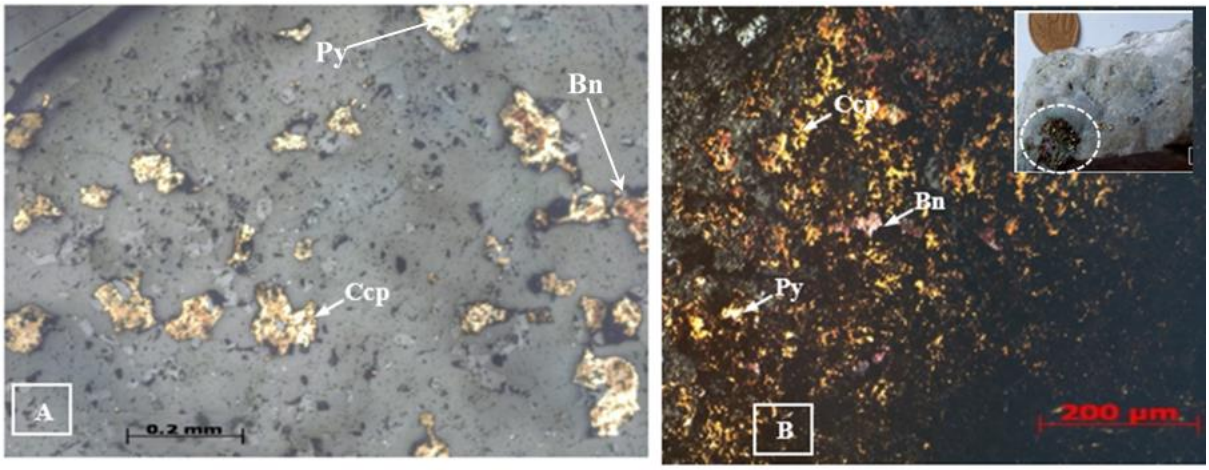


Figure 7.3: Microphotographs of fine-grained disseminated sulphides within amphibolite (A); and disseminated pyrite (Py), chalcopyrite (Ccp) and bornite (Bn) within quartz vein with some calcite (B) from sample Atcal01and CPqtz03 from Artonvilla and Campbell copper deposits respectively.

Brecciated Ore

Brecciation is a process whereby formation of breccia or masses of rock composed of fragments of older rocks are fused together. Thus, mineralisation in breccias is found as a cement to the breccia fragments which could indicate that the brecciation occurred prior to or, at the latest, contemporaneously with mineralisation (Shukla and Sharma, 2018; Misra, 2000; Macqueen and Thompson, 1978; Je´brak, 1997). Consequently, brecciated ore bodies are commonly interpreted as collapse features caused by a partial dissolution of underlying weak rocks, or interpreted as structures caused by hydraulic fracturing or in some cases are caused or controlled by older structures such as faults and fractures.

Some authors have attributed brecciation of the host rock to the action of ore-forming fluids where the hydrothermal fluids are likely to cause enlargement of pre-existing breccia bodies which could be evidenced by some dissolution of the host rock mineralisation (Shukla and Sharma, 2018; Je´brak, 1997; Misra, 2000; Ohle 1990; Gaylord and Brisky, 1983; Heyl, 1983). ,

In this study, brecciation was evidenced in several samples, for example, in ore samples CP03, CP01, CP05 and Atbr01 (Plate 7.3A, B, C and D) from Campbell and Artonvilla copper deposits.

© University of Venda



Plate 7.3: Hand specimen of brecciated ore samples of CP03 (A), CP05 (B) and CP01 (C) from Campbell, and Atbr01 from Artonvilla copper deposits: (A) sulphide mineralisation deposited as matrix around the brecciated quartz (Br qtz) grains; (B) sulphide mineralisation surrounds both the brecciated quartz (Br qtz) and amphibolite (Amp) fragments; (C) and (D) numerous breccias of both quartz and amphibolite fragments with minor sulphide mineralisation around the brecciated fragments.

In sample CP03, mainly pyrite and chalcopyrite were deposited within the brecciated quartz grains and infilling the microstructures between the breccias. This indicates that the mineralised hydrothermal solution followed the weak zones as their conduit (Plate 7.3A and B). Mostly sulphide mineralisation occurred within the brecciated quartz (Plate 7.3 A and B) and less within the brecciated amphibolite Plate 7.3C and D). The mineralised hydrothermal

© University of Venda

solution apparently was responsible for the localisation of quartz vein and emplacement of sulphide minerals.

Macroscopic and microscopic investigation of sample CP01 (Plate 7.3C and D; and Fig. 7.4), revealed brecciation of both host rock and quartz with some breccia ranging from 2 mm grains to 2.5 cm in diameter. Disseminated sulphide mineralisation occurred within the fragmented quartz breccia while little amount of mineralisation occurred within host rock breccia (Plate 7.3C and D; and Fig. 7.4). This could be indicative of hydrothermal solution influx into the brecciated rock that developed during the earlier processes that resulted into breccia formations. The infilling of mineralised solution occurred around the breccias and only in few instances, mineralisation occurred along the microfractures within the breccias. This resulted into the alteration of the host rock, amphibolite, with evidence of chloritization that apparently accompanied sulphide mineralisation.

In summary, the macroscopic and microscopic investigation of the Campbell and Artonvilla copper deposits revealed coarse textures of brecciated ore which was characterised mainly by quartz breccias and to some extent, amphibolite breccias. These breccias ranged in diameter ranged from 1 to 2.5 mm. Sulphide mineralisation occurred mainly around the breccias and in few cases, along the microfractures of these breccias. The process of sulphide mineralisation was apparently accompanied with chloritization.

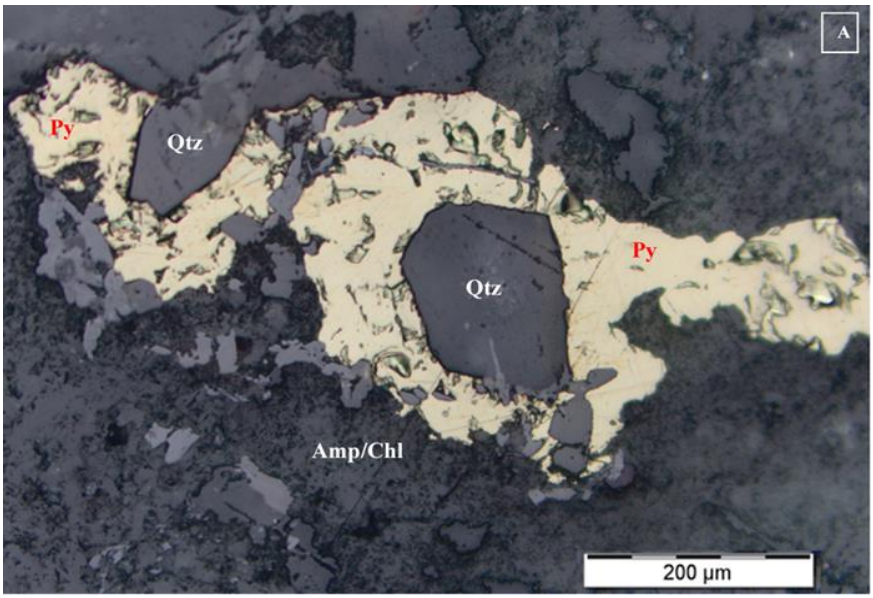


Figure 7.4: Microphotograph of minerals: pyrite (py) around the angular quartz (Qtz) and amphibolite breccias with alteration of amphibolite and deposition of chlorite.

© University of Venda

7.3.3.2 Industrial and Ore Minerals

Deposition of ore minerals at the Messina copper deposits included both the industrial minerals and metallic ore minerals. Industrial minerals associated with ore mineralisation included garnet ($A_3B_2Si_3O_{12}$) and graphite (C), while two groups of metallic ore minerals were established: the oxide minerals mainly magnetite (Fe_2O_3) and hematite (Fe_3O_4), and sulphide minerals comprising pyrite (FeS_2), chalcopyrite ($CuFeS_2$), sphalerite (ZnS), pyrrhotite(FeS) and pentlandite $(Fe, Ni)_9S_8$. The sulphide minerals were subjected to secondary alteration resulting in the formation of malachite [$Cu_2\ CO_3(OH)_2$], azurite [$Cu_3\ CO_3(OH)_2$], bornite (Cu_5FeS_4), covellite (CuS) and chalcocite(Cu_2S).

Industrial minerals

- **Garnet**

Garnet was found mainly within the granulite rocks such as garnet gneiss, quartzo-feldspathic gneiss, hornblende granulite at both Artonvilla and Campbell deposits but highly occurred at Artonvilla deposit. Formation of garnets within the host rock, however, is associated with regional metamorphism of the Limpopo mobile belt.

Hand specimen of host rock exhibited large crystals of garnet (Grt) up to 10 mm in diameter (Plate 7.4). The garnet (Grt) grains revealed red to brownish colour that occurred as octahedral to subhedral crystals with vitreous lustre and hardness greater than 7 in the Moh's scale of hardness. The specimens were strongly chloritized (Plate 7.4B and C) and this could be attributed to the influx of hydrothermal fluids that resulted into the deposition of sulphide minerals. The garnet occurred with magnetite (Mt) and large crystals of quartz (Qtz) (Pate 7.4B and C).

In polished surfaces and doubly polished thin sections, garnet exhibited large grains up to 10 mm in diameter that were distinguished by their optical properties (Fig. 7.5), such as isotropic, high relief.

© University of Venda

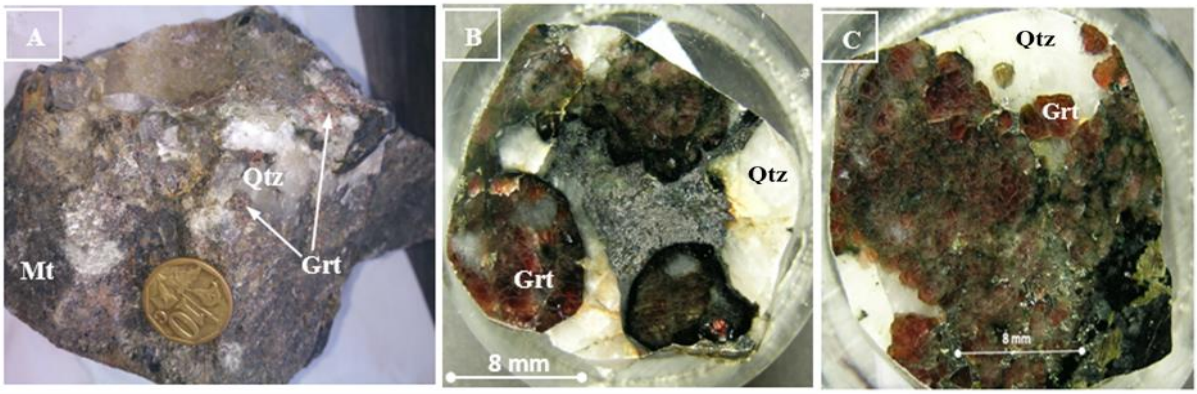


Plate 7.4: Garnet (Grt) and magnetite (Mt) minerals in quartz vein-amphibolite host rock from the Artonvilla copper deposit (A, B and C).

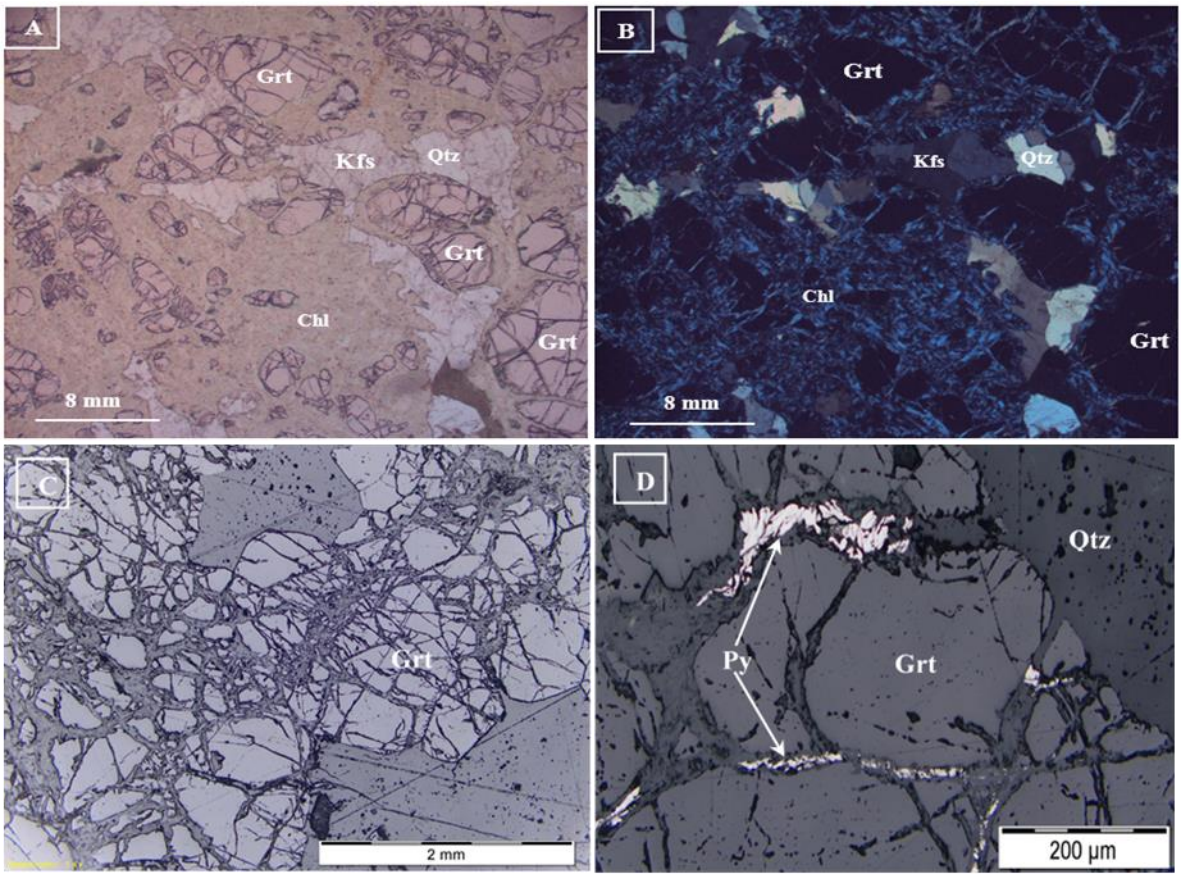


Figure 7.5: Photomicrographs of garnet (A) in plane polarized light; and (B) in crossed polarized light with potassium feldspar (Kfs) and chlorite (Chl); (C) highly fractured garnet (Grt) grains with micro-fractures filled with quartz; (D) quartz and pyrite (Py) deposited around and within microstructures in garnet (Grt) grains in reflected light.

© University of Venda

Garnet was associated with potassium feldspars (Kfs) (Fig. 7.5A and B), apparently orthoclase that is generally formed together with garnet in rocks of the granulite facies where almandine is developing from biotite and muscovite (Smirnov, 1976). In some places, the enclosed minerals included quartz and potassium feldspars. Garnet was replaced by quartz and pyrite along its grain boundary, in places within its microfractures (Fig. 7.5D).

Geochemical analysis of garnets from different samples using electron microprobe analysis (Section 6.3.6) revealed greater than 50% of almandine composition (55-68% almandine) using 50% rule, which suggested that all the garnet grains within the study area were almandine member with varying low composition of pyrope, grossular and spessartine. Following the Hunneman's concept, the garnets in this study can be classified as pyrope-almandanine (Hanneman, 2008), where in pyrope-almandine falls within the range of 30-70% almandine. Consequently. The alteration of garnet to anomalous blue chlorite (rich in Fe) is consistent with the presence of almandine member which is also Fe-rich.

Highly fractured garnet grains were infilled by mineralised solution containing mainly pyrite (Py) that was deposited together with first quartz generation (Fig. 7.5C and D). Large grains of almandine were mainly identified within the Artonvilla copper ores while small to medium sized grains were found within the Campbell copper ores.

- **Graphite**

Physical characteristics and occurrence: In Hand specimen, graphite occurred as visible laths of sizes up to 2 cm. It was identified through its physical characteristics such as grey colour, greasy/slippery feeling when rubbing off the finger and it is extremely soft with low specific gravity. At Artonvilla copper deposit, graphite occurred as plates within amphibolite schist and in granulite rocks. In places, it was found as inclusions within calcite vein (Plate 7.5A). Graphite was also identified within the brecciated ore (Plate 7.5B).

© University of Venda

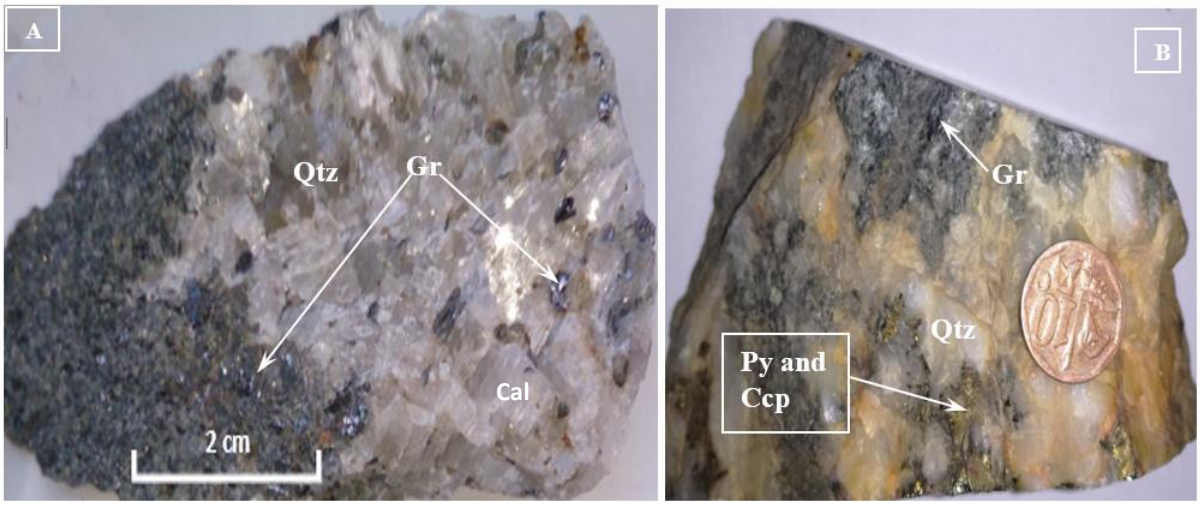


Plate 7.5: Ore specimens (Atcal01 and Cp03) with flakes of graphite (Gr) within amphibolite rock with calcite (Cal) vein from Artonvilla copper deposit (A), and within brecciated ore from Campbell copper deposit (B).

Grain size: Microscopically, the graphite is present as laths and/or folded thin flakes or plates (Fig. 6.6) disseminated within amphibolite schist and granulite rocks. In reflected light, the graphite appeared brownish grey in colour with thickness varying in size (Fig. 7.6 A-D). The elongated crystals ranged from 0.5 mm (500 µm) up to 4.3 mm (4300 µm) in length with thickness ranging from 50 µm to 100 µm with few cases greater than 100 µm such as thickness of 850 µm in Figure 7.6D. The grain size of graphite revealed fine textured flakes with few cases of coarse texture based on classification scheme from Mitchell (1993) whereby grain size ranging from 1 to 25 mm are classified as flakes. Flake graphite with grain thickness < 150 µm are classified as fine textured while those with thickness > 150 µm are coarse textured thickness and are of economic importance.

Other minerals: In places, later formed minerals such as chlorite formed during chloritization process and later formed quartz, cutting through graphite flakes (Fig. 7.6). In some cases, the microscopic study revealed formation of later quartz with pyrite mineralisation (Fig. 7.6A and C) and grains of sphalerite (Fig. 7.6C) interleaved the graphite into thinner flakes and sometimes cut the elongated flakes of graphite (Fig. 7.6C). The chloritization process also indicated alteration process that occurred across the graphite crystal (Fig. 7.6B).

© University of Venda

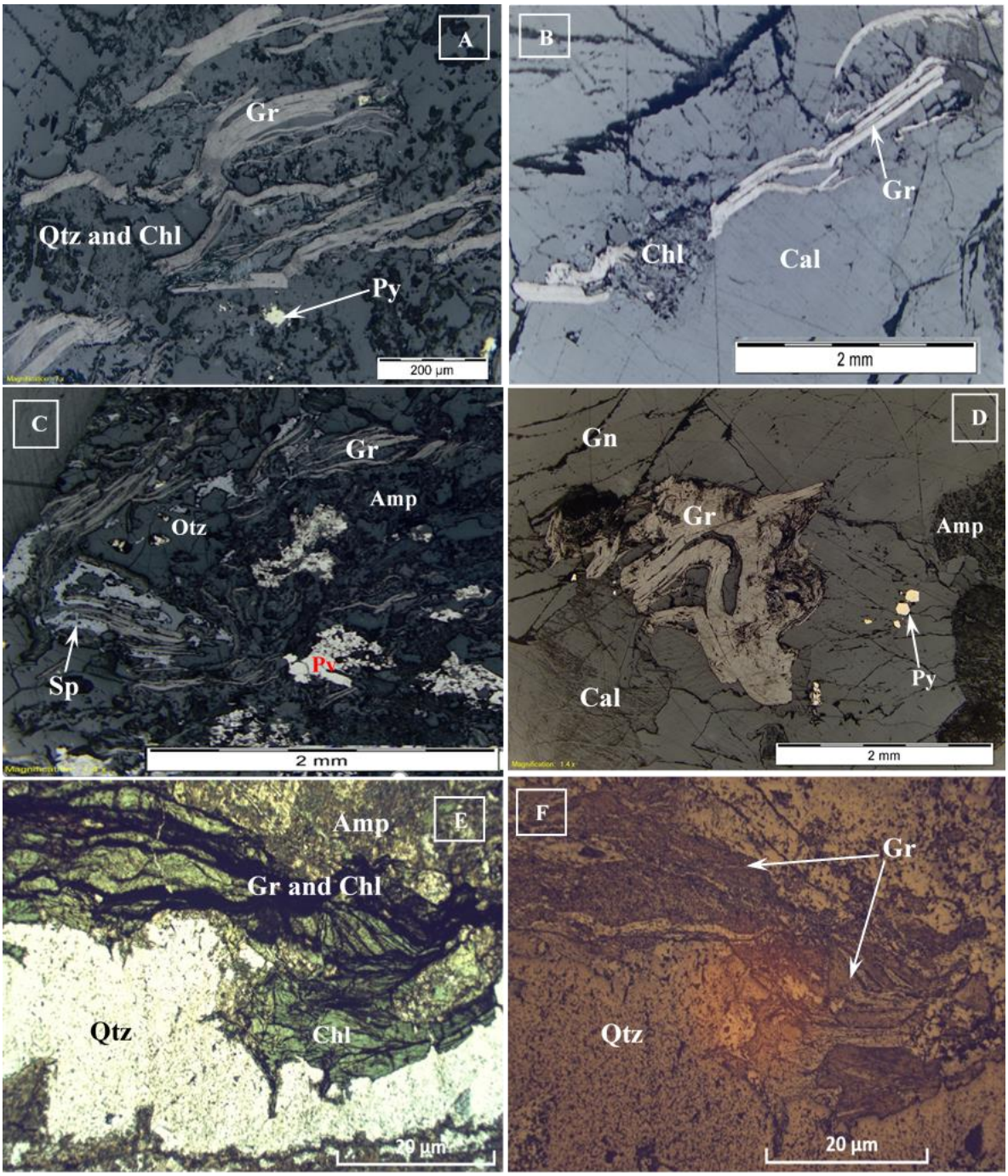


Figure 7.6: Microphotographs of Atcal01 (A, B. C, and D) in plane polarised reflected light and Cpqv01 (E and F) in plane and crossed polars of transmitted light from Artonvilla and Campbell copper deposits respectively. Flakes of graphite in association with sulphides such as pyrite (Py), sphalerite (Sp) and galena (Gn) and Chlorite (Chl), quartz, (Qtz) and amphibole (Amp).

© University of Venda

Graphite is also associated with minerals such as galena, calcite (Fig. 7.6D), quartz and amphibole (Fig. 7.6E). The graphite flakes appeared opaque in both plane and crossed polars of the transmitted light (Fig. 7.6E and F) with quartz, chlorite and amphibole oriented along with graphite flakes forming schistose structure (Fig. 7.6E and F). In places, the graphite flakes are highly folded and this was noted in granulite rocks (Fig. 7.6D). This suggest increase in metamorphic grade. The occurrence of graphite flakes was seen mainly within amphibolite schist and granulite rocks associated with disseminated and brecciated ores and rarely in veined ore at Campbell and Artonvilla deposits.

Ore Minerals

- **Oxides: magnetite and hematite**

Macroscopically, ore samples ATavr12 (Plate 6.6A) and CP01 (Plate 7.5B) from Artonvilla and Campbell copper deposit respectively, revealed large euhedral octahedral crystals of magnetite with grain size of up to 2 mm within the quartz vein and amphibolite host rock. Magnetite was identified through its distinctive properties such as magnetic, crystal form, colour, high density and semi-metallic to metallic lustre. In other samples magnetite occurred as tiny granular aggregates within the host rock (Plate 7.6B).

Hematite crystals were frequently found as irregular masses of earthy material mainly occurring together with magnetite. Hematite was identified by its bright brick red colour with brown-red streak colour indicating oxidation of magnetite to hematite and goethite due to chemical weathering processes (Plate 7.6A).

In reflected light, magnetite revealed crystal size of up to 200 µm as octahedral and bladed forms (Fig. 7.7). In Figure 7.7A, hematite (Hem) light grey in colour is replacing grey to brownish magnetite (Mt) and in some cases crystals of magnetite (Mt) are replaced by hematite as pseudomorphous crystals. The replaced magnetite retained its relics within the replacing hematite (Hem), thus the later mineral occurs as a replacement product.

Similar scenario was observed in Figure 7.7B, were euhedral grains of garnet (Grt) were replaced by hematite (Hem). However, in this case hematite occurs as tiny blades. Relics of replaced garnet were retained within the pseudomorphous grains.

© University of Venda

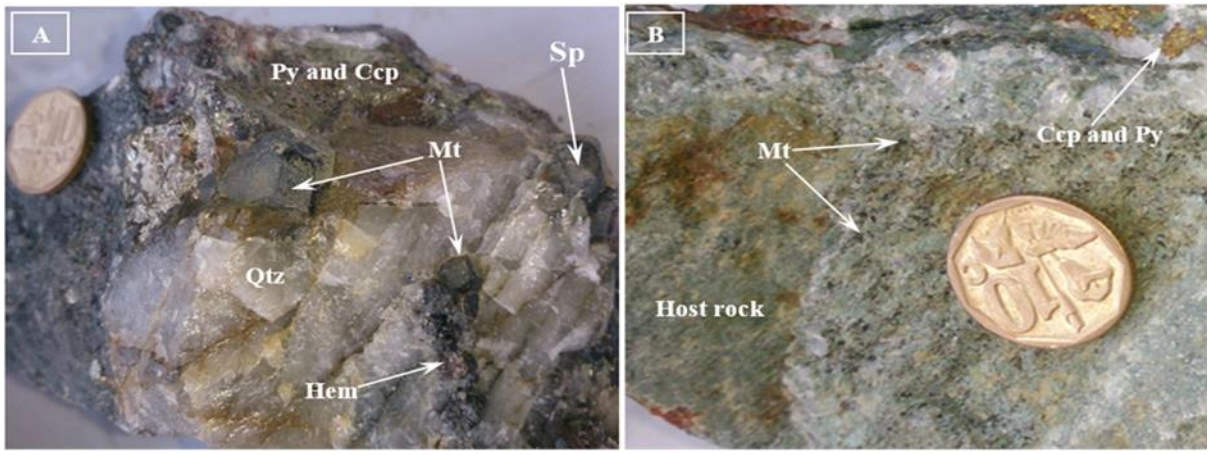


Plate 7.6: Occurrence of (A) large subhedral magnetite crystals (Mt) and hematite (Hem) with brownish to red colour within the quartz veined ore from Artonvilla copper deposit; (B) disseminated tiny magnetite crystals (Mt) within the amphibolite host rock of Campbell copper deposit.

Figure 7.7C depicts the effect of carbonate fluids that marked the end of sulphide mineralisation in this area, resulting in the formation of calcite. Apparently, this phenomenon triggered the replacement of pyrite (Py) by hematite (Hem). The allotriomorphic grains of pyrite were replaced along the grain boundary and through the microfractures within pyrite (Py). Relics of pyrite, however, were retained within the replacing mineral (hematite).

The relationship between pyrite and hematite, however, was complex as pyrite (Py) was noted to be filling the microfractures of platy hematite (Hem) which at the same time, was being replaced by goethite (Gt) along the grain margins and within the grain itself. Hematite was also replaced by the later infiltrating carbonate fluids, forming ankerite (Fig. 7.7D). In some places, subhedral crystals of pyrite cut across anhedral grains of magnetite (Mt) (Fig. 7.7E).

In summary, two types of magnetite were noted within these two deposits, apparently, earlier formed allotromorphic magnetite and later formed euhedral octrahedral crystals (Fig. 7.7A). Both types of magnetite were either totally or partially replaced by hematite. Hematite, however, was formed as thin plated during regional metamorphism (Fig. 7.7E) although at later stage hematite occured as a replacement product, having replaced either magnetite and garnet (Fig. 7.7A and B) or pyrite (Fig. 7.7C).

© University of Venda

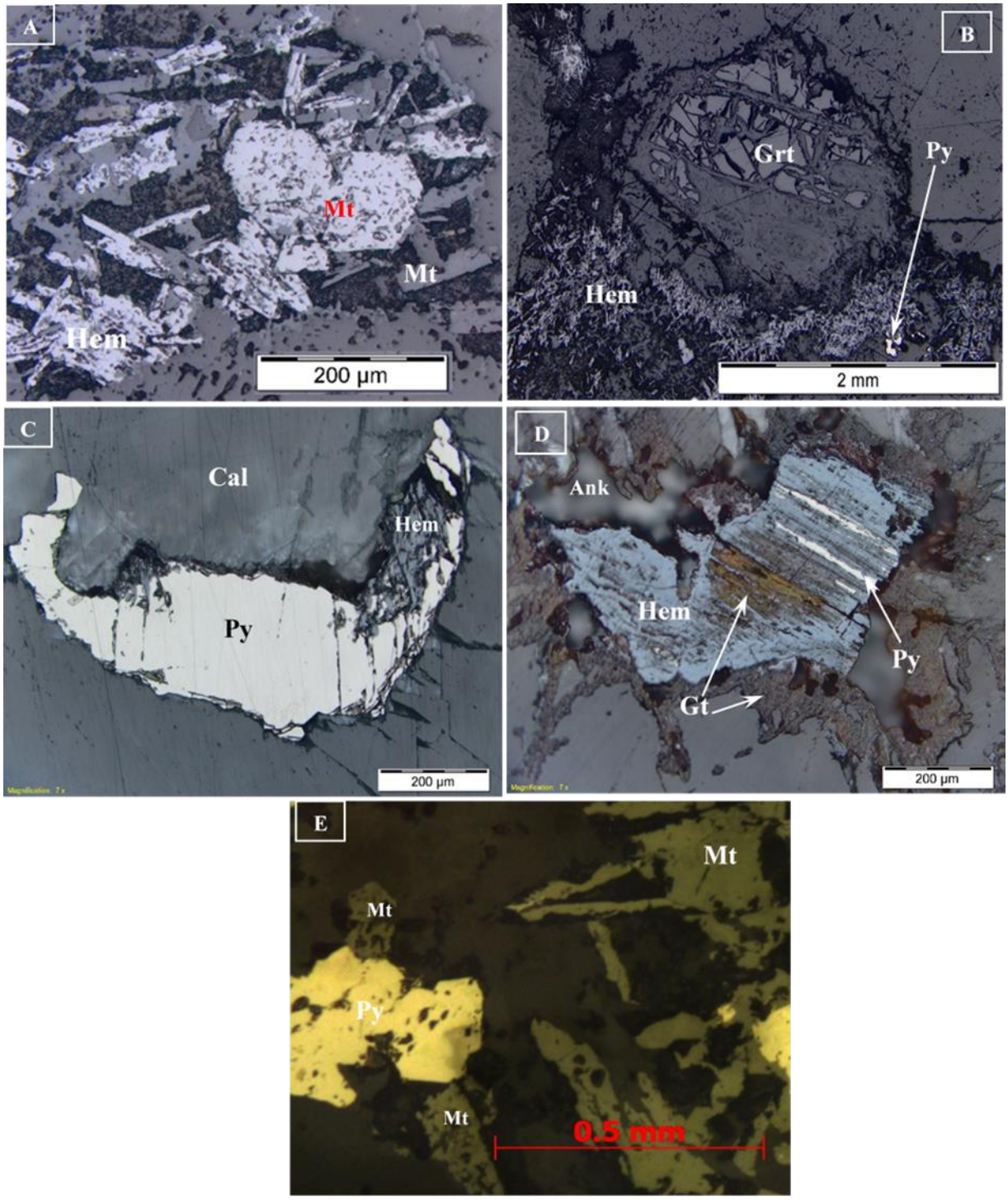


Figure 7.7: Photomicrographs of Atcal01, Atavr12 and Cp01 ore samples showing: (A) plated light grey crystals of hematite (Hem) in places, replacing euhedral magnetite crystals (Mt); (B) tiny blades of hematite (Hem), replacing euhedral crystals of garnet (Grt); (C and D) allotriomophic pyrite (Py) being replaced by hematite (Hem), along the grain boundary

© University of Venda

and microfractures, whereas hematite is replaced by goethite; (E) pyrite crystals (Py) cut across grains of magnetite (Mt).

- **Primary sulphide ore minerals**
  - **Pyrite**

Pyrite was one of the abundant primary sulphide minerals identified within Campbell and Artonvilla coper deposits. For example, sample CP02, CP03, CPqv01 from Campbell and ATcal01, ATavr12 from Artonvilla copper deposits were found to contain pyrite.

In hand specimen, pyrite exhibited a distinct pale yellow colour and occurred as anhedral and subhedral crystals (Fig. 7.1A). It is identifiable from similar minerals such as chalcopyrite, gold by its brassy yellow colour, crystal form, and strong metallic luster and its hardness is greater than 5.5. Pyrite was found to occur predominately within quartz vein and also in amphibolite host rock. It is also found as disseminated grains within both veined and disseminated ore (Plates 7.1 and 7.2) and it occurs around quartz grains (Plate. 7.3).

Under the ore microscope, pyrite appears yellowish white with euhedral, subhedral and anhedral grains (Figs. 7.2, 7.3, 7.4 and 7.8), which assumed the authigenic crystal appearance. In plane polarised reflected light, pyrite has no bireflectance and in crossed pollars, it does not have the play of colours, hence it belongs to the cubic minerals that are isotropic. Individual euhedral pyrite grains measure up to 330 µm (Fig. 7.2D). Two generations of pyrite were noted, viz: early formed pyrite that was emplaced along the microfractures of garnet together with early formed quartz (Fig. 7.2C), and later formed euhedral pyrite grains (Fig. 7.2D).

Both idiomorphic and allotriomorphic pyrite grains are replaced by chalcopyrite (Fig. 7.2C, D, Fig. 7.10D and Fig. 7.9B and C), hematite and calcite (Fig. 7.7C), chalcocite, bornite and covellite (Fig. 7.10).

Pyrite, sphalerite and chalcopyrite mineralisation together with later formed quartz were deposited around the grain boundaries and along the microfractures of garnet and or in between early formed garnets which was chloritized as evidenced by the presence of chlorite

© University of Venda

(Fig. 7.8A). Later formed euhedral pyrite together with chlorite were replaced by calcite resulting into the formation of subhedral to anhedral pyrite (Fig. 7.8B). Sphalerite was seen to replace pyrite.

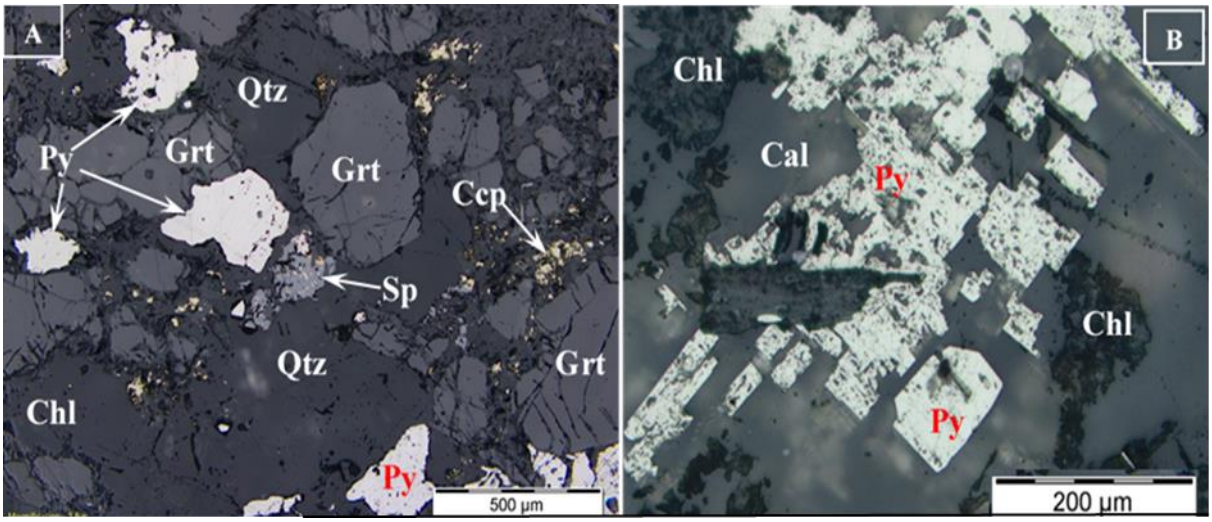


Figure. 7.8: Microphotograph illustrating: (A) sulphide mineralisation (pyrite (Py), sphalerite (Sp) and chalcopyrite (Ccp) within later formed quartz, in places, occurring between garnet grains (Grt); (B) later formed euhedral pyrite (Py) replaced by calcite.

- **Chalcopyrite**

It was established that chalcopyrite occurred within all ore samples collected from Campbell and Artonvilla copper deposits. It occurred within the veined, disseminated and brecciated ore samples (Plate 7.1, 7.2 and 7.3 respectively) commonly with other sulphide mineralisation such as pyrite, sphalerite and secondary minerals such as bornite, malachite and azurite (Plate 7.1, 7.2 and 7.3; and Fig. 7.2, 7.3, 7.6 and 7.7).

In hand specimen, chalcopyrite exhibited a distinct brassy dark yellow colour. It was differentiated from pyrite and gold by its distinct characteristic brassy dark yellow colour, its hardness which is less than that of pyrite, its brittleness and its greenish grey streak. It occurred within quartz vein, disseminated and brecciated ores.

Microscopically, chalcopyrite occurred as pale brassy dark yellow and always darker compared to pyrite. It exhibited anhedral crystal shapes and was always associated with other sulphide mineralisation such as pyrite, sphalerite and secondary minerals such as bornite, malachite and azurite. At some instances it was found enclosing early formed pyrite (Fig.

© University of Venda

7.9A and B) which was replacing hematite (Fig. 7.9A and B). In some instances, chalcopyrite was seen to replace pyrite (Fig. 7.9 B and C) while in some cases, it occurred as inclusions within sphalerite resulting into chalcopyrite disease (Fig. 7.9D).

The occurrence of chalcopyrite inclusions in sphalerite are considered to be due to exsolutions resulting into chalcopyrite disease as a result of replacement of Fe-rich sphalerite. This position has been contested by other researchers. For example, Bortnikov *et al.*, (1991) noted that chalcopyrite inclusions are formed in both Fe-rich (8 – 14wt% Fe) and Fe-poor (0.5 – 2wt% Fe) sphalerite. They further concluded from their study that chalcopyrite inclusions were produced by replacement as a result of interaction of sphalerite with solution that transported both copper and iron. They also proposed the coprecipitation of sphalerite and chalcopyrite.

- **Sphalerite**

Macroscopically, sphalerite was challenging to identify but using its diagnostic physical properties such as luster and streak colour, it was seen to occur as tiny grains with resinous luster. It was identified in few hand specimen from both Campbell and Artonvilla copper deposits (Plate 7.6).

Microscopically, sphalerite was identified in most of the samples from both Campbell and Artonvilla copper deposits. The sphalerite occurred as anhedral shaped crystals mostly light-bluish grey colour and grey to brownish colour. The crystals revealed chalcopyrite disease indicated by inclusions of chalcopyrite within the sphalerite. The chalcopyrite blebs within the sphalerite exhibited randomly distributed pattern (Figs. 7.8A; 7.9D, E and F).

At some places sphalerite was seen to be replacing anhedral pyrite (Fig. 6.9E) and sphalerite was mostly found associated with chalcopyrite and pyrite within influx of quartz wherein at some instances it revealed replacement by chalcopyrite (Fig. 7.9F). Sphalerite and chalcopyrite were seen to be replacing euhedral crystals of pyrite (Fig. 7.9G).

© University of Venda

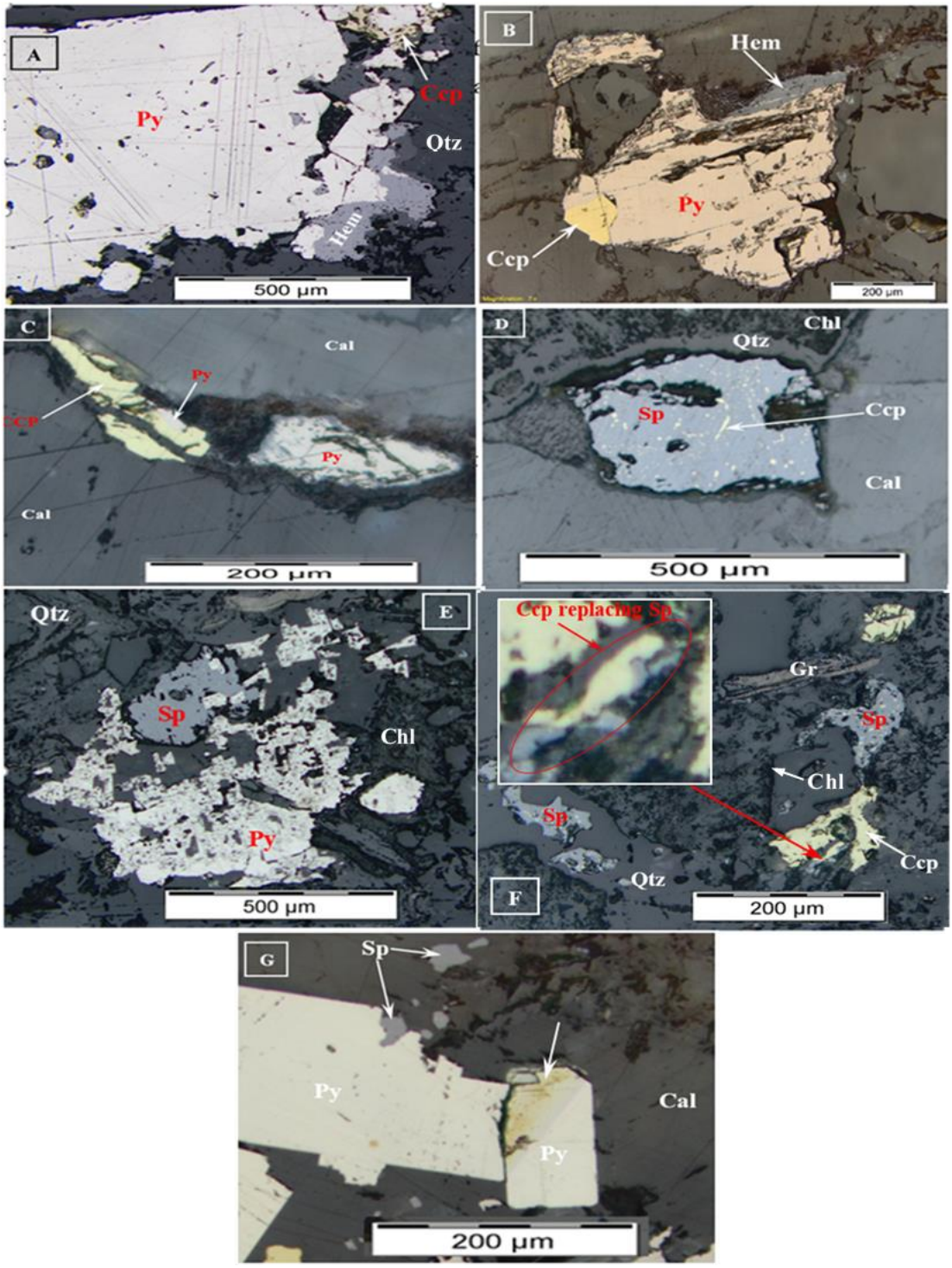


Figure 7.9: Microphotographs of ore samples from Artonvilla showing: (A) enclosed pyrite (Py) by chalcopyrite; (B) pyrite (Py) associated with chalcopyrite (Ccp) and hematite (Hem) where chalcopyrite (Ccp) is replacing pyrite (Py); (C) chalcopyrite (Ccp) replacing pyrite (Py); (D) chalcopyrite (Ccp) occurring as exsolution within sphalerite (Sp); (E) Early formed pyrite (Py) replaced by sphalerite (Sp); (F) Sphalerite (Sp) replacing chalcopyrite (Ccp); and (G) Later formed pyrite (Py) being replaced by sphalerite (Sp) and chalcopyrite (Ccp).

© University of Venda

- **Galena**

In hand specimen, identification of galena was not easy but its occurrence was easily identified under the ore microscope where it exhibited grains characterized by three or more parting or cleavage directions with parallel rows of triangular pits which are particularly characteristic of galena (Fig. 7.10). The triangular pits did not show any curvature characteristics, thus no evidence of deformation. In terms of colour, galena appears greyish brown and revealed intermediate reflectivity as compared to pyrite with high reflectance and sphalerite with low reflectance. At some instances in places, galena was seen occurring in association with anhedral pyrite sphalerite and pyrrhotite where anhedral pyrite was replaced by sphalerite (Fig. 7.10.A).

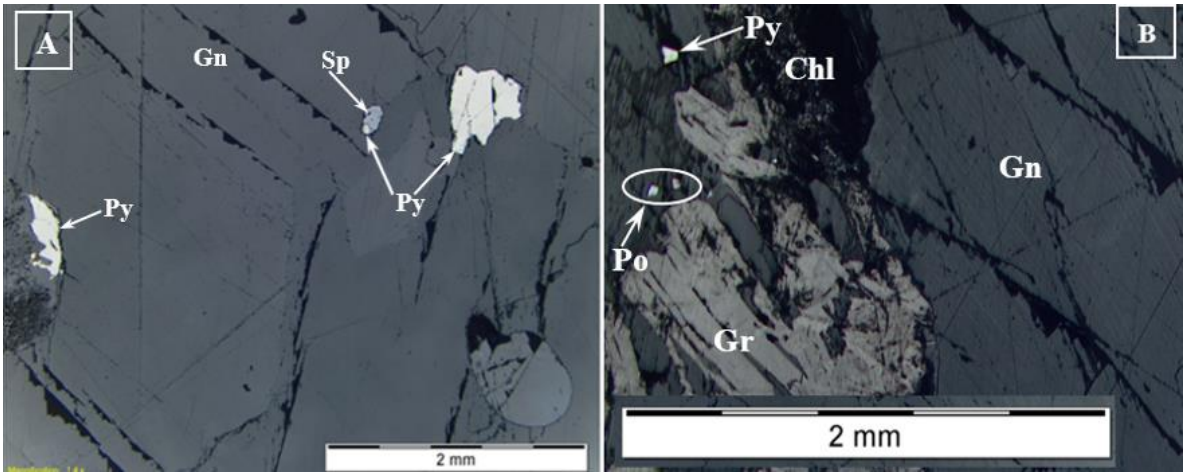


Figure 7.10: Photomicrograph of ore samples from Artonvilla copper deposit showing: (A) galena (Gn) with triangular pits, associated with anhedral pyrite (Py) and sphalerite (Sp) replacing pyrite (Py); (B) Galena (Gn) with graphite (Gr), tiny grains of pyrrhotite (Po), pyrite (Py) and chlorite.

- **Pyrrhotite**

In hand specimen, pyrrhotite could not be easily distinguished from pyrite as both have brassy, metallic colour and luster, however, they can be differentiated using crystal habit where pyrrhotite has flat and platy crystals while pyrite forms cubic crystal shape. But in this case, pyrrhotite occurred as subhedral to anhedral shaped crystals. Under ore microscopy,

© University of Venda

pyrrhotite occurred as tiny grains with creamish colour and with grain size less than a millimetre (Fig. 7.10.B) and was strongly anisotropic in crossed polars.

- **Secondary sulphide ore minerals**
  - **Malachite**

The brightly green coloured copper carbonate malachite [$Cu_2CO_3(OH)_2$] was commonly encountered on the surface and prospecting trenches. In hand specimen, malachite exhibited a bright green colour and mainly occurring as stains within the disseminated ore (Plate 7.7A). It was identified using its distinctive bright green colour and streak colour. It was found associated with oxidation of chalcopyrite and other copper minerals. It was seen commonly occurring with chalcopyrite, hematite, magnetite, azurite, bornite and in places with cuprite (Plate 7.7A). Malachite is a copper carbonate mineral which often resulted from weathering of copper ores. Because of its distinctive bright green colour and its presence in the weathered zones of copper mineralisation, it has often served as a prospecting guide for copper-sulphide mineralisation.

Microscopically, malachite exhibited its bright green colour with high internal reflection and often occurred together with blue azurite (Fig. 7.11A). In places, it occurred as pseudomorph of pyrite where it is replacing pyrite and retaining the pyrite original crystal habit (Fig. 7.11B). Replacement of euhedral pyrite by malachite together with chalcopyrite, bornite and chalcocite occurred along the margins of pyrite (Fig. 7.11B).

  - **Bornite**

In hand specimen, bornite (Cu_5FeS_4) exhibited a bright metallic purple-pinkish colour mixed with red colour. It was easy to identify by its distinctive coloration (Plate 7.7D). Bornite had a streak of grey-black. Microscopically, its pinkish brown colour allows it to be readily identified and it was mostly found to be replacing pyrite and chalcopyrite, especially along the grain boundaries and along the cracks (Fig. 7.11B, C and D). Bornite was found occurring together with other secondary copper minerals such as malachite, covellite and azurite (Fig. 7.11) and together with primary minerals mainly chalcopyrite, chalcocite and cuprite (Fig. 7.11). In places, it occurred as single grain that fully replaced pyrite that was earlier replaced by chalcopyrite (Fig. 7.10E).

© University of Venda

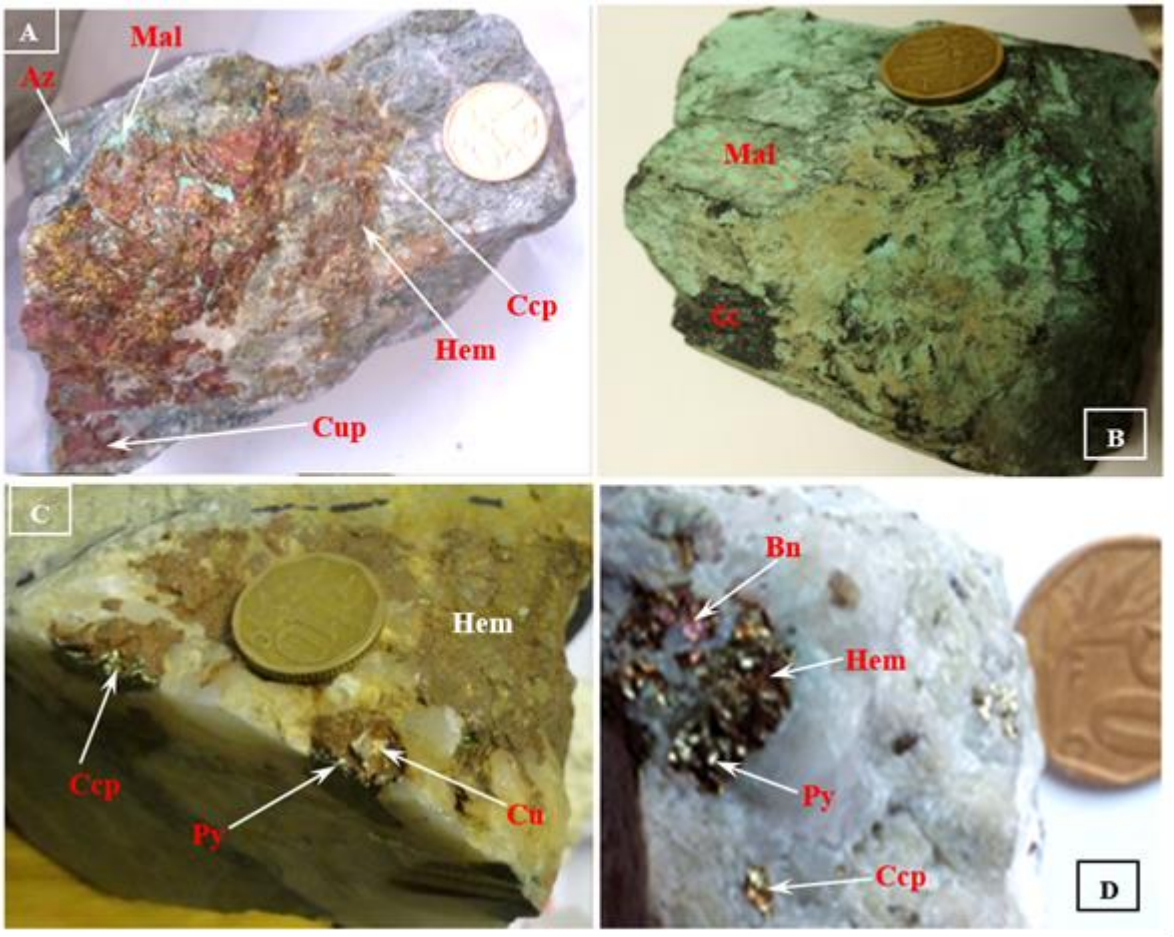


Plate 7.7: Hand specimen of sulphide secondary minerals: (A) malachite (Mal) in bright green colour after oxidation of chalcopyrite (Ccp) associated with hematite (Hem), cuprite (Cup) and azurite (Az); (B) Malachite (Mal) stains on chalcocite (Cc) with granular grains of chalcopyrite; (C) A grain of native copper surrounded by hematite (Hem) with tiny grains of pyrite and chalcopyrite (Ccp); and (D) Bornite (Bn) in pinkish colour occurring together with pyrite (Py), chalcopyrite (Ccp) and hematite (Hem).

- **Azurite**

Azurite [Cu3 $(CO_3)_2(OH)_2$] was clearly identified in hand specimen by its blue colour and its alteration to malachite while microscopically it exhibited its distinctive deep blue colour with high reflectance (Fig. 7.11A) while in places it revealed bluish colour and seen to replace late formed pyrite as its pseudomorph (Fig. 7.11C and D). Along the pyrite crystal azurite (blue) occurred together with bornite (pinkish) and covellite (blueish-purple) replacing the pyrite crystal (Fig. 7.11D).

© University of Venda

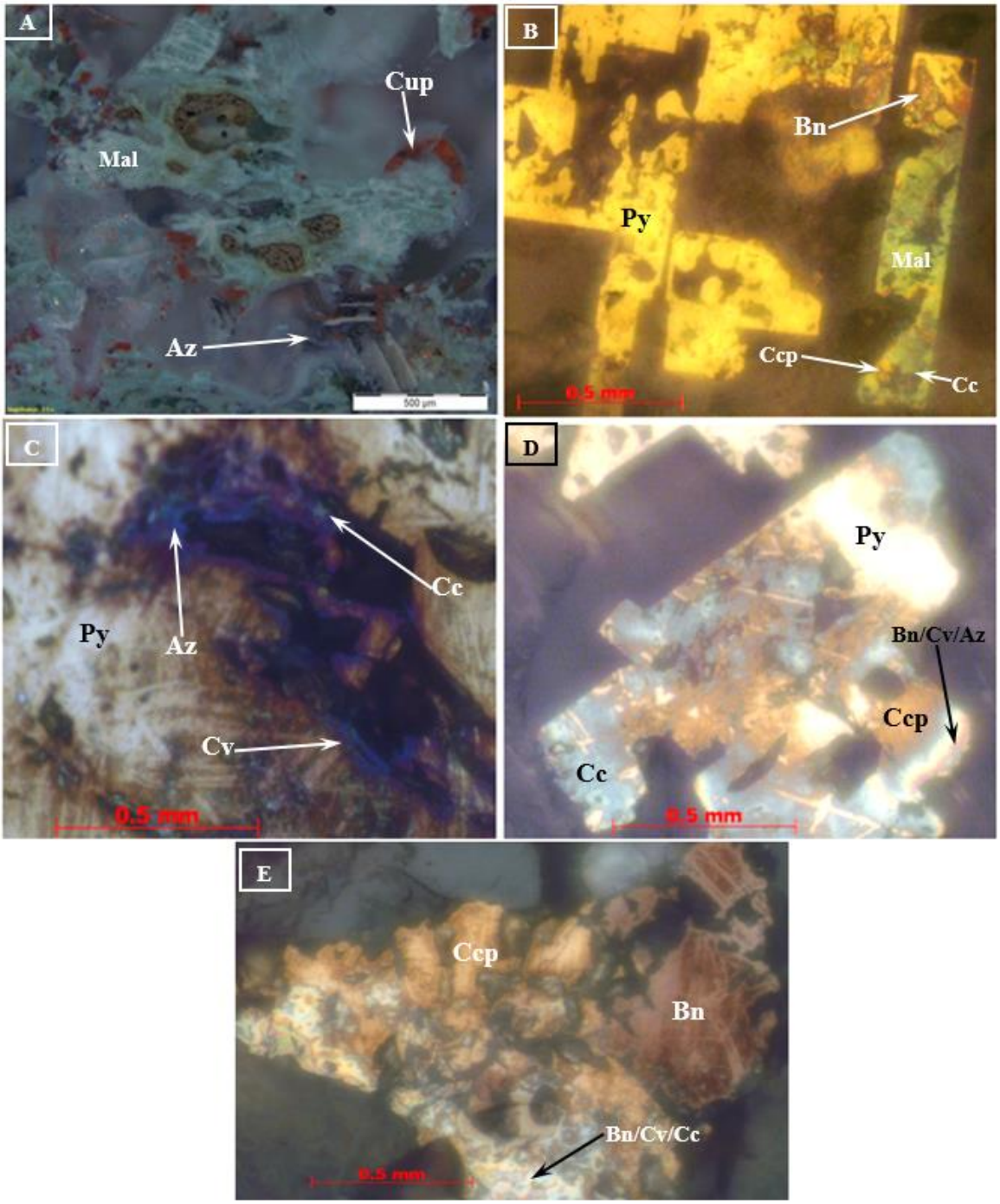


Figure 7.11: Photomicrographs showing: (A) internal reflection of malachite (Mal) and azurite (Az) occurring together with cuprite (Cup); (B) Replacement of euhedral pyrite (Py) by chalcopyrite (Ccp), malachite (Mal), bornite (Bn) and chalcocite (Cc) along the margins of pyrite (Py); (C) Pyrite (Py) and chalcopyrite (Ccp) twinning with purplish-blue covellite (Cv) along the grain boundary; (D) Euhedral crystals of pyrite (Py) replaced by chalcopyrite (Ccp), covellite (Cv), bornite (Bn) and chalcocite (Cc); and (E) Total replacement of

© University of Venda

chalcopyrite (Ccp) by bornite (Bn) and pale blue chalcocite (Cc), replacement starting along the grain boundary.

- **Covellite**

In polished sections, covellite (CuS) appeared as purplish blue in colour, strongly anisotropic and occurred along the chalcopyrite and pyrite twinned crystal (Fig. 6.11C and D). Covellite was usually found together with azurite, bornite and malachite replacing pyrite and chalcopyrite and forming pseudomorph of crystals (Fig. 6.11B, C and D). Replacement of chalcopyrite and pyrite generally starts along the grain boundaries and or along the microfractures of copper-sulphide minerals.

- **Chalcocite**

In hand specimen, chalcocite (Cu_2S) was identified by its diagnostic physical properties such as its grey colour, metallic luster, greyish black streak colour, softness, sooty appearance and its high density. It was noted in many samples from both Campbell and Artonvilla copper deposits. It occurred in disseminated and brecciated ores as granular tiny grains and found as individual grains in veined ores (Plate 6.1). It was also found as large specimen of about 10 cm with visible granular grains of chalcopyrite stained with malachite (Plate. 7.7B).

Under ore microscope, chalcocite exhibited pale blue colour with isotropism. Two shades of chalcocite were identified, pale blue and light whitish blue that commonly occurred along the grain boundary of euhedral pyrite. Chalcocite was observed as an end-product or later replacement process, thus replaced copper from the oxidised minerals. For example, in Figure 7.11 B, C, D and E, euhedral pyrite was replaced by chalcopyrite and bornite with covellite, azurite and malachite replacing chalcopyrite that replaced pyrite with chalcocite revealing later replacement process.

- **Cuprite and native copper**

In hand specimen, cuprite was identified as bright reddish brown colour and its reddish-brown streak colour with submetallic luster. Cuprite is commonly found as an oxidation product of copper-sulphide minerals such as chalcopyrite and pyrite, and often associated

© University of Venda

with malachite, azurite, and native copper (Plate 7.7A and C, and Fig. 7.11A). In polished section, the grey coloured mineral was not easy to distinguish from hematite but its reddish internal reflection colour proved to be the diagnostic feature (Fig. 7.11A).

Native copper occurred relatively rarely in the ore. It was identified by its distinctive bright metallic luster and its bronze brownish colour (Plate 7.7C). It was identified within an oxidised zone in association with hematite which was reddish brown in colour (Plate 7.7C).

Native copper generally form under reducing environments. It is postulated that copper was transported in the form of chlorite ($CuCl_2$ and $FeCl_2$) with Cu and Fe-rich hydrothermal solutions. This led to the oxidation of Fe as stated by Liu and Mcphail (2005).

$$CuCl_2 + 2FeCl_2 = \downarrow Cu + 2FeCl_3$$ Equation 7.1

Or

$$CuCl_2 + 2FeCl_2 + 3H_2O = \downarrow Cu + Fe_2O_3 + 6HCl$$ Equation 7.2

$FeCl_3$ then dissolved and later precipitated to form hematite:

$$FeCl_3 + 3H_2O \text{ (Hydrolysis)} = 3HCl + Fe(OH)_3$$ Equation 7.3

$$Fe(OH)_3 \text{ (precipitated) to } Fe_2O_3 + 3H_2O$$ Equation 7.4

7.4 Scanning Electron Microscopy

Scanning electron microscopy (SEM) was used to provide information on the crystalline structure and chemical composition at the range of 1 µm to 1 nm of the top surface of the specimen. In this study, the SEM was used for the identification of ore minerals in order to confirm the minerals identified through microscopy and most importantly for the identification of ore minerals which were not identified under ore microscopy because the SEM has higher magnification which is up 1000.000x with an ultimate resolution of 1nm (Vernon-Parry, 2000). The SEM enables identification of minerals with less than 3% within the ore sample which could not be detected by XRD (Vernon-Parry, 2000). This method is also important as it enables one to identify both ore and gangue minerals at the same time, thus association and relationship between these minerals could be revealed. Elemental mapping of individual grains was achieved with this method.

© University of Venda

7.4.1 Sample Preparation and Analysis

Sample preparation and analysis were both done at the Department of a Mineralogy, MINTEK, Johannesburg. From the polished sections used for optical microscopy, a total of 8 representative polished sections, (4 from Campbell and 4 from Artonvilla copper deposits), were used for scanning electron microscopic investigations. The polished sections were coated with a uniform carbon film to facilitate the accumulation of electrons from the beam. The samples were then placed in a special sample holder with platinum, aluminium, and cobalt standards which were embed in the rim of the sample holder which was also polished with 1 µm slurry.

Analysis was done using Carl Zeiss SMT Ltd. EVO/MAS 15 Scanning Electron Microscope (SEM) and Smart SEM software with EBSD and EDS spectral detectors used for processing the backscattered images and elementary analysis (Fig. 7.12).

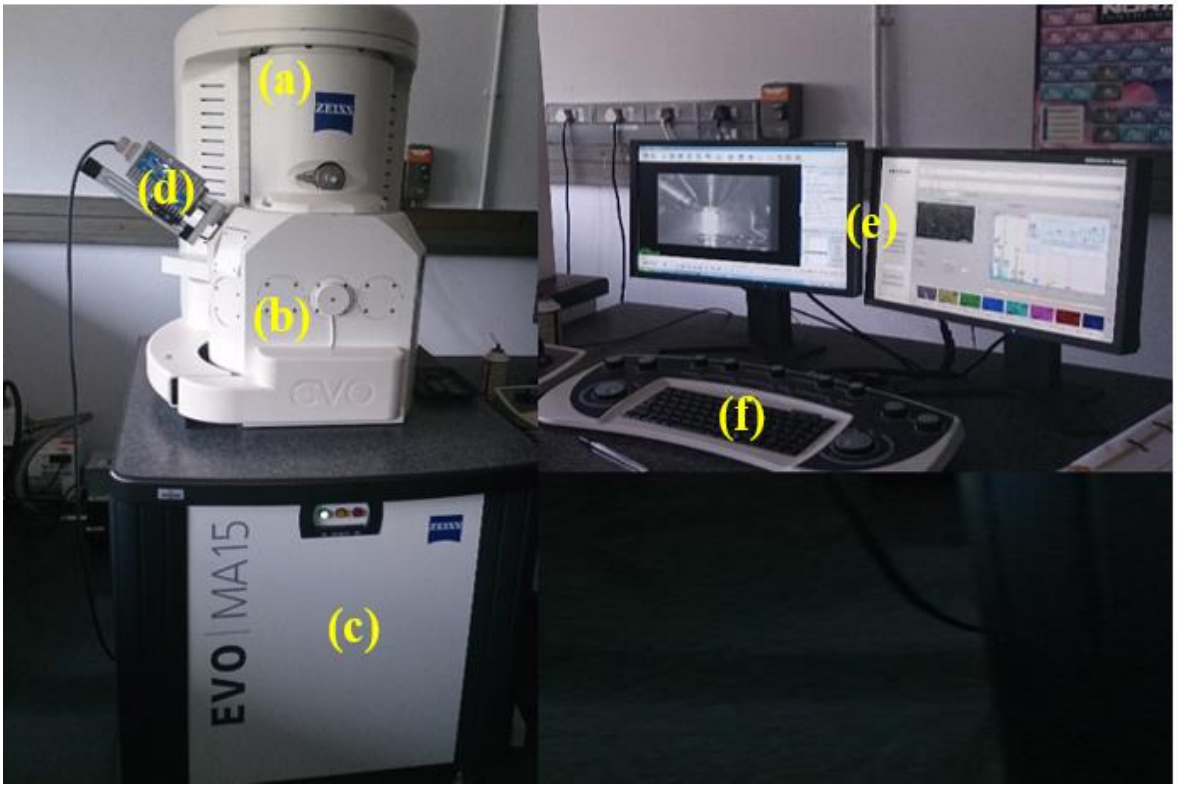


Figure 7.12: A photograph of Scanning electron microscope used for mineralogical analysis with (a) Electron column, (b) Sample chamber containing sample stage and back-scattered electron detector, (c) Electronics, (D) Energy dispersive spectrometer, and (e) Computer display with (f) joy stick.

© University of Venda

7.4.2 Results and Interpretation

Using this method, the following were achieved: (1) several minerals were identified, using optical microscopy; (2) microstructures that were invisible under ore microscopy were also revealed and that helped in deciphering mode of formation of the ore; and (3) identification of minerals, using SEM gave an insight on the association of minerals (ore and gangue minerals), thus helped in deciphering the mineral assemblages and paragenesis.

SEM study revealed and confirmed the occurrence of pyrite, chalcopyrite, and sphalerite in the ore which were among the minerals identified using ore microscopy mainly within the veined ore. Chalcopyrite occurred as inclusions within pyrite while quartz occurred as inclusions within both pyrite and chalcopyrite (Fig. 7.13A). This implied that pyrite was the first mineral to be formed along the grain boundary of garnets and in places cutting through earlier formed quartz grains. After the formation of earlier formed pyrite, the rejected Fe and Cu diffused to form inclusions of chalcopyrite in earlier formed pyrite (Fig. 7.3A).

Sphalerite with chalcopyrite inclusions was identified with chalcopyrite inclusions brighter in colour as compared to sphalerite which revealed light greyish colour (Fig. 7.12D), which is typical of chalcopyrite disease. The microstructures such as veinlets filled with mineralised solution were identified within later formed quartz (Qtz 2) that occurred between the garnet grains (Fig. 7.13B and C). In places, the infilling of mineralised solution within later formed quartz (Qtz 3) together with chlorite were identified along the boundaries of garnets and quartz (Qtz 2) (Fig. 7.13 D).

Brecciated ore revealed occurrence of sulphide mineralisation such as chalcopyrite and bornite with two generations of quartz (Qtz 1) and (Qtz 2). Chalcopyrite was identified occurring together with chlorite and later formed quartz (Qtz 2) which occurred around brecciated epidote (Fig. 7.13 E). In places, crystals of epidote were seen to have enclosed early formed quartz grains (Qtz 1) (Fig. 7.13 E). Bornite revealed brighter colour than chalcopyrite within an altered amphibole grain in quartz (Fig. 7.13F).

Scanning electron microscopy revealed occurrence of minerals such as pentlandite and nickel- rich pyrite which were not identified using ore microscopy (Fig. 7.14). The anhedral

© University of Venda

crystal of pentlandite was identified as slightly light grey as compared to the euhedral Ni-pyrite. It occurred as inclusions within the Ni-bearing pyrite and as small grains that were seen around the crystal boundary of the euhedral later formed quartz (Qtz 2) with relics of pyrite. The mineralisation was seen to be included within the early formed quartz (Qtz 1). The nickel content within the euhedral pyrite could be attributed to the occurrence of traces of pentlandite. Pyrite was the first to crystalize at high temperature and at a later stage second generation pyrite was crystallized from the solution with preferential concentration of nickel in this pyrite while rejected nickel and iron diffusing away to form pentlandite. Similar processes were observed in the formation of pyrite and pentlandite with nickel being concentrated in pyrite at low temperatures (Ewers and Hudson, 1972).

© University of Venda

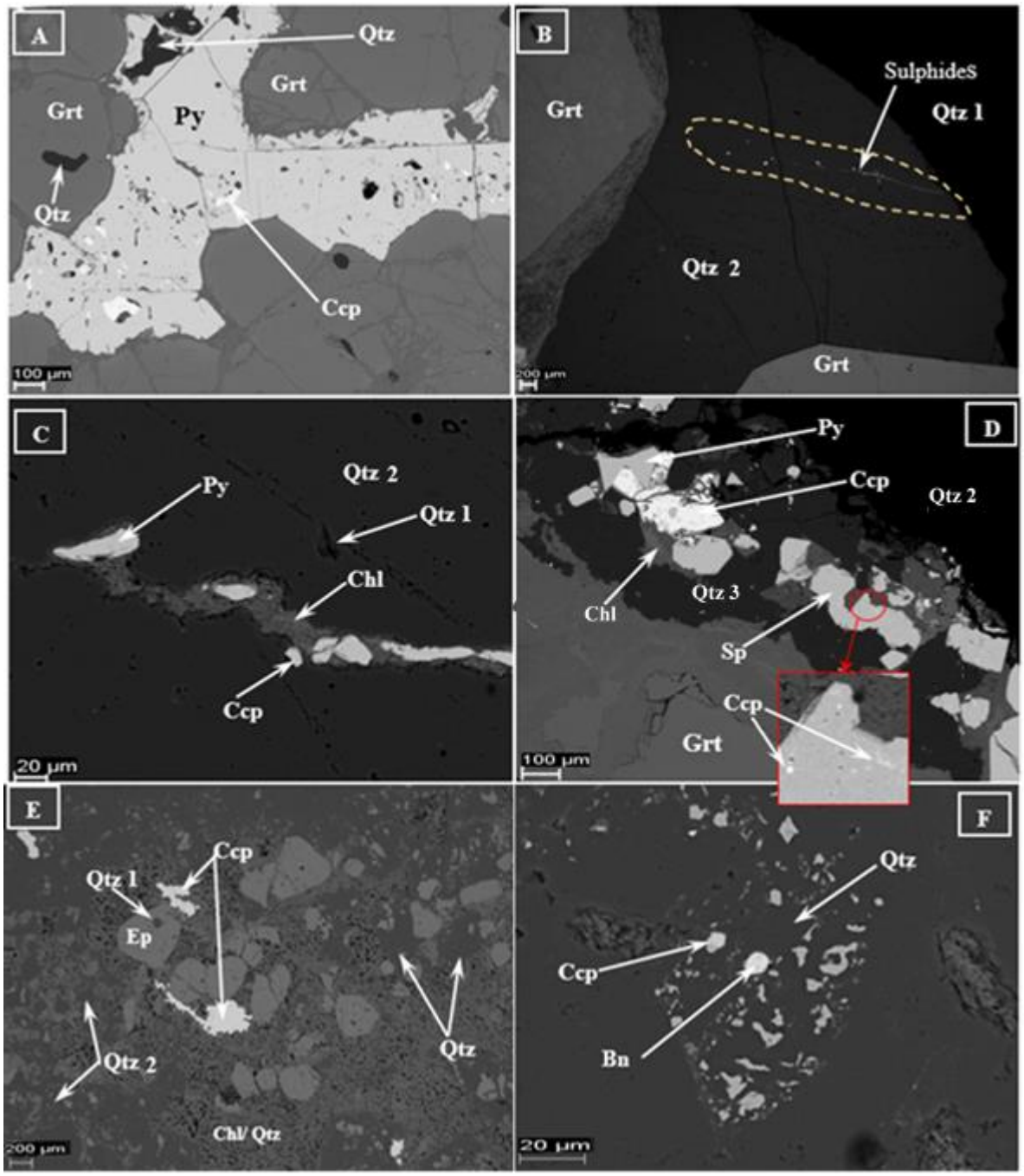


Figure 7.13: Scanning Electron backscattered images of veined ore (A, B, C and D) and brecciated ore (E and F) samples showing (A) pyrite (Py) with inclusions of chalcopyrite (Ccp); (B) Infilling of sulphide mineralised solution within later formed quartz (Qtz) in-between garnets crystals; (C) high magnification of B with pyrite (Py) and chalcopyrite (Ccp) within Quartz (Qtz) 1 and 2; (D) chalcopyrite (Ccp), pyrite (Py), sphalerite (Sp) within later quartz (Qtz 3) occurring between (Grt) and quartz (Qtz 2) boundaries; (E) Chalcopyrite (Ccp) within chlorite (Chl) and quartz (Qtz) surrounding the brecciated epidote (Ep); and (F) Quartz with bornite (Bn) showing lighter colour than chalcopyrite (Ccp) within altered amphibole.

© University of Venda

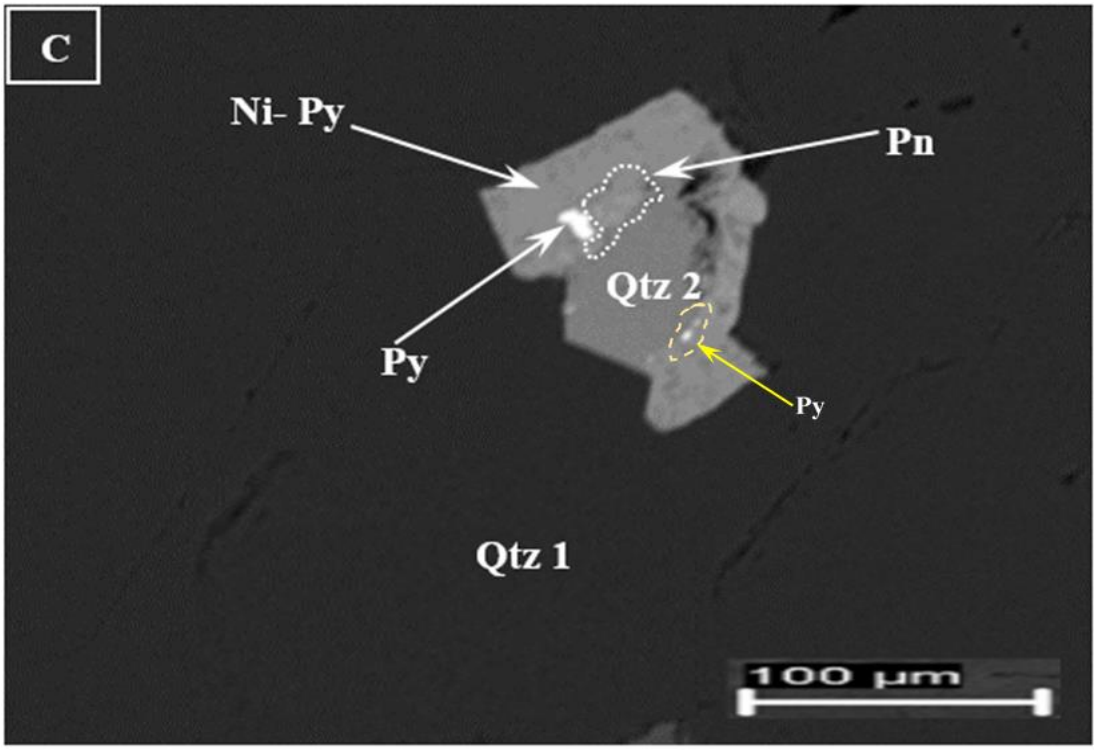


Figure 7.14: SEM backscattered electron image of disseminated ore sample showing fine-grained of pentlandite (Pn) with intergrowth of anhedral pyrite (Py) occurring as inclusion within the subhedral Ni-bearing pyrite (Ni-Py) forming around the quartz grain (Qtz 2) and at the boundary of the early formed quartz (Qtz 1).

7.5 X-ray Diffractometry

X- ray powdered diffraction spectrometry (XRD) and scanning electron microprobe are some of the ancillary techniques or methods which are commonly employed in conjunction with reflected light microscopy in order to obtain more detailed information on the identities and composition of mineral phases. Consequently, XRD was used in this study in order to identify different minerals and to determine the chemical composition of the ore samples from both Campbell and Artonvilla copper deposits.

7.5.1 Sample Preparation and Analysis

Sample preparation and analysis for XRD were both done at the Department of Mineralogy, MINTEK, Johannesburg, following the procedure used by Coelho (2007) and Jacobs (2016).

© University of Venda

The ore samples were subjected to crushing and milling, using McCrone micronizing millensure a particle size of less than 10 µm, which is a required particle size for XRD analysis (Coelho, 2007). The milled samples were left to dry overnight and thereafter used for analysis. Analysis of mineral phases was done through determination of XRD spectra, using Bruker D8 Advance powder diffractometer (Fig, 7.15) together with Vantec detector and fixed divergence and receiving slits with Co-Ka radiation. The conditions of the instrument were set at a step size of 0.01° at 2Θ with the total measurement run time of 1hour and 34 seconds (Coelho, 2007; Jacobs, 2016). X-ray diffraction patterns and chemical composition were obtained (Appendix 7A) using Bruker Topas 4.1 software.

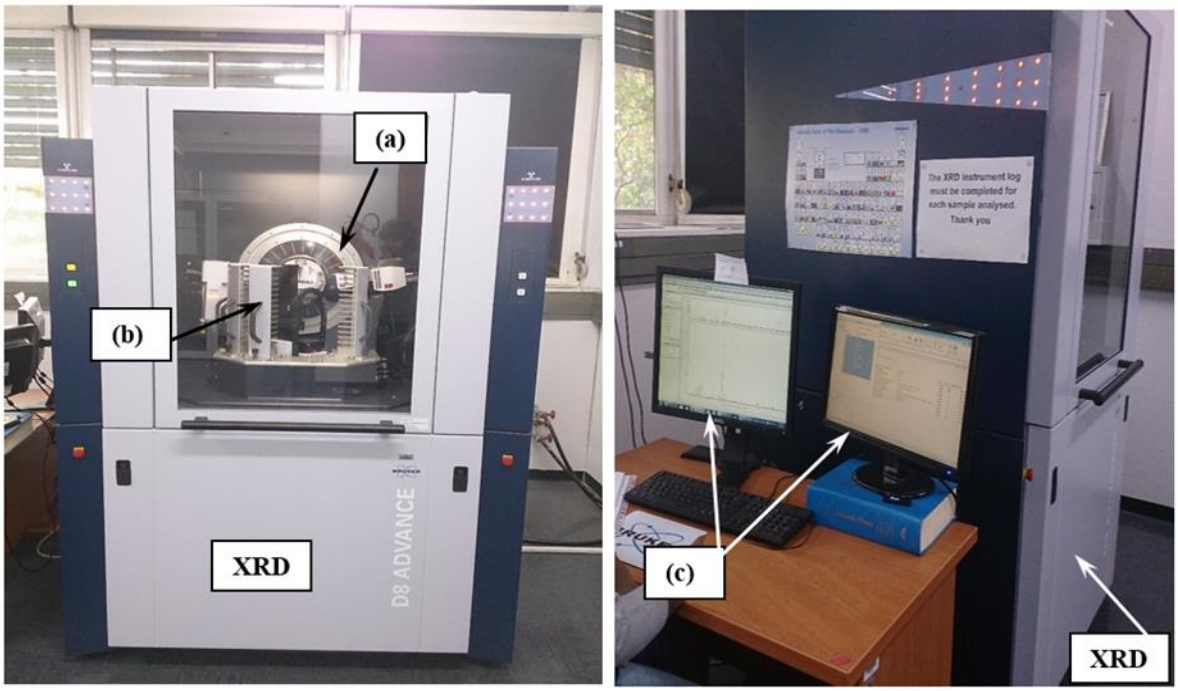


Figure 7.15: A photograph of X-ray powdered diffraction spectrometer used for mineralogical analysis with (a) XRD goniometer that enhouse the sample, optics and detector; (b) XRD sample magazines with sample holder; and (c) Computer monitors for displaying the results.

7.5.2 Results and Interpretation

The XRD patterns or scans and the chemical compositions (Appendix 7A) of the different mineral phases within the disseminated, veined, and brecciated ore samples from both Campbell and Artonvilla copper deposits were analysed and the results were summarised in Table 7.1. A total of 8 samples were analysed.

© University of Venda

The analysed samples revealed the presence of the following minerals in the ore: pyrite, chalcopyrite and sphalerite, pyrite occurring at the outer most alteration zone (Gossan cap of alteration zone). The analysis revealed also the occurrence of hematite, magnetite, graphite and almandine. Hematite is usually associated with oxidation zones of iron ores, formed as a result of the reduction or loss of water from limonite during metamorphic processes. While magnetite is an indicative mineral of high temperature environment which is usually oxidised to hematite and goethite.

Graphite is a carbon mineral that is indicative of metamorphic environment wherein carbon content is reduced which is an indication of high temperature metamorphic zone (Smirnov, 1976). Garnet of almandine group with high Fe content is known to be a high temperature mineral formed at high pressure in metamorphic environment.

The occurrence of several gangue minerals such as quartz, clinochlore, muscovite, calcite, pumpellyite, dolomite and orthoclase were noted in disseminated and veined ores, while quartz and clinochlore occurred in brecciated ore. Gangue minerals such as eastonite, vermiculite, lizardite, talc, ankerite and grunerite were found to occur in veined ore, while epidote, apatite and titanite were in brecciated ore (Table 7.1).

The presence of theses gangue minerals helps in deciphering the processes of ore formation and associated effects such as alteration. For example, pumpellyite is known to be a metamorphic mineral that is formed during the transition of zeolite to prehnite-pumpellyite metamorphic facies which is a low grade metamorphic facies occurring at low temperature and pressure (Harvey *et al.,* 2006). Consequently, the presence of this mineral indicates the early stage of alteration process.

The presence of gangue minerals such as lizardite and grunerite reveals the early alteration process of mafic minerals olivine and amphibole respectively, while mica minerals such as eastonite, vermiculite and muscovite are hydrothermal alteration minerals. Epidote commonly occurs or is generally associated with early hydrothermal alteration in copper deposits (Harvey *et al.,* 2006).

© University of Venda

Table 7.1: Minerals from different ore types detected using X-ray Diffractometry

Mineral Group	Mineral Name	Chemical composition	Ore type	Deposit/ sample ID	Comments
Sulphides	Pyrite	FeS_2	Disseminated Veined Brecciated		Gossan cap in alteration zone
	Chalcopyrite	$CuFeS_2$			Cu ore
	Sphalerite	ZnS			Zn ore, associated with Cu ore
Oxides	Hematite	Fe_2O_3	Veined Brecciated		Fe ore, oxidation zones of Fe ore – limonite loss - H_2O
	Magnetite	Fe_3O_4	Veined		Fe ore, high temp, oxidised -Hem +Gt
Industrial	Almandine	$(Ca_{0.51}Mg_{1.02}Mn_{0.04}Fe_{1.43})$ $Al_{1.98}(SiO_4)_3$	Veined		Fe-garnet–high grade metamorphism
	Graphite	C	Disseminated	Artonvilla Campbell	Reduction of C content - metamorphic zones
Gangue	Quartz	SiO_2	Disseminated Veined Brecciated		Silicate
	Clinochlore	$(Mg,Fe)_6(Si,Al)_4O_{10}(OH)_8$	Disseminated Veined Brecciated		Hydrothermal- altered mafic – association – epidote, sericite, Sulphide – late alt. stage
	Pumpellyite	$Ca_2(Al, Fe^{+2}, Mg)$ Al_2 (Si O_4) $(Si_2O_7)O(OH)\cdot H_2O$	Disseminated Veined		Early hydrothermal, prehnite-pumpellyite met. facies – low grade
	Calcite	$CaCO_3$	Disseminated Veined	Artonvilla Campbell	Late stage in sulphide deposits
	Dolomite	$CaMg(CO_3)_2$	Disseminated Veined		Late stage of mineralisation
	Talc	$3Mg_{O\cdot 4}\,SiO_2\cdot H_2O$	Veined		Late stage of alteration Chlorites altered -talc
	Ankerite	$Ca_{1.01}Mg_{0.45}Fe_{0.54}(CO_3)_2$	Veined		Carbonate – late stage of mineralisation
	Muscovite	$KAl_2(Si,Al)_4\,O_{10}\,(OH)_2$	Disseminated Veined		Alteration in Hydrothermal - sericite
	Vermiculite,	$Mg_3\,Si_4\,O_{10}\,(OH)_2$	Veined		Mica – alteration-
	Orthoclase	$Al_2O_3\cdot K_2O\cdot_6 SiO_2$	Disseminated Veined		Silicate – original rock comp
	Eastonite,	K - Mg - Fe - Al - Si - O - H_2O	Veined		Mica – alteration-hydrothermal
	Lizardite,	$(Mg, Fe)_3\,Si_2O_5\,(OH)_4$	Veined		Alteration of olivine
	Grunerite	$Fe_{5.5}\,Mg_{1.5}\,Si_8\,O_{24}\,H_2$	Veined		Amphibole- Fe host rock mineral
	Epidote	$Ca_2Al_{2.16}\,Fe_{0.84}\,Si_3\,O_{13}\,H$	Veined Brecciated		Early stage alteration
	Apatite	$Ca_5(PO_4)_3\,(OH)$	Brecciated	Campbell	Apatite alteration – indicator of Cu deposit - Last stage of hydrothermal alteration
	Titanite	$CaTi(SiO_4)O$	Brecciated		Indicator of cu mineralised zones/alteration

© University of Venda

Occurrence of clinochlore and talc within the copper orse could be attributed to the fact that in hydrothermal deposits mafic minerals are altered to chlorite which further undergoes intense alteration to talc which is an indication of late stage alteration process. Apatite and titanite minerals are known to be indicators of copper-sulphide mineralisation, thus are used as exploration guide

7.6 X-ray Fluorescence Spectrometry

X-ray Fluorescence Spectrometry (XRF) is currently one of the most widely used analytical technique in the determination of both major and trace elements in ores. Consequently, XRF was used in this study in order to determine the elemental chemistry of the ore from both Campbell and Artonvilla copper deposits. This was done in order to identify the occurrence and distribution of elements within the ore and also to characterize different ore types in terms of their concentration levels.

7.6.1 Sample Preparation and Analysis

Determination of the elemental composition within the ore samples was executed using X-ray fluorescence spectrometry (XRF) technique and for this purpose pressed pellets were prepared. Sample preparation (pellets preparation) and analysis for XRF were both done at the Department of Mineralogy, MINTEK, Johannesburg.

A total of 8 representative samples, four from each deposit, were selected for analysis. For the preparation of the pressed pellets samples, the ore samples were firstly subjected to crushing using a Sturtevant jaw crusher with C-steel plates and milled up to 75 µm particle size (fine powder) in a C-steel head using a Sebtechnik swing-mill (Willis, 1999). The powdered samples were then split into six portions or fractions using RS-212 Retsch rotatory sample splitter. From the divided samples, about 5-6 g of samples were inserted on a cylindrical ring of 13-35 mm diameter. Boric acid powder was used as a binder to prevent powdered samples from falling off or scattering from the pellet surface. The mixture was compressed or moulded using a manual compressor at 10 tons pressure. The pellets were then transferred to a furnace and reheated overnight at 950°C for the determination of loss on ignition (LOI) which is a composite of chemically bound water (H_2O+), carbonates (CO_2) and the oxidation of ferrous iron. Determination of loss on ignition was done following the

© University of Venda

procedure done by Willis (1990). Fusion of accurately weighed 0.0700± 0.001 g of roasted sample mixed with 6.000± 0.001 g of LiT/LiM at a ratio of 57:43 flux was achieved in a Pt-95%: Au-5% crucible with a gas burner to create a fusion disk (Willis, 1990).

Pressed pellets were then used for elemental analysis using a Panalytical Axios Wavelength XRF spectrometer with a 4kW tube. The calibration standards included natural standards of South African Reference Materials (SARM) range and United State Geological Survey (USGS) range as well as artificial standards doped with copper. For matrix corrections, the fundamental parameter method was used as described in Willis and Duncan (2008). The obtained results were saved on an excel spreadsheet (Appendix 7B) and summarised in Table 7.2.

7.6.2 Results and Interpretation

Elemental analysis results obtained from XRF analysis of different ores that included disseminated ore (ATCAL01) and veined ore (ATAVR12) from Artonvilla copper deposit together with veined ore (CPQV01) and brecciated ore (CAMP01) from Campbell copper deposit were interpreted and presented using bar graphs.

Occurrence and distribution of elements

Elements with concentration levels below detection limit (Ag, In, I, Cs, Hf, W and Th) and those with very low concentration values (Ti, V, Cr, and Te) were not included in the interpretation. Consequently, a total of 29 elements were recorded (Table 6.4) and analysed to deduce the distribution of the elements within different ore types (Fig. 7.16).

High concentration levels of various elements were identified in different ore types (Table 7.2 and Fig. 7.16). Disseminated ore had the highest concentration levels of (ppm); Zn (5969.00), Cd (16.90), Pb (115.80), Rb (67.00), Y (18.90), Sn (15.20), and Ba (53.00. Veined ore revealed highest concentration levels of (ppm): Co (153.00), Ni (279.60), As (21.30), Sr (351.70), Mo (15.30), La (24.30), Ce (45.60) and Ta (145.90), while brecciated ore showed highest concentration levels of (ppm): Cu (16430.00) and Zr (141.30).

© University of Venda

Copper and zinc revealed extremely high concentration values compared to other sulphide metals with values of 14950 and 16430 ppm for Cu in veined and brecciated ores respectively from Campbell deposit, and 5969 ppm for Zn within disseminated ore from Artonvilla deposit (Fig. 7.16). This indicates that the Artonvilla deposit is richer in sphalerite than copper minerals. The high concentration of cadmium within disseminated ore that registered the highest concentration of zinc is a further indication that Cd is genetically related to Zinc (Ogola, 1987; Wenk and Bulakh, 2008).

High content of sulphide elements such as Co; Ni; Zn; Cu; As; Mo; Cd and Pb could be attributed to the presence of Cobaltite (CoAsS); Pentlandite $(Ni,Fe)_9S_8$; Sphalerite (Zn,Fe)S; chalcopyrite, cuprite, chalcocite, bornite, tennantite; molybdenite (MoS_2) and galena. Minerals occurring in trace quantities such as tennantite, tetrahedrite, burnonite, boulagerite were deduced from the metal values in the ores (Table 7.2).

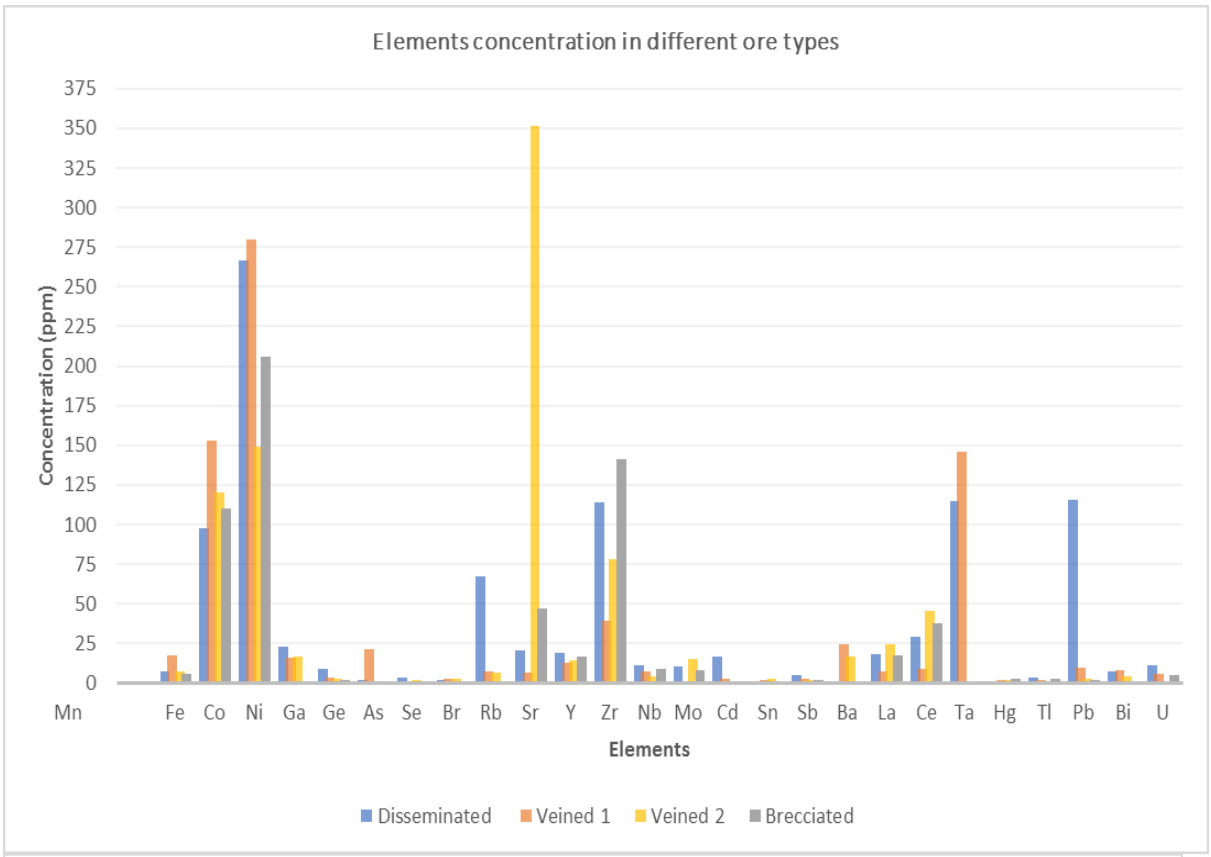
© University of Venda

Table 7.2: Distribution of elements within different ore types at Campbell and Artonvilla copper deposits

		Concentration (ppm)				Comments
Deposit		**Artonvilla**	**Artonvilla**	**Campbell**	**Campbell**	
Sample ID		**ATCAL01**	**ATAVR12**	**CPQV01**	**CAMP01**	
Ore type		**Disseminated**	**Veined**	**Veined**	**Brecciated**	
Element		**Concentration (ppm)**				
Sulphide elements	Mn	0.385	0.094	0.022	0.035	
	Fe	7.031	17.890	7.421	6.148	
	Co	98.000	153.000	120.000	110.000	Cobaltite (CoAsS)
	Ni	266.300	279.600	148.900	205.800	Pentlandite $(Ni, Fe)_9S_8$
	Cu	433.100	92.700	14950.000	16430.000	Cu minerals
	Zn	5969.000	197.000	41.800	49.800	Sphalerite (Zn,Fe) S
	As	2.100	21.300	<0.900	<0.800	Tennantite $Cu_{12}(AsS_3)_4S$
	Mo	10.700	<1.900	15.300	8.500	Molybdenite (MoS_2)
	Cd	16.900	2.400	1.300	0.600	
	Sb	5.400	2.500	2.300	2.100	Tetrahedrite $Cu_{12}(SbS_3)_4S$
	Hg	4.200	2.300	2.200	3.100	
	Pb	115.800	9.700	2.800	2.100	Galena, Bournonite, Boulangerite
	Bi	7.300	7.800	4.000	<1.500	
Trace elements	Ga	23.200	16.200	16.800	<2.300	
	Ge	8.900	3.400	2.400	2.200	
	Se	3.200	<0.900	1.900	1.200	
	Br	1.700	2.700	3.000	1.200	
	Rb	67.000	7.600	6.400	1.400	Lepidolite mica
	Sr	20.400	6.900	351.700	47.200	Strontianite ($SrCO_3$)
	Y	18.900	12.500	14.300	16.500	Yttrium metal
	Zr	113.800	39.700	78.100	141.300	Zircon ($ZrSiO_4$)
	Nb	11.500	7.300	3.900	8.800	
	Sn	15.200	2.100	2.400	<0.700	Cassiterite
	Ba	53.000	24.800	16.500	<4.400	Barite ($BaSO_4$)
	La	18.200	7.700	24.300	17.300	
	Ce	29.300	8.800	45.600	38.100	Monazite
	Ta	115.000	145.900	<99.000	<97.000	Tantalite (Fe, Mn)$Ta0_6$
	Tl	3.800	2.000	1.400	2.600	
	U	11.400	6.200	<3.300	4.900	

= *Highest concentration for each element*

© University of Venda



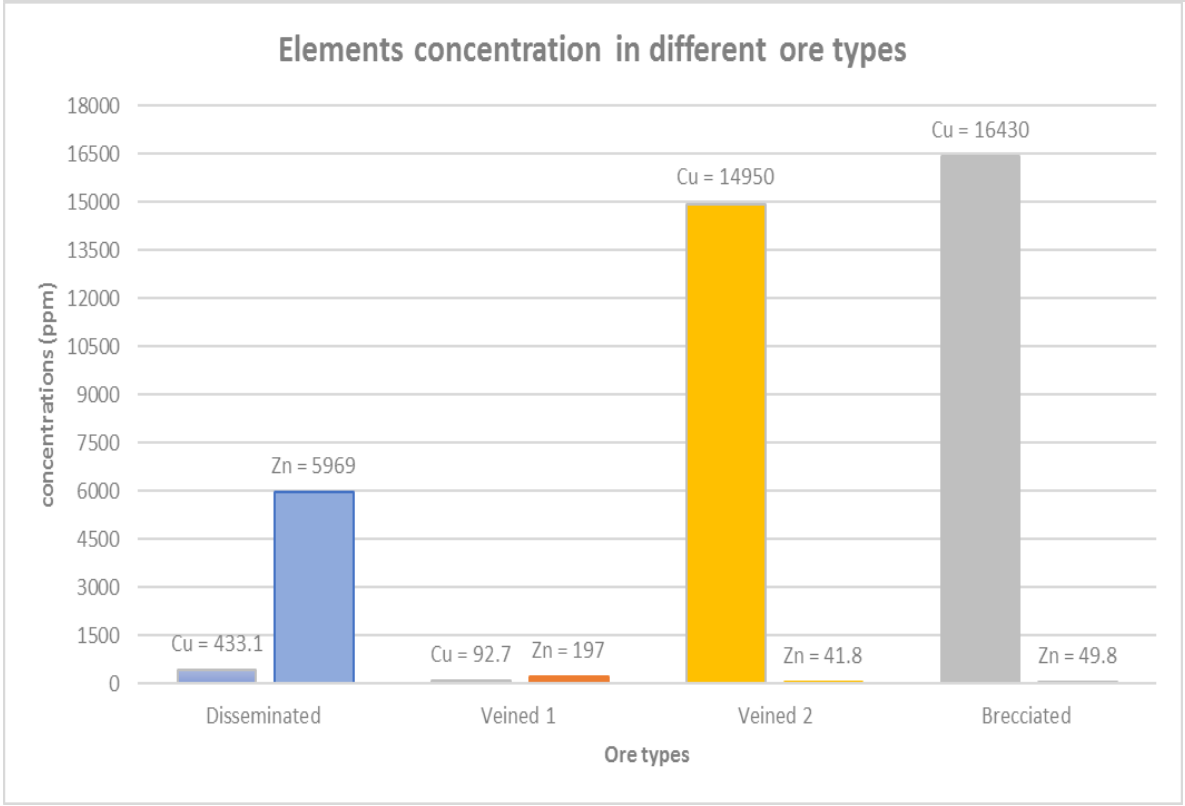


Figure 7.16: Distribution of elements within disseminated, veined and brecciated ores from Campbell and Artonvilla copper deposits (Note: Bar chart for Zn and Cu were plotted separately due to the high concentration).

© University of Venda

7.7 Monomineralic Analysis of Pyrite and Chalcopyrite

7.7.1 Sample Analysis

The same double polished thin sections and polished samples prepared for ore microscopy were used for monomineralic analysis. Two representative samples were selected from each deposit, i.e. CpAmp04 and CpQv01 from Campbell deposit and AtCal and AtGn04 from Artonvilla.

Monomineralic analysis of pyrite and chalcopyrite from Artonvilla and Campbell copper deposits respectively, was conducted so as to determine the elemental composition of these minerals, using JEOL JXA-8530F Hyperprobe from Fayetteville State University, North Carolina, USA. The analysis was done following the procedure by Chaumba *et al.* (2016). The Hyperprobe was operated at a beam current of 30 nA with the accelerating voltage set at 30 kV and a minimum beam diameter of 1mm. The elemental composition was analysed at first by using X-ray energy dispersive spectroscopy (EDS) for qualitative and semiqualitative analysis and thereafter followed by X-ray wavelength dispersive spectroscopy (WDS) for quantitative analysis, using Smithsonian standards. From each phase, three spots were analysed and 15 seconds counting times were used on peak and background measurements. The calculation of the oxides was done using the ZAF matrix correction system (Armstrong, 1988). The results were reported in weight percentages (Table 7.3).

7.7.2 Results and Interpretation

Monomineralic analysis of pyrite and chalcopyrite revealed the dominance of S and Fe in pyrite and S, Fe and Cu in chalcopyrite. Nickel (Ni), Pb, and Co were in trace quantities, whereas, Zn and Mn were below the detection level (Table 7.3).

The concentrations of elements within pyrite and chalcopyrite were used to plot scatter graphs (Fig. 7.17) in order to relate the composition of sulphides from Artonvilla and Campbell copper deposits with other similar previously studied deposits. For example, pyrite and chalcopyrite composition from Artonvilla and Campbell copper deposits compared quite well with the composition of these minerals from other deposits, for example, deposits in

© University of Venda

gabbro from South West Indian Ridge Spreading Centre (Millar and Cervantes, 2002); in South West Oregon Ophiolite from Ophiolite Complex (Foose, 1986); in layered intrusion of the Duluth Complex (Pateris, 1984) and also with the metamorphosed Keivitsansarvi Ni-Cu-PGE deposit in Keivitsa intrusion in Finland (Gervilla and Kojonen, 2002) (Fig. 7.17).

Table 7.3: Chemical composition of pyrite and chalcopyrite

Sulphide crystal	Sample ID	wt%								
		S	Ni	Zn	Cu	Pb	Fe	Co	Mn	Total
Pyrite	AtCal-P 76	53.784	b.d.l.	b.d.l.	b.d.l.	0.056	46.037	0.078	b.d.l.	99.958
	AtCal-P77	53.086	b.d.l.	b.d.l.	b.d.l.	0.068	46.073	0.071	b.d.l.	99.298
	AtCal-P78	52.815	b.d.l.	b.d.l.	b.d.l.	0.149	45.332	0.088	b.d.l.	98.39
	AtCal-P79	53.193	0.438	b.d.l.	b.d.l.	0.155	45.005	0.228	b.d.l.	99.028
	AtCal-P81	53.268	b.d.l.	b.d.l.	0.025	0.158	46.058	0.094	b.d.l.	99.613
	AtCal-P82	52. 697	b.d.l.	b.d.l.	0.009	0.064	45.93	0.1	b.d.l.	98.805
	AtCal-P83	53.176	b.d.l.	b.d.l.	0.014	0.148	46.255	0.086	b.d.l.	99.681
	AtCal-P84	53.285	0.008	b.d.l.	b.d.l.	0.189	46.104	0.072	b.d.l.	99.663
	AtCal-P85	51.4536	0.005	b.d.l.	b.d.l.	b.d.l.	44.72	0.074	b.d.l.	96.235
	AtGn04-P1	53.934	0.074	b.d.l.	0.01	0.142	45.194	0.113	b.d.l.	99.467
	AtGn04-P2	55.959	0.062	b.d.l.	b.d.l.	0.097	44.549	0.215	b.d.l.	100.882
	AtGn04-P3	52.238	0.07	b.d.l.	0.012	0.068	45.434	0.145	b.d.l.	97.967
	M.D.L.	0.003	0.0043	0.0053	0.0044	0.0273	0.0027	0.0033	0.0032	
Chalcopyrite	CpAmp04-P1	33.706	0.007	b.d.l.	33.474	b.d.l.	29.432	0.057	b.d.l.	96.68
	CpAmp04-P2	33.088	b.d.l.	b.d.l.	33.591	0.214	29.051	0.074	b.d.l.	96.018
	CpAmp04-P3	33.813	0.006	b.d.l.	33.405	0.038	29.489	0.053	b.d.l.	96.804
	CpAmp04-P4	33.794	b.d.l.	b.d.l.	33.722	0.1	29.742	0.069	b.d.l.	97.427
	CpAmp04-P5	34.115	b.d.l.	b.d.l.	33.452	b.d.l.	29.477	0.067	b.d.l.	97.128
	CpAmp04.P13	34.034	b.d.l.	b.d.l.	33.473	0.079	29.475	0.058	b.d.l.	97.126
	CpAmp04-P14	33.589	b.d.l.	b.d.l.	33.501	0,147	29.488	0.046	b.d.l.	96.771
	CpAmp04-P15	33.697	b.d.l.	b.d.l.	33.702	0.108	29.63	0.074	b.d.l.	97.23
	CpAmp04-P16	34.101	0.006	b.d.l.	33.626	0.048	29.584	0.055	b.d.l.	97.42
	CpAmp04-P17	33.673	b.d.l.	b.d.l.	33.438	0.03	29.336	0.059	b.d.l.	96.557
	CpQv01-P17	35.706	b.d.l.	b.d.l.	33.798	b.d.l.	29.117	0.053	b.d.l.	98.718
	CpQv01-P18	36.34	b.d.l.	b.d.l.	32.861	0.108	28.096	0.066	0.004	87.479
	M.D.L.	0.003	0.0043	0.0053	0.0044	0.0273	0.0027	0.0033	0.0032	

M.D.L = minimum detection limit; b.d.l = below detection level

Pyrite composition from the host rock and ore samples revealed Ni and Co concentrations which were comparable to the composition of the other previously studied deposits with the exception of the Keivitsansarvi Ni-Cu-PGE deposit (Fig. 7.17a and b) while Fe is comparable to those of Indian Ridge gabbro (Fig. 7.17a and b). The Fe from Artonvilla was seen to be higher than that of Keivitsansarvi Ni-Cu-PGE deposit, while Ni and Co were seen to be lower than that of the Keivitsansarvi Ni-Cu-PGE deposit (Fig. 7.17a and b).

© University of Venda

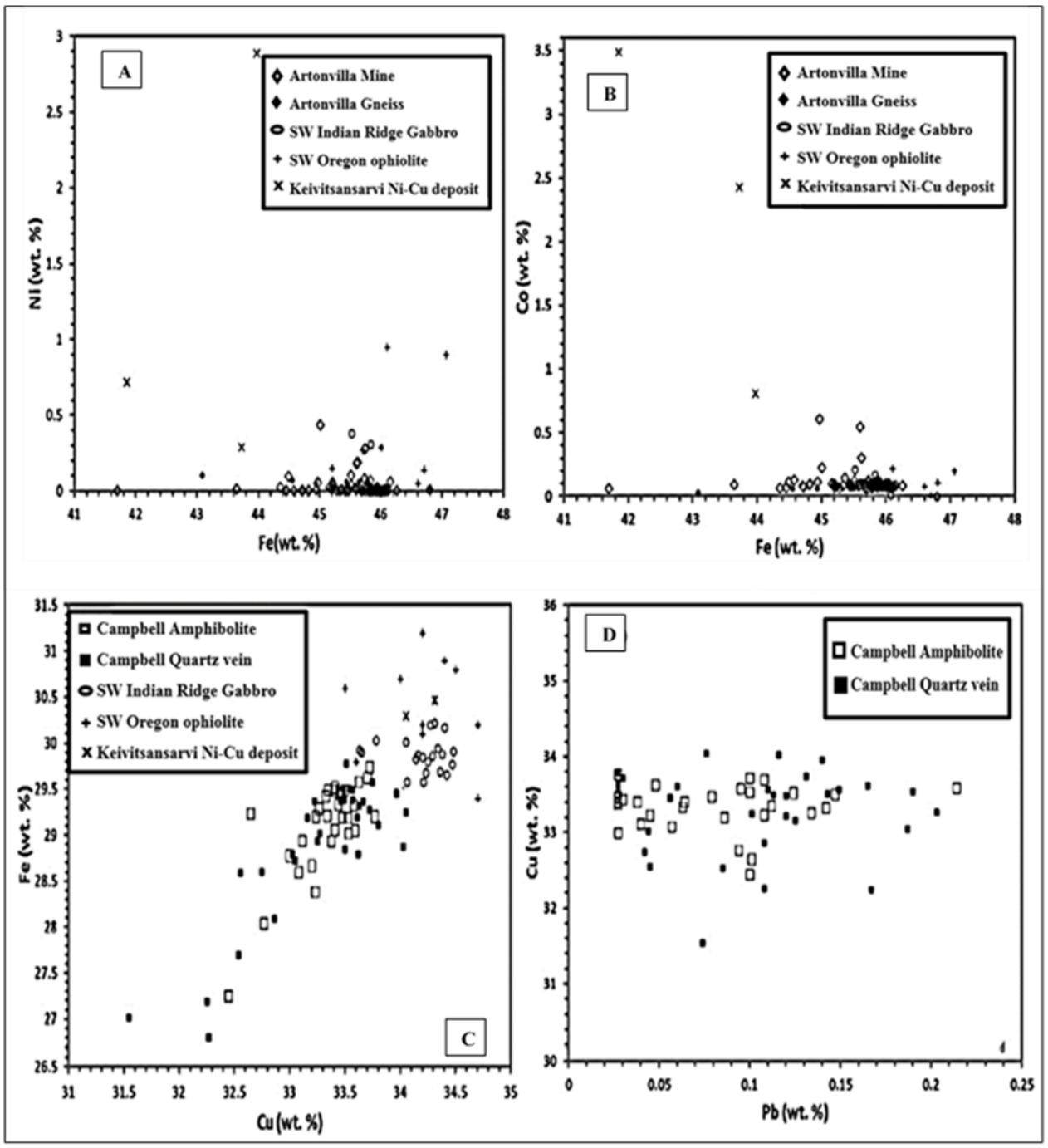


Figure 7.17: Scatter plots for pyrite and chalcopyrite composition form Artonvilla and Campbell copper deposits compared to sulphide compositions from previously studied deposits: (A) wt% Ni and wt% Fe scatter plot of pyrite; (B) wt% Co and wt% Fe scatter plot of pyrite; (C) wt% Fe and wt% Cu scatter plot of chalcopyrite; and (D) wt% Cu and wt% Pb scatter plot of chalcopyrite.

© University of Venda

This implied that there was more Fe substitution in the Keivitsansarvi Ni-Cu-PGE deposit than in Artonvilla copper deposit. Consequently, this means that pyrite from Artonvilla copper deposit was characterised by less substitution of Fe by Ni and Co to form pentlandite and cobaltite respectively.

Fe and Cu in chalcopyrite from Campbell copper deposit revealed positive correlation (Fig. 7.17c), but with Fe and Cu content lower than that of other deposits. This suggests that at Campbell, copper ore mineralisation was not hosted predominantly in chalcopyrite, but rather in other sulphide minerals such as bornite, chalcocite. Chalcopyrite from Campbell copper deposit revealed wide range concentration levels of Pb over a narrow range concentration levels of Cu with no correlation between Pb and Cu values (Fig. 7.17.d).

Pyrite and chalcopyrite composition were also used to plot ternary diagrams in order to relate the concentrations of S, Fe, Cu, Ni and Co (Fig. 7.18). The Fe-Ni-S ternary diagram (Fig. 7.18a) was used to plot the composition of pyrite from Artonvilla copper deposit. Low wt% Ni and Co was revealed and they plotted near the pyrite point which is consistent with pyrite crystallization.

A ternary diagram of Fe-Cu-S system at 300°C (Barton and Skinner, 1979) (Fig. 7.18b) was used to plot chalcopyrite composition from Campbell copper deposit. The chalcopyrite composition within quartz vein plots near chalcopyrite point with a trend from high S and low Fe to low S and high Fe next to copper constant concentration of about 33 wt% Cu. The chalcopyrite composition within amphibolite revealed Fe and Cu concentration trend of high Fe and low Cu of 31 wt% Cu to low Fe and high Cu concentration of about 36 wt % Cu (Fig. 7.18b). The trend shown by amphibolite is consistant with the immiscibility of both S and Fe, which then led to the increase of Cu in sulphide minerals thereafter settled out later leading to the formation of these deposits.

© University of Venda

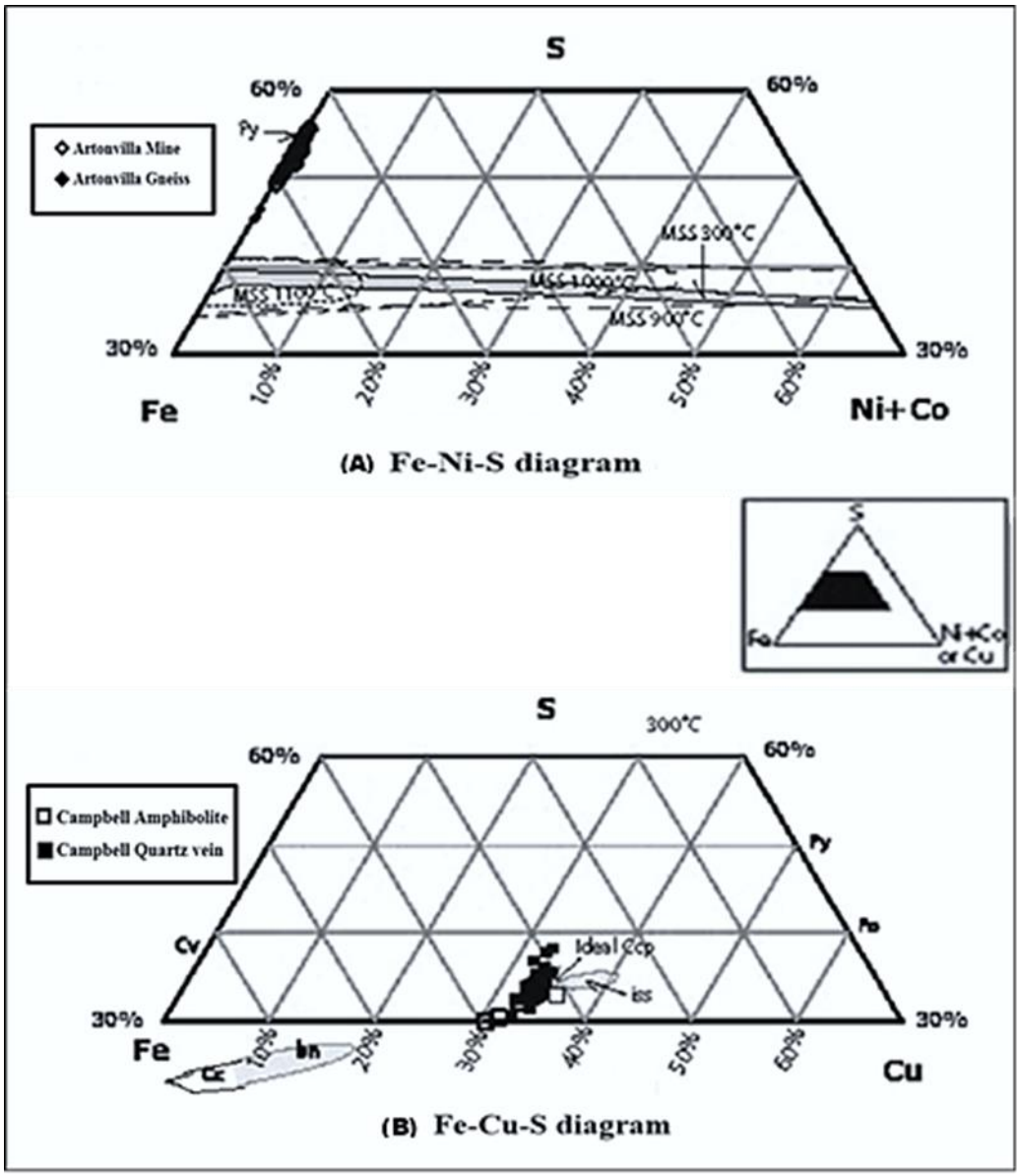


Figure: 7.18: (A) Fe- Ni-S ternary diagram showing pyrite (Py) elemental composition (wt%) from Artonvilla mine and high temperature mono-sulphide solid solution (mss) fields of Kullerud *et al.* (1969); (B) Fe-Cu-S ternary diagram at 300°C Fe-Cu-S system (Borton and Skinner, 1979) showing chalcopyrite (Ccp) elemental composition (wt%) from Campbell copper deposit. Different phases such as bornite (Bn), pyrite (py), pyrrhotite (Po), chalcocite (Cc), Chalcopyrite (Ccp), covellite (Cv) and intermediate solid solution (iss) are also indicated.

© University of Venda

7.8 Mineral Paragenesis

The process of mineral formation in the Messina copper deposits took place in two distinct stages: Firstly, the formation of industrial minerals such as garnet and graphite; and formation of ore minerals such as magnetite and hematite; and secondly, later sulphide mineralisation. The mineral formation processes occurred in four distinct stages: Stage I (Garnet- graphite – Fe oxides); stage II (Quartz- pyrite); stage III (Pyrite- sphalerite - chalcopyrite); and stage IV (Carbonate). The identification of these stages is based on processes of their formation, mineralogical assemblages, textural characteristics and on their mutual relationship, for example, grain boundaries. The mineral paragenesis (sequence of mineral formation) is illustrated in Table 7.4.

Stage I: Garnet - graphite – Fe oxides assemblage

Garnet, graphite, magnetite and hematite occurred in amphibolite that is highly chloritized and within granulite rocks, namely; garnet gneiss, quartzo-feldspathic gneiss, hornblende granulite from both Artonvilla and Campbell deposits. The garnet and graphite are associated with regional metamorphism of the Limpopo Mobile Belt. The magnetite grains were corroded by later minerals such as hematite, pyrite, chalcopyrite and carbonates. Regional metamorphosed deposits of iron ores are widespread in the Pre-Cambrian rocks and to some extent in the lower Paleozoic period. Occurrence of magnetite and hematite within such rocks as amphibolite are well documented (Smirnov, 1976).

The formation of these minerals is attributed to regional metamorphism of the Limpopo Mobile Belt that pre-ceded copper-sulphide mineralisation in the area. The current study established the presence of garnet, graphite, magnetite as primary minerals and hematite as secondary mineral by means of a range of analytical techniques comprising ore-microscopy, scanning electron microscopy and X-ray powder diffractometry.

Garnet of almandine type was identified within the granulite rocks which are associated with regional metamorphism. Mostly garnet was associated with feldspars mainly potassium feldspars such as orthoclase (Fig. 7.5) during the granulite stage of metamorphism where garnet mainly develops from biotite and muscovite. It was seen to have displaced and replaced early formed minerals such as quartz and potassium feldspars (Fig. 7.5). In some

© University of Venda

instances, inclusion of first generation of quartz were identified within the garnet grains which was found to be the same quartz infilling around the garnet grains and associated with pyrite. This implies that garnet is the earlier formed mineral and infiltrated by quartz (1st generation) with pyrite that were formed later (Fig. 7.5). Alteration of garnets occurred during replacement process which started around the grain boundaries and into its fractures, which implied that garnet was formed earlier and alteration process occurred later (Fig. 7.5).

Graphite is also a product of regional metamorphism. It was seen to occur in the form of undulating laths running parallel to each other (Fig. 7.6). In some instances, graphite laths were separated into thinner flakes by chlorite and later formed quartz (Fig. 7.6). In places, alteration process triggered by chloritization occurred across the graphite crystal (Fig. 7.6B). In some instances, folded flakes of graphite (Fig. 7.6D) occurred in granulite rocks suggesting the increase in metamorphism.

Magnetite was seen to occur as grains in polished ore surface (Fig. 7.7A and B). In places, it was either partially or totally replaced by hematite as pseudomorphous crystals, replacement that started from the grain boundaries to the centre (Fig. 7.7A). Hematite occurred either as blades within the replaced magnetite or as needles within the quartz grains (Figs. 7.A and B). In some instances, partially or totally replaced magnetite was cut across by early formed anhedral to subhedral pyrite crystals separating the magnetite into two (Fig. 7.7E). Euhedral grains of garnets were seen to be replaced by hematite where hematite occurred as tiny blades and relics of replaced garnet were retained within the psuedomorphous grains (Fig. 7.6B). The allotriomorphic grains of pyrite were replaced along the grain boundary and within the microfractures triggered by the influx of carbonate solution (Fig. 7.C and D).

Stage II: Quartz – pyrite assemblage

Quartz veins and stringers which conform to the regional strike of the host rocks were encountered with early formed quartz intruding amphibolite (Plate 7.1B) and in places, filling the microfractures of garnet, resulting in box-work texture with remnants of garnet in quartz (Fig. 7.5C). An early generation of quartz vein is rarely mineralised, but later formed quartz veins contain sulphide mineralisation mainly pyrite and some chalcopyrite (Plate 7.1A). Later formed quartz (Qtz 2) with sulphide mineralisation mainly pyrite and some

© University of Venda

chalcopyrite occurred as influx between the early formed quartz (Qtz 1) grains (Figs. 7.13B, C, D and 7.19).

Table 7.4: Paragenesis of the Campbell and Artonvilla minerals

Stages	**I**	**II**	**III**		**IV**
Assemblages / **Minerals**	**Garnet – graphite - Fe Oxides**	**Quartz – pyrite**	**Pyrite – sphalerite-chalcopyrite**		**Carbonate**
Garnet	▬▬				
Graphite	▬▬				
Magnetite	———				
Hematite	———				
Quartz	▬▬▬	▬▬▬	▬▬▬		
Pyrite		———	▬▬▬		
Sphalerite				▬▬▬	
Chalcopyrite				▬▬▬	
Pyrrhotite				———	
Galena				———	
Pentlandite				- - - - - - -	
Tennantite. molybdenite cobaltite Tetrahedrite				- -	
Calcite Dolomite Ankerite					|||||||| - - - - - - - - - - - - - - - -
Characteristic of paragenetic association	Garnet, graphite, magnetite, hematite, early formed quartz (Qtz 1)	Later formed quartz (Qtz 2), early formed pyrite	Later formed quartz (Qtz 3), sphalerite, chalcopyrite, later formed pyrite,		Calcite, dolomite, ankerite
Ore structure	Veined disseminated, brecciated,	Veined, brecciated, disseminated	Veined, disseminated, brecciated	Brecciated, veined, disseminated	Brecciated, veined, disseminated
▬▬ Dominant	||||| Major	——— Minor	- - - - - - Trace		

Note: Secondary copper minerals: Bornite, chalcocite, malachite, azurite, covellite, cuprite
Native mineral: Copper

© University of Venda

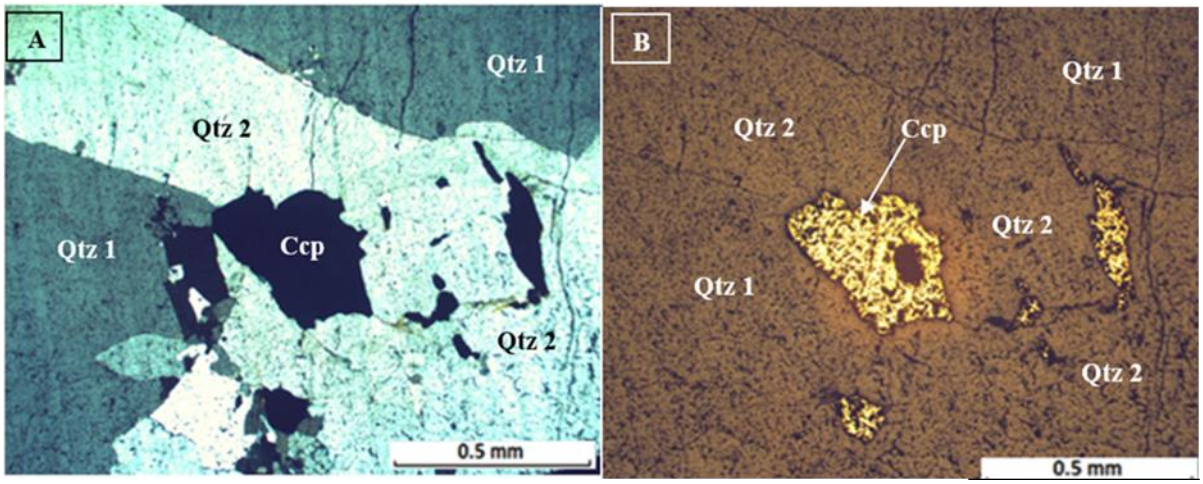


Figure 7.19: Photomicrograph of sample CPQtz03 from Campbell copper deposit showing: (A) early formed quartz (Qtz 1) grains in transmitted light; and (B) in reflected light of later formed quartz (Qtz 2) grains with chalcopyrite (Ccp) within quartz 2.

Early formed pyrite is usually anhedral. Allotriomorphic pyrite was emplaced along the microfractures of garnet together with early formed quartz (Fig. 7.5D). In places, anhedral pyrite was oxidised to hematite which was further oxidised to goethite and oxidation started from the grain boundary (Fig. 7.7C and D; and Fig. 7.9A). At this stage, early formed quartz is evidenced by relics of quartz within pyrite grains and the latter was seen to be replaced by sphalerite (Fig. 7.9A and E). At the same time, pyrite was seen to be enclosed by later formed chalcopyrite (Fig. 7.9A). Sulphide mineralisation mainly pyrite and traces of chalcopyrite were deposited within later formed quartz (Qtz 2) (Figs. 7.13 B and C).

Stage III: Pyrite - sphalerite - chalcopyrite assemblage

Pyrite-sphalerite-chalcopyrite assemblage is typical of veined, brecciated and disseminated ores. The assemblage is mainly characterised by later formed quartz (Qtz 3), later formed euhedral pyrite as well as sphalerite and chalcopyrite with minor pyrrhotite and galena while pentlandite, tennantite, tetrahedrite, molybdenite and cobaltite occurred as traces (Table 7.4). Chalcopyrite, pyrite and sphalerite occurred together with later quartz (Qtz 3) between garnet (Grt) and earlier quartz (Qtz 2) (Fig. 7.13 D). Sphalerite was seen to be replacing anhedral pyrite (Fig. 7.9E) and in places, sphalerite and chalcopyrite replaced euhdral pyrite (Fig. 7.9G). In places, the replacement was at advanced stage, whereby the euhedral pyrite was replaced by secondary copper minerals, namely; covellite, bornite and chalcocite (Fig.

© University of Venda

7.11D). Disseminated blebs of chalcopyrite were seen in several crystals of sphalerite within all types of ores (Fig. 7.9D and F). Inclusion of chalcopyrite in sphalerite, apparently, is due to both co-precipitation and influx of iron and copper in early formed sphalerite (Bortnikov *et al.,* 1991).

Pyrrhotite occurred as tiny grains in trace amounts (Table 7.4) and was strongly anisotropic in crossed polars. It was seen to occur together with galena (Fig. 7.10B). High concentration of As, Mo and Co revealed by XRF apparently suggests the presence of tennantite, molybdenite, and cobaltite in the ore. Galena was characterized by parting or cleavage with parallel rows of triangular pits that showed no sign of deformation (Fig. 7.10A and B). Galena occurred in association with anhedral pyrite and sphalerite with sphalerite replacing pyrite (Fig.7.10.A).

Anhedral pentlandite was identified by SEM and it occurred as inclusions within nickel-rich pyrite, while small grains of pyrite occurred either along the margins of pentlandite and Ni-rich pyrite or at the crystal margin of euhedral later formed quartz (Qtz 2) (Fig. 7.14). Nickel content within the euhedral pyrite could be attributed to the occurrence of traces of pentlandite. The presence of pyrite together with nickel-rich pyrite and pentlandite implies that pyrite was the first sulphide mineral to crystalize at high temperature, but at a later stage, later pyrite was crystallized from the solution with preferential concentration of nickel in this pyrite while rejected nickel and iron diffused away to form pentlandite. During this stage mineralisation took place together with alteration processes of host rock such as chloritization of amphiboles and pyroxenes (Fig. 7.9E and F).

Stage IV: Carbonate Assemblage

Minerals of this assemblage comprised calcite, dolomite and ankerite with calcite occurring as major carbonate while dolomite and ankerite occurred in trace amounts. These minerals were the last to be deposited in both Campbell and Artonvilla copper deposits (Table 7.4).

X-ray diffractometry revealed the occurrence of calcite ($CaCO_3$), dolomite [$CaMg(CO_3)_2$] and ankerite [$Ca_{1.01}Mg_{0.45}Fe_{0.54}(CO_3)_2$] within the ore (Appendix 6A). These minerals were difficult to differentiate under ore microscopy. Hand specimen investigation, however, established the occurrence of calcite veins within the ore (Plate 7.8). Calcite was

© University of Venda

characterised by whitish to creamy colour with rhombic crystals exhibiting vitreous luster and was transparent. Calcite formed veins that cross-cut mineralised amphibolite (Plate 7.8).

In Figure 7.2, the sharp contact between calcite and fractured garnet, microfractures of which are filled with quartz (Qtz 2) and earlier formed pyrite. The contact between calcite and later formed quartz (AQtz 3) is also sharp (Fig. 7.2C). Calcite was also seen to be replacing later formed euhedral pyrite (Fig. 7.8B). Calcite veinlets were further confirmed through the study of cathodoluminescence that cross- cut quartz in sample CPdis03 from Campbell copper deposit (Fig. 8.15). Consequently, this assemblage marks the end of ore mineralisation within the Campbell and Artonvilla copper deposits.

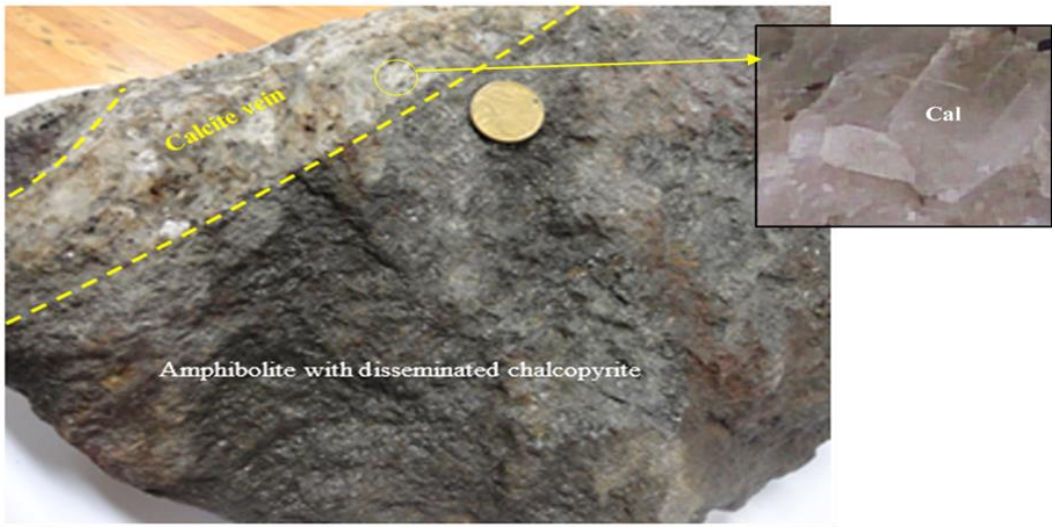


Plate 7.8: A photograph showing calcite (Cal) vein cutting across amphibolite with disseminated sulphide mineralisation from Artonvilla copper deposit (Sample Atcal01).

Dolomite and ankerite are carbonate minerals with closely related mineral composition wherein ankerite differs from dolomite by having magnesium that is replaced by varying amounts of iron (II) and manganese (Reeder and Dollase, 1989). These two minerals occurred in trace amounts, thus were only detected by XRD analysis (Appendix 7A).

7.9 Discussion

Ore mineralogy and ore-microscopy study aimed at the investigation of ore types, mode of occurrence, mineral assemblages and paragenesis of the Campbell and Artonvilla copper deposits.

© University of Venda

7.9.1 Ore Types and Mode of Occurrence

According to Evans and Moon (2006) and Misra (2000), mode of ore occurrence is defined as the pattern of distribution of ore minerals within a host rock which could be either visible or invisible with a naked eye, but could be visible using ore microscopy. For example, mineralisation style could be of disseminated, veined, brecciated, stockwork, strata-bound.

Jacobsen and McCathy (1976) noted that the orebodies of the Messina deposits were of three types; breccia pipes, fissure deposits and disseminated replacement ore bodies. They further noted that the breccia pipes were either mineralised or were devoid of any sulphide mineralisation. Two mineralised breccia pipes were each identified at Campbell and Artonvilla deposits. Söhnge (1946), however, noted that the breccia pipes exhibited collapse features with interfragmental quartz, albite and sulphide fillings.

Veined ore apparently was associated with the structural features within the Musina area such as the Messina and Towe-Tokwe faults. Söhnge (1946) noted that vein deposits were generally found to emanate from the breccia pipes.

Jacobsen (1974) concluded that disseminated replacement ores occurred in suitable structural traps accompanied by extensive hydrothermal alteration especially in the Artonvilla deposit. Sawkins (1977) noted that hydrothermal replacement of the host rock resulted in dissolution of silica and formation of central core of albetized rock surrounded by an envelope of sericitic alteration. He further observed that the orebodies were concentrically zoned in much the same way as the alteration sequences, with disseminated pyrite forming an envelope around the ore bodies succeeded inwards by a zone of chalcopyrite then bornite. The central potion was occupied by chalcocite and small amounts of native copper.

The current study identified three different types of mode of ore occurrence within the Campbell and Artonvilla copper deposits in the Musina area, namely; veined, disseminated, and brecciated ores. Both macro- and microscopic investigation revealed veined ore that occurred in quartz vein that was seen to cut across the host rocks, mainly amphibolite. Within quartz vein, mineralisation occurred along micro-fractures, resulting in ore stockworks with quartz stringers. Fine to medium-grained disseminated ore consisted mainly of pyrite and

© University of Venda

chalcopyrite and rarely bornite, distributed within host rocks such as amphibolite and quartz vein. Coarse texture of brecciated ore with sulphide mineralisation surrounding quartz and amphibolite breccias, was identified at the two deposits. Formation of ore was accompanied with chloritization.

7.9.2 Mineralisation

Mineralisation within Campbell and Artonvilla copper deposits consisted of industrial and ore minerals. Current study established different types of industrial minerals such as garnet and graphite. Garnet was mainly found associated with granulite rocks such as garnet gneiss, quartzo-feldspathic gneiss, hornblende granulite. Formation of garnet in the granulite rocks was associated with regional metamorphism that occurred during the formation of the Limpopo Mobile Belt. The occurrence of garnet was associated with orthoclase which according to Smirnov (1976) is generally formed together with garnet in rocks of the granulite facies, where almandine is developing from biotite and muscovite. Large grains of garnet revealed fracturing that was infilled with sulphide minerals and the host rocks were seen to have undergone chloritization. The presence of infilled mineralised microfractures and occurrence of chlorite were attributed to the influx of hydrothermal fluids that resulted in the deposition of sulphide minerals. Traditionaly, mineralogists used to classify garnets using 50 to 50% rule as stated by Hanneman (2008) who later developed the Hanneman's concept. The geochemical analysis of the garnet grains, suggested an almandine member following the traditional classification, with varying proportion of low composition of pyrope, grossular and spessartine . Following the Hunneman's concept, the garnet in this study was found to be pyrope-almandine (Hanneman, 2008), where in pyrope-almandine falls within the range of 30-70% almandine. Consequently, the alteration of garnet to deep blue chlorite (rich in Fe) is consistent with the presence of almandine member which is also Fe-rich. This pyrope-almandine was found to be associated with potassium feldspar that is generally formed together with rocks of granulite facies, where almandine is developing from muscovite and biotite (Smirnov, 1976). This indicates that garnet was formed during the early stages of mineralisation.

The study also revealed the occurrence of graphite in both Campbell and Artonvilla copper deposits. Visible laths of graphite occurred within the amphibolite schists and garnet gneiss.

© University of Venda

Microscopically, the laths occurred as elongated flakes ranging from 500 µm up to 4300 µm with a thickness range of 50 µm to 100 µm and rarely greater than 100 µm. Consequently, these flakes of graphite were classified as fine textured using Mitchell's classification scheme (Mitchel, 1993), hence they are of economic importance. Highly folded flakes of graphite are attributed to high grade metamorphism.

The main oxide minerals within these deposits included magnetite and hematite with magnetite oxidised to hematite then to goethite due to chemical weathering. Two types of magnetite were revealed within these two deposits, apparently, earlier formed allotromorphic magnetite and later formed euhedral octahedral crystals which were both either totally or partially replaced by hematite. In the same manner, hematite was formed in two stages that was due to regional metamorphism, forming plates and the second that occurs as replacement product, having replaced garnet.

The study revealed the occurrence of primary sulphide ore minerals such as pyrite, chalcopyrite, sphalerite, galena, pyrrhotite and pentlandite. Both idiomorphic and allotriomorphic pyrite were revealed together with chalcopyrite and sphalerite**.** Chalcopyrite inclusions in sphalerite are considered to be due to exsolution resulting into chalcopyrite disease as a result of replacement of Fe-rich sphalerite. This position has been contested by other researchers, for example, Bortnikov *et al.* (1991) noted that chalcopyrite inclusions are formed in both Fe-rich (8 – 14wt% Fe) and Fe-poor (0.5 – 2wt% Fe) sphalerite. They further concluded from their study that chalcopyrite inclusions were produced by replacement as a result of interaction of sphalerite with solution that transported both copper and iron. They also proposed the coprecipitation of sphalerite and chalcopyrite. Galena occurred with triangular pits which did not show any curvature features, thus no evidence of deformation. While pyrrhotite occurred as tiny grains. These primary sulphide minerals were subjected to secondary alteration resulting in the formation of malachite, azurite, bornite, covellite, cuprite, and chalcocite. Native copper was relatively rare in the ore.

The use of scanning electron microscopy revealed occurrence of anhedral crystal of pentlandite together with euhedral Ni-pyrite occurring around the crystal boundary of euhedral later formed quartz (Qtz 2) with relics of pyrite. The nickel content within the euhedral pyrite could be attributed to the occurrence of traces of pentlandite. Pyrite was the

© University of Venda

first to crystalize at high temperature and at a later stage second generation pyrite was crystallized from the solution with preferential concentration of nickel in this pyrite while rejected nickel and iron diffusing away to form pentlandite.

The use of XRD and XRF revealed presence of the following minerals: Pyrite, chalcopyrite, sphalerite, hematite, magnetite, almandine, graphite, quartz, clinochlore, muscovite, calcite, pumpellyite, dolomite, orthoclase, eastonite, vermiculite, lizardite, talc, ankerite, grunerite, epidote, apatite, titanite, cobaltite, tennantite, molybdenite, bournonite, boulangerite, lepidolite mica, strontianite, yttrium metal, zircon, cassiterite, barite, monazite and tantalite. The study thus, identified a number of new ore minerals which were previously unknown in these deposits. This included; tennantite, cobaltite and tetrahedrite.

Sulphide mineralisation were composed mainly of pyrite, chalcopyrite and sphalerite and other sulphide minerals such as cobaltite, tennantite, molybdenite, bournonite,, boulangerite and were associated with oxides minerals namely; magnetite and hematite as well as the gangue minerals such as quartz, calcium, dolomite, and other rock forming minerals. This study confirms that sulphide mineralisation took place within metamorphosed terrain in which earlier formed minerals such as magnetite, hematite, graphite and almandine were product of metamorphism. The study also confirms that the processes of sulphide mineralisation was associated with host rock alteration resulting into the formation of the secondary minerals such as chlorites, epidote, sericite, apatite, titanite etc. Thus, these analyses confirm alteration of host rocks as was identified during petrographic studies. The carbonates mainly calcite, dolomite, ankerite mark the last stage of sulphide mineralisation in Campbell and Artonvilla copper deposits. These have further been confirmed by ore microscopy and cathodoluminescence studies. These processes support hydrothermal mode of ore formation.

Mineralogical investigation of the Messina copper deposits revealed that the Artonvilla deposit was richer in sphalerite than copper minerals. The high concentration of cadmium within disseminated ore that registered the highest concentration of zinc is a further indication that Cd is genetically related to Zinc. This genetically relationship between Zn and Cd has been confirmed through other studies. For example, a study conducted by Ogola (1987) at Migori Greenstone Belt Macalder in Kenya; and study conducted by Wen *et al.* (2016) on

© University of Venda

determination of Zn/Cd ratio and cadmium isotope as evidence for the classification of lead zinc deposits.

Monomineralic analysis of pyrite and chalcopyrite revealed the dominance of S and Fe in pyrite and S, Fe and Cu in chalcopyrite. Nickel (Ni), Pb, and Co were in trace quantities. The elemental composition of these minerals compared quite well with pyrite and chalcopyrite from other deposits, for example, deposits in gabbro from South West Indian Ridge Spreading Centre (Millar and Cervantes, 2002); in South West Oregon Ophiolite from Ophiolite Complex (Foose, 1986); in layered intrusion of the Duluth Complex (Pateris, 1984) and also with the metamorphosed Keivitsansarvi Ni-Cu-PGE deposit in Keivitsa intrusion in Finland (Gervilla and Kojonen, 2002).

A comparison of the Fe, Ni and Co content in pyrite from Artonvilla deposit to that of the Keivitsansarvi Ni-Cu-PGE deposit revealed that Fe in pyrite from Artonvilla was higher than that of Keivitsansarvi Ni-Cu-PGE deposit, while Ni and Co was the opposite. This implied that there was more Fe substitution in the Keivitsansarvi Ni-Cu-PGE deposit than in Artonvilla copper deposit. Consequently, pyrite from Artonvilla copper deposit was characterised by less substitution of Fe by Ni and Co to form pentlandite and cobaltite respectively, hence the low values of these metals at Artonvilla deposit. A comparison of Fe and Cu content in chalcopyrite from Campbell deposit with other deposits mentioned above revealed lower values, suggesting that at Campbell deposit, copper ore mineralisation was not hosted predominantly in chalcopyrite, but rather in other sulphide minerals such as bornite, chalcocite.

7.9.3 Mineral Assemblages and Paragenesis

Mineral formation in the Messina copper deposits took place in two distinct phases: Firstly, the formation of minerals such as garnet, graphite, magnetite and hematite; and secondly, later sulphide minerals. Previously, Jacobsen and McCathy (1976) had presented an idealized paragenetic chart for the mineralised breccia pipes of the Messina copper deposits. This chart indicated both rock forming minerals and their alteration, and sulphides in general. The chart did not specify the paragenetic sequence of the industrial and sulphide minerals.

© University of Venda

The current study, however, identified four stages of mineralisation that occurred within two main phases, namely: Stage I (Garnet- graphite – Fe oxides) from regional metamorphism; stage II (Quartz- pyrite); stage III (Pyrite- sphalerite - chalcopyrite); and stage IV (Carbonates). In Stage I, it was noted that garnet, graphite and magnetite occurred as primary minerals and hematite as both primary and secondary mineral. These industrial minerals were formed during regional metamorphism of the Limpopo Mobile Belt that pre-ceded copper-sulphide mineralisation in the area. Both magnetite and garnet were replaced by hematite. Magnetite was replaced from the grain boundary inwards, whereas garnet was replaced along its grain boundary and microfractures as this mineral was highly fractured. Magnetite was either partially or totally replaced by hematite as pseudomorphous crystals. Graphite, also a product of regional metamorphism, consisted of laths which were separated into thin flakes due to chloritization. These minerals occurred within early quartz (Qtz 1) that was also a product of metamorphism characterised by highly chloritized amphibolite, garnet gneiss, quartzo-feldspathic gneiss and hornblende granulite. Consequently, the paragenesis of these minerals revealed mineral assemblages of the first stage. This is also supported by Smirnov (1976) who pointed out that regional metamorphosed deposits of iron ores are widespread in the Pre-cambrian rocks and to some extent in the lower Paleozoic period. Consequently, occurrence of magnetite and hematite within such rocks as amphibolite are well documented.

Stage II of ore mineralisation in the Musina area was characterised by the occurrence of quartz - pyrite assemblage. The assemblage consisted of 2nd generation quartz and minor early formed pyrite that occurred within veined, brecciated and disseminated ores. Quartz occurred as veins and stringers which conform to the regional strike of the host rocks and in places intruded amphibolite. Both quartz and pyrite were seen to feel the microfractures within garnet.

Stage III of ore mineralisation comprised pyrite, sphalerite, chalcopyrite with minor pyrrhotite and galena as well as traces of pentlandite, tennantite, molybdenite, cobaltite and tetrahedrite. Ore mineralisation was accompanied by chloritization. This assemblage occurred within disseminated, veined and brecciated ores. The occurrence of sphalerite with blebs of chalcopyrite suggested both co-precipitation and influx of Fe and Cu contentment into the early formed sphalerite (Bortnikov *et al.* (1991). This was the main stage of sulphide mineralisation in the Musina area.

© University of Venda

Stage IV of ore mineralisation consisted of carbonates, namely; calcite, dolomite and ankerite. Calcite was the dominant mineral in this stage accompanied with minor dolomite and ankerite. This stage marked the end of ore mineralisation in the area as these carbonates cross cut earlier formed ore minerals (Ogola, 1987; de Melo *et al.*, 2014). For example, Ogola (1987) noted that carbonate minerals cross-cut and replace all earlier formed minerals and there was no sulphide deposition during carbonate formation, although pyrite was altered to marcasite at this stage. de Melo *et al.* (2014) also noted that late calcite crystals were observed in veinlets of approximately 2 mm in width that cross-cut zones of previous stages of hydrothermal alteration.

© University of Venda

CHAPTER 8

CATHODOLUMINESCENCE INVESTIGATION

Preamble

This chapter focuses on the study of cathodoluminescence (CL) in different minerals associated with copper ores from Campbell (CAMP) and Artonvilla (ARTV) copper deposits using cathodoluminescence microscopy technique. The chapter first introduce the basic aspects of cathodoluminescence study that include the following: principles, instrumentation, and application of cathodoluminescence microscopy. It thereafter explains in detail the cathodoluminescence investigation of the Messina copper deposits focusing on the objectives, sample selection, preparation and analysis; results and interpretation, and finally discusses the findings of the study.

8.1 Principles of Cathodoluminescence

Luminescence is one of the common phenomenon in both inorganic and organic substances, resulting from an emission transition of anions, molecules, or resulting from a crystal from an excited electronic state to a lesser energy state (Marfunin, 1979). Due to the excitation method, different types of luminescence can be distinguished such as photo, cathode, thermos or X-ray luminescence (Göetze, 2002). Due to wide range of individual luminescence behaviour of mineral phases, luminescence techniques are used for the investigation and interpretation of the composition and structure of minerals and materials (Göetze, 2002).

Much is known about the origin of CL in artificial crystals as they are the most common in terms of their economic importance in the manufacture of electronics such as computers, television. However, less is known about the origin of CL in naturally occurring minerals. Most of the minerals emit radiation which is referred to as luminescence. This occurs when minerals are bombarded by an energy source and emissions are commonly in the visible range, but ultraviolet (UV) and infrared (IR) emissions may also occur (Marshall, 1988; Götze, 2009). When the energy source is bombarded by high-energy, cathodoluminescence is produced (Fig. 8.1), unlike when bombarded by high-energy UV photons where a beam of energetic ions and X-rays produce photo-luminescence, iono-luminescence and radio-

© University of Venda

luminescence (Pagel *et al*., 2000). Boggs and Krinsley (2006) defined cathodoluminescence as an emission of visible (and UV) luminescence by a substance that is bombarded by electrons, where the cathode is the source of the electrons. They further defined CL as a phenomenon in which electrons impacting on a luminescent material such as fluorite, calcite, quartz, cause the emission of photons with wavelengths in the visible spectrum.

There are several factors that are responsible for CL emissions and to visualize this, one has to consider atoms in crystals in terms of the band theory of solids (Fig. 8.1). The energy state of electrons depends on two factors, bounding of electrons in particular atoms or electrons are delocalized, hence the electrons are not associated with individual atoms but are shared by all atoms (Boggs and Krinsley, 2006). Delocalized electrons have waves that traverse through the entire crystals whereas waves in bound electrons have discrete energy states associated with shells of electrons within the atom. This brings the fact that energy bands will be formed because of large number of atoms that interact in a solid material and the energy levels are closely spaced (Boggs and Krinsley, 2006). These energy bands are referred to as valence and conduction bands where valence bands (Fig. 8.2) are analogous to the highest occupied molecular orbital and conduction bands are analogous to the lowest unoccupied molecular orbital (Boggs and Krinsley, 2006; Gucsik, 2009).

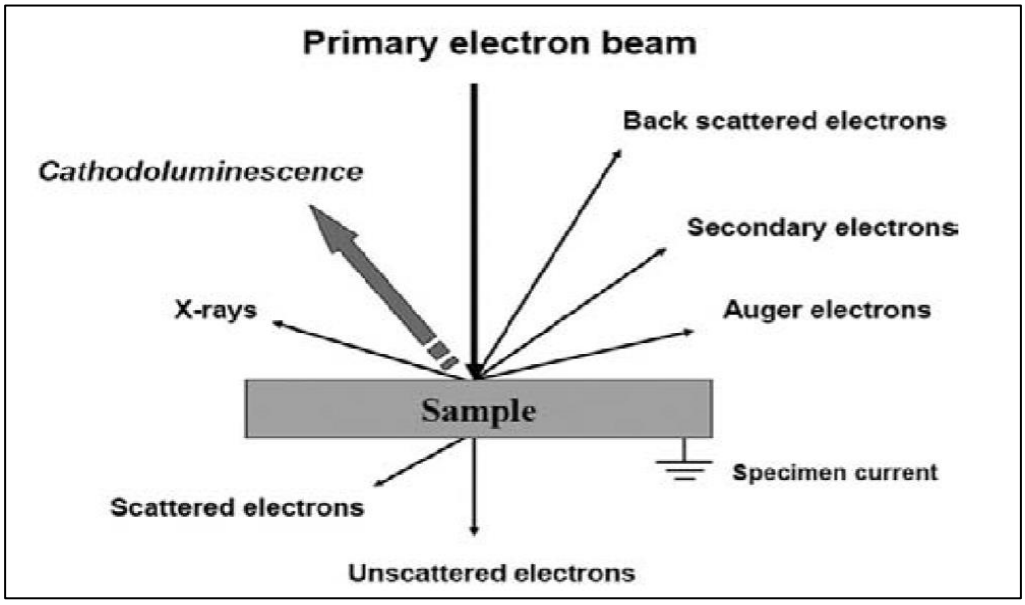


Figure 8.1: Schematic illustration of interactions of an electron beam with a solid surface (Gucsik, 2009 modified after Yacobi and Holt, 1990).

© University of Venda

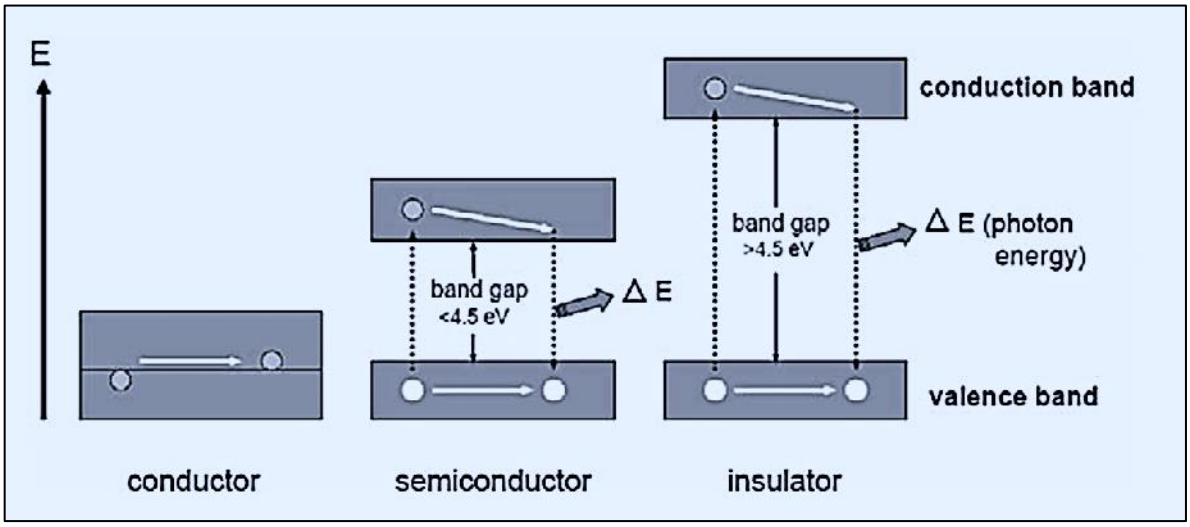


Figure 8.2: Schematic illustration of energy levels in a band scheme for different crystal types: conductor with overlapping valence and conduction band, semiconductor with small inter-band and insulator with large band gap (Götze and Kempe, 2009).

The electrons from conduction band are easily removed by the electric field and if there are many electrons from this band it then acts as a good conductor of heat. Electrons from valence band can be removed easily with the application of energy (Boggs and Krinsley, 2006; Götze and Kempe, 2009). In the case of CL, this energy is supplied by bombardment with high-energy electrons. In insulators, such as quartz, a forbidden zone exists between the valence band and the conduction band, which is referred to as the band gap (Fig.8.2). Electrons do not reside permanently in the forbidden zone, however, they can travel back and forth through it. The band gap is quite wide in insulators but much narrower in semiconductors, and is absent in conductors (Boggs and Krinsley, 2006; Götze and Kempe, 2009).

Fundamental causes of cathodoluminescence

In insulator minerals, all electrons occupy the lower energy valence band while the conduction band is empty. The electrons are thus excited and promoted to the conduction band leaving holes in the valence band when sufficient energy is applied to a mineral (Fig. 8.3). The electrons will then lose energy and attempt to return to the valence band, hence the de-energized electrons may be trapped within the band gap for microseconds by extrinsic luminescence centers (defects) which are often called impurity defects, which are incorporated within the crystal owing to some property of the fluid, or melt from which a

© University of Venda

mineral crystallized. The de-energized electrons may be trapped by intrinsic luminescence centers (defects) which are often called structural defects owing to the presence of varieties of defects in a crystal structure. All this occurs within the band gap in wide band-gap insulators such as quartz and feldspar (Marshall, 1988; Walker and Burley, 1991; Machel *et al*., 1991; Götze *et al*., 2001; Boggs and Krinsley, 2006; Götze and Kempe, 2009).

The energy lost when electrons vacate traps and continue their transit to the valence band is converted into photons of light (Fig. 8.3), which have characteristic wavelengths. Most photons have wavelengths in the visible light range of the electromagnetic spectrum, however, emissions may also occur in the near ultraviolet and infrared rays which are the basis for cathodoluminescence. The greater the number of electrons being trapped within the band gap, the greater the intensity of CL (Marshall, 1988; Walker and Burley, 1991; Machel *et al*., 1991; Götze *et al*., 2001; Boggs and Krinsley, 2006; Götze and Kempe, 2009).

In summary, the CL of minerals results from substitutional and interstitial incorporation of trace elements and from different types of intrinsic and extrinsic defect centers in mineral lattice. Consequently, CL behaviour is the complex function of trace elements such as Al, Fe, Ti concentrations that may act as activators or quenchers. It is therefore, related to conditions of crystallization and alterations of minerals (Marshall, 1988; Walker and Burley, 1991; Machel *et al*., 1991; Müller *et al*., 2000; Götze *et al*., 2001; Boggs and Krinsley, 2006; Gucsik, 2009).

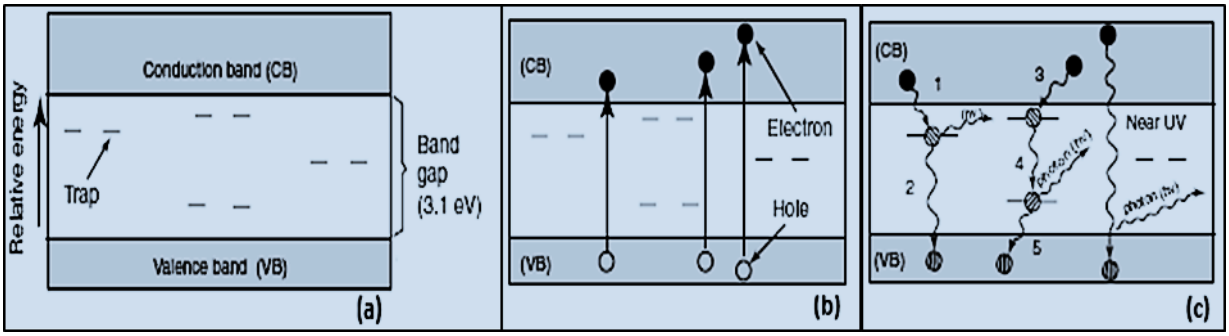


Figure 8.3: Schematic representation of the processes that cause CL generation in minerals: (a) Defects within the band gap with electron traps; (b) De-localized electrons from valence band move to conduction band leaving holes in valence band; and (c) Trapped de-excited electrons emit photons (CL) in the visible light range (Boggs *et al*., 2001).

© University of Venda

8.2 Cathodoluminescence Instrumentation

Cathodoluminescence (CL) microscopy and spectroscopy are luminescence techniques with widespread applications in geoscience studies. Many rock-forming and accessory minerals show CL characteristics, which can be successfully used in geoscientific investigations (Götze, 2002). The earliest observations of CL were realized in 1960's when using an electron probe microanalyzer (EPMA) which is also referred to as an electron microprobe which is an exciting source (Long, 1963;; Stenstrom and Smith, 1964; Long and Agrell, 1965Smith and Stenstrom, 1965).

Although CL images can be viewed in an EPMA, the EPMA is primarily used for compositional analysis (Boggs and Krinsley, 2006). Recently, a number of CL detectors on scanning electron microscope (SEM) have been used. The samples may be analysed under high magnification scanning electron microscopy cathodoluminescence SEM-CL, which provides high special resolution of CL features. The arrangement of the CL detector on a SEM allows one to carry out micro-chemical analysis (Götze, 2002).

The combination of CL and light microscopy was first performed in geoscience studies in early 1960's (Smith and Stenstrom, 1965) and was referred to as optical cathodoluminescence microscopy (OCM). The optical microscope is a microscope on which a cathodoluminescence stage is attached and allows specimen to be bombarded by high-energy electrons from a cathode gun that allows one to alternate from transmitted and polarized light and CL viewing (Götze, 2002; Boggs and Krinsley, 2006).

The electron gun of the optical cathodoluminescence microscope may be performed as cold-cathode or as hot-cathode of which the two differ in several ways such as electrons discharge, CL intensity, minerals transmission of CL, vacuum pressure and coating substances (Table 8.1).

© University of Venda

Table 8.1: Differences between Cold-cathode and Hot-cathode cathodoluminescence summarized from Marshall (1988); Yacobi and Holt (1990); Redmond *et al.* (1992); Marshall (1993); Götze (2002) and; Boggs and Krinsley (2006)

Parameters	**Cold-cathode CL**	**Hot-cathode CL**
Discharge of electrons	Between cathode and high voltage anode in an ionized gas	Emitted from low voltage heated filament
Intensity	Low CL intensity	High CL intensity
Types of minerals	Strongly CL minerals	Both strongly and weakly CL minerals
Vacuum pressure	Moderate vacuum ~ 10^{-2} Torr	Lower vacuum < 10^{-5} – 10^{-6} Torr
Coating	Carbon or gold coating is not necessary	Carbon or gold coating is important

In cold-cathode CL, the electron gun discharges electrons between the cathode and anode in an ionized gas at a moderate vacuum of approximately 10^{-2} Torr, while in hot-cathode CL the electrons are discharged from heated filament at low vacuum pressure less than 10^{-5}-10^{-6} Torr (Marshall, 1988; Yacobi and Holt, 1990; Redmond *et al.*, 1992; Boggs and Krinsley, 2006). The hot-cathode technique provides higher CL intensity as compared to low intensity from cold-cathode technique. Consequently, the hot-cathode is appropriate for weakly luminescence minerals (Marshall, 1993; Götze, 2002). In cold-cathode technique some electrical charges in the discharge may reach the specimen and neutralize the static charge created at the surface by modifying the secondary electron yield of the specimen thus it is not necessary to coat the sample with a conductive coating such as gold or carbon coating. It is important to coat the sample in hot-cathode technique to prevent any buildup of the electrical charge during CL operation (Götze, 2002; Boggs and Krinsley, 2006).

There are two main commercially produced CL stages, which include Luminoscope and Technosyn stages (Fig. 8.4a). The two stages have the same basic components, which are; vacuum chamber with upper and lower windows enclosing an X-Y stage movement with an

© University of Venda

attached cold-cathode or hot-cathode electron source (Fig. 8.4a and b). The two stages differ in that Technosyn uses an electron gun aimed at a sample centered on the optical microscope whereas the Nuclide uses magnets to deflect the electron beam (Yacobi and Holt, 1990).

The stage can be attached to a standard petrographic microscope (Fig. 8.4b) which allows the CL image to be viewed in colour through the objectives of the microscope. The major advantage of CL microscopy compared to SEM-CL is that the real colours of CL can be detected and compared directly with transmitted light observations.

The most important analytical parameters of CL microscope equipment include electron beam and source, voltage and beam current, spectral range and spatial resolution (Table 8.2). The sample to be analysed is a polished thin section with 30 µm thickness.

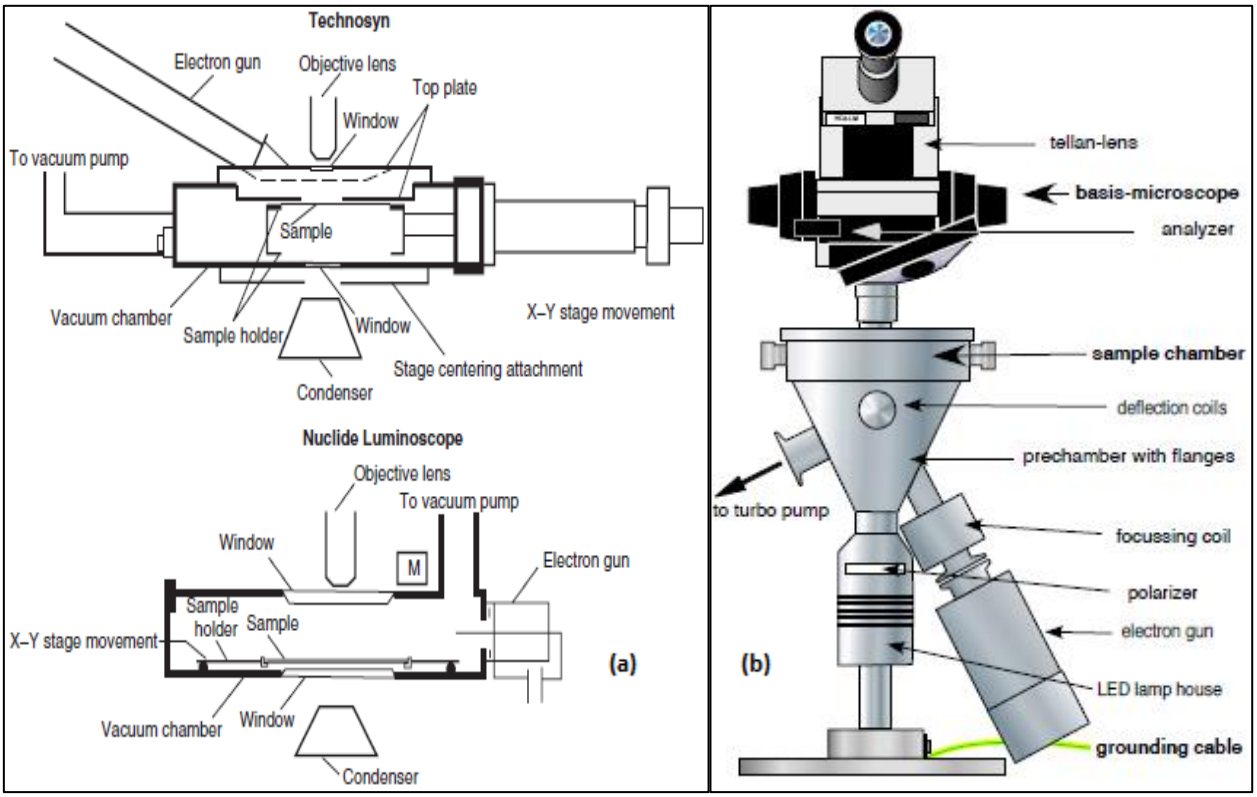


Figure 8.4: Schematic cross-sectional view of (a) cathodoluminescence stages and (b) Cl microscope - HC5-LM (Boggs and Krinsley, 2006; Neuser, 2009).

© University of Venda

Table 8.2: Important analytical parameters of CL microscopy (Götze, 2002)

Parameter	**CL Microscope**
Electron beam	Defocused, stationary mode
Electron source	Heated filament for hot-cathode or ionized gas for cold cathode
Acceleration voltage	14 Kv
Beam current	0.1 – 0.5 mA
Vacuum chamber	< 10-6 bar
Optics	Glass optics
Spectral range	380 – 1200nm (Vis-IR)
Spot of spectral analysis	Ca. 30 µm
Luminescence imaging	True luminescence colours
Spatial resolution	1-2 µm
Analytical combination	Polarizing microscopy

8.3 Application of Cathodoluminescence

Cathodoluminescence microscopy has become a standard technique in several fields of investigations in geoscience and material science (Sittner and Götze, 2018; den Engelsen *et al.*, 2017; Götze *et al.*, 2015; Götze. 2012; Gucsik, 2009; Boggs and Krinsley, 2006; Müller *et al*., 2000; Pangel *et al*., 2000). Some of the main applications of CL microscopy in the field of geoscience include quantitative separation of different mineral species, evidence of different mineral generations (phase distribution), analysis of real structures (defects, zonal growth, internal structures), microstructural characteristics (micro-fracturing, brecciation and crushing), textural relationship between minerals and reconstruction of processes of mineral formation and alteration (Götze, 2002; Pangel *et al*., 2000).

© University of Venda

Quantitative separation of different mineral species: It is easier to quantify different mineral species under a quick look of CL and to estimate the percentage of the mineral present in a given sample. For example, minerals such as diamond (element), sphalerite (sulphide), periclase, corundum, cassiterite (oxides), fluorite, halite (halides), anhydrite, alunite (sulphates), scheelite (wolframate), apatite (phosphates), calcite, dolomite, magnesite (carbonates), feldspar, quartz, zeolites, kaolinite, zircon, garnet (silicates) have distinct CL which makes such minerals to be distinguished easily (Götze, 2002).

Evidence of different mineral generations (phase distribution): Some of the minerals may show distinct CL properties allowing a rapid identification of phase distribution or different generations and phase transformation (Götze, 2002; Sittner and Götze, 2018). For certain minerals, it is often difficult to recognize the different generations if present in thin section. Quartz is the best example because it contains very low trace element amount (Pangel *et al.*, 2000; den Engelsen *et al.*, 2017; Sittner and Götze, 2018).

Analysis of structures such as zonal growth: A study conducted by Müller *et al.* (2000) yielded important information on the nature and evolution of the melt from which the crystal grew through the study of quartz texture, size distribution growth zonation and growth textures using CL technique. Boggs and Krinsley (2006) illustrated the oscillatory-zonation in volcanic quartz phenocryst from a volcanic clast in the Lake Hill Conglomerate in New Zealand.

Microstructural characteristics (micro-fracturing, brecciation and crushing): The existence of a micro-fractured healed plane is easily detected in many minerals by CL observations (Pangel *et al.*, 2000). Milliken and Laubach (2000) showed that in certain cases of recrystallization CL is a powerful tool to detect brecciation events.

Textural relationship between minerals: Cathodoluminescence observations help in the establishment of the succession of paragenetic associations in rocks when considering textural parameters such as growth zone, microfructuring, replacement, alteration, dissolution and recrystallization grain boundary features (den Engelsen *et al.*, 2017; Götze *et al.*, 2015; Pangel *et al.*, 2000). The knowledge about the above mentioned parameters in a mineral enable one to reconstruct the processes of mineral formation and alteration of rock materials.

© University of Venda

University of Venda
Creating Future Leaders

In this study, cathodoluminescence microscopy was applied in order to identify and characterize different types of minerals, their textures, internal structures and different mineral generations and interrelations. The study led to the reconstruction of the processes of mineral formation and their alteration at the Campbell and Artonvilla deposits in Musina area.

8.4 Cathodoluminescence Investigation of the Messina Copper Deposits

8.4.1 Objectives

In this study, cathodoluminescence study was conducted for the purpose of:

- Identification and characterisation of different types of CL minerals associated with copper sulphide mineralisation within the Campbell and Artonvilla copper deposits;
- Identification and characterisation of the textural relationship between the CL minerals and associated minerals within the deposits;
- Investigation of the microstructural characteristics of the CL minerals; and
- Identification and characterization of mineral generations and their interrelations.

8.4.2 Sample Selection

A total of 11 polished thin-sections at a thickness of 30 µm (see preparation in chapter 6) used for petrographic investigation were also used for cathodoluminescence studies in order to identify cathodoluminescence minerals associated with copper sulphide mineralisation. The thin-sections used were prepared from mineralised samples collected from both Campbell (CPdis01, CPdis02, CP02, CPA4, CP03, CPqtz03, and CPqv01) and Artonvilla (ATcal01, AT01, ATavr12 and AT02) copper deposits. The samples were selected from the mineralised ore specimens sampled within the study area. The selected samples were considered to be ideal for this study because they had copper-sulphide mineralisation such as chalcopyrite, pyrite, bornite and chalcocite minerals.

8.4.3 Sample Preparation

The selected thin-sections were prepared for CL investigation at the Department of Applied Geology, Geoscience Centre of the University of Göttingen in Germany. The thin-sections

© University of Venda

were first scanned by putting them in the thin section holder (Fig. 8.5a) and inserting them in a Nikon Super Scoolscan 5000 ED 1.023 scanner (Fig.8.5b). The obtained scans were saved using the Nikon Scan version 4.0.3 software installed in a computer (Fig.8.5c). Scanning was done so as to be able to trace back the location of the minerals identified during petrographic study.

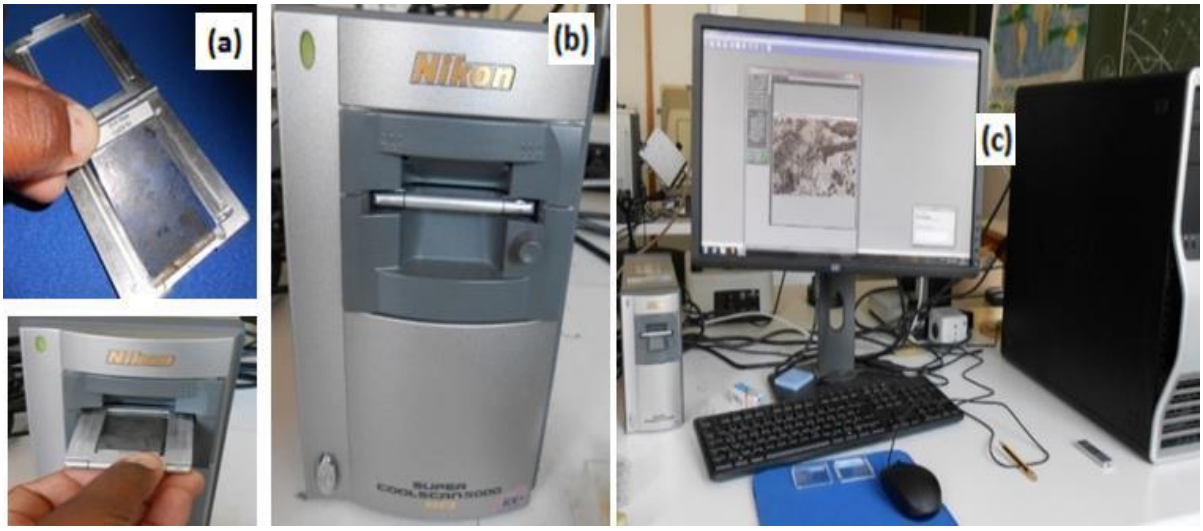


Figure 8.5: Nikon Super Coolscan 5000 ED 1.03 scanner used for scanning the thin-sections: (a) thin-section holder; (b) Scanner; (c) computer and monitor connected to the scanner.

After scanning, the thin-sections were coated with carbon layer using Cressington *208* carbon coater (Fig.8.6a) with thickness monitor MTM-10 unit (Fig. 8.6b) for precise and reproducible coating thickness, metal evaporation accessory for prevention of metal evaporation, rotary-planetary-tilting stage (Fig. 8.6c) for multiple sample coating and auxiliary power supply stage unit (Fig. 8.6d) to drive the metal evaporation. The carbon coating was done to prevent any build-up of electrical charge during CL operation.

The thin-sections were put into the specimen chamber and the chip of carbon was inserted into carbon holder and closed. The coater was switched on and air was pumped in for about 1.5 minute at $1x10^{-4}$ mb pressure. The automatic coating took about 30 to 60 seconds. The thin sections were then removed from the specimen chamber, and ready for CL investigation.

© University of Venda

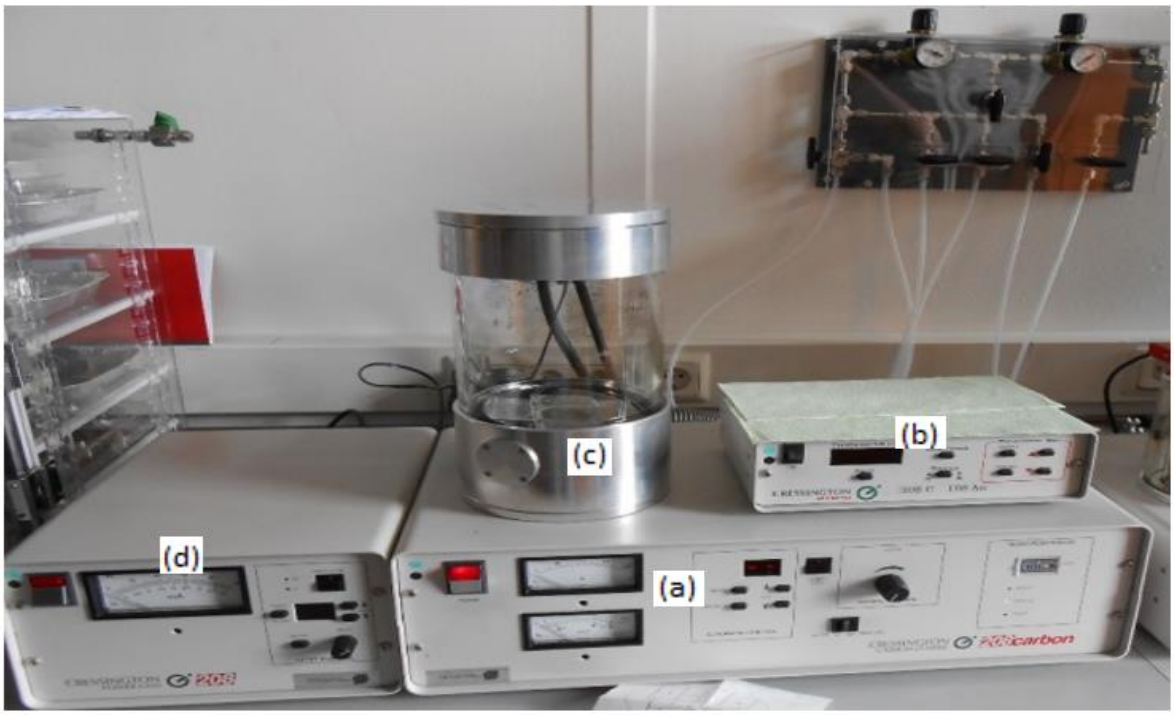


Figure 8.6: (a) *208*C High vacuum turbo carbon coater with; (b) Thickness monitor MTM-10; (c) Rotary-planetary-tilting stage with Metal evaporation accessory; and (d) Auxiliary power supply used for coating the thin-sections.

8.4.4 Sample Analysis

Hot cathodoluminescence microscope HC3-LM attached to a pump (Fig. 8.7) was used to identify different types of minerals under cathodoluminescence (CL), Transmitted light (TL) and Polarized light (PL).

The external switch was switched on and the coated thin-section was inserted in a sample chamber and the sample chamber cover was then closed. The rotatory pump (Fig. 8.7a) was always kept on. The vacuum system was then switched on to start both the rotatory and the diffusion pumps (Fig. 8.7b) and waited until the vacuum pump reached 5 x 10-4 mbar in the sample chamber which is the maximum pressure needed for working vacuum. The main switch of the power supply rack HC3-LM/SG was switched on for the power supplies. The high voltage was switched on to 14 kV and observation was then made through the microscope (Fig. 8.7c) tube while controlling the potentiometer until the desired intensity of luminescence was achieved with the current value from 0.2 mA and not exceeding 0.45 mA. The meter for the filament current was kept at < 1.6 to 2.7A because too high filament current may overheat the sample and break it. The optical microscope used was attached to the

© University of Venda

cathodoluminescence stage connected to the hot cathode (Fig.8.7d) that bombard high-energy electrons and allows one to alternate from transmitted, polarized light and CL viewing.

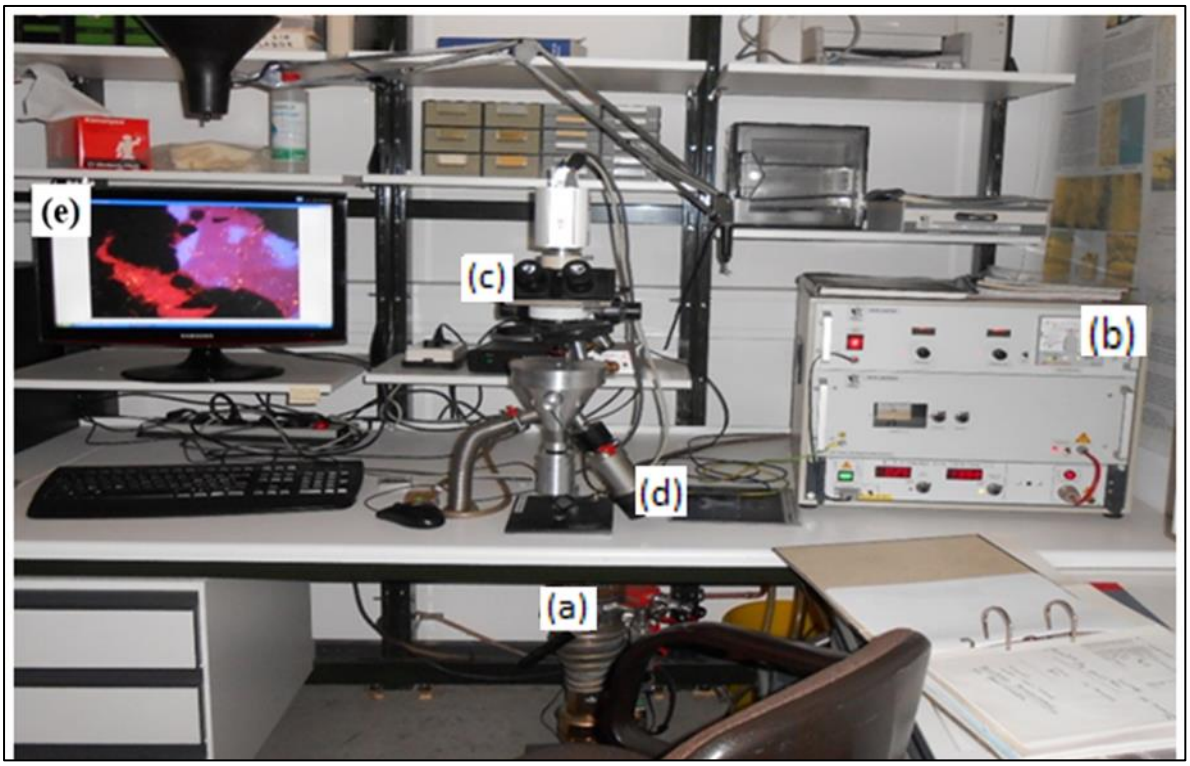


Figure 8.7: Hot cathodoluminescence microscope HC3-LM stage used for the CL investigation: (a) Rotatory pump; (b) Diffusion pump; (c) Microscope; (d) Hot cathode; and (e) Computer and monitor.

To change the sample, the electron beam was switched off after switching off the high voltage. The filament current potentiometer was turned down and power supply was switched off for the electron gun. The vacuum and the pumps were then turned off and the device was completely vented after about 2 minutes.

The images were captured using a built-in high sensitivity Kappa camera Dx40c-285FW and version 1.4.2.9031 software installed in an attached computer (Fig.8.7e). Images were characterised, described, taking note of features such as: CL, crystal structure, mineral species, mineral generations (phase distribution), zonal growth, microstructures, textures, replacement, alteration, dissolution and recrystallization and labeled accordingly (Table 8.3 and 8.4, and Fig. 8.8 – 8.20). The identification was done under cathodoluminescence (CL), crossed polarized light (PL) and plane transmitted light (TL).

© University of Venda

Table 8.3: Campbell deposit minerals and their characteristics identified under cathodoluminescence

Locat -ion	Mineral type (Macro)	Sample ID	Mineral species	Mineral Type (Micro)	Generation	CL	TL	PL	Zoning	Texture	Fracture	Replacement	Alteration
Campbell deposit	Quartz vein	CP02, CPA4	Quartz	Qtz 1	Early formed	Dark blue to dark violet,	Grey - greenish	Blue to light grey and dark brown	Zoned	Xenormophic phenocryst	Fractured/ in-filled/ open	Qtz 2 replacing Qtz 1	Grain boundary altered
				Qtz 2	Late formed	Dark red							
		CP03	Quartz	Qtz 1	Early formed	Dark blue to dark violet,	Grey - greenish	Blue to light grey	Oscilla-Tory/concentric	Sub-idiomorphic Rings qtz	Fructured	Qtz 2 replacing Qtz 1	Grain boundary altered
				Qtz 2	Late formed	Dark red							
		CPqv01	Quartz	Qtz 1	Early formed	Dark blue to dark violet,	Grey - greenish	Blue and light grey	-	Anhedral	veinlet	Qtz 2 replacing Qtz 1	Strongly altered -
				Qtz 2	Late formed	Dark red							
		CPqtz03	Quartz	Qtz 1	Early formed	Dark blue to dark violet,	Grey - greenish	Dark brown and blue-light grey	-	Fine grained matrix	Massive qtz texture	Qtz 2 replacing Qtz 1	-
				Qtz 2	Late formed	Dark red							
		CP02, CPA4	Apatite	Secondary apatite	Secondary apatite	Yellowish to light greenish	Grey - greenish	Black	-	Xenomorphic phenocryst	Open fractures filled qtz	Qtz filling open fractures	Strongly altered
		CPqtz03	Prehnite	Rim prehnite	-	Bright greenish to yellowish green	Grey - greenish	Brownish-bluish-greish - oroange	Zoned	Rim of columinar prehnite comb structure	-	Engulfment of amygdale	-
	Brecciated quartz	CPdis0, CPdis02	Quartz	Qtz 1	Early formed	Dark blue to dark violet, bright blue	Grey - greenish	Blue to dark grey	-	Graphic Cataclastic	In-filled/ open	Qtz 2 replacing Qtz 1	Altered
				Qtz 2	Late formed	Dark red							
		CPdis0, CPdis02	Calcite	Veined Calcite	Cross-cutting -late formed	Bright red to orange	Light grey-brownish	Light grey -brownish	-	Massive veined	Infilled vein with calcite	-	-
		CPdis0, CPdis02	Apatite	Secondary apatite	Secondary apatite	Yellowish to light greenish	Grey - greenish	Black	-	Xenomorphic	fractured	-	Strongly altered
		CPdis0, CPdis02	Apatite	Primary apatite	Primary apatite	Deep blue	Blue/ greyish green	Black	-	Subidiomorphic	-	Replacement by qtz	Slightly altered

Note: CL- cathodoluminescence, PL- crossed polarized light; TL- plane transmitted light

© University of Venda

Table 8.4: Artonvilla deposit minerals and their characteristics identified under cathodoluminescence

Locat -ion	Mineral type (Macro)	Sample ID	Mineral species	Mineral Type (Micro)	Generation	CL	TL	PL	Zoning	Texture	Fracture	Replacement	Alteration
Artonvilla deposit	Quartz vein	ATavr12 AT02	Quartz	Qtz 1	Early formed	Bright blue to violet,	Grey - greenish	Blue to light grey	-	Xenomorphic	-	Qtz 2 replacing Qtz 1	Grain boundary altered
				Qtz 2	Late formed	Dark red							
		ATavr12 AT02	Quartz	Qtz 1	Early formed	Dark blue to violet,	Grey - greenish	Blue to light grey brown	-	Xenomorphic	Fractured	In-filled fractures by qtz 2	-
				Qtz 2	Late formed	Dark red							
		AT02 ATavr12	Quartz	Qtz 1	Early formed	Dark blue to dark violet,	Grey - greenish	Blue to light grey	Oscillatory/ zoning	Xenomorphic	-	Qtz 2 replacing Qtz 1	Grain boundary altered
				Qtz 2	Late formed	Dark red							
		ATavr12 AT02	Apatite	Secondary apatite	Secondary apatite	Yellowish to light greenish	Grey – greenish pinkish	Black	-	Broken , xenomorphic phenocryst	Open fracture filled rock fragments		Strongly altered
	Calcite vein	ATcal01 AT01	Quartz	Qtz 1	Early formed	dark red brown	Grey - greenish	Blue to light grey	-	Xenomorphic	Slightly fractured	-qtz replacing rock materials	Along fractures
		ATcal01 AT01	Quartz	Qtz 1	Early formed	Dark violet	Grey - greenish	Blue to light grey and dark brown	-	Xenomorphic	-	-	Altered by rock fragments
		ATcal01 AT01	Calcite	Sub-idiomorphic calcite	Late formed	Bright red to orange	Light greyish brownish	Pinkish – greenish-bluish	-	Smooth, phenocryst, sub-idiomorphic	-	Rock fragments replacing calcite	Altered/dissolution
		ATcal01 AT01	Calcite	Sub idiomorphic calcite	Late formed	Bright red to orange	Light greyish brownish	Blue to light grey and dark brown	-	Scattered spotted , Xenomorphic	-	Rock fragments replacing calcite	Altered/dissolution
		ATcal01 AT01	Apatite	Subidiomorphic apatite	Primary apatite	Deep blue	Blue/ greyish green	Black	-	Sub-idiomorphic phenocryst	One prominent fracture	Sharp grain boundary	Grain boundary altered

Note: CL- cathodoluminescence, PL- crossed polarized light; TL- plane transmitted light

© University of Venda

8.4.5 Results and Interpretation

Using CL microscopy, different types of minerals that showed cathodoluminescence were identified. This included; quartz (SiO_2), calcite ($CaCO_3$), apatite ($Ca_{10}(PO4)_6(OH,F,Cl)_2$ and Prehnite ($Ca_2Al_2Si_3O_1(OH)_2$).

8.4.5.1 Quartz

Through the study of quartz cathodoluminescence, different types of quartz were identified based on the crystal generations and interrelation, crystal structure and state of the quartz grains. Consequently, the following types of quartz were identified: first (Qtz 1), second (Qtz 2) and third (Qtz 3) generations of quartz revealing different structural features such as graphic structure, growth zonation.

Generations of quartz (Qtz 1 and Qtz 2)

Cathodoluminescence was one of the distinctive properties used in the characterization of different types of quartz. Crossed polarized and plane transmitted light were also used in order to supplement the findings from CL. Four different luminescence types of quartz from Campbell and Artonvilla deposits (Table 8.3 and 8.4) were identified; the dark blue to dark violet, bright blue, dark red and dark brown luminescence. Different luminescence in a sample revealed replacement processes that characterized Qtz 1 and Qtz 2. For example, in sample CP01 from Campbell, Qtz 1 displayed dark blue to dark violet luminescence that was being replaced by Qtz 2 in dark red CL leaving relics of Qtz 1 surrounded by thin concentric coatings of bright red luminescence, which is indicative of replacement process (Fig. 8.8a).

This replacement process was also evidenced using plane polarized and transmitted light of the same thin section in Figure 8.8a and 8.8b respectively. For example, in PL, Qtz 1 (dark brown black) was seen to be replaced by blue-grey Qtz 2 leaving some relics of Qtz 1 (Fig. 8.8b). Figure 8.8c also displayed replacement process where Qtz 1 (white-grey) was replaced by Qtz 2 (dark grey-brown) leaving relics of Qtz 1. At the Centre of the images (Fig. 8.8 a and c), ore mineralisation occurred (dark black colour) in association with a later formed quartz (Qtz 2).

© University of Venda

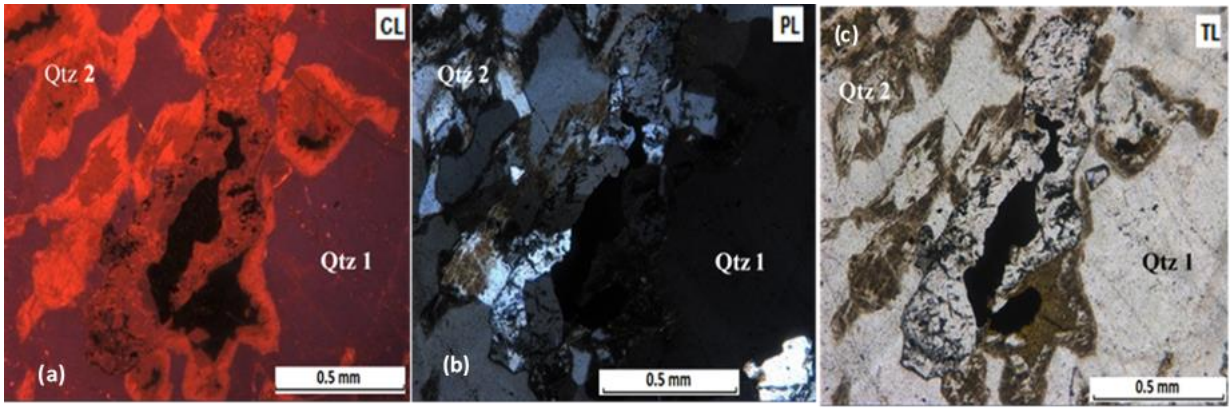


Figure 8.8: Early formed quartz (Qtz 1) in dark blue to violet CL being replaced by late formed quartz (Qtz 2) in dark red CL in sample CPdis01 from Campbell deposit.

In sample ATavr12 and AT02 from Artonvilla, the nature of CL displayed by Qtz 2, i.e. dark red and violet colours are indicative of the state of replacement of early quartz by the late quartz. For instance, the dark-red to violet colour reflects a mixture of the two types of quartz before total replacement of early formed quartz. In polarized light (PL) and transmitted light (TL) quartz showed no distinction between the two types of quartz (Fig. 8.9b and c).

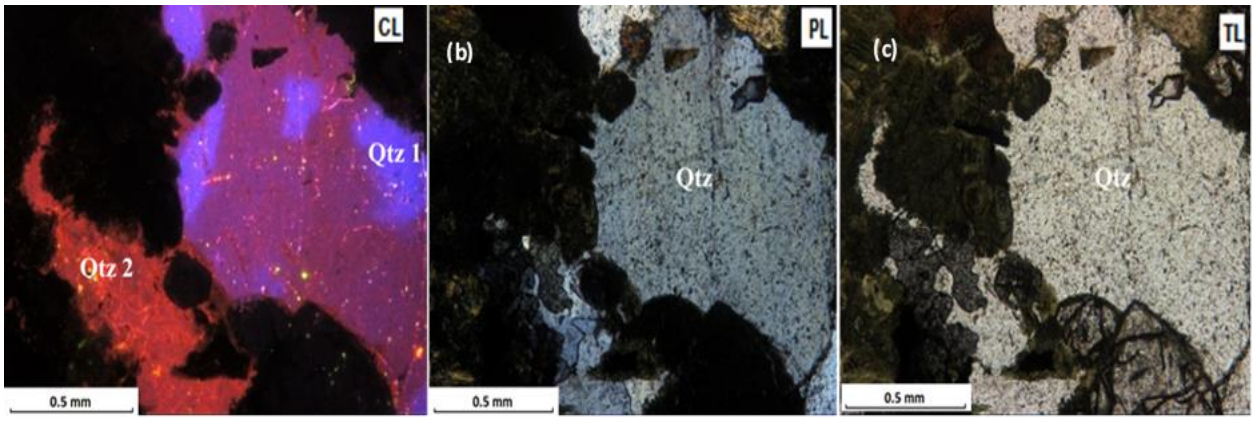


Figure 8.9: Early formed quartz in (a) bright blue CL replaced by late formed quartz in dark red CL and quartz showing no distinction between the two quartz types in (b) PL, (c) TL in sample ATavr12 from Artonvilla deposit.

The dark red-brown CL was revealed in sample CPdis01 and CPdis02 from Campbell and sample ATcal01 and AT01 from Artonvilla deposits, where it indicated late formed quartz (Qtz 2). This type of quartz was always associated with apatite crystals in all the four samples (CPdis01, CPdis02, ATcal01 and AT01). For example, sample CP01 indicated the dark red-brown CL colour (Qtz 2) replacing Qtz 1 appeared black around the bright blue CL apatite

© University of Venda

phenocryst leaving relics of early formed quartz (Qtz 1) (Fig. 8.10a). Early formed quartz displayed white-grey colour and was seen being replaced by later formed quartz replacing early formed quartz with apatite clearly seen in the centre (Fig. 8.10c).

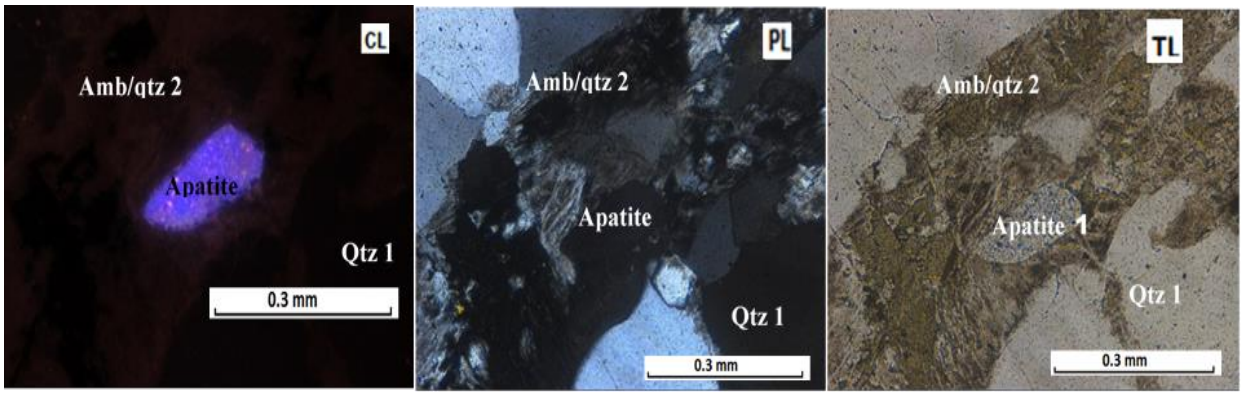


Figure 8.10: (a) Dark red-brown luminescence indicating late formed quartz replacing early formed quartz appeared black with apatite phenocryst that displayed blue luminescence (CL) and (b) in dark colour (PL). It is embedded within the altered rock materials and with quartz grains within and around the altered amphibole.

Consequently, four CL of quartz were identified and these included quartz with dark blue to dark violet, bright blue, dark red and dark red-brown colour and revealed a distinction between 1st and 2nd generations of quartz that indicated replacement processes.

Graphic textured quartz

Graphic texture was revealed from sample CPdis01 and CPdis02 of Campbell deposit (Fig. 8.11). This occurred when replacement of Qtz 1 by Qtz 2 continued along the fractures of quartz 1. For example, in sample CPdis01, Qtz 1 appearing dark blue to dark violet CL as a result of replacement. The combination of relics of the replaced quartz 1 and newly formed qua rtz 2 result into graphic intergrowth

Fractured quartz

Fractured quartz was revealed in sample CPdis01, CPdis02, CP02, CPA4, CP03, ATcal01, AT01, ATavr12 and AT02. In this case, earlier formed quartz 1was being replaced by later formed quartz 2 along the micro-fractures. infilling occurred resulting from precipitation of

© University of Venda

late formed quartz and leaves the infilling fractured surface intact. For example, highly fractured quartz of sample AT02 from Artonvilla, displayed the in-filled fractures displaying dark red-brown CL (Qtz 2) with lots of secondary fluid inclusions along the fractured zones that displayed bright cathodoluminescence. Infilled micro fracture of quartz was clearly revealed under CL as compared to TL and TL images whereas occurrence of fluid inclusions was clearly displayed in CL, PL and TL images (Fig. 8.12).

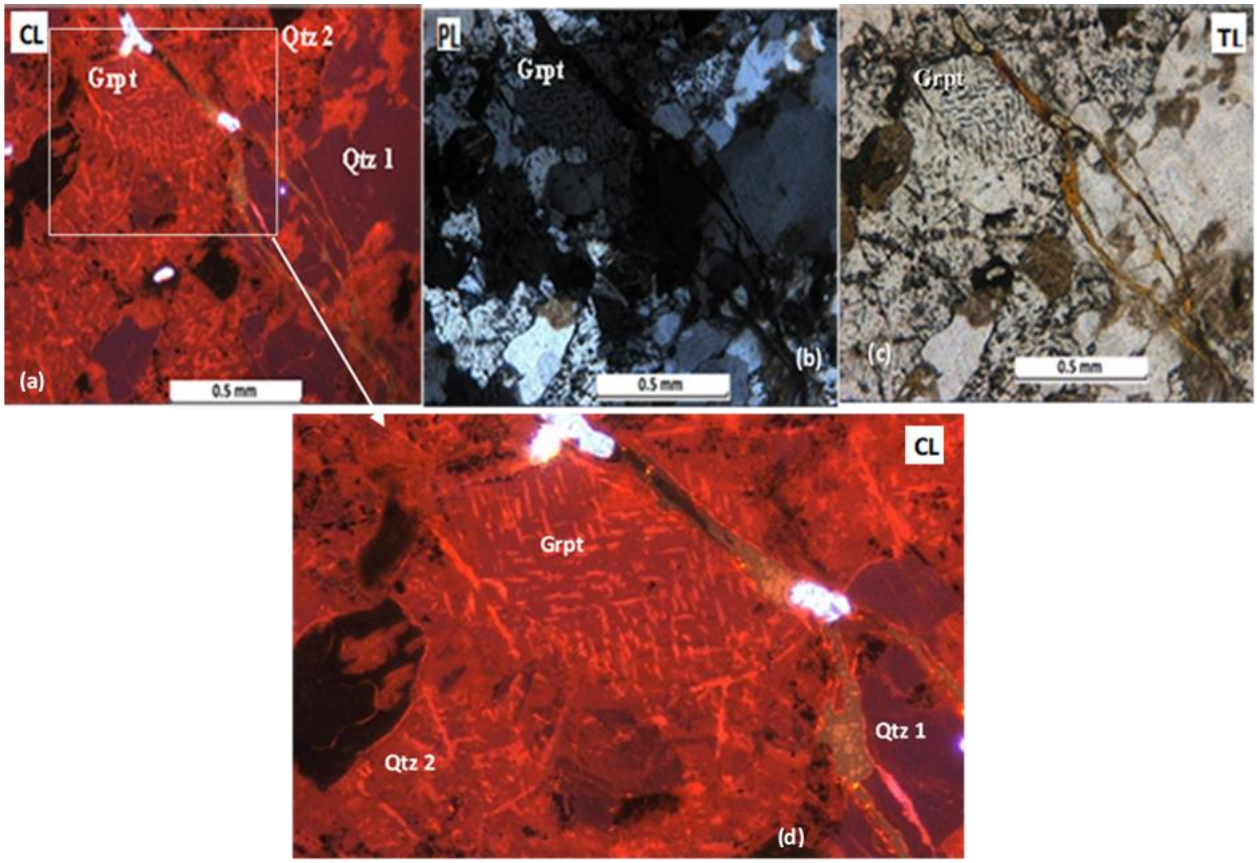


Figure 8.11: (a) Early formed qtz (Qtz 1) replaced by late formed Qtz 2 with graphic intergrowth (Grpt) in Qtz 2 of sample CP01, and also viewed in (b) polarized light (PL); (C) transmitted light (TL) and (d) enlarged part of (a) from Campbell copper deposit.

© University of Venda

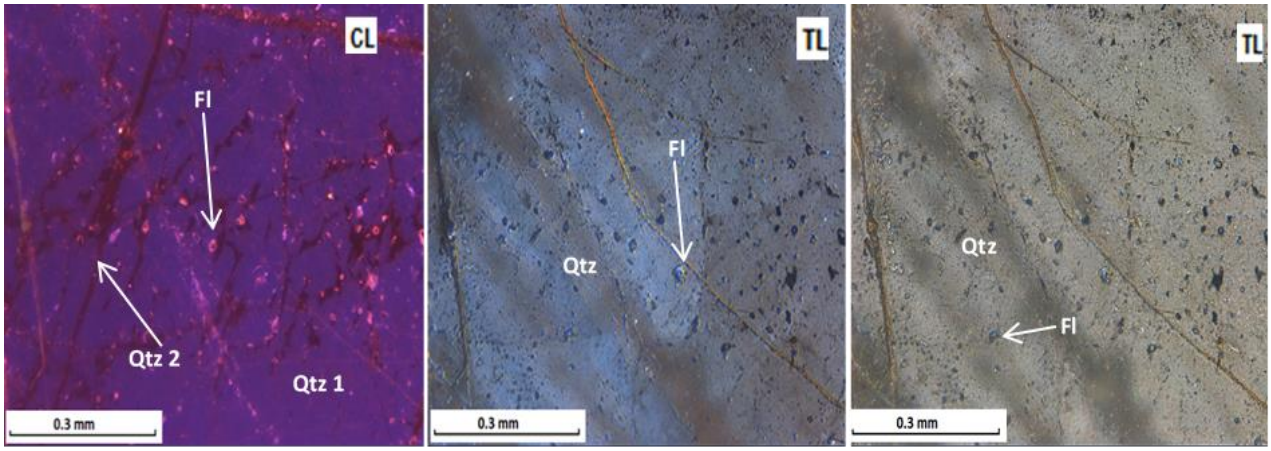


Figure 8.12: Internal structure of highly fractured quartz (CL) showing infilling of micro-fractures by late formed quartz with large secondary fluid inclusions in sample AT02 from Artonvilla copper deposit.

3rd generation of quartz (Qtz 3)

Crystal zonation in both macro or micro texture of a crystal can be either characterized by change in colour or by extinction angle of the mineral from the core to the rim, sometimes crystals zones are developed that indicate different period of crystallization (Van der Kerkhof and Hein, 2001). Crystal zonation was therefore used in characterization of quartz using Cathodoluminescence microscopy. Crystal zonation was identified in sample Cp02, CPA4 and Cp03 from Campbell deposit, and in sample AT02 and ATavr12 from Artonvilla deposit. Two types of crystal zonations were revealed; oscillatory and concentric growth zonation. The oscillatory growth zonation was identified in sample CP03 with layers displaying dark red and dark violet CL alternating each other which is an indication of multiple compositionally varying growth-layers (Fig. 8.13). The oscillatory growth zoning was mainly displayed in sub-hedral crystals which partly displayed their faces (Fig. 8.13 and Fig. 8.14) and overlaid by three distinctive early formed xenomorphic quartz crystals which is an indication of deformation due to stress along the crystal boundaries that occurred during the development of late formed quartz crystals (Fig. 8.13).

© University of Venda

The concentric zoning was clearly indicated in sample CP03 from Campbell which was indicated by successive sub-idiomorphic stepped crystal zones indicating different stages of crystal formation, where the top most crystal is the early formed quartz crystal while the bottom most crystal indicates late formed crystal growth (Fig. 8.14).

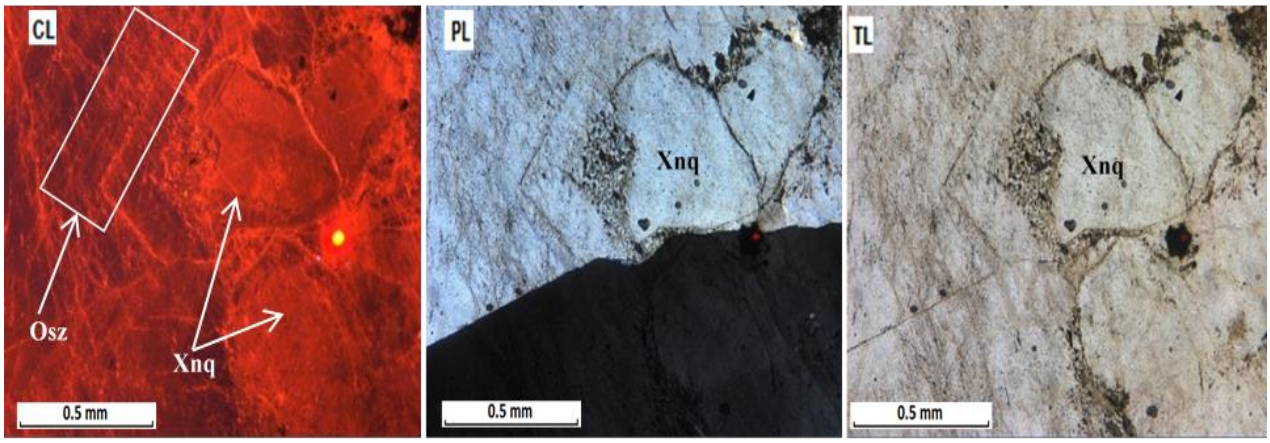


Figure 8.13: Zoned quartz indicating oscillatory zoning (Osz) in late formed sub-idiomorphic quartz crystals with early formed xenomorphic quartz crystals (Xnq) at the top which is displayed in CL, PL and TL in sample CP02 from Campbell.

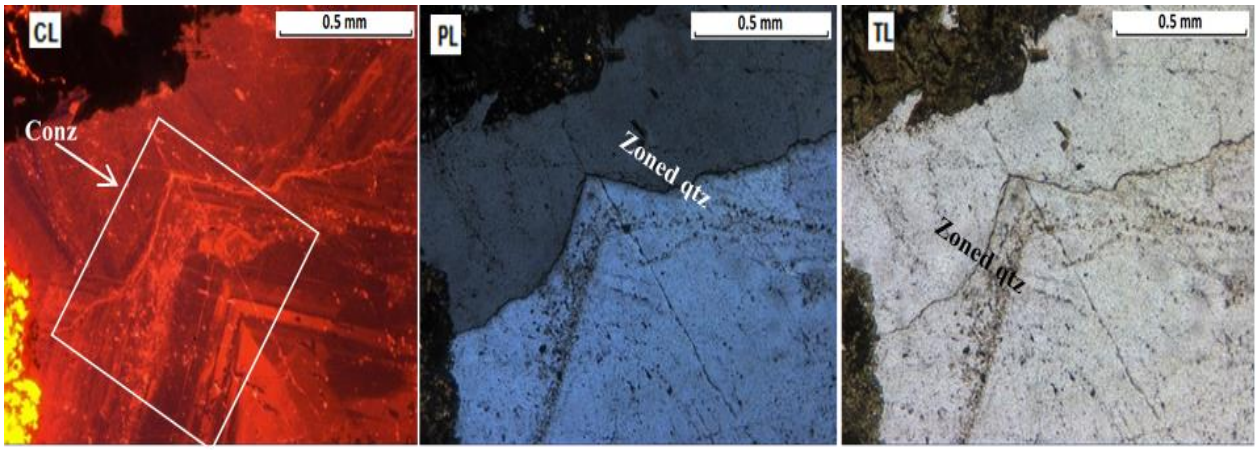


Figure 8.14: Zoned quartz displaying concentric zoning (Conz) indicated by stepped sub-idiomorphic crystals growth revealing different stages of crystal formation where the top most crystal is the older (early formed) and the bottom most crystal is the younger (late formed) crystals.

© University of Venda

8.4.5.2 Apatite

Apatite crystals were identified in samples CPdis01, CPdis02, CP02 and CPA4 from Campbell copper deposit, and in samples ATcal01, AT01, ATavr12 and AT02 from Artonvilla copper deposit. The study of apatite cathodoluminescence revealed different types of apatite based on period of formation, crystal structure and state of the grains. Consequently, the following types of apatite were identified; Primary and secondary apatite.

Primary and secondary apatite

Sub-idiomorphic crystals identified in samples CPdis01, CPdis02, ATcal01 and AT01 displayed deep blue CL surrounded by green CL rim which is an evidence of primary apatite (Figs. 8.15 and 8.16). In plane polarized light the apatite revealed black colour and showed white grey colour in transmitted light. Xenomorphic crystals of apatite in samples CPdis01, CPdis02, CP02, CPA4, ATavr12 and AT02 displayed yellowish to light greenish CL and infilled fractures by rock material that appeared black in CL while in polaraised light the apatite displayed black colour and in transmitted light it appeared white grey. The altered rock materials that appeared brown grey altered the apatite crystals that were separated due to alteration. Light greenish brown colour in cathodoluminescence image is an evidence of secondary apatite occurrence (Fig. 8.16).

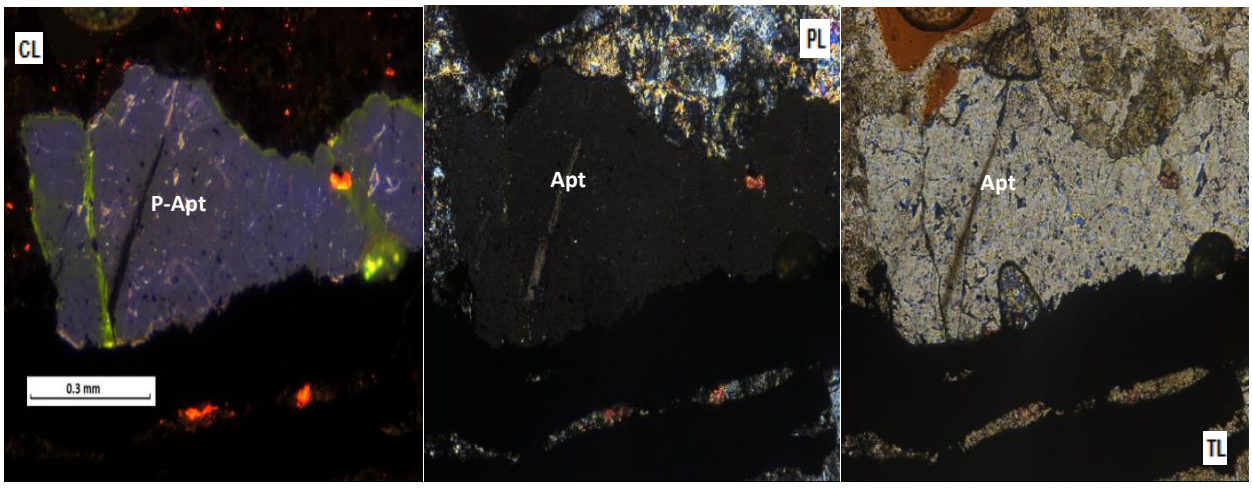


Figure 8.15: Primary apatite (P-Apt) displayed by deep blue CL, with bright green rim indicating replacement in sample ATcal01 from Artonvilla copper deposit.

© University of Venda

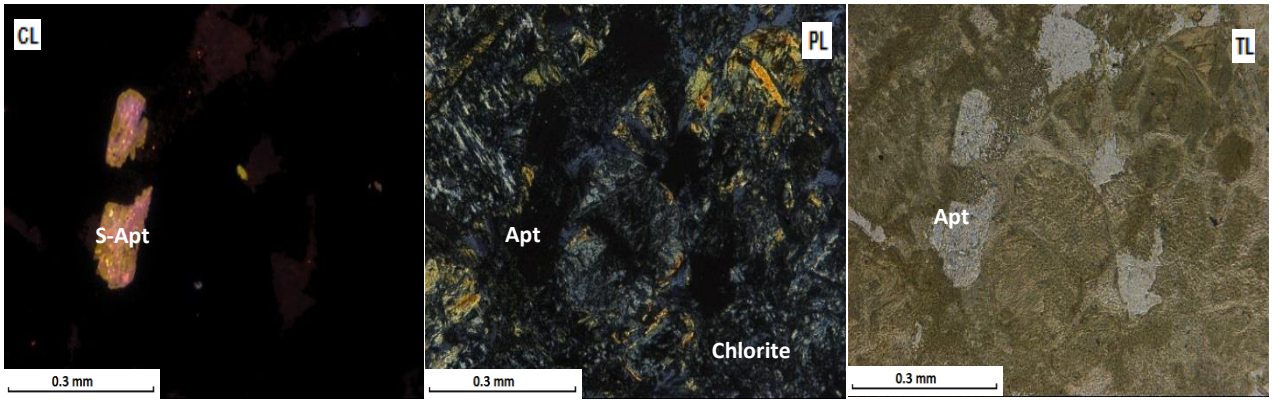


Figure 8.16: Sample AT02 from Artonvilla: Strongly altered secondary apatite (S-Apt) displayed by yellowish to light greenish-pinkish CL with open fracture filled by chlorite.

8.4.5.3 Prehnite

Prehnite crystals were identified based on period of formation, crystal structure and state of the quartz grains. The rim of columnar prehnite crystals displayed by bright greenish to yellowish green cathodoluminescence, projecting into the cavity with preserved crystal face termination and overgrown on top of the amygdule grain (Fig.8.17) was revealed in sample CPqtz03 from Campbell copper deposit. Both the polarized and transmitted light images revealed Prehnite surrounding the quartz crystal that appeared light grey in PL and brownish grey in TL. This is an indicative of nucleation of prehnite on the vesicle wall and followed by deposition of prehnite in free space from the influx solution.

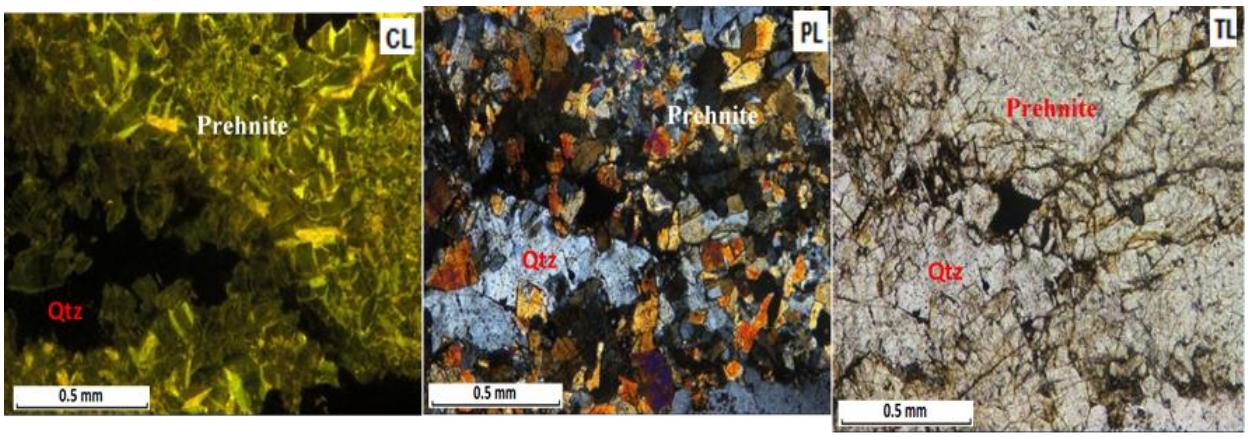


Figure 8.17: Prehnite crystals from sample CPqtz03 from Campbell copper deposit, displayed by bright green to yellowish green CL around and overgrowing on top of the idiomorphic black crystal of the host rock. Prehnite showed bright orange to yellow colours in plane polarized light surrounding white grey quartz. Prehnite in transmitted light showed brown to grey colour surrounding the light grey quartz.

© University of Venda

8.4.5.4 Calcite

The study of calcite cathodoluminescence revealed different types of calcite based on period of formation, crystal structure and state of the calcite grains. Consequently, the following types of calcite were identified: veined calcite and subhedral calcite.

Veined calcite

Veined calcite was identified in sample CPdis01 and CPdis02 from Campbell copper deposit displaying bright red to orange CL (Fig.8.18a) and light grey to brownish colour in TL and PL images (Figs. 8.18.b and c respectively). The lenticular calcite veined the early formed quartz in dark brown CL, which is an indication of calcite being formed late after the earlier formed quartz (Fig. 8.18). In polarized and transmitted light, the vein was seen cutting through the most of the earlier formed minerals (Figs. 18b and c).

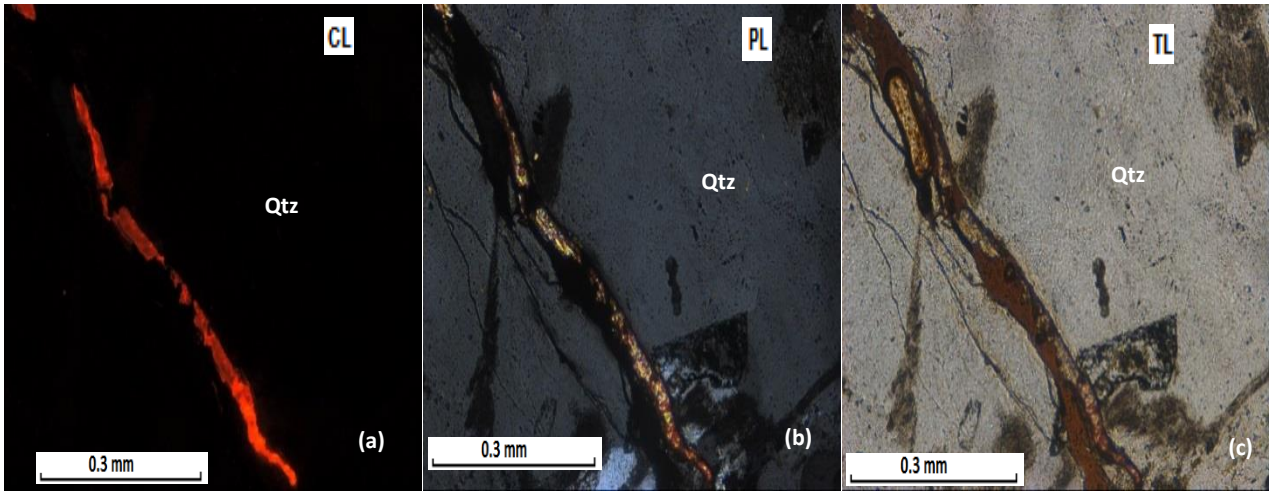


Figure 8.18: Late carbonate vein (calcite) in (a) bright red to orange CL cutting through earlier formed quartz and also cutting through (b and c) other earlier formed minerals such as altered amphiboles with quartz 2 in sample CPdis01 from Campbell copper deposit.

Sub-hedral calcite

The bright red to orange CL of calcite revealed sub-hedral shape calcite crystals with most of its boundaries revealing a sharp crystal boundary contact (indicated by yellow lines) with

© University of Venda

quartz and host rock materials. The calcite crystals appeared sub-hedral in texture. At some instances, the calcite displayed an influx of solution cutting the earlier formed minerals such as early formed quartz, later formed quartz and altered amphiboles showing also the sharp crystal boundary contact between the crystals (Fig. 19). The sharp crystal boundary contacts were revealed in CL image and as well as in polarized and transmitted light images (Figs. 19a, b and c respectively).

At some instances calcite revealed xenomorphic crystal shape enclosing quartz and host rock fragments in dark CL with thin layer of sharp contact bright red around the crystal, which is an indication of clear and visible sharp crystal boundaries with other earlier formed crystals, hence confirming a later calcite influx solution that occurred at the later stage (Fig. 8.19).

Influx of calcite were identified from samples ATcal01 and AT01 at Artonvilla copper deposit. It displayed a bright red to orange CL. This late calcite is cutting across altered rock materials displaying broken crystal grains of calcite and remnants of rock materials engulfed by calcite which could have been caused by later alteration processes (Fig. 8.20). This calcite was also seen to have cut across the apatite crystal leaving a sub-idiomorphic apatite which displayed deep blue CL with light green thin layer around the apatite crystal and few calcite crystal grains engulfed within the apatite which is an evidence of replacement and alteration process. In this case calcite revealed late stage of mineralisation, which occurred even after some of the alteration processes (Fig. 8.20).

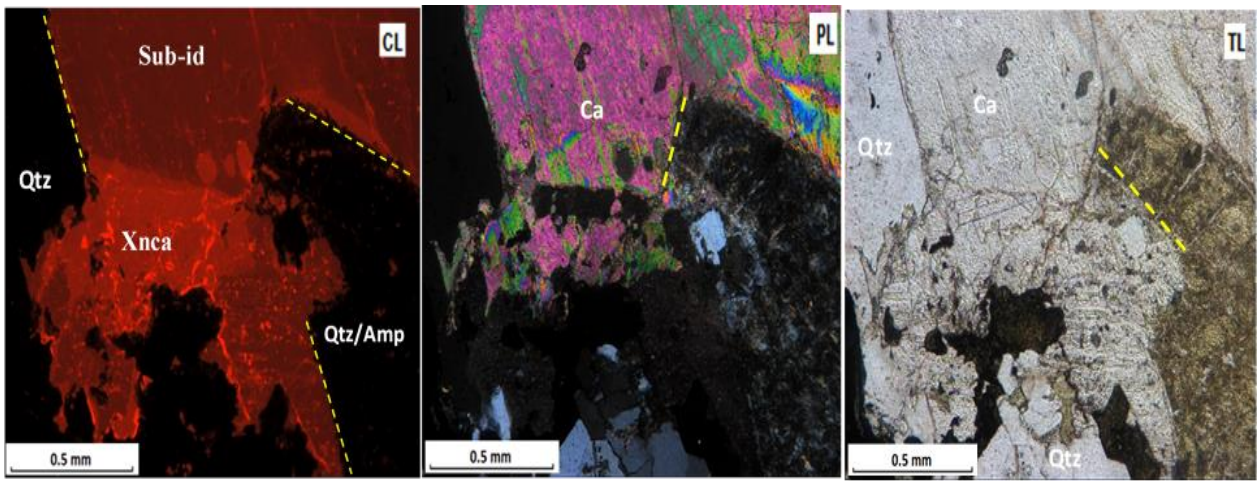


Figure 8.19: Sub-hedral calcite (Sub-id) in bright red CL displaying sub-idiomorphic crystal shape with a distinct crystal boundary and xenomorphic calcite (Xnca) cutting the earlier formed minerals from AT01 of Artonvilla copper deposit.

© University of Venda

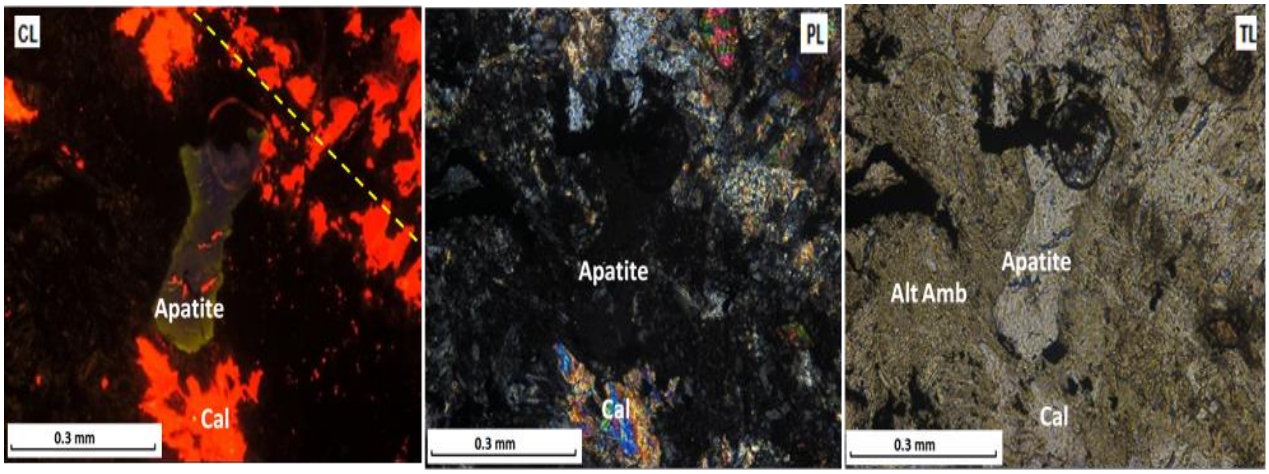


Figure 8.20: Influx of calcite displayed in bright red to orange CL cutting across altered rock materials and cutting through apatite in deep blue CL in sample ATcal01 from Artonvilla copper deposit.

8.5 Discussion

Cathodoluminescence microscopy was used to study minerals associated with the Campbell and Artonvilla copper orebodies. This was done in order to identify different mineral generations, in this case, identification of different generations of quartz, identification of micro-fractures within the mineral grains, zonal growth, brecciation and textural relationships between minerals. Cathodoluminescence study of these features assist in the reconstruction of processes of mineral formation and alteration.

The study involved 11 polished thin sections prepared from mineralized samples from Campbell and Artonvilla copper deposits. The thin sections were investigated, using the Cathodoluminescence microscope HC3-LM under transmitted light (TL) and polarized light (PL). The images were captured, using an in-built high sensitivity Kappa camera DX40-285FW and version 1.4.2.9031 software.

Using Cathodoluminescence microscopy, the following features were captured; mineral species, mineral generations, zonation, texture, and defects such as micro-fractures within mineral grains and infilling of such structures and open space, replacement and mineral alterations (Table 8.3 and 8.4). Cathodoluminescence was revealed by quartz, calcite, apatite and prehnite. Quartz revealed three generations; quartz 1 (Q1), quartz 2 (Q2) and quartz 3 (Q3). For example, Q1 from Campbell copper deposit displayed dark blue to dark violet

© University of Venda

Cathodoluminescence and it was being replaced by Q2 that displayed dark red Cathodoluminescence. Quartz 2 was seen as a replacement product of quartz 1. In places, this replacement resulted in graphic intergrowth. Internal structure of quartz 1 was also revealed by Cathodoluminescence, depicting the micro-fractures that were infilled with later formed quartz 2. The last quartz to from within the Messina copper orebodies was quartz 2 which under Cathodoluminescence was characterized by crystal zonation. Two types of crystal zonation were observed, oscillatory and concentric growth zonation. The oscillatory zonation was displayed mainly by idiomorphic crystals.

Identification of three generations of quartz within the Messina copper deposits is of great significance as there has been different schools of thought in this with connection to the genesis of these deposits. For example, Sawkins and Rye (1979) while conducting fluid inclusions, had identified only one type of quartz that registered low temperature of ore formation ranging from 210^{o} to 15^{o}C. Jacobsen and McCathy (1980) while opposing this finding noted that Sawkins and Rye (1979) had used quartz which was late in the paragenesis sequence. According to these latter researchers, in the Messina orebodies, the early fluids reactions involved desilication and only during the terminal stages of ore mineralization did the fluids become silica rich. The current study, however, has identified three generations of quartz, and quartz 1 was formed at the early stages of ore formation, hence was formed during the 1st stage of ore paragenetic sequence.

Cathodoluminescence microscopy also identified the occurrence of carbonate minerals, mainly calcite, dolomite and ankerite in the Messina orebodies. Dominant among the carbonates was calcite that displayed bright red to orange Cathodoluminescence. Veinlets of calcite were seen cutting across earlier formed minerals including quartz and sulphide ore minerals. Apart from calcite infilling micro-fractures of these minerals, calcite apparently formed within the open space as can be judged by its idiomorphic crystals. Formation of calcite within the Messinc copper deposits, apparently marked the end of ore mineralisation in the area as it cuts through all earlier formed minerals.

Cathodoluminescence microscopy revealed also the alteration of some rock-forming minerals in the area. Of great genetic importance was the alteration of apatite that presented two types, primary and secondary. Primary apatite with subhedral crystals displayed deep blue Cathodoluminescence with bright green rims along its grain boundaries and micro-fractures.

© University of Venda

Secondary apatite was a product of alteration, thus had xenomorphic crystal grains and it displayed yellowish to greenish-pinkish Cathodoluminescence with open fractures filled with chlorite.

© University of Venda

CHAPTER 9

FLUID INCLUSION INVESTIGATION

Preamble

This chapter focusses on fluid inclusion study of minerals associated with copper ores from Campbell and Artonvilla copper deposits. The chapter firstly, review different types and classification of fluid inclusions, principles, importance and application of fluid inclusions to the understanding of geologic processes, using petrographic investigation, microthermometry and Laser Raman microprobe spectroscopy. Secondly, the chapter focuses on fluid inclusion investigation of the ore samples from Campbell and Artonvilla deposits, using different techniques that include; optical microscopy, microthermometry and Raman spectroscopy and then dealt with the interpretation of the obtained results as well as discussion of the findings.

9.1 Types and Classification of Fluid Inclusions

Fluid inclusions are small volumes of fluids with sizes usually < 50 µm, trapped within a crystal during its original growth from that fluid or during subsequent healing of fractures in the presence of fluids which are filled with liquids and/or gases (Roedder and Bodnar, 1997; Roedder, 1984; Wilkinson, 2001; Roedder, 2002). Misra (2000) simply defined fluid inclusion as a minute aliquot of fluid that was trapped inside a crystal at some stage of its formation and this is referred to as primary fluid that is associated with that particular crystal in space and time. Fluid inclusions provide information about the genesis of mineral deposits and their characteristics during their formation (Roedder and Bodnar, 1997; Roedder, 1984; Wilkinson, 2001; Roedder, 2002).

Based on the descriptive classification, which involves describing fluid inclusions in terms of visual parameters such as size, shape, colour, refractive index and most importantly, by the phases: Liquid (L), vapour (V), solid (S) phases present at room temperature (Van den Kerkhof and Hein, 2001), the most common inclusions in ore deposits fall into four general types: Type I- Liquid-rich; type II- Gas-rich; type III- daughter mineral-rich; and type IV- Gas-rich (Nash, 1976) (Fig. 9.1).

© University of Venda

Type I: Is a moderate salinity inclusion. It is a common type of inclusion that contains generally two phases consisting of liquid and a small vapour bubble (Fig. 9.1) ranging from 10% to 40% of the volume of the inclusion (Nash, 1976). The presence of vapour bubble indicates trapping at an elevated temperature and formation of bubble on cooling (Nash, 1976). The volume of vapour is roughly proportional to the temperature whereby calculated curves may be used in estimating temperature (Kalyuzhnyi, 1965). Heating of fluid inclusions on a microscope stage causes homogenization to single liquid phase and the homogenization temperature indicates the temperature at which the inclusion was trapped which represents the temperature of growth of that part of crystal (provided the necessary pressure correction is made). Previous studies revealed the presence of sodium, potassium, calcium and chlorine, and salinity ranging from 0.1-23 wt% NaCl equivalent during freezing tests and chemical analysis of extracted fluids (Roedder, 1972). In some of these inclusions small amounts of daughter salts (carbonates and anhydrite) may be precipitated during cooling (Roedder, 1972; Nash, 1976).

Type II: This is a gas-rich inclusion (Fig. 9.1) that generally contains two fluid phases: liquid and more than 60% vapour (Nash, 1976). The salinity ranges from 0.4 to 7 wt% where the higher salinity indicates trapping of some higher salinity liquid with vapour (Roedder, 1971; Nash and Theodore, 1971). This type is dominantly aqueous but $C0_2$ may be present in small amounts. They appear to represent trapped steam. The simultaneous presence of gas-rich and gas-poor aqueous inclusions is good evidence that the fluids were boiling at the time of trapping (Nash, 1976).

Type III: This type of inclusion contains well developed cubic halite and generally several other daughter minerals, particularly sylvite and anhydrite (Roedder, 1971; Moore and Nash, 1974) (Fig. 9.1) with salinities commonly above 23 wt% and in some cases it ranges from 40% to more than 50% (Roedder, 1971; Moore and Nash, 1974; Nash, 1976).

Type IV: Type IV inclusion has three fluid phases which are liquid, vapour and CO_2 (CH_4) (Fig. 9.1). It is rich in CO_2. The CO_2:H_2O ranges from 3 to more than 30 mol%. Some have salinity of about 2 wt% (Nash and Cunningham, 1973) and some have halite with salinity of about 30 wt% (Nash and Theodore, 1971).

Based on their genetic classification, fluid inclusions may be classified as primary, secondary and pseudo-secondary fluid inclusions. Primary inclusions are those fluid inclusions that

© University of Venda

were formed during the formation of the enclosing crystal. Texturally, they tend to be either solitary or isolated within the crystal, and are best identified by being trapped parallel to a growth zone or crystal face (Fig. 9.2). During analysis of such inclusions, information on the conditions of formation or crystallization of the host mineral is revealed (Bodnar, 2003; Van den Kerkhof and Hein, 2001; Misra, 2000; Goldstein and Reynolds, 1994).

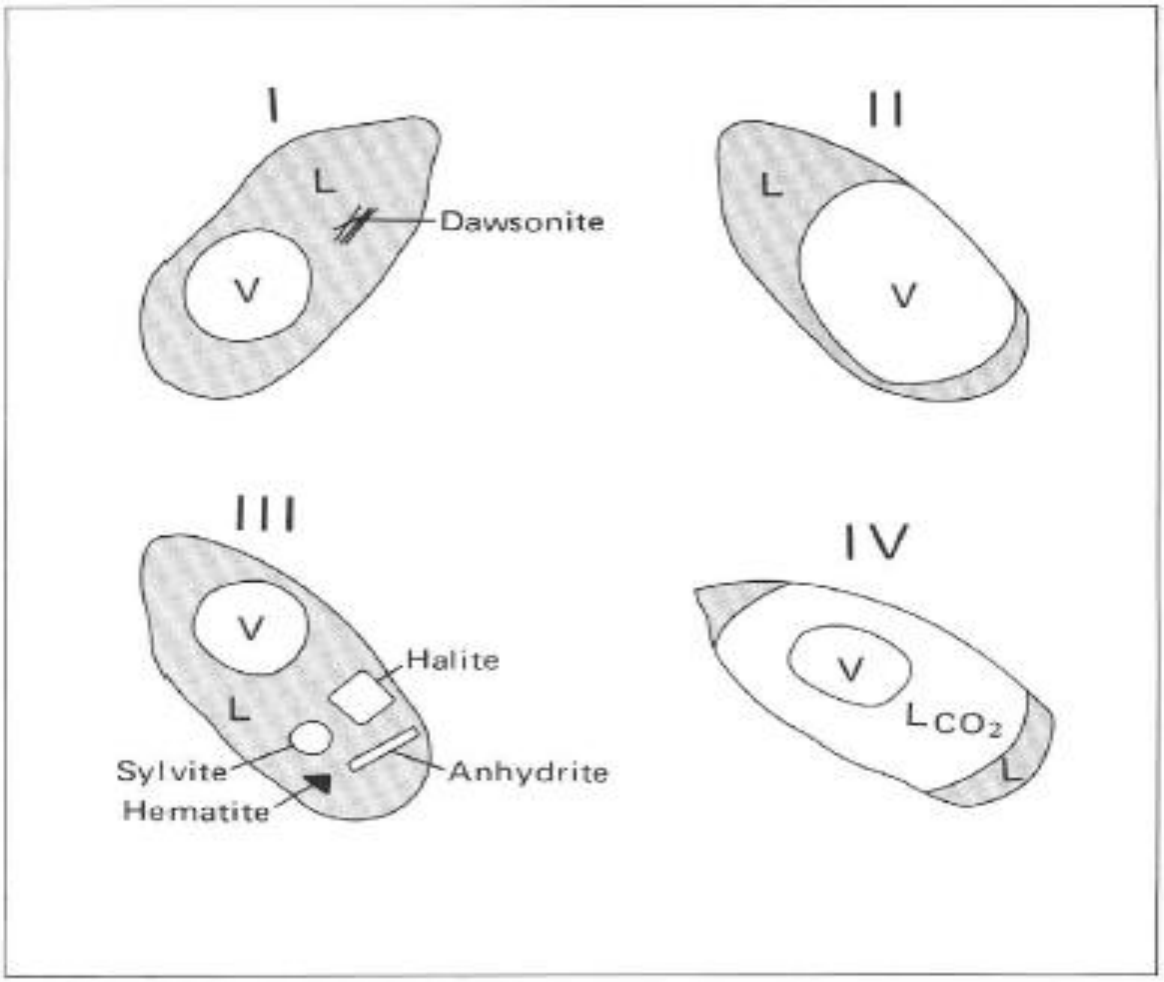


Figure 9.1: Sketches illustrating the common types of fluid inclusions at room temperature, classified based on the presence of phases within the fluid inclusion: L= aqueous fluid, V= vapour, LCO_2 = liquid CO_2 (Nash, 1976).

Secondary inclusions as those inclusions that occur along fractures that developed after the formation of the host mineral and the fractures healed in the presence of fluids (Bodnar, 2003; Misra, 2000; Van den Kerkhof and Hein, 2001; and Goldstein and Reynolds, 1994). Texturally these fluid inclusions are recognized by their occurrence in trails or clusters that often cut across grain boundaries (Bodnar, 2003; Misra, 2000; Van den Kerkhof and Hein, 2001 (Fig. 9.2).

© University of Venda

Pseudosecondary inclusions (Fig. 9.2) originate from trapping of fluid in a fracture that formed during the growth of the crystal and such inclusions show a distribution similar to that of secondary inclusions but are primary in terms of their age relative to the host crystal although not necessarily of the same composition as the primary inclusions (Van den Kerkhof and Hein, 2001; Misra, 2000; Goldstein and Reynolds, 1994). Texturally these inclusions occur along trails that end abruptly against grain boundaries, or one of the growth zones (Van den Kerkhof and Hein, 2001).

According to Bodnar (2003), sometimes the origin of the fluid inclusions relative to the formation of the crystal cannot be determined with certainty and the inclusions origin is said to be indeterminable (i). Texturally the fluid inclusion will mostly be in isolation (Fig. 9.2).

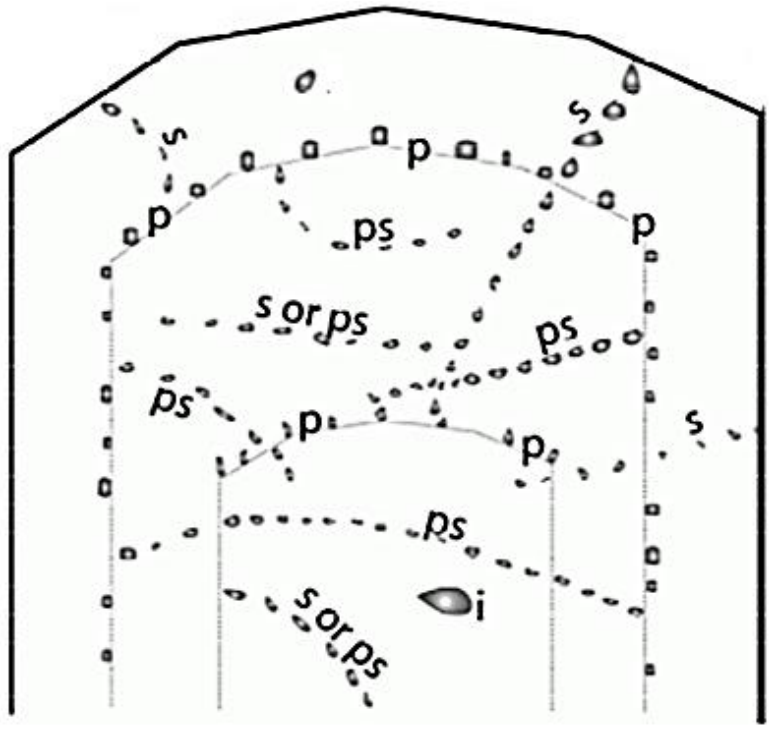


Figure 9.2: Sketch illustrating distinction among primary (p); pseudo-secondary (ps); secondary (s); and indeterminable (i) fluid inclusions (Goldstein and Reynolds, 1994).

© University of Venda

9.2 Fundamentals of Fluid Inclusions

9.2.1 Assumptions of Fluid Inclusion Studies

Fluid inclusion studies are based on several major assumptions (Roedder, 1979b, Goldstein and Reynolds, 1994). It is assumed that the inclusion represents a chemically closed (isoplethic) system from the time of entrapment implying that there has been no leakage or necking since entrapment. If an inclusion shows evidence of necking, it should not be used for microthermometry as it is not a primary inclusion.

It is also assumed that the volume of the inclusion remains constant (isochoric) since entrapment (Roedder, 1979b, Goldstein and Reynolds, 1994). This implies that the inclusion followed a path of constant density along one of the isochores for the system in question (Fig. 9.3).

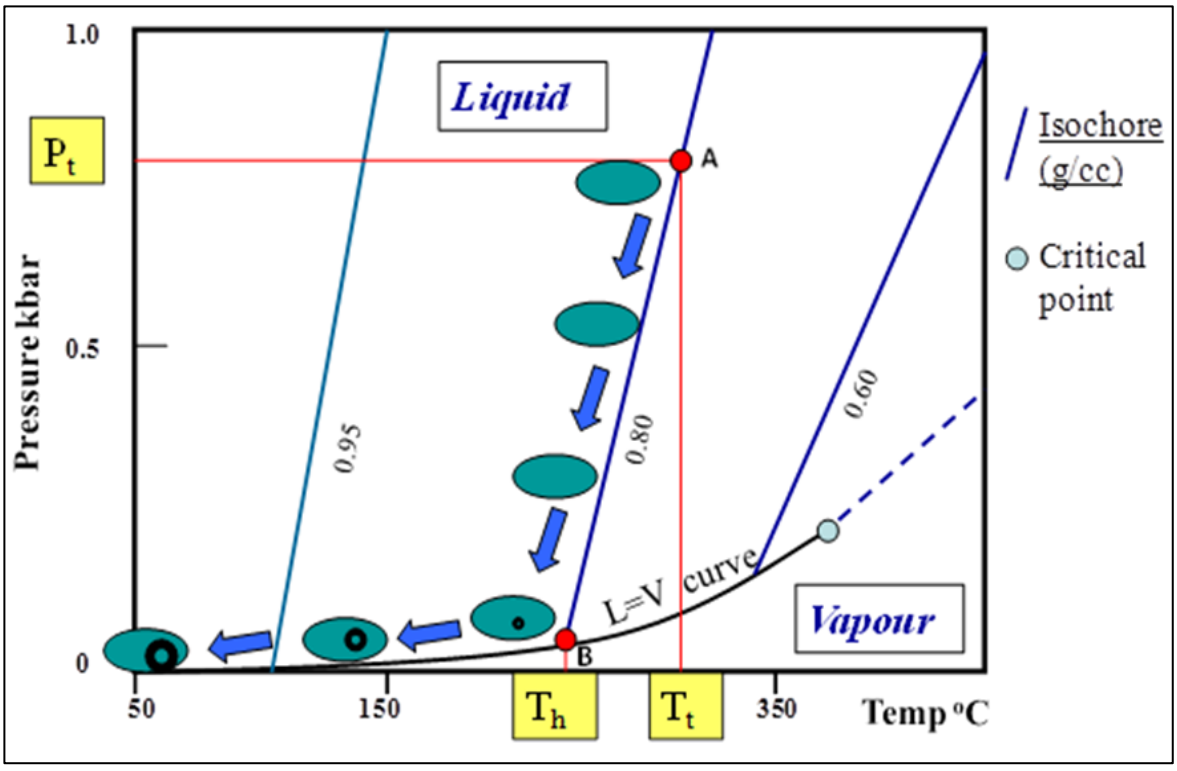


Figure 9.3: Pressure -Temperature diagram showing changes occurring in a fluid inclusion as the rock is cooled and decompressed along an isochore and a phase boundary. Pt: entrapment pressure; T_t: entrapment temperature; T_h: homogenization temperature; L: liquid; V: vapour (www.kingston.ac.uk/esg/facilities/fluidinc.pp)

© University of Venda

9.2.2 Measurements in Fluid Inclusion Studies

A careful study of fluid inclusions provide a wealth of information about the system through the measurements of the following: Freezing point (T_{mf}); first melting temperature or initial melting temperature (T_i), homogenization temperature (T_h), the temperature at which a fluid inclusion transforms from a heterogeneous phase to a homogeneous state, temperature of entrapment (T_t), the temperature at the time of trapping (formation) of a fluid inclusion; and decrepitating temperature (T_d), the temperature at which a fluid inclusion irreversibly ruptures or "decrepitates", upon heating (Roedder, 1984; Goldstein and Reynolds, 1994; Diamond, 2003).

Information derived from the fluid inclusion studies include; fluid composition, salinity of the fluids, fluid density and temperature of entrapment, and T-P history of the sample (Bordnar, 2014; Roedder, 1984, Misra, 2000, Van den Kerkhof and Hein, 2001).

9.2.3 Principles of Fluid Inclusion Analysis

Generally, when fluid inclusion is trapped at a specific temperature (T_t) and pressure (P_t) during formation of a mineral at a certain depth in the earth crust or mantle, the mineral will undergo cooling process. Assuming there is no change in the mass or volume of such inclusion during cooling, the inclusion will cool along lines of constant density on a P-T diagram known as isochores (Fig. 9.3). This implies that fluid inclusions with different composition will have isochores of different slopes in P-T space. For example, isochores of H_2O are much steeper than those of CO_2 (Roedder and Bodnar, 1980; Roedder, 1984; Misra, 2000). While the inclusion is cooling along the isochores (from point A to point B) as a homogeneous liquid phase, it will then intersect the liquid – vapour univariant curve (point B) whereby the bubble will appear and increase with further cooling (Fig. 9.3). When the inclusion is heated on a heating-cooling stage, the inclusion will reverse its path and homogenize to liquid phase giving a homogenization temperature (T_h) and minimum estimate of its trapping temperature (T_t) (Fig. 9.3) (Roedder and Bodnar, 1980; Roedder, 1984; Misra, 2000). If the inclusions were trapped from a boiling fluid (point B in Fig. 9.3), the homogenization temperature is the same as the trapping temperature and the corresponding pressure (P_h) is the trapping pressure (Roedder and Bodnar, 1980; Roedder, 1984; Misra,

© University of Venda

2000). For the inclusion that is filled with CO_2 may intersect the liquid-vapour boundary from the vapour side depending on the fluid inclusion density and the vapour bubble shrinks as the bubble condenses into liquid phase (Roedder and Bodnar, 1980; Roedder, 1984). While for the fluid inclusion with a mixture of two fluids that are miscible at high temperature, then upon cooling and decompression the two components will unmix and the two phases of immiscible fluids will appear in the inclusion (Misra, 2000).

9.3 Importance and Application of Fluid Inclusions

The fluid inclusion studies in ores, rocks and minerals dates back to 17th century when the presence of fluid inclusions in minerals were employed to support the Neptunist theories (Goldstein and Reynolds, 1994). The first modern approach was done by Hennry Clifton Soby in 1858 (Fig. 9.4) where he showed that fluid inclusions were present in samples from many geological environments, including ore deposits and that it was trapped in the crystal and was preserved for million or billion years (Goldstein and Reynolds, 1994; Roedder and Bodnar, 1997; Touret, 1977).

After Hennry Clifton Soby, between 1873 and 1920 (stage II, in Fig, 9.4) during the 1st World War a number of researchers including Harry Rosenbusch, Ferdinand Zirkel, Ferdinand André Fouqué, Auguste Michel-Lévy and Alfred Lacroix conducted systematic studies of fluid inclusions. However, from 1920 to 1960 (stage III, Fig. 9.4) there was a decline in fluid inclusion research in the western world, whereas the Russians did the extensive fluid inclusion investigations lead by G.G. Lemmlein, and N.P. Ermakov. From 1960 to date (stage IV, Fig. 9.4), the French and the European groups (Deicha, Nancy Group, Shephen), and the USA researchers (Edwin Roedder and Robbert Bodnar) have continued with the systematic studies of fluid inclusions.

Since then fluid inclusion study has become an integrative part of almost all the disciplines of earth sciences (Roedder, 1984). Today the study of fluid inclusions is widely applied in the understanding of the genesis of ore deposits, igneous, sedimentary and metamorphic rocks, and geothermal systems (Li *et al.*, 2015, Maydagán *et al*., 2015; Glassley, 2014; Gilg *et al*., 2014; Gueye *et al.*, 2013; Van den Kerkhof, 2014; Touret, 2001; Van den Kerkhof *et al.*, 2014; Wilkinson, 2001).

© University of Venda

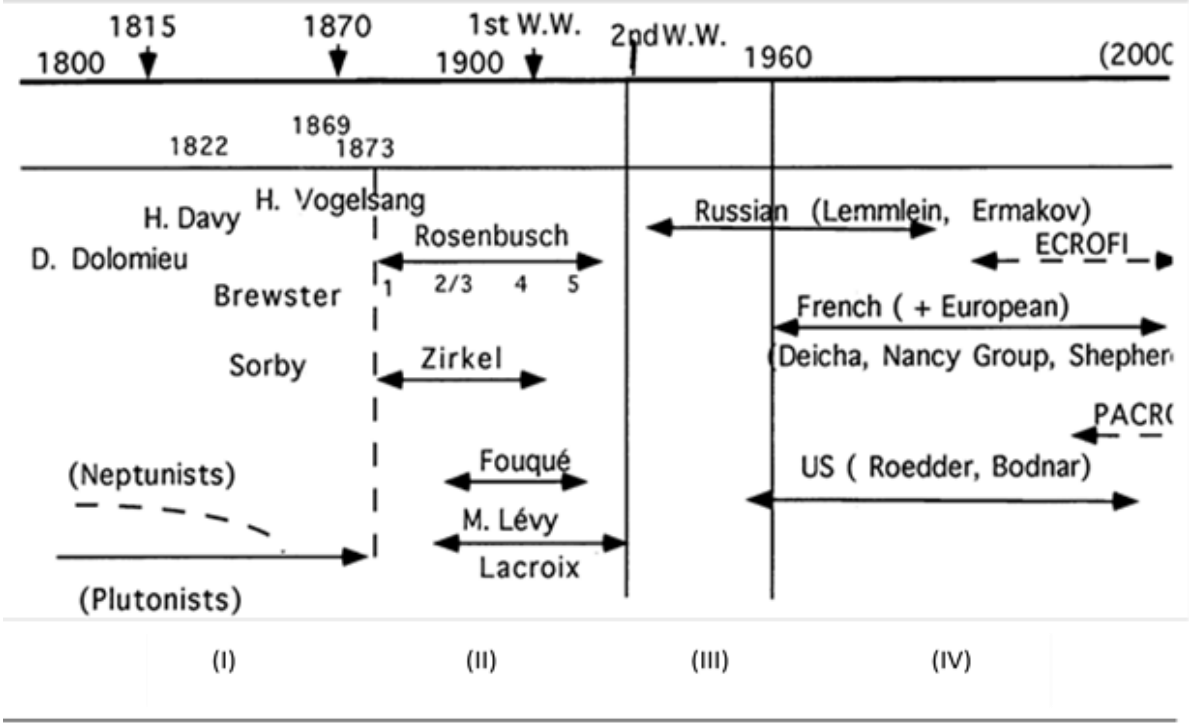


Figure 9.4: Historical overview of the study of fluid inclusions (Touret, 1977).

Fluid inclusion studies on ore deposits revealed many complexities in an attempt to use fluid inclusions as a tool to understand ore deposition while these same complexities have been shown to provide greater wealth of clues concerning ore deposition process (Roeder and Bodnar, 1997). They provide valuable information using simple petrographic observation, microthermometric analysis, or sophisticated geochemical analysis of fluid inclusion content which include: temperature, pressure, composition and origin of fluids of mineral precipitation, improve interpretation of petroleum migration history and reconstructions of thermal history (Misra, 2000; Goldstein and Reynolds, 1994).

Temperature: Fluid inclusions can be used to obtain a minimum temperature at which a mineral was formed or deposited. Many companies make use of fluid inclusions in the determination of temperature in order to understand the processes that went on to form known deposits and also in the exploration for new deposits (Li *et al*., 2015; Han *et al*., 2014; Yoo *et. al*., 2011; Hein *et. al*., 1994). Oil companies look at the temperature of inclusions of core samples to determine whether the rocks have been hot enough to generate oil (Hall *et. al*., 2002; Roedder, 2002). In geothermal exploration, fluid inclusions temperature is used in siting boreholes for the exploitation of the geothermal resources (Glassley, 2014; Roedder, 2002). Gemologists use fluid inclusion temperature data to validate the place of origin of gemstones (Limtrakun *et al.,* 2001; Roedder, 2002).

© University of Venda

Pressure: Some fluid inclusions are suitable for determination of the trapping pressure, which is the pressure of the environment at the time of the fluid entrapment (Roedder and Bodnar, 1980). The ability to interpret the pressure data is dependent on the particular suite of the fluid inclusions present in the minerals studied (Goldstein and Reynolds, 1994). Estimates of the pressure and hence the depth at which some ore veins have formed have aided in the search for similar veins in otherwise unknown new areas (Zhong *et al.,* 2014, Roedder, 2002).

Composition and origin of fluids: In appropriate primary fluid inclusions, many aspects of aqueous fluid composition can be established such as salinity, concentrations of ions, isotopes, dissolved components such as sulphate and gas which are important in deducing the origin of the deposit (Goldstein and Reynolds, 1994). In recent years, there has been a breakthrough on understanding the chemistry of ore metal transportation and deposition and thus fluid compositions have helped to refine these models (Bodnar, 2014; Roedder, 2002).

The study of fluid inclusions has been widely used in improving understanding of subsurface fluid evolution such as subsurface brines, porosity evolution in petroleum exploration, petroleum migration history, reconstructions of thermal history and reconstruction of tectonic or stratigraphic history (Roedder, 2002, Misra, 2000; Goldstein and Reynolds, 1994).

Consequently, this study focused on the investigation of fluid inclusions in quartz associated with copper-sulphide mineralisation of the Campbell and Artonvilla copper sulphide deposits so as to establish the classification of fluid inclusion in terms of their chronological relationship (relative age) and also to ascertain the physiochemical conditions of ore forming minerals within the Messina copper-sulphide deposits for the purpose of understanding the genesis of the deposits.

9.4 Methods for Fluid Inclusion Analysis

Several methods have been used in the analysis of fluid inclusions and these are divided into non-destructive and destructive methods (Table 9.1). The non-destructive methods include those in which the analysis takes place without destroying the fluid inclusion vacuole, and the destructive methods are those in which the fluid inclusion is opened for the analysis (Passchier and Trouw, 2014; Goldtein and Reynolds, 1994; Roedder and Bodnar, 1997). Non-destructive analyses include several techniques such as optical microscopy,

© University of Venda

microthermometry, vibrational spectroscopy and particle beams techniques (Table 9.1) (Passchier and Trouw, 2014; Goldtein and Reynolds, 1994, Roedder and Bodnar, 1997).

The optical microscopy include different methods such as petrographical microscopy which is used for fluid abundance and chronology; Cathodoluminescence microscopy/Scanning electron microscopy which deal with textural relations within the mineral; UV-microscopy used for the detection of hydrocarbons; and IR-microscopy applied for visualization of fluid inclusion in a mineral, while transmission electron microscopy (TEM) is used to identify the micro-cracks (Table 9.1) (Passchier and Trouw, 2014; Goldtein and Reynolds, 1994; Roedder and Bodnar, 1997).

Microthermometry is used for determination of composition and molar volume within fluid inclusion; while vibrational spectroscopy is used for determination of no-aqueous fluids and daughter crystals, using Laser excited micro-Raman spectroscopy; Fourier Transform Infrared (FT-IR) used for detecting CO_2, H_2O; and fluorescence spectroscopy used for detection of hydrocarbons. The particle beams techniques use Electron microprobe (EPMA), Proton probes and Electron synchrotron in order to analyse fluid inclusion near the surface (Table 9.1) (Passchier and Trouw, 2014; Roedder and Bodnar, 1997; Goldtein and Reynolds, 1994).

The destructive analysis of fluid inclusions can be conducted, using bulk analysis or single inclusion analysis techniques. The bulk analysis involves three techniques namely: mechanical stepwise heating, crushing and leaching techniques. Mechanical technique uses crushing stage method for determination of non-aqueous fluids, while stepwise heating technique involves acoustic emission decreptometry method that is used for pressure determination, gas chromatography which is used for the determination of fluid inclusion composition, and mass spectroscopy which is used for the determination of bulk fluid composition and isotopes concentrations.

The crushing and leaching is used for determination of composition of aqueous fluids, element ratio and dissolved daughter crystals. Single inclusion analysis mainly uses electron microprobe analysis (EMPA) or secondary ion mass spectroscopy (SIMS) and laser ablation inductively coupled plasma mass spectroscopy (LA-ICPMS) to identify daughter crystals, composition of fluid inclusion and trace elements respectively (Table 9.1) (Passchier and Trouw, 2014; Roedder and Bodnar, 1997; Goldtein and Reynolds, 1994).

© University of Venda

Table 9.1: Overview of methods for studying inclusions

Non –destructive analysis			
Technique		**Method**	**Application**
1. Optical microscopy and visualization techniques		Petrographical microscopy	Fluid inclusion abundance and chronology (relative age)
		CL- microscopy/SEM-CL	Textural relation with host mineral, secondary quartz
		UV-Microscope	Detection of hydrocarbons
		IR-Microscope	Visualizing inclusions in opaque minerals (e.g. chromite, cassiterite, pyrite)
		Transmission electron microscopy (TEM)	Dislocation/ micro-cracks around FI
2. Microthermometry		Heating and cooling stage	Composition and molar volume
3. Vibrational Spectroscopy		Laser excited micro-Raman spectroscopy	Composition of non-aqueous fluids, identification of daughter crystals
		Fourier Transform Infrared (FT-IR)	Detection of CO_2, H_2O, Hydroxyl
		Fluorescence spectroscopy	Detection of hydrocarbons
4. Particle beams techniques		Electron microprobe (EMPA)	Inclusion near the surface
		Proton probes: PIXE, SXRF	
		Electron synchrotron	
Destructive analysis			
Bulk analysis	1. Mechanical	Crushing stage method	Non-aqueous, qualitative
	2. Stepwise heating	Acoustic emission decreptometry	Finger print of fluid inclusion content (pressure determination)
		Gas chromatography	Bulk fluid composition
		Mass spectrometry	Bulk fluid composition, isotopes
	3. Crush and leach	micro-chemical analysis, AAS	Composition of aqueous fluids, element, ratios, dissolved daughter crystals
Single inclusions	EPMA or SIMS (opened inclusions)		Identification of daughter minerals, composition of FI (Freezing method)
	LA-ICPMS		Composition including trace elements

© University of Venda

9.5 Fluid Inclusion Investigation of the Messina Copper Deposits

In this study, fluid inclusion investigation was done using three methods classified under non-destructive techniques, viz.; optical microscopy (fluid inclusion petrography), microthermometry, and vibrational spectroscopy (Laser excited Raman spectroscopy). Optical microscopy involves petrological investigation of fluid inclusions for the determination of fluid inclusion abundance and chronology, and textural relations with host mineral. Microthermometry is a heating and cooling method used for the determination of fluid inclusion composition, molar volume and physical conditions of the fluid entrapment, while Laser excited Raman spectroscopy involves determination of composition of non-aqueous fluids and identification of daughter crystals.

9.5.1 Fluid Inclusion Petrography

Fluid inclusion petrography entails identification of fluid inclusions, their classification in terms of their chronology (relative age), composition, and textural relations with the host mineral.

9.5.1.1 Sample Selection

A total of 12 samples were selected for fluid inclusion studies. The selected mineralised samples were both from Campbell (CPdis01, CPdis02, CP02, CPA4, CP03, CPqtz03, CPqv01 and Cpq03) and Artonvilla (ATcal01, AT01, ATavr12 and AT02) copper-deposits (Table 9.2). The samples were collected randomly from the waste rock dump and were considered to be ideal for this study because they had quartz veins, associated with copper-sulphide mineralisation comprising chalcopyrite, pyrite, bornite and chalcocite minerals.

9.5.1.2 Sample Preparation

Sample preparation for fluid inclusion study using, petrographic microscopy was done by making doubly polished thick sections (plates) of 100 µm thickness. From the 12 doubly polished plates, 7 were prepared at Société Générale de Surveillance (SGS) Laboratory in Johannesburg, South Africa and 5 were prepared at the Department of Applied Geology, Geoscience Institute, Göttingen University, Germany.

© University of Venda

Table 9.2: Quartz-sulphide ore samples from Campbell and Artonvilla deposits used for fluid inclusion studies

Deposit	**Sample ID**	**Host Mineral**	**Rock type with sulphide mineralisation**
Campbell	CPdis01	Quartz	Amphibolite schist with disseminated chalcopyrite and quartz vein
	CPdis02	Quartz	
	CP02	Quartz	Amphibolite schist with chalcopyrite, pyrite and bornite sulphide mineralisation within quartz vein
	CPA4	Quartz	
	CP03	Quartz	Quartz vein with brecciated chalcopyrite, and pyrite
	CPqtz03	Quartz	Quartz vein with veined chalcopyrite, pyrite and bornite
	CPqv01	Quartz	Quartz vein with veined chalcopyrite, pyrite and bornite
	CPq03	Quartz	Quartz vein with veined chalcopyrite, bornite, and covellite
Artonvilla	ATcal01	Quartz	Amphibolite schist with disseminated chalcopyrite, and calcite vein
	AT01	Quartz	
	ATavr12	Quartz	Mafic rock with quartz vein, garnet and disseminated chalcopyrite
	AT02	Quartz	

According to van den Kerkhof and Hein (2001), it is ideal for polished thin-section to be made from the same sample for microscopic studies, electron microprobe analysis, mineral thermobarometry, and also for cathodoluminescence microscopy. Consequently, the doubly polished plates in this study were prepared from the same selected ore samples used for the preparation of the thin-sections and polished sections.

The preparation was done following the doubly polished thick section preparation procedures set by van den Kerkhof and Hein (2001); Goldstein and Reynolds 1994; Shepherd *et al.* (1985) and Roedder (1984).

Cutting: The slab or chip of a slide size was cut using diamond saw and trimmed using trim saw. The cutting was done with care to minimize any harm to fluid inclusions and this was

© University of Venda

done by cutting gently and having ample coolant during cutting process and by using precision high speed trim saw which can be adjusted so that the blade will not wobble.

*Grinding:*Grinding was done using a Precision Lapping machine. The lapping powders, silicon carbide 120 grit, 400 grit, 1000 grit and 1200 grit and deionized water were added during the process in order to achieve flat and smooth surface of the plate.

*Polishing:*Polishing was firstly done on well ground side of the plate. The section was polished, lapped on MD-Mol Cloth together with 1 μm Diaduo and again with 3 μm Diaduo diamond solution to a final standard thickness of 100 μm using Struers Rtopol-35 lapping machine. Final stage of polishing was done using MD-Pan fine Cloth used with 6μm Diaduo diamond solution which has finer grain size of 3 μ - 1 μ. The plate was then cleaned with deionized water and air dried to remove remaining grit and some diamond solution.

Mounting and trimming: Once the surface of the section was polished it was then glued to a petrographic slide, using epoxy solution (2 parts of hardener: 15 parts of resin) (SGS sample preparation) and araldite solution (Gottingen sample preparation). Bubbles were removed by placing the section into an Epo-vacuum chamber. The section was then trimmed from the glass side to a desired size using slow-speed trimming saw. The process was repeated for the opposite surface of the plate. The achievement of the proper thickness was also checked by observing the section under the petrographic microscope to ensure light transmission and visibility of inclusions.

Based on the laboratory procedures of the two respective laboratories, the prepared plates were immersed in acetone for about 24 hours for those samples that were prepared using epofix bonding solution, whereas those that were prepared using araldite epoxy solution were immersed in acetone for about 6 hours. This was done in order to separate the plates from the glass slides. The plates were then cleaned up using a fine brush immersed in acetone to remove any excess bonding solution. Each plate was then numbered accordingly, ready for fluid inclusion investigation.

9.5.1.3 Fluid Inclusion Analysis

Identification of fluid inclusion was done at the Department of Applied Geology, Geoscience Institute, Göttingen University, Germany. Firstly, by using Zeiss Axiophot petrographic

© University of Venda

microscope attached with a KCC Zelos camera which uses 1.2.2.12101 Kappa GiG Vision Kappa camera software (Fig. 6.2) for the determination of the fluid inclusion occurrence in quartz. The identified portion of the plate was chipped off and then used for classification in terms of genetic types (relative age: primary, secondary and pseudosecondary inclusions) and phase assemblages of fluid inclusions (liquid, vapour and solid phases). This was done using BH-2 Olympus standard petrographic microscope connected to of KCC Zelos version 1.2.2.12101 Kappa GiG Vision Kappa camera and Linksys 32 software (Fig. 9.11) while Heating-freezing microscope system, TMS94, LNP System Controllers, and Nitrogen gas pump were switched off at this stage.

During analysis, photos were taken (Appendix 9A) using the attached camera and software connected to the computer for documentation purposes and sketches were drawn in a note book. Different characteristics such as abundance, fluid inclusion type, phase assemblages, relative age (primary, pseudosecondary, secondary), relative phase volumes (spherical fluid inclusion – Volume % and flat fluid inclusions – area %), inclusion size and morphology were noted, documented (Appendix 9B) and summarized (Table 9.3).

9.5.1.4 Results and Interpretation

Occurrence and abundance

The identification of fluid inclusions in quartz veins from veined, disseminated and brecciated ores was done using petrographic microscopy in order to determine the occurrence of fluid inclusions. The fluid inclusions were identified in quartz crystals from both Campbell and Artonvilla copper deposits. For example, occurrence of fluid inclusions was revealed along crisscrossing planes of veined quartz crystals from Campbell copper deposit (Fig. 9.5).

The fluid inclusions appeared tiny with majority of them having minute bubbles. Some appeared as dark spots, but also forming crisscrossing planes of which some of the planes followed the microfractures within the quartz crystal. Some fluid inclusions were scattered within the quartz crystals (Fig. 9.5). Following the classification in terms of trails terminology proposed by Simons and Richter (1976) and Kranz (1983); transgranular, intergranular and intragranular trails of fluid inclusions were identified, viz: transgranular inclusions are

© University of Venda

formed in healed micro-cracks, cross-cutting grain boundaries; intergranular formed along the grain boundary; and intragranular fluid inclusions occur within single grains and do not cross-cut grain boundary (Fig. 9.5).

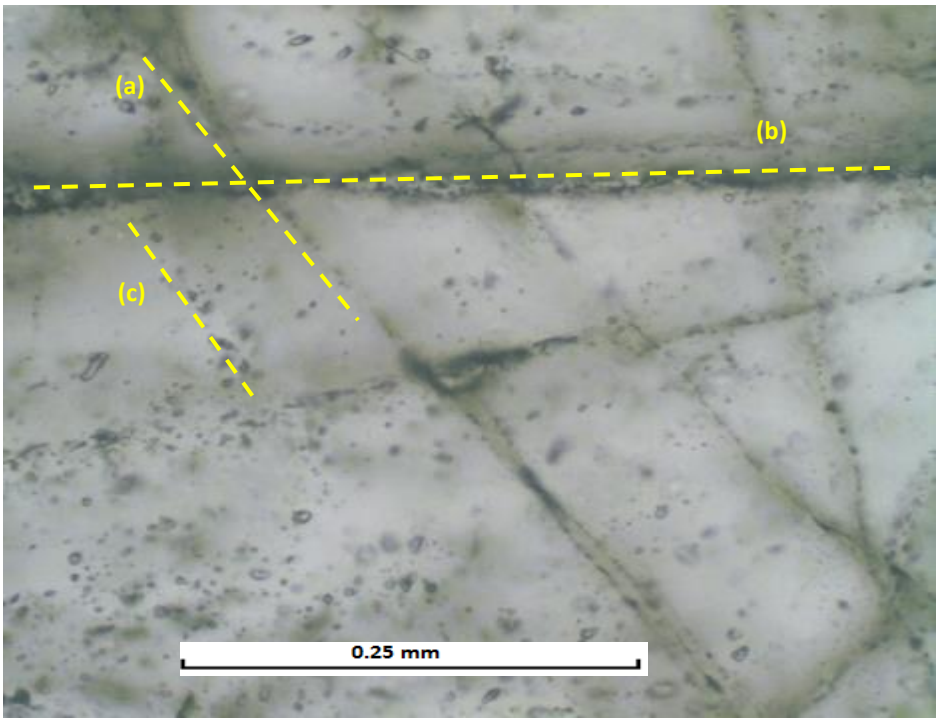


Figure 9.5: Photomicrograph of crisscrossing planes of fluid inclusions along microfractures of quartz vein in sample CPqtz03 from Campbell copper deposit. Trails of fluid inclusions indicating (a) transgranular, (b) intergranular and (c) intragranular textures.

Types of fluid inclusions and their characteristics

Following classification pointed out by Nash (1976), four types of fluid inclusions were identified at room temperature from both Campbell and Artonvilla deposits, namely: Type I - L-rich (L + V); Type II - V-rich (L + V); Type III – High salinity + daughter minerals (L + V + D_{1+2}) and Type IV - Gas rich (L + V + Gas).

Type I - L - rich (L + V)

Type I was identified as multiphase liquid rich two phases which comprised liquid and vapour phases at room temperature. The fluid inclusions were generally small with size ranging from 2x2 to 15 x10 µm and vapour bubbles were small ranging from 5 to 20% in volume. These were found in abundance in most of the samples with high occurrence of primary fluid

© University of Venda

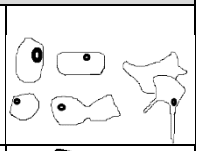
inclusions as compared to secondary fluid inclusions. Textually in both deposits, they occurred as clusters, scattered and as isolated fluid inclusions. Some of the fluid inclusions occurred as trails along fractures and along crystal growth zones. Fluid inclusions along crystal growth were only identified within samples from Campbell copper deposit, whereas both Campbell and Artonvilla revealed isolated, scattered and cluster textures including trails of fluid inclusions along fractures (Table 9.3 and Fig. 9.6). Both spherical and irregular shapes were exhibited at these deposits, while rectangular and necking-down shapes were revealed only at Campbell deposit (Table 9.3 and Fig. 9.7).

Type II - V-rich (L + V)

Type II was identified as multiphase vapour-rich inclusions comprising both liquid and vapour phases at room temperature and generally small in size (3x2 µm). The vapour bubbles were $\geq$ 60% in volume (Table 6.3 and Fig. 6.8a). These inclusions were dominant within the Artonvilla deposit. In both deposits, vapour rich inclusions occurred as isolated inclusions with spherical shape (Table 9.3 and Fig. 9.8). The presence of gas (vapour) and aqueous solution was an indication that the fluids were boiling during the time of trapping. Consequently, the fluids were trapped at elevated temperature.

© University of Venda

Table 9.3: Characteristics of fluid inclusions identified in quartz associated with sulphide mineralisation within Campbell and Artonvilla copper deposits using optical microscopy method

Copper deposit	Fluid inclusion type		Fluid inclusion characteristics						
			Phase assemblages	**Relative abundance**	**Primary (P), *Secondary* (S)**	**Size ((µm) Volume (%)**	**Textures**	**Morphology**	
Campbell	L-rich two phase Multiphase	Type I: Liquid rich, Moderate salinity	L + V	High	High P, Low S	2x2 – 15x10 5 – 20%	Isolated, scattered clusters, trails along fracture and growth zones	Spherical, Rectangular, irregular, necking down	
	Multiphase	Type II: Vapour rich	L + V V ≥ 60%	Low	High P	3x2 80%	Isolated	Spherical	
	Multiphase solid	Type III: High salinity + daughter minerals	L + V + D_{1+2} Halite /Calcite	Low	High P	12x8 10- 15%	Isolated	Spherical	
	Multiphase	Type IV: Gas rich	L + V + Gas	Low	Moderate P and S	2x2 – 7x5 5-10%	Isolated, clusters, scattered, trails along fractures and growth zones	Spherical, irregular	
Artonvilla copper deposit	L-rich two phases Multiphase	Type I: Moderate salinity	L + V	High	High P, Low S	2x2 – 6x2 10– 20%	Clusters, scattered, trails along fractures	Spherical, rectangular, irregular	
	Multiphase	Type II: Vapour rich	L + V V ≥ 60%	Moderate	High P	4x3 80%	Isolated	Spherical	
	Multiphase	Type III: High salinity + daughter minerals	L + V + D_{1+2} Halite /Calcite	Low	High P	3x2 -5x4 10-15%	Scattered, clusters and isolated	Spherical, rectangular	
	Multiphase	Type IV: Gas rich	L + V + Gas	Low	High P Low S	3x2–6x4 5-10%	Clusters, scattered,	Spherical, irregular	

N.B: P- primary; S-secondary; L-liquid; V- vapour; D_{1+2} - Daughter minerals 1and 2

© University of Venda

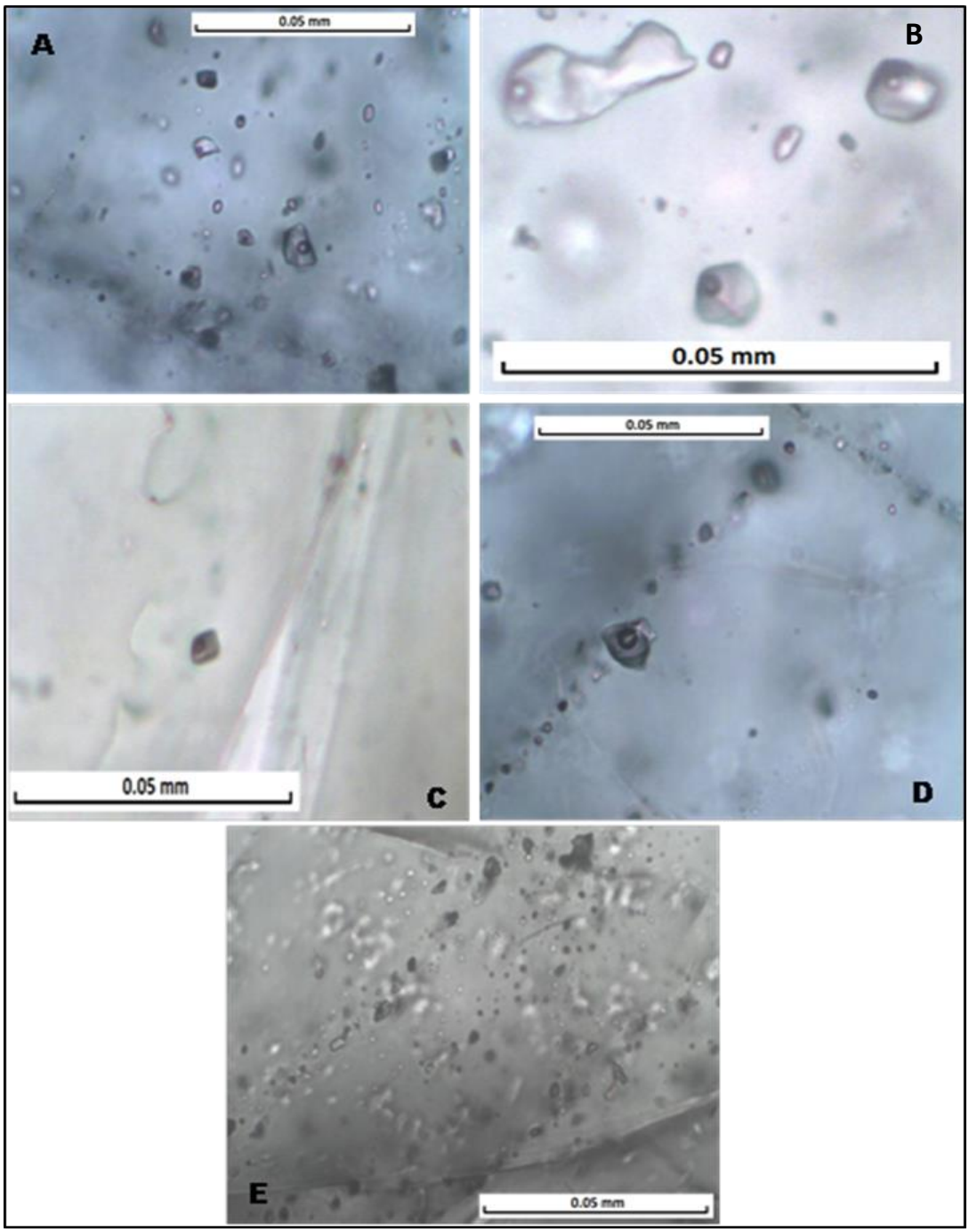


Figure 9.6: Photomicrographs of representative types of fluid inclusions in quartz crystals from disseminated, veined and brecciated ores from Campbell and Artonvilla copper deposits indicating different types of textures and relative age: (A) clustered and primary, (B) scattered and primary, (C) isolated and primary, (D) trails of fluid inclusions along fractures and secondary (E) along crystal growth zones and are primary inclusions.

© University of Venda

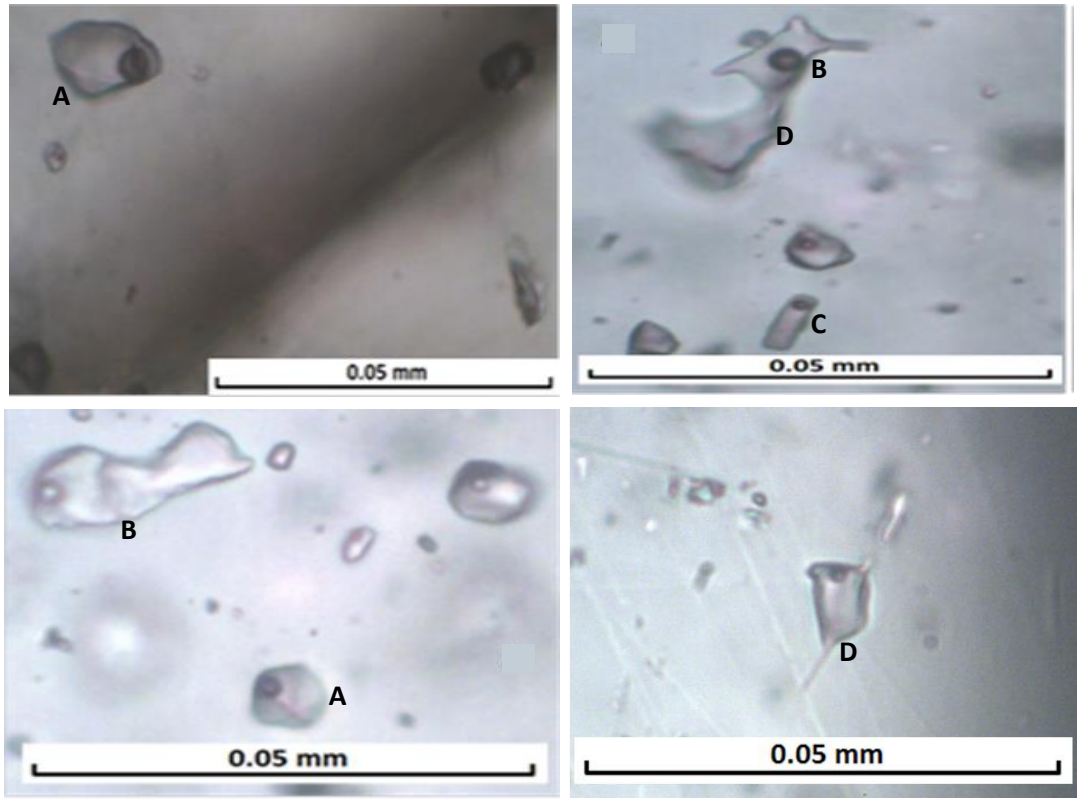


Figure 9.7: Fluid inclusions indicating different types of morphology: (A) Spherical; (B) irregular; (C) rectangular; and (D) necking-down of fluid inclusion only from Campbell deposit.

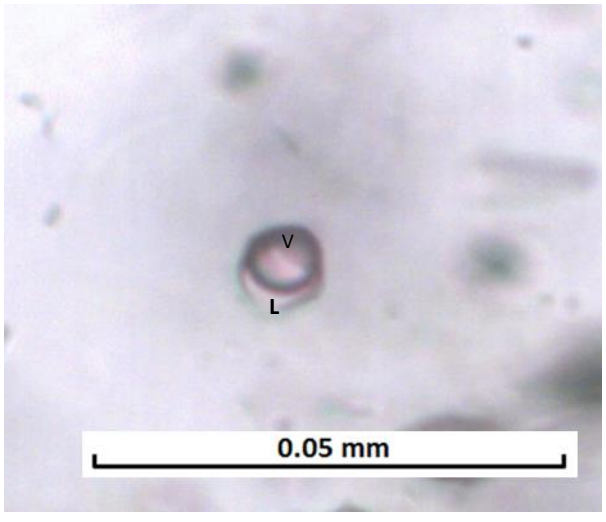


Figure 9.8: Type II vapour-rich (V + L) fluid inclusion with large vapour phase with volume ≥ 60% exhibiting isolated texture and spherical shape.

© University of Venda

Type III – High salinity + daughter minerals (L + V + D_{1+2})

Type III was identified in both deposits as multiphase with high salinity and daughter minerals which include halite and calcite. The halite was identified through its reflectance and cubic crystal shape, using optical microscopy. Halite had refractive index of 1.54 and was isotropic with cubic habit. The crystal revealed light green colour. Calcite indicated high birefringence with prismatic habit. Similarly, several studies revealed same optical properties for the same daughter minerals (Van den Kerkhof and Hein, 2001). This type was less abundant as compared to type I. Most of type III inclusions occurred as primary fluid inclusions with size ranging from 2x2 to 7x5 µm. The vapour bubbles were small with volume ranging from 10% to 15% (Table 9.3 and Fig. 9.9). Textually, these fluid inclusions occurred isolated with spherical shape within Campbell deposit, whereas at Artonvilla they occurred as scattered, clustered and isolated fluid inclusions, with spherical and rectangular shapes (Table 9.3). Type III inclusions were mostly identified within Artonvilla deposit.

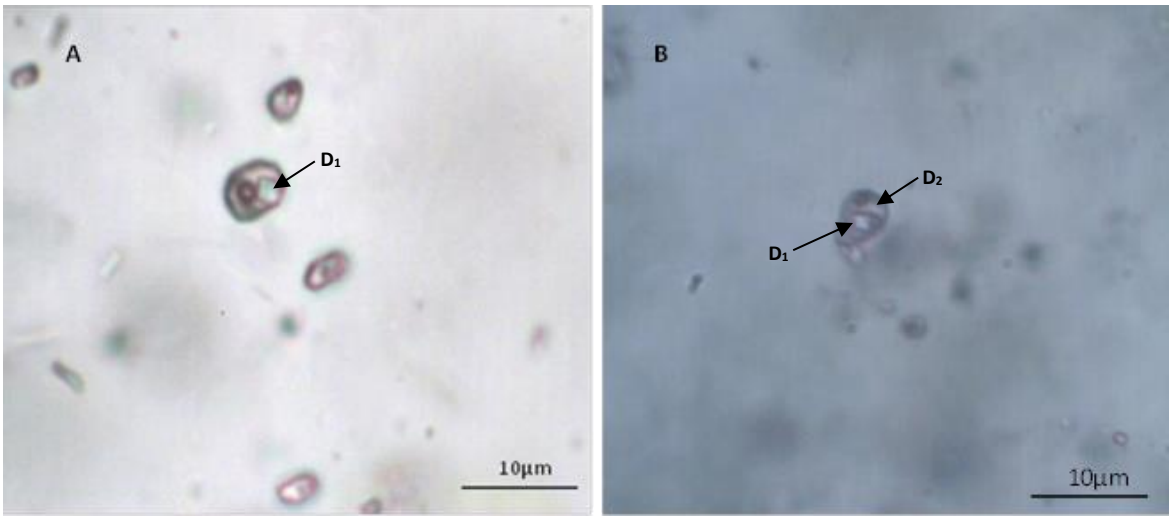


Figure 9.9: Type III – High salinity + daughter minerals (L + V + D_{1+2}) fluid inclusions with (A) and (B) showing cubic daughter mineral (D_1); while (B) having a second daughter mineral (D_2).

© University of Venda

Type IV – Gas-rich (L + V + Gas)

Type IV was identified as multiphase gas-rich that comprised liquid and vapour phases at room temperature. Most of these fluid inclusions had size ranging from 2x2 to 4x6 µm. The vapour bubbles were small with volume ranging from 5% to 10% and some with no visible bubbles (Table 9.3 and Fig. 9.10). They occurred along crystal growth zones and also scattered and clustered within the crystal. They were identified from both Campbell and Artonvilla deposits and occurred as primary and secondary fluid inclusions. Textually, they occurred as clustered and scattered with spherical and irregular shape (Table 9.3 and Fig. 9.10).

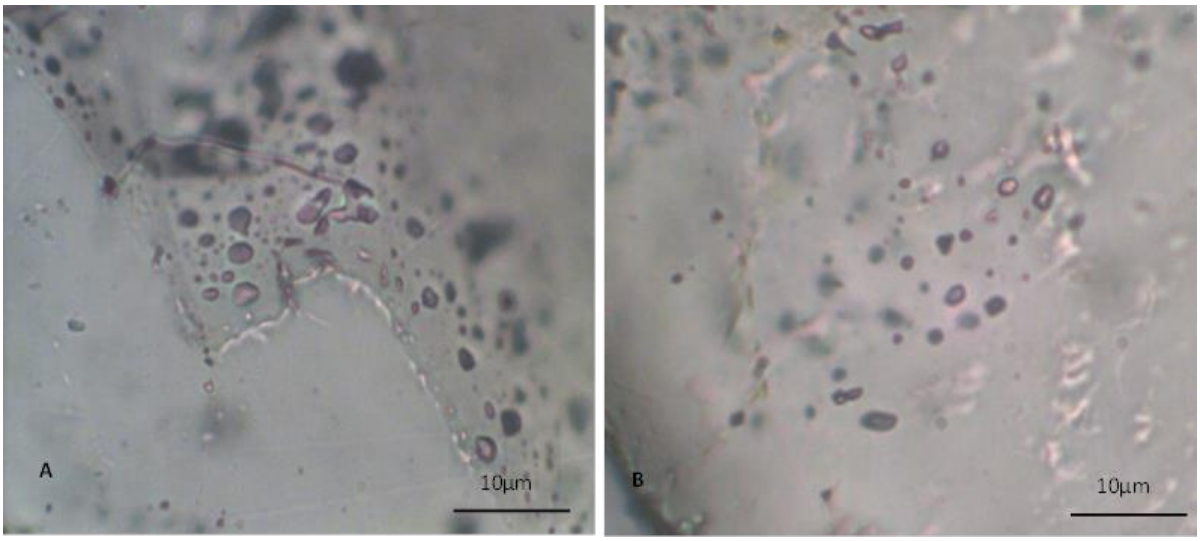


Figure 9.10: Type IV – Gas-rich fluid inclusions from sample CPdis02 (A) along the crystal growth zones and AT02 (B) scattered and clustered within the crystal, with less liquid and vapour, while some had no visible bubbles.

9.5.2 Microthermometry

Microthermometry is the most common non-destructive analytical technique used in fluid inclusion studies. It is used for the determination of fluid inclusion composition, molar volume and physical conditions of the fluid inclusion entrapment which include temperature and pressure. The microthermometry analysis of fluid inclusions from Campbell and Artonvilla copper deposits was conducted with the aim of establishing the physical and chemical conditions of cupper-sulphide mineralisation within these two deposits.

© University of Venda

9.5.2.1 Sample Selection

The same samples used for microscopical investigation (fluid inclusion petrography) (Table 9.4) were also used for microthermometry investigation. The same samples were used in order to achieve full description of the fluid inclusions studied within the same specific host mineral. The selection was also based on the identified abundance of fluid inclusions in quartz crystals and that they were having suitable size for conducting fluid inclusion investigation.

9.5.2.2 Sample Preparation and Analysis

The chips from the doubly polished plates used previously were used to identify and analyse the fluid inclusions using Linkam THMS 600 heating and freezing stage (Fig. 9.11a) connected to TMS94 and LNP System Controllers (Fig. 9.11c) and Nitrogen gas pump (Fig. 9.11d). The CPU and Monitor (Fig. 9.11e and f) were used for the storage and display of the results. The study was conducted at the Department of Applied Geology, Geoscience Institute, Göttingen University, Germany. Liquid nitrogen and thermal resistor were used for cooling and heating respectively. The heating-freezing stage was mounted on a binocular Olympus BHI82 Infrared microscope with a maximum magnification of 50X (Fig. 9.11b).

The precision, accuracy and calibration of the stage was done following Yoo *et al.* (2011) procedure whereby the precision of temperature measurements was calculated as ±0.1°C in the temperature range of the observed phase changes. Accuracy was estimated to be ±0.2 °C between −180°C and −10°C on cooling. On heating, the acuracy was estimated to be ±0.5°C between −10°C and +30°C and estimated to be ±2°C at temperatures above +100°C. The calibration of the stage was done at low temperature using synthetic H_2O and CO_2 inclusions at 0°C and −56.6°C respectively. Heating rates were maintained at ~2°C/min for measurements of total homogenization temperatures. Vapour volumetric percentage within fluid inclusions was determined at room temperature using standard graphical charts (Roedder, 1984; Shepherd *et al.*, 1985).

© University of Venda

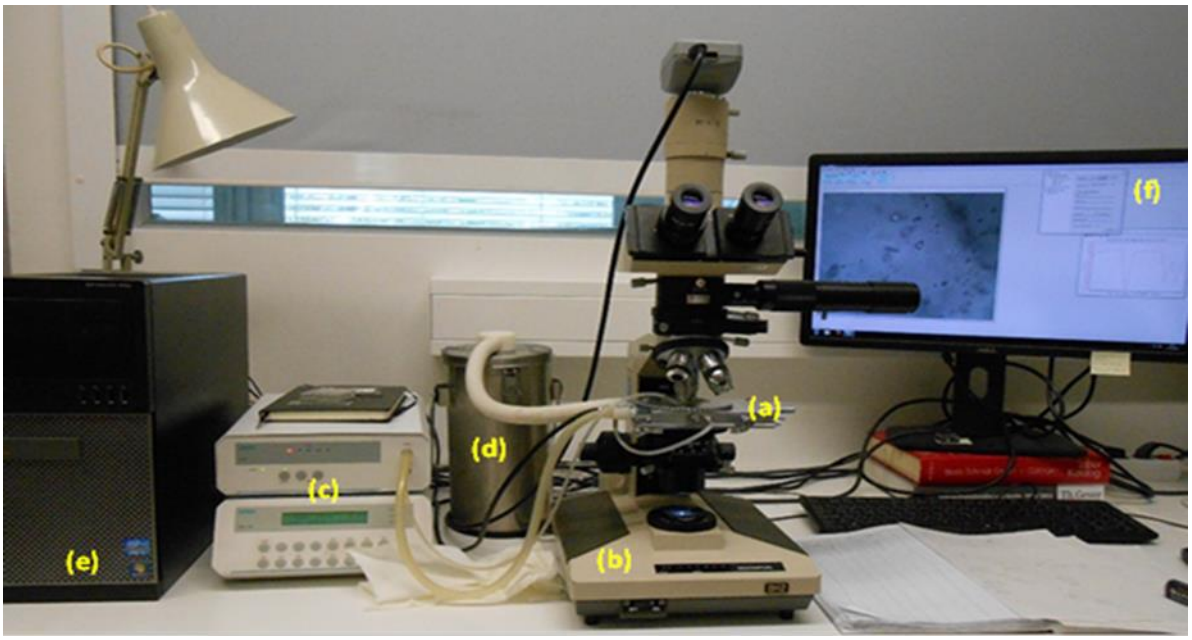


Figure 9.11: (a) Linkam THMS 600 heating-freezing microscope stage connected to (b) BH-2 standard petrographic microscope (c) TMS94 and LNP System Controllers (d) Nitrogen gas pump (e) CPU and (f) Monitor used for fluid inclusion study.

During the analysis it was assumed that there was no leakage of the fluid inclusions since the time of entrapment and that the volume remained constant throughout (Roedder, 1979b, Goldstein and Reynolds, 1994). Consequently, the inclusions that showed necking were not used for Microthermometry analysis.

For the microthermometry study, a total 126 inclusions from Campbell and 40 inclusion from Artonvilla were measured for the determination of homogenisation temperature (T_h), final melting temperature (T_m) and eutectic temperature (T_e). Each fluid inclusion was measured three times and the average value was used (Appendix 9B). Homogenization measurements were carried out on liquid and vapour fluid inclusions, whereby through heating and cooling process, the fluid inclusion homogenized to liquid. The cooling was done up to -80°C and heated up to 400°C. This was done while noting and recording the phase transition of each fluid inclusion.

© University of Venda

9.5.2.3 Results and Interpretation

The Microthermometry data obtained (Appendix 9B) were used for the determination of fluid inclusion types (composition) and phase transition; T_h population groups, salinity range, and T-P conditions of entrapment.

Fluid inclusion types and phase transition

The following four different types of fluid inclusions were identified based on their composition:

- Type I - L-rich (L + V) = Aqueous H_2O-NaCl;
- Type II - V-rich (L + V) = Vapour + Aqueous H_2O-NaCl;
- Type III – High salinity + daughter minerals (L + V + D_{1+2}) = Aqueous H_2O-NaCl + Halite(HL) and Calcite(CC) solids; amd
- Type IV - Gas rich (L + V + Gas) = Aqueous H_2O + $CH_4 \pm N_2$.

During the measurement of both $T_{m(ice)}$ and T_h of fluid inclusions, phase transitions of different types of inclusions were observed and recorded as follows:

- Type Ia and Type Ib: Aqueous H_2O-NaCl system
  - Final melting of ice ($T_{m(ice)}$): ice + L + V = L + V
  - Homogenization (T_h): L + V = L

- Type II: Aqueous H_2O-NaCl + HL/CC solids
  - Final melting of ice ($T_{m(ice)}$): ice + L + V + $Sol_{(HL/CC)}$ = L + V + $Sol_{(HL/CC)}$
  - Final melting of ice ($Tm_{(HL/CC)}$): L + V + $Sol_{(HL/CC)}$ = L + V + $Fluid_{(HL/CC)}$
  - Homogenization (T_h): $Fluid_{(HL/CC)}$ + L + V = L

- Type III: Aqueous H_2O + $CH_4 \pm N_2$
  - Final melting of ice ($T_{m(ice)}$): ice + L + V + $Sol_{(CH_4)}$ = L + V + $Sol_{(CH_4)}$
  - Final melting ($Tm_{(CH_4)}$): $Sol_{(CH4 \pm N2)}$ + L + V = L + V + $Fluid_{(CH_4)}$
  - Homogenization (T_h): Fluid $_{(CH4 \pm N2)}$+ L + V = L

© University of Venda

The phase transition was also illustrated using Binary water-salt (H_2O-NaCl) system which is a temperature-composition diagram at constant pressure (1 bar) (Fig. 9.12). This example was chosen because fluid inclusions within this system were abundant. The graph shows that the frozen fluid inclusion with salinity of 10 wt% which was heated and reached at T_e of -21.1°C at which the ice started melting. Upon further heating, the ice + L + V fluid inclusion reached the T_m (ice) at -5°C following the liquidus line. At $Tm_{(ice)}$, the total ice melted and the phase changed to L + V. Further heating lead to homogenization of vapour and liquid phase at T_h of 154°C.

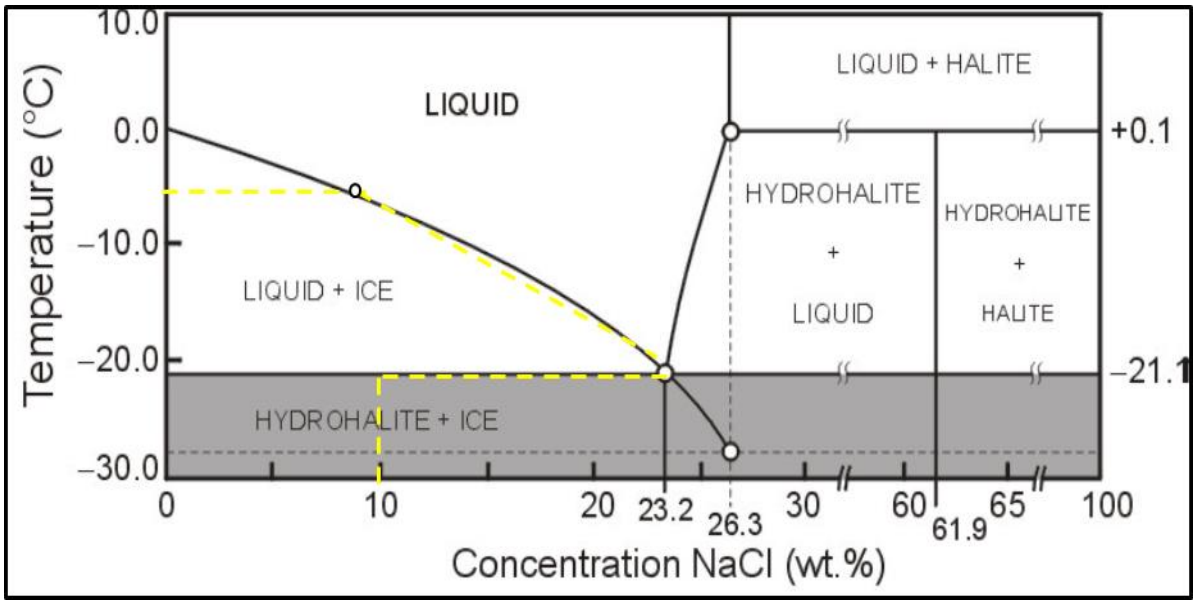


Figure 9.12: Phase diagram for the Binary water-salt system (H_2O – NaCl) indicating phase transition of fluid inclusion with – 10 wt% salinity (Modified after Huizenga, 2014).

Through determination of phase transitions, three major groups were identified; aqueous H_2O-NaCl system (liquid rich and vapour rich), aqueous H_2O-NaCl + HL/CC solids, and aqueous H_2O + CH_4±N_2 system. Among the three groups deduced, aqueous H_2O-NaCl system was found to be abundant (Figs. 9.13 and 9.14) for both Campbell and Artonvilla fluid inclusions with 92% and 55% respectively, followed by aqueous H_2O-NaCl + HL/CC solids that showed 7% from Campbell deposit and 25% from Artonvilla copper deposit, and lastly followed by aqueous H_2O + CH_4±N_2 system that revealed 1% from Campbell deposit and 20% from Campbell.

© University of Venda

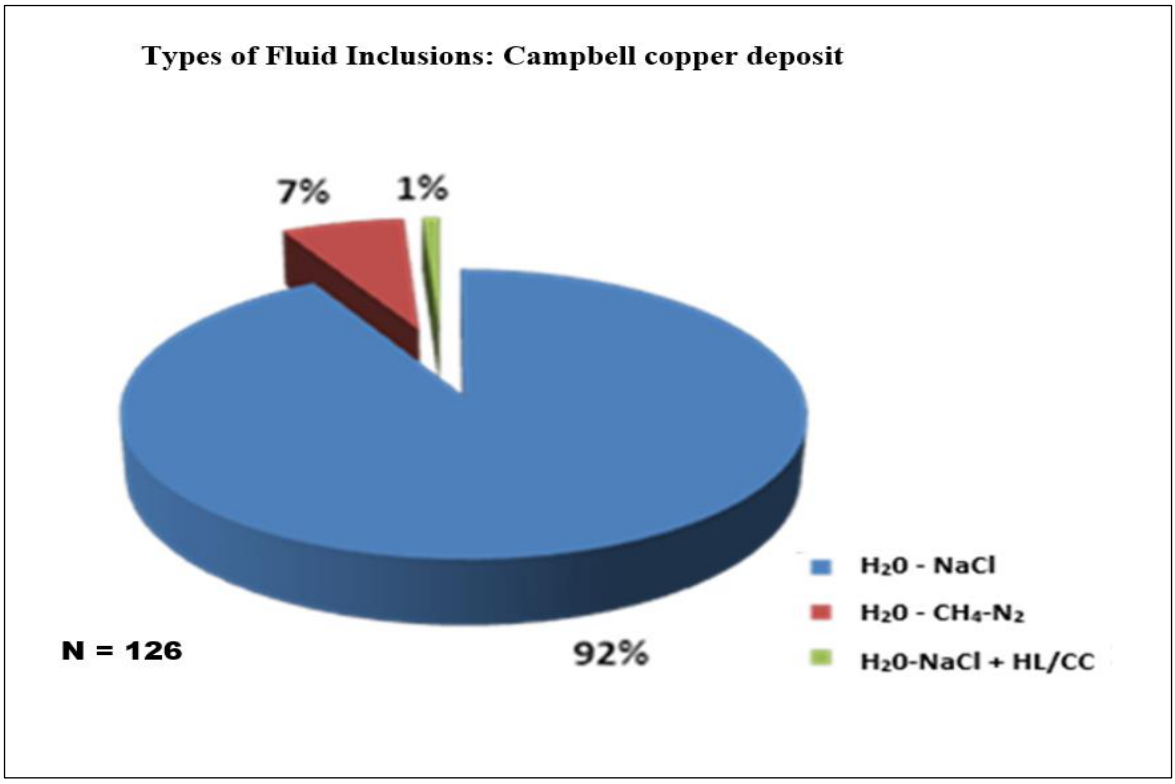


Figure 9.13: Pie chart illustrating abundance of different types of fluid inclusions in terms of phase composition for Campbell copper deposit.

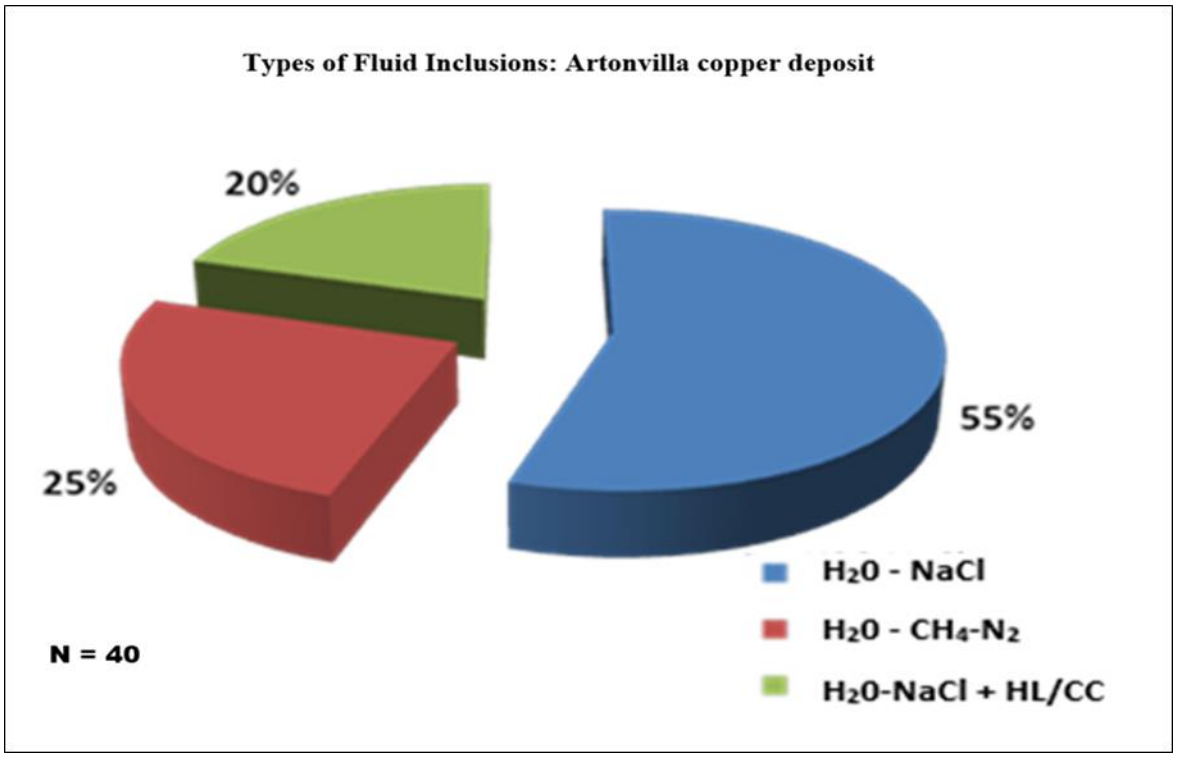


Figure 9.14: Pie chart illustrating abundance of different types of fluid inclusions in terms of phase composition for Artonvilla copper deposit.

© University of Venda

Homogenization temperature (T_h) population groups of aqueous fluid inclusions

The minimum and maximum homogenization temperatures (T_h) of fluid inclusions from Campbell copper deposit were found to be 80°C and 223°C respectively, while the minimum and maximum T_h for Artonvilla fluid inclusions were found to be 120°C and 199°C respectively. Homogenization temperature was used to determine the population of different fluid inclusions in terms of T_h range and this was deduced, using frequency histograms for both Campbell and Artonvilla copper deposits (Figs. 9.15 and 9.16).

The aqueous inclusions from Campbell copper deposit was found to be widely distributed within the homogenization temperature range of 82°C to 223°C. The highest population group was within the range of 135°C to 155°C, while the lowest pollution group had homogenization temperature range of 215°C - 235°C (Fig. 9.15). The distribution of aqueous fluid inclusions from Artonvilla copper deposit revealed highest T_h at the range of 150°C to 170°C with the lowest range of 110°C to 130°C (Fig. 9.16). Generally, the aqueous fluid inclusions were widely spread within the minimum and maximum T_h from both deposits (Figs. 9.15 and 9.16).

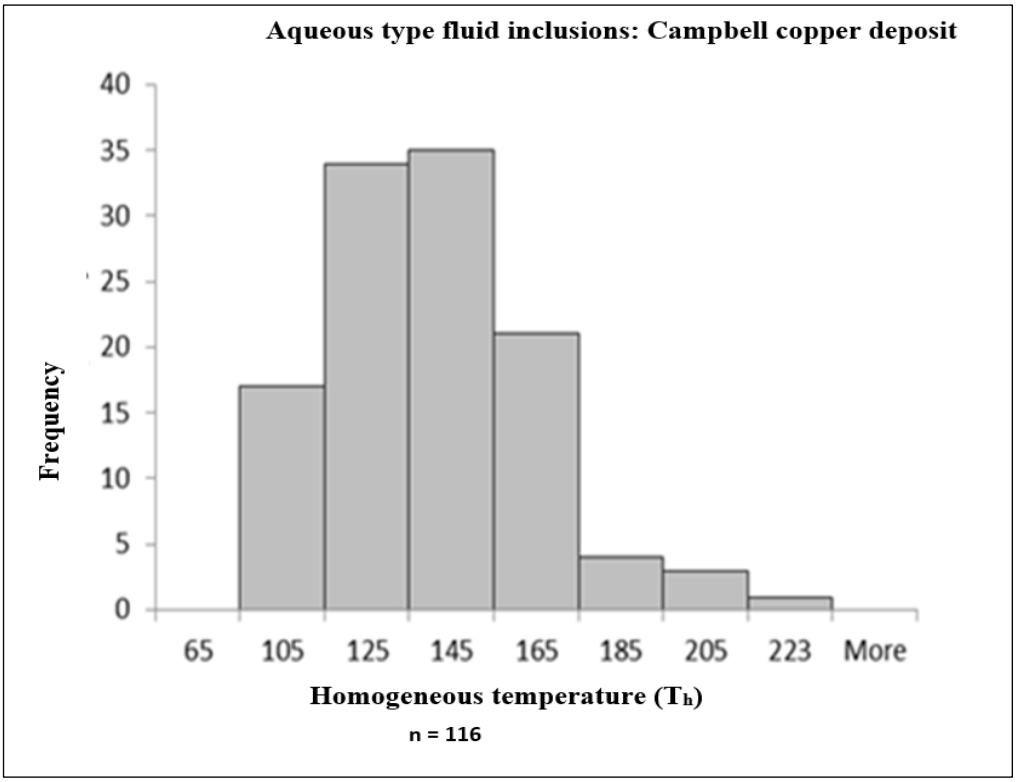


Figure 9.15: Frequency histogram of the homogenization temperatures of samples from Campbell copper deposits.

© University of Venda

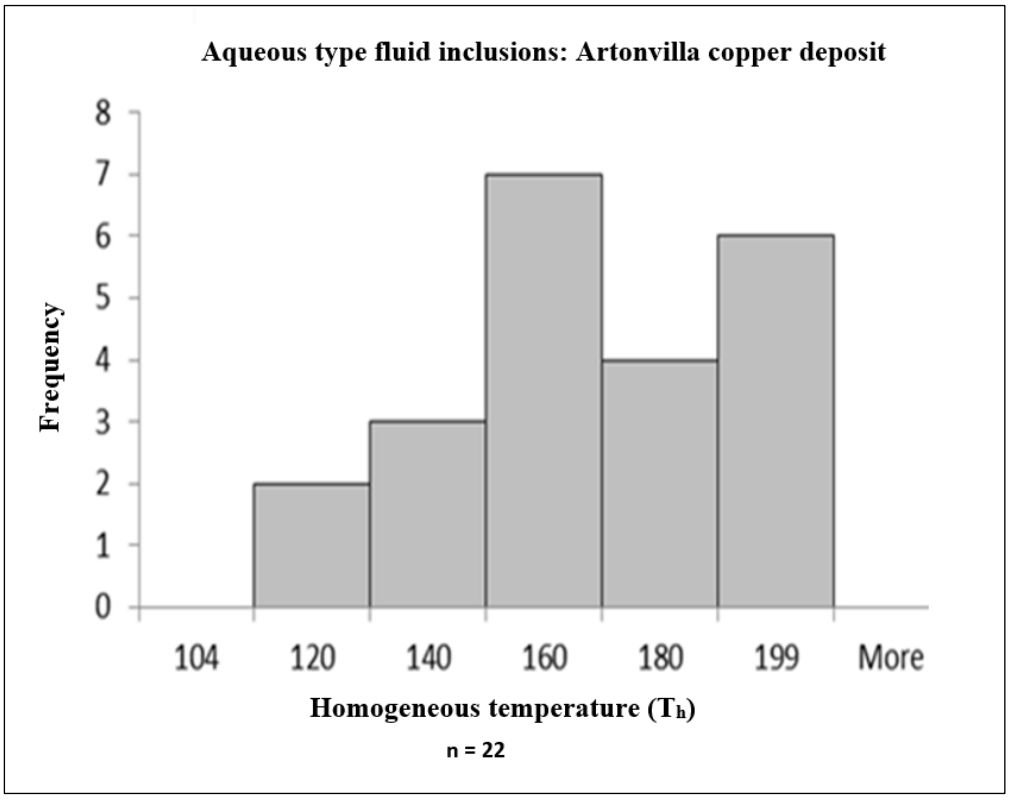


Figure 9.16: Frequency histogram of the homogenization temperatures of samples from Artonvilla copper deposits.

Determination of temperature range (T_h/T_m)

Melting ($T_{m(ice)}$) and homogenization temperatures (T_h) were used to plot the $T_{m(ice)}$ /T_h graphs in order to deduce the temperature range of fluid inclusions (Figs. 9.17 and 9.18 and Table 9.4). The T_h range of the Campbell deposit was from 82°C - 223°C with more population of T_h range between 85°C - 175°C while the $T_{m(ice)}$ temperature ranged from -28.2 to -0.1°C (Fig. 9.17 and Table 9.4).

Melting ($T_{m(ice)}$) and homogenization temperatures (T_h) of the Artonvilla copper deposit had homogenization temperature range of 104°C - 200°C with $T_{m(ice)}$ temperature ranging from -25°C to -0.5°C (Fig. 9.17 and Table 9.4). Generally, the T_h at Artonvilla deposit was not widely spread but $T_{m(ice)}$ was found to be widely distributed within the minimum and maximum $T_{m(ice)}$, while at Campbell deposit, both the $T_{h\ and}$ $T_{m(ice)}$ were found to be widely distributed within the minimum and maximum $T_{h\ and}$ $T_{m(ice)}$ (Figs. 9.17 and 9.18 and Table 9.4).

© University of Venda

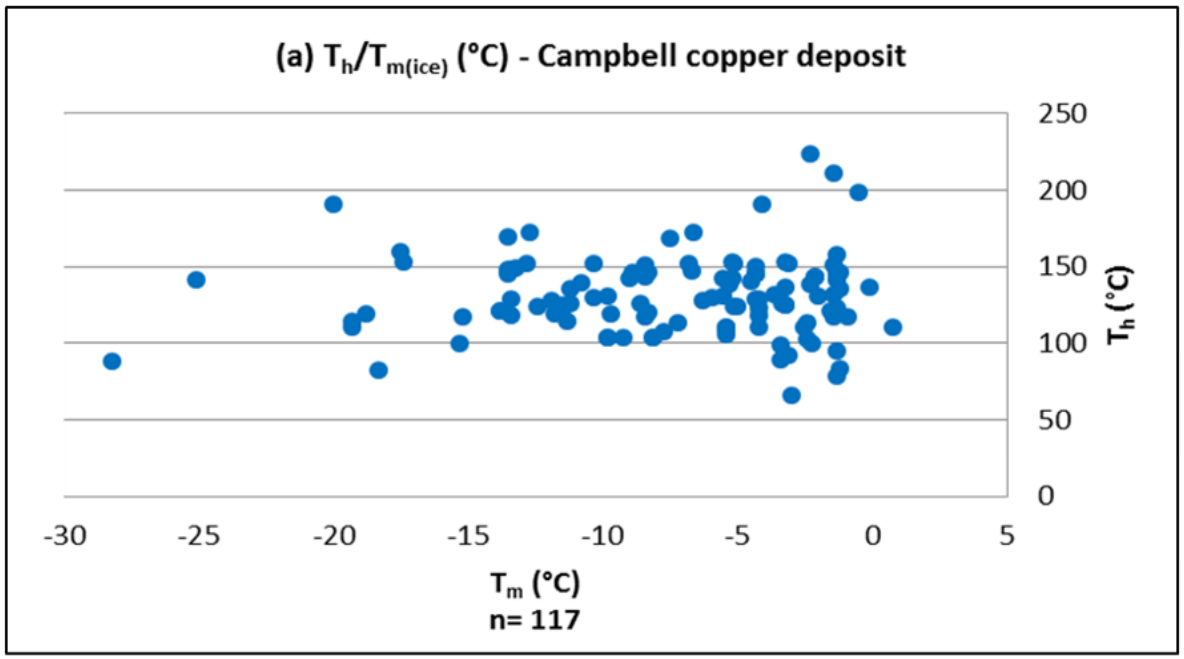


Figure 9.17: Bivariate plot illustrating $T_h/T_{m(ice)}$ graph for H_2O-NaCl and aqueous H_2O-NaCl + HL/CC fluid inclusion types for Campbell copper deposit.

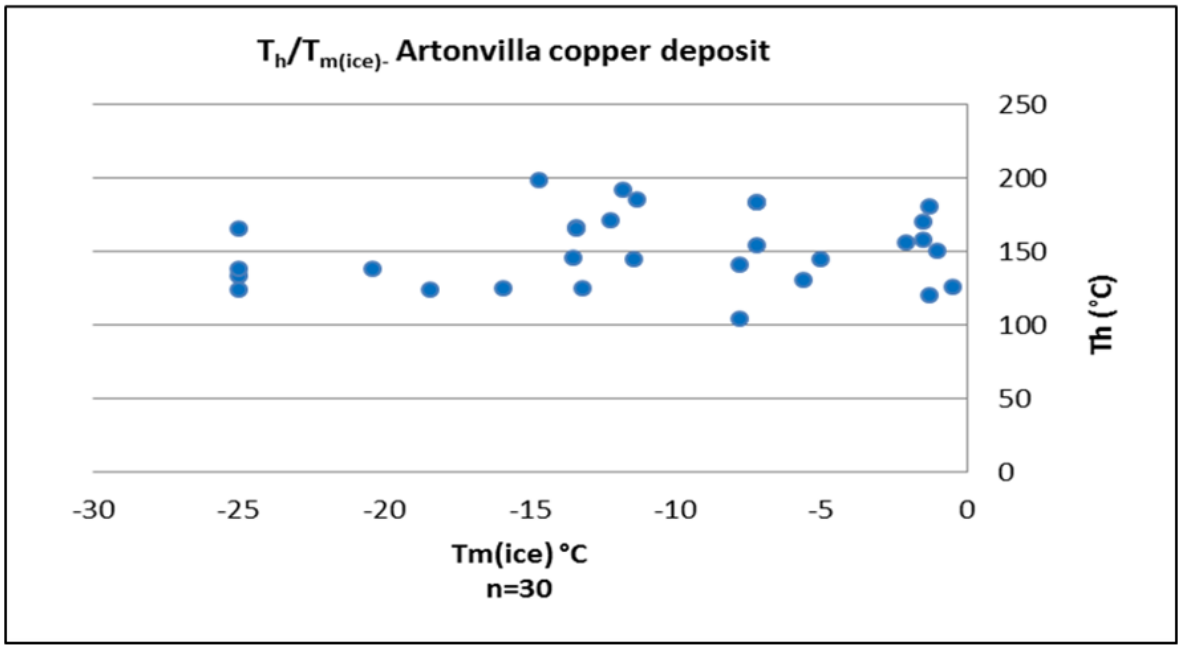


Figure 9.18: Bivariate plots illustrating $T_h/T_{m(ice)}$ graphs for H_2O-NaCl and aqueous H_2O-NaCl + HL/CC fluid inclusion types for Campbell and Artonvilla copper deposits.

© University of Venda

Salinity of Fluid inclusions

Final melting temperatures (T_m) of the aqueous inclusions were used to determine the salinity status of the fluid inclusions studied within the two deposits (Figs. 9.19 and 9.20). The T_m temperatures were converted to NaCl wt% equivalent (Appendix 9B). This was done using empirical formula of Bodnar and Vityk (1994) whereby:

$$\text{Salinity (wt\% NaCl equivalent)} = [-1.78\ (T_m)] - [(0.0442\ (T_m)^2] + [(0.000557\ (T_m^3)] \quad \text{Equation 9.1}$$

The calculated salinity was plotted against T_h (Figs. 9.19 and 9.20) in order to deduce the salinity range of the aqueous fluid inclusions and summarised in Table 9.4.

Determination of the salinity range also helped in the determination of those inclusions with daughter minerals such as halite and calcite. According to Wilkinson (2001); Roedder (1971); and Nash and Theodore (1971) fluid inclusions with high salinity indicate the presence of such salts and these are mainly classified as aqueous H_2O-NaCl + HL/CC solid type.

The study revealed low to high salinity. For example, fluid inclusions from Campbell deposit and Artonvilla copper deposits had salinity range of 0.2 to 27.5 wt% NaCl and 0.9 to 25.6 wt% NaCl respectively, although for Campbell deposit, most of the salinity values fall between 1.5 wt% NaCl and 22 wt% NaCl (Figs. 9.19 and 9.20). Inclusions with daughter minerals (Type III) revealed salinity ranging from 13.5 wt% NaCl to 25.6 wt% NaCl. Consequently, fluid inclusions from the Messina copper deposits revealed variations of salinity ranging from low to high with Type III fluid inclusions revealing high salinity range.

© University of Venda

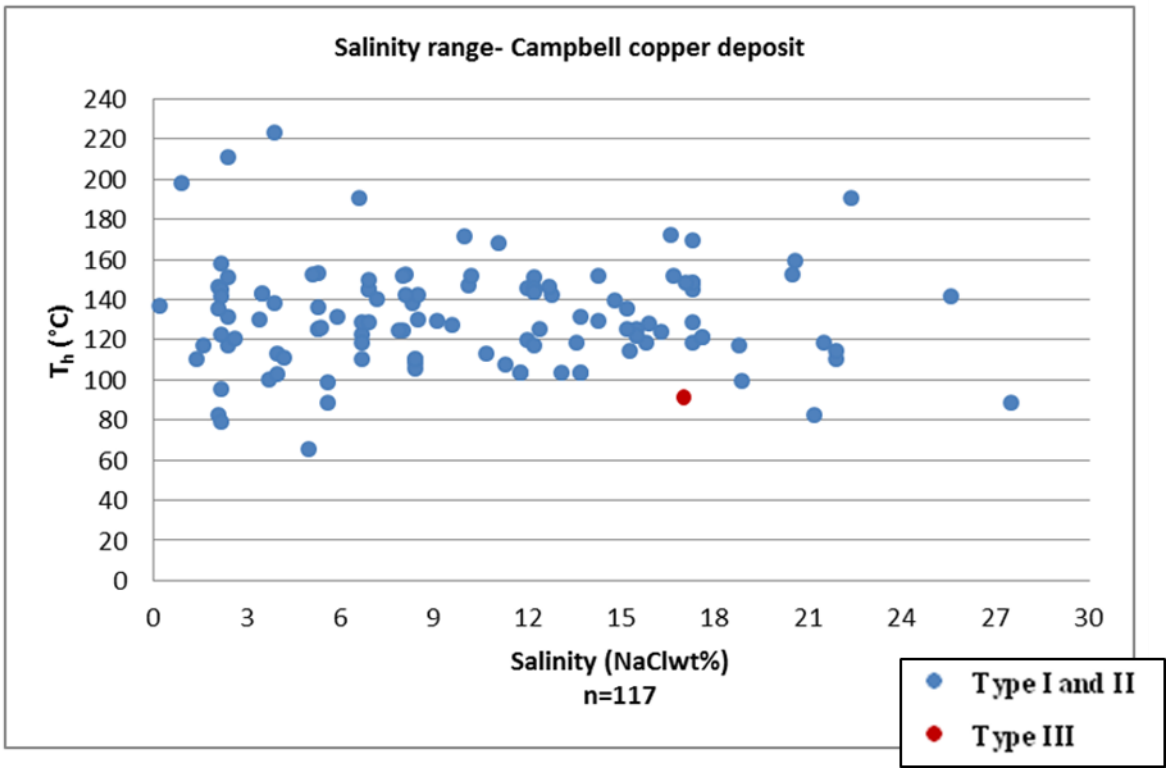


Figure 9.19: Bivariate plot illustrating salinity range of aqueous fluid inclusions, Type I – liquid-rich H_2O-NaCl, Type II - vapour-rich H_2O-NaCl and Type III- H_2O-NaCl-HL/CC from Campbell copper deposits.

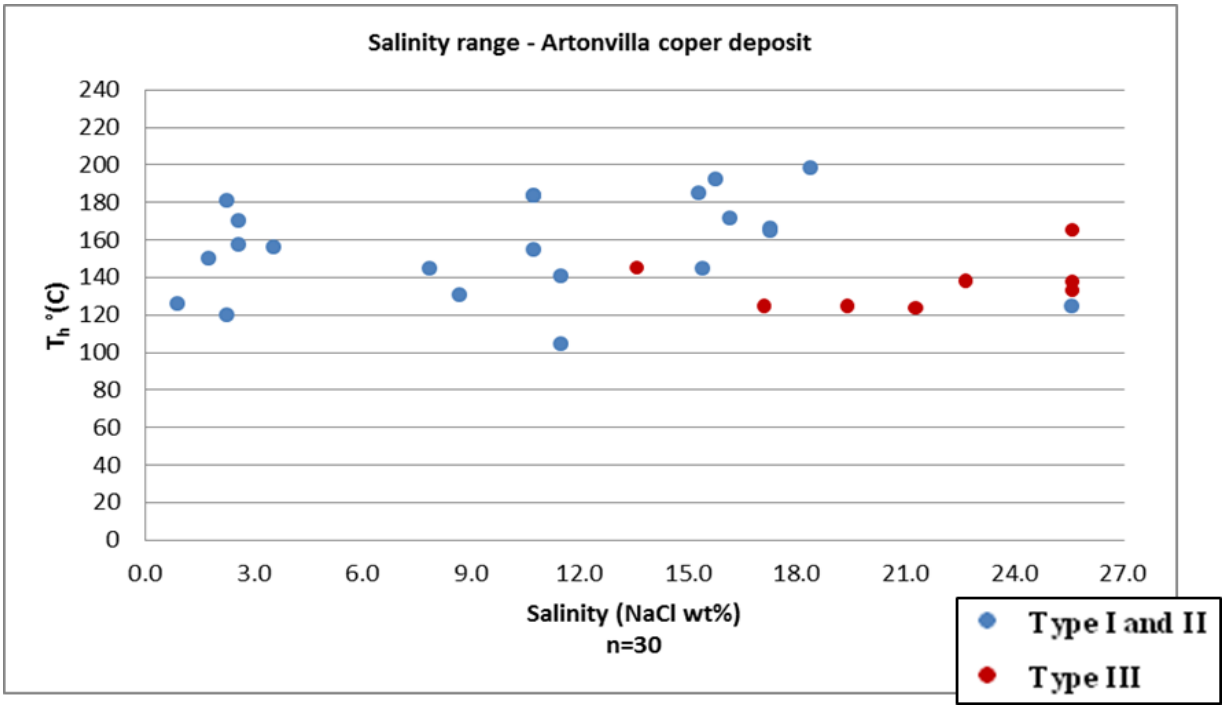


Figure 9.20: Bivariate plot illustrating salinity range of aqueous fluid inclusions, Type I – liquid-rich H_2O-NaCl, Type II - vapour-rich H_2O-NaCl and Type III- H_2O-NaCl-HL/CC from Artonvilla copper deposits.

© University of Venda

Table 9.4: Summary of fluid inclusion petrography and microthermometry data for measured fluid inclusions in quartz from veined, disseminated and brecciated ores of the Campbell and Artonvilla copper deposits

Types of fluid inclusion	**Type I**		**Type II**	**Type III**
	Type Ia	**Type Ib**		
Composition	L-rich (L + V) = H_2O-NaCl	V-rich (L + V) = H_2O-NaCl Low	(L + V + D1+2) = H_2O-NaCl + Halite(HL) and Calcite (CC)	Gas rich (L + V + Gas) = H_2O -CH_4±N_2
Salinity	Low - high Salinity	High Salinity	High salinity	
	0.2 - 27.5 wt% NaCl			
Tm(ice)	(CAMP) = -28.2°C to -0.01°C and (ARTV) = -25°C to -0.5°C			
T_h	(CAMP) = 82 – 223°C and (ARTV) = 104°C – 200°C			
Vapour%	5-10%V	80%V extremely few	10-15%V	5-10%V
Abundance	High (Type I and II) = 92% (CAMP) and 55%(ARTV)	Low -moderate (Type I and II) = 92% (CAMP) and 55%(ARTV)	Low = 1% (CAMP) and 20%(ARTV)	Low= 7% (CAMP) and 25% (ARTV)
Primary/Second	High P, low S	High P. Low S	High P	Moderate -high P, low S
Texture	Isolated, scattered clusters, trails along fracture and growth zones	Isolated	Isolated, clustered and scattered	Isolated, scattered clusters, trails along fracture and growth zones
Morphology	Spherical, Rectangular, irregular, necking down	Spherical, Rectangular, irregular, necking down	Spherical	Spherical and irregular

© University of Venda

University of Venda
Creating Future Leaders

Temperature and pressure conditions of entrapment

The temperature and pressure conditions at which mineralisation took place could be deduced through determination of Isochores graphs and have been widely used in several fluid inclusion studies (Huizenga *et al*., 2014; Van Reenen *et al.*, 2014; Gueye *et al*., 2013; Harlov *et al.,* 2013, Yoo *et al*., 2011). Isochores are important part of fluid inclusion studies and mainly used for the interpretation of the data accumulated through microthermometry study. The isochores were used in order to determine the temperature and pressure conditions at which the fluid inclusions were trapped.

For the determination of isochores, parameters such as salinity, density, bulk molar volume and bulk composition are the most important parameters. Salinity was calculated using the above empirical formula (Equation 9.1) in Bodnar and Vityk (1994).

Fluids-package of computer programs such as program 1: BULK, version 01/03 was used to calculate bulk molar volume and bulk composition of the fluid inclusions, while program 2: ISOC, version 01/03 was used to determine the isochores temperatures and pressures of fluids entrapment and both programs were developed by Bakker (2003) and improved in Bakker (2018). The 40°C/Km geothermal gradient was used together with the water isochores and aqueous (brine) fluid inclusions (Figs. 9.21 and 9.22).

For the construction of isochores for the fluid systems in this study, lines of constant density, with constant molar volume in a Pressure –temperature diagram was constructed using ISOC programme in *FLUIDS* computer programme for a selected fluid compositions . In this case, compositional information for the selected types of fluid system was obtained from the BULK programme within the *FLUIDS* computer software programme. In some instances, hypothetical density was used as an input. The BULK programme calculated densities and or molar volumes together with bulk compositions of fluid inclusions selected, following the procedure from Barker and Brown (2003) (Appendix C).

The calculated isochores were derived from microthermometry data of fluid inclusions for different types of quartz. For example, isochores of idiomorphic quartz (zoned), quartz with carbonic (CH_4) fluid inclusions and quartz with prehnite were used, wherein zoned quartz was from brecciated ore and gas fluid inclusions were from disseminated ore, while quartz with prehnite was from veined ore.

© University of Venda

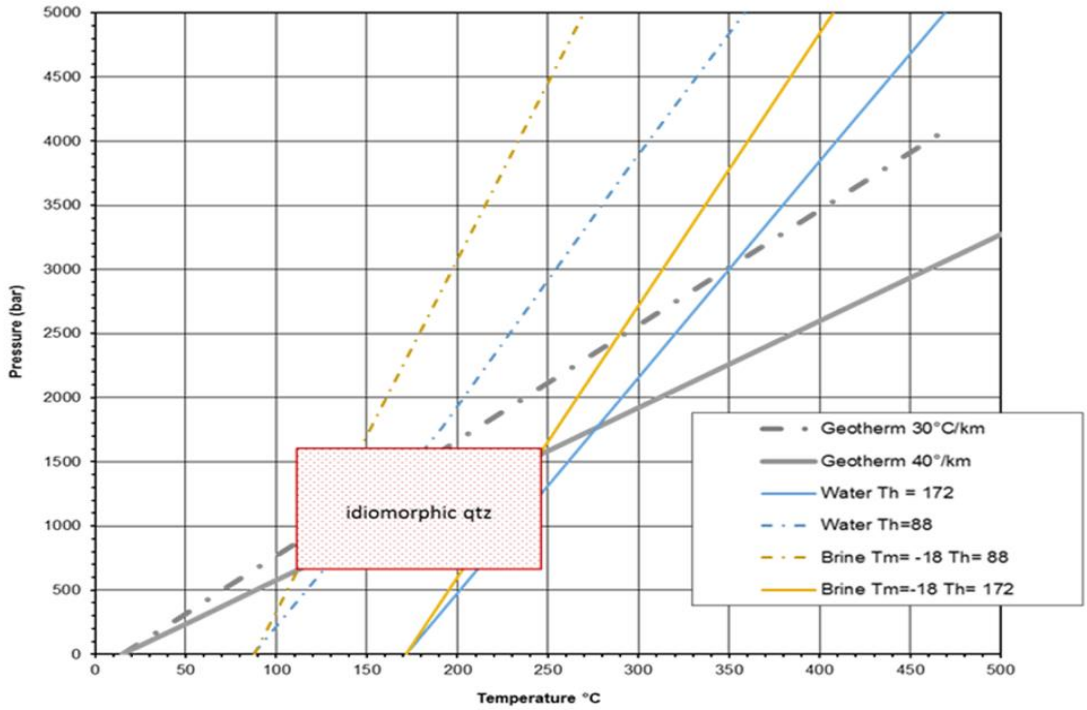


Figure 9.21: Temperature-pressure graph showing representative isochores of aqueous inclusions from idiomorphic zoned quartz (brecciated ore) from Campbell copper deposit.

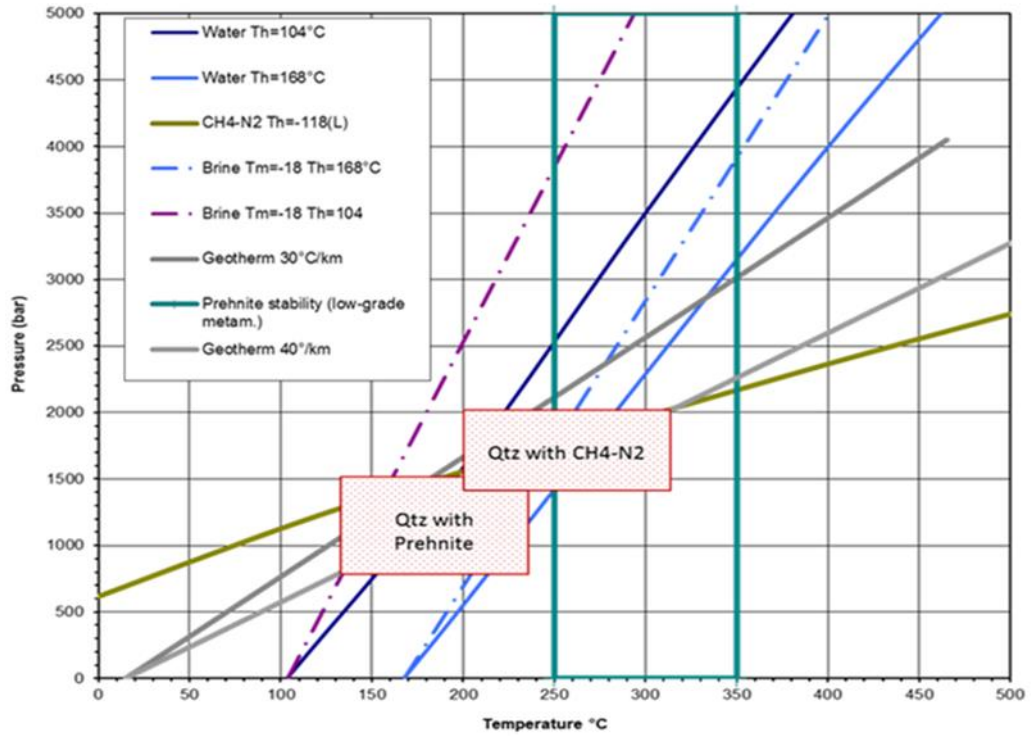


Figure 9.22: Temperature-pressure graph showing representative isochores of aqueous inclusions from quartz with prehnite (veined ore) and isochores of quartz with aqueous carbonic fluid inclusions (disseminated ore) from Artonvilla copper deposit.

© University of Venda

For the trapping temperature and pressure, unless fluid immiscibility was clearly demonstrated, homogenization temperatures are not to be used as trapping temperature (Potter, 1977; Gueye et al., 2013; Huizenga *et al*., 2014; Van Reenen *et al*., 2014;). Potter, (1977) pointed out that fluid inclusion cannot homogenize below the temperature at which they were trapped thus; homogenization temperature is the minimum temperature at which the fluid inclusions were formed. Consequently, the independent pressure estimates are required in order to deduce the true trapping temperature of aqueous solutions or aqueous carbonic solutions from isochores (Potter, 1977).

In this study, the pressure and temperature estimation was estimated following where the 40°C/Km geothermal gradient together with the water isochores and aqueous (brine) fluid inclusions isochores lines intersect each other. From the intersection points, an area of rectangular shape was drawn which revealed both minimum and maximum pressure and temperature at which the fluid inclusions were trapped (Figs. 9.21 and 9.22).

From T-P graph of idiomorphic quartz, it was revealed that the earliest carbonic aqueous fluid inclusions in idiomorphic quartz from veined ore were formed at 1.4 to 2.0 kbar from a hot solution between 315°C and 200°C (Fig. 9.21). The fluid inclusions in quartz vein from disseminated ore and quartz vein from brecciated ore were formed at more or less similar pressure (1.5 – 0.8 kbar and 1.6 – 0.6 kbar respectively) with temperature range of 235°C - 135 °C and 240°C - 115 °C respectively (Table 9.5).

Table 9.5: Entrapment temperature-pressure conditions of fluid inclusions of Messina copper deposits

Temperature (°C)	**Pressure**		**Host mineral**
	(bar)	**(kbar)**	
315 - 200	2000 - 1400	2 – 1.4	Quartz with gas fluid inclusions - Quartz vein
235 - 135	1500 - 800	1.5 – 0.8	Quartz with prehnite - Quartz vein
240 - 115	1600 - 650	1.6 – 0.65	Idiomorphic quartz (zoned quartz) - quartz vein

© University of Venda

9.5.3 Raman Spectroscopy

Raman spectroscopy is a non-destructive technique used for fluid inclusion analysis. It better characterizes the liquid and gaseous compounds, solid phase and solute species within the fluid inclusion (Frezzotti *et al*., 2012). The main advantage of this method is that it is able to characterize the chemical and structural properties in fluid inclusion of the size as small as 1µm in diameter. This resolution is not possible using other methods such as conventional petrography, microthermometry and other spectroscopic methods. This method has been widely used successfully to analyze fluid inclusions with an increasing number of publications throughout the years (Krenn and Le Thi-Thu Huong, 2019; Kowalski and Kissin, 2018; *Gueye et al*., 2013; Frezzotti at al., 2012; Nasdala *et al.*, 2004; Burruss, 2003; Burke, 2001; Touret, 2001; McMillan *et al.*, 1996; van den Kerkhof, 1990, 1988a and b); Burke and Lustenhouwer, 1987; Seitz *et al.*, 1987).

9.5.3.1 Sample Selection and Analysis

The same samples used for microthermometry were also used for Raman spectrometry analysis. Samples with carbonic inclusions were analysed for the determination of composition within the fluid inclusions at the Department of Applied Geology, Geoscience Institute, Göttingen University, Germany. Selection of gas fluid inclusions (AT02) and (ATavr12) was done for the purpose of determining the composition, using Horiba Jobin Yvon LabRam HR800-UV Raman spectrometer with optics including microscope connected to Olympus UC30 camera at the excitation laser of 488 nm (Fig. 9.23).

6.5.3.2 Results and Interpretation

Samples AT02 and ATarv 12 comprised of gas fluid inclusions that were identified during microthermometry analysis, consequently, analysis of fluid inclusions for the determination of composition of the gas fluid inclusion was done using Raman spectrometer. Three gas inclusions were selected and composition of the gas fluid inclusions were measured and the Raman spectra graph was deduced (Fig. 9.24).

© University of Venda

The Raman spectra graph revealed Raman shift peak at 2915 cm^{-1} wavelength for all the three gas fluid inclusions indicated by blue green and red colour graphs with the density of 7,6 g/cm3 and the Raman shift peak at 2330 cm-1 wavelength was also detected with density of 1 g/cm3, thus revealing the presence of both methane and nitrogen (CH_4-N_2) gases within the gas fluid inclusions (Fig. 9.24).

The gas composition of fluid inclusion 1 was deduced to be CH_4 (76%) and N_2 (28%); gas composition for fluid inclusion 2 was found to be CH_4 (79%) and N_2(21%) and for fluid inclusion 3 was found to be CH_4 (79%) and N_2(21%). Consequently, the average composition of CH_4 and N_2 from fluid inclusion 1, 2 and 3 were found to be ~80% and ~20% respectively.

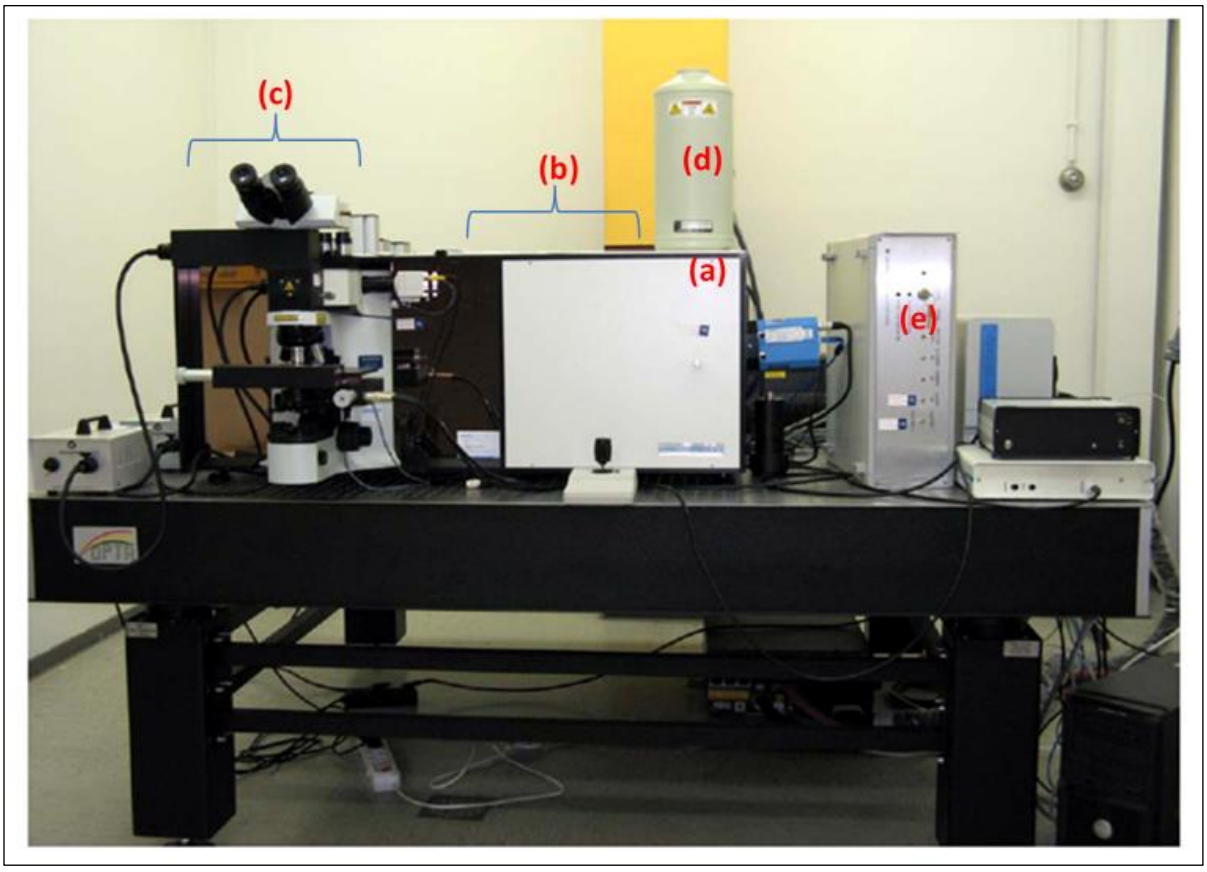


Figure 9.23: Horiba Jobin Yvon LabRam HR800-UV Raman spectrometer, (a) Spectrometer running underneath top optic; (b) lasers behind main unit with citation laser of 488 nm used for determination of gas fluid composition; (c) Optic box with Olympus UC30 camera connected to a microscope (d) In-Gas detector and (e) silver control box.

© University of Venda

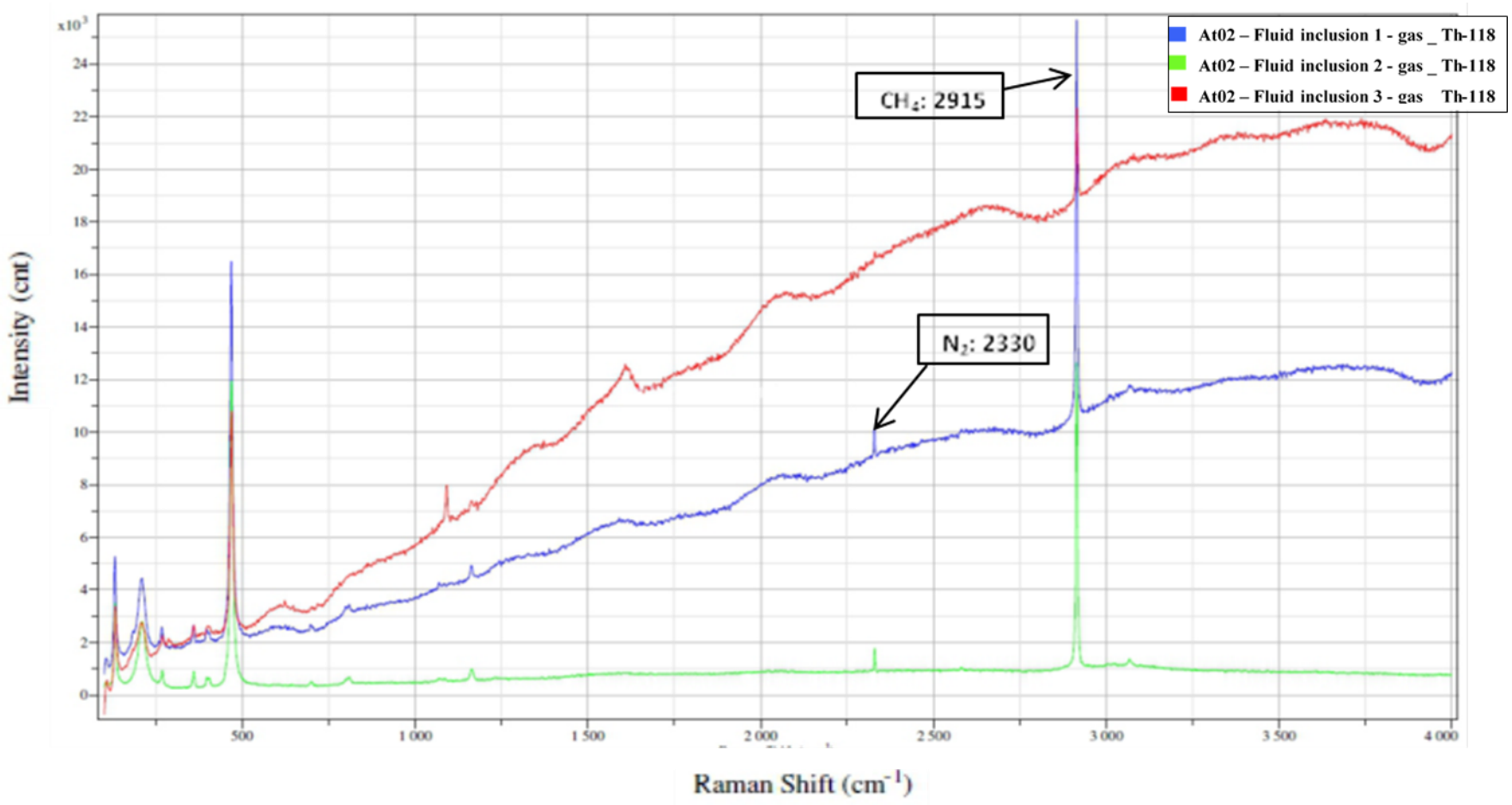


Figure 9.24: Raman spectra indicating relative wave numbers of gas fluid inclusions from three fluid inclusions of samples AT01 and AT02.

© University of Venda

9.6 Discussion

The study of primary inclusions formed during the growth of crystals provide information on the physical and chemical conditions of ore formation. The study is based on a number of assumptions, viz: that the fluid inclusions in the minerals represent a closed system from the time of entrapment, hence there was no leakage or necking; the chemical compositions of the inclusions remains the same from the time of entrapment and even during the experiment, thus the inclusion followed a path of constant density; and the partly filled vacuoles were completely filled with a single fluid phase when the mineral formed.

If the inclusion is more than half liquid at room temperature, the ore fluid was hydrothermal, if more than half gas, the ore fluid was pneumatolytic (www.geol-amu.org/notes/m7-1-12.htm). The homogenization temperature marks a lower limit for the temperature of mineral formation.

One of the challenges in the study of fluid inclusions is that diffusion may occur especially at high temperatures and when the hydrogen fugacity difference between the inclusion and its surroundings is large (www.geol-amu.org/notes/m7-1-12.htm). Bodnar (2003), however, recons that sometimes the origin of the fluid inclusions relative to the formation of the crystal cannot be determined with certainty, thus the origin of the fluid inclusion is indeterminable.

The study of fluid inclusions in ore minerals at the Campbell and and Artonvilla deposits focused on primary inclusions. Primary fluid inclusions occurred as isolated, scattered and as clusters within the quartz crystal and also along the growth zones of the quartz crystals.

Fluid inclusion have been defined as fluids - filled vacuoles that are sealed within minerals and if they are trapped within diagenetic minerals, they provide the only direct means of examining the fluids present in ancient diagenetic environments. Using petrographic observation, microthermometry analysis, and Raman spectroscopy methods, fluid inclusion may provide valuable information such as, temperatures, pressures, and fluid composition. This study has been conducted way back in 18th centuries (Fig. 9.4) and still being actively applied recently in the Geoscience field with lots of improvement in the techniques used (e.g. Testa (2018); Li *et al.* (2018); Li (2019); refs). Consequently, above mention valuable information have been deduced in this study to suggest the mineralisation processes within the Messina copper deposits.

© University of Venda

9.6.1 Occurrence and Types of Fluid Inclusion

Occurrence and type of fluid inclusion in a crystal is important to unpack the information about the origin of mineral deposits and their characteristics. Descriptive and genetic classification of the fluid inclusion are most crucial in ore genesis as stated and confirmed by several authors such as Roeder (2002) and Li *et al.* (2018).

According to Van der Kerkhof (2001), fluid inclusions may occur in most minerals, but in practice more than 90% of fluid inclusions studies consider fluid inclusion in quartz. Consequently, in this study, quartz associated with mineralisation were selected and used. Based on the genetic classification, the study revealed the occurrence of primary and secondary fluid inclusions in quartz from both Campbell and Artonvilla copper deposits, with high abundance of primary inclusions. Primary fluid inclusions occurred as isolated, scattered and as clusters within the quartz crystal and also along the growth zones of the quartz crystals. Secondary fluid inclusions were associated with fracture zones of the quartz crystals. Implications. Consequently, the primary fluid inclusions were trapped during the time of quartz crystal formation. the primry fluid inclusions were then used for further fluid inclusion analysis rather than secondary fluid inclusion that could indicate trapping t any time of ore genesis or formed due to other processes that do not involve mineralisation period. Based on the descriptive classification that deals with phase assemblages of fluid inclusion, the study revealed both aqueous and gas multiphase fluid inclusions grouped into four types, which included Type I: liquid-rich (L + V); Type II: Vapour-rich (L + V); Type III: High salinity + daughter minerals (L + V + HH/CC); and Type IV: Gas rich fluid inclusions. Both Campbell and Artonvilla copper deposits comprised mainly Type I as compared to Type II, Type III and Type IV. The study also identified small inclusions with average size of 4µm, although few large inclusions were up to 15 µm, while most of the fluid inclusions densities were about 10% volume with few cases of 80% volume from vapour rich fluid inclusions. The presence of both liquid and vapour phases in fluids that occurred in small size and at some instances large size could be attributed to the fact that the fluid with small vapour size originated from a liquid-like fluid because of its relatively high density. The occurrence of fluid with large vapour size could be attributed to the fact that the fluid was derived from a vapour-like fluid because of its relatively low density. The presence of vapour bubbles also implied that the trapping was at an elevated temperature. The study conducted by Komeili

© University of Venda

(2017) confirmed that the presence of gas rich together with liquid rich fluid inclusions and multiphase in quartz vein is an indicative of boiling event in Kahang magmatic-hydrothermal copper porphyry deposit of northeast of Isfahan. Similar conditions were also noted in several studies on magmatic-hydrothermal copper deposits such as; Li (2019); Testa (2018); Kamilli and Ohmoto (1997).

9.6.2 Microthermometry Analysis

Homogenisation temperature, salinity and composition of fluid inclusions

The most important, obvious and simplest way of characterising the fluid inclusions present in mineralised system is mainly in terms of homogenisation temperature and salinity NaCl equivalent (Wilkson. 2001). Homogenisation temperature is a temperature at which the fluid inclusion was trapped while high salinity determines the presence salts daughter minerals.

The current study revealed salinity that ranged from 0.2 to 27.5 wt% NaCl with 17 wt% NaCl salinity of Type III fluid inclusion from Campbell copper deposits, while fluid inclusions from Artonvilla copper deposit revealed salinity that ranged from 0.9 to 25.6 wt% NaCl with salinity range of 13.5 to 25.6 wt% NaCl for Type III fluid inclusions. The Campbell copper deposit had salinity that ranged from 0.2 to 27.5 wt% NaCl with 17 wt% NaCl salinity of Type III fluid inclusion, while, fluid inclusions from Artonvilla copper deposit revealed salinity that ranged from 0.9 to 25.6 wt% NaCl with salinity range of 13.5 to 25.6 wt% NaCl for Type III fluid inclusions. Consequently, fluid inclusions from the Messina copper deposits revealed variations of salinity raging from low to high (0.2 to 27.5 wt% NaCl) with Type III fluid inclusions revealing high salinity range. The high salinity range was an indication of presence of halite and calcite crystal within the type III inclusion at room temperature. Similarly, the study of fluid inclusions in quartz associated with magmatic-hydrothermal mineralisation revealed more or less similar ranges of salinity with the presence of soluble salts. For example studies conducted by (Testa *et al.*, 2018; Li and Zhang, 2019).

The current study deduced the composition of gases in the fluid inclusions using Raman Spectroscopy and the identified gases were CH_4 and N_2 with ~80% and ~20% composition respectively. The presence of these gases in inclusions together with those of liquid phase and multiphase with different salinities are indicative of boiling fluids at the time of boiling, hence implies hydrothermal type of deposits.

© University of Venda

The T_h of fluid inclusions of the Campbell copper deposit ranged from 80 – 223°C with $Tm_{(ice)}$ ranging from- -28.2 to -0.1°C, while T_h of fluid inclusions of the Artonvilla copper deposit ranged from 104 – 199°C with $T_{m(ice)}$ ranging from -25 to -0.5°C. Consequently, the overall T_h and $Tm_{(ice)}$ of the Messina copper deposits ranged from 80 -223°C and from -25 to -0.5°C respectively.

Temperature- pressure estimation

Temperature-pressure estimation method revealed that the earliest carbonic aqueous fluid inclusions in idiomorphic quartz from veined ore were formed at 1.4 to 2 kbar from a hot fluid between 315°C and 200 °C. This was followed by fluid inclusions in quartz vein from disseminated ore and quartz vein from brecciated ore which were formed at more a less similar pressure (1.5 – 0.8 kbar and 1.6 – 0.65 kbar respectively) with temperature range of 235°C – 130°C and 240°C - 115°C respectively. Consequently, the fluid inclusion study revealed temperature range of 115 - 235°C.

Freely (2018), pointed out that several studies had been undertaken with similar fluid inclusion conditions and were of magmatic-hydrothermal origin. For example, the hydrothermal evolution of vein sets at Pipeline Gold mine , Nevanda was investigated by Blamely *et al*. (2017). The authors argued that the geochemical results from fluid inclusion Microthermometry and gas analysis revealed that the fluids from quartz were sourced from condensing magmatic volatiles and were trapped at approximately 300°C at 2 kbar lithospheric pressure.

9.6.3 Possible Sources and Evolution of Ore-forming Fluids

The ore forming fluids of the Messina copper deposits were aqueous/vapour H_2O-NaCl and some with halite/calcite and gasses ($CH_4 \pm N_2$) bearing fluids with low to high salinity values (2 to 27.5 wt% NaCl equivalent) and, trapping conditions were 315°C to 115°C and 0.8 to 2kbar. These fluids are similar to those observed in many deposits interpreted to be mainly magmatic origin (e,g Li and Zhang, 2019).

© University of Venda

CHAPTER 10

SULPHUR ISOTOPE GEOCHEMISTRY

Preamble

This chapter focuses on the study of sulphur isotope geochemistry in different ore samples and country rocks associated with copper ores from the Campbell and Artonvilla copper deposits. The chapter first introduces the fundamentals of isotope geochemistry in general and thereafter summarizes major aspects of sulphur isotope geochemistry, which include; fundamentals of sulphur isotope geochemistry, analytical techniques, equilibrium fractionations, geothermometry in sulphur isotope analysis, and application of sulphur isotope geochemistry in different geochemical environments. The second part of the chapter, deals with the investigation of stable isotopes in samples from the study area as well as interpretation of the results and discussion.

10.1 Fundamentals of Isotope Geochemistry

10.1.1 Types and Classification of Isotopes

Isotopes are atoms of the same element that have the same numbers of protons and electrons but different numbers of neutrons. Isotopes are also defined as atoms of the same element that have the same atomic number (number of protons) but different mass numbers (neutrons) (Kendall *et al*., 1995; Kendall and Caldwell, 1998; Kendall, 2004). The original composition of isotopes in planetary systems is a function of nuclear processes in stars (Kendall, 2004). In the terrestrial environment, isotopic composition is changed due to radioactive decay, cosmic ray interactions and also due to anthropogenic activities such as nuclear fuels processing, reactor accidents and nuclear weapons testing (Kendall *et al*., 1995; Kendall and Caldwell, 1998; Kendall, 2004).

The two main types of isotopes include; radioactive and stable isotopes. Radioactive also referred as radioisotope, radionuclide, radioactive nuclide or unstable isotopes are isotopes whose nuclei are unstable and dissipate or disintegrate over time to form other isotopes through emitting excess energy by spontaneously emitting radiation in the form of alpha (results of excess mass), beta (results of excess protons or neutrons) and gamma rays

© University of Venda

(produced after electron capture). Examples of radioactive elements include; Lead, uranium, thorium (Kendall *et al*., 1995; Kendall and Caldwell, 1998; Kendall, 2004; Misra, 2012; Encyclopedia Britannica, 2016). Depending on the creation process, radioactive isotopes are classified into four types; long-lived, cosmogenic, anthropogenic and radiogenic radioactive isotopes. Long-lived radioactive isotopes emerged during the creation of the solar system, cosmogenic radioactive isotopes occur as a reaction of the atmosphere to cosmic rays emitted by stars, anthropogenic isotopes are purely man-made and created through nuclear activities (weapons testing, nuclear fuel), while radiogenic isotopes are the results of radioactive decay (Kendall *et al*., 1995; Kendall and Caldwell, 1998; SAHRA, 2005; Claude, 2008; White, 2015). In Geochemistry, the main applications of radioactive isotopes include; dating of rocks, minerals and archeological artifacts; tracing geochemical processes such as the evolution of the Earth's oceans, crust, mantle, and atmosphere through geologic time scale, and magmatic differentiation and assimilation (DePaolo and Wasserburg, 1979; DePaolo, 1981) and tracing the sources and transport paths of dissolved and detrital constituents involved in the formation of rocks and mineral deposits (Hemming *et al*., 1995; Panneerselvam *et al*., 2006).

Stable isotopes are isotopes whose nuclei do not appear to decay to other isotopes on geologic timescale, but they may themselves be the product of the decay of radioactive isotopes. They have stable proton –neutron combination and do not display any sign of decay. Since they don't decay, thus they do not pose any physiological effects to human and living organisms. Examples of stable isotopes include those of; oxygen, hydrogen, sulfur, nitrogen and carbon and are used in the environmental and ecological studies and most commonly in geochemistry for the determination of historical geological processes (SAHRA, 2005; Hoefs, 2015).

10.1.2 Stable Isotope Fractionation

As isotopes are atoms of same element, their chemical and physical properties differ slightly due to their atomic mass difference. Difference in atomic mass affects physical properties such as densities and temperatures. Elements with low atomic numbers have large mass difference which is enough for physical, chemical and biological processes or reaction to fractionate or change the relative proportions of various isotopes (Kendall *et al.*, 1995;

© University of Venda

Kendall and Caldwell, 1998; Kendall, 2004; SAHRA, 2005; Hoefs, 2015; Encyclopedia Britannica, 2016).

The group of elements whose isotopes are especially susceptible to natural isotope fractionation include those of; oxygen, hydrogen, sulfur, nitrogen and carbon. These elements are among the most abundant elements in the Earth and intimately associated with biosphere, hydrosphere and lithosphere. Consequently, the study of fractionation of their isotopes provides information on geological processes occurring in many different geological environments (Faure, 1986; Sharp, 2007; Misra, 2012; White, 2015). Thus, basic principles of stable isotopes can be explained through stable isotope fractionation processes.

Isotope fractionation describes processes that affect the relative abundance of isotopes. It describes the partitioning of isotopes of an element between co-existing substances resulting in different isotopic ratios in the two substances (Kendall, 2004; Misra, 2012).

It is important to note that physical and chemical properties of isotopic elements play a major role in fractionation process. This is so because various isotopic elements have slightly different chemical and physical properties because of their mass difference (Kendall *et al.*, 1995; Kendall and Caldwell, 1998; Kendall, 2004; Misra, 2012). In element of low atomic numbers, these mass differences are large enough for physical, chemical and biological processes or reactions to fractionate the relative proportions of different isotopes of the same element in various compounds. Due to this process, water and solutes often develop unique isotopic compositions (ratio of heavy to light isotopes) and these may be an indicative of their source or origin (Gat, 1980; Gat and Gonfiantini, 1981; O'Neil, 1986b; Kendall *et al.*, 1995; Kendall and Caldwell, 1998; Kendall, 2004).

Causes of stable isotopic fractionation

Isotopic fractionation arises because of energies produced during the vibrational, rotational and transitional motions of electrons and atoms within a molecule of which these energies are mass dependent (Misra, 2012). For instances, when a heavier isotope replaces a lighter isotope, the vibrational energy of a molecule is decreased and the molecule tends to be more stable as compared with a molecule containing the lighter isotope. For example, in liquid vapour system, such as H_2O (liquid) – H_2O (vapour), the liquid phase is enriched in the

© University of Venda

heavier isotopes (^{18}O and ^{2}H), whereas the vapour phase preferably concentrates the lighter isotopes (^{16}O and ^{1}H) (Kendall, 2004; Misra, 2012). The other reason or causes of mass depended isotopic fractionation is the kinetic energies of the molecules. The kinetic energy of a molecule is a function of its mass and can be expressed as (Misra, 2012):

$$E_{\text{kinetic}} = 1/2mv^2 \qquad \text{Equation 10.1}$$

Where E is kinetic energy, m = mass, and v = velocity of a molecule. This is the same for all ideal gases at a given temperature (Misra, 2012). In this case if velocity (v) of isotope molecules differs, this lead to isotopic fractionation. For instants, light isotope molecules can diffuse out of the system and leave the reservoir enriched with heavier isotope (Misra, 2012). In the case of evaporation of water, the lighter isotopes with high transitional velocity will break through the liquid surface, resulting into fractionation between liquid and vapour (O'Neil, 1986a).

Types of isotopic fractionation

According to Faure (1986), Hoefs (2004), Misra (2012) and Hoefs (2015) the main types or processes that produce isotopic fractionations include; isotope exchange reaction effects, unidirectional reactions (kinetic effects) and physical processes such as evaporation, and condensation, melting, and crystallization, adsorption and desorption, and diffusion of molecules (Faure, 1986; SAHRA, 2005; Sharp, 2007; Misra, 2012; Hoefs, 2015; Encyclopedia Britannica, 2016).

Isotopic exchange reaction effect

Isotopic exchange reaction effect is also referred as equilibrium isotopic effect produced by equilibrium isotope exchange reactions and entails the redistribution of isotopes of an element among various species or compounds without any change in the chemical make-up of reactants or products. It is partial separation of isotopes between two or more substances in chemical reaction (Horita and Wesolowski, 1994; Kendall *et al*., 1995; Kendall and Caldwell, 1998; Chacko *et al*., 2001; Maggi and Riley, 2010; Misra, 2012).

© University of Venda

At equilibrium, the forward and backward reaction rates of any particular isotope are identical, meaning that the ratios of the different isotopes in each compound are constant. In this process the heavier isotope become enriched in the species with higher energy state (high oxidation state). For example, sulphate is enriched in ^{34}S relative to sulphide, meaning that sulphide is depleted in ^{34}S relative to sulphate. As a rule of thumb, among different species of the same element (different phases of the compound) the denser the material, the more it tends to be enriched in the heavier isotope. During phase changes the ratio between the heavy and light isotopes from the molecules in the two phases changes. Generally, the higher the temperature the less is the difference between the equilibrium isotopic compositions of any two species (Kendall *et al*., 1995; Kendall and Caldwell, 1998; Chacko *et al.*, 2001; Maggi and Riley, 2010).

Fractionation factor: The equilibrium exchange fractionation of the two substances (A and B) can be expressed by the use of fractionation factor (α). The equilibrium exchange can be expressed as (Misra, 2012):

$$^{1}A + {}^{2}B \Leftrightarrow {}^{2}A + {}^{1}B \qquad \text{Equation 10.2}$$

Where A and B are phases, and subscripts 1 and 2 are isotopes.

The equilibrium constant (fractionating factor) may be expressed as (Misra, 2012):

$$K = \frac{[^{1}B][^{2}A]}{[^{2}B][^{1}A]} \qquad \text{Equation 10.3}$$

Or can be expressed as:

$$R_A = \frac{[^{2}A]}{[^{1}A]} \quad \text{and} \quad R_B = \frac{[^{2}B]}{[^{1}B]} \qquad \text{Equation 10.4}$$

$$K = \frac{R_A}{R_B} = \alpha_{A-B} \qquad \text{Equation 10.5}$$

where $\alpha_{A\text{-}B}$ is the fractionation factor and *R* is the ratio of the heavy (less abundant) to light (more abundant) isotope, for example: $^{34}S/^{32}S$ in compounds A and B (SAHRA, 2005). Thus, Fractionation factor is defined as the ratio of the numbers of any two isotopes in one chemical compound A divided by the corresponding ratio for another chemical compound B (Friedman and O'Neil, 1977; SAHRA, 2005; Hoefs, 2015).

© University of Venda

Fractionation factor (α) is similar to distribution factor and this is the most important quantity used in the evaluation of stable isotope variations observed in nature. Several factors influence the sign and magnitude of fractionation factors and these include; temperature, pressure, chemical composition, crystal structure and chemical bonds (O'Neil, 1986b). Variation of Fractionation factor as a function of temperature is the basis of Isotope Geo-thermometry. For instance, at high temperature the fractionation factor approaches zero. Variation in chemical bonds results in the fractionation factor effect because heavier isotopes are more stable than lighter isotopes which are less stable with weaker hydrogen bonds which are easy to break (Kendall and Caldwell 1998; Misra 2012; Hoefs, 2015). Effect caused by crystal structure are minor compared to those caused by chemical bonding while the effect of pressure on fractionation factor is negligible, not more than 1.1 ‰ over 20 kbar (Misra, 2012; Hoefs, 2015). This is so because the change in molar volumes of solids on isotopic distribution is very small (Misra, 2012; Hoefs, 2015).

The delta (δ) notation:

Stable isotope ratios are generally reported as delta (δ) values in units of parts per thousand or as per mil (‰) relative to appropriate reference standards (Misra, 2012; Hoefs, 2015). The delta (δ) value of two compounds A and B whose isotopic compositionS are measured in the laboratory by conventional spectroscopy is defined as (Misra, 2012):

$$\delta_A = \left(\frac{R_A}{R_{st}} - 1\right) 10^3 \ (\%) \qquad \text{(Equation 10.6)}$$

and

$$\delta_B = \left(\frac{R_B}{R_{st}} - 1\right) 10^3 \ (\%), \qquad \text{(Equation 10.7)}$$

where R_A and R_B are the respective atomic ratio of the heavy to light isotope and R_{st} is the defined ratio of a standard sample (Misra, 2012; Hoefs, 2015). For the compounds A and B, the δ-values and fractionation factor (α) are related by (Misra, 2012):

$$\delta_A - \delta_B = \Delta_{A-B} \approx 10^3 \ln \alpha_{A-B} \qquad \text{(Equation 10.8)}$$

© University of Venda

A positive δ-value means enrichment of the heavier isotopes in the sample relative to the standard while a negative value means depletion of heavier isotopes in the sample relative to the standard. For example, a sample with δ ^{15}N value of +30 ‰ means that there are 30 part-per-thousand or 3% more ^{15}N in the sample relative to the standard (Kendall *et al.*, 1995; Kendall and Caldwell, 1998; Misra, 2012; Hoefs, 2015). Typical ranges of stable isotopes, for example, sulphur and oxygen in different geologic systems have been compiled by Faure (1986), Hoefs (1997) and Misra (2000) (Fig. 10.1).

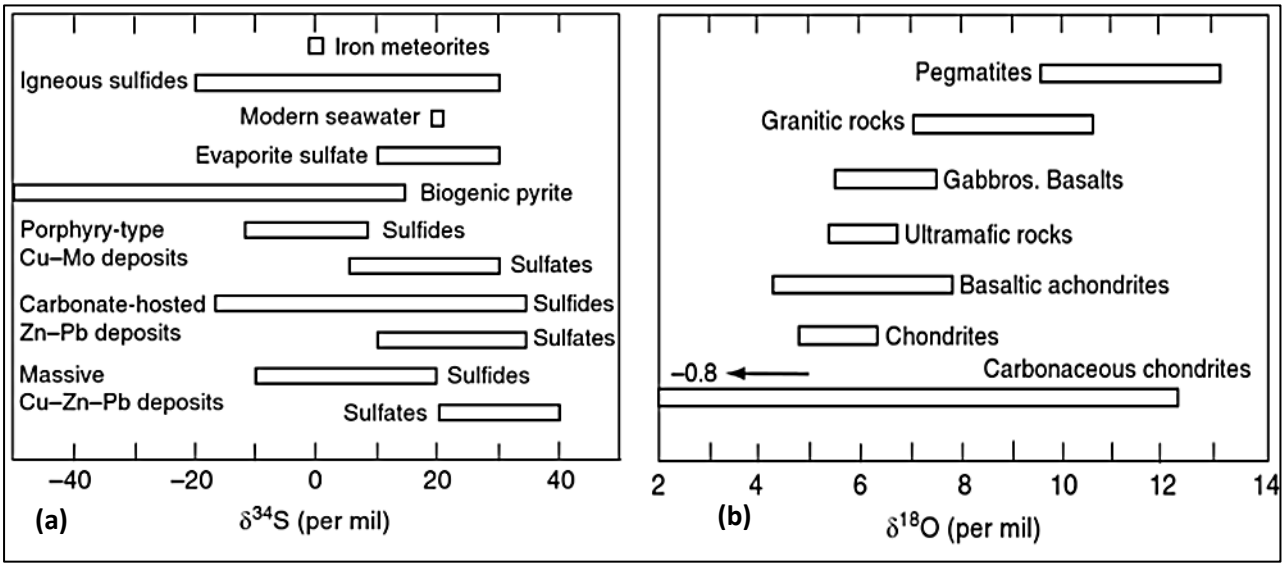


Figure 10.1: Typical ranges of stable isotope ratios in geologic systems: (a) Sulphur; (b) oxygen (Thode, 1970; Ohmoto and Rye, 1979; Faure, 1986; Hoefs, 1997, 1997; Misra, 2000).

Kinetic isotope effect

Kinetic fractionation is the fractionation process that is unidirectional and where equilibrium is not attained. It is dependent on the ratios of the masses of the isotopes and their vibrational energies. Biochemical processes are unidirectional and are good examples of kinetic isotopic reaction, for example, bacterially mediated reduction of SO_4^{2-} to H_2S, which depends on reaction mechanisms and possible intermediate products (Misra, 2012). In this process the lighter isotope is faster reacting and becomes concentrated in the product causing the residual reactants to become enriched in the heavy isotopes. Consequently, the organisms preferentially use lighter isotopic species because of low energy costs (Kendall *et al.*, 1995;

© University of Venda

Kendall and Caldwell, 1998; SAHRA, 2005; Misra, 2012). Some chemical reactions such as evaporation, diffusion, and dissociation are also unidirectional (Misra, 2012).

10.1.3 Reference Standards of Stable Isotopes

The isotopic composition of analysed materials using mass spectrometry is usually reported relative to international reference standards (Kendall and Caldwell, 1998; Misra, 2012). This could be done in several ways; samples are either analysed at the same time as these reference standards or with some internal laboratory standards that have been calibrated relative to the international standards. The other method is to use absolute ratios of isotopes. These reference standards are available for calibration purposes from either the National Institute of Standards and Technology (NIST) in the USA (Kendall and Caldwell, 1998).

Isotope laboratories use various working standards for the measurement of δ values, but to facilitate comparisons, the δ values are scaled to internationally accepted standards (Table 10.1) Troilite (FeS) from the Canyon Diablo iron meteorite is the standard used for reporting $\delta^{34}S$ values whereas Standard Mean Ocean Water (SMOW) is commonly used for reporting $\delta^{18}O$ and δD values which was defined by Graig (1961b) or the equivalent Vienna- Standard Mean Ocean Water (VSMOW) standard. The $\delta^{13}C$ values are reported relative to either the Pee Dee Belemnite (PDB) standard or the equivalent Vienna Pee Dee Belemnite (VPDB) standard (Kendall and Caldwell, 1998; Misra 2012; Hoefs, 2015).

The VSMOW and VPDB whose scales are identical to those of SMOW and PDB standards within the limits of analytical uncertainty, refer to standards available from the International Atomic Energy Commission (IAEA) in Vienna (Kendall and Caldwell, 1998; Misra 2012; Hoefs, 2015).

© University of Venda

Table 10.1: Abundance of selected stable isotopes and reference standards used for measurement of isotope ratio (O'Neil 1986b; Kyser, 1987a)

Element	Isotopes	Relative abundance (%)	Primary reference standards
Hydrogen	^{1}H(protium)	99.9844	V-SMOW
	^{2}H(D)	0.0156	
Carbon	^{12}C	98.89	PDB
	^{13}C	1.11	
Nitrogen	^{14}N	99.63	N2 in the atmosphere
	^{15}N	0.37	
Oxygen	^{16}O	99.763	V-SMOW
	^{17}O	0.0375	PDB
	^{18}O	0.1995	
Sulphur	^{32}S	95.02	CDT (Canyon Diablo Troilite)
	^{33}S	0.75	
	^{34}S	4.21	
	^{36}S	0.02	

10.1.4 Methods of Stable Isotope Analysis and Instrumentation

A number of different methods may be used for the measurement of stable isotopes abundance, these include; neutron activation, analysis of electromagnetic spectra, determination of the specific gravity of fluids, and analysis of mass spectra (Hoefs, 2009). Mass spectrometric methods are by far the most effective means of measuring isotope abundances, consequently the most widely used method (Hoefs, 2015). The major contribution on the invention of the mass spectrometer is by Thomson (1914) and Aston (1919). Subsequent improvements were made by Bainbridge and Jordan (1936), Nier (1940), Inghram and Hyden (1954), Arrience and Compston (1968) and Wasserburg *et al.*, (1969). The principle of mass spectrometry involves ionization of atoms of the chemical element whose isotopic composition is to be measured in a vacuum chamber. Ions are produced and accelerated using potential difference of 3-20 kV and this produces electric current that passes through magnetic field (Misra, 2012). The force from magnetic field is produced and is perpendicular to the current resulting in the bending of the beam of ions. During this

© University of Venda

process, the lighter ions are deflected more than the heavier ones and so the ions will be sorted according to their masses. The relative abundance of each isotope is then measured from the relative values of the electron currents produced by separated beam of ions (Hoefs, 1973, 1980, 2009 and 2015; Allegre, 2008).

The mass spectrometer is divided into four different parts; the inlet system, the ion source, the mass analyzer and the ion detector (Hoefs, 1973, 1980, 2009 and 2015; Allegre, 2008).

The inlet system: The inlet system (Fig. 10.2) has a changeover valve that allows rapid and consecutive analysis between gas samples (sample and standard gas) within few seconds. The gases are fed into the system through the capillaries. The dual inlet system is designed to enable one gas to flow into the ion source and the other one to flow into a waste pump so that the flow through the capillaries remains uninterrupted.

The ion source: The functions of the source are to generate, accelerate and shape the electron beam. The ions are generated from atoms whereby the electrons are bombarded and emitted by a heated tungsten or rhenium filament. The ions are then accelerated by electrostatic potentials between 50 and 150Ev and enter the ionization chamber. The ionized molecules are shaped into a beam that enters the analyzer that deviates and separates the ions. The ion beam is deviated when the beam passes through the magnetic field and this causes ion beam deflection which separates the ions by mass (Fig. 10.2).

The ion detector: The function of the detector is to collect and integrate the ion charges. The separated ions are collected and converted into electrical impulse which is then fed into the amplifier connected to the voltage /frequency converter and the measurement is obtained from the output device (computer) (Fig. 10.2).

There are two main different types of mass spectrometers, namely; the dual viscous –flow mass spectrometers and the continuous flow-isotope ratio monitoring mass spectrometers. The development of the continuous flow isotope ratio monitoring mass spectrometer was done through improvement or modification of the hardware of the classic dual viscous flow mass spectrometer.

© University of Venda

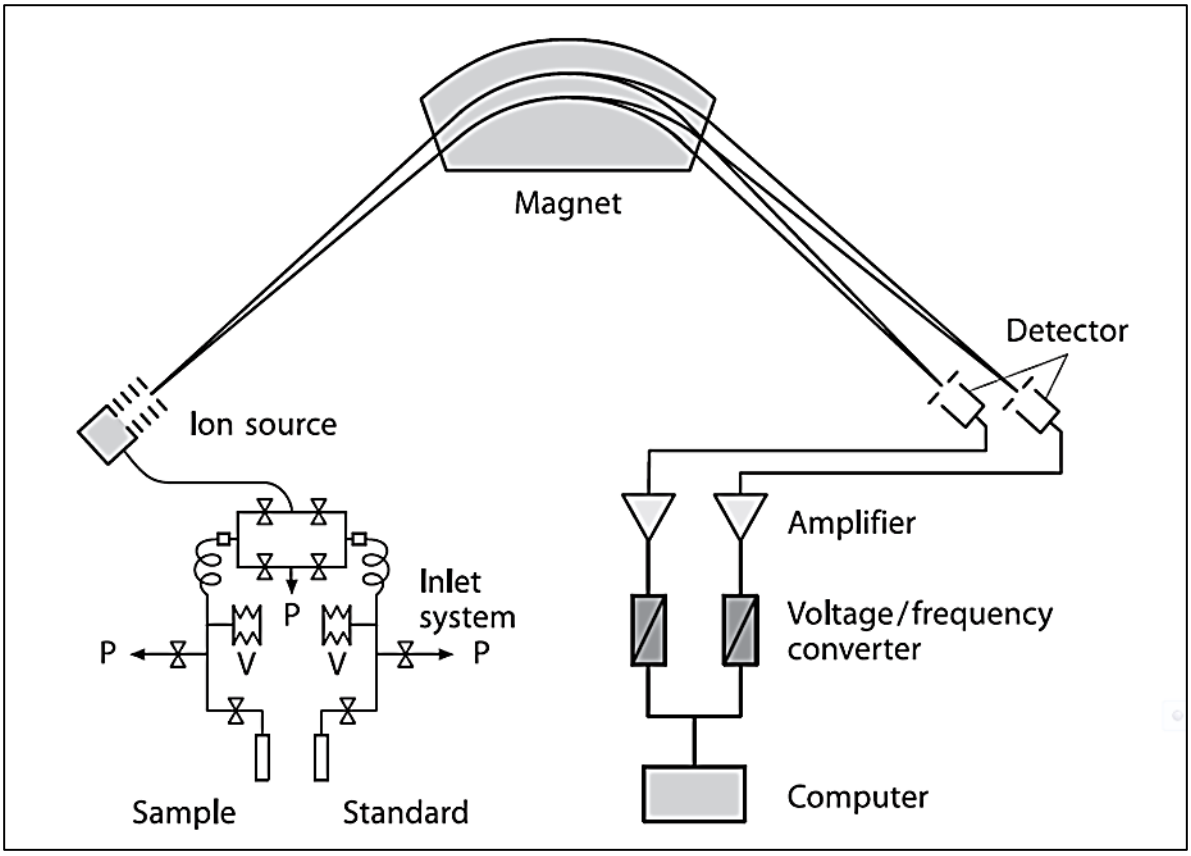


Figure 10.2: Schematic representation of a gas-source spectrometer used for stable isotope analysis. P denotes pumping system and V denotes variable volume (Hoefs, 2009).

The modification was done due to sample size factor, wherein the dual inlet spectrometer uses large sample size. Consequently, to reduce the sample size led to modification of the classic dual viscous –flow to continuous flow isotope ratio monitoring mass spectrometer in which the gas to be analysed is a trace gas in a stream of carrier gas (Hoefs, 1973, 1980, 2009 and 2015; Allegre, 2008). For this technique the size of the sample has been drastically reduced to the nano or even pico-molar range (Merritt and Hayes, 1994), but the major disadvantage of this method is that it gives lots of problems with homogeneity of sample, while the dual inlet gives little problems with homogeneity of samples (Seal, 2006).

© University of Venda

10.2 Importance and Application of Stable Isotopes

There are several characteristics that render stable isotopes of H, C, N, O and S to be useful for interpretation of geological, geochemical and biological processes. These include the following (Misra, 2012):

- These elements (H, C, N, O and S) are the main components of most minerals, rocks, and fluids, and they are also basic constituents of most forms of life;
- The relative difference in mass between heavy and light isotopes of these elements is fairly large (Table 10.1);
- The occurrence of more than one oxidation state as with C, N and S enhances the mass-depended isotopic fractionation of these elements;
- Having different types of bonds as in H-O, C-O and S-O that ranges from ionic to highly covalent also enhances the mass-depended isotopic fractionation of these elements; and
- For these elements, the abundance of the least common isotope is high (few tenths of percentage to percentage) that allow high precision measurements.

Variations of stable isotope ratios in minerals, rocks and fluids provide important insights into wide spectrum of geologic issues ranging from the formation of minerals to the evolution of the Earth and its biosphere through time (Misra, 2012). Some notable applications include geo-thermometry; recognition and quantification of crystal assimilation by magmas and mixing of hydrothermal fluids; interferences about the sources of metals in rocks and ore deposits; estimation of water: rock ratios in water-mineral reactions; and tracing the evolution of the atmosphere –biosphere system (Misra, 2012).

For example, carbon isotopes investigations have been undertaken in several deposit types such as; vein, replacement and Mississippi Valley types. In the study discussed by Ohmoto and Ryem (1979), it was deduced that hydrothermal deposits contain different generations of hydrothermal carbonate minerals and in most cases with a trend of increasing $\delta\ ^{13}C$ for later stage carbonates (Misra, 2000). Yang *et al.* (2013) used carbon and oxygen isotope compositions of lacustrine carbonate sediments from the Palacogene Shahejie Formation of the Qikou depression, Bohaiwan Basin in China for the determination of the palaeo-environmental conditions in the region.

© University of Venda

Oxygen and hydrogen isotopes have been widely applied in hydrothermal deposits as water is the main constituent of the hydrothermal fluids. The combination of the two isotopes is useful in tracing the origin and evolution of hydrothermal fluids (White, 1968; Taylor, 1974; 1979, 1997; Ohmoto, 1986; Sheppard 1986; Han, 2014).

10.3 Sulphur Isotopes Geochemistry

10.3.1 Fundamental Aspects of Suphur Isotopes

Sulphur is the 10th most abundant element in the Universe and it is the 14th most abundant element in the Earth's crust. Sulphur is the defining element of the sulphide minerals and provides insights into the origins of sulphide minerals through its stable isotopes. The four sulphur isotopes are ^{32}S, ^{33}S, ^{34}S, ^{35}S and ^{36}S which are defined by the presence of 16 protons, but can have either 16,17,18,19, or 20 neutrons, thus having atomic masses of 32,33,34,35 and 36 respectively (Seal, 2006). Four of the five isotopes are stable (^{32}S, ^{33}S, ^{34}S, ^{36}S) while ^{35}S is unstable or radiogenic (Seal, 2006). The four isotopes have terrestrial abundance of 95.02, 0.75, 4.21 and 1.02% respectively (Table 8.1).

The understanding of the origin and evolution of sulphide minerals is revealed from variations of the isotopic composition of sulphide minerals and related compounds such as sulphate minerals or aqueous sulphate species caused by fractionation processes (Seal, 2006). The isotopic composition of sulphur isotopes is defined as (Seal, 2006):

$$\delta^{34}S = \left(\frac{\left(^{34}S/^{32}S\right)_{sample} - \left(^{34}S/^{32}S\right)_{reference}}{\left(^{34}S/^{32}S\right)_{reference}} \right) \times 1000 \quad \text{(Equation 10.9)}$$

with its units given as parts per thousand or permil (‰). The values of $\delta^{33}S$ and $\delta^{36}S$ are defined the same way ($\delta^{33}S/\ \delta^{32}S$ and $\delta^{36}S/\delta^{32}S$) (Seal, 2006; Misra, 2012).

© University of Venda

10.3.2 Standards and Analytical Methods

The reference standard material (Table 10.1) commonly used for sulphur isotopes is from troilite of the Canyon Diablo iron meteorite, with the absolute ratio $^{32}S/S^{34}$ for Canyon Diablo Troilite of 4.50045 x 10^{-3}.

For conventional analysis, mineral separation is done through handpicking or gravitational technique or using wet chemical technique. This is done until the desired compound is concentrated and sulphur is extracted and converted to gaseous form (SO_2 or SF_6). The amount of sample required for conventional technique is 5 to 20 mg and the analytical uncertainties are 0.1 ‰ for $\delta^{34}S$ and in this method, sulphide mineral is reacted with oxidant (CuO, Cu_2O or V_2O_5) at temperature of 1000 to 1200°C under vacuum (Seal, 2006).

Isotopic analysis is done using gas-source, sector-type, isotope ratio mass spectrometer where the gas molecules are ionized to positively charged particles (Section 10.1.5). The *in-situ* microanalysis technique is one new method which has been developed through technological advancement. This technique uses the secondary ion mass spectrometry (SIMS) also referred as microprobe (Paterson *et al*., 1997; Eldridge *et al*., 1988; McKibben and Riciputi, 1998). The recent advance is the development of continuous-flow techniques. This technique uses the combination of elemental analyser and gas chromatograph for online combustion and purification of gases (Seal, 2006).

10.3.3 Sulfur Isotope Geo-thermometry

Factors that control suphur isotope fractionation include; composition variation, temperature and oxidation and reduction reactions acting upon the Sulphur. The oxidation and reduction processes may occur at high temperature, such as in igneous processes; at intermediate temperatures such as in hydrothermal processes; and at low temperature such as in sedimentary processes (Seal, 2006).

The temperature-dependence of sulphur isotope fractionation between two phases forms the basis of sulphur isotope geo-thermometry. Sulphur isotope geo-thermometry is based on fractionation of sulphur isotopes between two phases such as sphalerite and galena, or pyrite and galena, or pyrite and chalcopyrite or pyrite and sphalerite (Seal, 2006). The use of sulphur

© University of Venda

isotopes geo-thermometry is based on several assumptions, which include the following (Seal, 2006):

- The minerals must have been formed in equilibrium with one another at a single temperature;
- No re-equilibration or alteration of one or both minerals;
- Pure minerals must have been separated for isotopic analysis; and
- Temperature dependence of the fractionation factors must be known; and greater precision will be achieved when using mineral pairs that have greatest temperature dependence in their fractionation.

Ohmoto and Rye (1979) developed equations that can be used to calculate the temperature recorded by the coexisting pairs of the above mentioned sulphide minerals (Table 10.2).

Table 10.2: Sulphur isotope geo-thermometers (Ohmoto and Rye, 1979)

Mineral pair in equilibrium (M1-M2)	**Equation (T in Kelvin):** $\Delta^{34}S = \delta^{34}S_{M1} - \delta^{34}S_{M2}$	**Equation No.** 10.10	**Uncertainties: Calculated temperature** *1	*2
Pyrite – galena	$T = \frac{(1.01 \pm 0.04) \times 10^3}{\sqrt{\Delta^{34}S}}$	10.11	±25	±20
Sphalerite (or pyrrhotite) – galena	$T = \frac{(0.85 \pm 0.03) \times 10^3}{\sqrt{\Delta^{34}S}}$	10.12	±20	±25
Pyrite-chalcopyrite	$T = \frac{0.67 \pm 0.04) \times 10^3}{\sqrt{\Delta^{34}S}}$	10.13	±35	±40
Pyrite - sphalerite (or pyrrhotite)	$T = \frac{0.55 \pm 0.04) \times 10^3}{\sqrt{\Delta^{34}S}}$	10.14	±40	±55
	*1 = Estimated temperature uncertainty *2 = Analytical uncertainty of ±0.2‰ for Δ values at 300°C			

© University of Venda

10.3.4 Processes that Result in the Fractionation of Sulphur Isotopes

The most important processes that cause fractionation of sulphur isotopes include mass-dependent fractionation (Section 10.1.3) and mass-independent fractionation processes. The processes under mass-depended fractionation include; kinetic of isotope exchange reactions, sulphate reduction, sulphide oxidation, sulphide precipitation, and disproportionation of SO_2, while example of mass-independent processes is photochemical processes (Seal, 2006).

10.3.5 Sulphur Isotopes in Various Geological Environments

There are various geological environments where sulphur isotopes have been applicable and provide an insight in the genesis of ore deposits. These geological environments include; meteorite, marine sediments, coal deposits, mantle and igneous rocks, magmatic sulfide deposits, porphyry and epithermal deposits, sea floor hydrothermal systems and Mississippi Valley-type deposits (Seal, 2006; Misra, 2000, 2012). The typical ranges of sulphur isotopes ratios in geologic systems have been summarized in Figure 10.1 (Section 10.1.3.2).

10.4 Sulphur Isotopes Geochemistry Investigation of the Musina Copper Deposits

10.4.1 Objectives

In this study, sulphur isotope geochemistry investigation was conducted in order to:

- Determine sulphur isotope composition of the sulphide minerals and rocks from the Artonvilla and Campbell copper deposits;
- Identify the possible sources of sulphur during ore formation;
- To compare the sulphur isotope signatures of the Artonvilla and Campbell copper deposits and with other previous studied deposits; and
- Determine the temperature of ore formation at Artonvilla and Campbell deposits.

The above mentioned objectives are important in the study of sulphur isotope geochemistry for the purposes of better understanding the genesis of the Musina copper deposits.

© University of Venda

10.4.2 Sample Selection

A total of 8 samples were selected for sulphur isotope geochemistry investigation. The selected mineralised samples were collected from both Campbell (CpAm04, CpQv02 and CpQv02) and Artonvilla (Atcal01, Atcal02, Atgn03, Atgn04 and Atgn05) copper deposits (Table 10.3). The samples were collected randomly from near the closed shaft and waste rock dump, and were considered to be ideal for this study because they had sulphide mineralisation such as chalcopyrite, pyrite and bornite.

The collected samples were dominant in chalcopyrite and pyrite with minor content of bornite (CpQv01). The amount of sulphide mineralisation ranged from low, medium to high. Most of the ore sample collected had quartz veins and indicated brecciated structures of quartz, amphiboles and potassium feldspars (see chapter 6 and 7). The country rocks collected composed gneissic rocks which included: biotite gneiss, biotite garnet gneiss and quartzo-feldspathic gneiss that were associated with sulphide mineralization (Table 10.3).

10.4.3 Sample Preparation

The laboratory work was conducted at the Department of Geology, University of Georgia, Athens, GA in United States of America (USA). The laboratory work was supervised by Dr. Jeff, B. Chaumba together with Ms. Julia, A. Cox and Christopher, J. Fleisher. Monomineralic separation of sulphide minerals (Pyrite, Chalcopyrite and Bornite) from both Campbell and Artonvilla copper deposits was done from the selected samples.

Manual drilling method was used to separate these minerals using a diamond drill bit. The isotopic analysis of sulphur isotope requires the production of suitable gaseous compound of the element which is to be introduced to a source region of a gas source mass spectrometer (Hoefs, 1973, 1980, 2009 and 2015; Yanagisawa and Sakai, 1983; Rees and Holt, 1991).

© University of Venda

Table 10.3: Description of samples from Campbell and Artonvilla copper deposits used for sulphur isotope geochemistry

Deposit	Sample ID	Rock type	Degree of alteration	Colour	Texture/structure	Mineral composition	Amount sulphide mineralisation
Campbell	CpQv01	Quartz vein	Medium	Felsic	Course grained-quartz and k-feldspar breccia	Quartz, chalcopyrite, pyrite,	Medium -high
	CpQv02	Amphibolite with mineralisation within quartz veins	Low	Mafic	Course grained, quartz and amphibole breccia	Quartz, amphibole, chalcopyrite, pyrite, Bornite	Low
	CpAm04	Amphibolite with minor quartz veins hosting sulphides	Low	Mafic	Medium to course, quarts and k-fepdspar breccia	Amphiboles, Chalcopyrite-pyrite, quartz, chalcopyrite partly oxidised	Low
Artonvilla	Atcal01	Amphibole with elongated calcareous and quartz crystals forming veins	Low	Mafic	Medium to course grained /veinlets of quartz and calcite	Amphiboles, mafic minerals, calcitic minerals, quartz, disseminated sulphides within amphibole	Medium
	Atbr02	Brecciated amphibole with angular and veined quartz grains	Low	Mafic	Medium to course grained- quartz and amphibole breccia	Amphiboles, quartz, minor micas, low content of sulphides	Low
	Atgn03	Biotite garnet gneiss with disseminated sulphide mineralisation	Medium	Mafic	Medium to course grained, gneissic foliation	Layers of mafic and felsic minerals, micas and spotted garnets	Medium
	Atgn04	Biotite gneiss with disseminated sulphides	Low	Felsicto mafic	Course grained, foliations	Alternating layers of mafic and felsic minerals, minor spots of garnets, sulphides disseminated	Low
	Atgn05	Quartzo-feldspathic gneiss	Low	Felsic	Course grained	Not fully developed interlayers of quartz feldspathic and minor mafic minerals	Very low

© University of Venda

The gas used for sulphur isotope is sulphur dioxide (SO_2) which is produced using several methods but commonly following a method modified from Yanagisawa and Sakai (1983). The same method was used in this study where high temperature oxidation of sulphide using vanadium pentoxide (V_2O_5) as a solid oxygen donor was used and a simplified schematic diagramme was used to illustrate the procedure (Fig. 10.3).

About 4 to 6 mg of each pyrite, chalcopyrite and bornite were weighed and combined with elemental copper, quartz, and vanadium pentoxide (V_2O_5) and the mixture was then finely crushed. An offline V_2O_5 combustion line with variable cryogenic temperature (low temperature) trap (Fig. 10.4) was used following a modified method from Yanagisawa and Sakai (1983). The samples were then heated at 1050°C combustion furnace (Fig. 10.4a) and this was done in order to produce SO_2. The gas produced at this stage is highly contaminated by the other gases such as carbon dioxide (CO_2) and H_2O vapour.

Water was removed and trapped along water trap (Fig. 10.4b) cryogenically using dry ice-ethanol slush, and the remaining sample was collected in a variable temperature cryogenic trap (Fig. 10.4c).

Carbon dioxide was removed from the sample by raising the temperature from -190°C to -145°C. The temperature was finally raised from -145°C to -90°C and this was done in order to convert solid SO_2 to gaseous SO_2.

The SO_2 was collected in a conventional Pyrex break-seal tubes in a collection port (Fig. 10.4d) and was then measured using a calibrated mercury manometer (Fig. 10.4e), converted and reported as actual SO_2 yield. The conventional Pyrex break-seal tubes were used to collect the SO_2 because they offer secure long-term storage (Rees and Holt, 1991).

© University of Venda

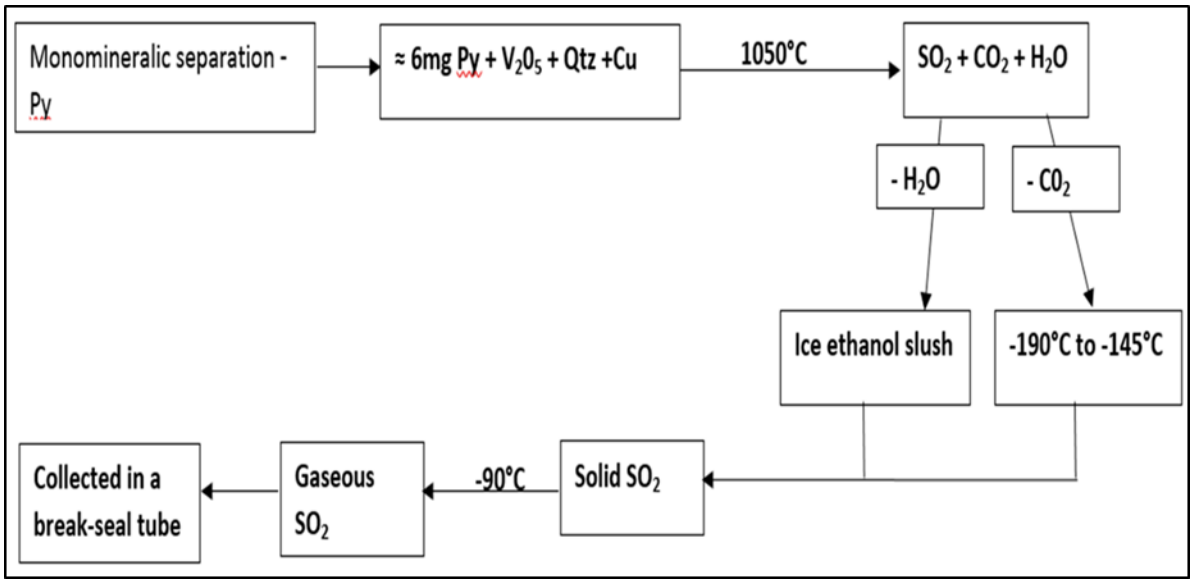


Figure 10.3: Schematic representation of the procedure followed for the production of gaseous SO_2 using vanadium pentoxide (V_2O_5) as a solid oxygen donor.

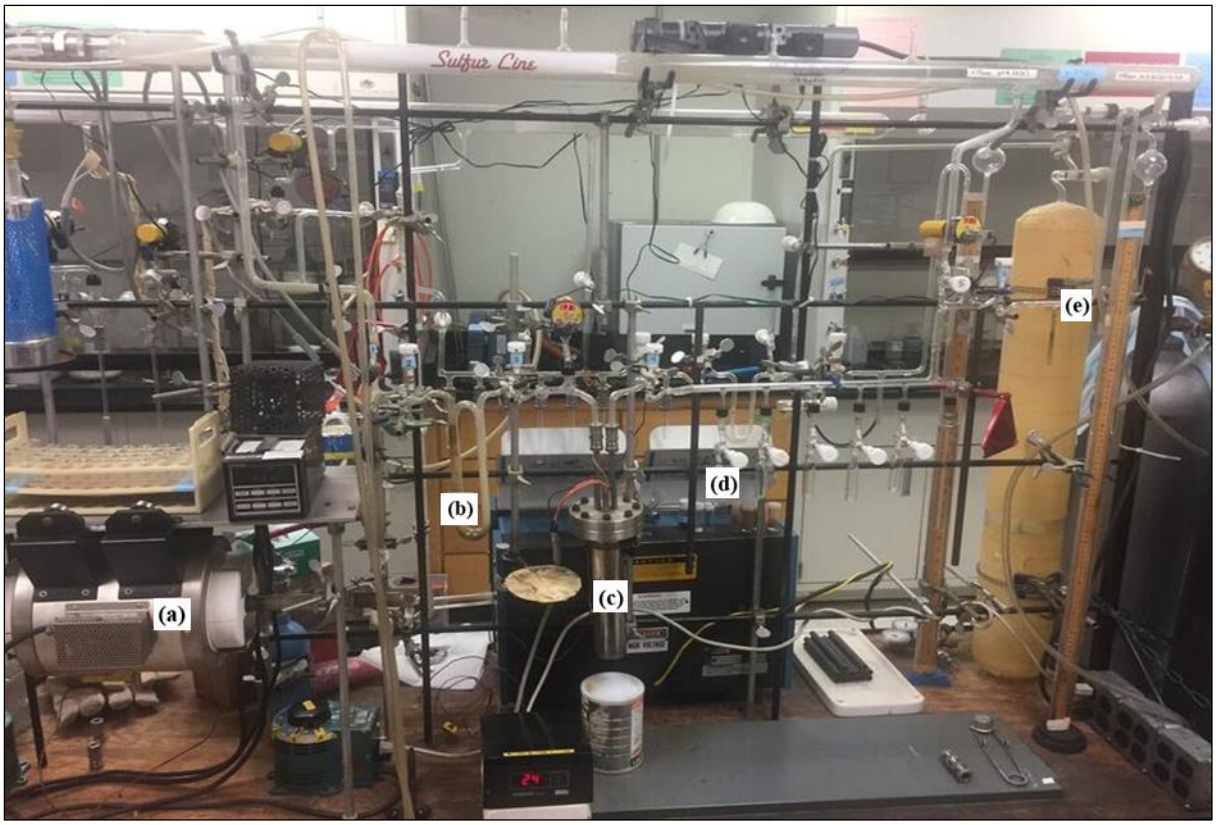


Figure 10.4: An offline V_2O_5 combustion line with variable cryogenic temperature trap used for the production of pure SO_2 from sulphide minerals: (a) Combustion furnace; (b) water trap; (c) variable temperature trap; (d) sample collection port; (e) sample cold-finger and manometer.

© University of Venda

10.4.4 Sample Analysis

The collected purified SO_2 gas was analysed using Finnigan MAT 252 dual inlet mass spectrometer (Fig. 10.5) from the Department of Geology, University of Georgia, USA. The sample and the standard reference gas were admitted in the sample inlet pot (Fig. 10.5a) and reference inlet pot (Fig. 10.5b) respectively. The sample and the reference were admitted alternatively so that isotopic differences can be determined under constant conditions and with no consequent elimination of many instrumental bias following Rees and Holt (1991) procedure adopted from (Nier, 1947; Wanless and Thode, 1953). An accelerating potential of 8 kV was set on the mass spectrometer. The ions were generated, accelerated and the electron beam shaped within the ion source (Fig. 10.5c) and controlled using ion source controls (Fig. 10.5d). The ion beam passes through the electromagnetic field where the electromagnet (Fig. 10.5e) deviates the ions according to their mass and focus each ion beam direct to the ion collector (Fig. 10.5f) which then integrates the ion charges so as to generate the electric current.

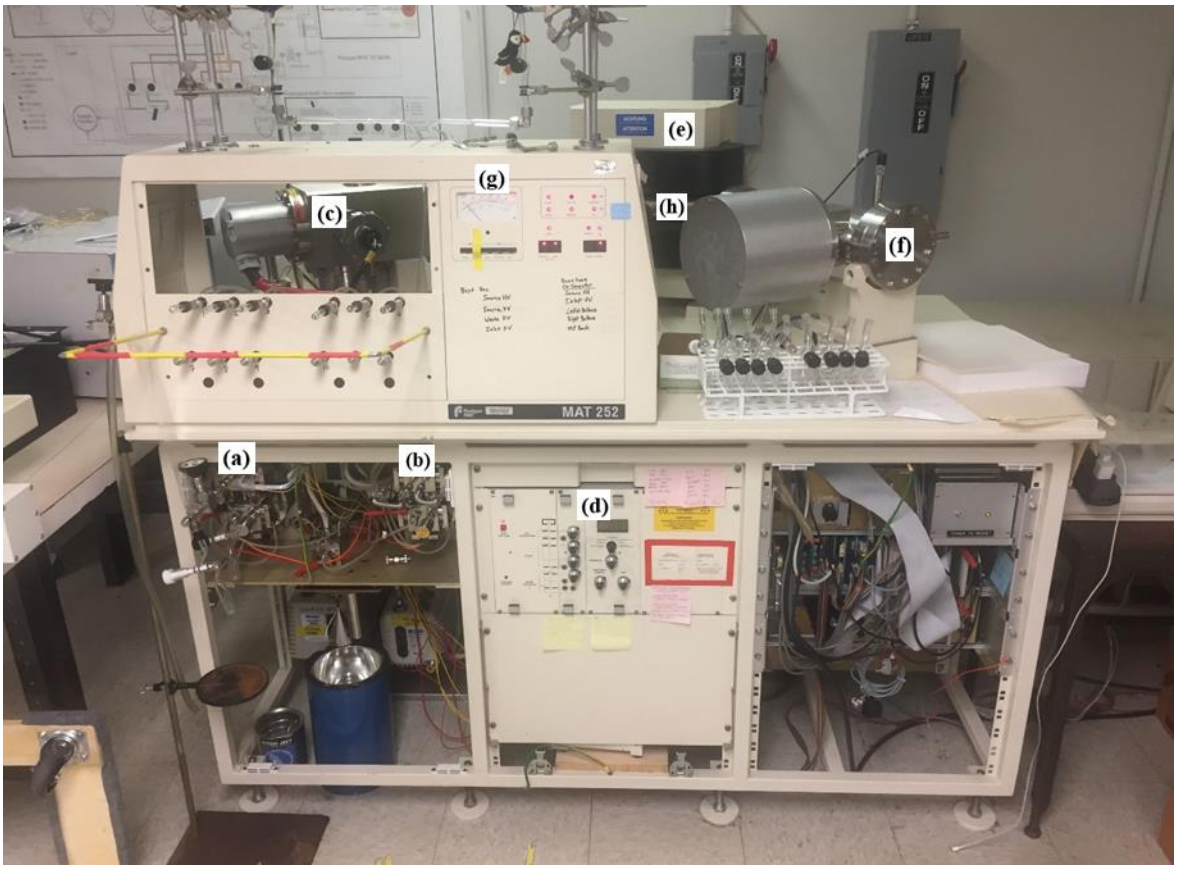


Figure 10.5: Finnigan MAT 252 dual inlet mass spectrometer used for sulphur isotope analysis: (a) Sample inlet pot; (b) reference inlet pot; (c) ion source; (d) ion source control; (e) electromagnet; (f) ion collectors; (g) vacuum gauge; and (h) flight tube.

© University of Venda

The whole system (from the ion source to ion collectors) is built in a vacuum tube within which the vacuum pressure can be maintained.

The element isotopic composition was measured in a vacuum gauge (Fig.10.5g) and detected using an electron multiplier in pulse-counting mode. During analysis, each sample was measured for 8 seconds for 8 standard sample cycles against the appropriate SO_2 reference gas.

The sulphur samples were measured with a1000-2000 mV signal intensity, with an open Variable Ion Source Conductance (VISC) referred as 'sulfur window' and recorded (Table 10.4). An error of ±0.2 ‰ was determined based upon replicate analysis of Esperanza and ZS495 standards. The results were expressed in the Delta notation ‰ (per mil) (Table 10.4) and reported relative to the Vienna Canyon Diablo Troilite (VCDT) Standard which is a well known recognized International reference material used for sulphur isotope analysis (Zoran *et al.,* 2009; Sharman *et al.,* 2013; Donoghue, *et al.,* 2014; Bekker *et al.,* 2016) defining $\delta^{34}S$ as in equation 10.9. The absolute $^{32}S/\ ^{34}S$ ratio for VCDT is 4.50045 x 10^{-3} (Ault and Jensen, 1963).

Table 10.4: $\delta^{34}S_{(VCDT)}$ data for Campbell and Artonvilla copper deposit samples

Deposit	**Sample ID**	**Phase**	**$\delta^{34}S$ (‰, VDCT)**	**Average**
Campbell	CpQv01py	Pyrite	0.5	
	CpQv01Ccp2	Chalcopyrite	0.7	
	CpQv01Ccp	Chalcopyrite	0.4	0.5286
	CpQv02Ccp	Chalcopyrite	-0.3	(~ 0.5‰)
	CpAm04Ccp	Chalcopyrite	0.3	
	CpAm04Ccp2	Chalcopyrite	-1.1	
	CpQv01bn	Bornite	0.4	
Artonvilla	Atcal01py	Pyrite	3.1	3.5333
	Atcal01py2	Pyrite	3.6	(~ 4‰)
	Atcal01Ccp	Chalcopyrite	3.9	
	Atgn04wr	Granatic gneiss	8.2	

© University of Venda

10.4.5 Results and Interpretation

10.4.5.1 Campbell Copper Deposit $\delta^{34}S$ Values

Pyrite, chalcopyrite and bornite sulphide minerals from selected samples of Campbell copper deposit were used for sulphur isotope composition analysis. The pyrite and chalcopyrite analysed were from quartz vein sample (CpQv01) characterised by medium to high sulphide mineralisation with course grained quartz and potassium feldspar grains that formed breccia structures (Table 10.3). The analysed pyrite sample from sample CpQv01 revealed positive $\delta^{34}S_{pyrite}$ value of 0.5‰ whereas the chalcopyrite from the same sample, but drilled at two different positions revealed positive $\delta^{34}S_{chalcopyrite}$ values of 0.4‰ and 0.7‰ (Table 10.4). Sulphur isotope analysis was also done on bornite from the same sample (CpQv01) and revealed positive $\delta^{34}S_{bornite}$ value of 0.4‰ (Table 10.4). The average $\delta^{34}S$ values from the sulphides of the Campbell copper deposit was 0.5‰. Consequently, this implies that sample CpQv01 was enriched with $\delta^{34}S$ rather than depleted in $\delta^{34}S$ as all the $\delta^{34}S$ showed positive values rather than negative values as in samples CpQv02 and CpAm04 (Table 10.4).

The $\delta^{34}S$ chalcopyrite values were also determined from sample CpQv02 and CpQAm04 both from Campbell copper deposit. The sample (CpQv02) had quartz vein within the amphibolite with low content of sulphide mineralisation and displayed quartz and amphibole brecciated structures (Table 10.3). Amphibolite with minor quartz veins hosting sulphide minerals (CpQAm04) displayed low content of sulphide mineralisation with medium to course brecciated quartz and k-feldspar (Table 10.3). The two samples (samples CpQv02 and CpQAm04) revealed negative $\delta^{34}S_{chalcopyrite}$ values of -0.3‰ and -1.1‰ respectively meaning that the sample was depleted with $\delta^{34}S_{chalcopyrite}$. While $\delta^{34}S_{chalcopyrite}$ value of sample CpQAm04 analysed at different position revealed positive $\delta^{34}S_{chalcopyrite}$ of 0.3‰ (Table 10.4).

The sulphur isotopic compositions from Campbell copper deposit for a pyrite, chalcopyrite and bornite were plotted using frequency diagram (Fig. 10.6). The $\delta^{34}S$ values within Campbell copper deposit samples were clustered within a range of -1.5 to 1.5‰ with highest frequency within a range of -0.5 to 0.5‰ (Fig. 10.6).

© University of Venda

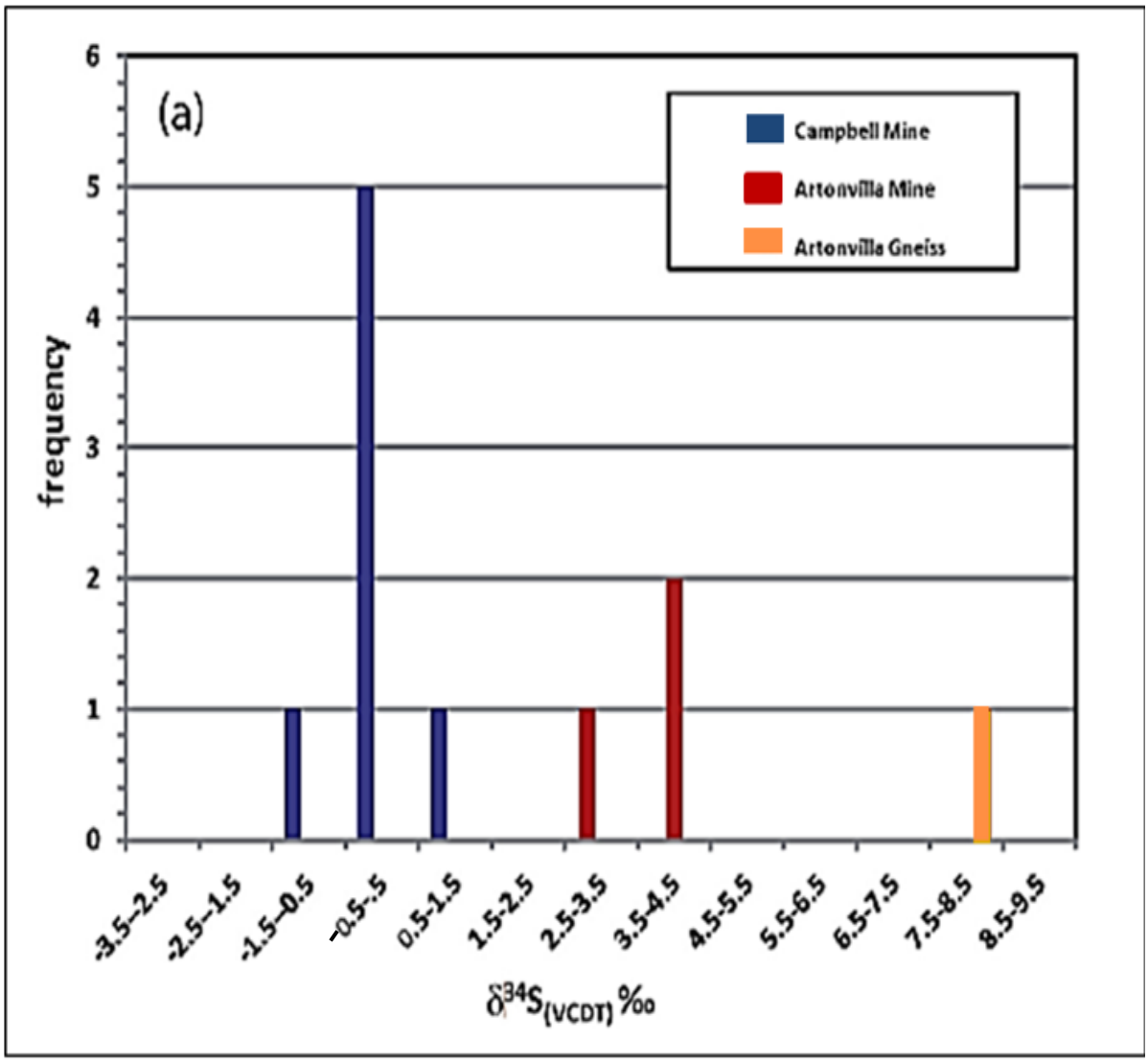


Figure 10.6: Frequency plot of $\delta^{34}S$ values of pyrite, chalcopyrite, bornite from Campbell copper deposit and $\delta^{34}S$ values of pyrite, chalcopyrite and country rock (whole rock) from Artonvilla copper deposit.

10.4.5.2 Artonvilla Copper Deposit $\delta^{34}S$ Values

From Artonvilla samples, an ore sample (Atcal01) and country rock samples (Atgn04) were used for sulphur isotope composition determination. The Atcal01sample was characterized medium content of sulphide mineralisation that occurred as disseminated grains within

© University of Venda

amphibolite. The sample exhibited medium to coarse texture and had elongated calcareous and quartz crystals forming a veined structure with the amphibolite rock (Table 10.3).

Determination of $\delta^{34}S$ values in pyrite of sample Atcal01 yielded $\delta^{34}S_{pyrite}$ values of 3.1 and 3.6‰ while chalcopyrite from the same sample revealed $\delta^{34}S_{chalcopyrite}$ value of 3.9‰. The analysed pyrite from country rock (Atgn04) revealed $\delta^{34}S_{pyrite}$ value of 8.2‰. Thus, the average $\delta^{34}S$ value from the sulphides of the Artonvilla copper samples was found to be 3.5333 which is about 4‰. All the samples from Artonvilla copper deposit revealed positive $\delta^{34}S$ values implying that the samples were enriched with S.

The sulphur isotopic compositions for a pyrite and chalcopyrite from Artonvilla copper deposit samples were plotted using frequency diagram (Fig. 10.6). The $\delta^{34}S$ values within Artonvilla copper deposit samples were found to be clustered within a range of 2.5 to 4.5‰ while the the most frequent $\delta^{34}S$ values falls within 3.5 to 4.5 ‰ (Fig. 10.6).

10.4.5.3 Comparison of $\delta^{34}S$ Values with other Previous Studies

The results obtained from both Campbell and Artonvilla samples were compared with the results of the previous investigation done by Sawkins and Rye (1979) and also compared with similar study undertaken from the Mantos Blancos breccia copper deposit in Chile and Ilkwang breccia pipe from South Korea (Fig. 10.7). The comparison was done using the frequency diagram (Fig. 10.7).

The sulphur isotope study on hypogene sulphide mineralisation of the Mantos Blancos breccia copper pipe in Chile, conducted by Ramirez *et al*. (2006) revealed a narrow range of $\delta^{34}S$ (-3.5 to 2.5‰) that are clustered around 0‰ (Fig.10.7), suggesting a magmatic source of sulphur and indicated a co-genetic relationship for the investigated sulphide mineralisation. The sulphide isotopic compositions of the sulphide minerals from the Ilkwang breccia pipe deposit investigated by Yang and Bodna (2004) revealed $\delta^{34}S$ values ranging from -2.5 to 2.5‰ (Fig.10.7) and were consistent with the magmatic origin for the hydrothermal fluids.

© University of Venda

Sulphur isotopic composition of sulphide mineralisation within the Campbell copper deposit revealed sulphur isotopic composition clustering around 0‰ with highest frequency within a range of -0.5 to 0.5‰ (Figs. 10.6 and 10.7). This range showed a similar trend with sulphur isotopic data from the previous study undertaken by Sawkins and Rye (1979) and also relate very well with the data from both Mantos Blancos and Ilkwang breccia copper pipes (Fig. 10.7). On this basis, this study revealed that samples from Campbell copper deposit are consistent with the magmatic source for the sulphide mineralisation.

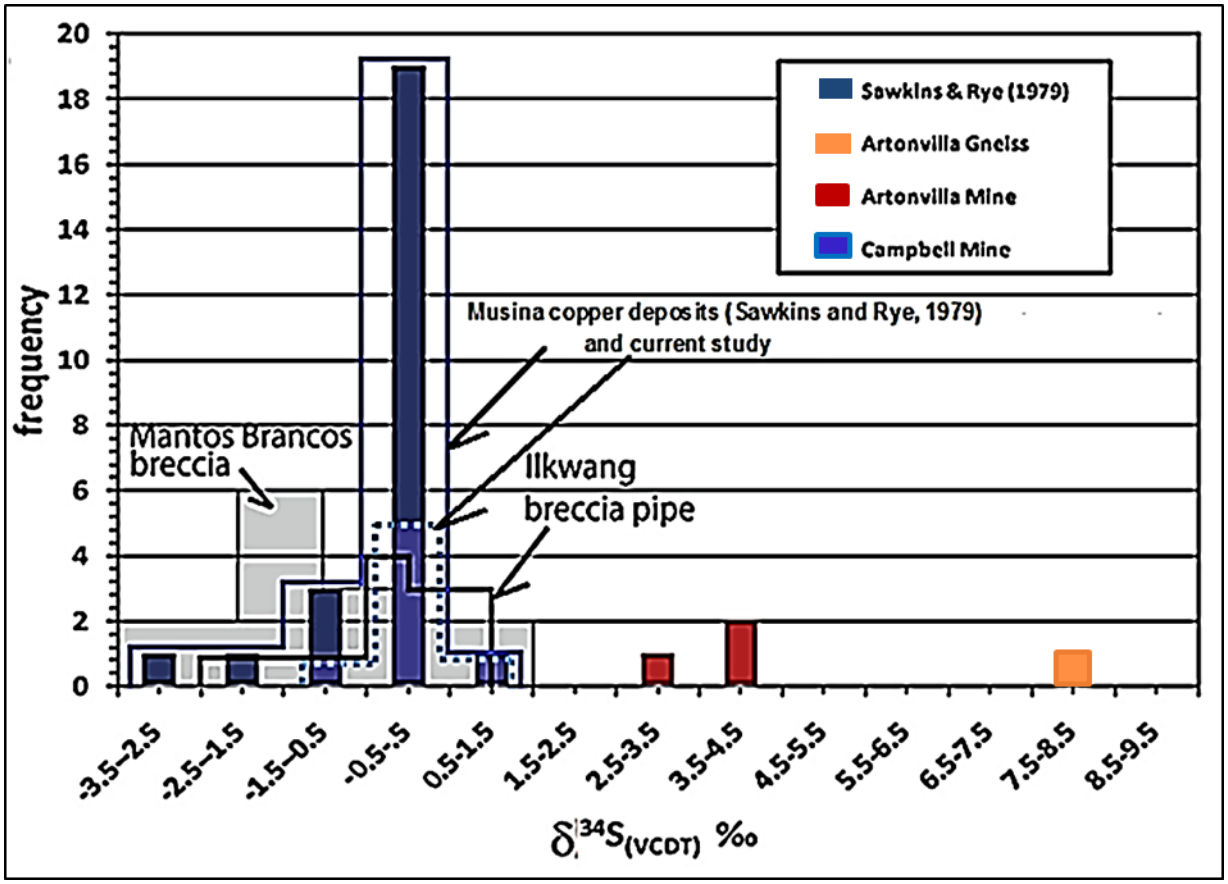


Figure 10.7: Frequency diagram showing a comparison of sulphur isotope values for sulphide minerals from both Campbell and Artonvilla copper deposits with sulphur isotope data of Mantos Brancos breccia pipes, Northern Chile and Ilkwang breccia pipe, South Korea.

© University of Venda

10.4.5.4 Comparison of δ^{34}S Values within Artonvilla Sulphide Ore and Country Rock Samples

Monomineralic analysis of chalcopyrite within the country rock sample (AtGn04) from Artonvilla copper deposit yielded δ^{34}S value of 8.2‰ (Table 10.4) indicating the enrichment of heavy sulphur isotope (δ^{34}S) within the country rocks. Monomineralic analysis of the sulphides within the Artonvilla copper deposit revealed average δ^{34}S value of ~ 4‰ (Table 10.4). This gives an immense difference of about 4.2/8.2‰*100 = 51.2%.

An immense difference between the Artonvilla copper deposit country rock and ore samples implies that magmatic sulphur may have been contaminated by sulphur from sulphur that comes from the Artonvilla country rock. The sulphur could have also been sourced from the mantle which was affected by hydrothermal fluid which comprised of sulphur generated when the hydrothermal fluids affected the sulphur enriched country rock.

Generally, if mineralisation of a deposit pre-dates metamorphism, its ore samples and its country rock are likely to be characterised by more or less similar δ^{34}S values. If mineralisation of a deposit post-dates metamorphism, its ore samples and country rocks are likely to be characterised by different δ^{34}S values (Chaumba *et al.*, 2016) which is the case in this study. Consequently, this could imply that ore mineralisation within the Musina deposits took place after regional metamorphism.

10.4.5.5 Comparison of the Campbell and Artonvilla with the Mantle δ^{34}S Values

The determined δ^{34}S values from Campbell sulphide mineralisation yielded a range from -1.1 to 0.7‰ (Table 10.4) with highest frequency δ^{34}S values clustered between -0.5 to 0.5‰ (Fig. 10.6 and 10.7) while the δ^{34}S values Artonvilla sulphide mineralisation yielded a range from 3.1 to 3.9‰ (Table 10.4) with highest frequency δ^{34}S values clustered between 3.5 to 4.5‰ (Fig.10.6 and 10.7). According to Ohmoto and Rye (1979) and Ohmoto and Goldhaber (1997), the mantle is characterised by δ^{34}S of 0±5‰ (Fig. 10.8). The δ^{34}S from Campbell and Artonvilla sulphide mineralisation were found to be within the δ^{34}S range of the mantle derived Sulphur (Fig. 10.8). This implies that the sulphur from sulphide mineralisation within Campbell and Artonvilla sulphide mineralisation were derived from the mantle. The

© University of Venda

Campbell and Artonvilla $\delta^{34}S$ values were also found to be within the $\delta^{34}S$ values of the previously studied copper deposits (Fig. 10.8), where it was also concluded that the sulphur from the sulphide mineralisation was derived from the mantle. For example, the $\delta^{34}S$ values from Ilkwang breccia copper deposit, Mantos Blancos breccia copper deposit and the six hydrothermal deposits reported by Rye and Omoto (1974) revealed $\delta^{34}S$ values that ranged from -2.5 to 2.5; -3.5 to 2.5; -5.0 to 5.0 per mil respectively (Fig. 10.8), thus, gave a cluster between -5.0 to 5.0 per mil which is the same as that of the mantle (0±5‰). Similarly, Campbell and Artonvilla copper deposits $\delta^{34}S$ range (-1.1 to 0.7‰ and 3.1 to 3.9‰ respectively) were found to be within 0±5‰ (Fig. 10.8).

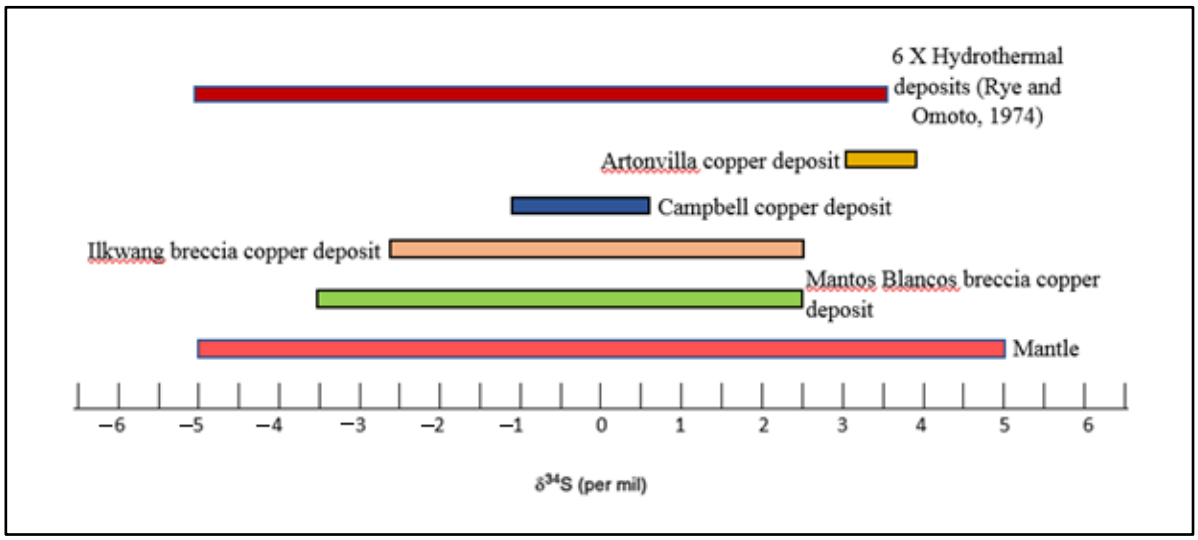


Figure 10.8: Comparison of the Campbell and Artonvilla copper deposits $\delta^{34}S$ values and the Mantle $\delta^{34}S$ values.

10.4.5.6 Sulphur Isotope Geo-thermometry of Musina Deposits

Sulphur isotope geo-thermometry was conducted whereby temperature of the Musina copper sulphide ore formation was determined. Ohmoto and Rye (1979) developed several equations (Table 10.2) which are used for the determination of temperature of ore formation from the coexisting pairs of sulphide minerals such as pyrite-galena; sphalerite (or pyrrhtite)-galena; pyrite-chalcopyrite and pyrite-sphalerite (or pyrrhtite) pairs (Table 10.2). For example, the pyrite-chalcopyrite pair from quartz vein sample (CPQv01) of the Campbell copper deposit

© University of Venda

was used to determine the temperature of ore formation of the deposit using equation 10.13 (Ohmoto and Rye, 1979):

$$T = \frac{0.67 \pm 0.04) \times 10^3}{\sqrt{\Delta^{34}S}} \qquad \text{Equation 10.13}$$

where,

$\Delta^{34}S = \delta^{34}S_{M1} - \delta^{34}S_{M2}$

$= \delta^{34}S_{\text{pyrite}} - \delta^{34}S_{\text{chalcopyrite}}$

$= 0.5 - (-0.3)$ ‰

$= 0.8$‰

Thus,

$$T = \frac{(0.67 \pm 0.04) \times 10^3}{\sqrt{0.8‰}}$$

$T(K) = 749$

$T\ (°C) = 749 - 273$

$= 476°C$

Thus, the temperature determination of mineral pair pyrite and chalcopyrite from Campbell sample (CPQv01) with pyrite $\delta^{34}S_{\text{pyrite}}$ value of 0.5‰ and $\delta^{34}S_{\text{chalcopyrite}}$ values of -0.3‰ yielded $\Delta^{34}S$ of 0.8‰. Thus, temperature determination using Campbell sample yielded temperatures of 476°C.

Following the same procedure, the temperature determination of mineral pair pyrite and chalcopyrite from Artonvilla sample (Atcal01) with pyrite $\delta^{34}S_{\text{pyrite}}$ values of 3.1‰ and $\delta^{34}S_{\text{chalcopyrite}}$ value of 3.9‰ yielded $\Delta^{34}S$ of 0.8‰. Using $\Delta^{34}S$ of 0.8‰, temperatures of 476°C was deduced.

Chalcopyrite and bornite isotope composition (Table 10.4) from the Campbell quartz vein (CpQv01) were used following the equation derived by Li and Liu (2006). In this method, modification of the increment method to calculate thermodynamic isotopic fractionation factors of sulphides was done. This was done based on the chemical features of Sulphur - metal bonds and crystal features of sulphide minerals wherein the Madelung constant (C_m)

© University of Venda

was introduced (Li and Liu, 2006). The general modified equation derived by Li and Liu (2006) is as follows:

$0.12 * 10^6/T^{-2}$ where T is in Kelvin Equation 10.15

$0.12 * 10^6/T^{-2} = \Delta^{34}S$

This equation was then used for the determination of temperature of ore formation using coexisting pairs of sulphide minerals chalcopyrite-bornite.

Where,

$\Delta^{34}S = \delta^{34}S_{M1} - \delta^{34}S_{M2}$

$= \delta^{34}S_{\text{chalcopyrite}} - \delta^{34}S_{\text{bornite}}$

= 0.7 ‰ – 0.4 ‰ (Table 10.4)

= 0.3‰

Thus,

$0.12 \text{ X } 10^6/T^{-2} = 03$

$120\,000/ T^{-2} = 0.3$ >>> $T^{-2} = 0.3/120\,000$ >>> $T^2 = 120\,000/0.3$

$T = 400\,000$

$= \sqrt{400\,000}$

T (K) = 632.46

T(°C) = 632.46 – 273

= 359°C

Following the same procedure (equation 10.15), temperature determination of mineral pair chalcopyrite and bornite from Artonvilla sample (Atcal01) with $\delta^{34}S_{\text{chalcopyrite}}$ values of 0.7 and -0.3‰ and $\delta^{34}S_{\text{bornite}}$ value of 0.4‰ yielded $\Delta^{34}S$ of 0.3 and 0.7‰ respectively, with temperature values of 359°C and 141°C respectively.

Consequently, the temperature of ore formation within Campbell and Artonvilla copper deposit yielded temperature value of 476°C deduced from pyrite-chalcopyrite pair. While

© University of Venda

Artonvilla copper deposit yielded temperature values of 141°C and 359°C deduced from chalcopyrite-bornite pair.

The temperatures deduced from both Campbell and Artonvilla pyrite-chalcopyrite pair registered high temperature value of 476°C while temperature values deduced from Artonvilla and Campbell chalcopyrite-bornite pair registered temperatures with a range of 141°C to 359°C with average value of 250°C.

10.5 Discussion

Sulphur isotope geochemistry is one of the major recent advances and most appropriate geochemical tool used in the field of economic geology to identify possible sources of sulphur in sulphide ore formation, used on inferring about the sources of metals in rocks and ore deposits, used to draw conclusions about the geochemical conditions and mechanisms of ore formation, and used in sulphur isotope geo-thermometry which is temperature determination of ore formation (Ohmoto, 1986; Misra, 2000; Seal, 2006; Misra, 2012). All of the four factors stated above have a profound influence on the sulphur isotope signatures of sulphide minerals and therefore these factors were taken into consideration in the discussion of the results obtained in this study.

10.5.1 Possible Sources of Sulphur in Sulphide Ore Formation

Positive value of δ means enrichment of the heavier isotope in the sample relative to the standard while a negative δ value means relative depletion of the heavier isotope in the sample (Kendall *et al.*, 1995; Kendall and Caldwell, 1998; Misra, 2000; Misra, 2012; Hoefs, 2015). The isotopic investigation of the Campbell copper deposit revealed positive $\delta^{34}S$ from sample CpQv01 and negative values from samples CpQv02 and CpQamp04 (Table 10.4) with high frequency $\delta^{34}S$ values within -0.5 to 0.5‰ (Fig. 10.6), which is indication of enrichment (+ve) and depletion (-ve) of sulphur. The Artonvilla copper deposit registered positive $\delta^{34}S$ values that were clustered within 2.5 to 4.5‰ (Fig.10.6), thus implying enrichment of sulphur, with a country rock registering highly enriched $\delta^{34}S$ values (8.2‰). Similarly, the study conducted by Sawkins and Rye (1979), revealed sulphur isotope values from Campbell copper deposit that were both enriched and depleted by sulphur in their ore

© University of Venda

samples. However, Sawkins and Rye (1979) did not analyse samples from Artonvilla copper deposit nor country rock from the deposit, rather samples analysed were mostly from Campbell and two from Harper and one from Spence which were mostly showing negative δ values, thus showing depletion of sulphur and two samples showing positive δ values.

A comparison of the δ^{34}S values from both Artonvilla and Campbell copper deposits with other previously studied deposits was executed using a frequency versus δ^{34}S values plot (Fig. 10.7). Previously studied deposits such as Mantos Brancos breccia pipes, Northern Chile (Ramírez *et al.*, 2006) and Ilkwang breccia pipe, South Korea (So and Shelton, 1983) concluded that the mineralisation of these deposits is related to hydrothermal circulation driven by magmatic intrusions based on sulphur isotope values, temperature, petrography and sulphide mineral composition. A comparison between the Artonvilla and Campbell δ^{34}S values with these previously studied deposits together with the results from Sawkins and Rye (1979) broadly compare well (Fig. 10.7). Consequently, this implied that ore minerals from Campbell and Artonvilla copper deposits were of magmatic origin.

10.5.2 Sources of Metals in Rocks and Ore Deposits

Artonvilla copper deposit samples revealed average delta values of about 4‰ whereas a country rock granitic gneiss from the same deposit registered 8.2‰ (Table 10.4 and Fig. 10.6). Artonvilla country rock was found to be highly enriched with sulphur.

The mantle is generally characterised by δ^{34}S of 0±5‰ (Ohmoto and Rye 1979; Ohmoto and Goldhaber, 1997). Both the Artonvilla and Campbell samples registered δ^{34}S values (3.5 to 4.5 ‰ and -0.5 to 0.5‰) that are within the mantle δ^{34}S range (0±5‰) as represented in Figure 10.8 together with previously studied deposits which also had sulphur derived from the mantle. For example, the six hydrothermal deposits studied by Rye and Ohmoto (1974), Ilkwang, and Mantos Blancos breccia pipe deposits studied by So and Shelton (1983), and Ramírez *et al*. (2006) respectively. Consequently, both Artonvilla and Campbell sulphur was apperently derived from the mantle.

A wide gap was found between the average δ^{34}S values of 4.2‰ from Artonvilla sulphides and country rock granitic gneiss value of 8.2‰, giving over 50% difference. Generally, if mineralisation of a deposit pre-dates metamorphism, its ore samples and its country rock are likely characterised by more or less similar δ^{34}S values. If mineralisation of a deposit post-

© University of Venda

dates metamorphism, its ore samples and country rocks are likely characterised by a wide range of $\delta^{34}S$ values (Chaumba *et al.*, 2016) which is the case in this study. Consequently, this therefore confirms that ore mineralisation occurred after regional metamorphism of the Limpopo Mobile Belt.

10.5.3 Geochemical Conditions and Mechanisms of Ore Formation

The elevated $\delta^{34}S$ values from Artonvilla copper deposit (3.1 to 3.9‰) can be explained by the fact that mantle-derived sulphur might have been affected by either contamination by country rock sulphides with elevated $\delta^{34}S$ value of 8.2‰ or affected by hydrothermal activity that had interacted with country rocks, or both.

The narrow $\delta^{34}S$ values from Campbell copper deposits (-0.5 to 0.5‰) can be explained by the fact that immiscibility of both S and Fe occurred, leading to increased concentration of Cu in sulphide mineralisation which then settled out later leading to the formation of the Musina copper deposits (Chaumba *et al.*, 2016).

According to Sawkins and Rye (1979), the narrow range (-0.5 to 0.5‰) is due to the removal of S and Fe during oxidation of sulphides, while McCarthy and Jacobsen (1976) suggested that it is due to the addition of Cu to originally early formed pyrite and chalcopyrite while Fe is oxidized to conserve electrons. This position is also supported by Chaumba *et al*. (2016).

10.5.4 Sulphur Isotope Geo-thermometry of the Messina Copper Deposits

Determination of temperature of ore formation using sulphur isotope ratio is one of the advanced and recent method used in deciphering ore genesis. Its limitation is that the determined temperature relates to the last event of equilibration, which may or may not be the main stage of mineralisation, especially if the deposit is of hydrothermal metamorphism origin (Misra, 2000).

In the current study, the calculated temperatures from Campbell and Artonvilla pyrite-chalcopyrite revealed high temperature value of 476°C while temperature values deduced from chalcopyrite-bornite pair from Campbell registered temperature value of 359°C and temperature values from Artonvilla of 141°C to 359°C.

© University of Venda

The high temperatures obtained from pyrite-chalcopyrite pair are due to the fact that pyrite is the most sensitive sulphide geo-thermometer, and temperatures involving pyrite may show an appreciable high and wide range of temperature. This is due to common occurrence of several stages of pyrite crystallisation and that it is commonly within the outermost layer of mineralization (Misra, 2000; Li and Liu, 2006). Consequently, the temperature derived from pyrite were not reliable. The order of δ^{34}S enrichment of sulphides is generally pyrite > pyrrhotite > greenockite > sphalerite > chalcopyrite > cubanite > sulvanite > bornite > violarite > galena (Misra, 2000; Li and Liu, 2006). The temperatures derived from bornite in this study were considered because bornite is one of the sulphide minerals which is highly enriched with δ^{34}S. Consequently, the temperature of the Musina copper deposits revealed a range of 141°C – 359°C with average value of 250°C, which is consistent with stability of this mineral pair (Borton and Skinner, 1979). This temperature was also broadly consistent with hydrothermal imprint on the Musina copper deposits as derived from the study undertaken by Jacobsen *et al.* (1976) where replacement minerals were inferred to have been formed at temperatures of ~ 375°C.

Similar previously studied deposits such as Mines Gaspe´ in Quebec, Canada (Shelton and Rye, 1982; Yang and Bodma, 2004), the Ilkwang Mine breccia pipe deposit in the Republic of Korea (So and Shelton, 1993) and Mantos Blancos breccia copper deposit (Ramírez *et al*., 2006) recorded comparable temperatures of ore formation.

In summary, sulphur isotope geochemistry studies currently widely used in the deciphering genesis of mineral deposits, particularly in relation to sources of sulphur within sulphide mineralisation. However, in the Musina area few studies had been previously conducted (Sawkins and Rye, 1979) and McCarthy and Jacobsen (1976) and in these studies only narrow ranges δ^{34}S were used to determine the source of sulphur and that brought the controversial on the issue on the mechanism of ore formation. No previous studies had focused on the use of isotope geothermometry to determine the temperature of ore formation within the Messina deposits.

Consequently, this study was one of the few studies done within the study area with respect to sulphur isotope geothermomerty. The δ^{34}S values were used not only in terms of narrow δ^{34}S values but considered for a wide range of factors such as in the comparison with several previously similar studied deposits, comparison with the country rock's δ^{34}S value and the

© University of Venda

mantled derived $\delta^{34}S$ values, mechanism of ore formation and for the determination of the temperature of ore formation. Therefore, this study has contributed to new knowledge on the processes of ore mineralisation in the study area.

© University of Venda

CHAPTER 11

GENESIS OF MESSINA COPPER-SULPHIDE DEPOSITS

Preamble

This Chapter focuses on the genesis of the Messina Copper-sulphide deposits. It includes a review of the previous genetic hypotheses on the mode of ore mineralisation within the deposits and their interrogation, based on the current findings. The chapter presents also a genetic model that describes the source and nature of the mineralised solution of the Messina Cu-sulphide deposits.

11.1 Review of Previous Studies on Ore Genesis

The genesis of the Messina copper deposits is highly debatable as often the case with most ore deposits of the world. Ore genesis has always remained controversial due to the fact that the observed features and obtained analytical data often present conflicting results. In the case of Messina copper deposits, two opposing hypotheses have been proposed:

(a) Formation of copper deposits as a result of descending meteoric waters that resulted in the extraction of Cu and S from overlying Karoo basalt (Sawkins and Rye, 1979). According to these researchers, meteoric waters contained also dissolved salts, collected in playa lakes. These fluids migrated downwards along faults and were superheated by a hot body, but on their return towards the surface, they picked up ore elements from the country rock incorporating them into a hydrothermal solution that later formed breccia and disseminated orebodies. In support of their genetic model, they listed the following points::

- Low temperature of formation ranging from 150°C to 210°C;
- Strong variations in the salinity that ranged from 1% to 26% of hydrothermal fluids that are independent of $\delta^{18}O_{H2O}$ variations in the fluids;
- A relatively narrow range of negative sigma $\delta^{18}O_{H20}$ values for the quartz fluids that is indicative of largely un-exchanged meteoric fluids;

© University of Venda

University of Venda
Creating Future Leaders

- Intense alteration during mineralisation involving formation of albite, zoisite, epidote, sericite and chlorite;
- Presence of only limited alteration outside the ore bodies;
- Concentric sulphide zoning and paragenetic generations reflecting a time and/or a space increase in Cu/Fe and Fe/S ratios of the minerals;
- A narrow range of $\delta^{34}S$ values in chalcopyrite, bornite and chalcocite despite evidence for increasing f_{O2} in later fluids and concluded that this is as a result of formation of bornite and chalcocite from original chalcopyrite;
- Gas and fluid inclusion analyses compatible with a meteoric origin for hydrothermal fluids; and
- Occurrence of highly oxidized mineral assemblages in reduced granulite facies metamorphic host rocks.

Jacobsen and McCarthy (1980), however, opposed the points made by Sawkins and Rye (1979). For example, on low temperature of ore formation, they noted that Sawkins and Rye (1979) had used quartz and calcite in their fluid inclusion and isotope studies which according to them were late in the paragenetic sequence. Jacobsen and McCarthy (1976), noted that in the ore bodies at Messina, the early ore fluid reactions involved desilication, and only during the terminal stages of mineralisation did the fluids become silica saturated. Consequently, McCarthy and Jacobsen (1980) concluded that quartz was very late in the paragenetic sequence.

(b) Formation of copper deposits as a result of magmatic hydrothermal origin of the ores as a result of copper-bearing solutions that were derived from a deep-seated alkaline magma of the Karoo igneous suite and migrated upward along suitable structures and at suitable environments became trapped (Jacobsen and McCarthy 1976; McCarthy and Jacobsen 1976; Jacobsen *et al.,* 1976; Jacobsen 1974). They further noted that the reaction between fluid rich in sodium and aluminum and host granulites produced the ore deposits in these trapped structures.

© University of Venda

Jacobsen *et al.* (1976) noted that the Messina copper-sulphide deposits are hosted in three primary sulphide minerals, namely; chalcopyrite, bornite and chalcocite. Chalcopyrite tends to be found along the periphery of the ore bodies, while bornite and chalcocite occupy the central part followed by the bornite zone then bornite/chalcopyrite zone (Fig. 11.1).

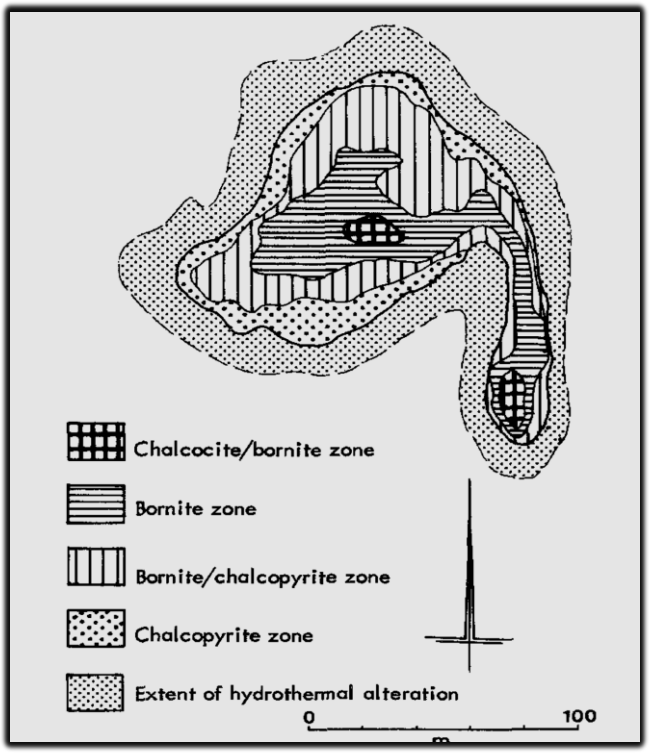


Figure 11.1: Distribution of sulphide mineralisation and hydrothermal alteration within the Messina copper sulphide deposits (Jacobsen *et al*., 1976).

As stated above, previous studies proposed two opposing hypotheses on the genesis of the Messina copper-sulphide deposits, hence the genesis of these deposits is still a subject of further research.

11.2 Findings of the Current Study

The current study looked at the factors and geological processes that are responsible for ore mineralisation in order to decipher the genesis of the Messina copper-sulphide deposits. These included; mode of occurrence, rock alteration and role of structures on ore formation, ore

© University of Venda

mineralisation and paragenesis, sulphur isotope geochemistry, cathodoluminescence and fluid inclusions.

Mode of occurrence: The Messina orebodies occurred as veined, disseminated, and brecciated ores with veined ore occurring in quartz veins mainly within amphibolite schist. Mineralisation in quartz veins occurred along micro-fractures, resulting in ore stockworks with quartz stringers. Fine to medium-grained disseminated ore consisted mainly of pyrite and chalcopyrite and rarely bornite, distributed within host rocks such as amphibolite and quartz veins. Coarse texture of brecciated ore with sulphide mineralisation surrounding quartz and amphibolite breccias, was identified at the Campbell and Artonvilla deposits. Formation of ore was accompanied with chloritization.

Epidote alteration and geological structures: Remote sensing data revealed the occurrence of geological structures and epidote alteration within the area. Spatial distribution and intensity of epidote alteration within the Limpopo Mobile Belt mainly coincided either with the known copper deposits or structural features such as faults and folds. The epidote alteration trend was oval in shape, striking in the same direction as the geological structures in the area, however, within the deposits the intensity of alteration was high at the centre, but dying outwards in a concentric manner. It is therefore deduced that geological structures in the area acted as conduits for hydrothermal fluids that resulted in the alteration of the host rocks and mineralisation of copper sulphide ore.

Occurrence of epidote alteration over the known ore deposits and geological structures, and also over other geological structures discovered through remote sensing, coupled with geochemical anomalies identified through geochemical survey led to the identification of target areas for future mineral exploration in the Musina area.

Ore mineralisation and paragenesis: The process of mineral formation in the Messina area took place in two distinct phases: Firstly, the formation of garnet, graphite, magnetite and hematite that are attributed to regional metamorphism in the area; and secondly, later sulphide ore mineralisation. Sulphide mineralisation within the Messina copper deposits represented complex ore mineralisation that is typical of hydrothermal mode of ore formation, for example, the main stage of sulphide mineralisation comprised pyrite, chalcopyrite, sphalerite with minor pyrrhotite and galena as well as traces of pentlandite, tennantite, molybdenite, cobaltite and tetrahedrite. The final stage of ore formation (Stage IV) comprising carbonates, namely; calcite, dolomite and ankerite, was typical of the final stage of hydrothermal ore mineralisation.

© University of Venda

University of Venda
Creating Future Leaders

In this current study, paragenetic sequence of minerals confirmed the occurrence of three generations of quartz; 1st generation being associated with garnet, graphite and iron oxides, 2nd generation of quartz associated with pyrite, and 3rd generation of quartz was associated with pyrite, sphalerite and chalcopyrite. Cathodoluminescence investigation also confirmed three generations of quartz within the ore, whereby early formed quartz (Q1) appeared as bright blue cathodoluminescence and was being replaced by later quartz (Q2) that displayed dark red Cathodoluminescence (Fig. 8.9). In Cathodoluminescence, latest quartz to form (Q3) appeared as concentric zonation with successive sub-idiomorphic stepped crystal zones, revealing different stages of crystal formation (Fig. 8.13 and 8.14). The notion held by Jacobsen and McCarthy (1976) that in the ore bodies at Messina, the early ore fluid reactions involved desilication, and only during the terminal stages of mineralisation did the fluids become silica saturated is not supported by these findings.

Ore mineralogy and ore-microscopy revealed replacement processes whereby pyrite was being replaced initially by chalcopyrite and later by bornite, chalcocite and covellite (Fig. 7.11B, C and D). In the secondary zone of sulphide enrichment, these minerals were replaced by azurite and malachite. In places, these minerals form pseudomorph of the original pyrite crystals. The study further confirmed the replacement of chalcopyrite by bornite and chalcocite.

The above findings were also supported by a narrow range of $\delta^{34}S$ values (-0.5 to 0.5‰) obtained in this study which is attributed to the formation of chalcopyrite from pyrite, and bornite from chalcopyrite, which was also confirmed by ore microscopy. This could also be attributed to the addition of Cu to pyrite to form chalcopyrite and addition of Cu and S to form bornite during which iron was oxidised from Fe^{+2} to Fe^{+3} as follows:

$FeS_2 + Cu \text{------} \rightarrow CuFeS_2$ Equation 11.1

$CuFeS_2 + 4Cu + 2S \text{----} \rightarrow Cu_5FeS_4$ Equation 11.2

The current study revealed replacement processes whereby chalcopyrite was gradually replaced by bornite, chalcocite and native copper. Similarly, Jacobsen *et al.* (1976) noted that these replacement processes occurred towards the centre of the orebodies (Fig. 11.1).

The paragenetic study identified four stages of mineral formation: Stage I-Garnet-Graphite-Fe oxides-Quartz (Q1); Stage II- Quartz (Q2)-Pyrite; Stage III- Quartz (Q3)-Pyrite-Sphalerite-Chalcopyrite; and Stage IV-Calcite-dolomite-ankerite. Garnet occurred in form of almandine in granulite rocks and was associated with potassium feldspars. Garnet developed mainly from

© University of Venda

University of Venda
Creating Future Leaders

biotite and muscovite during the granulite stage of regional metamorphism. In places, micro-fractures of highly fractured garnet grains are filled with quartz and pyrite (Fig. 7.5). This confirms that garnet formed before quartz. At Artonvilla copper deposit, graphite occurred as plates within amphibolite schist and in granulite rocks (Plate 7.5b). Graphite plates were cut by chlorite and later quartz with pyrite mineralisation.

Two types of magnetite were noted in the study area; earlier formed allotriomorphic magnetite and later formed euhedral octahedral magnetite crystals. Both types of magnetite were partially or totally replaced by hematite. Hematite was formed as thin plates during regional metamorphism in the area, although it also formed as a replacement product, having replaced magnetite and garnet.

Pyrite, sphalerite and chalcopyrite together with late formed quartz were deposited around garnet grains and in places, filling the micro-structures in garnet. Paragenetic sequence confirmed that pyrite was formed earlier among the sulphide minerals, hence was subjected to oxidation, resulting in the formation of later sulphide minerals, mainly chalcopyrite, bornite and chalcocite.

The occurrence of chalcopyrite inclusions in sphalerite is considered to be due to chalcopyrite disease as a result of replacement of Fe-rich sphalerite, although some researchers dispute this. For example, Bortinikov *et al.* (1991) concluded that chalcopyrite inclusions in sphalerite were produced by replacement as a result of interaction of sphalerite with solution that transported both Cu and Fe.

In the current study, the Fe-Cu-S system (Fig.7.18) indicated the immiscibility of both S and Fe, which led to the increase of Cu in sulphide minerals and thereafter settled out later leading to the fornmation of Messina copper deposits.

Fluid inclusion investigation: Fluid inclusion studies established that the entrapment temperatures of 1st generation quartz ranged from 315°C to 200°C; 2nd generation quartz from 235°C to 135°C; and 3rd generation quartz from 240°C to 115°C, however, sulphur isotope investigation of chalcopyrite-bornite pair from Campbell deposit registered temperature of 359°C and temperature values from Artonvilla deposit were between 359°C -141°C with average value of 250°C. These findings indicate that the low temperature that was determined by Sawkins and Rye (1979) represented later formed quartz. The assertion by McCarthy and Jacobsen (1980) that quartz could not have been formed in the earlier paragenetic sequence of

© University of Venda

University of Venda
Creating Future Leaders

ore formation is disputable as our findings revealed the occurrence of early formed quartz that was associated with regional metamorphism and mineralisation of garnet, graphite, magnetite and hematite.

The current study on salinity of fluid inclusions revealed a wide range of 0.2-27.6wt% NaCl, however as was previously noted by Sawkins and Rye (1979), fluid inclusions with daughter minerals such as halite and calcite had salinity ranging from 13.5wt% NaCl to 25.6wt% NaCl. In some of these inclusions small amounts of daughter salts (carbonates and anhydrite) may be precipitated during cooling (Roedder, 1972; Nash, 1976).

Raman Spectroscopy revealed the composition of gases in the fluid inclusions. The identified gases were CH_4 and N_2 with ~80% and ~20% composition respectively; however, some inclusions were gas-poor. According to Nash (1976), the simultaneous presence of gas-rich and gas-poor aqueous inclusions is good evidence that the fluids were boiling at the time of trapping. Wakita and Sano (1983) noted that the source of methane in fluid inclusion is likely to have come from the upper mantle magmatic activity.

In this study, the pressure and temperature estimation was done (Fig. 9.17) and it revealed that the earliest carbonic aqueous fluid inclusions in quartz from veined ore were formed from 2000 to 1400 bars from a hot solution between 315°C and 200°C. The fluid inclusions in quartz vein from disseminated ore and idiomorphic quartz veins from brecciated ore were formed at more or less similar pressure (1.5-0.8 kbar and 1.6 -0.65 kbars respectively) with temperature range of 135 - 235°C and 115 - 240°C respectively (Table 9.5).

Sulphur isotope investigation: Sulphur isotope investigation of the Campbell ore revealed $\delta^{34}S$ frequency values of -1.5 to 1.5‰ with highest frequency range of -0.5 to 0.5‰, whereas Artonvilla ore indicated $\delta^{34}S$ frequency values of 2.5 to 4.5‰ while the most frequent $\delta^{34}S$ frequency values falls within 3.5 to 4.5 ‰. This frequency range showed a similar trend with sulphur isotopic data from the previous study undertaken by Sawkins and Rye (1979) and also relate well with the data from Mantos Blancos that revealed a narrow range of $\delta^{34}S$ (-3.5 to 2.5‰), suggesting a magmatic source of sulphur (Ramirez *et al*., 2006). According to Ohmoto and Rye (1979) and Ohmoto and Goldhaber (1997), the mantle is characterised by a $\delta^{34}S$ narrow range of 0±5‰. The $\delta^{34}S$ from Campbell and Artonvilla sulphide mineralisation were found to be within the narrow $\delta^{34}S$ range of the mantle-derived Sulphur. On this basis, this study concluded that the Messina copper-sulphide mineralisation is of magmatic origin.

© University of Venda

Investigation of sulphur isotopes from the country rock from Artonvilla copper deposit yielded δ^{34}S value of 8.2‰ indicating the enrichment of heavy sulphur isotope within the country rock, while the Artonvilla copper deposit revealed average δ^{34}S value of ~ 4‰, resulting into a wide range between the country rock and the ore. This implies that ore mineralisation in the study area post-dated metamorphism (Chaumba *et al.*, 2016).

11.3 Genetic Model of Messina Copper-Sulphide Deposits

The genesis of ore deposits is sometimes complex such that researchers tend to attribute the origin of the source material to be associated with the depositional environment. Copper can form under diverse environmental conditions ranging from magmatic representing Copper-Nickel (PGEs) deposits, Porphyry Copper deposits associated with igneous intrusions, Volcanogenic Massive Sulphide Deposits, Skarn Copper Deposits, and Carbonatite Copper Deposits to Sediment-hosted Copper Deposits and Copper-sulphide Mineralisation within Metamorphic Terrain. In the case of Copper-sulphide mineralisation within metamorphic terrain, the occurrence of copper deposit may not necessarily be due to metamorphism. The Messina Copper deposits are typical examples of deposits found within the metamorphic terrain that are not necessarily genetically linked to regional metamorphism of the area. Tourtelot and Vine (1976) noted that Copper can form:

- As spongy masses of native copper in a peat bog as is the case of the Beartooth Mountains near Cooke City, Montana, where it occurs in thin beds of black muck;
- A pond that is coloured blue by the large amount of copper coming from spring waters feeding the pond, which are also blue, contain as much as 38 ppm copper and other metals, which are attributed to leaching of older copper deposits or copper-rich sedimentary rocks; and
- Copper-rich brines that involve varying proportions of meteoric, connate, metamorphic, and magmatic waters and are enriched in metals as is the case along the East Pacific Rise (Corliss *et al.*,1972).

Most copper deposits, however, are associated with magmatic segregation and fluids that may either result into copper deposition within ultramafic and mafic rocks or magmatic fluids on ascent culminate into hydrothermal fluids, resulting into either volcanogenic massive sulphide

© University of Venda

deposits on or below the seafloor or porphyry copper deposits and sediment-hosted copper deposits. In more or less every case, magmatic fluids appear to have played a role as the source material. Examples of these types of deposits include (Smirnov, 1976; John, 2010; Shanks III and Koski, 2010; Colin-Garcia, 2016; Misra, 2000; Bell, 1994; Cox *et al.*, 2007):

- Copper-Nickel deposits of Norilsky, Mocha_Tundra and Pachenga, Sudbury, Lynn Lake, Mystery Lake, Alaska and Stillwater, and the Bushveld Complex;
- Porphyry Copper Deposits, a typical example being the Chuquicamata porphyry copper deposit;
- Volcanogenic Massive Sulphide Deposits associated with deposits of Copper, Zinc, Lead, Gold, and Silver;
- Skarn Copper Deposits associated with granitic intrusive in contact with carbonate rocks; and
- Sediment-hosted Copper Deposits where the Zambian-Katanga Sediment-hosted Stratiform Copper Mineralisation is a classic example.

A mineral deposit model is the systematically arranged information describing the essential attributes of a class of mineral deposits. The model may be: empirical (descriptive), in which instance the various attributes are recognized as essential even though their relationships are unknown; and theoretical (genetic), in which case the attributes are interrelated through some fundamental concept.

Genetic model requires that: a) it must be open so that new types of deposits can be added in the future; and b) the user must be able to find easily the appropriate models to apply to the rock and tectonic environments being investigated (Cox *et al.*, 2007). The first thing to consider when trying to identify the genetic model of a deposit is its mode of formation, for example, whether the deposit is of syngenetic or epigenetic origin. The genetic concepts are used to distinguish the critical from the incidental attributes, hence models are constructed so as to be independent of site-specific attributes and therefore contain only those features which are transferable from one deposit to another.

The critical attributes bring to the fore, the genetic link with the host rock, for example, contemporaneous formation of the host rock and ore mineralisation as there is direct link

© University of Venda

University of Venda
Creating Future Leaders

between the lithotectonic environment of the formation of the host rock and the lithotectonic environment of the mineralisation process (Cox *et al.*, 1986). For igneous mode of ore formation, the genetic models fall under either geological-tectonic environment or intrusive and extrusive environment. Under intrusive are mafic-ultramafic, alkaline and basic, and felsic, whereas under extrusive are mafic, and felsic-mafic (Cox *et al.*, 1986).

The Messina copper-sulphide deposits were of epigenetic in nature. The copper orebodies were localized along the fault planes and within the alteration zones of metamorphic rocks, namely; amphibolite schists and granitic gneisses. Consequently, the role of geological structures on the formation of the ore deposits were of paramount importance. According to Brandl (1981), faulting in the Musina area was post-Karroo (<145 Ma) and was associated with dolerite, syenite, ejiolite and granitic intrusives. This took place after the area had been subjected to regional metamorphism (2650-2000 Ma), resulting in the formation of the Limpopo Mobile Belt that was accompanied with the tilting and folding of the rocks (Kramers *et al.*, 2006; Brandl, 1981).

Faulting, however, was of pre-ore mineralisation in the area, but the faults acted as conduits for hydrothermal fluids for copper-sulphide mineralisation that finally resulted in the localization of copper sulphide ore bodies along the Messina fault, and also at the intersection of the Messina and Dowe-Tokwe faults. The ore occurred as veins, disseminated and brecciated orebodies. Veined ore occurred in quartz veins within amphibolite schist. In places, ore mineralization took place along microfractures in quartz grains, resulting in stockworks.

The source of fluids for ore formation was of magmatic origin, although the actual deposition of copper occurred from hydrothermal fluids. This position is supported by the arguments raised above under Ore Mineralogy and Ore-microscopy, Remote Sensing, Cathodoluminescence, Fluid Inclusion Geothermometry, and Sulphur Isotope study as well as structural control on ore mineralisation. Disseminated ore also occurred within quartz vein. Disseminated ore was in form of tiny grains of anhedral chalcopyrite replacing pyrite and in some places, chalcopyrite was replaced by bornite (Fig. 7.3 A and B). Brecciated ore comprised mainly pyrite and chalcopyrite. These minerals were deposited within brecciated quartz grains and infilling the microstructures between the breccias. This indicates that the mineralised hydrothermal solution followed the weak zones as their conduit, upon which the ore minerals were deposited.

© University of Venda

The Messina copper deposits are of polymetallic vein type. According to John *et al.* (2010), polymetallic vein type deposits are genetically associated with porphyry copper deposits. These are copper orebodies formed from hydrothermal fluids originating from magma. Messina copper deposits possess some of the generic characteristics possessed by porphyry copper deposits, such as ore types being veined, disseminated and brecciated.

Söhnge (1945) had stipulated that the nearest large intrusion, apparently associated with the ore in the Musina area is a batholith of augite granophyre, about 113 km east of Messina. But previous studies of copper-sulphide ore mineralisation associated with granitic batholiths within the greenstone complexes had, however, established that ore localization usually takes place within the greenstone rocks roughly 5-10 km away from the batholith contact (Ogola, 1985). Consequently, it is unlikely for a batholith which occurs about 113 km east of Messina to have been the source of mineralized solution for the Messina deposits as stated by Söhnge (1945). Jacobsen and McCarthy (1976), proposed that hydrothermal solutions came from a deep-seated alkaline magma of the Karoo igneous suite. The mineralized solution, apparently originated from a batholith at the time of its crystallization (Fig. 11.2), although the apparent location of the batholith is still unknown.

The localization of the ore was influenced by the Messina fault that acted as the conduit for mineralized solution transportation as well as the Messina-Dowe Tokwe faults intersection at Campbell and the pre-and post-Karroo dyke intrusions. The final deposition of the orebody, however, occurred along the minor fractures or at the intersection of the two faults. The role of the dykes in ore mineralisation was equally important as observed at the Campbell and Harper deposits. For instance, the Messina sulphide mineralized dyke trends to the N40^{o}E and N60^{o}E (Söhnge, 1945). The dykes seem to have followed the structures within the granitic gneisses, although some are not associated with fault or breccia zones. Söhnge (1945) noted that the Messina dyke occupying the complex strike-slip fault branching out from the Dowe-Tokwe fault near Campbell deposit is prominent underground and it continues from Harper deposit northeastwards to the western border of Antonvilla deposit. At the same time, minor dolerite dykes running nearly parallel to the Messina fault are found in Antonvilla deposit.

At the Harper deposit, the dyke cuts through the Messina fault zone without any displacement, whereas at the Campbell deposit, the dyke is displaced by the Messina fault (Söhnge, 1945). This indicates that the dykes cutting the Messina fault zone over the Campbell deposit were intruded earlier, apparently being pre-Karroo in age, whereas those over the Harper deposit

© University of Venda

University of Venda
Creating Future Leaders

were post-Karroo in age. At the same time, the occurrence of copper ore mineralisation at the intersections of the Messina fault zone and the dykes is an indication that both the fault and the dykes pre-determined the location of copper ore within the Musina area. Apparently, both the pre-Karroo and post-Karroo dykes had structural control on copper-sulphide mineralisation in the area.

The ingression of hydrothermal fluids was influenced by the fractured and brecciated zones, apparently due to faulting. Söhnge (1945) noted that Campbell deposit lies within the Messina fault zone, about 1.6 km of its junction with the Dowe-Tokwe fault. He further observed that at the intersection of these two fault systems, the mineralized area is strongly fractured by a number of branching shears. Apparently, the localization of the Campbell ore bodies was influenced by the intersection of the two fault zones, the Messina fault and the Dowe-Tokwe faults. This is an area that was subjected to maximum fracturing, thus created an enabling environment for the ingress of the mineralized solution and the actual deposition of the ore.

Similar observations had been noted elsewhere, for example, Ogola (1988) while conducting a study of the Macalder copper deposit in the Migori gold belt in Kenya noted that the Macalder deposit was situated over an area marking the intersection of different faults. Söhnge (1945) also noted that ore precipitation in the Musina area took place along minor fractures parallel to either foliation or along the Messina fissure system.

© University of Venda

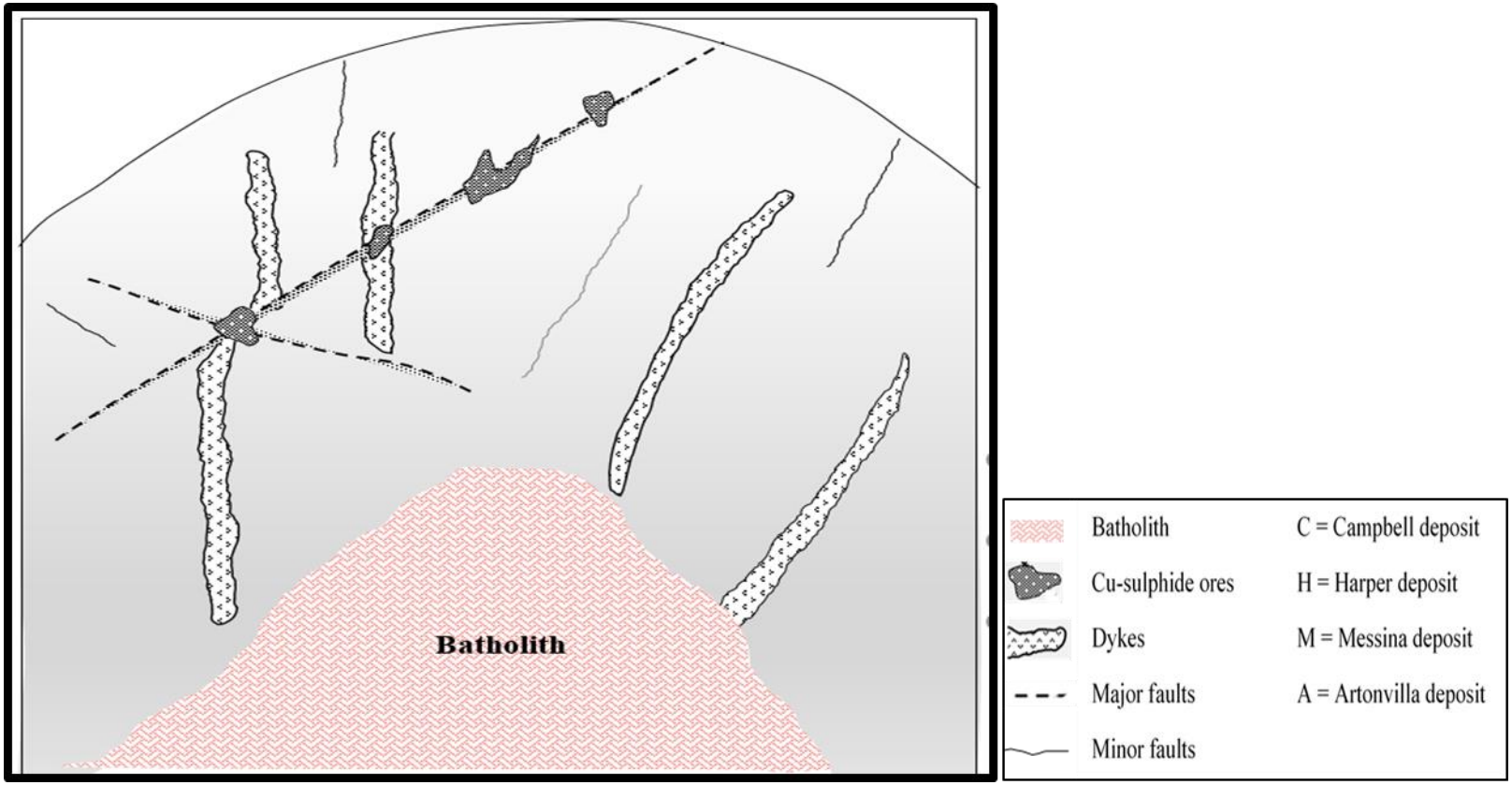


Figure 11.2: Genetic model of copper-sulphide mineralisation in the Musina area. Mineral deposits occurred either along the fault planes or at the interaction of faults and dykes with rock alteration along the weak zones.

© University of Venda

CHAPTER 12

CONCLUSIONS AND FUTURE RESEARCH DIRECTIONS

Preamble

The chapter focuses on the main findings of the study. From the conclusions, gaps were identified and recommendations made for further studies so as to answer some of the questions that emanated from the study.

12.1 Conclusions

Petrographic studies from the Messina copper deposits confirmed the host rocks to be amphibolite-quartz granulite, biotite-garnet-quartz granulite, amphibolite, quartzite, hornblende schist, biotite schist, hornblend gneiss, quatrzo-feldspathic gneiss, potassium-feldspathic gneiss and calc-silicate gneiss. These rocks were subjected to hydrothermal alteration during ore mineralisation within the area. It was further noted that epidote as an alteration product was much intensive in ore samples while un-mineralized rock samples had less occurrence of epidote.

Remote sensing data revealed the occurrence of geological structures such as faults and folds, and epidote alteration within the study area. Spatial distribution and intensity of epidote alteration within the study area mainly coincided either with the known copper deposits or structural features such as faults and folds. The epidote alteration trend was oval in shape, striking in the same direction as the geological structures in the area, however, within the deposits the intensity of alteration was high at the centre, but dying outwards in a concentric manner. It is therefore deduced that geological structures in the area acted as conduits for hydrothermal fluids that resulted in the alteration of the host rocks and mineralisation of copper sulphide ore. Spatial distribution and intensity of epidote alteration within the study area also led to the identification of exploration areas for future mineral exploration in the Musina area.

Geochemical survey revealed anomalous areas of Pb, Zn, Cu, As and Ni over the known copper deposits at Campbell, Harper, Messina and Artonvilla as well as over six other areas

© University of Venda

that have not been associated with any sulphide mineralization. Such new anomalous areas have been identified as target areas for future exploration of sulphide ore mineralisation.

Messina Copper deposits were of magmatic-hydrothermal origin and were epigenetic in nature. The orebodies were localized along the fault planes and within the altered metamorphic rocks, mainly amphibolite schists and granitic gneisses. Sulphide mineralisation was composed mainly of pyrite, chalcopyrite and sphalerite with bornite, chalcocite and minor cobaltite, tennantite, molybdenite, bournonite and boulangerite.

The process of mineral formation in the Messina copper deposits took place in two distinct phases: Firstly, the formation of minerals such as garnet, graphite, and magnetite and hematite that are attributed to regional metamorphism in the area; and secondly, later sulphide mineralisation which represented complex ore mineralisation that is typical of hydrothermal mode of ore formation. The main stage of sulphide mineralisation comprised pyrite, chalcopyrite, sphalerite with minor pyrrhotite and galena as well as traces of pentlandite, tennantite, molybdenite, cobaltite, tetrahedrite, bournonite and boulangerite.

Chalcopyrite was formed as a product of pyrite replacement whereby later hydrothermal solutions rich in copper resulted in the oxidation of pyrite to form chalcopyrite and further addition of copper and sulphur resulted in the formation of bornite during which iron was oxidized from Fe^{+2} to Fe^{+3}. Chalcopyrite was later gradually replaced by bornite, chalcocite and native copper.

The Messina ore bodies occurred as veined, disseminated, and brecciated ores with veined ore occurring in quartz veins mainly within amphibolite schist. Mineralisation in the quartz veins occurred along micro-fractures, resulting in ore stockworks with quartz stringers.

Ore mineralogy and ore-microscopy identified four stages of mineralisation, namely: Stage I (Garnet- graphite – Fe oxides); stage II (Quartz- pyrite); stage III (Pyrite- sphalerite - chalcopyrite); and stage IV (Carbonates). Stage III was the dominant stage for sulphide ore mineralisation, while stage IV comprising calcite, dolomite and ankerite marked the last stage of sulphide ore mineralisation.

Paragenetic sequence of minerals confirmed the occurrence of three generations of quartz; 1st generation being associated with garnet, graphite and iron oxides, 2nd generation of quartz

© University of Venda

associated with pyrite, and 3rd generation of quartz was associated with pyrite, sphalerite and chalcopyrite. Cathodoluminescence investigation also confirmed three generations of quartz within the ore, whereby early formed quartz (Qtz1) appeared as bright blue Cathodoluminescence and was being replaced by later quartz (Qtz2) that displayed dark red Cathodoluminescence while quartz 3 formed zonation intergrowth of two types namely, oscillation and concentric zonation.

Three generations of quartz had entrapment temperatures of 1st generation ranging from 200°C to 315°C; 2nd generation from 135°C to 235°C and 3rd generation from 115°C to 240°C. Sulphur isotope investigation of chalcopyrite-bornite pair also indicated a temperature of 359°C. The study therefore confirmed that the temperature of ore formation within the Messina copper deposits ranged between 359°C and 115°C. The pressure of ore formation was found to be from 2000 to 1400 bars.

Halite and calcite were identified as the dominant daughter minerals in the fluid inclusions that is responsible for high salinity of fluid inclusions. The presence of daughter minerals in the fluid inclusion is indicative of direct ex-solution of crystalizing magma.

Methane and Nitrogen gases were found to be the dominant gases within fluid inclusions with the composition of 80% and 20% respectively. The presence of gases in the fluid inclusions is an indication that there was boiling at the time of entrapment.

A genetic model for the formation of copper ores within the Messina deposits was proposed. Messina copper deposits are of polymetallic vein type that are genetically associated with porphyry copper deposits. The genetic model considers this type of ore formation to have been from hydrothermal fluids originating from a magmatic source. The mineralized solution, apparently originated from a batholith at the time of its crystallization, although the apparent location of the batholith is still unknown. The copper orebodies were localized along the fault planes and within the alteration zones of metamorphic rocks. Faulting, however, was of pre-ore mineralisation in the area, but the faults acted as conduits for hydrothermal fluids for copper-sulphide mineralisation that finally resulted in the localization of copper sulphide ore bodies along the Messina fault, and also at the intersection of the Messina and Dowe-Tokwe faults.

© University of Venda

Based on geological investigation, remote sensing study, ore mineralogy and ore-microscopy, petrology, cathodoluminescence, fluid inclusion, and isotope investigation, the study therefore concluded that the Messina copper deposits were of magmatic hydrothermal origin.

12.2 Future Research Directions

- The potential for sulphide ore mineralisation in the Musina area and it's environs is quite high, thus there is need to continue with further exploration in the region, based on the following:
    - Areas that have undergone "moderate" to "high" degree of epidote alteration and lie in close proximity to geological structures such as thrust folds that could have acted as conduits for hydrothermal fluids and resulted in sulphide ore mineralisation should be targeted; and
    - Anomalous concentration areas comprising Pb, Zn, As, and Ni as possible targets for sulphide ore mineralisation.
- Further research work should focus on the discovery of location of the batholith that is presumed to have been the magmatic source of sulphide ore mineralisation of the Messina copper deposits.
- Dating of later intrusive rocks as well as orebody is essential for understanding the processes of ore formation in this area.
- Detailed geostatistical analysis for delineation of homogeneous sub-areas based on the investigation of lineaments, combination of interpolated soil geochemical data and thematic maps such as soil and topographic maps.

© University of Venda

APPENDICES

© University of Venda

Appendix 3AI: Sample location and characteristics of soil in the western direction of the study area (Campbell)

Sample No	Sample ID	Latitude	Longitude	Elevation (m)	Vegetation	Colour	Texture	Type of soil	Comment
1	D1T1S1	22˚20'46.0"	29˚59'36.9"	575	MO, G	Grey	Med-Co	Loamy soil	Presence of calcrete,
2	D1T1S2	22˚20'57.9"	29˚59'42.3"	570	MO, G, TH	Brown	Med-Co	Loamy soil	
3	D1T1S3	22˚21'15.5"	29˚59'56.0"	555	MO, TH	Red	Fine	Loamy soil	
4	D1T1S4	22°21'30.0"	29°59'55.0"	564	MO, TH	Red	Med-Co	Loamy soil	
5	D1T1S5	22˚21'45.0"	29˚59'55.0"	571	MO, G, TH	Brown	Med-Co	Loamy soil	
6	D1T1S6	22˚22'00.0"	29˚59'00.0"	569	MO, TH	Brown	Med-Co	Loamy soil	
7	D1T1S7	22˚22'15.1"	29˚59'55.2"	572	MO, G, TH, BA	Brown	Med-Co	Loamy soil	
8	D1T1S8	22˚22'34.5"	29˚59'55.2"	574	MO, G, TH, BA	Brown	Med-Co	Loamy soil	
9	D1T1S9	22˚22'50.4"	29˚59'55.3"	567	MO,G, BA, MA	Brown	Med-Co	Loamy soil	
10	D1T1S10	22˚23'07.2	29˚59'55.2"	571	MO, G,BA, MA	Red	Med-Co	Loamy soil	
11	D1T1T11	22°23'27.3"	29°59'55.2"	573	MO,G, BA, MA	Brown	Med-Co	Loamy soil	
12	D1T1T12	22°23'51.0"	29°59'55.3"	572	MO, G,BA, MA	Red	Med-Co	Loamy soil	
13	D2T2S2	22˚21'06.0"	29˚59'19.8"	574	MO, G	Grey	Med-Co	Loamy soil	
14	D2T2S4	22˚21'40.8"	29˚59'19.8"	574	MO, G, TH, MA	Red	Med-Co	Loamy soil	
15	D2T2S6	22°21'57.6"	29˚59'19.8"	580	Vegetables	Red	Fi-Med	Loamy soil	
16	D2T2S7	22˚22'36.6"	29˚59'19.8"	568	MO, G, MA	Red	Med-Co	Loamy soil	Collected 15m away from railway line on the northern side of it
17	D2T2S8	22˚22'49.2"	29˚59'19.8"	580	MO,G, BA, MA	Red	Med-Co	Loamy soil	
18	D2T2S9	22˚23'06.0"	29˚59'19.8"	584	MO,G, BA, MA	Red	Med-Co	Loamy soil	
19	D2T3S1	22°23'14.9"	29°59'01.2"	576	MO, G, TH	Brown	Med-Co	Loamy soil	Collected next to the stream
20	D2T3S2	22°23'06.0"	29°59'01.2"	587	MO, G, TH, BA	Red	Coarse	Sandy soil	
21	D2T3S3	22°22'49.2"	29°59'01.2"	589	MO, G, TH	Red	Fi-Med	Loamy soil	Collected next to gravel road

© University of Venda

Appendix 3AI: Continued…….

22	D2T3S4	22°22'36.6''	29°59'01.2''	598	MO, G, TH	White	Coarse	Sandy soil	collected at the bank of mine dumps of Campbell Copper mine
23	D2T3S5	22°22'14.4''	29°59'01.2''	590	MO, G, TH	Brown	Med-Co	Loamy soil	
24	D3T3S3	22°21'30.3''	29°59'01.2	588	Mo, G, TH	Red	Med-Co	Loamy soil	
25	D3T3S6	22°21'57.6''	29°59'01.2''	580	MO, G, TH	Red	Fi-Med	Clay soil	
26	D3T3S7	22°21'40.8''	29°59'01.2''	577	MO, G, TH, MA	Red	Coarse	Sandy soil	
27	D3T3S8	22°21'24.0''	29°59'01.2''	578	MO, G, TH	Brown	Med-Co	Loamy soil	
28	D3T3S9	22°21'06.0''	29°59'01.2''	580	MO, G, TH	Brown	Med-Co	Loamy soil	
29	D3T3S10	22°20'54.0''	29°59'01.2''	579	G, TH	Red	Coarse	Sandy soil	Collected on the northern side of the tar road
30	D3T4S1	22°20'58.6''	29°58'45.6''	588	MO, G, TH	Brown	Med-Co	Loamy soil	
31	D3T4S2	22°21'06.0''	29°58'45.6''	586	MO, G, TH	Grey	Med-Co	Loamy soil	
32	D3T4S4	22°22'38.6''	29°58'45.6''	597	MO, G, TH, BA	Red	Med-Co	Loamy soil	
33	D3T4S6	22°22'14.4''	29°58'45.6''	595	MO, G, TH	Red	Coarse	Sandy soil	
34	D3T4S8	22°22'49.2''	29°58'45.6''	588	MO, G,TH	Red	Med-Co	Loamy soil	
35	D3T4S9	22°23'06.6''	29°58'45.6''	576	MO, G, TH, BA	Brown	Med-Co	Loamy soil	
36	D3T5S3	22°22'33.6''	29°58'28.8''	604	MO, G, TH, BA	Red	Coarse	Sandy soil	
37	D3T5S5	22°21'57.6''	29°58'28.8''	597	MO, G,TH	Red	Coarse	Sandy soil	
38	D3T5S7	22°21'24.0''	29°58'28.8''	584	MO, G, TH,MA	Brown	Med-Co	Loamy soil	
39	D3T5S8	22°21'06.6''	29°58'28.8''	581	MO, G,TH	Brown	Med-Co	Loamy soil	
40	D3T5S9	22°21'01.3''	29°58'28.8''	590	G, TH	Red	Med-Co	Loamy soil	Collected few meters from the road next to the Munati farm
41	D6S1FA	22°23'56.6''	29°57'28.1''	580	MO, G,TH	Red	Coarse	Sandy soil	
42	D6S2FA	22°24'03.3''	29°57'12.3''	578	MO, G,TH	Brown	Med-Co	Loamy soil	
43	D6S3FA	22°24'07.3''	29°57'00.1''	582	MO, G, TH, BA	Brown	Coarse	Sandy soil	
44	D6S4FA	22°24'20.9''	29°57'09.6	580	MO, G,TH	Red	Coarse	Sandy soil	
45	D6S6FA	22°24'10.4''	29°57'36.4''	582	MO, G,TH	Brown	Coarse	Sandy soil	

© University of Venda

Appendix 3AI: Continued…….

46	D6SC/B1	22°23'55.6"	29°56'51.2"	601	MO, G, TH,MA	Red	Coarse	Sandy soil
47	D6SC/B2	22°23'49.1"	29°57'07.3	576	Pumpkins	Red	Coarse	Sandy soil
48	D6SC/B3	22°23'42.1"	29°57'20.2"	578	MO, G, TH,MA	Red	Coarse	Sandy soil
49	D6S1FD	22°23'18.8"	29°57'06.6"	599	MO, G,TH	Brown	Med-Co	Loamy soil
50	D6S2FD	22°23'25.0"	29°56'50.0"	595	MO, G, TH,MA	Red	Coarse	Sandy soil
51	D6S4FD	22°23'31.5"	29°56'33.1"	591	MO, G,TH	Brown	Med-Co	Loamy soil
52	D7S2FE	22°23'13.7"	29°57'25.5"	591	MO, G,TH	Grey	Coarse	Sandy soil
53	D7S1FF	22°23'14.8"	29°57'37.3"	598	MO, G, TH, BA	Red	Coarse	Sandy soil
54	D7S2FF	22°23'07.9"	29°57'34.1"	597	MO, G, TH, BA	Red	Coarse	Sandy soil
55	D7S3FF	22°23'25.9"	29°57'32.4"	593	MO, G, TH, BA	Red	Coarse	Sandy soil
56	D7S4FF	22°23'29.3"	29°57'44.1"	590	MO, G, TH, BA	Brown	Coarse	Sandy soil
57	D7S1FG	22°23'25.4"	29°57'52.4"	598	MO, G, TH,MA	Brown	Coarse	Sandy soil
58	D7S2FG	22°23'10.5"	29°57'46.4"	611	MO, G, TH,MA	Red	Coarse	Sandy soil
59	D7S3FG	22°23'04.4"	29°57'43.8"	614	MO, G, TH,MA	Red	Coarse	Sandy soil
60	D7S2FH	22°23'24.0"	29°58'03.5"	604	MO, G, TH,MA	Red	Coarse	Sandy soil
61	D7S3FH	22°23'07.7"	29°58'03.3"	624	MO, G, TH,MA	Red	Coarse	Sandy soil
62	D7S4FH	22°22'56.3"	29°58'03.3"	618	MO, G, TH,MA	Red	Coarse	Sandy soil
63	D7S2FI	22°23'44.2"	29°58'39.1"	572	MO, G, TH,MA	White	Coarse	Sandy soil
64	D8S1FI	22°23'44.2"	29°58'21.5"	579	MO, G, TH,MA	Brown	Coarse	Sandy soil
65	D8S3FI	22°23'59.4"	29°58'15.6"	599	MO, G, TH,MA	Red	Coarse	Sandy soil
66	D8S4FI	22°24'15.3"	29°58'19.4"	580	MO, G, TH,MA	Grey	Coarse	Sandy soil
67	D8S5FI	22°23'28.3"	29°58'07.9"	596	MO, G, TH,MA	Red	Coarse	Sandy soil
68	D8S6FI	22°23'21.1"	29°58'24.3"	593	MO, G, TH,MA	Brown	Coarse	Sandy soil
69	D8S7FI	22°23'15.4"	29°58'40.1"	580	MO, G, TH,MA	Red	Coarse	Sandy soil
70	D8S2FJ	22°23'59.7"	29°57'43.0"	579	MO, G,TH	Grey	Coarse	Sandy soil
71	D8S4FJ	22°23'47.5"	29°57'42.6"	588	MO, G,TH	Grey	Coarse	Sandy soil
72	D8S2FI	22°23'51.3"	29°58'20.5"	583	Mo, G, TH	Red	Coarse	Sandy soil
73	D9S1FM	22°24'27.6"	29°58'15.2"	567	MO, G,TH	Brown	Med-Co	Loamy soil
74	D13S4FM2	22°21'25.2"	30°00'17.6"	562	MO, G,TH	Red	Coarse	Sandy soil

© University of Venda

Appendix 3AI: Continued…….

75	D13S5FM2	22°21'41.3"	30°00'22.5"	556	MO, G,TH	Red	Coarse	Sandy soil	
76	D14S3FM3	22°21'04.5"	30°00'39.2"	556	MO, G,TH	Brown	Coarse	Sandy soil	
77	D14S5FM3	22°21'36.7"	30°00'39.0"	551	MO, G,TH	Red	Coarse	Sandy soil	
78	D14S6FM3	22°21'52.8"	30°00'39.4"	559	MO, G,TH	Brown	Coarse	Sandy soil	Collected on resided area next to Apollo lights
79	D14S2FM4	22°20'26.4"	30°00'53.2"	552	NONE	Red	Coarse	Sandy soil	Collected next to the sealed shaft of Harper mine
80	D14S4FM4	22°21'02.4"	30°00'52.2"	572	MO, G,TH	Brown	Coarse	Sandy soil	Collected at western part of municipality waste dump site
81	D14S5FM4	22°21'18.5"	30°00'52.2"	558	MO, G,TH	Brown	Coarse	Sandy soil	Collected 8m away from the railway line
82	D14S6FM4	22°21'36.1"	30°00'59.3"	548	MO, G,TH	Brown	Coarse	Sandy soil	
83	D14S7FM4	22°21'56.0"	30°00'58.3"	554	MO, G,TH	Brown	Coarse	Sandy soil	Collected 15m from Green Shade church
84	D14S1FM4	22°20'06.2"	30°00'52.2"	551	MO, G,TH	Red	Coarse	Sandy soil	Collected next to the road and board written "food shop"
85	D15S1FM5	22°19'56.7"	30°01'05.3"	551	MO, G, TH,MA	Brown	Coarse	Sandy soil	Collected next to the hillside, dumping side
86	D15S2FM5	22°20'12.8"	30°01'18.3"	545	MO,G,TH, MA, BA	Red	Coarse	Sandy soil	
87	D15S3FM5	22°20'28.9"	30°01'23.6"	573	MO,G,TH, MA, BA	Red	Coarse	Sandy soil	Collected 60m away from Hamper mine
88	D15S5FM5	22°21'01.1"	30°01'33.1"	562	MO,G,TH, MA, BA	Red	Coarse	Sandy soil	Collected 200m towards N1
89	D15S1FM6	22°19'42.6"	30°01'15.1"	549	MO, G,TH	Brown	Coarse	Sandy soil	Collected next to soccer field at Extension 2
90	D15S2FM6	22°19'58.7"	30°01'20.9"	538	MO, G,TH	Brown	Coarse	Sandy soil	Collected at Extension 8 (Venetia mine settlement)
91	D15S5FM6	22°20'39.6"	30°01'49.9"	566	MO, G, TH, MA	Red	Coarse	Sandy soil	

© University of Venda

Appendix 3AI: Continued…….

92	D16S1FM7	22°19'25.3"	30°01'32.7"	529	MO, G, TH, MA, BA	Brown	Coarse	Sandy soil	
93	D16S2FM7	22°19'11.2"	30°01'29.5"	522	MO, G,TH	Brown	Coarse	Sandy soil	Collected 5m away from railway line
94	D16S3FM7	22°18'55.1"	30°01'24.1"	516	MO, G,TH	Brown	Coarse	Sandy soil	Collected 10m from N1 road and 20m to the traffic police station
95	D16S1FM8	22°19°'30.0"	30°01'50.3"	533	MO, G,TH	Brown	Coarse	Sandy soil	Collected at northern part of the tiling dump
96	D16S5FM8	22°19'48.7"	30°02'38.0"	527	MO, G, TH, BA	Grey	Coarse	Sandy soil	Collected within the settlement
97	D17S8FM8	22°20'19.6"	30°00'48.3"	548	G, TH	Brown	Coarse	Sandy soil	Collected 10m from Baobab trees near N1 road
98	D17S9FM8	22°19'43.3"	30°02'04.7"	534	G, TH, BA	Brown	Coarse	Sandy soil	Collected 150m away from Shoprite store
99	D17S10FM8	22°20'32.0"	30°02'22.9"	547	G, TH, MA	Brown	Coarse	Sandy soil	Collected 80m away from rugby ground
100	D17S11FM8	22°20'48.5"	30°02'06.9"	553	MO, G, TH	Grey	Coarse	Sandy soil	Collected 10m away from rugby ground
101	D17S12FM8	22°21'11.9"	30°01'56.0"	548	TH, MA, BA	Brown	Coarse	Sandy soil	Collected 35m from Shell garage
102	D17S13FM8	22°21'23.4"	30°02'04.1"	541	MO, G, MA, BA	Brown	Coarse	Sandy soil	

MA *– Marula trees/shrubs,* ***MO*** *– Mopani trees/shrubs,* ***GR*** *– Grass,* ***TH*** *- Thorny shrubs -,* ***BA*** *– Baobab tree,* ***Med-Co*** *– Medium coarse*

© University of Venda

Appendix 3AII: Sample location and characteristics of soil in the eastern direction of the study area (Artonvilla)

Sample No.	Sample ID	Latitude	Longitude	Elevation (m)	Vegetation	Colour	Texture	Type of soil	Comment
1	SS 1.1	-22.386	30.1045	455	GR, MO, TH	Brown		Loamy soil	
2	SS 1.2	-22.3821	30.10442	443	GR, MO, TH	Red		Loamy soil	
3	SS 1.3	-22.378	30.10422	455	GR, MO, TH	Red		Loamy soil	
4	SS 1.4	-22.3738	30.10447	425	GR, MO, TH	Red		Loamy soil	
5	SS 1.7	-22.3488	30.10447	451	MO, TH	Red Brown		Loamy soil	
6	SS 1.8	-22.3446	30.10467	466	GR, TH	Red Brown		Loamy soil	
7	SS 1.9	-22.3404	30.10447	436	GR, MO	Brown		Loamy soil	
8	SS 1.10	-22.3362	30.10422	477	MO, TH	Red Brown		Loamy soil	
9	SS 1.11	-22.3321	30.10442	465	MO, TH	Red Brown		Loamy soil	
10	SS 1.12	-22.3278	30.10414	465	GR, MO, TH	Red Brown		Loamy soil	
11	SS 1.13	-22.324	30.10417	442	GR, MO, TH	Red Brown		Loamy soil	
12	SS 1.14	-22.3196	30.10389	432	MO, TH	Red		Loamy soil	
13	SS 1.15	-22.3154	30.38633	422	MO, TH	Red		Loamy soil	
14	SS 2.1	-22.3863	30.10028	455	GR, MO, TH	Brown		Loamy soil	
15	SS 2.2	-22.3822	30.10028	479	GR, MO, TH	Brown		Loamy soil	
16	SS 2.3	-22.3779	30.1	469	GR, MO, TH	Brown		Loamy soil	
17	SS 2.4	-22.3736	30.1	486	MO, TH	Brown		Loamy soil	
18	SS 2.5	-22.3614	30.1	460	GR, TH	Brown		Loamy soil	
19	SS 2.6	-22.3572	30.1	462	GR, TH	Red		Loamy soil	
20	SS 2.7	-22.353	30.10028	453	GR, TH	Dark brown		Loamy soil	High content of organic materials

© University of Venda

Appendix 3AII: Continued……

21	SS 2.8	-22.3488	30.1	439	GR, MO, TH	Red	Loamy soil
22	SS 2.9	-22.3447	30.1	498	BA, GR, MO, TH	Red	Loamy soil
23	SS2.10	-22.3405	30.1	467	GR, TH	Red	Loamy soil
24	SS 2.11	-22.3363	30.1	460	GR, TH	Red	Loamy soil
25	SS2.12	-22.3319	30.10028	462	GR, BA, TH	Red	Loamy soil
26	SS 2.13	-22.3279	30.1	472	GR, MO, TH	Red	Loamy soil
27	SS 2.14	-22.3239	30.1	462	GR, MO, TH	Red	Loamy soil
28	SS 2.15	-22.3197	30.1	445	MO, TH	Red	Loamy soil
29	SS 9.1	-22.3614	30.09583	455	MO, TH	Red Brown	Loamy soil
30	SS 9.2	-22.3654	30.09583	484	GR, MO	Red Brown	Loamy soil
31	SS 9.3	-22.3696	30.09583	488	GR, MO	Red Brown	Loamy soil
32	SS 9.4	-22.3736	30.09583	477	GR, MO, TH	Red Brown	Loamy soil
33	SS 9.5	-22.3778	30.09583	479	GR, MO, TH	Red Brown	Loamy soil
34	SS 9.6	-22.382	30.09583	494	MO, TH	Red	Loamy soil
35	SS 9.7	-22.3862	30.09583	491	MO, TH	Red	Loamy soil
36	SS 9.8	-22.3573	30.09583	477	MO, TH	Red	Loamy soil
37	SS 9.9	-22.3529	30.096	463	GR, MO, TH	Red Brown	Loamy soil
38	SS 9.10	-22.3486	30.09583	457	GR, MO, TH	Red Brown	Loamy soil
39	SS 9.11	-22.3445	30.09583	495	GR, MO, TH	Red Brown	Loamy soil
40	SS 9.12	-22.3403	30.09583	470	GR, MO, TH	Red Brown	Loamy soil
41	SS 9.13	-22.3363	30.09583	451	GR, MO, TH	Red Brown	Loamy soil
42	SS 9.14	-22.332	30.09583	471	GR, MO, TH	Red Brown	Loamy soil
43	SS 9.15	-22.3279	30.09583	490	GR, MO, TH	Red Brown	Loamy soil
44	SS 10.1	-22.3863	30.09172	508	GR, MO, TH	Red Brown	Loamy soil
45	SS 10.2	-22.3821	30.09192	490	GR, MO, TH	Red Brown	Loamy soil
46	SS 10.3	-22.3779	30.09164	450	GR, MO, TH	Red Brown	Loamy soil
47	SS 10.4	-22.3736	30.09172	433	GR, MO, TH	Red Brown	Loamy soil
48	SS 10.5	-22.3655	30.09192	439	GR, MO, TH	Brown	Loamy soil

© University of Venda

Appendix 3AII: Continued……

49	SS 10.6	-22.3613	30.09164	431	GR, MO, TH	Brown	Loamy soil	
50	SS 10.7	-22.3569	30.09181	461	GR, MO, TH	Light Brown	Silty soil	
51	SS 10.8	-22.353	30.09172	476	MO, TH	Brown	Loamy soil	
52	SS 10.9	-22.3487	30.09192	463	MO, TH	Brown	Loamy soil	
53	SS 10.10	-22.3443	30.09164	446	MO, TH	Red Brown	Loamy soil	
54	SS 10.11	-22.3403	30.09172	487	MO, TH	Brown	Loamy soil	
55	SS 10.12	-22.3361	30.09192	486	MO, TH	Brown	Loamy soil	
56	SS 10.13	-22.3321	30.09164	477	MO, TH	Brown	Loamy soil	
57	SS 10.14	-22.3279	30.09172	497	GR, MO, TH	Red	Loamy soil	
58	SS 10.15	-22.3241	30.09192	474	GR, MO, TH	Red brown	Loamy soil	
59	SS 10.16	-22.3195	30.09164	457	GR, MO, TH	Red	Loamy soil	
60	SS 11.1	-22.3573	30.0875	467	GR, MO, TH	Light Brown	Silty soil	
61	SS 11.2	-22.3611	30.08775	451	GR, MO, TH	Light Brown	Silty soil	
62	SS 11.3	-22.3653	30.08758	438	GR, MO, TH	Light Brown	Silty soil	Few pebbles
63	SS 11.4	-22.3694	30.08767	483	MO, TH	Red Brown	Loamy soil	
64	SS 11.5	-22.3738	30.08767	446	BA, GR, MO, TH	Red Brown	Loamy soil	
65	SS 11.6	-22.3779	30.0875	505	GR, MO, TH	Red Brown	Loamy soil	
66	SS 11.7	-22.382	30.08775	528	MO, TH	Red Brown	Loamy soil	
67	SS 11.8	-22.3861	30.08758	512	GR, MO	Brown	Loamy soil	
68	SS 11.9	-22.353	30.0875	485	GR, MO, TH	Brown	Loamy soil	
69	SS 11.10	-22.3486	30.08775	488	GR, MO, TH	Brown	Loamy soil	
70	SS 11.11	-22.3442	30.08758	466	GR, MO, TH	Red	Loamy soil	
71	SS 11.12	-22.3398	30.0875	482	GR, MO, TH	Red	Loamy soil	
72	SS 11.13	-22.3362	30.08775	477	GR, MO, TH	Light Brown	Loamy soil	Calcrete grains
73	SS 11.14	-22.332	30.08758	485	GR, MO, TH	Red	Loamy soil	
74	SS 11.15	-22.328	30.0875	474	MO, TH	Red	Loamy soil	
75	SS 11.16	-22.324	30.08775	477	MO, TH	Red	Loamy soil	

© University of Venda

Appendix 3AII: Continued……

76	SS 11.17	-22.3196	30.08758	469	MO, TH	Red	Loamy soil
77	SS 12.1	-22.3863	30.08333	509	GR, TH	Red Brown	Loamy soil
78	SS 12.2	-22.382	30.08333	481	GR, TH	Red Brown	Loamy soil
79	SS 12.3	-22.3779	30.08333	479	GR, MO, TH	Red Brown	Loamy soil
80	SS 12.4	-22.3737	30.08333	459	MO, TH	Red Brown	Loamy soil
81	SS 12.5	-22.3694	30.08333	462	GR, MO, TH	Red Brown	Loamy soil
82	SS 12.6	-22.3653	30.08361	471	GR, MO, TH	Red Brown	Loamy soil
83	SS 12.7	-22.3609	30.08333	483	GR, MO, TH	Brown	Loamy soil
84	SS 12.8	-22.3573	30.08333	488	GR, MO, TH	Red Brown	Loamy soil
85	SS 12.9	-22.3529	30.08333	471	MO, TH	Light Brown	Loamy soil
86	SS 12.10	-22.3484	30.08333	461	MO, TH	Brown	Loamy soil
87	SS 12.11	-22.3445	30.08333	494	MO, TH	Red Brown	Loamy soil
88	SS 12.12	-22.3403	30.08361	499	MO, TH	Red	Loamy soil
89	SS 12.13	-22.3362	30.08333	502	GR, MO, TH	Red	Loamy soil
90	SS 12.14	-22.332	30.08333	486	GR, MO, TH	Red	Loamy soil
91	SS 12.15	-22.3281	30.08361	486	GR, MO, TH	Red	Loamy soil
92	SS 12.16	-22.3239	30.08361	471	MO, TH	Red	Loamy soil
93	ATN 1	30.10417	-22.29583	480	GR, MO, TH	Red Brown	Loamy soil
94	ATN 2	30.10417	-22.30139	468	GR	Light Brown	Sandy soil
95	ATN 3	30.10417	-22.30722	447	GR, TH	Light Brown	Sandy soil
96	ATN 5	30.10417	-22.31222	488	GR, MO, TH	Light Brown	Sandy soil
97	ATN 6	30.10417	22.317222	474	GR, TH	Brown	Loamy soil
98	ATN 17	30.099722	-22.32056	445	GR, MO, TH	Light Brown	Loamy soil
99	ATN 18	30.099722	22.316667	449	GR, MO, TH	Light Brown	Loamy soil
100	ATN 19	30.099722	-22.31278	462	GR	Red Brown	Loamy soil
101	ATN 20	30.099722	-22.31167	463	GR, MO, TH	Dark Brown	Loamy soil
102	ATN 21	30.099722	-22.3075	458	GR, MO, TH	Brown	Loamy soil
103	ATN 22	30.099722	-22.30111	478	GR, MO, TH	Dark Brown	Loamy soil

© University of Venda

Appendix 3AII: Continued……

104	ATN 23	30.099722	-22.29611	467	GR, MO, TH	Light Brown	Loamy soil	
105	ATN 24	30.099722	-22.2925	452	GR, MO, TH	Light Brown	Loamy soil	
106	ATN 26	30.09583	22.291667	480	GR, MO, TH	Brown	Silty soil	
107	ATN 27	30.09583	-22.3	460	GR, MO, TH	Brown	Silty soil	
108	ATN 28	30.09583	22.304167	466	GR, MO, TH	Light Brown	Loamy soil	
109	ATN 29	30.09583	-22.30778	460	GR, TH	Brown	Loamy soil	
110	ATN 30	30.09583	-22.3125	457	GR, TH	Dark Brown	Loamy soil	
111	ATN 31	30.09583	22.316667	450	GR	Red Brown	Loamy soil	
112	ATN 32	30.09583	22.320833	445	GR, TH	Brown	Loamy soil	
113	ATN 45	30.09167	-22.31278	457	GR, MO, TH	Brown	Loamy soil	
114	ATN 46	30.09167	22.307222	460	GR, TH	Red Brown	Sandy soil	
115	ATN 47	30.09167	22.304167	457	GR, TH	Brown	Loamy soil	
116	ATN 48	30.09167	-22.29917	456	GR, MO	Red Brown	Silty	
117	ATN 49	30.09167	22.295833	453	GR	Dark Brown	Silty soil	
118	ATN 50	30.09167	-22.29111	451	GR	Brown	Silty soil	Organic materials
119	ATN 51	30.0875	-22.28944	439	GR, MO, TH	Dark Brown	Loamy soil	
120	ATN 52	30.0875	-22.29389	455	GR, MO, TH	Brown	Loamy soil	
121	ATN 53	30.0875	-22.29833	453	GR, MO, TH	Light Brown	Loamy soil	
122	ATN 54	30.0875	-22.30361	465	GR, MO, TH	Brown		
123	ATN 55	30.0875	-22.30694	468	GR, MO, TH	Light Brown	Loamy soil	
124	ATN 56	30.0875	-22.31194	465	GR, MO, TH	Brown	Loamy soil	
125	ATN 57	30.0875	-22.31667	472	GR, MO, TH	Brown	Loamy soil	
126	ATN 69	30.08333	-22.32083	460	GR,MO, TH	Red Brown	Loamy soil	
127	ATN 70	30.083333	-22.31667	480	GR, MO	Brown	Loamy soil	
128	ATN 71	30.08333	-22.31167	472	GR, MO, TH	Dark Brown	Loamy soil	
129	ATN 72	30.08333	-22.30722	472	GR, MO, TH	Brown	Loamy soil	
130	ATN 75	30.08333	-22.29389	466	GR	Brown	Loamy soil	
131	ATN 76	30.08333	-22.28944	458	GR	Brown	Loamy soil	

© University of Venda

Appendix 3AII: Continued……

132	ATN 77	30.07917	-22.28975	462	GR, TH	Dark Brown	Loamy soil
133	ATN 81	30.07917	22.308333	483	GR, TH	Brown	Loamy soil
134	ATN 82	30.07917	-22.3125	483	GR	Brown	Sandy soil
135	ATN 83	30.07917	22.316611	485	GR, MO, TH	Light Brown	Loamy soil
136	ATN 84	30.07917	22.320833	481	GR, MO, TH	Light Brown	Loamy soil
137	ATN 85	30.07917	22.325028	482	GR, MO, TH	Red Brown	Loamy soil
138	ATN 86	30.07917	-22.32917	499	GR, MO, TH	Brown	Loamy soil
139	ATN 87	30.07917	22.333139	503	GR, MO, TH	Red Brown	Loamy soil
140	ATN 88	30.07917	-22.3375	481	GR	Dark Brown	Loamy soil
141	ATN 89	30.07917	-22.34167	470	GR, MO, TH	Light Brown	Loamy soil
142	ATN 90	30.075	-22.34167	496	GR, MO, TH	Light Brown	Loamy soil
143	ATN 91	30.075	-22.33778	510	GR, MO, TH	Dark Brown	Loamy soil
144	ATN 92	30.075	-22.3325	519	GR, MO, TH	Brown	Loamy soil
145	ATN 93	30.075	-22.32889	500	GR, MO, TH	Light Brown	Loamy soil
146	ATN 94	30.075	-22.32389	500	GR, TH	Brown	Loamy soil
147	ATN 95	30.075	-22.32056	513	GR, MO, TH	Light Brown	Loamy soil
148	ATN 96	30.075	-22.31611	510	GR, MO, TH	Light Brown	Loamy soil
149	ATN 97	30.075	-22.305	490	GR, MO, TH	Red Brown	Loamy soil
150	ATN 99	30.075	-22.31167	500	GR, MO, TH	Dark Brown	Loamy soil
151	ATN 100	30.075	-22.30694	520	GR, MO, TH	Light Brown	Loamy soil
152	ATN 101	30.075	-22.30167	500	GR, MO, TH	Brown	Loamy soil
153	ATN 103	30.07083	22.291417	480	GR, MO, TH	Light Brown	Loamy soil
154	ATN 104	30.07083	22.295333	460	GR, MO, TH	Dark Brown	Loamy soil
155	ATN 105	30.07083	22.299722	459	GR, MO, TH	Brown	Loamy soil
156	ATN 106	30.07083	22.303944	445	GR, MO,TH	Light Brown	Loamy soil
157	ATN 107	30.07083	22.308361	480	GR, MO, TH	Brown	Loamy soil
158	ATN 108	30.07083	22.312361	484	GR	Dark Brown	Loamy soil
159	ATN 109	30.07083	22.316389	483	GR, MO, TH	Red	Loamy soil

© University of Venda

Appendix 3AII: Continued……

160	ATN 110	30.07083	-22.32028	489	GR, MO, TH	Red Brown	Loamy soil
161	ATN 111	30.07083	-22.32417	496	GR, TH	Red	Loamy soil
162	ATN 112	30.07083	-22.32889	494	GR, TH	Dark Brown	Loamy soil
163	ATN 113	30.07083	-22.33278	494	GR, MO, TH	Dark Brown	Loamy soil
164	ATN 114	30.07083	-22.3375	494	GR, MO, TH	Brown	Loamy soil
165	ATN 115	30.07083	-22.34167	498	GR, MO, TH	Brown	Loamy soil
166	ATN 116	30.06667	-22.34139	505	GR, MO, TH	Brown	Loamy soil
167	ATN 117	30.06667	-22.33722	518	GR, MO, TH	Brown	Loamy soil
168	ATN 118	30.06667	-22.33278	563	GR, MO, TH	Brown	Loamy soil
169	ATN 119	30.06667	-22.32889	601	GR, TH	Brown	Loamy soil
170	ATN 120	30.06667	-22.32417	506	GR MO TH	Brown	Loamy soil
171	ATN 121	30.06667	-22.32056	516	GR MO TH	Red	Loamy soil
172	ATN 124	30.06667	-22.30694	503	GR	Red Brown	Loamy soil
173	ATN 125	30.06667	-22.30361	517	GR, MO, TH	Light Brown	Loamy soil
174	ATN 126	30.06667	-22.29917	494	GR, MO, TH	Light Brown	Loamy soil
175	ATN 128	30.06667	-22.29028	476	GR, MO, TH	Light Brown	Loamy soil
176	ATN 131	30.0625	-22.3	401	GR, MO, TH	Brown	Loamy soil
177	ATN 132	30.0625	-22.3045	431	GR, MO, TH	Brown	Loamy soil
178	ATN 133	30.0625	-22.3085	421	GR, MO, TH	Light Brown	Loamy soil
179	ATN 134	30.0625	22.312917	465	GR, MO, TH	Light Brown	Loamy soil
180	ATN 135	30.0625	22.317222	459	GR, MO, TH	Brown	Loamy soil
181	ATN 136	30.0625	-22.32056	475	GR, MO, TH	Light Brown	Loamy soil
182	ATN 137	30.0625	-22.32472	468	GR, MO, TH	Light Brown	Loamy soil
183	ATN 139	30.0625	-22.33306	489	GR, MO, TH	Light Brown	Loamy soil
184	ATN 140	30.0625	-22.33722	495	GR, MO, TH	Brown	Loamy soil
185	ATN 141	30.0625	22.341389	497	GR	Brown	Loamy soil
186	ATN 151	30.041833	22.333056	519	GR	Greyish Brown	Loamy soil
187	ATN 152	30.041833	22.329389	526	BA, GR, TH	Light Brown	Loamy soil

© University of Venda

Appendix 3AII: Continued……

188	ATN 153	30.041833	22.325028	561	GR, TH	Light Brown	Loamy soil
189	ATN 154	30.041833	22.321139	514	GR. TH	Red	Loamy soil
190	ATN 155	30.041833	22.316694	522	MO, TH	Red Brown	Loamy soil
191	ATN 157	30.05	-22.32075	524	GR, MO, TH	Red Brown	Loamy soil
192	ATN 158	30.05	22.324967	523	MO, TH	Red	Loamy soil
193	ATN 159	30.05	22.329167	519	TH, FT	Red	Loamy soil

GR *- Grass,* ***MO*** *- Mopane,* ***TH*** *- Thorn tree,* ***BA*** *- Baobab tree****, FT*** *- Fern tree*

© University of Venda

Appendix 3BI: Physical characteristics of different rock types identified from Campbell copper deposit

Deposit	Specimen ID	Name of the rock	Colour	Texture	Structure	Grain size	Minor minerals	Major minerals	Sulphides
Campbell copper deposit	CPR 01	Grey gneiss	Grey	Medium - coarse	Foliated	2 mm – 5 mm	Quartz, plagioclase, orthopyroxene	Biotite and garnet	Not visible
	CPR 02	Quartzite	Light green	Coarse	Well laminated	5 mm – 2 cm	Quartz	Plagioclase, biotite, magnetite	Not visible
	CPR 03	Hornblende gneiss	Black	Fine to medium	Well-developed foliation	10 µm – 2 mm	Hornblende and pyroxene	Biotite, quartz and feldspar	Not visible
	CPR 04	Amphibolite	Black	Fine to medium	Non foliated	10 µm 2 mm	Hornblende and magnetite	Plagioclase, biotite and quartz	Few grains
	CPR 05	Amphibolite-Quartz granulite	Greyish black	Medium to coarse	Non foliated	2 mm – 5 mm	Hornblende and quartz	Feldspar, biotite and magnetite	Few grains
	CPR 06	Biotite-Garnet-Quartz granulite	Brown to grey	Coarse	Non foliated	5 mm – 2 cm	Biotite, garnet and quartz	Orthoclase and epidote	Not visible
	CPR 07	Quartzo-Feldspathic gneiss	Pinkish grey	Medium to coarse	Irregular foliation	2 mm - 5 mm	Plagioclase, orthoclase and orthopyroxene	Quartz and garnet	Not visible

© University of Venda

Appendix BI: continued …….

	CPR 08	Potassium Feldspathic gneiss	Pinkish	Medium to coarse	Irregular foliation	2 mm – 5 mm	Orthoclase and orthopyroxene	Biotite and quartz	Not visible
	CPR 09	Pegmatite	White	Coarse	Non foliation	5 mm – 2 cm	Plagioclase and quartz	Plagioclase and quartz	Not visible
	CPR 10	Marble	Whitish green	Coarse	Non foliated	10 µm – 2 mm	Calcite	Quartz, garnet and epidote	Not visible
Campbell copper deposit	CPR 11	Grey gneiss	Dark grey	Medium - coarse	Slightly Foliated	-	Quartz, plagioclase, orthopyroxene	Biotite and garnet	Not visible
	CPR 12	Amphibolite schist	Blackish	Fine to medium	Non foliated	-	Hornblende and magnetite	Plagioclase, biotite and quartz	Not visible
	CPR 13	Potassium Feldspathic gneiss	Pinkish	Medium to coarse	Slightly foliation	-	Orthoclase and orthopyroxene	Biotite and quartz	Not visible
	CPR 14	Grey gneiss	Blackish grey	Fine to medium	Well-developed foliation	-	Amphibole and pyroxene	Biotite, quartz and feldspar	Not visible

© University of Venda

Appendix 3BI: Physical Characteristics of different rock types identified from Artonvilla copper deposit

Deposit	Specimen ID	Name of the rock	Colour	Texture	Structure	Grain size	Minor minerals	Major minerals	Sulphides
Artonvilla copper deposit	ATR 01	Calc-Silicate gneiss	Whitish grey	Medium to coarse	Lineation	1 – 2 mm	Calcite, Quartz and Feldspars	Boitite, Garnet and Amphibole	Not visible
	ATR 02	K-feldspathic gneiss	Pinkish	Fine to medium	Well foliated	1 - 4 mm	Biotite	Quartz and K-feldspars	Not visible
	ATR 03	Quartzo-feldspathic gneiss	Grey	medium	Poorly laminated	1mm – 1 cm	Biotite, Quartz and Feldspars	Garnet and muscovite	Not visible
	ATR 04	Garnet-Quartzo-feldspathic gneiss	Pinkish grey	Medium to Coarse	Well foliated	2 - 5 mm	Plagioclase , quartz	Garnet, biotite , amphibole, microcline	Not visible
	ATR 05	Biotite-Garnet gneiss	Pinkish white	Coarse	Poorly foliated	2 – 5 mm	Feldspars, quatrz	Amphibole , garnet, bioyite	Not visible
	ATR 06	Amphibolite	Greyish black	Fine to medium	Non foliated	2 – 15 mm	Amphibolite schist	Amphiboles and Feldspars	Few grains

© University of Venda

Appendix 3BII: Continued…….

	ATR 07	Hornblende Schist	Greenish black	Coarse	Schistocity				Not visible
Artonvilla copper deposit	ATR 08	Biotite Schist	Brownish white	Medium to coarse	Non foliated	5 – 20 mm	Biotite and quartz	Feldspar	Not visible
	ATR 09	Ultramafic granulite	Greyish black	Fine	Non foliation	1 - 4 mm	Amphiboles	Feldspars	Not visible
	ATR 10	Silicate gneiss	Whitish grey	coarse	Lineation		Calcite, Quartz and Feldspars	Boitite, Garnet	Not visible
	ATR 11	Feldspathic gneiss	Light pinkish	Medium	Poorly foliated		K-feldspars	Quartz	Not visible
	ATR 12	Quartzo-feldspathic gneiss	Grey	medium	Poorly laminated		Biotite, Quartz and Feldspars	Garnet and muscovite	Not visible
	ATR 13	Garnet gneiss	Pinkish grey	Coarse	Well foliated		Plagioclase , quartz	Garnet, biotite and amphibole	Not visible
	ATR 14	Biotite gneiss	Pinkish brownish white	Coarse	Poorly foliated		Feldspars, quatrz	Amphibole , biotite	Not visible

© University of Venda

Appendix 3BII: Continued……

	ATR 15	Amphibolite Schist	Greyish black	Fine to medium	Non foliated		Amphibolite	Felsic minerals	Not visible
	ATR 16	Biotite Schist	Brownish	coarse	Non foliated		Biotite and quartz	Feldspar, muscovite	Not visible
	ATR 17/ Atgn03	Biotite garnet gneiss	Dark greyish	Medium to coarse	Gneissic foliation		Feldspars, quartz	Biotite, garnet	Disseminated sulphides
	ATR 18/ Atgn04	Biotite gneiss	Greyish	Coarse grained	Gneissic foliation		Mafic and felsic minerals	garnets	Disseminated sulphides
	ATR 19/ Atgn05	Quartzo-feldspathic gneiss	Light grey	Course grained	Gneissic foliation		quartz feldspar	Amphiboles	Not visible

© University of Venda

Appendix 3CI: Physical Characteristics of different ore samples identified from Campbell copper deposit

Deposit	Specimen No.	Specimen ID	Plate No.	Specimen name	Colour	Texture	Structure	Grain size	Mineralisation	Type of ore
Campbell copper deposits	CP01	CP01	Plate 7.3A	Brecciated ore	Whitish brown	Course	Angular grains, filled microstructures	Up to 2 cm	Amphiboles, quartz, pyrite, chalcopyrite, magnetite, chlorites	Brecciated ore
	CP02	CP02		Quartz vein-amphibolite	Light Greyish black	Coarse	Vein	Up to 2 mm	Quartz, amphibole, pyrite, chalcopyrite	Veined ore
	CP03	CP03	Plate 7.3B	Brecciated ore	Whitish grey	Course	Angular grains, filled microstructures	Up to 2 cm	Amphiboles, quartz, pyrite, graphite, chalcopyrite, chlorites	Brecciated ore
	CP04	CPA4		Quartz vein-amphibolite	Greyish black	Coarse	Vein	Up to 2 mm	Quartz, amphibole, sulphides	Vein ore
	CP05	CPAm04		Quartz vein-amphibolite	Greyish black	Coarse	Vein	Up to 2 mm	Quartz, amphibole, sulphides	Vein ore
	CP06	CP05	Plate 7.3C	Brecciated ore	Greenish grey	Course	Angular grains, filled microstructures	Up to 2 cm	Amphiboles, quartz, pyrite, chalcopyrite	Brecciated ore
	CP07	CPqv01	Plate 7.1A	Quartz vein ore	Whitish	coarse	Large grains	Up to 10 mm	Quartz, pyrite, chalcopyrite	Veined ore

© University of Venda

Appendix 3CI: Continued…….

Campbell copper deposits	CP08	CPqv02		Quartz vein ore	Whitish	coarse	Large grains	10 mm	Quartz, pyrite, chalcopyrite	Veined ore
	CP09	CPqtz03	Plate 7.2B	Quartz vein	White	Fine to medium	vein	Up to 1 mm	Quartz, chalcopyrite, pyrite, bornite	Vein/Disseminated ore
	CP10	CPdis01		Amphibolite	Greyish black	Fine to medium	Disseminated grains	Up 1 mm	Amphibole, sulphides	Disseminated ore
	CP11	CPdis02		Amphibolite	Greyish brownish grey	Medium to coarse	Disseminated grains	Up 1 mm	Amphibole, malachite, pyrite, chalcopyrite, bornite	Disseminated ore
	CP12	CPmal01	Plate 7.7B	Malachite-Amphibolite	Greenish	Fine to medium	Stains of malachite		Malachite, chalcocite	Disseminated ore
	CP13	CPbr01	Plate 7.7C	Brecciated quartz	whitish	Coarse	Angular grains	Up to 2 cm	Quartz, pyrite , bornite, copper	Brecciated ore

© University of Venda

Appendix 3CII: Physical Characteristics of different ore samples identified from Artonvilla copper deposit

Deposit	Specimen No.	Specimen ID	Plate No.	Specimen name	Colour	Texture	Structure	Grain size	Mineralisation	Type of ore
Artonvilla copper deposit	AT01	ATbr01	Plate 7.3	Brecciated amphibolite	Greenish black	Medium to coarse	Angular grains	Up to 2 cm	Amphiboles, quartz, minor sulphides	Brecciated ore
	AT02	ATavr12	Plate 7.4	Quartz vein amphibolite	Brownish grey	coarse	Large grains,	Up to 10 mm	Quartz, garnet, magnetite, sulphides	Veined ore
	AT03	Atcal01	Plate 7.5	Cal-amphibolite	White-greyish black	Medium to coarse	Calcite-quartz vein	Up to 2 cm	Calcite, quartz, amphiboles, graphite, pyrite, chalcopyrite	Veined/disseminated ore
	AT04	ATavr11	Plate 6,1	Amphibolite with quartz vein	Darkish greyish black	Fine to medium	Quartz vein	Few mm	Amphiboles, quartz, low sulphide occurrence	Veined ore
	AT05	AT01		Calcite amphibolite	Whitish-grey	coarse	Vein	Up to 2 cm	Calcite, quartz, amphiboles, sulphides	Veined/disseminated ore
	AT06	AT02		Quartz vein amphibolite	Light brownish grey	coarse	Large grains	Up to 12 mm	Quartz, garnet, magnetite, sulphides	Veined ore
	AT07	ATavr22		Quartz vein	Whitish	Coarse	Large grains	Up to 10 mm	Quartz, amphiboles, magnetite, sulphides	Veined ore
	AT08	ATavr26		Amphibolite schist	Greenish black	Coarse	Veinlets of quartz	Up to 2 mm	Amphiboles, quartz, sulphide, chlorites	Disseminated ore

© University of Venda

Appendix 4A: Hierarchical metadata structure for data collected within the study area

(MD_Metadata)
- **contact**: (CI_Responsibility)
  - **role**: (CI_RoleCode) author *(party who authored the resource)*
  - **party**: (CI_Organisation)
    - **name**: University of Venda
- **dateInfo**: (CI_Date)
  - **date**: (DateTime)
    - **date**: *YYYY-MM*
  - **dateType**: (CI_DateTypeCode) creation *(date identifies when the resource was brought into existence)*
- **metadataStandard**: (CI_Citation)
  - **title**: 19115-1
  - **editionDate**: 2014-07
- **referenceSystemInfo**: (MD_ReferenceSystem)
  - **referenceSystemIdentifier**: (MD_Identifier)
    - **code**: *alphanumeric value identifying a the spatial and temporal reference systems used in the resource*
- **identificationInfo**: (MD_Identification)
  - **citation**: (CI_Citation)
    - **title**: *name by which the cited resource is known*
  - **abstract**: *brief narrative summary of the resource*
  - **credit**: *recognition of those who contributed to the resource*
  - **pointOfContact**: (CI_Responsibility)
    - **role**: (CI_RoleCode) originator *(party who created the resource)*
    - **party**: (CI_Party)
      - **contactInfo**: (CI_Contact)
        - **phone**: (CI_Telephone)
          - **number**: *(telephone number by which individuals can contact responsible organisation or individual)*
        - **address**: (CI_Address)
          - **deliveryPoint**: *address line for the location*
          - **city**: *city of the location*
          - **postalCode**: *ZIP or other postal code*
          - **electronicMailAddress**: *address of the electronic mailbox of the responsible organisation or individual*

© University of Venda

Appendix 4A: Continued…….

topicCategory: (MD_TopicCategoryCode) geoscientificInformation

extent: (EX_Extent)

description: Limpopo Province, South Africa

geographicElement: (EX_GeographicBoundingBox)

westBoundLongitude: *western-most coordinate of the limit of the resource extent, expressed in longitude in decimal degrees (positive east)*

eastBoundLongitude: *eastern-most coordinate of the limit of the resource extent, expressed in longitude in decimal degrees (positive east)*

southBoundLatitude: *southern-most coordinate of the limit of the resource extent, expressed in latitude in decimal degrees (positive north)*

northBoundLatitude: *northern-most coordinate of the limit of the resource extent expressed in latitude in decimal degrees (positive north)*

additionalDocumentation: (CI_Citation)

title: *name of thesis or study that discusses the cited resource*

resourceFormat: (MD_Format)

formatSpecificationCitation: (CI_Citation)

title: pdf

descriptiveKeywords: (MD_Keywords)

keyword: *commonly used word(s) or formalised word(s) or phrase(s) used to describe the subject*

keyword:

keyword:

keyword:

resourceSpecificUsage: (MD_Usage)

specificUsage: *brief description of the resource and/or resource series usage*

resourceConstraints: (MD_Constraints)

useLimitation: *limitation affecting the fitness for use of the resource or metadata*

resourceLineage: (LI_Lineage)

statement: *general explanation of the data producer's knowledge about the lineage of a resource*

scope: (MD_Scope)

level: (MD_ScopeCode) dataset

© University of Venda

Appendix 4BI: Concentration levels of heavy metals in soil samples from Campbell area

Sample No.	Sample ID	Latitude	Longitude	Elevation (m)	As (ppm)	Cd (ppm)	Co (ppm)	Cr (ppm)	Cu (ppm)	Mn (ppm)	Ni (ppm)	Pb (ppm)	Zn (ppm)
1	D1T1S1	22˚20'46.0"	29˚59'36.9"	575	10	<4	6.8	37	24.6	160.8	30.6	6.8	4.6
2	D1T1S2	22˚20'57.9"	29˚59'42.3"	570	8	<4	5.6	32	9.6	118.4	22	6.2	4.4
3	D1T1S3	22˚21'15.5"	29˚59'56.0"	555	12	<4	8.8	56.2	16.6	187.8	33.2	6.2	4.0
4	D1T1S4	22°21'30.0"	29°59'55.0"	564	12	<4	10	58.4	17.4	178.8	27	9.4	4.6
5	D1T1S5	22˚21'45.0"	29˚59'55.0"	571	12	<4	5	23.4	10.6	97.4	11.6	5.4	4.4
6	D1T1S6	22˚22'00.0"	29˚59'00.0"	569	8	<4	9.8	39.4	13.6	180	19.8	4.4	4.6
7	D1T1S7	22˚22'15.1"	29˚59'55.2"	572	10	<4	4.8	27.2	10	101.6	13	4.4	4.2
8	D1T1S8	22˚22'34.5"	29˚59'55.2"	574	4	<4	6.8	25.8	19	147.2	13.6	5.6	4.
9	D1T1S9	22˚22'50.4"	29˚59'55.3"	567	12	<4	6.8	36.6	17.2	181.8	16.6	4.6	4.2
10	D1T1S10	22˚23'07.2	29˚59'55.2"	571	4	<4	7.6	39.8	14.4	198.6	18.4	4.2	5
11	D1T1S11	22°23'27.3"	29°59'55.2"	573	10	<4	6.6	39	12.8	141.2	16	<4	4.6
12	D1T1S12	22°23'51.0"	29°59'55.3"	572	8	<4	4	43.6	30.6	115.6	15	<4	4.2
13	D2T2S2	22˚21'06.0"	29˚59'19.8"	574	12	<4	10	85.4	23	189	45.8	6.6	4.4
14	D2T2S4	22˚21'40.8"	29˚59'19.8"	574	12	<4	8	55.6	14.6	159.8	24	6.2	4.4
15	D2T2S6	22°21'57.6"	29˚59'19.8"	580	8	<4	6	27.8	15.4	148.4	15.4	6.2	4.8
16	D2T2S7	22˚22'36.6"	29˚59'19.8"	568	14	<4	6.6	29.2	22.4	120.4	13.4	4.4	4.6
17	D2T2S8	22˚22'49.2"	29˚59'19.8"	580	10	<4	7	34	24.8	193.2	18	7.2	4.4

© University of Venda

Appendix 4BI: Continued…….

Sample No.	Sample ID	Latitude	Longitude	Elevation (m)	As (ppm)	Cd (ppm)	Co (ppm)	Cr (ppm)	Cu (ppm)	Mn (ppm)	Ni (ppm)	Pb (ppm)	Zn (ppm)
18	D2T2S9	22˚23'06.0"	29˚59'19.8"	584	6	<4	6.4	37.6	10	146.2	8.8	4	4.2
19	D2T3S1	22°23'14.9"	29°59'01.2"	576	8	<4	11.4	72.4	20.8	204.2	45.2	8.2	24
20	D2T3S2	22°23'06.0"	29°59'01.2"	587	6	<4	5.6	37.8	18.8	65.2	12	<4	<4
21	D2T3S3	22°22'49.2"	29°59'01.2"	589	4	<4	6	40.8	21.4	148.6	17	6.2	16.4
22	D2T3S4	22°22'36.6"	29°59'01.2"	598	8	<4	14.8	54.8	1107	181.2	34.2	12.8	31
23	D2T3S5	22°22'14.4"	29°59'01.2"	590	8	<4	8.4	67.4	129.6	181	31.8	8	10.2
24	D3T3S3	22°21'30.3"	29°59'01.2	588	<4	<4	7.6	56.8	13.8	228	23.4	6.6	11.8
25	D3T3S6	22°21'57.6"	29°59'01.2"	580	8	<4	13	63.2	20.4	283.4	26.6	8.8	16.4
26	D3T3S7	22°21'40.8"	29°59'01.2"	577	12	<4	11	64.6	21.8	231.4	31.8	7	17.2
27	D3T3S8	22°21'24.0"	29°59'01.2"	578	18	<4	8	52.2	14.8	140.2	22.8	8	13.2
28	D3T3S9	22°21'06.0"	29°59'01.2"	580	14	<4	13.6	97.2	22	151	59.6	8.2	26.4
29	D3T3S10	22°20'54.0"	29°59'01.2"	579	8	<4	15	61	20.2	267.4	43.4	8.4	27.8
30	D3T4S1	22°20'58.6"	29°58'45.6"	588	10	<4	11.8	66.8	24.2	144.6	43	8	21.4
31	D3T4S2	22°21'06.0"	29°58'45.6"	586	6	<4	10.8	81	23.2	177.2	47	7.4	21.6
32	D3T4S4	22°22'38.6"	29°58'45.6"	597	18	<4	12.2	65	19.8	254.2	30	10.8	17.8
33	D3T4S6	22°22'14.4"	29°58'45.6"	595	4	<4	4.2	41.2	9.4	78.2	22.8	<4	<4
34	D3T4S8	22°22'49.2"	29°58'45.6"	588	12	<4	9.6	60.2	46.6	184.6	26.6	6.6	14.2
35	D3T4S9	22°23'06.6"	29°58'45.6"	576	6	<4	12	65	33.4	223	35.2	6.8	22.8

© University of Venda

Appendix 4BI: Continued…….

Sample No.	Sample ID	Latitude	Longitude	Elevation (m)	As (ppm)	Cd (ppm)	Co (ppm)	Cr (ppm)	Cu (ppm)	Mn (ppm)	Ni (ppm)	Pb (ppm)	Zn (ppm)
36	D3T5S3	22°22'33.6"	29°58'28.8"	604	8	<4	9.8	39.4	13.6	180	19.8	4.4	4.6
37	D3T5S5	22°21'57.6"	29°58'28.8"	597	8	<4	8.2	60.6	17.5	173.6	22.6	5.4	11.8
38	D3T5S7	22°21'24.0"	29°58'28.8"	584	4	<4	11	67.4	26.8	164	32.8	6.6	17.2
39	D3T5S8	22°21'06.6"	29°58'28.8"	581	10	<4	5.6	28.6	9.2	134	14.8	5	4.2
40	D3T5S9	22°21'01.3"	29°58'28.8"	590	14	<4	8.6	37.8	26.6	167.4	19.2	9	17.2
41	D6S1FA	22°23'56.6"	29°57'28.1"	580	8	<4	<4	21.8	16.8	79.8	12	<4	4.6
42	D6S2FA	22°24'03.3"	29°57'12.3"	578	14	<4	5.6	29.2	11.6	140.4	17	7.2	4.6
43	D6S3FA	22°24'07.3"	29°57'00.1"	582	<4	<4	4	12.8	7.8	77.4	11.4	4.4	4.2
44	D6S4FA	22°24'20.9"	29°57'09.6	580	8	<4	7.6	38.4	29	172	21.2	4.8	4.4
45	D6S6FA	22°24'10.4"	29°57'36.4"	582	14	<4	6.4	22.2	9.6	115.8	21.6	6.4	4
46	D6S1Fc/b	22°23'55.6"	29°56'51.2"	601	<4	<4	7.2	55	14.2	116.2	28.2	5.8	4.6
47	D6S2Fc/b	22°23'49.1"	29°57'07.3	576	<4	<4	6.8	31.2	37	148.8	15.4	5	4.8
48	D6S3Fc/b	22°23'42.1"	29°57'20.2"	578	18	<4	7.2	21.86	16.2	155.6	23.6	7.2	5.4
49	D6S1FD	22°23'18.8"	29°57'06.6"	599	14	<4	6.2	36.2	12.4	186.8	24.4	<4	4.2
50	D6S2FD	22°23'25.0"	29°56'50.0"	595	10	<4	7.4	33	14.6	152.8	21	7.4	4.2
51	D6S4FD	22°23'31.5"	29°56'33.1"	591	8	<4	5.6	37.8	14.2	225.8	22.2	4.4	4.4

© University of Venda

Appendix 4BI: Continued…….

Sample No.	Sample ID	Latitude	Longitude	Elevation (m)	As (ppm)	Cd (ppm)	Co (ppm)	Cr (ppm)	Cu (ppm)	Mn (ppm)	Ni (ppm)	Pb (ppm)	Zn (ppm)
52	D7S2FE	22°23'13.7"	29°57'25.5"	591	<4	<4	10.6	23.2	16	67	23.4	6.4	4
53	D7S1FF	22°23'14.8"	29°57'37.3"	598	12	<4	11.2	70.4	17.6	246.2	52	6	4.4
54	D7S2FF	22°23'07.9"	29°57'34.1"	597	12	<4	10.4	19.8	19.8	148.2	20.6	13.2	4.4
55	D7S3FF	22°23'25.9"	29°57'32.4"	593	10	<4	4.2	26.4	13.6	116	15.8	<4	4.4
56	D7S4FF	22°23'29.3"	29°57'44.1"	590	8	<4	8	44.8	12.4	143.6	18.4	4.2	4.2
57	D7S1FG	22°23'25.4"	29°57'52.4"	598	12	<4	14.4	109.8	24.6	329.4	63.4	5.6	4.4
58	D7S2FG	22°23'10.5"	29°57'46.4"	611	8	<4	9.4	54	19	327.2	29.8	5.8	4.4
59	D7S3FG	22°23'04.4"	29°57'43.8"	614	<4	<4	<4	23.8	9.2	78.6	15	<4	4.6
60	D7S2FH	22°23'24.0"	29°58'03.5"	604	12	<4	5.8	46.6	15.4	327.2	29.8	5.8	4.4
61	D7S3FH	22°23'07.7"	29°58'03.3"	624	<4	<4	13.2	60.4	30.6	227.6	35.2	5.6	4.6
62	D7S4FH	22°22'56.3"	29°58'03.3"	618	8	<4	6.8	26	12.6	108.2	9.2	<4	9.2
63	D7S2FI	22°23'44.2"	29°58'39.1"	572	12	<4	10.4	19.8	19.8	148.2	20.6	13.2	4.4
64	D8S1FI	22°23'44.2"	29°58'21.5"	579	20	<4	9.6	55.4	19.2	214.8	33.8	5.4	4.4
65	D8S3FI	22°23'59.4"	29°58'15.6"	599	6	<4	5	47.6	11.2	102.4	19.2	<4	4.4
66	D8S4FI	22°24'15.3"	29°58'19.4"	580	12	<4	10.8	54	21.6	276	37.4	5.2	4.2
67	D8S5FI	22°23'28.3"	29°58'07.9"	596	4	<4	5.8	33.6	19.6	111.4	20.6	<4	4.2
68	D8S6FI	22°23'21.1"	29°58'24.3"	593	12	<4	10.4	33	28.4	255.6	28	5.6	4.2

© University of Venda

Appendix 4BI: Continued…….

Sample No.	Sample ID	Latitude	Longitude	Elevation (m)	As (ppm)	Cd (ppm)	Co (ppm)	Cr (ppm)	Cu (ppm)	Mn (ppm)	Ni (ppm)	Pb (ppm)	Zn (ppm)
69	D8S7FI	22°23'15.4"	29°58'40.1"	580	6	<4	6.4	56	11.8	111.2	26	<4	4.2
70	D8S2FJ	22°23'59.7"	29°57'43.0"	579	16	<4	8.8	28.4	21.2	239.8	29.2	6.6	4.2
71	D8S4FJ	22°23'47.5"	29°57'42.6"	588	16	<4	10	32.8	60.2	162.8	30	5.8	4.4
72	D8S2FI	22°23'51.3"	29°58'20.5"	583	<4	<4	<4	39.8	19.6	90.2	19.2	<4	4.2
73	D9S1FM	22°24'27.6"	29°58'15.2"	567	6	<4	11.8	29.4	54	260.8	30.8	6	4.8
74	D13S4FM2	22°21'25.2"	30°00'17.6"	562	12	<4	12.4	96.4	18.6	241.8	42.4	11.2	23.4
75	D13S5FM2	22°21'41.3"	30°00'22.5"	556	8	<4	9.2	55.2	17.4	176	25.8	10.4	23.4
76	D14S3FM3	22°21'04.5"	30°00'39.2"	556	4	<4	<4	20	134	112	9	6.8	13
77	D14S5FM3	22°21'36.7"	30°00'39.0"	551	10	<4	5.8	20.4	13	185.4	11.6	8.6	38.2
78	D14S6FM3	22°21'52.8"	30°00'39.4"	559	4	<4	4.6	18.2	9.2	185	12.4	5	4.2
79	D14S2FM4	22°20'26.4"	30°00'53.2"	552	4	<4	6.4	35.2	52.6	173.4	19.2	5.6	4.4
80	D14S4FM4	22°21'02.4"	30°00'52.2"	572	4	<4	5	20.4	150	123	9.6	7.4	11
81	D14S5FM4	22°21'18.5"	30°00'52.2"	558	6	<4	4.6	18.4	36.8	148	10	5.8	22.2
82	D14S6FM4	22°21'36.1"	30°00'59.3"	548	4	<4	<4	37.6	18.4	170.6	16.4	<4	4.2
83	D14S7FM4	22°21'56.0"	30°00'58.3"	554	6	<4	<4	14.8	22.8	138.8	8.8	4	4.2
84	D14S1FM4	22°20'06.2"	30°00'52.2"	551	4	<4	9.2	87.8	18.4	351.6	49	5.4	4.4
85	D15S1FM5	22°19'56.7"	30°01'05.3"	551	4	<4	10.6	70.4	133.8	260.2	43	5.2	4.2

© University of Venda

Appendix 4BI: Continued…….

Sample No.	Sample ID	Latitude	Longitude	Elevation (m)	As (ppm)	Cd (ppm)	Co (ppm)	Cr (ppm)	Cu (ppm)	Mn (ppm)	Ni (ppm)	Pb (ppm)	Zn (ppm)
86	D15S2FM5	22°20'12.8"	30°01'18.3"	545	12	<4	5.4	22.8	15.4	166	10.2	5.2	14.4
87	D15S3FM5	22°20'28.9"	30°01'23.6"	573	4	<4	10.4	33	28.4	255.6	28	5.6	4.2
88	D15S5FM5	22°21'01.1"	30°01'33.1"	562	16	<4	9.6	59.8	33.8	239.8	29.2	6.6	4.4
89	D15S1FM6	22°19'42.6"	30°01'15.1"	549	12	<4	6.8	31	12.6	147.6	14.4	11	13.6
90	D15S2FM6	22°19'58.7"	30°01'20.9"	538	6	<4	6	22.8	29	140.4	13.2	7	4.8
91	D15S5FM6	22°20'39.6"	30°01'49.9"	566	8	<4	7.4	64.6	46.8	170.6	30.2	6.4	4
92	D16S1FM7	22°19'25.3"	30°01'32.7"	529	<4	<4	8	37.2	36.2	194.8	22.8	13.4	32.2
93	D16S2FM7	22°19'11.2"	30°01'29.5"	522	14	<4	11	67.8	36.4	192.2	34.4	8	23.4
94	D16S3FM7	22°18'55.1"	30°01'24.1"	516	14	<4	15.4	86	33.2	197.4	48.2	10	30.8
95	D16S1FM8	22°19°'30.0"	30°01'50.3"	533	<4	<4	7	31.6	67	128.4	15.8	10	26.2
96	D16S5FM8	22°19'48.7"	30°02'38.0"	527	<4	<4	17	70.6	671.4	130	39	8.8	19
97	D17S8FM8	22°20'19.6"	30°00'48.3"	548	<4	<4	8.6	38.2	17.6	161.2	25.2	10.4	20.6
98	D17S9FM8	22°19'43.3"	30°02'04.7"	534	4	<4	9.4	68.4	133.8	134.4	29.2	7.8	19
99	D17S10FM8	22°20'32.0"	30°02'22.9"	547	10	<4	6.2	28	200.2	152.8	14.4	11	29.2
100	D17S11FM8	22°20'48.5"	30°02'06.9"	553	10	<4	15.8	54.6	1580.2	179	29.6	11.6	26.2
101	D17S12FM8	22°21'11.9"	30°01'56.0"	548	<4	<4	13	94.6	95.6	277.6	49.8	14.4	141
102	D1S13FM8	22°21'23.4"	30°02'04.1"	541	8	<4	11.4	46.4	27.6	182.6	25.8	10	29.6

© University of Venda

					As	Cd	Co	Cr	Cu	Mn	Ni	Pb	Zn
Min					3.5	4	3.5	12.8	7.8	6	8.8	3.5	3.5
Max					20	4	17	109.8	1580.2	351.6	260.8	30.8	141
Mean					8.70	4	8.33	45.45	64.78	172.18	27.70	6.86	11.60
Median					8	4	7.8	39.2	19.8	165	23.4	6.2	4.6
SD					4.16		3.15	20.96	198.74	72.64	26.50	3.55	15.75
LBV					12.86		11.47	66.41	263.52	244.82	54.21	10.42	27.35

© University of Venda

Appendix 4BII: Concentration levels of heavy metals in soil samples from Artonvilla area

Sample No.	Sample ID	Latitude	Longitude	Elevation (m)	As ppm	Cd ppm	Co ppm	Cr Ppm	Cu ppm	Mn ppm	Mo ppm	Ni ppm	Pb ppm	Zn ppm
1	SS 1.1	-22.386	30.1045	455	5	0.2	8	13	12	94	5	20	5	9
2	SS 1.2	-22.381	30.10442	443	5	0.196	12	82	26	163	12	42	7	27
3	SS 1.3	-22.378	30.10422	455	12	0.2	16	158	32	165	16	97	10	42
4	SS 1.4	-22.3738	30.10447	425	5	0.2	13	78	24	255	18	42	12	25
5	SS 1.7	-22.3488	30.10447	451	12	0.195	10	56	26	138	8	22	8	8
6	SS 1.8	-22.3446	30.10467	466	18	0.198	11	55	23	172	24	25	7	9
7	SS 1.9	-22.3404	30.10447	436	14	0	13	61	16	220	10	28	8	12
8	SS 1.10	-22.3362	30.10422	477	12	0.391	32	75	35	281	35	57	13	28
9	SS 1.11	-22.3321	30.10442	465	16	0.196	20	89	37	228	20	79	11	38
10	SS 1.12	-22.3278	30.10414	465	20	0	22	93	30	298	23	51	17	36
11	SS 1.13	-22.324	30.10417	442	26	0.198	18	106	42	263	18	71	13	3
12	SS 1.14	-22.3196	30.10389	432	22	0.2	17	100	29	263	24	49	15	25
13	SS 1.15	-22.3154	30.38633	422	20	0	18	47	28	240	28	48	15	27
14	SS 2.1	-22.3863	30.10028	455	6	0.2	10	20	18	221	38	48	12	20
15	SS 2.2	-22.3822	30.10028	479	12	0.197	9	21	15	155	28	42	10	10
16	SS 2.3	-22.3779	30.1	469	10	0.2	20	51	45	300	26	41	16	10
17	SS 2.4	-22.3736	30.1	486	16	0.2	11	32	22	184	22	26	11	9
18	SS 2.5	-22.3614	30.1	460	12	0.393	12	35	34	197	20	31	13	10

© University of Venda

Appendix 4BII: Continued…….

Sample No.	Sample ID	Latitude	Longitude	Elevation (m)	As ppm	Cd ppm	Co ppm	Cr Ppm	Cu ppm	Mn ppm	Mo ppm	Ni ppm	Pb ppm	Zn ppm
19	SS 2.6	-22.3572	30.1	462	14	0.196	21	40	45	264	20	55	14	19
20	SS 2.7	-22.353	30.10028	453	22	0	24	61	50	563	30	70	17	21
21	SS 2.8	-22.3488	30.1	439	16	0.2	14	43	28	239	22	36	12	18
22	SS 2.9	-22.3447	30.1	498	13	0.192	16	51	25	253	21	38	11	13
23	SS 2.10	-22.3405	30.1	467	19	0.193	10	19	10	151	21	23	13	10
24	SS 2.11	-22.3363	30.1	460	20	0	10	20	18	290	20	24	14	12
25	SS 2.12	-22.3319	30.10028	462	24	0.2	11	21	22	336	28	22	15	16
26	SS 2.13	-22.3279	30.1	472	27	0	22	22	41	285	29	32	14	41
27	SS 2.14	-22.3239	30.1	462	27	0.194	10	20	21	538	33	22	15	27
28	SS 2.15	-22.3197	30.1	445	8	0.195	23	27	81	3	25	38	17	53
29	SS 9.1	-22.3614	30.09583	455	34	0.2	15	33	25	27	42	26	15	19
30	SS 9.2	-22.3654	30.09583	484	14	0.2	5	14	11	119	26	10	12	<5
31	SS 9.3	-22.3696	30.09583	488	8	0.389	7	12	23	89	27	25	12	5
32	SS 9.4	-22.3736	30.09583	477	16	0.2	14	43	24	40	34	32	14	1
33	SS 9.5	-22.3778	30.09583	479	18	0.2	13	37	24	54	30	31	14	1
34	SS 9.6	-22.382	30.09583	494	14	0.2	11	30	28	42	34	26	15	3
35	SS 9.7	-22.3862	30.09583	491	16	0	16	38	23	14	37	40	15	3

© University of Venda

Appendix 4BII: Continued…….

Sample No.	Sample ID	Latitude	Longitude	Elevation (m)	As ppm	Cd ppm	Co ppm	Cr Ppm	Cu ppm	Mn ppm	Mo ppm	Ni ppm	Pb ppm	Zn ppm
36	SS 9.8	-22.3573	30.09583	477	16	0.398	9	17	15	69	40	12	12	6
37	SS 9.9	-22.3529	30.096	463	10	0	17	19	17	48	37	17	13	8
38	SS 9.10	-22.3486	30.09583	457	12	0.2	20	43	20	40	38	20	13	14
39	SS 9.11	-22.3445	30.09583	495	6	0.195	35	65	33	12	41	70	19	29
40	SS 9.12	-22.3403	30.09583	470	12	0.196	18	44	31	20	45	61	18	15
41	SS 9.13	-22.3363	30.09583	451	16	0	21	50	28	14	41	49	18	26
42	SS 9.14	-22.332	30.09583	471	5	0	33	67	64	32	47	110	20	42
43	SS 9.15	-22.3279	30.09583	490	5	0.399	28	41	34	63	46	46	18	28
44	SS 10.1	-22.3863	30.09172	508	8	0.2	17	68	25	3	58	51	13	12
45	SS 10.2	-22.3821	30.09192	490	6	0.2	19	31	94	14	44	38	16	19
46	SS 10.3	-22.3779	30.09164	450	14	0.2	16	23	28	42	52	24	16	8
47	SS 10.4	-22.3736	30.09172	433	12	0.196	17	81	25	40	51	78	15	4
48	SS 10.5	-22.3655	30.09192	439	5	0	14	38	25	20	52	31	17	20
49	SS 10.6	-22.3613	30.09164	431	5	0.2	10	28	21	64	50	21	17	24
50	SS 10.7	-22.3569	30.09181	461	14	0	22	51	165	3	55	55	16	35
51	SS 10.8	-22.353	30.09172	476	21 5	0.199	27	50	45	21	54	71	19	24
52	SS 10.9	-22.3487	30.09192	463	20	0	18	33	32	31	58	58	18	20
53	SS 10.10	-22.3443	30.09164	446	16	0.196	10	24	19	56	59	20	15	11

© University of Venda

Appendix 4BII: Continued…….

Sample No.	Sample ID	Latitude	Longitude	Elevation (m)	As ppm	Cd ppm	Co ppm	Cr Ppm	Cu ppm	Mn ppm	Mo ppm	Ni ppm	Pb ppm	Zn ppm
54	SS 10.11	-22.3403	30.09172	487	22	0.2	10	42	30	59	58	39	16	17
55	SS 10.12	-22.3361	30.09192	486	26	0	19	51	52	3	65	47	19	34
56	SS 10.13	-22.3321	30.09164	477	91	0.396	29	34	33	9	125	46	19	24
57	SS 10.14	-22.3279	30.09172	497	16	0	21	34	39	42	61	45	17	32
58	SS 10.15	-22.3241	30.09192	474	10	0.198	7	22	8	75	67	26	15	8
59	SS 10.16	-22.3195	30.09164	457	49	0	14	25	48	34	115	27	15	34
60	SS 11.1	-22.3573	30.0875	467	22	0.198	14	26	44	51	69	27	17	22
61	SS 11.2	-22.3611	30.08775	451	18	0	28	75	52	13	76	90	19	53
62	SS 11.3	-22.3653	30.08758	438	10	0.197	20	58	37	34	75	82	23	38
63	SS 11.4	-22.3694	30.08767	483	16	0.196	10	36	20	82	73	22	14	7
64	SS 11.5	-22.3738	30.08767	446	20	0.196	11	40	14	54	78	31	15	8
65	SS 11.6	-22.3779	30.0875	505	6	0.196	11	16	19	36	74	15	13	9
66	SS 11.7	-22.382	30.08775	528	10	0	33	84	94	56	92	114	18	41
67	SS 11.8	-22.3861	30.08758	512	10	0	26	139	30	55	96	125	25	30
68	SS 11.9	-22.353	30.0875	485	20	0.196	17	19	28	4	92	40	19	30
69	SS 11.10	-22.3486	30.08775	488	20	0.196	17	36	36	30	106	50	16	22
70	SS 11.11	-22.3442	30.08758	466	16	0	16	33	31	32	103	41	17	20
71	SS 11.12	-22.3398	30.0875	482	18	0.199	12	27	22	38	100	21	16	13

© University of Venda

Appendix 4BII: Continued…….

Sample No.	Sample ID	Latitude	Longitude	Elevation (m)	As ppm	Cd ppm	Co ppm	Cr Ppm	Cu ppm	Mn ppm	Mo ppm	Ni ppm	Pb ppm	Zn ppm
72	SS 11.13	-22.3362	30.08775	477	21	0	11	20	16	41	107	19	19	17
73	SS 11.14	-22.332	30.08758	485	8	0.392	23	26	13	68	104	36	18	13
74	SS 11.15	-22.328	30.0875	474	25	0.196	11	18	18	56	108	26	16	15
75	SS 11.16	-22.324	30.08775	477	14	0.196	12	32	26	42	112	32	16	11
76	SS 11.17	-22.3196	30.08758	469	32	0.198	11	22	25	28	111	27	14	12
77	SS 12.1	-22.3863	30.08333	509	17	0.193	10	16	16	51	104	25	14	11
78	SS 12.2	-22.382	30.08333	481	27	0.196	7	18	13	69	102	23	13	6
79	SS 12.3	-22.3779	30.08333	479	20	0	14	43	27	88	112	39	16	15
80	SS 12.4	-22.3737	30.08333	459	30	0.189	18	45	33	46	102	39	17	19
81	SS 12.5	-22.3694	30.08333	462	24	0.196	19	39	39	38	98	39	18	24
82	SS 12.6	-22.3653	30.08361	471	18	0	20	42	34	20	109	44	19	30
83	SS 12.7	-22.3609	30.08333	483	20	0.198	21	32	41	13	113	43	19	39
84	SS 12.8	-22.3573	30.08333	488	22	0.2	14	13	23	8	116	20	22	43
85	SS 12.9	-22.3529	30.08333	471	37	0	13	34	31	10	116	28	19	32
86	SS 12.10	-22.3484	30.08333	461	38	0.199	15	31	37	40	106	35	20	31
87	SS 12.11	-22.3445	30.08333	494	36	0	16	22	39	26	116	24	17	20
88	SS 12.12	-22.3403	30.08361	499	28	0	8	17	26	7	116	15	14	10
89	SS 12.13	-22.3362	30.08333	502	24	0	12	18	30	66	120	20	14	13

© University of Venda

Appendix 4BII: Continued…….

Sample No.	Sample ID	Latitude	Longitude	Elevation (m)	As ppm	Cd ppm	Co ppm	Cr Ppm	Cu ppm	Mn ppm	Mo ppm	Ni ppm	Pb ppm	Zn ppm
90	SS 12.14	-22.332	30.08333	486	30	0.2	11	17	19	47	120	18	14	8
91	SS 12.15	-22.3281	30.08361	486	20	0	10	27	14	48	120	21	13	6
92	SS 12.16	-22.3239	30.08361	471	50	0	17	25	38	66	114	62	17	16
93	ATN 1	30.10417	-22.29583	480	44	0.37	17	59	22	277	9	65	10	32
94	ATN 2	30.10417	-22.30139	468	47	0.195	9	32	24	239	8	29	9	26
95	ATN 3	30.10417	-22.30722	447	71	0.375	13	43	26	303	6	34	11	19
96	ATN 5	30.10417	-22.31222	488	50	0.18	8	32	14	154	11	32	8	15
97	ATN 6	30.10417	22.31722	474	11 9	0.377	11	46	26	278	15	62	11	32
98	ATN 17	30.09972	-22.32056	445	76	0.378	15	29	54	318	6	26	9	26
99	ATN 18	30.09972	22.31666	449	63	0.192	7	27	77	196	8	31	7	19
100	ATN 19	30.09972	-22.31278	462	71	0.197	6	17	37	179	10	16	8	16
101	ATN 20	30.09972	-22.31167	463	55	0.189	7	37	11	189	11	30	9	23
102	ATN 21	30.09972	-22.3075	458	73	0.382	17	52	42	442	8	57	12	30
103	ATN 22	30.09972	-22.30111	478	84	0.375	11	41	38	285	0	38	9	21
104	ATN 23	30.09972	-22.29611	467	73	0.753	36	107	85	1009	6	135	14	61
105	ATN 24	30.09972	-22.2925	452	63	0.185	13	32	65	279	7	36	9	23
106	ATN 26	30.09583	22.29167	480	87	0.389	28	79	37	286	2	289	14	50
107	ATN 27	30.09583	-22.3	460	70	0.379	36	129	67	290	9	166	15	82

© University of Venda

Appendix 4BII: Continued…….

Sample No.	Sample ID	Latitude	Longitude	Elevation (m)	As ppm	Cd ppm	Co ppm	Cr Ppm	Cu ppm	Mn ppm	Mo ppm	Ni ppm	Pb ppm	Zn ppm
108	ATN 28	30.09583	22.30416	466	71	0.198	7	26	80	203	6	21	15	31
109	ATN 29	30.09583	-22.30778	460	85	0.387	26	85	203	342	0	64	10	26
110	ATN 30	30.09583	-22.3125	457	61	0.191	6	33	14	162	2	31	10	17
111	ATN 31	30.09583	22.31666	450	82	0.196	12	102	20	350	2	31	8	27
112	ATN 32	30.09583	22.32083	445	83	0.197	3	11	7	117	12	10	8	7
113	ATN 45	30.09167	-22.31278	457	74	0.186	8	28	20	168	7	22	6	11
114	ATN 46	30.09167	22.30722	460	61	0.197	12	36	110	261	10	30	7	21
115	ATN 47	30.09167	22.30417	457	63	0.191	11	44	32	249	0	39	9	21
116	ATN 48	30.09167	-22.29917	456	72	0.4	34	202	48	388	2	349	15	49
117	ATN 49	30.09167	22.29583	453	67	0.384	59	95	23	427	6	1004	17	41
118	ATN 50	30.09167	-22.29111	451	53	0.195	14	50	20	200	4	80	8	20
119	ATN 51	30.0875	-22.28944	439	111	0.189	20	66	22	469	15	80	12	35
120	ATN 52	30.0875	-22.29389	455	116	0.19	27	39	32	352	6	43	10	26
121	ATN 53	30.0875	-22.29833	453	62	0.194	6	29	55	157	8	20	7	12
122	ATN 54	30.0875	-22.30361	465	115	0.195	13	37	9	233	14	24	12	15
123	ATN 55	30.0875	-22.30694	468	106	0.192	12	9	18	146	10	147	11	30
124	ATN 56	30.0875	-22.31194	465	152	0.197	27	9	33	381	12	94	14	37
125	ATN 57	30.0875	-22.31667	472	98	0.188	15	17	11	193	11	26	7	12

© University of Venda

Appendix 4BII: Continued…….

Sample No.	Sample ID	Latitude	Longitude	Elevation (m)	As ppm	Cd ppm	Co ppm	Cr Ppm	Cu ppm	Mn ppm	Mo ppm	Ni ppm	Pb ppm	Zn ppm
126	ATN 69	30.08333	-22.32083	460	118	0	10	32	9	72	12	20	6	5
127	ATN 70	30.08333	-22.31667	480	58	0.387	20	52	42	540	4	55	8	24
128	ATN 71	30.08333	-22.31167	472	94	0.384	21	71	40	245	8	98	10	38
129	ATN 72	30.08333	-22.30722	472	86	0.195	21	88	49	295	8	93	12	34
130	ATN 75	30.08333	-22.29389	466	79	0.196	17	61	32	240	10	79	10	32
131	ATN 76	30.08333	-22.28944	458	119	0	7	60	5	62	14	14	4	4
132	ATN 77	30.07917	-22.28975	462	81	0.188	4	20	16	62	6	11	5	5
133	ATN 81	30.07917	22.308333	483	122	0	27	53	27	379	12	51	8	28
134	ATN 82	30.07917	-22.3125	483	96	0.191	19	24	37	327	17	42	9	19
135	ATN 83	30.07917	22.316611	485	98	0.382	30	40	92	516	10	55	9	36
136	ATN 84	30.07917	22.320833	481	105	0.397	21	39	68	315	12	46	13	31
137	ATN 85	30.07917	22.325028	482	98	0.199	10	30	16	120	8	22	5	6
138	ATN 86	30.07917	-22.32917	499	104	0.197	12	26	23	166	10	26	6	9
139	ATN 87	30.07917	22.333139	503	110	0.197	16	49	29	257	2	43	8	23
140	ATN 88	30.07917	-22.3375	481	103	0.382	29	64	74	408	13	73	12	55
141	ATN 89	30.07917	-22.34167	470	80	0.199	10	16	23	224	2	25	13	14
142	ATN 90	30.075	-22.34167	496	67	0.196	6	11	16	230	12	13	10	32

© University of Venda

Appendix 4BII: Continued…….

Sample No.	Sample ID	Latitude	Longitude	Elevation (m)	As ppm	Cd ppm	Co ppm	Cr Ppm	Cu ppm	Mn ppm	Mo ppm	Ni ppm	Pb ppm	Zn ppm
143	ATN 91	30.075	-22.33778	510	81	0.193	12	27	22	149	6	25	7	18
144	ATN 92	30.075	-22.3325	519	72	0.199	19	54	41	245	2	56	9	26
145	ATN 93	30.075	-22.32889	500	95	0.194	19	56	39	207	6	64	10	29
146	ATN 94	30.075	-22.32389	500	73	0.197	12	38	18	196	10	25	7	25
147	ATN 95	30.075	-22.32056	513	83	0.19	11	27	21	181	2	23	6	13
148	ATN 96	30.075	-22.31611	510	139	0.385	20	55	39	308	8	61	10	23
149	ATN 97	30.075	-22.305	490	122	0.197	9	3	16	257	6	26	11	13
150	ATN 99	30.075	-22.31167	500	104	0.189	17	25	34	229	11	58	8	14
151	ATN 100	30.075	-22.30694	520	110	0.187	12	64	24	213	13	32	10	23
152	ATN 101	30.075	-22.30167	500	91	0.19	10	14	15	213	15	26	9	20
153	ATN 103	30.07083	22.29142	480	101	0.199	20	60	30	266	16	50	6	15
154	ATN 104	30.07083	22.29533	460	112	0.385	32	71	18	376	17	738	15	27
155	ATN 105	30.07083	22.29972	459	120	0.581	37	97	52	422	12	417	12	47
156	ATN 106	30.07083	22.30394	445	115	0.398	30	45	123	511	12	53	9	49
157	ATN 107	30.07083	22.30836	480	112	0.199	13	44	31	233	18	75	8	22
158	ATN 108	30.07083	22.31236	484	102	0.186	10	36	39	248	4	55	10	20
159	ATN 109	30.07083	22.31639	483	109	0.191	7	16	15	224	10	16	12	17
160	ATN 110	30.07083	-22.32028	489	92	0	5	15	12	121	11	15	9	7

© University of Venda

Appendix 4BII: Continued…….

Sample No.	Sample ID	Latitude	Longitude	Elevation (m)	As ppm	Cd ppm	Co ppm	Cr Ppm	Cu ppm	Mn ppm	Mo ppm	Ni ppm	Pb ppm	Zn ppm
161	ATN 111	30.07083	-22.32417	496	105	0.198	20	89	249	281	10	49	8	25
162	ATN 112	30.07083	-22.32889	494	99	0.191	15	40	38	313	10	40	10	34
163	ATN 113	30.07083	-22.33278	494	106	0.199	19	51	17	224	18	49	12	26
164	ATN114	30.07083	-22.3375	494	100	0.398	24	58	55	433	14	60	11	34
165	ATN 115	30.07083	-22.34167	498	91	0.193	14	31	34	314	4	29	12	34
166	ATN 116	30.06667	-22.34139	505	97	0.198	9	19	34	211	8	16	8	19
167	ATN 117	30.06667	-22.33722	518	84	0.196	21	48	68	342	14	45	10	24
168	ATN 118	30.06667	-22.33278	563	99	0.199	8	24	20	214	18	21	12	17
169	ATN 119	30.06667	-22.32889	601	109	0.192	17	43	48	264	8	47	9	15
170	ATN 120	30.06667	-22.32417	506	117	0.194	9	26	25	211	14	34	10	13
171	ATN 121	30.06667	-22.32056	516	94	0.192	14	29	46	283	8	30	10	25
172	ATN 124	30.06667	-22.30694	503	75	0.581	29	80	50	369	17	266	19	40
173	ATN 125	30.06667	-22.30361	517	139	0.198	12	32	16	282	8	60	15	32
174	ATN 126	30.06667	-22.29917	494	117	0.191	12	36	17	329	8	59	16	34
175	ATN128	30.06667	-22.29028	476	111	0.195	15	31	41	314	6	32	11	26
176	ATN131	30.0625	-22.3000	401	106	0.392	49	69	20	346	8	962	16	18
177	ATN132	30.0625	-22.3045	431	94	0.189	10	35	31	160	9	61	8	15
178	ATN133	30.0625	-22.3085	421	105	0.198	9	25	13	205	10	30	23	12

© University of Venda

Appendix 4BII: Continued…….

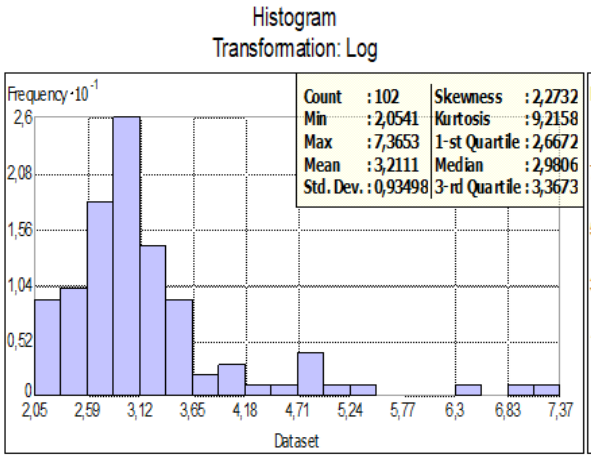
Sample No.	Sample ID	Latitude	Longitude	Elevation (m)	As ppm	Cd ppm	Co ppm	Cr Ppm	Cu ppm	Mn ppm	Mo ppm	Ni ppm	Pb ppm	Zn ppm
179	ATN134	30.0625	22.31292	465	91	0	5	11	7	114	8	14	12	8
180	ATN135	30.0625	22.31722	459	133	0.192	10	20	14	278	29	26	15	18
181	ATN 136	30.0625	-22.32056	475	143	0.191	7	28	17	237	13	23	15	16
182	ATN 137	30.0625	-22.32472	468	120	0.197	31	89	34	431	8	88	15	49
183	ATN 139	30.0625	-22.33306	489	98	0.195	7	18	504	229	4	18	12	38
184	ATN 140	30.0625	-22.33722	495	99	0.194	5	10	69	122	12	12	12	19
185	ATN 141	30.0625	22.34138	497	89	0	5	10	65	128	14	13	12	21
186	ATN 151	30.04183	22.33306	519	132	0.384	30	37	548	165	35	53	16	31
187	ATN 152	30.04183	22.32939	526	116	0.387	17	52	1321	188	14	43	17	24
188	ATN153	30.04183	22.32503	561	96	0.178	9	36	371	141	12	25	12	23
189	ATN 154	30.04183	22.32114	514	100	0.192	11	36	21	244	13	29	8	43
190	ATN 155	30.04183	22.31669	522	106	0.193	22	49	18	289	14	44	7	17
191	ATN 157	30.05	-22.32075	524	108	0.193	8	35	16	185	19	31	6	18
192	ATN 158	30.05	22.32497	523	123	0	7	32	22	129	20	25	6	10
193	ATN 159	30.05	22.32917	519	103	0.191	10	31	433	202	10	34	7	12
Statistics	**Min.**				5	0	3	3	5	3	0	10	4	1
	Max.				215	0.753	59	202	13.1	1009	125	1004	25	82
	Median				61	0.196	14	36	28	188	17	36	12	20

© University of Venda

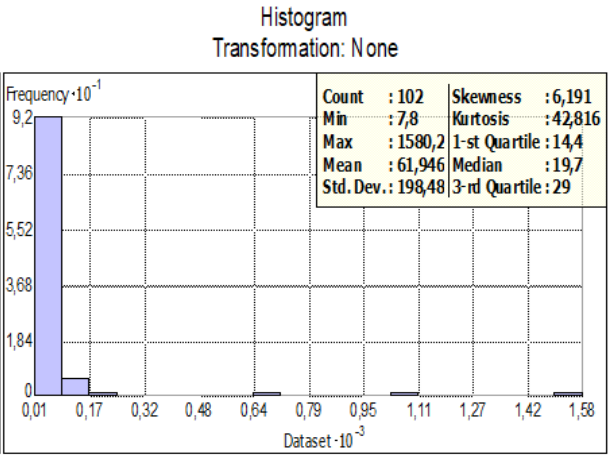
					As ppm	Cd ppm	Co ppm	Cr Ppm	Cu ppm	Mn ppm	Mo ppm	Ni ppm	Pb ppm	Zn ppm
Statistics	**Mean**				59.1	0.195	15.97	42.76	50.57	186.93	34.05	61.32	12.67	22.27
	SD				43.6	0.126	8.416	27.96	114.67	114.58	36.04	117.56	4.14	12.80
	LBV				102.9	0.322	24.7	70.7	165.3	331.9	74.6	179	17.4	52.6

© University of Venda

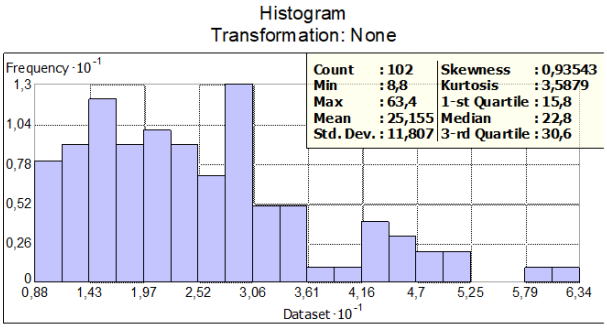
Appendix 4CI: Frequency diagrammes showing both non-transformed and log transformed data of the metals in soil within the western side of the study area (Campbell)



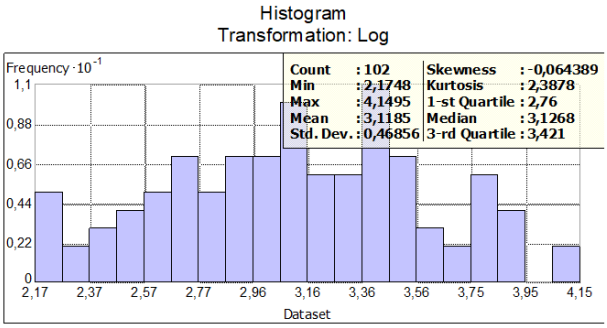
Dataset : Campbell_Copper_Soil_sample Attribute: Cu__ppm_



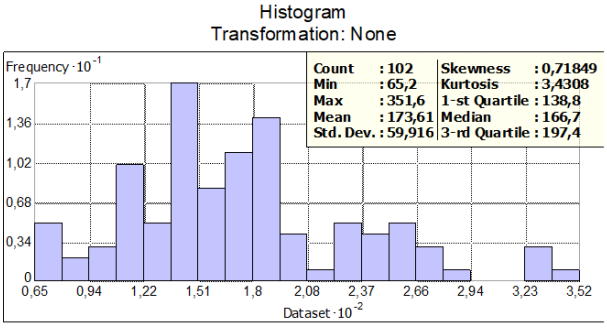
Dataset : Campbell_Copper_Soil_sample Attribute: Cu__ppm_



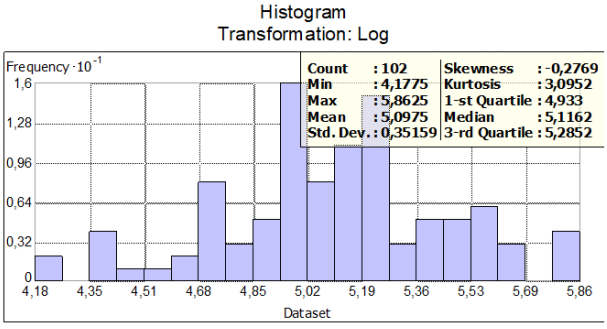
Dataset : Campbell_Nickel_soil_samples Attribute: Ni__ppm_



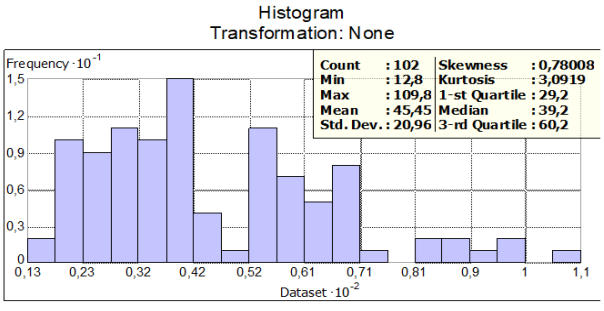
Dataset : Campbell_Nickel_soil_samples Attribute: Ni__ppm_



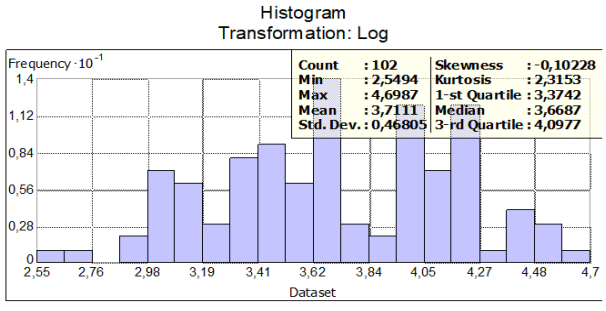
Dataset : Campbell_Manganese_soil_samples Attribute: Mn__ppm_



Dataset : Campbell_Manganese_soil_samples Attribute: Mn__ppm_



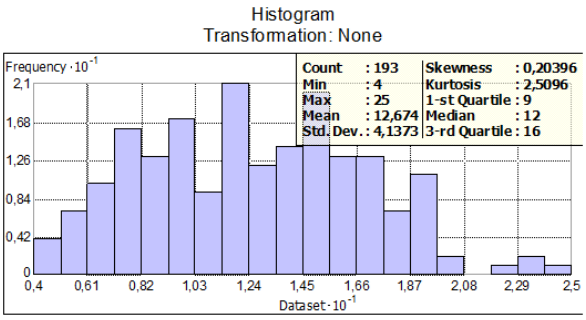
Dataset : Campbell_Chromium_soil_samples Attribute: Cr__ppm_



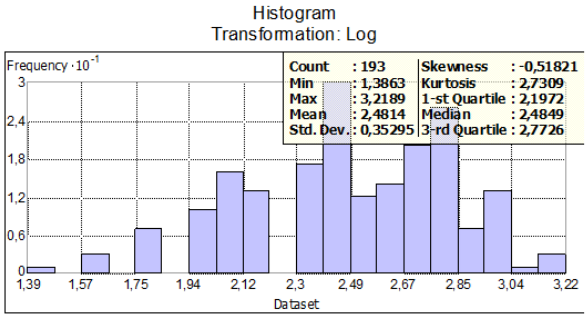
Dataset : Campbell_Chromium_soil_samples Attribute: Cr__ppm_

© University of Venda

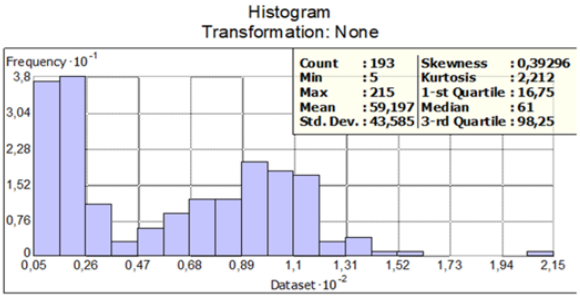
Appendix 4CII: Frequency diagrammes showing both non-transformed and log transformed data of the metals in soil within the eastern side of the study area (Artonvilla)



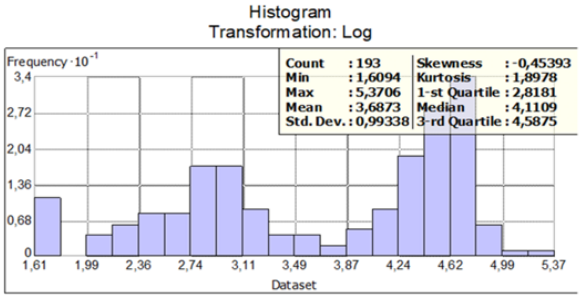
Dataset : Artonville_Lead_soil_samples Attribute: Pb__ppm_



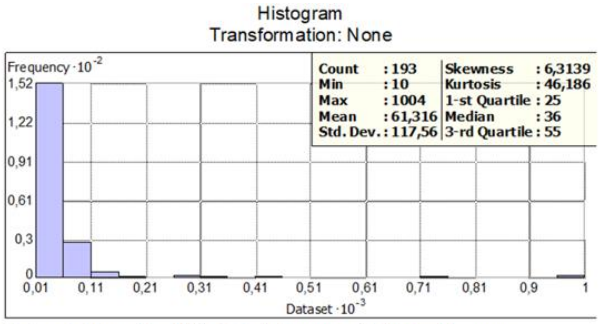
Dataset : Artonville_Lead_soil_samples Attribute: Pb__ppm_



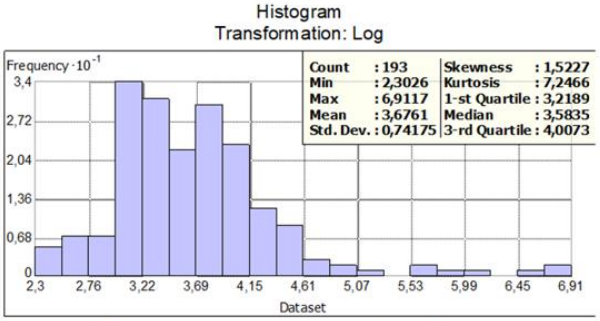
Dataset : Artonville_Arsenic_Soil_Samples Attribute: As_ppm



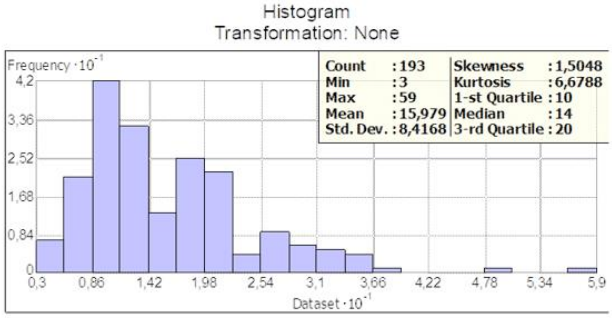
Dataset : Artonville_Arsenic_Soil_Samples Attribute: As_ppm



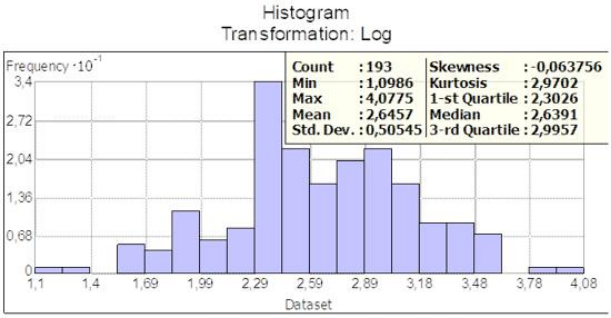
Dataset : Artonville_Nickel_Soil_Samples Attribute: Ni__ppm_



Dataset : Artonville_Nickel_Soil_Samples Attribute: Ni__ppm_



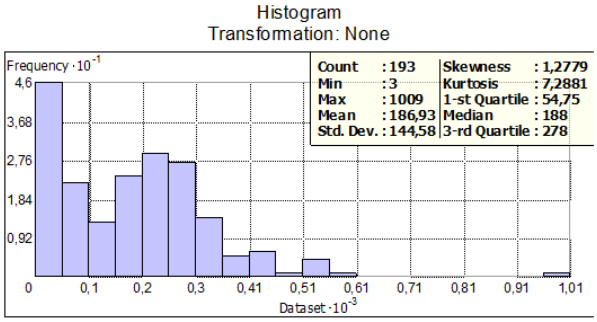
Dataset : Artonville_Cobalt_Soil_samples Attribute: Co__ppm_



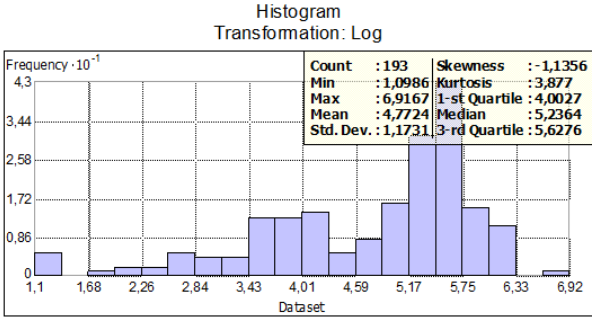
Dataset : Artonville_Cobalt_Soil_samples Attribute: Co__ppm_

© University of Venda

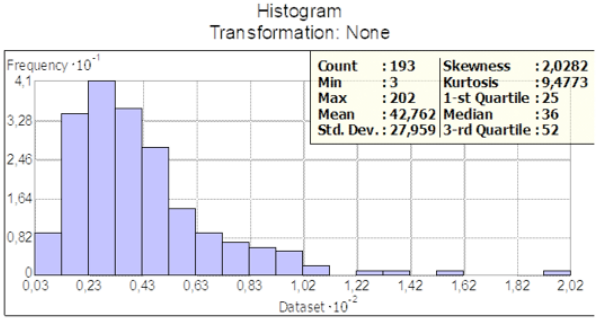
Appendix 4CII:Continued ……



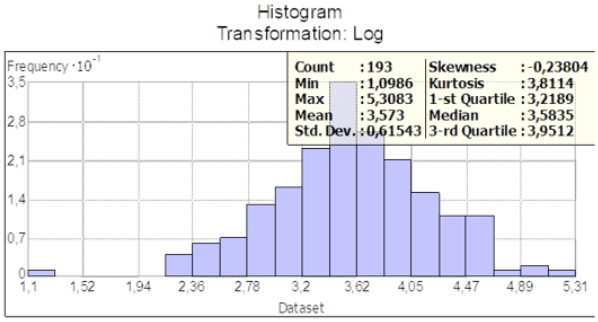
Dataset : Artonville_Manganese_soil_samples Attribute: Mn



Dataset : Artonville_Manganese_soil_samples Attribute: Mn



Dataset : Artonville_Chromium_soil_samples Attribute: Cr__ppm_



Dataset : Artonville_Chromium_soil_samples Attribute: Cr__ppm_

© University of Venda

Appendix 5A: Commonly used band ratios for of different minerals (Kalinowski and Oliver, 2004)

Feature	Band or Ratio	Comments	Reference
Iron			
Ferric iron, Fe^{3+}	2/1		Rowan; CSIRO
Ferrous iron, Fe^{2+}	5/3 + 1/2		Rowan
Laterite	4/5		Bierwith
Gossan	4/2		Volesky
Ferrous silicates (biot, chl, amph)	5/4	Fe oxide Cu-Au alteration	CSIRO
Ferric oxides	4/3	Can be ambiguous*	CSIRO
Carbonates / Mafic Minerals			
Carbonate / chlorite / epidote	(7+9)/8		Rowan
Epidote / chlorite / amphibole	(6+9)/(7+8)	Endoskarn	CSIRO
Amphibole / MgOH	(6+9)/8	Can be either MgOH or carbonate*	Hewson
Amphibole	6/8		Bierwith
Dolomite	(6+8)/7		Rowan, USGS
Carbonate	13/14	Exoskarn (cal/dolom)	Bierwith, Nimoyima, CSIRO
Silicates			
Sericite / muscovite / illite / smectite	(5+7)/6	Phyllic alteration	Rowan (USGS); Hewson (CSIRO)
Alunite / kaolinite / pyrophyllite	(4+6)/5		Rowan (USGS)
Phengitic	5/6		Hewson
Muscovite	7/6		Hewson
Kaolinite	7/5	Approximate only*	Hewson
Clay	$(5x7)/6^2$		Bierwith
Alteration	4/5		Volesky
Host rock	5/6		Volesky
Silica			
Quartz rich rocks	14/12		Rowan
Silica	(11x11)/10/12		Bierwith
Basic degree index (grt, cpx, epi, chl)	12/13	Exoskarn (grt, px)	Bierwith, CSIRO
SiO2	13/12	Same as 14/12	Palomera
SiO_2	12/13		Nimoyima
Siliceous rocks	(11x11)/(10x12)		Nimoyima
Silica	11/10		CSIRO
Silica	11/12		CSIRO
Silica	13/10		CSIRO
Other			
Vegetation	3/2		
NDVI	(3-2)/(3+2)	Normalised difference vegetation index	

© University of Venda

Appendix 5B: List of common ASTER false colour composites for enhancing mineral features band ratios (Kalinowski and Oliver, 2004)

Features	Red	Green	Blue	Reference
Vegetation and visible bands**	3, 3/2, or NDVI	2	1	
AlOH minerals/advanced argillic alteration***	5/6 (phen)	7/6 (musc)	7/5 (kaol)	Hewson (CSIRO)
Clay, amphibole, laterite	(5x7)/6^2 (clay)	6/8 (amph)	4/5 (lat)	Bierwith
Gossan, alteration, host rock	4/2 (goss)	4/5 (alt)	5/6 (host)	Volesky
Gossan, alteration, host rock	6 (goss)	2 (alt)	1 (host)	
Decorellation (envi)	13	12	10	Bierwith
Silica, carbonate, basic degree index	(11x11)/10/12 (silica)	13/14 (carb)	12/13 (basic)	Bierwith
Silica, carbonate	(11x11)/(10x12)	13/14	12/13	Nimoyima
Silica	11/10	11/12	13/10	CSIRO
Discrimination for mapping	4/1	3/1	12/14	Abdelsalam
Discrimination in sulphide rich areas	12	5	3	
Discrimination	4/7	4/1	(2/3) x (4/3)	Sultan
Discrimination	4/7	4/3	2/1	Abrams (USGS)
Silica, Fe^{2+}	14/12	(1/2) + (5/3)	MNF Band 1	Rowan (USGS)
Enhanced structural features	7	4	2	Rowan (USGS)

*Comments by Hewson
**Equivalent to Landsat RGB 432
***Alunite/pyrophyllite, mica, kaolinite/dickite

© University of Venda

Appendix 6A: Physical characteristics of different rock types identified from Campbell copper deposit

Deposit	Specimen ID	Plate No.	Name of the rock	Colour	Texture	Structure	Grain size	Minor minerals	Major minerals	Sulphides
Campbell copper deposit	CPR 01	Plate 6.9	Grey gneiss	Grey	Medium - coarse	Foliated	2 mm – 5 mm	Quartz, plagioclase, orthopyroxene	Biotite and garnet	Not visible
	CPR 02	Plate 6.5	Quartzite	Light green	Coarse	Well laminated	5 mm – 2 cm	Quartz	Plagioclase, biotite, magnetite	Not visible
	CPR 03	Plate 6.8	Hornblende gneiss	Black	Fine to medium	Well-developed foliation	10 µm – 2 mm	Hornblende and pyroxene	Biotite, quartz and feldspar	Not visible
	CPR 04	Plate 6.3	Amphibolite	Black	Fine to medium	Non foliated	10 µm 2 mm	Hornblende and magnetite	Plagioclase, biotite and quartz	Few grains
	CPR 05	Plate 6.1	Amphibolite-Quartz granulite	Greyish black	Medium to coarse	Non foliated	2 mm – 5 mm	Hornblende and quartz	Feldspar, biotite and magnetite	Few grains
	CPR 06	Plate 6.2	Biotite-Garnet-Quartz granulite	Brown to grey	Coarse	Non foliated	5 mm – 2 cm	Biotite, garnet and quartz	Orthoclase and epidote	Not visible
	CPR 07	Plate 6.9	Quartzo-Feldspathic gneiss	Pinkish grey	Medium to coarse	Irregular foliation	2 mm - 5 mm	Plagioclase, orthoclase and orthopyroxene	Quartz and garnet	Not visible

© University of Venda

Appendix 6A: Continued…….

	Specimen ID	Plate No.	Name of the rock	Colour	Texture	Structure	Grain size	Minor minerals	Major minerals	Sulphides
	CPR 08	Plate 6.18	Potassium Feldspathic gneiss	Pinkish	Medium to coarse	Irregular foliation	2 mm – 5 mm	Orthoclase and orthopyroxene	Biotite and quartz	Not visible
	CPR 09	-	Pegmatite	White	Coarse	Non foliation	5 mm – 2 cm	Plagioclase and quartz	Plagioclase and quartz	Not visible
	CPR 10	-	Marble	Whitish green	Coarse	Non foliated	10 µm – 2 mm	Calcite	Quartz, garnet and epidote	Not visible
Campbell copper deposit	CPR 11	-	Grey gneiss	Dark grey	Medium - coarse	Slightly Foliated	-	Quartz, plagioclase, orthopyroxene	Biotite and garnet	Not visible
	CPR 12	-	Amphibolite schist	Blackish	Fine to medium	Non foliated	-	Hornblende and magnetite	Plagioclase, biotite and quartz	Not visible
	CPR 13	-	Potassium Feldspathic gneiss	Pinkish	Medium to coarse	Slightly foliation	-	Orthoclase and orthopyroxene	Biotite and quartz	Not visible
	CPR 14	-	Grey gneiss	Blackish grey	Fine to medium	Well-developed foliation	-	Amphibole and pyroxene	Biotite, quartz and feldspar	Not visible

© University of Venda

Appendix 6AII: Physical Characteristics of different rock types identified from Artonvilla copper deposit

Deposit	Specimen ID	Plate No.	Name of the rock	Colour	Texture	Structure	Grain size	Minor minerals	Major minerals	Sulphides
Artonvilla copper deposit	ATR 01	Plate 6.3	Calc-Silicate gneiss	Whitish grey	Medium to coarse	Lineation	1 – 2 mm	Calcite, Quartz and Feldspars	Boitite, Garnet and Amphibole	Not visible
	ATR 02	Plate 6.10	K-feldspathic gneiss	Pinkish	Fine to medium	Well foliated	1 - 4 mm	Biotite	Quartz and K-feldspars	Not visible
	ATR 03	Plate 6.9	Quartzo-feldspathic gneiss	Grey	medium	Poorly laminated	1mm – 1 cm	Biotite, Quartz and Feldspars	Garnet and muscovite	Not visible
	ATR 04	Plate 6.11	Garnet-Quartzo-feldspathic gneiss	Pinkish grey	Medium to Coarse	Well foliated	2 - 5 mm	Plagioclase , quartz	Garnet, biotite , amphibole, microcline	Not visible
	ATR 05	Plate 6.12	Biotite-Garnet gneiss	Pinkish white	Coarse	Poorly foliated	2 – 5 mm	Feldspars, quatrz	Amphibole , garnet, bioyite	Not visible
	ATR 06	Plate 6.4	Amphibolite	Greyish black	Fine to medium	Non foliated	2 – 15 mm	Amphibolite schist	Amphiboles and Feldspars	Few grains
	ATR 07	Plate 6.6	Hornblende Schist	Greenish black	Coarse	Schistocity				Not visible
Artonvilla copper	ATR 08	Plate 6.7	Biotite Schist	Brownish white	Medium to coarse	Non foliated	5 – 20 mm	Biotite and quartz	Feldspar	Not visible

© University of Venda

Appendix 6AII: Continued…….

	Specimen ID	Plate No.	Name of the rock	Colour	Texture	Structure	Grain size	Minor minerals	Major minerals	Sulphides
Artonvilla copper deposit	ATR 09	-	Ultramafic granulite	Greyish black	Fine	Non foliation	1 - 4 mm	Amphiboles	Feldspars	Not visible
	ATR 10	-	Silicate gneiss	Whitish grey	coarse	Lineation	-	Calcite, Quartz and Feldspars	Boitite, Garnet	Not visible
	ATR 11	-	Feldspathic gneiss	Light pinkish	Medium	Poorly foliated	-	K-feldspars	Quartz	Not visible
	ATR 12	-	Qtz-feldspathic gneiss	Grey	medium	Poorly laminated	-	Biotite, Qtz and Feldspars	Garnet and muscovite	Not visible
	ATR 13	-	Garnet gneiss	Pinkish grey	Coarse	Well foliated	-	Plagioclase , quartz	Garnet, biotite and amphib	Not visible
	ATR 14	-	Biotite gneiss	Pinkish brownish	Coarse	Poorly foliated	-	Feldspars, quatrz	Amphibole , biotite	Not visible
	ATR 15	-	Amphibolite Schist	Greyish black	Fine to medium	Non foliated		Amphibolite	Felsic minerals	Not visible
	ATR 16	-	Biotite Schist	Brownish	coarse	Non foliated	-	Biotite and quartz	Feldspar, muscovite	Not visible
Artonvilla Copper deposit	ATR 17/ Atgn03	-	Biotite garnet gneiss	Dark greyish	Medium to coarse	Gneissic foliation	-	Feldspars, quartz	Biotite, garnet	Disseminated sulphides
	ATR 18/ Atgn04	-	Biotite gneiss	Greyish	Coarse grained	Gneissic foliation	-	Mafic and felsic minerals	garnets	Disseminated sulphides
	ATR 19/ Atgn05	-	Quartzo-feldspathic gneiss	Light grey	Course grained	Gneissic foliation	-	quartz feldspar	Amphiboles	Not visible

© University of Venda

Appendix 6B: Procedure on the calculation of molecular proportions of the oxides

Table of molecular proportions of oxides for Grey gneiss rock as an example

Oxide	Sample Wt %	Mol. Weight of Oxide	Mol. Prop of Oxide (Wt %÷Mol. Weight)
SiO_2	71.96	60.08	1.1977
TiO_2	0.26	79.86	0.0033
Al_2O_3	14.51	101.96	0.1423
Fe_2O_3	1.80	159.64	0.0113
MnO	0.034	70.94	0.0005
MgO	0.42	40.30	0.0104
CaO	1.72	56.08	0.0307
Na_2O	3.29	61.98	0.0531
K_2O	4.99	94.20	0.0530
P_2O_5	0.051	141.94	0.0530
Cr_2O_3	<0.001	<0.001	<0.001

The ACF diagram plots the following components: A= Al_2O_3; C= CaO and, and F= FeO +MgO

Where, A is the value of excess Al_2O_3 left after allocating Na_2O and K_2O to form alkali feldspar. Fe_2O_3 is combined with Al_2O_3 because Fe^{3+} typically substitute for Al^{3+}. The C value that is needed is the excess CaO after allocating P_2O_5 to form apatite, assuming that any P_2O_5 in the rock will suck up CaO to form apatite. P_2O_5 is combined with CaO in the ratio 1:3.3 in order to create apatite while F is the combined pseudo-component based on common exchangeability of Fe, Mg, and Mn in solid solution of most mafic rocks. It is then assumed that all mineral assemblages plotted may also contain alkalis feldspar and quartz (Winter, 2014).

Molecular proportions of all components were calculated to obtain the plotting parameters as indicated below:

A= $[Al_2O_3 + Fe_2O_3] - [Na_2O + K_2O]$; C= $[CaO] -3.33[P_2O_5]$; and F= [FeO + MgO + MnO]

The chemical analysis of the rock is first recalculated to molecular proportions by dividing the sample's weight percentage of each oxide constituent by the molecular weight of that oxide (Table above). Since only three components have to be plotted, they have to be nominalized so that they add up to 1 or 100% (Winter, 2014).

© University of Venda

Appendix 6B: Continued……..

If 't' is the total number of molecular proportions of the plotting parameters, therefore, t= A + C + F, and then the plotting parameters were:

A= 100×A/t; C= 100×C/t, F= 100×F/t

Example using plate 6.1 Grey gneiss

$A = [Al_2O_3 + Fe_2O_3] - [N_2O + K_2O]$

$= [0.1423 + 0.0113] - [0.0531 + 0.0530]$

$= 0.0475$

$C = [CaO] - 3.33\,[P_2O_5]$

$= 0.0307 - 3.33\,[0.0004]$

$= 0.0294$

$F = [MnO + MgO]$

$= [0.0005 + 0.0104]$

$= 0.0109$

Therefore t= A + C + F

$= [0.0475 + 0.0294 + 0.0109]$

$= 0.0878$

Therefore,

A%= 100×A/t

= 100×0.0475/0.0878

= 54.1 %

C%= 100×C/t

= 100×0.0294/0.0878

= 33.5%

F%= 100×F/t

= 100×0.0109/0.0878

= 12.4 %

© University of Venda

Appendix 6B: Continued……..

Oxides molecular proportions

Sample ID	Specimen name	Oxides molecular proportions									
		SiO_2	TiO_2	Al_2O_3	Fe_2O_3	MnO	MgO	CaO	N_2O	K_2O	P_2O_5
Camp03	Grey gneiss	1.1977	0.0033	0.1423	0.0113	0.0005	0.0104	0.0307	0.0531	0.0530	0.0004
Camp04	Quartzite	1.3565	0.02442	0.0629	0.0169	0.0003	0.0012	0.0925	0.0010	0.0044	0.0022
Camp/A17	Hornblende gneiss	1.2360	0.0049	0.0360	0.0685	0.0014	0.2179	0.0105	0.0047	0.0097	4.23×10^{-5}
Camp/07	Amphibolite	0.8172	0.0103	0.1476	0.06452	0.0035	0.2402	0.1701	0.0419	0.0172	0.00035
Camp/a24	Amphibolite-Quartz granulite	0.8331	0.0460	0.1216	0.0829	0.0031	0.1310	0.1537	0.0405	0.0228	0.0049
Camp/A18	Biotite-gnt-Qtz granulite	1.1128	0.0011	0.1694	0.0096	0.0002	0.0112	0.0446	0.1554	0.0003	0.0004
Camp05	Quartzo-Feldspathic gneiss	1.2179	0.0006	0.1418	0.0066	0.0015	0.0002	0.0196	0.0741	0.0493	0.0007
Camp02	Quartzo-Feldspathic gneiss	1.6022	0.0015	0.0135	0.0053	0.0001	0.0015	0.0023	0.0055	0.0046	4.93×10^{-5}
AVR01	Calc-Silicate gneiss	1.2350	0.0008	0.1349	0.0039	0.0001	0.0035	0.0111	0.0465	0.0754	0.0004
AVR08	K-feldspathic gneiss	0.8286	0.0144	0.1768	0.0956	0.0014	0.1047	0.0166	0.0902	0.0125	0.0008
AVR20	Quartzo-feldspathic gneiss	1.0013	0.0115	0.1638	0.0639	0.0023	0.1002	0.0512	0.0382	0.0199	0.00014
ATN01	Gnt-Qtz feldsp-gneiss	1.2665	0.0009	0.1306	0.0115	0.0010	0.0057	0.0638	0.0560	0.0075	$9.16x10^{-5}$
ATN03	Biotite-Garnet gneiss	1.0146	0.0088	0.2135	0.0481	0.0019	0.0963	0.0102	0.0097	0.0320	$1.76x10^{-4}$
AVR13	Amphibolite	1.5158	0.0048	0.0231	0.0148	0.0004	0.0146	0.0401	0.0015	0.0003	0.0002
AVR13a	Amphibolite Schist	1.4817	0.0050	0.0278	0.0159	0.0006	0.0310	0.0508	0.0016	0.0004	0.0002
AVR15	Biotite Schist	1.1639	0.0103	0.1292	0.0213	0.0003	0.0814	0.0259	0.0415	0.0460	0.0002
AVR25	Ultramafic granulite	0.8893	0.0416	0.1253	0.0931	0.0029	0.0769	0.0765	0.0390	0.0255	0.0069

© University of Venda

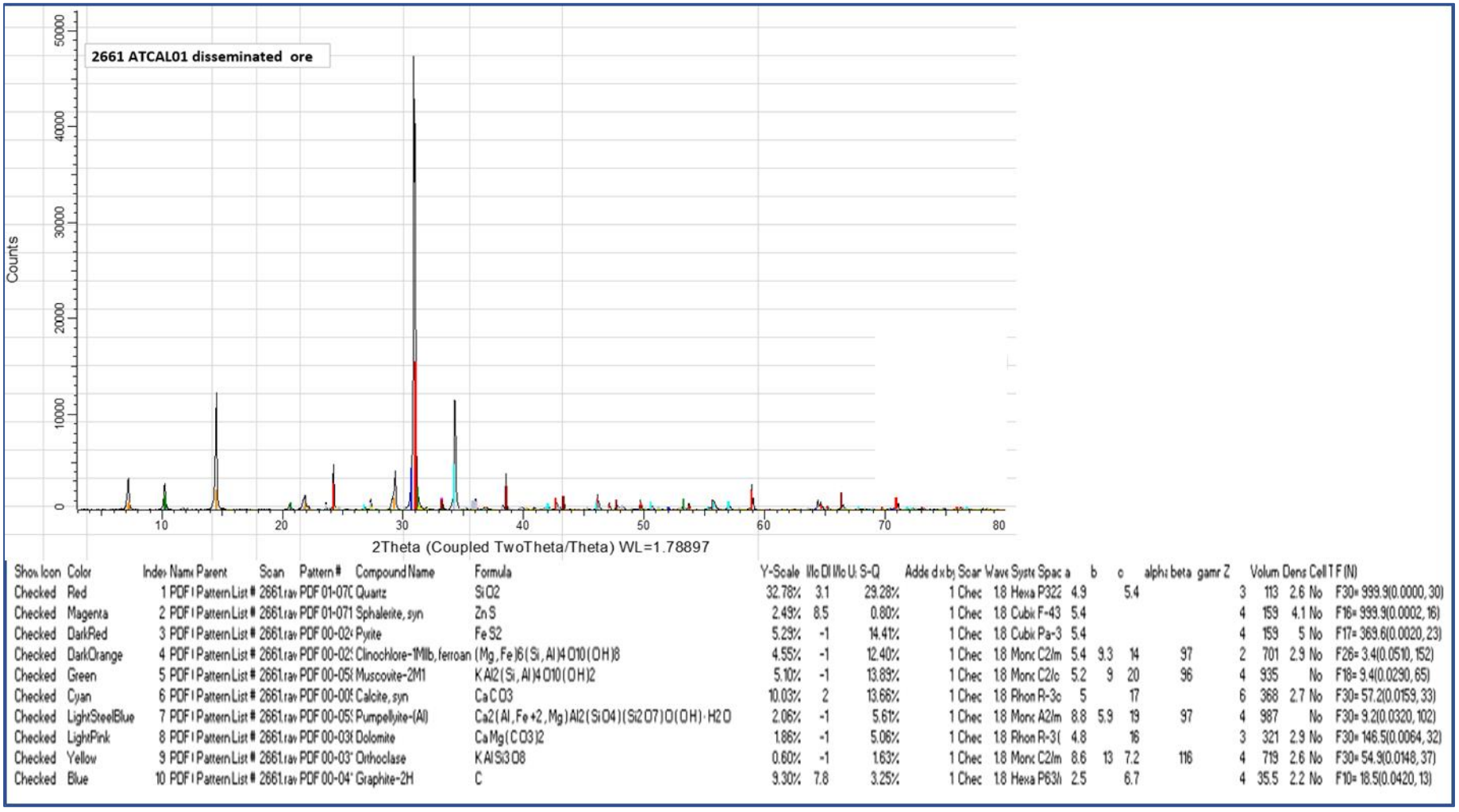
Appendix 6B: Continued……..

Molecular proportions of components

Specimen name	Molecular proportions of components			Percentage of components		
	A	C	F	A	C	F
Grey gneiss	0.0475	0.0294	0.0109	54.1	33.5	12.4
Quartzite	0.0744	0.0852	0.0042	45.4	52	2.6
Hornblende gneiss	0.0901	0.0103	0.2193	28.2	3.2	68.6
Amphibolite	0.153	0.16878	0.2437	27.1	29.8	43.1
Amphibolite-Quartz granulite	0.1412	0.1374	0.1341	34.2	33.3	32.5
Biotite-Garnet-Quartz granulite	0.0233	0.0433	0.0114	29.9	55.5	14.6
Quartzo-Feldspathic gneiss	0.025	0.0173	0.0017	56.8	39.3	3.9
Quartzo-Feldspathic gneiss	0.0087	0.0021	0.0016	70.2	16.9	12.9
Calc-Silicate gneiss	0.0169	0.0098	0.0036	55.8	32.3	11.9
K-feldspathic gneiss	0.1697	0.0139	0.1061	58.6	4.8	36.6
Quartzo-feldspathic gneiss	0.1696	0.0507	0.1025	52.5	15.7	31.8
Garnet-Quartzo-feldspathic gneiss	0.786	0.0635	0.0067	52.8	42.7	4.5
Biotite-Garnet gneiss	0.2199	0.0095	0.0982	67.1	2.9	30
Amphibolite	0.0361	0.0394	0.015	39.9	43.5	16.6
Amphibolite Schist	0.0417	0.0501	0.0316	33.8	40.6	25.6
Biotite Schist	0.063	0.0252	0.0817	37.1	14.8	48.1
Ultramafic granulite	0.1539	0.0535	0.0798	53.6	18.6	27.8

© University of Venda

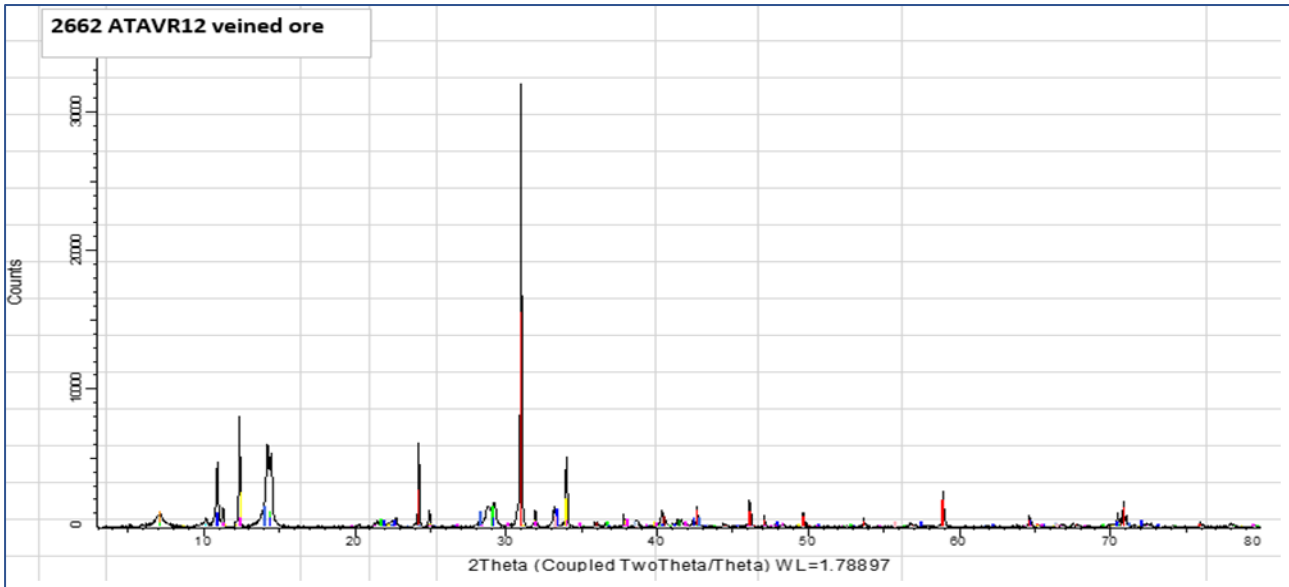
Appendix 7A: X – Ray powder difraction results of dessiminated, veined and brecciated ore samples from Campbell and Artonvilla copper deposits in Musina area



Show	Icon	Color	Index	Name	Parent	Scan	Pattern #	Compound Name	Formula	Y-Scale	Mic	Dl	Mic	U	S-Q	Added	dx by	Scan	Wave	Syste	Spac	a	b	c	alpha	beta	gamr	Z	Volum	Dens	Cell	T F (N)
Checked		Red	1	PDF	Pattern List	#	2661.rav	PDF 01-070	Quartz	SiO2	32.78%	3.1			29.28%		1	Chec	1.8	Hexa	P322	4.9		5.4				3	113	2.6	No	F30= 999.9(0.0000, 30)
Checked		Magenta	2	PDF	Pattern List	#	2661.rav	PDF 01-071	Sphalerite, syn	Zn S	2.49%	8.5			0.80%		1	Chec	1.8	Cubi	F-43	5.4						4	159	4.1	No	F16= 999.9(0.0002, 16)
Checked		DarkRed	3	PDF	Pattern List	#	2661.rav	PDF 00-02	Pyrite	Fe S2	5.23%	-1			14.41%		1	Chec	1.8	Cubi	Pa-3	5.4						4	159	5	No	F17= 369.6(0.0020, 23)
Checked		DarkOrange	4	PDF	Pattern List	#	2661.rav	PDF 00-02	Clinochlore-1Mlb, ferroan	(Mg, Fe)6(Si, Al)4O10(OH)8	4.55%	-1			12.40%		1	Chec	1.8	Monc	C2/m	5.4	9.3	14		97		2	701	2.9	No	F26= 3.4(0.0510, 152)
Checked		Green	5	PDF	Pattern List	#	2661.rav	PDF 00-05	Muscovite-2M1	KAl2(Si, Al)4O10(OH)2	5.10%	-1			13.89%		1	Chec	1.8	Monc	C2/c	5.2	9	20		96		4	935		No	F18= 9.4(0.0290, 65)
Checked		Cyan	6	PDF	Pattern List	#	2661.rav	PDF 00-05	Calcite, syn	Ca C O3	10.03%	2			13.66%		1	Chec	1.8	Rhon	R-3c	5		17				6	368	2.7	No	F30= 57.2(0.0159, 33)
Checked		LightSteelBlue	7	PDF	Pattern List	#	2661.rav	PDF 00-05	Pumpellyite-(Al)	Ca2(Al, Fe+2, Mg)Al2(SiO4)(Si2O7)O(OH)·H2O	2.06%	-1			5.61%		1	Chec	1.8	Monc	A2/m	8.8	5.9	19		97		4	987		No	F30= 9.2(0.0320, 102)
Checked		LightPink	8	PDF	Pattern List	#	2661.rav	PDF 00-03	Dolomite	Ca Mg(C O3)2	1.86%	-1			5.06%		1	Chec	1.8	Rhon	R-3(	4.8		16				3	321	2.9	No	F30= 146.5(0.0064, 32)
Checked		Yellow	9	PDF	Pattern List	#	2661.rav	PDF 00-03	Orthoclase	K Al Si3 O8	0.60%	-1			1.63%		1	Chec	1.8	Monc	C2/m	8.6	13	7.2		116		4	719	2.6	No	F30= 54.9(0.0148, 37)
Checked		Blue	10	PDF	Pattern List	#	2661.rav	PDF 00-04	Graphite-2H	C	9.30%	7.8			3.25%		1	Chec	1.8	Hexa	P63/	2.5		6.7				4	35.5	2.2	No	F10= 18.5(0.0420, 13)

© University of Venda

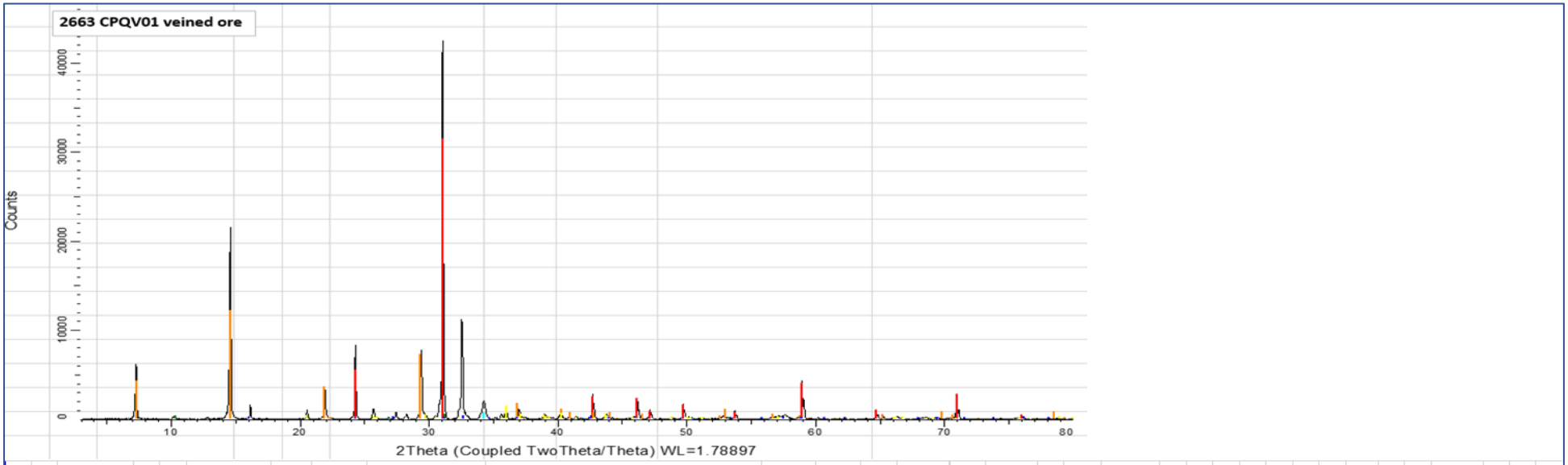
Appendix 7A: X – Ray powder difraction results continued ……..



Show	Icon	Color	Inde	Nam	Parent	Scan	Pattern #	Compound Name	Formula	Y-Scale	I/Ic DB	I/Ic Us	S-Q	d x by	Scan WL	Wav	Systen	Space Gro	a	b	c	alph	beta	gam	Z	Volun	Dens	Cell	F (N)
Checked		Red	1	PDF	Pattern List #4	2662.ra	PDF 01-07	Quartz	Si O2	32.78%	3.05		26.38%	1	Checked	1.8	Hexag	P3221 (154	4.9		5.4				3	113	2.6	No	F30= 999.9(0.0000, 30)
Checked		Cyan	2	PDF	Pattern List #4	2662.ra	PDF 00-00	Eastonite (Mica)	K - Mg - Fe - Al - Si - O - H2 O	3.46%	-1		8.49%	1	Checked	1.8											0		No	
Unchecke		DarkOrange	3	PDF	Pattern List #4	2662.ra	PDF 00-06	Clinochlore, ferroan, (	(Mg , Fe , Al)6 (Si , Al)4 O10 (O H)8	10.23%	-1			1	Checked	1.8	Monoc	C (0)	5.4	9.3	14		97		2	707		No	F6= 4.2(0.0260, 55)
Checked		DarkOrange	4	PDF	Pattern List #4	2662.ra	PDF 01-07	Vermiculite-2M	Mg3 Si4 O10 (O H)2	3.61%	21.49		0.41%	1	Checked	1.8	Monoc	Cc (9)	5.3	9.2	29		93		4	1409	1.8	No	F30= 225.5(0.0042, 32)
Checked		Lime	5	PDF	Pattern List #4	2662.ra	PDF 00-06	Clinochlore, ferroan	(Mg , Fe , Al)6 (Si , Al)4 O10 (O H)8	4.56%	-1		11.19%	1	Checked	1.8	Monoc	C (0)	5.4	9.3	14		97		2	707		No	F26= 4.6(0.0370, 152)
Checked		RoyalBlue	6	PDF	Pattern List #4	2662.ra	PDF 00-05	Lizardite-1M	(Mg , Fe)3 Si2 O5 (O H)4	4.57%	-1		11.22%	1	Checked	1.8	Monoc	C (0)	5.3	9.2	15		97		4	715	2.5	No	F30= 7.9(0.0300, 128)
Checked		DarkRed	7	PDF	Pattern List #4	2662.ra	PDF 01-07	Almandine, magnesia	(Ca0.51 Mg1.02 Mn0.04 Fe1.43) Al1.98 (Si O4)3	2.36%	2.19		2.64%	1	Checked	1.8	Cubic	Ia-3d (230	12						8	1547	3.9	No	F30= 999.9(0.0000, 30)
Checked		Blue	8	PDF	Pattern List #4	2662.ra	PDF 00-00	Talc Steatite Soapston	3 Mg O ·4 Si O2 · H2 O	4.00%	-1		9.82%	1	Checked	1.8	Monoc	C2/c (15)	5.3	9.1	19		100			887	2.8	No	F30= 2.7(0.0530, 211)
Checked		Green	9	PDF	Pattern List #4	2662.ra	PDF 01-07	Magnetite, syn	Fe3 O4	1.39%	5.05		0.68%	1	Checked	1.8	Cubic	Fd-3m (227	8.4						8	588	5.2	No	F30= 999.9(0.0002, 30)
Checked		Yellow	10	PDF	Pattern List #4	2662.ra	PDF 00-02	Grunerite, (Amosite)	Fe5.5 Mg1.5 Si8 O24 H2	7.68%	-1		18.86%	1	Checked	1.8	Monoclinic		9.5	18	5.3		102			903		No	F19= 0.5(0.0780, 447)
Checked		Fuchsia	11	PDF	Pattern List #4	2662.ra	PDF 01-08	Magnesiocummingtor	(Fe3.16 Mg3.84) (Si8 O22 (O H)2)	1.99%	0.69		7.08%	1	Checked	1.8	Monoc	C2/m (12)	9.5	18	5.3		102		2	897	3.3	No	F30= 999.9(0.0000, 31)
Checked		Magenta	12	PDF	Pattern List #4	2662.ra	PDF 01-07	Iron Oxide	Fe2 O3	0.64%	2.9		0.54%	1	Checked	1.8	Rhomb	R-3c (167)	5		14				6	291	5.5	No	F30= 604.9(0.0015, 32)
Checked		LightSteelBlue	13	PDF	Pattern List #4	2662.ra	PDF 00-04	Pyrite	Fe S2	1.32%	1.6		2.03%	1	Checked	1.8	Cubic	Pa-3 (205)	5.4						4	159	5	No	F27= 97.8(0.0095, 29)
Checked		LightPink	14	PDF	Pattern List #4	2662.ra	PDF 01-07	Sphalerite, syn	Zn S	2.28%	8.36		0.67%	1	Checked	1.8	Cubic	F-43m (216	5.4						4	158	4.1	No	F16= 999.9(0.0003, 16)

© University of Venda

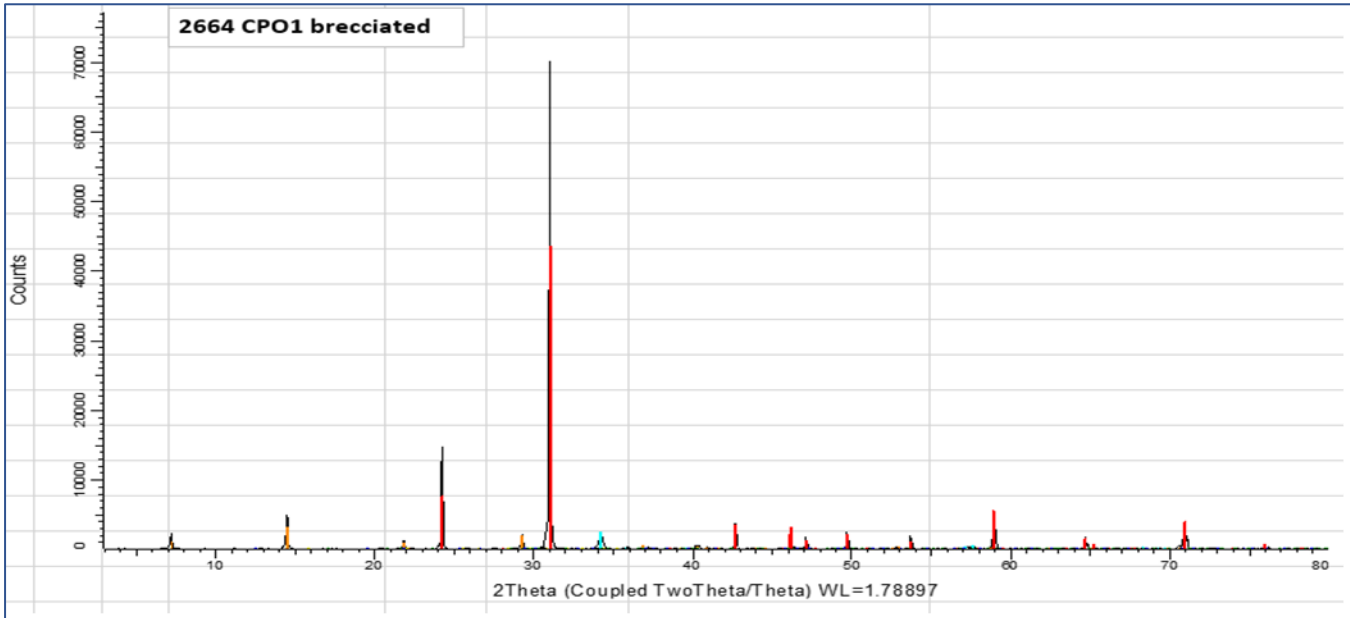
Appendix 7A: X – Ray powder difraction results continued …….



Show	Icon	Color	Inde	Nam	Parent	Scan	Pattern #	Compound Name	Formula	Y-Scale	I/Ic DB	I/Ic Us	S-Q	d x by	Scan WL	Wav	Systen	Space Gro	a	b	c	alph	beta	gam	Z	Volun	Dens	Cell	F (N)
Checked		Red	1	PDF	Pattern List #4	2663.ra	PDF 01-07	Quartz	Si O2	66.61%	3.05		39.45%	1	Checked	1.8	Hexag	P3221 (154	4.9		5.4				3	113	2.6	No	F30= 999.9(0.0000, 30)
Unchecke		Magenta	2	PDF	Pattern List #4	2663.ra	PDF 01-07	Sphalerite, syn	Zn S	0.20%	8.49			1	Checked	1.8	Cubic	F-43m (21	5.4						4	159	4.1	No	F16= 999.9(0.0002, 16)
Checked		DarkRed	3	PDF	Pattern List #4	2663.ra	PDF 00-02	Pyrite	Fe S2	0.21%	-1		0.37%	1	Checked	1.8	Cubic	Pa-3 (205)	5.4						4	159	5	No	F17= 369.6(0.0020, 23)
Checked		DarkOrange	4	PDF	Pattern List #4	2663.ra	PDF 00-02	Clinochlore-1MIIb, fer	(Mg , Fe)6 (Si , Al)4 O10 (O H)8	25.87%	-1		46.73%	1	Checked	1.8	Monoc	C2/m (12)	5.4	9.3	14		97		2	701	2.9	No	F26= 3.4(0.0510, 152)
Checked		Green	5	PDF	Pattern List #4	2663.ra	PDF 00-05	Muscovite-2M1	K Al2 (Si , Al)4 O10 (O H)2	1.21%	-1		2.19%	1	Checked	1.8	Monoc	C2/c (15)	5.2	9	20		96		4	935		No	F18= 9.4(0.0290, 65)
Checked		Cyan	6	PDF	Pattern List #4	2663.ra	PDF 00-00	Calcite, syn	Ca C O3	1.69%	2		1.53%	1	Checked	1.8	Rhomt	R-3c (167)	5		17				6	368	2.7	No	F30= 57.2(0.0159, 33)
Unchecke		LightSteelBlue	7	PDF	Pattern List #4	2663.ra	PDF 00-05	Pumpellyite-(Al)	Ca2 (Al , Fe +2 , Mg) Al2 (Si O4) (Si2 O7) O (O H	2.00%	-1			1	Checked	1.8	Monoc	A2/m (12)	8.8	5.9	19		97		4	987		No	F30= 9.2(0.0320, 102)
Unchecke		LightPink	8	PDF	Pattern List #4	2663.ra	PDF 00-03	Dolomite	Ca Mg (C O3)2	1.86%	-1			1	Checked	1.8	Rhomt	R-3 (148)	4.8		16				3	321	2.9	No	F30= 146.5(0.0064, 32)
Checked		Blue	9	PDF	Pattern List #4	2663.ra	PDF 00-00	Orthoclase	Al2 O3 · K2 O ·6 Si O2	0.91%	-1		1.64%	1	Checked	1.8	Monoc	C2/m (12)	8.5	13	7.2		116			700	2.6	No	F30= 2.5(0.0930, 131)
Unchecke		Lime	10	PDF	Pattern List #4	2663.ra	PDF 01-08	Ankerite	Ca1.01 Mg0.45 Fe0.54 (C O3)2	2.73%	3			1	Checked	1.8	Rhomt	R-3 (148)	4.8		16				3	325	3.1	No	F30= 999.9(0.0000, 31)
Checked		Yellow	11	PDF	Pattern List #4	2663.ra	PDF 01-07	Epidote	Ca2 Al2.16 Fe0.84 Si3 O13 H	3.57%	0.87		7.41%	1	Checked	1.8	Monoc	P21/m (11	8.9	5.6	10		115		2	459	3.5	No	F30= 199.9(0.0038, 39)
Checked		Black	12	PDF	Pattern List #4	2663.ra	PDF 00-00	Hematite	Fe2 O3	0.38%	-1		0.69%	1	Checked	1.8	Rhomt	R-3c (167)	5		14				6	300	5.3	No	F26= 11.4(0.0500, 46)

© University of Venda

Appendix 7A: X – Ray powder difraction results continued …….



Show	Icon	Color	Inde	Nam	Parent	Scan	Pattern #	Compound Name	Formula	Y-Scale	I/Ic DB	I/Ic Us	S-Q	d x by	Scan WL	Wav	System	Space Gro	a	b	c	alph	beta	gam	Z	Volun	Den	Cell	F (N)
Checked		Red	1	PDF	Pattern List #4	2664.ra	PDF 01-07	Quartz	Si O2	62.17%	3.05		64.11%	1	Checked	1.8	Hexag	P3221 (15	4.9		5.4				3	113	2.6	No	F30= 999.9(0.0000, 30)
Checked		DarkOrange	2	PDF	Pattern List #4	2664.ra	PDF 00-02	Clinochlore-1MIIb, fer	(Mg , Fe)6 (Si , Al)4 O10 (O H)8	6.65%	-1		20.92%	1	Checked	1.8	Monoc	C2/m (12)	5.4	9.3	14		97		2	701	2.9	No	F26= 3.4(0.0510, 152)
Checked		Yellow	3	PDF	Pattern List #4	2664.ra	PDF 00-00	Anorthite, sodian, ord	(Ca , Na) (Al , Si)2 Si2 O8	0.21%	-1		0.66%	1	Checked	1.8	Triclini	C-1 (2)	8.2	13	7.1	94	116	90	4	334	2.7	No	F19= 5.3(0.0850, 42)
Checked		Cyan	4	PDF	Pattern List #4	2664.ra	PDF 00-03	Chalcopyrite	Cu Fe S2	3.44%	-1		10.84%	1	Checked	1.8	Tetrag	I-42d (122	5.3		10				4	292	4.2	No	F30= 159.5(0.0052, 36)
Checked		Black	5	PDF	Pattern List #4	2664.ra	PDF 01-07	Epidote	Ca2 Al2.16 Fe0.84 Si3 O13 H	0.55%	0.87		1.99%	1	Checked	1.8	Monoc	P21/m (11	8.9	5.6	10		115		2	459	3.5	No	F30= 199.9(0.0038, 39)
Checked		ForestGreen	6	PDF	Pattern List #4	2664.ra	PDF 01-07	Titanite, syn	Ca Ti (Si O4) O	0.31%	1.52		0.64%	1	Checked	1.8	Monoc	P21/a (14)	7.1	8.7	6.6		114		4	370	3.5	No	F30= 332.5(0.0023, 39)
Checked		Red	7	PDF	Pattern List #4	2664.ra	PDF 01-07	Iron Oxide	Fe1.766 O3	0.21%	2.73		0.24%	1	Checked	1.8	Rhomb	R-3c (167)	5		14				6	303	4.8	No	F30= 372.7(0.0024, 33)
Checked		Blue	8	PDF	Pattern List #4	2664.ra	PDF 00-00	Apatite-(CaOH), syn	Ca5 (P O4)3 (O H)	0.19%	-1		0.60%	1	Checked	1.8	Hexag	P63/m (17	9.4		6.9				2	529	3.1	No	F30= 54.6(0.0157, 35)

© University of Venda

Appendix 7.B: X-ray fluorescence spectroscopy results from Campbell and Artonvilla copper deposits in Musina area

MINTEK
Specialists in mineral and metallurgical technology

200 Malibongwe Drive
Randburg
2125

ANALYTICAL SERVICES TEST REPORT

XRF Section

Sheet No. / ID: W068663
Project No: MNC-50002379-20
Date Recieved: 2014/03/25
Date Authorized: 2014/03/28
Samp. Type SOLID
Method: TQK-2364

Customer: MNLArchie Corfield
Address: MNL
E-Mail: ArchieC@mintek.co.za

Sample Name	nls DESCRIPTION	Rep	Semi quant Al %	Si %	P %	S %	Cl %	K %	Ca %	Ti %	V %
W068663/1	WCL/14/2661	1	2.510	**9.919**	0.205	1.122	0.015	0.732	7.622	0.188	0.012
W068663/2	WCL/14/2662	1	0.042	**11.260**	0.218	0.134	0.022	<0.008	0.504	0.126	0.006
W068663/3	WCL/14/2663	1	1.670	**15.640**	0.219	1.203	0.021	<0.009	2.369	0.077	0.005
W068663/4	WCL/14/2664	1	0.351	**17.270**	0.380	1.228	0.019	<0.007	1.095	0.215	0.007

Sample Name	nls DESCRIPTION	Rep	Cr %	Mn %	Fe %	Co ppm	Ni ppm	Cu ppm	Zn ppm	Ga ppm	Ge ppm
W068663/1	WCL/14/2661	1	0.021	0.385	7.031	98.000	266.300	433.100	5969.000	23.200	8.900
W068663/2	WCL/14/2662	1	0.059	0.094	17.890	153.000	279.600	92.700	197.000	16.200	3.400
W068663/3	WCL/14/2663	1	0.012	0.022	7.421	120.000	148.900	14950.000	41.800	16.800	2.400
W068663/4	WCL/14/2664	1	0.018	0.035	6.148	110.000	205.800	16430.000	49.800	<2.300	2.200

Sample Name	nls DESCRIPTION	Rep	As ppm	Se ppm	Br ppm	Rb ppm	Sr ppm	Y ppm	Zr ppm	Nb ppm	Mo ppm
W068663/1	WCL/14/2661	1	2.100	3.200	1.700	67.000	20.400	18.900	113.800	11.500	10.700
W068663/2	WCL/14/2662	1	21.300	<0.900	2.700	7.600	6.900	12.500	39.700	7.300	<1.900
W068663/3	WCL/14/2663	1	<0.900	1.900	3.000	6.400	351.700	14.300	78.100	3.900	15.300
W068663/4	WCL/14/2664	1	<0.800	1.200	1.200	1.400	47.200	16.500	141.300	8.800	8.500

COMMENTS

Elements from Al to Ca are unreliable as these elements are too light and were not determined under vacuum.

Authorized by:
makatso Mokgosi

EndOfLIMSDesktopMFields

The results relate only to the items tested

Accredited : ASD-MET-OES-SP005;ASD-MET-AAS-SP001;ASD-MET-C16/26;ASD-MET-C06/37;ASD-MET-SPT006;ASD-MET-SPT007;
ASD-MET-SPT008;ASD-MET-FA002;ASD-MET-XRF002;ASD-MET-XRF004;ASD-MET-XRF019

© University of Venda

Appendix 7B: Continued…….

MINTEK
Specialists in mineral and metallurgical technology

200 Malibongwe Drive
Randburg
2125

ANALYTICAL SERVICES TEST REPORT

XRF Section

Sheet No. / ID: W068663
Project No: MNC-50002379-20
Date Recieved: 2014/03/25
Date Authorized: 2014/03/28
Samp. Type SOLID
Method: TQK-2364

Customer: MNLArchie Corfield
Address: MNL
E-Mail: ArchieC@mintek.co.za

Sample Name	nls DESCRIPTION	Rep		Ag ppm	Cd ppm	In ppm	Sn ppm	Sb ppm	Te ppm	I ppm	Cs ppm	Ba ppm
W068663/1	WCL/14/2661	1		5.400	16.900	<0.500	15.200	5.400	<0.900	<1.800	3.700	53.000
W068663/2	WCL/14/2662	1		<0.700	2.400	<0.500	2.100	2.500	1.700	<1.800	3.100	24.800
W068663/3	WCL/14/2663	1		<0.600	1.300	<0.400	2.400	2.300	1.000	1.600	<3.100	16.500
W068663/4	WCL/14/2664	1		<0.500	0.600	<0.300	<0.700	2.100	<0.800	1.300	<2.900	<4.400

Sample Name	nls DESCRIPTION	Rep		Ba ppm	La ppm	Ce ppm	Hf ppm	Ta ppm	W ppm	Hg ppm	Tl ppm	Pb ppm
W068663/1	WCL/14/2661	1		53.000	18.200	29.300	<15.000	115.000	<24.000	4.200	3.800	115.800
W068663/2	WCL/14/2662	1		24.800	7.700	8.800	<10.000	145.900	<11.000	2.300	2.000	9.700
W068663/3	WCL/14/2663	1		16.500	24.300	45.600	<79.000	<99.000	<11.000	2.200	1.400	2.800
W068663/4	WCL/14/2664	1		<4.400	17.300	38.100	<77.000	<97.000	<11.000	3.100	2.600	2.100

Sample Name	nls DESCRIPTION	Rep		Bi ppm	Th ppm	U ppm
W068663/1	WCL/14/2661	1		7.300	<1.300	11.400
W068663/2	WCL/14/2662	1		7.800	<4.000	6.200
W068663/3	WCL/14/2663	1		4.000	12.800	<3.300
W068663/4	WCL/14/2664	1		<1.500	4.600	4.900

COMMENTS
Elements from Al to Ca are unreliable as these elements are too light and were not determined under vacuum.

Authorized by:
makatso Mokgosi

EndOfLIMSDesktopMFields

The results relate only to the items tested
Accredited : ASD-MET-OES-SP005;ASD-MET-AAS-SP001;ASD-MET-C16/26;ASD-MET-C06/37;ASD-MET-SPT006;ASD-MET-SPT007;
ASD-MET-SPT008;ASD-MET-FA002;ASD-MET-XRF002;ASD-MET-XRF004;ASD-MET-XRF019

Sample ID

WCL/14/2661 = ATCAL01 = Disseminated ore

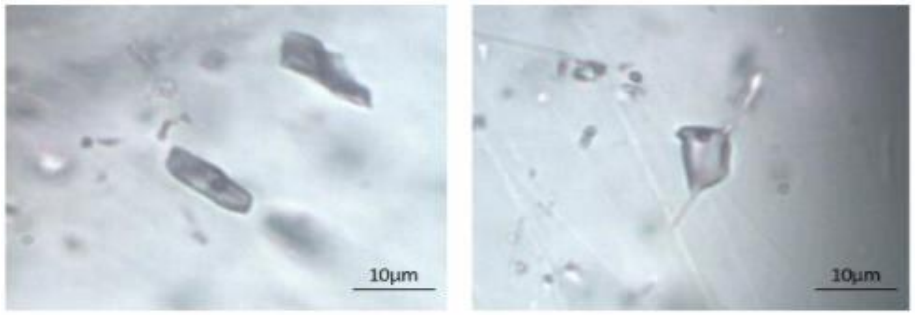
WCL/14/2662 = ATAVR12 = Veined ore

WCL/14/2663 = CPQV01 = Veined ore

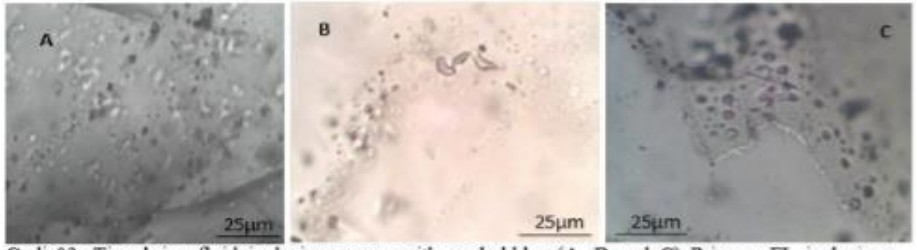
WCL/14/2664 = CAMP01 = Brecciated ore

© University of Venda

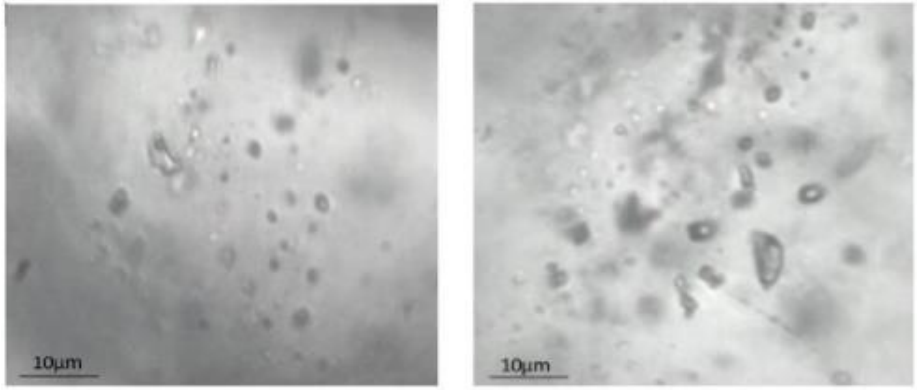
Appendix 9A: Fluid inclusion photographs Appendix 9AI: Fluid inclusions photographs for Campbell copper deposit



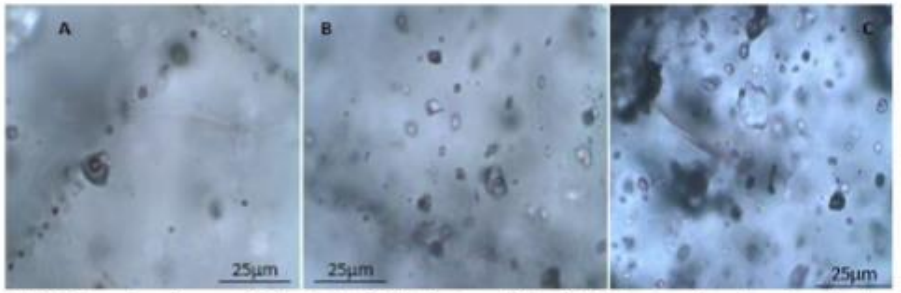
Cpdis02: Primary L+V phases brine fluid inclusions within qtz crystal.



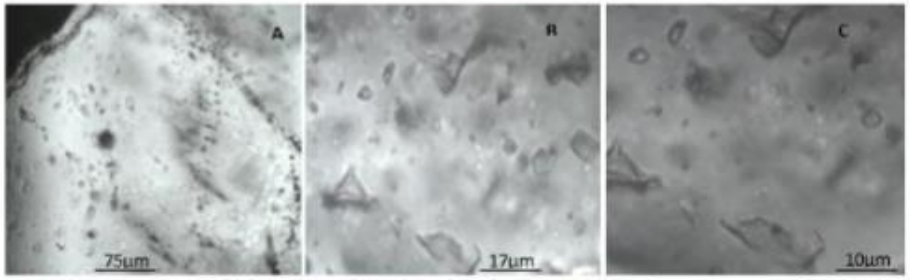
Cpdis02: Tiny brine fluid inclusions some with no bubbles (A, B and C) Primary FL inclusions following the milky qtz crystal zones and (C) along the crystal growth zones.



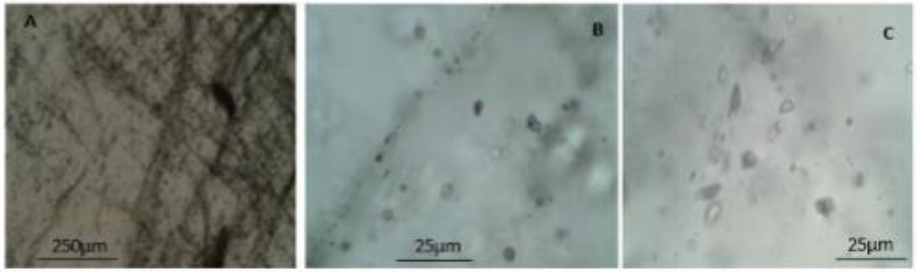
Cp01: Brine fluid inclusions with few fluid inclusions with bubbles within the milky qtz crystal.



A4: (A) Secondary, large and high salinity fluid inclusion and tiny fluid inclusions along the micro-fractures within qtz crystal, (B) both secondary and primary fluid inclusions and (C) large fluid inclusion with small bubble (5% V) with tiny fluid inclusions scattered within qtz crystal.



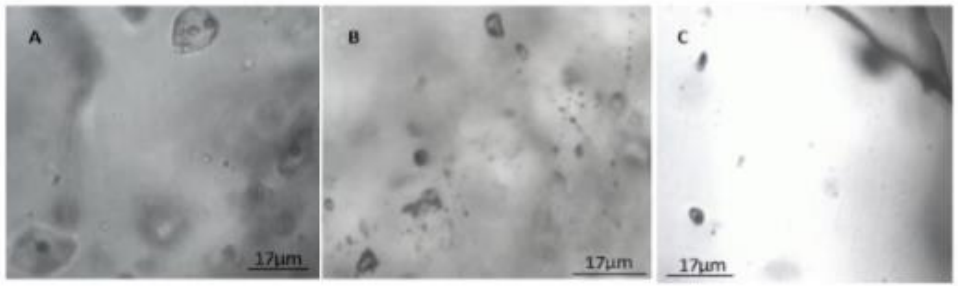
Cp02: (A) Secondary fluid inclusions along the micro-fractures, photo taken at 20x magnification (B) scattered primary large and high salinity fluid inclusion and tiny fluid inclusions within qtz crystal, (C) Large fluid inclusion with tiny bubble 5% V both.



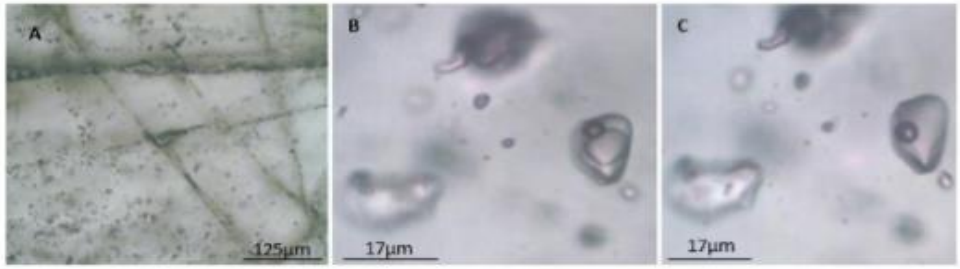
CpQV01: (A) Secondary fluid inclusions along the micro-fractures, photo taken at 20x magnification (B) Secondary brine fluid inclusions along the fractures and (C) both primary and secondary fluid inclusions

© University of Venda

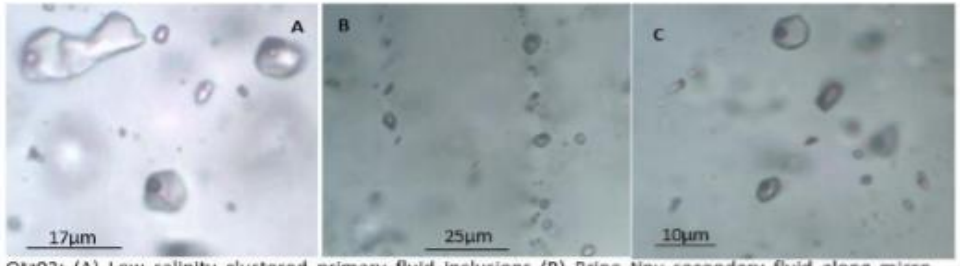
Appendix 9AI: Continued…….



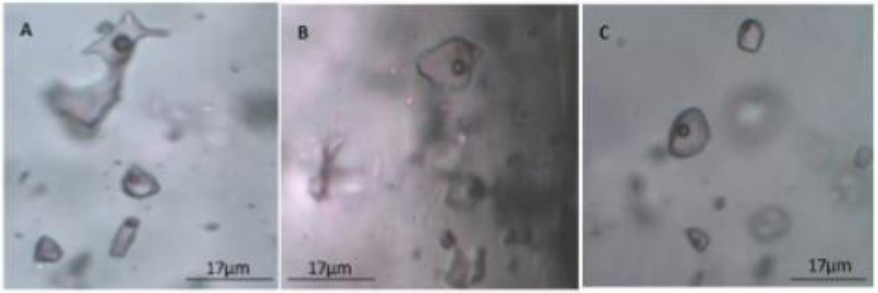
Cp03: (A) Brine fluid inclusion with V + L + S phases (top)with solid phase comprised of halite mineral and 2 high salinity fluid inclusions. (B) Brine primary fluid inclusions and tiny secondary fluid along micro-fractures. (C) Isolated fluid inclusions within the qtz crystals.



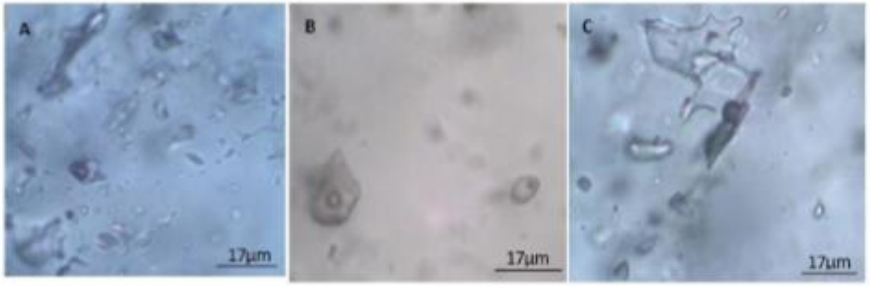
Qtz03: (A) Primary and secondary fluid inclusions with secondary fluid inclusions along the micro-fractures, photo taken at 10x magnification (B) Brine primary fluid inclusion (V + L + ice) upon heating (-30°C)from freezing state and (C) V + L phases at Tm(ice) -10 °C.



Qtz03: (A) Low salinity clustered primary fluid inclusions (B) Brine tiny secondary fluid along micro-fractures. (C) Clustered primary fluid inclusions within the qtz crystals.



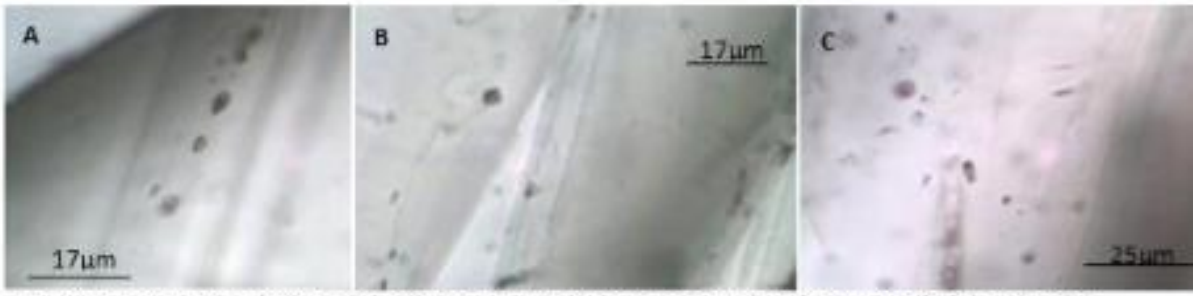
CPQ03: (A) Deformed fluid inclusion within the early qtz generation (B) and (C) Clusters of brine fluid inclusions within the early formed qtz.



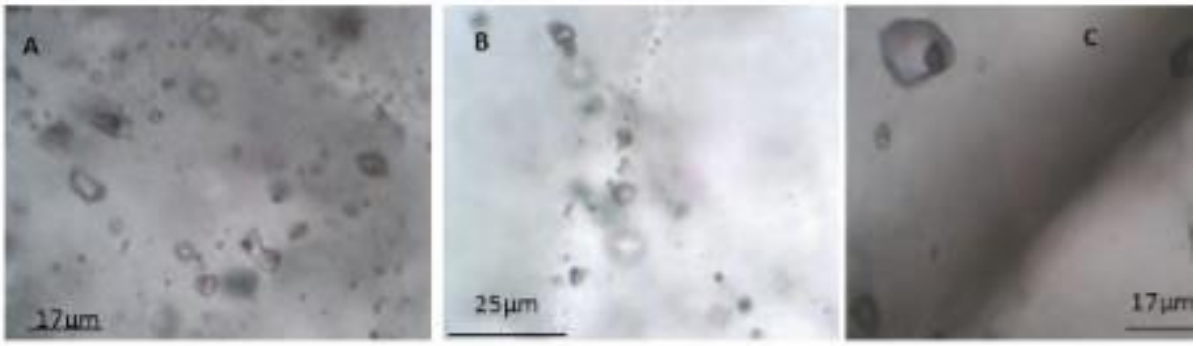
CPQ03: (A) Brine fluid inclusion with 60% volume of Vapour within the late qtz generation (B) Brine fluid inclusions within the late formed qtz and (C) Two large fluid inclusions with tiny fluid inclusions within the late formed qtz.

© University of Venda

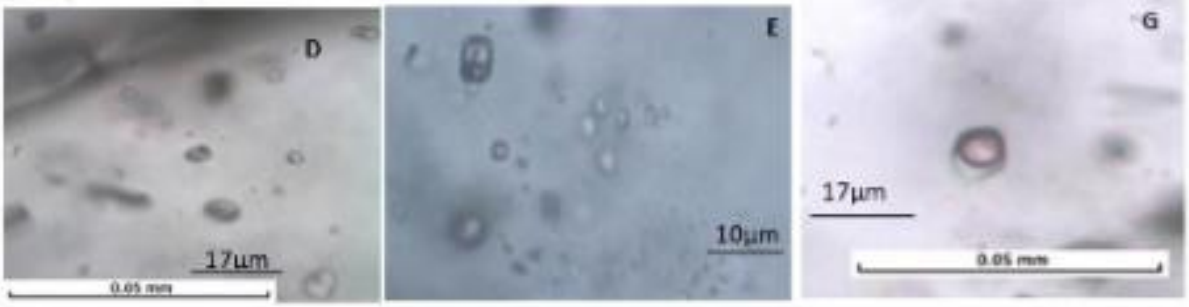
Appendix 9AII: Fluid inclusions photographs for Artonvilla copper deposit



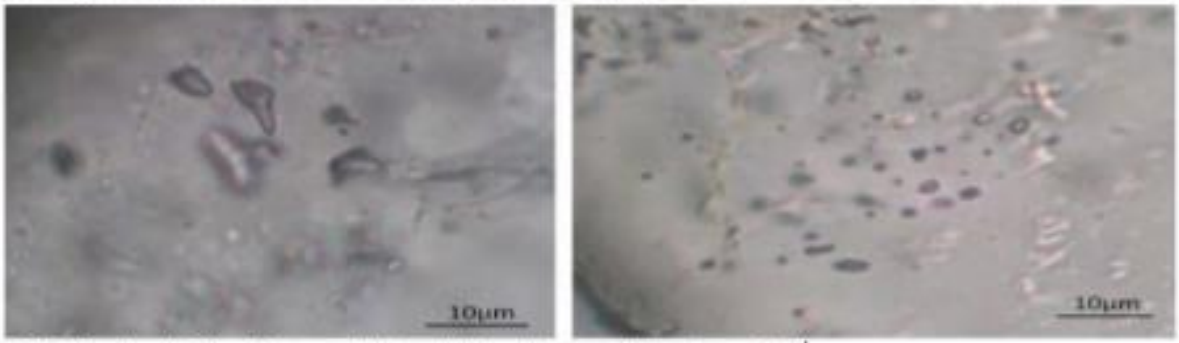
ATcal01: Brine Fluid inclusions, (A) Secondary FL inclusions in qtz within the host rock, (B) Isolated FL inclusion in calcite and (C) Secondary FL inclusion in calcite in sample Atcal01.



ATavr12: Brine Fluid inclusions, (A) clustered primary FL inclusions in between garnets and sulphides mineralisation, (B) Secondary FL inclusions along the fractures (C) Isolated primary FL inclusion in younger zone of qtz.



ATavr12: Brine Fluid inclusions, (D) clustered primary FL inclusions in older qtz zone, (D and F) L+V+D primary FL inclusions with halite as solid phase and (G) vapour rich L + V isolated fluid inclusion.



AT02: Clustered $CH_4 - N_2$ gas and brine fluid inclusions within qtz crystal.

© University of Venda

Appendix 9BI: Characteristics of fluid inclusions identified within Campbell copper deposit samples

Quartz	Sample	Plate No.	Inclusion type		Size (µm) %V Composition				Temperature (%)					Daughter mi	Salinity	Drawing (Page No.	Photo No.	Comments: specific fluid
						Liquid (L)	Vapour(V)	Solids (S	Te	Tm(ice)	xNaCl w	Th (L)	Th (L) D			Fluid Incl Flip file		
Quartz v	Cpdis01	Cp01 A	P	Brine	3x5	✓	✓	-		-7.5	11.1	168.1				Cp01 Pg 35	1 Cp01 A	Isolated
(which qtz)		Cp01 A	P	Brine	3x3	✓	✓	-		-1.2	2.1	146				Cp01 Pg 35	2 Cp01 A	Scattered
		Cp01 A	P	Brine	3x5	✓	✓	-		-4.2	6.7	110				Cp01 Pg 35	2 Cp01 A	
		Cp01 A	P	Brine	2x3	✓	✓	-		-5.3	8.3	137.8				Cp01 Pg 35	2 Cp01 A	
		Cp01 A	P	Brine	2x2	✓	✓	-		-3.2	5.3	153				Cp01 Pg 35	2 Cp01 A	
		Cp01 A	P	Brine	2x3	✓	✓	-		-1.2	2.1	82.5				Cp01 Pg 35	2 Cp01 A	
		Cp01 A	P	Brine	2x2	✓	✓	-		-5.4	8.4	108.3				Cp01 Pg 35	3 Cp01 A	Clusters
		Cp01 A	P	Brine	5x4	✓	✓	-		-5.4	8.4	105				Cp01 Pg 35	3 Cp01 A	
		Cp01 A	P	Brine	2x3	✓	✓	-		-3.2	5.3	125				Cp01 Pg 35	3 Cp01 A	
		Cp01 A	P	Brine	4x3	✓	✓	-		-1.3	2.2	78.5				Cp01 Pg 35	4 Cp01 A	Along fracture
		Cp01 A	S	Brine	4x3	✓	✓	-		0.8	1.4	110				Cp01 Pg 35	4 Cp01 A	Along fracture
		Cp01 A	S	Brine	4x3	✓	✓	-		-1.3	2.2	144.5				Cp01 Pg 35	4 Cp01 A	Along fracture
		Cp01 A	S	Brine	4x2	✓	✓	-		-5.5	8.5	142				Cp01 Pg 35	4 Cp01 A	Along fracture
		Cp01 A	S	Brine	2x2	✓	✓	-		-5.2	8.1	142.3				Cp01 Pg 36	4 Cp01 A	Along fracture
Quartz v	Cpdis02	Cpdis02 A	S	Gas	4x3	✓	✓	-		-	-	-118				Cpdis02 Pg 27	1 Cpdis02 A	Frature
(which qtz)		Cpdis02 A	S	Gas	4x2	✓	✓	-		-	-	-108				Cpdis02 Pg 27	1 Cpdis02 A	Frature
		Cpdis02 A	S	Gas	4x3	✓	✓	-		-	-	-107				Cpdis02 Pg 27	1 Cpdis02 A	Frature
		Cpdis02 A	P	Gas	5x3	✓	✓	-		-	-	-108				Cpdis02 Pg 27	2 Cpdis02 A	Cluster
		Cpdis02 A	P	Gas	7x5	✓	✓	-		-	-	-109				Cpdis02 Pg 27	2 Cpdis02 A	Cluster
		Cpdis02 A	P	Gas	4x3	✓	✓	-		-	-	-118				Cpdis02 Pg 27	2 Cpdis02 A	near grwoth zone
		Cpdis02 A	P	Gas	4x3	✓	✓	-		-	-	-101.4				Cpdis02 Pg 27	3 Cpdis02 A	Isolated
		Cpdis02 A	P	Gas	5x3	✓	✓	-		-	-	-109.3				Cpdis02 Pg 27	3 Cpdis02 A	Isolated
		Cpdis02 A	P	Gas	2x2	✓	✓	-		-	-	-112				Cpdis02 Pg 27	3 Cpdis02 A	Isolated
		Cpdis02 A	P	Brine	10x4 10% V	✓	✓	-		-7.7	11.3	107.4				Cpdis02 Pg 28	4 Cpdis02 A	Clusters
		Cpdis02 A	P	Brine	5x3 20% V	✓	✓	-		-3.4	5.6	98.3				Cpdis02 Pg 28	4 Cpdis02 A	Clusters
		Cpdis02 A	P	Brine	5x7 10% V	✓	✓	-		-18.3	21.2	82.3				Cpdis02 Pg 28	4 Cpdis02 A	Clusters
		Cpdis02 A	S	Brine	5x3 10% V	✓	✓	-		-1.3	2.2	141				Cpdis02 Pg 28	4 Cpdis02 A	Clusters
		Cpdis02 A	S	Brine	3x2 10% V	✓	✓	-		-13.4	17.3	118				Cpdis02 Pg 28	4 Cpdis02 A	Clusters
Quartz v	Cp02	Cp02 A	p	Brine	3x6 10% V	✓	✓	-		-13.5	17.3	144.9				Cp02 Pg 32	1 Cp02 A	
(which qtz)		Cp02 A	P	Brine	2x4 10% V	✓	✓	-		-13.4	17.3	148.1				Cp02 Pg 32	1 Cp02 A	
		Cp02 A	P	Brine	2x2 10% V	✓	✓	-		-13.4	17.3	128.5				Cp02 Pg 32	1 Cp02 A	
		Cp02 A	P	Brine	2x3 10% V	✓	✓	-		-13.5	17.3	148.1				Cp02 Pg 32	1 Cp02 A	
		Cp02 A	P	Brine	2x3 10% V	✓	✓	-		-13.2	17.1	148.3				Cp02 Pg 32	1 Cp02 A	
		Cp02 A	P	Brine	3x5 10% V	✓	✓	-		-13.8	17.6	121.1				Cp02 Pg 32	1 Cp02 A	
		Cp02 A	P	Brine	2x3 10% V	✓	✓	-		-13.8	17.6	121.1				Cp02 Pg 32	1 Cp02 A	
		Cp02 A	P	Brine	3x5 10% V	✓	✓	-		-10.3	14.3	151.5				Cp02 Pg 32	1 Cp02 A	
		Cp02 B	P	Brine	4x3 10% V	✓	✓	-		-9.2	13.1	103.4				Cp02 Pg 32	1 Cp02 B	Brine scattered
		Cp02 B	P	Brine	12x4 10% V	✓	✓	-		-5.4	8.4	110.3				Cp02 Pg 32	1 Cp02 B	
		Cp02 B	P	Brine	5x4 10% V	✓	✓	-		-8.1	11.8	103.4				Cp02 Pg 32	1 Cp02 B	
		Cp02 B	P	Brine	8x3 10% V	✓	✓	-		-8.1	11.8	103.4				Cp02 Pg 32	1 Cp02 B	
		Cp02 B	P	Brine	3x3 10% V	✓	✓	-		-9.8	13.7	103.01				Cp02 Pg 32	1 Cp02 B	
		Cp02 B	P	Brine	3x2 10% V	✓	✓	-		-9.8	13.7	103.1				Cp02 Pg 32	1 Cp02 B	
		Cp02 B	P	Brine	12x5 10% V	✓	✓	-		-5.4	8.4	110.2				Cp02 Pg 32	1 Cp02 B	
		Cp02 B	P	Brine	6x4 10% V	✓	✓	-		-19.3	21.9	110.3				Cp02 Pg 32	1 Cp02 B	
		Cp02 B	P	Brine	6x2 10% V	✓	✓	-		-19.3	21.9	114.2				Cp02 Pg 32	1 Cp02 B	
Quartz v	A4	A4 A	S	Brine	5x5 20%V	✓	✓	-		-1.4	2.4	210.4				A4 A Pg 19	A4 A	Along the fractures, dark
(which qtz)		A4 A	P	Brine	2x2 10%V	✓	✓	-		-8.3	12.0	119.3				A4 A Pg 19	A4 A	
		A4 A	S	Brine	1x3 10%V	✓	✓	-		-8.3	12.0	145.6				A4 A Pg 19	A4 A	Along the fractures, dark
		A4 A	S	Brine	1x3 10%V	✓	✓	-		-11.3	15.3	114.3				A4 A Pg 19	A4 A	Clusters
		A4 A	P	Brine	5x4 10%V	✓	✓	-		-5.2	8.1	152.2				A4 A Pg 19	A4 A	Clusters
		A4 A	P	Brine	4x2 10%V	✓	✓	-		-3.1	5.1	152				A4 A Pg 19	A4 A	Clusters
		A4 A	P	Brine	2x1 10%V	✓	✓	-		-2.1	3.5	142.9				A4 A Pg 19	A4 A	Clusters
		A4 A	P	Brine	2x1 10%V	✓	✓	-		-2.1	3.5	142.9				A4 A Pg 19	A4 A	Clusters
		A4 A	P	Brine	4x3 10%V	✓	✓	-		-3.2	5.3	125				A4 A Pg 19	A4 A	
		A4 A	S	Brine	3x2 10%V	✓	✓	-		-8.4	12.2	150.7				A4 A Pg 19	A4 A	Along the fracture

© University of Venda

Appendix 9BI: Continue…….

		A4 B	P	Brine	7x4 10%V	√	√	-		-8.6	12.4	125.3				A4_A Pg 19	A4_A	Deformed
		A4 B		Brine	6x2 10%V	√	√	-		-1.4	2.4	117				A4_A Pg 19	A4_A	
		A4 B		Brine	5x2 10%V	√	√	-		-5.1	8.0	124				A4_A Pg 19	A4_A	
		A4 B		Brine	6x4 10%V	√	√	-		-5	7.9	124				A4_A Pg 19	A4_A	
		A4 B		Brine	4x2 10%V	√	√	-		-1.4	2.4	131				A4_A Pg 19	A4_A	
		A4 C		Brine	15x10 5%V	√	√	-		-2.2	3.7	99.8				A4_A Pg 19	A4_A	
		A4 C		Brine	6x8 5%V	√	√	-		-4.2	6.7	122.3				A4_A Pg 19	A4_A	
Quartz v	Cp03	Cp03 B	P	Brine	12x8 15% V	√	√	HL/CC		-3.1	5.1	91.3	HAL 180	-		Cp03_Pg 33	1_Cp03_B	Brine with halite, carbon
(which c	with zon	Cp03 B	P	Brine	6x4 40% V	√	√	-		-17.4	20.5	152.3				Cp03_Pg 33	1_Cp03_B	Brine with vapour
	rings qtz	Cp03 B	P	Brine	7x5 10% V	√	√	-		-7.2	10.7	112.6				Cp03_Pg 33	1_Cp03_B	
	different	Cp03 A	P	Brine	4x3 15% V	√	√	-		-12.4	16.3	123.5				Cp03_Pg 34	2_Cp03_A	Brine and clustered
	generatic	Cp03 A	P	Brine	5x4 10% V	√	√	-		-8.4	12.2	145.6				Cp03_Pg 34	2_Cp03_A	
		Cp03 A	P	Brine	3x2 10% V	√	√	-		-4.3	6.9	145				Cp03_Pg 34	2_Cp03_A	
		Cp03 A	P	Brine	3x3 10% V	√	√	-		-4.3	6.9	145				Cp03_Pg 34	2_Cp03_A	
		Cp03 A	P	Brine	4x3 10% V	√	√	-		-8.4	12.2	143.2				Cp03_Pg 34	2_Cp03_A	
		Cp03 A	P	Brine	3x3 10% V	√	√	-		-8.4	12.2	117				Cp03_Pg 34	2_Cp03_A	
		Cp03 A	S	Brine	5x6 20% V	√	√	-		-1.3	2.2	157.8				Cp03_Pg 34	3_Cp03_A	Along fracture
		Cp03 A	P	Brine	4x2 10% V	√	√	-		-2.4	4.0	102.3				Cp03_Pg 34	3_Cp03_A	
		Cp03 A	P	Brine	5x3 20% V	√	√	-		-0.9	1.6	117				Cp03_Pg 34	3_Cp03_A	
		Cp03 A	S	Brine	2x2 10% V	√	√	-		-2.4	4.0	113				Cp03_Pg 34	3_Cp03_A	Along fracture
Quartz v	Qtz03	Qtz03A	P	Brine	10%V	√	√	-		-9	12.8					Qtz03 Pg_1	0_Qtz03A	
(which qtz)		Qtz03A	P	Brine	10%V	√	√	-		-4.2	6.7			_		Qtz03 Pg_1	0_Qtz03A	clusters
	chaged t	Qtz03A	P	Brine	10%V	√	√	-		-10.3	14.3			_		Qtz03 Pg_2	0_Qtz03A	clusters
	CPQtz 0	Qtz03A	S	Brine	10%V	√	√	-		-15.2	18.8	117				Qtz03 Pg_2	0_Qtz03A	fractures
		Qtz03A	P	Brine	10%V	√	√	-	-55	-28.2	27.5	88		_		Qtz03 Pg_3	0_Qtz03A	cluster -high salinity
		Qtz03A	P	Brine	10%V	√	√	-		-0.5	0.9	198				Qtz03 Pg_4	0_Qtz03A	clusters
		Qtz03A	P	Brine	10%V	√	√	-		-5.5	8.5	130				Qtz03 Pg_4	0_Qtz03A	clusters
		Qtz03B	P	Brine	10%V	√	√	-		-6.6	10.0	171.5				Qtz03 B Pg_5	1_Qtz03B	Clusters
		Qtz03B	P	Brine	10%V	√	√	-		-12.8	16.7	151.4				Qtz03 B Pg_5	1_Qtz03B	Clusters
		Qtz03B	P	Brine	10%V	√	√	-		-13.5	17.3	169.5				Qtz03 B Pg_5	1_Qtz03B	Clusters
		Qtz03B	P	Brine	10%V	√	√	-		-1.4	2.4	150.8				Qtz03 B Pg_6	2_Qtz03B	Clusters
		Qtz03B	P	Brine	10%V	√	√	-		-6.7	10.1	147				Qtz03 B Pg_6	2_Qtz03B	Clusters
		Qtz03B	P	Brine	10%V	√	√	-		-4.2	6.7	128.6				Qtz03 B Pg_6	2_Qtz03B	Clusters
		Qtz03B	P	Brine	10%V	√	√	-		-3.6	5.9	131.2				Qtz03 B Pg_7	3_Qtz03B	Clusters
		Qtz03B	P	Brine	10%V	√	√	-		-6.3	9.6	127				Qtz03 B Pg_7	3_Qtz03B	Clusters
		Qtz03B	S	Brine	10%V	√	√	-		-0.1	0.2	136.5				Qtz03 B Pg_8	4_Qtz03B	along fracture
		Qtz03B	S	Brine	10%V	√	√	-		-4.3	6.9	128.4				Qtz03 B Pg_8	4_Qtz03B	along fracture
Quartz v	CPQV01	CPQV01A	P	Brine		√	√	-		-3	5.0	65.1				CPQV01 Pg 9		
(which qtz)		CPQV01A	P	Brine		√	√	-		-10.8	14.8	139.3				CPQV01 Pg 9		
		CPQV01A	P	Brine		√	√	-		-8.9	12.7	145.9				CPQV01 Pg 9		
		CPQV01A	P	Brine		√	√	-		-2.3	3.9	223.1				CPQV01 Pg 9		
		CPQV01A	P	Brine		√	√	-		-4.1	6.6	190.3				CPQV01 Pg 9		
		CPQV01A	P	Brine		√	√	-		-25.1	25.6	141.3				CPQV01 Pg 9		
		CPQV01A	P	Brine		√	√	-		-2	3.4	130				CPQV01 Pg 9		
		CPQV01A	P	Brine		√	√	-		-20	22.4	190.3				CPQV01 Pg 9		
		CPQV01A	S	Brine		√	√	-		-6.8	10.2	151.8				CPQV01 Pg 9		
		CPQV01A	S	Brine		√	√	-		-5.1	8.0	151.8				CPQV01 Pg 9		
		CPQV01A	S	Brine		√	√	-		-5.9	9.1	129.4						
Quartz v	CPQ03	CPQ03A	P	Brine	5x4 15%V	√	√	-		-3.2	5.3	135.7				CPQ03 Pg 16	CPQ03 older	
(which c	zoned qt	CPQ03A	P	Brine	3x2 10%V	√	√	-		-2.3	3.9	137.8				CPQ03 Pg 16	no	
		CPQ03A	P	Brine	6x4 15%V	√	√	-		-9.8	13.7	130.8				CPQ03 Pg 16	CPQ03	isolated
		CPQ03A	P	Brine	2x1 10%V	√	√	-		-1.3	2.2	122.4				CPQ03 Pg 16	no photo	
		CPQ03A	P	Brine	4x3 10%V	√	√	-		-1.5	2.6	120.4				CPQ03 Pg 16	no photo	
		CPQ03A	P	Brine	5x1 10%V	√	√	-		-9.7	13.6	118.3				CPQ03 Pg 16	no photo	
		CPQ03A	P	Brine	7x4 10%V	√	√	-		-11.9	15.9	127.5				CPQ03 Pg 16	CPQ03	Clusters
		CPQ03A	P	Brine	3x2 10%V	√	√	-		-11.5	15.5	124.9				CPQ03 Pg 16	CPQ03	Clusters
		CPQ03A	P	Brine	4x4*2 10%V	√	√	-		-3.3	5.4	125.8				CPQ03 Pg 16	CPQ03	Clusters
		CPQ03A	P	Brine	15x5 5%V	√	√	-		-11.8	15.8	118.5				CPQ03 Pg 16	CPQ03	necking down
		CPQ03A	P	Brine	4x3 10%V	√	√	-		-18.8	21.5	118.3				CPQ03 Pg 16	CPQ03	
		CPQ03A	P	Brine	5x4 10%V	√	√	-		-11.5	15.5	121.9				CPQ03 Pg 16	CPQ03	Tube like
		CPQ03B	P	Brine	8x4 15%V	√	√	-		-17.5	20.6	159.2				CPQ03 Pg 17	CPQ03 younger	
		CPQ03B	P	Brine	5x4 10%V	√	√	-		-15.3	18.9	99				CPQ03 Pg 17	CPQ03 younger	
		CPQ03B	P	Brine	4x3 10%V	√	√	-		-4.3	6.9	149.3				CPQ03 Pg 17	CPQ03 younger	
		CPQ03B	P	Brine	15x8 10%V	√	√	-		-11.2	15.2	135.4				CPQ03 Pg 17	CPQ03 younge	deformed
		CPQ03B	P	Brine	12x5 5%V	√	√	-		-12.7	16.6	172				CPQ03 Pg 17	CPQ03 younger	
		CPQ03B	P	Brine	5x4 10%V	√	√	-		-11.2	15.2	125.3				CPQ03 Pg 17	CPQ03 younger	
		CPQ03B	P	Brine	5x3 10%V	√	√	-		-1.2	2.1	135.4				CPQ03 Pg 17	CPQ03 younger	
		CPQ03B	P	Brine	5x4	√	?	-		-3.4	5.6	88.5				CPQ03 Pg 17	CPQ03 younge	one phase liquid phase
		CPQ03B	P	Brine	6x5	√	?	-		-1.3	2.2	94.8				CPQ03 Pg 17	CPQ03 younge	one phase liquid phase
		CPQ03B	P	Brine	6x5	√	?	-		-2.5	4.2	110.4				CPQ03 Pg 17	CPQ03 younge	one phase liquid phase
		CPQ03B	P	Brine	4x4 60%V	√	√	-		-4.5	7.2	140				CPQ03 Pg 17	CPQ03 younge	large bubble

© University of Venda

Appendix 9BII: Fluid Inclusion Characteristics of Campbell and Artonvilla Copper Deposits

Quartz ty	Sample No.	Plate No.	Inclusion type		Size (µm) %V	Composition			Temperature (%)		Salinity			Daughter mineral	Drawing (Page No.)	Photo No.	Comments specific fluid	Geneal Comments
						Liquid (L)	Vapour(V)	Solids (S)	Te	Tm(ice)	xNaCl wt%	Th (L)	Th (L) D		Fluid Incl Flip file			
	Atcal 01	Atcal01	P	Brine	4*2 10%V	X	X			-7.2	10.7	154.4			Atcal01 Pg_10	1_Atcal01_A	cluster lineer form	Calcite is mostly less than 160°C, You use polariser
		Atcal01	P	Brine	3*2 10%V	X	X			-7.8	11.5	104.3			Atcal01 Pg_10	1_Atcal01_A	cluster lineer form	Few fluid inclusions - some fluids are in qtz within host rock
		Atcal01	P	Brine	3*2 10%V	X	X			-7.8	11.5	140.3			Atcal01 Pg_10	1_Atcal01_A	cluster lineer form	some are in calcite at the calcite vein
		Atcal01	P	Brine	4*3 20%V	X	X			-11.8	15.8	192.1			Atcal01 Pg_10	2_Atcal01_A	scattered	isolated - scattered
		Atcal01	P	Brine	3*2 20%V	X	X			-1.3	2.2	180.7			Atcal01 Pg_10	2_Atcal01_A	scattered	
		Atcal01	P	Brine	3*4 20%V	X	X			-14.7	18.4	198.5			Atcal01 Pg_10	3_Atcal01_A	scattered	
		Atcal01	P	Brine	4*2 10%V	X	X			-11.3	15.3	185			Atcal01 Pg_10	3_Atcal01_A	scattered	
						X	X				0.0							
	AVR12	AVR12	P	Brine	3*5 10%V	X	X			-1	1.7	150.3			AVR12 Pg_10	1_AVR12_A	Scattered	Large fluid inclusions - low salinity - high salinity - due to immiscibility
		AVR12	P	Brine	6*2 10%V	X	X			-1.3	2.2	120			AVR12 Pg_10	1_AVR12_A	Scattered	low- is with big vapour - high is with calcite and salt
		AVR12	P	Brine	3*2 10%V	X	X			-5	7.9	144.5			AVR12 Pg_10	1_AVR12_A	Scattered	
		AVR12	P	Brine	4*6 10%V	X	X			-0.5	0.9	126			AVR12 Pg_10	1_AVR12_A	Scattered	
		AVR12	P	Brine	4*2 10%V	X	X			-5.6	8.7	130.6			AVR12 Pg_10	1_AVR12_A	Scattered	
		AVR12	S	Brine	4*3 10%V	X	X			-11.4	15.4	144.4			AVR12 Pg_10	2_AVR12_A	along fracture	
		AVR12	S	Brine	4*2 10%V	X	X			-2.1	3.5	155.7			AVR12 Pg_10	2_AVR12_A	along fracture	
		AVR12	s	Brine	3*2 10%V	X	X	HL		-25	25.6	165.6	Th(HL)256	Halite	AVR12 Pg_11	3_AVR12_B	scattered	So many in AVR12 - Clusters - also scattered -
		AVR12	S	Brine	4*3 10%V	X	X	HL and CC		-25	25.6	133.4	Th(HL)241	Halite and Calcite	AVR12 Pg_13	4_AVR12_A	scattered	hitgh salinity - high temperature--ANALYNSED FOR RAMA
		AVR12	S	Brine	4*2 10%V	X	X			-25	25.6	124.2	?		AVR12 Pg_13	4_AVR12_A	scattered	Minus 25 is an eutectic temperature
		AVR12	P	Brine	4*3 10%V	X	X	HL and CC		-25	25.6	138.1	235.1	Halite and Calcite	AVR12 Pg_13	4_AVR12_A	scattered	
	AVR12	AVR12	P	Brine	4*3 60%L	x	x	HL/CC		-2.1	3.5	145.3	322 HL	Halite and calcite	AVR12 Pg_18	4_AVR12_A	three phases: L, V and Solid	Lots of bubble measurable ,
		AVR13	P	Brine	5*4 65%L	x	x	HL		-18.4	21.3	124	?	Halite	AVR12 Pg_18	4_AVR12_A	three phases: L, V and Solid	lots of bubbles with halite(HL) and calcite
		AVR14	P	Brine	4*4 65%L	x	x	HL		-20.4	22.6	138.2	245 HL	Halite	AVR12 Pg_18	4_AVR12_A	three phases: L, V and Solid	scattered in qtz
		AVR15	P	Brine	4*3 75%L	x	x	HL/CC		-13.2	17.1	124.7	271 HL	Halite	AVR12 Pg_18	4_AVR12_A	three phases: L, V and Solid	
		AVR16	P	Brine	4*3 80%V	x	x	HL/CC		-15.9	19.4	124.7	248 HL	Halite	AVR12 Pg_18	4_AVR12_A	three phases: L, V and Solid	
	At01	At01 A	P	Brine	3*2 10% V	X	X			-1.5	2.6	170.3			At01 _Pg 30	1_At01 _A	Clusters	Brine fluids scattered
		At01 A	P	Brine	3*2 10% V	X	X			-1.5	2.6	157.5			At01 _Pg 30	1_At01 _A	Clusters	
		At01 A	P	Brine	3*2 10% V	X	X			-13.4	17.3	165.8			At01 _Pg 30	1_At01 _A	Clusters	
		At01 A	P	Brine	2*4 10% V	X	X			-13.4	17.3	165			At01 _Pg 30	1_At01 _A	Clusters	
		At01 A	P	Brine	2*3 10% V	X	X			-12.2	16.1	171.3			At01 _Pg 30	1_At01 _A	Clusters	
		At01 A	P	Brine	2*3 10% V	X	X			-7.2	10.7	183.2			At01 _Pg 30	1_At01 _A	Clusters	
		At01 A	P	Brine	2*2 10% V	X	X			-7.2	10.7	183.2			At01 _Pg 30	1_At01 _A	Clusters	
	At 02	At 02 A	P	Gas	5*3	x	x				0.0	-110			At02 _Pg 20	01_At02_A	G-phase- one phase at room temp	Methane- Nitrogen gas
		At 02 A	P	Gas	4*3	x	x				0.0	-118			At02 _Pg 21	01_At02_A	G-phase- one phase at room temp	Critical temp of CH4 IS -183 and of N2 is -143
		At 02 A	P	Gas	3*2	x	x				0.0	-114			At02 _Pg 21	01_At02_A	G-phase- one phase at room temp	
		At 02 A	P	Gas	4*3	x	x				0.0	-118.8			At02 _Pg 22	01_At02_A	G-phase- one phase at room temp	
		At 02 A	S	Gas	6*4	x	x				0.0	-112.3			At02 _Pg 22	02_At02_A	G-phase- one phase at room temp	
		At 02 A	P	Gas	3*2	x	x				0.0	-116			At02 _Pg 23	03_At02_A	Th(L) not clear	
		At 02 A	P	Gas	3*2	x	x				0.0	-105.5			At02 _Pg 24	04_At02_A	Clusters	
		At 02 A	P	Gas	3*3	x	x				0.0	-120			At02 _Pg 24	04_At02_A	Clusters	
		At 02 A	P	Gas	3*4	x	x				0.0	-109.3			At02 _Pg 24	04_At02_A	Clusters	
		At 02 A	P	Gas	3*5	x	x				0.0	-122.3			At02 _Pg 24	04_At02_A	Clusters	

© University of Venda

Appendix 9C: Calculation instructions in the program BULK, according to the heating experiment (Bakker, 2003)

a

```
FLUIDS, package of computer programs for fluid inclusion studies

Program 1: BULK, version 08/02
Product Development Ronald J. Bakker

Included components:

    1. Fluids : H2O-CO2-CH4-N2-C2H6-H2S-NH3-H2-O2-CO
    2. Salts  : NaCl-KCl-CaCl2-MgCl2-FeCl2

Bulk fluid V-X properties of inclusions are calculated from:

    - Homogenisation temperatures/pressures
    - Ice melting temperatures
    - Volume fraction estimates

Properties of individual phases are calculated at room temperature


_____________________________________________________________________
Component definition:

    (1) predefined systems
    (2) manually defined system

                              choose number: 1


    (1)  H2O
    (2)  H2O-NaCl
    (3)  H2O-CO2
    (4)  H2O-CO2-NaCl
    (5)  H2O-CH4
    (6)  H2O-CH4-NaCl
    (7)  CO2-CH4
    (8)  H2O-CO2-CH4
    (9)  H2O-NaCl-CO2-CH4
    (10) changed my mind

                              choose number: 7
```

b

```
Non-aqueous phase: mixture CO2 CH4

Composition of the homogeneous non-aqueous phase
(amount-of-substance fraction, number between 0 and 1):

    x(CO2) = 0.07
    x(CH4) = 0.93

Density of non-aqueous phase is obtained from:

    (1) Density (g/cc)
    (2) Molar Volume (cc/mol)
    (3) Homogenisation Temperature
    (4) Homogenisation Pressure

                              choose number: 3

    Homogenisation Temperature (°Celsius) = -77

    Mode of homogenisation:

        (1) Vapour
        (2) Liquid
        (3) Critical

                              choose number: 1

Equation of state for homogenisation conditions of the non-aqueous phases:

    (1)  Redlich & Kwong (1949) any gas mixture
    (2)  Chueh & Prausnitz (1967) CO2-CH4-N2-C2H6-H2S-H2
    (3)  Soave (1972) any gas mixture
    (4)  Lee & Kesler (1975) CH4-C2H6-H2S-H2
    (5)  Peng & Robinson (1976) any gas mixture
    (6)  Holloway (1977, 1981) Flowers (1979) any gas mixture
    (7)  Bowers & Helgeson (1983), Bakker (1999) any gas mixture
    (8)  Duan et al. (1992) H2O-CO2-CH4
    (9)  Thiery et al. (1994), Soave (1972) CO2-CH4-N2
    (10) Duan et al. (1996) H2O-CO2-CH4-N2-C2H6-H2S-H2-O2-CO

                              Choose number : 9
```

© University of Venda

Appendix 9C: Continue…….

C

```
**************************************************************************
Homogenisation conditions are numerically analysed. Conversion depends on
the chosen initial parameters. The trivial solution may regularly occur,
especially if the temperature exceeds the immiscibility field.
You may adjust the initiation until you reach a satisfying result.

Iteration number: 1 2 3 4 5 6 7 8 9 10 11 12 13 14 15 16 17 18 19
**************************************************************************
Result of Liquid-Vapour Equilibria Calculations

Temperature = 196.15 K, -77 °C
Pressure = 7.89673 MPa, 78.9673 bar
Zero function = -1.17795e-13
Number of iterations : 19

Phase 1      63.2349 cc/mol
 x(CO2)      0.0700001 (f = 0.0724819 MPa)
 x(CH4)      0.93 (f = 3.67113 MPa)

Phase 2      63.2349 cc/mol
 x(CO2)      0.07 (f = 0.0724817 MPa)
 x(CH4)      0.93 (f = 3.67113 MPa)

Warning: phases have nearly equal compositions, possible trivial solution
Warning: phases have nearly equal densities, possible trivial solution

Do you want to change the numerical approximation? (y/n) y

    Initial liquid composition (amount-of-substance fractions):

    x(CO2) = 0.2
    x(CH4) = 0.8

    New Pressure Approach (in MPa) = 2.5

    New Precision (default is 1e-12) = 1e-12

Iteration number:  44 45 46 47 48 49 50 51 52 53 54 55 56 57 58 59 60 61 62
63 64 65 66 67 68 69 70 71 72 73 74 75 76 77 78 79 80 81 82 83 84 85 86
**************************************************************************
Result of Liquid-Vapour Equilibria Calculations

Temperature = 196.15 K, -77 °C
Pressure = 4.32529 MPa, 43.2529 bar
Zero function = -2.04059e-13
Number of iterations : 86

Phase 1      64.3344 cc/mol
 x(CO2)      0.175803 (f = 0.135217 MPa)
 x(CH4)      0.824197 (f = 2.89235 MPa)

Phase 2      201.733 cc/mol
 x(CO2)      0.07 (f = 0.135217 MPa)
 x(CH4)      0.93 (f = 2.89235 MPa)


Do you want to change the numerical approximation? (y/n) n

--------------------------------------------------------------------------
Gas mixture calculations:

    Homogenisation temperature = 196.15 K (-77 °C)
    Homogenisation pressure = 4.32529 MPa (43.2529 bar)
    Molar volume = 192.467 cc/mole
    Density = 0.0935249 g/cc

--------------------------------------------------------------------------
Calculation fluid inclusion properties at 20 °C

--------------------------------------------------------------------------
Total Homogenisation and Volume Fractions

Gas mixture:

    Total homogenisation at 196.15 K (-77 °C)
    Molar Volume = 192.467 cc/mol

--------------------------------------------------------------------------
Write results in file : test3
```

© University of Venda

REFERENCES

Abersteiner, A., Kamenetsky, V.S., Golovin, A.V., Kamenetsky, M. and Goemann, K. (2018). Was Crustal Contamination Involved in the Formation of the Serpentine-Free Udachnaya-East Kimberlite? New Insights into Parental Melts, Liquidus Assemblage and Effects of Alteration. *Journal of Petrology*. Vol. 59, No. 8, pp. 1467 -1492.

Abrams, M. and Hook, S. (2006). ASTER User Handbook, Version 2. California: Jet Propulsion Laboratory, California Institute of Technology, 135pp.

Agangi, A., Gucsik, A., Nishido, H., Ninagawa, K and Kamenestsky, V.S. (2016). Relation between Cathodoluminescence and Trace Elements Distribution of Magmatic Topaz from the Ary-Bulk Massif, Russia, Vol. 80, Issue 5, pp. 881 – 899.

Aggarwal, S. (2003). Satellite Remote Sensing and GIS Applications in Agricultural Meteorology: Principles of Remote Sensing. Dehra Dun, World Meteorological Organization, pp. 22-38.

Ali, R.G.M., Khidir, S.O.H., Abdelgalil, M.Y. (2017). Application of ASTER Data in the Identification of Alteration Zones – Related to Mineralisation around Wadi E1 Milk, North Kordofan, Sudan. *Al Neelain Journal of Geosciences*, Vol. 1, Issue No. 1, pp. 38-46.

Allaby, M. (2008). A Dictionary of Earth Sciences. 3rd Edition. Oxford University Press, 672pp.

Allègre, C. J. and Sutcliffe, C. (2008). Isotope Geology. Cambridge University Press, New York, pp.550.

Allum, A.F. (1954). Geological Mapping of the Mine Workings. Mine Records, Macalder Mine, Kenya (unpublished).

Almasi, A., Yousefi, M., Carranza, E.J.M. (2017). Prospectivity Analysis of Orogenic Gold Deposits in Saqez-Sardasht Goldfield, Iran. *Ore Geology Reviews*, Vol. 91, pp. 1066-1080.

Anhaeusser, C.R. (1990). Precambrian Crust Evolution and Metallogeny of Southern Africa. In Naqvi, S.M. (Ed.). *Precambrian Continental Crust and its Economic Resources*, Amsterdam, Elsevier, Chapter 2, pp. 123– 156.

Annels, A.E. (1974). Some Aspects of the Stratiform Ore Deposit of the Zambian Copperbelt and their Genetic Significance. In Barthlome, P. (Ed.). Gisements Stratiformes Forms et Provinces Cuprifères. Sociètè Gèologique de Belgique, Liege, pp. 235-254.

Annels, A.E. (1984). The Geotectonic Environment of the Zambian Copper-cobalt Mineralisation. *Journal of Geological Society, London*, Vol. 141, pp. 279 – 289.

© University of Venda

Annels, A.E. (1989). Ore genesis in the Zambian Copper Belt with Particular Reference to the Northern Sector of the Chambeshi Basin. *Geological Association of Canada*, Special Paper 36, pp. 427-452.

Anthony, R.P. and Ague, J.J. (2009). *Principles of Igneous and Metamorphic Petrology*. 2nd Edition, Cambridge University Press, New York, 667 pp.

Antibachi, D., Kelepertzis, E., Kelepertsis, A. (2012). Heavy Metals in Agricultural Soils of the Mouriki–Thiva Area (Central Greece) and Environmental Impact Implications. Soil and Sediment Contamination: *An International Journal*, Vol. 21, pp. 434–450.

Armstrong, J.T. (1988). Quantitative Analysis of Silicate and Oxide Minerals: Comparison of the Monte Carlo, ZAF and Φ(ρZ) Procedures. In: Newbury, D.E. (Ed.). *Microbeam Analysis*. San Francisco Press, San Francisco, USA, pp. 239-246.

Aronoff, S. (2005). Remote Sensing for Gis Managers. 1st Ed. Esri Press, 95 pp.

Arriens, P.A. and Compston, W. (1968). A method for Isotopic Ratio Measurement by Voltage Peak Switching and its Application with Digital Input. *International Journal of Spectrom,* Ion Physics, Vol. 1, pp. 471 - 481.

Asadzadeh, S. and de Souza Filho, C.R. (2015). A Review on Spectral Processing Methods for Geological Remote Sensing. International Journal of Applied Earth Observation and Geo-information, Vol. 4, pp. 60-90.

Arriens, P.A. and Compston, W. (1968). A method for Isotopic Ratio Measurement by Voltage Peak Switching and its Application with Digital Input. *International Journal of Spectrom,* Ion Physics, Vol. 1, pp. 471 - 481.

Atkison, W. Jr. and Einaudi, 1M.T. (1978). Skarn Formation and Mineralization in the Contact Areole at Carr Fork, Bingham, Utah. Economic Geology, Vol. 73, Bahnemann K.P. (1986). A Review of the Geology of the Messina Copper Deposits, Northern Transvaal. In Anhaeusser, C.R. and Masker, S. (eds.): *Mineral Deposits of Southern Africa*, Geological Society of South Africa, Vol. 11, pp. 1671-1688.

Ault, W.U. and Jensen, M.L. (1963). Summary of Sulfur Isotope Standards. In Jensen, M.L. (ed.): Biogeochemistry of Sulfur Isotopes. National Science Foundation Symposium Proceedings, Yale University, pp. 16 - 29.

Bahnemann, K.P. (1972). A Review of the Structure, the Stratigraphy and the Metamorphism of the Basement Rocks in the Messina District Northern Transvaal. D.Sc. Thesis (unpublished). University of Pretoria, Pretoria, 354pp.

Bahnemann K.P. (1986). A Review of the Geology of the Messina Copper Deposits, Northern Transvaal. In Anhaeusser, C.R. and Masker, S. (Eds.). *Mineral Deposits of Southern Africa*, Geological Society of South Africa, Vol. 11, pp. 1671-1688.

© University of Venda

Bakker, R.J. (2003). Package FLUIDS 1. Computer Programs for Analysis of Fluid Inclusion Data and for Modelling Bulk Fluid Properties. *Chemical Geology*, Vol. 194, pp. 3 - 23.

Bakker, R.J. (2018). AqSo_NaCl: Computer program to calculate p-T-V-x Properties in the H2O-NaCl Fluid System Applied to Fluid Inclusion Research and Pore Fluid Calculation. *Computer and Geoscience,* Elsevier, Vol. 115, pp. 122 – 123.

Bakker, R.J. and Brown, B.P. (2003). Computer Modelling in Fluid Inclusions Research. In Samson, I., Anderson, A. and Marshall, D. (Eds.). Fluid Inclusions: Analysis and Interpretation. *Mineralogical Association of Canada*, Short Course, Vol. 32, Chapter 7, published by fluids.unileoben.ac.za. PDF.

Ballinger, J. and Shugar, G. (2011). Chemical Technicians' Ready Reference Handbook. 5th Edition, McGraw-Hill Professional, 704 pp.

Barton, P.B. Jr. and Skinner, B.J., (1979). Sulfide Mineral Stabilities. In Barnes, H.L. (Ed.). *Geochemistry of Hydrothermal Ore Deposits*. 2nd Edition. J. Wiley and Sons, pp. 278-485.

Barton, J.M. Jr, Fripp, R.E.P., Horrocks, P. and McLean, N. (1979a). The Geology, Age and Tectonic Setting of the Messina Layered Intrusion, Limpopo Mobile Belt, Sourhern Africa: American Journal of Science, Vol. 279, pp. 1 108-1 134.

Bei, y., Shufang, T., Jia, G. and Yagqin, S. (2017). Assessment of WorldView-3 Data for Lithological Mapping. *Remote Sensing,* Vol. 9, Issue No. 11. www.mdpi.com/2072-4292/9/11/1132/htm.: Accessed: 22 January 2019).

Bekker, A. Grokhovskaya, T.L., Hieberts, R., Sharkovs, E.V., Bui, T.H., Stadnek, K.R., Chashchin, V.V. and Wing, B.A. (2016). Multiple Sulfur Isotope and Mineralogical Constraints on the Genesis of Ni-Cu-PGE Magmatic Sulfide Mineralization of the Monchegorsk Igneous Complex, Kola Peninsula, *Russia. Mineral Deposita*, Springer-Verlag Berlin Heidelberg, Vol. 51, pp.1035 – 1053.

Bell, K. (1994). Carbonatites and Mantle Evolution: A Review. Ottawa-Carleton Geoscience Centre, Department of Earth Sciences, Carleton University, Ottawa, Canada K1S 5B6. *Mineralogical Magazine*, Vol. 58A, PP.69-70.

Bensid, M., Strauss, S. and Billay, A. (2016). Mineral Prospectivity Mapping of the Tugela Terrane, KwaZulu-Natal: Semiregional Soil Survey. *Council for Geoscience Conference,* In pursuit of Excellence in the Geosciences, Pretoria,

Bernhardt, H.J. (1987). A Simple, Fully-Automated System for Ore Mineral Identification. *Mineralogy and Petrology*, Springer, Issue 3-4, Vol. 36, pp. 241-245.

Bernhardt, H.J. (1990). Microscopic Identification, and Identification Schemes, of Ore Minerals. In Jambor, L. and Vaughan, D. (Eds.), Advanced Microscopic Studies of Ore Minerals. *Mineralogy Association of Canada*, Short Course, Hand book, Ottawa, pp. 89-211.

© University of Venda

Bettge, M. (2014). Integration of Data to Support Mineral Exploration with Special use of GIS within the Musina Area, Limpopo Province, South Africa (unpublished).

Beus, A. A. and Grigorian, S. V. (1977). Geochemical Exploration Methods for Mineral Deposits. Applied publishing, Wilmette, IL, translated from Russian, 287 pp.

Bevelander, M. (1994). Nigramoep- From Exploration Target to Mine. XVth CMMI, Congress, Johannesburg, *South African Institute of Mining and Metallurgy*, Vol. 3, pp. 225-231.

Billay, A. (2016). The Role of the Council for Geoscience in Promoting Mining and Exploration Investment in South Africa: Current Exploration Projects. *Proceedings of the Council for Geoscience Conference*, Pretoria.

Blatt, H., Tracy, R. J. and Owens, B. E. (2006). Petrology: Igneous, Sedimentary and Metamorphic. Third Edition. W.H. Freeman and Company, New York, 530 pp.

Blamey, N., Campbell, A.R., Heizler, M.T. (2017). The Hydrothermal Fluid Evolution of Vein Sets at the Pipeline Gold Mine, Nevada. *Minerals*, MDPI, Vol. 7.

Blenkinsop, T.G., Kröner, A. and Chiwara, V. (2004). Singlione Stage, Late Archaean Exhumation of Granulites in the Northern Marginal Zone, Limpopo Belt, Zimbambwe, and Relevance to Gold Mineralisation at Renco Mine, *South African. Journal of Geology*, Vol. 107, pp. 377-396.

Boardman, J. W. and Kruse, F. A. (2011). Analysis of Imaging Spectrometer Data Using N-Dimensional Geometry and a Mixture-Tuned Matched Filtering Approach. IEEE Transactions on Geoscience and Remote Sensing, Vol. 49, No.11, pp. 4138-4152.

Bodnar, R.J, Vityk, M.O. (1994). Interpretation of Microthermometric Data for H_20-NaC1 Fluid Inclusions. In De Vivo, B., Frezzotti, M.L. (eds.): Fluid Inclusions in Minerals: Methods and Application. Virginia Polytechnic Institute and State University, Blacksburg, VA, pp. 117 - 130.

Bodnar, R.J. (2003). Introduction to Fluid Inclusions. In Samson, I., Anderson, A. and Marshall, D. (Eds.): Fluid Inclusions: Analysis and Interpretation. *Mineral Association of Canada*, Short Course, Vol. 32, pp.1 - 8.

Bodnar, R.J. (2014). Fluid Inclusions in Hydrothermal Ore Deposits. In Turekia, K. K. Holland, H. D. (Eds.): Treatise on Geochemistry. 2nd Edition, Chapter 13.5. Oxford, Elsevier Ltd, pp. 119 - 142.

Boggs, S., Jr., Krinsley, D.H, Goles, G.G., Seyedolali, A. and. Dypvik, H. (2001). Identification of Shocked Quartz by Scanning Cathodoluminescence Imaging. *Meteoritics and Planetary Sciences*, Vol. 36, pp. 783–91.

Boggs, Jr. S. and Krinsley, D. (2006). Application of Cathodoluminescence Imaging to the Study of Sedimentary Rocks. United State of America, Cambridge University Press, New York, 178pp.

© University of Venda

Bohling, G. (2005). Introduction to Geostatistics and Variogram Analysis. Lawrence: The University of Kansas.

Booth, P.W.K. (2011). Stratigraphic, Structural and Tectonic Enigmas associated with the Cape Fold Belt: Challenges for Future Research. *South African Journal of Geology*, Geological Society of South Africa, Vol. 114. No. 3-4, pp. 235-248.

Bortnikov, N.S, Genkin, A.D., Dobrovol'skaya, M.G., Muravitskaya, G.N. and Filimonova, A.A. (1991). The Nature of Chalcopyrite Inclusions in Sphalerite: Exsolution, Coprecipitation or "Disease". *Economic Geology*, Vol. 86, No. 5, pp.1070 - 1082.

Borzov, S.M., Melnikov, P.V., Pestunov, I.A. (2016). Complex Processing of Hyperspectral Images on the Basis of Spectral and Spatial Information. *Vych. Tekhnol*. Vol. 21, Issue No. 1, pp.25-39.

Brandl, G. (1981). The Geology of the Messina area: Explanation of Sheet 2230. Geological Survey, Republic of South Africa, Pretoria, 35 pp.

Brandl, G. (2001). The Limpopo Belt and its Environs: Explanation of Geological Map of the Limpopo Belt and its Environs. Council for Geoscience, 46 pp.

Butterfield, N., Rowe, M.R., Stewart, E., Roesel, D. and Neshyba, S. (2017). Quantitative Three-dimensional Ice Roughness from Scanning Electron Microscopy. *Journal of Geophysical Research: Atmosphere.* Vol. 122, Issue 5, AGU publications, pp. 2527-3170.

Burke, E.A.J. (2001). Raman Microspectrometry of Fluid Inclusions. *Lithos*, Elsevier, Vol. 55, pp. 139 - 158.

Burke, E.A.J. and Lustenhouwer, W.J. (1987). The Application of a Multichannel Laser Raman Microprobe (Microdril-28) to the Analysis of Fluid Inclusions. *Chemical Geology*, Vol. 61, pp. 11 - 17.

Burrough, P. A. (1986). Principles of Geographical Information Systems for Land Resources Assessment. Oxford: Oxford University Press.

Burruss, R.C. (2003). Raman Spectroscopy of Fluid Inclusions. In Samson, I., Anderson, A. and Marshall, D. (eds.): Fluid Inclusions: *Analysis and Interpretation: Mineralogical Association of Canada*, Short Course Series, Vol. 32, pp. 279 - 289.

Burrough, P. A. (1991). Soil Information Systems. In Maguire, D. J. Goodchild, M. F. and Rhind, D. W. (Eds.): Geographical Information Systems Essex, Longman Scientific and Technical, pp. 153 - 169.

Burrough, P. A., and McDonnell, R. A. (1998). Principles of Geographical Information Systems. New York: Oxford University Press, pp.1-19.

Burt, D.M. (1977). Mineralogy and Petrology of Skarn Deposits. *Society of Italiana Mineralogia Petrologia*, Rendiconti, Vol. 33, pp. 859-873.

© University of Venda

Cairncross, B. (1991). The Messina District, South Africa, Mineralogical Records, Vol. 22, pp. 187-199.

Cambell, J. B. and Wynne, R. H. (2011). Introduction to Remote Sensing, 5th Ed. London, The Guilford Press, 683 pp.

Carranza, E. J. M. (2011). Geochemical Sampling for Geological–Environmental Studies. *Journal of Geochemical Exploration*, Vol. 111, No. 3. pp. 57-58.

Carranza, E.J.M. (2012). Geochemical Characteristics of Mineral Deposits: Implications for Ore Genesis. *Geochemistry: Exploration, Environment, Analysis*, Vol. 12, Issue 2, pp.89-92.

Carranza, E.J.M. Sadeghi, M. and Billay, A. (20165). Prediction Mapping of the Prospectively for Orogenoic Gold, Giyani Greenstone Belt, South Africa. *Ore Geology Reviews.* Vol. 71, pp. 703-718.

Centre for Remote Imaging, Sensing and Processing. (2001). Interpretation of Optical Images. http://www.crisp.nus.edu.sg/_~research/_tutorial/opt_int.htm: [Accessed: 5 July 2016].

Chacko T., Cole D.R., and Horita J. (2001). Equilibrium Oxygen, Hydrogen and Carbon Isotope Fractionation Factors Applicable to Geologic Systems. In Valley, J.W. and Cole, D.R. (eds.): Reviews in Mineralogy and Geochemistry. *Mineralogical Society of America,* Chantilly, VA, Vol. 43, pp. 1 - 81.

Chang, I.C. (2003). Hyperspectral Imaging: Techniques for Spectral Detection and Classification, Vol. 1. New York, Kluwer Academic Publishers, 377 pp.

Chaumba, J. B., Mundalamo, H.R., Ogola, J.S., Cox, J.A. and Fleisher, C.J. (2016). Petrography, Sulphide Mineral Chemistry, and Sulfur Isotope Evidence for a Hydrothermal Imprint on Musina Copper Deposits, Limpopo Province, South Africa: Evidence for a Breccia Pipe Origin. *Journal of African Earth Sciences*, Elsevier, Vol. 120, pp. 141-159.

Chinoda, G., Moyce, W., Matura, N. and Owen, R. (2009). The Geology of the Limpopo Basin area. WaterNet Working Paper 7, Mineral Resources Centre, University of Zimbabwe, Harare, 44 pp.

Chon, H.T. and Hwang, I.H. (2007).Geochemical Soil Survey for Au Exploration in the Kenieba District in Mali, Africa. Geochemical Case History and Geochemical Exploration Methods. Proceedings of Exploration, *Fifth International Conferences*, p.p. 997-1001.

Clark, R. (1999). Spectroscopy of Rocks and Minerals, and Principles of Spectroscopy. In: Rencz, A. (Ed.). Manual of Remote Sensing. Chapter 1, New York: John Wiley and Sons, pp. 3-58.

© University of Venda

Clark Labs. (2008). IDRISI Guide to GIS and Image Processing Vol. 1, Worcester: Clark Labs.

Claude, J.A. (2008). Isotope Geology. Cambridge University Press, New York, USA, 534pp.

Clifford, T.N., Barton, E.S., Retief, E.A. and Rex, D.C. (1995). A Crustal Progenitor for the Intrusive Arnothosite-Charnokite Kindred of the Cupriferous Koperberg Suite, O'kiep District, Namaqualand, South Africa: New Isotope Data for the Country Rocks and Intrusives. *Journal of Petrology*, Vol. 36, pp. 231 – 258.

Cloutier, J., Piercey, S.J., Layn, G., Heslop, J. and Hussey, A. (2015). Style, Textural Evolution, and Sulfur from the Cambrian Whalesback Volcanogenic Massive Sulphide Deposit, Central Newfounded, Canada. Economic Geology, Vol. 110, No. 5, pp. 1215-1234.

Coelho, A. (2007). TOPAS, Version 4.2, Copyright _ 1999–2009 Bruker AXS. Technical Reference.

Colín-García, M., A. Heredia,G. Cordero, A. Camprubí, A. Negrón-Mendoza, F. Ortega-Gutiérrez, H. Beraldi, S. Ramos-Bernal. (2016). "Hydrothermal Vents and Prebiotic Chemistry: A Review". *Boletín de la Sociedad Geológica Mexicana*, Vol. 68, No. 3, pp. 599–620.

Cole, D.I. and Wipplinger, P.E. (2001). Sedimentology and Molybdenum Potential of the Beaufort Group in the Main Karoo Basin, South Africa. Memoir, Council for Geoscience, South Africa, Vol. 80, 225pp.

Cornell, D.H., Thomas, R.J., Moen, H.F.G., Reid, D.L., Moore, J.M. and Gibson, R.L. (2006). The Namaqua-Natal Province. In Johnson, M.R., Anhaeusser, C.R. and Thomas, R.J. (Eds.). *The Geology of South Africa, Geological Society of South Africa*, Johannesburg/Council for Geoscience, Pretoria, Chapter 16, pp. 325-380.

Cornradie, J.A. and Schoch, A.E. (1986). Petrographic Characteristics of the Koperbergsuite, South Africa: An Anology to Massive-Type Anorthosite. *Precambrian Research*, Vol. 31, pp. 157-188.

Coward, M.P., James, P.R. and Wright, L. (1976). Northern Margin of the Limpopo Belt, Southern Africa. *Geological Society of America*, Vol. 87, pp. 601-611.

Cox, K.G., Johnson, R., Monkman, L.G., Stillman C.J., Vail, V.R. and Wood, D.N. (1965). The Geology of the Naunetsi Igneous Province, Philosophical Transaction of the Royal Society of London, Vol. 257A, pp. 71-218.

Cox, D.P., Lindsey, D.A., Singer, D.A., Moring, B.C. and Diggles, M.F. (2007). Sediment-Hosted Copper Deposits of the World: Deposit Models and Database. Open-File Report 03-107, Version 1.3, 53 pp.

Craig, H. (1961b). Standard for Reporting Concentrations of Deuterium and Oxygen-18 in Natural Waters. *Science*, Vol. 133, Issue 3467, pp. 1833 - 1834.

© University of Venda

Craig, J.R. and Vaughan, D.J. (1994). Ore Mineralogy and Ore Microscopy. 2nd Edition. John Wiley and Sons. Inc. Canada, 434pp.

Cressie, N. (1986, September). Kriging Nonstationary Data. *Journal of the American Statistical Association*, pp. 625-634.

Cui, Z., Wang, Y., Gao, X., Jie, L., and Zheng, Y. (2016). Multispectral Image Classification Based on Improved Weighted MRF Bayesian. Neurocomputing, Vol. 212, pp. 75-87.

Cutten, H., De Waele, B., Fernandez-Alonso, M. and Tack, L. (2004). Age Constraints for Basin Evolution and Sedimentation in the "Northeastern Kibaran Belt". *20th Colloquium of African Geology*, 20th Colloquium of African Geology, Orleans, France. pp.123.

Darnley, A. G., Bjorklund, A., Bolviken, B., Gustavsson, N., Koval, P. V., Plant J. A., Steenfelt, A., Tauchid M. and Xie Xuejing (1995). A Global Geochemical Database for Environmental and Resource Management. *Earth Science Series* No. 19, UNISECO, Paris, France, 122 pp.

Davidson, C.F. (1966). Some Genetic Relationships between Ore Deposits and Evaporites. *Institution of Mining and Metallurgy,* Section B, Vol. 75, pp. B216-B225.

de Melo, G. H. C., Monteiro, L. V. S., Moreto, C. P. N., Xavier, R. P. and da Silva, M. A. D. (2014). Paragenesis and Evolution of the Hydrothermal Bacuri Iron - Oxide -Copper – Gold Deposit, Carajás Province. *Brazilian Journal of Geology*, Vol. 44, No. 1, Sãu Paulo.

DePaolo, D.J. (1981). Trace Elements and Isotopic Effects of Combined Wallrock Assimilation and Fractional Crystallization. *Earth and Planetary Science Letters*, Vol. 53, Issue 2, pp. 189 - 202.

DePaolo, D.J. and Wasserburg, G.J. (1979). Sm-Nd age of the Stillwater Complex and the mantle evolution curve for neodymium. *Geochimica, Cosmochica Acta.* Vol. 43, pp. 999 -1008.

De Wijs, H.J. (1951). Statistics of Ore Distribution Part 1: Frequency Distribution of Assay Values. *Journal of the Royal Netherlands Geological and Mining Society*. Vol. 13, pp. 365-375.

Deer, W.A., Howie, R.A. and Zussman, J. (1992). An Introduction to the Rock Forming Minerals. Pearson Prentice Hall, Second Edition, United Kingdom, pp 31-46.

den Engelsen, D., Fern, G. R., Harris, P. G., Ireland, T. G. and Silver, J. (2017). New Developments in Cathodoluminescence Spectroscopy for the Study of Luminescence Materials. *Materials*, Vol. 10, Issue 312, pp. 1-16.

Deutsch, C.V. and Journel, A.G. (1997). GSLIB: Geostatistical Software Library and User's Guide, Second Edition, Oxford University Press, New York, 369 pp.

© University of Venda

Devaraj, C. and Shah, C.A. (2014). Automated Geometric Correction of Multispectral Images from High Resolution CCD Camera (HRCC) On-board CBERS-2 and CBERS-2B. *ISPRS Journal of Photogrammetry and Remote Sensing*, Vol. 89, pp. 13-24.

Diamond. (2003). Glossary: Terms and Symbols Used in Fluid Inclusion Studies. In Samson, I., Anderson, A. Marshall, D. (eds.): Fluid Inclusions: *Analysis and Interpretation. Mineral Association of Canada*, Short Course, pp. 365-374.

DigitalGlobe Core Imagery Products Guide. (2015). http://www.genesiis.com/pdf/ Digital-globe-core-imagery-products-guide.pdf: [Accessed: 17 October 2016].

Donoghue, K.A., Ripley, E.M. and Li, C. (2014). Sulfur Isotope and Mineralogical Studies of Ni-Cu Sulfide Mineralization in the Bovine Igneous Complex Intrusion, Baraga Basin, Northern Michigan. Economic Geology, Vol. 109, pp. 325 - 341.

Dinnebier, R and Friese, K. (2018). Modern XRD Methods in Mineralogy - Vol III. In De Vivo, B., Grasemann, B, and Stuwe, K. (Eds.). Geology, Encyclopedia of Life Support System, Vol IV, pp. 93-157.

Dodson, R., and Santa, B. (1998). Projecting Data. Unit 10. http://www.ncgia.ucsb.edu/cctp/units/unit10/10.html: [Accessed: 9 July 2016].

Drew, L. J. (2006). A Tectonic Model for the Spatial Occurrence of Porphyry Copper and Polymetallic Vein Deposits - Applications to Central Europe. Scientific Investigation Report 2005-5272, U.S. Geological Survey, 36 pp.

Du Toit, M.C., Van Reenen, D.D. and Roering, C. (1983). Some Aspects the Geology, Structure and Metamorphism of the Southern Marginal Zone of the Limpopo Metamorphic Complex. *Special Publication Geological Society of South Africa*, Vol. 8, pp.121-142.

Duda, K., Daucsavage, J., Siemonsma, D., Brooks, B., D., Oleson, R., Meyer, D and Doescher, C. (2015). Advanced Space-borne Thermal Emission and Reflection Radiometer (ASTER) Level 1 Precision Terrain Corrected Registered At-Sensor Radiance Product (AST_L1T). AST_L1T Product User's Guide. Department of the Interior U.S. Geological Survey, USGS, NASA, Version 1.0, 74pp.

Einaudi, M.T. Meinert, L.D. and Newberry, R.J. (1981). Skarn Deposits. *Economic Geology*, 75th Anniversary Vol. 75, pp.317-391.

Einaudi, M.T. and Burt, D.M. (1982). Terminology, Classification and Composition of Skarn Deposits. *Economic Geology*, Vol. 77, pp. 745-754.

Eldridge, C.S., Compston, W., Williams, I.S., Both, R.A., Walshe, J, L. and Ohmoto, H. (1988). Sulfur Isotope Variability in Sediment-hosted Massive Sulfide Deposits as Determined using the Ion Microprobe SHRIMP: An Example from the Rammelsberg Orebody. *Economic Geology*, Vol. 83, pp. 443 - 449.

© University of Venda

Encyclopedia Britannica, (2016). Radioactive Isotope: Encyclopedia Britannica Britannica Online. http://global.britannica.com/science/radioactive-isotope: [Retrieved: 24 May 2016]

Environmental Systems Research Institute. (2012). GIS Dictionary. http://support.esri.com/other-resources/gis-dictionary/term/band%20ratio: [Accessed: 4 July 2016].

Errington, K. (1963). Geological Mapping of the Mine Workings. Mine Records, Macalder Mine, Kenya (unpublished).

Evans, A. M. and Moon, C. J. (2006). Mineral Deposit Geology and Models. In Moon, C. J., Whateley, M. K. G. and Evans, A. M. (Eds.). *Introduction to Mineral Exploration*. 2nd Edition, Chapter 3, Blackwell Publishing, pp. 33-52.

Evans, J.G., Moyle, P.R., Frank, D.G. and Olson, D.W. (2006). Garnet - An Essential Industrial Mineral and January Birthstone. In Hendley, J.W. (Ed.). United State Geological Survey, Fact Sheet 2000 - 3149.

Ewers, W. E. and Hudson, D. R. (1972). An interpretation Study of a Nickel-Irin Sulphide Ore Intersection, Lunnon Shoot, Kambalda, Western Australia. *Economic Geology*, Vol. 8, pp. 1075-1092.

eXtension. (2013). What's the difference between a supervised and unsupervised image classification. https://articles.extension.org/pages/40214/whats-the-difference-between-a-supervised-and-unsupervised-image-classification: [Retrieved: 10 July 2016].

Fagereng, A. (2012). A Note on Folding Mechanisms in the Cape Fold Belt. *South African Journal of Geology*, Geological Society of South Africa, Vol. 115, No. 2, pp. 137-144.

Farber, K., Dziggel, A., Meyer, F.M. and Harris, C. (2016). Petrology, Geochemistry and Fluid Inclusion Analysis of Altered Komatiites of the Mendon Formation in the BARB4 drill Core, Barberton Greenstone Belt, South Africa. *South African Journal of Geology*, Geology of South Africa, Vol. 119. No. 4, pp. 639-654.

Faure, G. (1986). Principles of Isotope Geology. 2nd Edition. John Wiley and Sons, Inc., New York, USA, 589pp.

Feely, M. (2018). Editorial for Special Issue: Fluid Inclusions - Study Methods, Applications, and Case Histories. Minerals, Vol. 8. MDPI, Vol. 7.

Ferreira, S.L.C., Bezerra, M.A., Santos, A.S.S., Dos Santos, W.N.L., Novaes, C.G., de Oliviera, O.M.C., Oliviera, M.L. and Garcia, R.L. (2018). Atomic Absorption Spectroscopy - A Multi Element Technique. Trends in Analytical Chemistry, Elsevier, Vol. 100, pp. 1-6.

© University of Venda

Foster, R.P., Leahy,K., Hunns, S.R., Pelham, D.A., Lawrence, S.R. and Harison, A.E. (2001). Pan African Terranes: Realizing the Metal Potential. *Australian Trans. Intitute of Mining and Metallurgy*, Vol.110, pp. 15 – 21.

Foose, M.P. (1986). Setting of a Magmatic Sulfide Occurrence in a Dismembered Ophiolite, Southwestern Oregon. *USGS Bulletin 1626-A*, pp. 1-23.

Frelinger, S.N., Ledvina, M.D., Kyle, J.R and Zhao, D. (2015). Scanning Electron Microscopy Cathodoluminescence of Quartz: Principles, Techniques and Applications in Ore Geology. *Ore Geology Reviews*, Vol. 65, pp. 840 – 852.

Frezzotti, M.L., Tecce, F. and Casagli, A. (2012). Raman Spectroscopy for Fluid Inclusion Analysis. *Journal of Geochemical Exploration*, Elsevier, Vol. 112, pp. 1 - 20.

Friedman, I. and O'Neil, J.R. (1977). Compilation of Stable Isotope Fractionation Factors of Geochemical Interest. In Fleischer, M. (Ed.): Data of Geochemistry. U.S. Geological Survey Professional Paper 440-KK, 6th Edition, Reston, VA.

Gałuszka, A. (2007). Different Approaches in using and Understanding the Term "Geochemical Background" - Practical ImplicationsfFor Environmental Studies. *Polish Journal of Environmental Studies*, Vol. 16, No. 3, pp. 389-395.

Gałuszka, A. and Migaszewski, Z.M. (2011). Geochemical Background: An Environmental Perspective. Mineralogia, *Mineralogical Society of Poland Polskie Towarzystwo Mineralogiczne*, Vol. 42, No. 1, pp. 7-17.

Gallon, M.L. (1986). Structural Re-interpretation of the Selebi –Phikwe Nicke-copper Sulphide Depsits, Estern Botswana. In Anhaeuser, C.R. and Maske, S. (eds.): *Mineral Deposits of Southern Africa*. Geological Society of South Africa, Johannesburg, pp.1663-1669.

Garlick, W.G. and Fleischer, V.D. (1972). Sedimentary Environment of Zambian Copper Deposition, *Geologie en Mijnbouw*, Vol. 51, No. 3, pp. 277-298

Gat, J.R. (1980). The Isotopes of Hydrogen and Oxygen in Precipitation. In Fritz, P. and Fontes, J. Ch. (eds.): Handbook of Environmental Isotope Geochemistry. Elsevier, The Terrestrial Environment, Elsevier, Amsterdam, pp. 21 - 48.

Gat, J.R. and Gonfiantini, R. (1981). Stable Isotope Hydrology: Deuterium and Oxygen-18 in the Water Cycle. International Atomic Energy Agency Technical Report Series No. 210, Vienna, 339pp.

Gaylord, W.B. and Brisky, J.A. (1983). Geology of the Elmwood and Gordonsville Mines, Central Tennessee Zinc District. In Craig, J.R. (Ed.): Zinc Deposits Fieldtrip Guidebook, *Geological Science Guide Book*. Chapt. 9, pp. 116 - 151.

Gervilla, F. and Kojonen, K. (2002). The Platinum-Group Minerals in the Upper Section of the Keivitsansarvi Ni-C-PGE Deposit, Northern Finland. Canadian Mineralogist. Vol. 40, No. 2, pp. 377-394.

© University of Venda

Ghosh A.K. (1972). Trace Element Geochemistry And Genesis Of The Copper Ore Deposits Of The Singbhum Shear Zone, Eastern India. *Mineralium Deposita*, Vol. 7, pp.292–313.

Gillan, J. (2013). Landsat Thematic Mapper 4 and 5 (TM4 and TM5). Abstract. The Landscape Toolbox: Tools and Methods for Effective Land Health Monitoring. http://wiki.landscapetoolbox.org/doku.php/remote_sensor_types:landsat_tm_5: [Accessed: 28 November 2016].

Giri, C., Pengra, B., Long, J. and Loveland, T.R. (2013). Next Generation of Global Cover Characterisation, Mapping, and monitoring. *International Journal of Applied Earth Observation and Geoinformation*, Vol. 25, pp. 30-37.

Glassley, W.E. (2014). Geothermal Energy: Renewable Energy and the Environment. 2nd Edition. *CRC Press Energy and the Environment*, 423pp.

Goldstein, R.H. and Reynolds, T.J. (1994). Systematics of Fluid Inclusions in Diagenetic Minerals. SEPMN Short Course 31, *Society of Sedimentary Geology*, USA, 213pp.

Götze, J. (2002). Potential of Cathodoluminescence (CL) Microscopy and Spectroscopy for the Analysis of Minerals and Materials. Special Issue Paper, *Anal. Bioanal. Chem.*, Springer-Verlag, Vol. 374, pp.703–708.

Götze, J. (2009). Cathodoluminescence in Applied Geosciences. In Pagel, M., Barbin, V. Blanc, P. and Ohnenstetter, D. (Eds.). *Cathodoluminescence in Geosciences.* Springer-Verlag, Berlin Heidelberg, New York, Chapter 18, pp.457-477.

Götze, J. (2012). Application of Cathodoluminescence Microscopy and Spectroscopy in Geosciences. Special Section: Cathodoluminescence. *Journal of Microscopy and Analysis*, Microscopy Society of America, Vol. 18, Issue 06, pp.1270-1284.

Götze, J., Plötze, M. and Habermann, D. (2001). Origin, Spectral Characteristics and Practical Applications of the Cathodoluminescence (CL) of Quartz: A Review. *Mineralogy and Petrology*, Vol. 71, Springer-Verlag, Australia, pp. 225–250.

Götze, J. and Kempe, U. (2009). Physical Principles of Cathodoluminescence (CL) and its Applications in Geosciences. In: Gucsik, A. (Ed). Cathodoluminescence and its Application in the Planetary Science. Chapter 1, Springer-Verlag Berlin Heidelberg, Germany, pp 1-22.

Götze, J., Pan, Y., Stevens-Kalceff, M., Kempe, U. and Müller, A. (2015). Origin and Significance of the Yellow Cathodoluminescence (CL) of quartz. *Am. Miner*, Vol. 100, pp. 1469–1482.

Government of Canada. (2013). Visible and Infrared. http://www.nrcan.gc.ca/earth-sciences/geomatics/satellite-imagery-air-photos/sensors-methods/visible-infrared/10966: Accessed: 5 July 2016].

© University of Venda

Government of Canada, (2015). Pre-processing. http://www.nrcan.gc.ca/earth-sciences/geomatics/satellite-imagery-air-photos/satellite-imagery-products/educational-resources/9403: [Accessed: 14 June 2016].

Government of South Australia. (2014). Remote Sensing-Using Spectral Imaging to Map Surface Geology and Mineralogy. http://minerals.statedevelopment.sa.gov.au/geoscience/geoscientific_data/remote_sensing: [Accessed: 5 July 2016].

Gregory, A.F. (1979). Remote Sensing in the Search for Metallic Ores: A Review of Current Practice and Future Potential. In: Hood, P. J. (Ed.). Geophysics and Geochemistry in the Search for Metallic Ores. Geological Survey of Canada, *Economic Geology Report 31*, pp. 511-526.

Gilg, H.A., Krüger, Y., Taubald, H., Van den Kerkhof, A.M., Frenz, M., Morteani, G. (2014). Mineralisation of Amethyst-bearing Geodes in Ametista do Sul (Brazil) from Low-Temperature Sedimentary Brines: Evidence from Monophase Liquid Inclusions and Stable Isotopes. *Mineralium Deposita*, Vol. 49, pp. 861 - 877.

Gueye, M., Van Der Kerkhof, A.M., Hein, U.F., Diene, M., Mucke, A. and Siegesmund, S. (2013). Structural Control, Fluid Inclusions and Cathodoluminescence Studies of Birimian Gold-Bearing Quartz Vein Systems in the Paleoproterozoic Mako Belt, Southeastern Senegal. *South African Journal of Geology, Geological Society of South Africa*, Vol. 116, No. 2, pp. 199 - 218.

Gucsik, A. (2009). Shock Metamorphism of Terrestrial Impact Structures and its Application in the Earth and Planetary Sciences. In: Gucsik, A. (Ed): *Cathodoluminescence and its Application in the Planetary Science.* Chapter 2, Springer-Verlag Berlin Heidelberg, Germany, pp. 23-44.

Habibzadeh F. (2017). Statistical Data Editing in Scientific Articles. *Journal of Korean Medical Science*, Vo. 32, No. 7, pp. 1072-1076.

Halder, S.K. (2018). Mineral Exploration: Principles and Applications. Second Edition. Elsevier, Amsterdam, Netherlands, 378pp.

Haldar, S. K., and Tišljar, J. (2014). Introduction to Mineralogy and Petrology. Elsevier, Chapter 3, 338 pp.

Hall, D.L., Sterner, S.M., Shentwu, W. and Bigge, M.A. (2002). Applying Fluid Inclusions to Petroleum Exploration and Production. Tulsa Geological Society, Online *Journal for Exploration and Production Geoscientists*, Data Pages, Inc. Search and Discovery Article No. 40042.

Han, J. S., Yao, J. M.., Chen, H. Y., Deng, X. H., Dingc, J. Y. (2014). Fluid inclusion and Stable Isotope Study of the Shagou Ag–Pb–Zn deposit, Luoning, Henan Province, China: Implications for the Genesis of an Orogenic lode Ag–Pb–Zn system. *Journal of Ore Geology Reviews*, Vol. 62, pp. 199 - 210.

© University of Venda

Hanisch, E.O.M (1974). Copper Workings in the Messina District. *Journal of the Southern African Institute of Mining and Metallurgy* – Pre-colonial Mining in Southern Africa, Vol. 100, Issue 1, pp. 49-56.

Hanneman, W.W. (2008). Naming Garnets. Sinkankas Symposium. *Gemmological Instruments*, Poulsdo, Washingtorn, 25pp.

Hanson, R.E., Hargrove, U.S., Martin, M.W., Bowring, S.A., Krol, M.A., Hodges K.V., Munyanyiwa, H. and Blenkinsop, T.G. (1998). New Geochronological Constraints on the Tectonic Evolution of the Pan-African Zambezi Belt, South-Central Africa. *Journal of African Earth Sciences*, Vol. 27, pp. 104– 105.

Harlov, D.E., Van den Kerkhof, A.M. and Johansson, L. (2013). The Varberg-Torpa Charnockite-granite Association, SW Sweden: Mineralogy, Petrology, and Fluid Inclusion Chemistry. *Journal of Petrology*, Vol. 54, No. 1, pp. 3 - 40.

Harris, P. (2000). At the Cutting Edge-Abbrasives and their Markets. *Industrial Minerals*. Issue No. 388, 19 pp.

Harris, D. C. (2007). Quantitative Chemical Analysis (Seventh ed.). New York: W. H. Freeman and Company.

Harris, N.B. and Einaudi, M.T. (1982). Skarn Deposits in the Yerington District, Nevada: Metasomatic Skarn Evolution near Ludwig. *Economic Geology*, Vol. 77, No. 04, pp. 877 – 898.

Harsanyi, J.C. and Chang, I.C. (1994). Hyperspectral Image Classification and Dimensionality Reduction: An Orthogonal Subspace Projection Approach. IEEE *Transactions on Geoscience and Remote Sensing*, Vol. 32, No. 4, pp. 779-785.

Harvey, B., Robert, J.T. and Brent, E.O. (2006). Petrology: Igneous, Sedimentary, and Metamorphic. Third Edition. W.H. Freeman and Company, England, 530 pp.

Hauff, P. (2005). An Overview of VIS-NIR-SWIR Field Spectroscopy as Applied to Precious Metals Exploration: *Spectral International Inc*, 71 pp.

Hedenquest, J.W., Simmons, S.F., Giggenbach, W.F. and Eldridge, C.S. (1993). Volcanic-hydrothermal System Represents the Geochemical Environment of High-sulfidation Cu and Au Ore Deposition. *Geology*, White Island, New Zealand, 21, pp.731-734.

Hein, U.F., Behr, H.J., Van den Kerkhof, A.M., Osswald, U., Reutel, Chr. and Scho¨ttler, T., (1994). Untersuchungen von Flu¨ssigkeitseinschl¨ussen fu¨r die lagerst¨attengenetische Interpretation der Gold-Mineralisationen in NW-Burundi. Z. *Angew. Geol.* Vol. 111, pp. 40-52.

Heinrich, E.W. (1966). The geology of carbonatite. Rand McNally and Co. 555 pp.

Heinrich, E.W. (1970). The Palabora Carbonatitic Complex- A Unique Copper Deposit. *The Canadian Mineralogist*, Vol. 10, pp. 585-598.

© University of Venda

Hemming, S.R., McLennan S.M. and Hanson, G.N. (1995). Geochemical and Nd/Pb Isotopic Evidence for the Provenance of the Early Proterozoic Virginia Formation, Minnesota: Implications for the Tectonic Setting of the Animikie Basin. *Journal of Geology*, Vol. 103, pp.147 - 168.

Heyl, A.V. (1983). Geologic Characteristics of Three Major Mississippi Valley Districts. *International Conference on Mississippi Valley-type Lead-Zinc Deposits*, University of Missouri, Rolla Press, Proceedings, pp. 27 - 60.

Hiller, N. and Snowden, P.A. (1983). Structural and Stratigraphic Relationships in the Cape Fold Belt South of Steytlerville. *Transaction of Geological Society of South Africa*, Vol. 86, pp. 263-271.

Hoefs, J. (1973). Stable Isotope Geochemistry. Springer-Verlag, Berlin Heidelberg, New York, 137pp.

Hoefs, J. (1997). Stable Isotope Geochemistry. 4th Edition. Springer-Verlag, Berlin, 202pp.

Hoefs, J. (1980). Stable Isotope Geochemistry. Completely Second Revised and Updated Edition. Springer-Verlag, Berlin, 205pp.

Hoefs, J. (2004). Stable Isotope Geochemistry. 5th Edition. Springer-Verlag, Berlin, 212pp.

Hoefs, J. (2009). Stable Isotope Geochemistry. 6th Edition. Springer-Verlag, Berlin Heidelberg, New York, 281pp.

Hoefs, J. (2015). Stable Isotope Geochemistry. 7th Edition. Springer, New York, 389pp.

Holmes, A. and Cahen, L. (1957). Geochronologie Africaine. Memoir. Acad. Roy. Sci. Coloniales, Section 8, Vol. 15, No, 1, pp. 1-169.

Hohn, M.E. (1988). Geostatistics and Petroleum Geology. Van Norstrand Reinhold, New York, 400pp.

Horita, J. and Wesolowski, D.J. (1994). Liquid-vapor Fractionation of Oxygen and Hydrogen Isotopes of Water from the Freezing to the Critical Temperature. *Geochimica et Cosmochimica Acta*, Elsevier, Vol. 58, Issue 16, pp. 3425 - 2437.

Huizenga, J.M., van Reenen, D.and Touret, J. (2014). Fluid-rock Interaction in Retrograde Granulites of the Southern Marginal Zone, Limpopo High Grade Terrain, South Africa. *Geoscience Frontiers*, Vol. 5, No. 5, pp. 673 - 682.

Hulbert LJ. and Von Gruenewaldt, G. (1982). Nickel, Copper and Platinum Mineralisation in the Lower Zone of the Bushveld Complex, South of Potgietersrus. *Economic Geology*, Vol. 77, pp. 1296–1306.

Hurai V., Harčova E., Huraiová, Ozdín D., Prochaska W., Wiegerová V. (2002). Origin of Siderite Veins in the Western Carpathians I. P-T-X-Δ13 C-Δ18o Relations in Ore-forming Brines of the Rudňany Deposits. *Ore Geology Reviews*, Vol. 21, pp.67–101.

© University of Venda

Ichikawa, S., Matsumoto, T., NakamUra, T. and Kurisaki, T. (2019). Provenance Determination of Prehistorical Pottery from Oshima Island Belonging to Izu Islands (Tokyo, Japan) using X-ray Fluorescence Spectrometry. X-ray *Fluorescence Spectrometry*, pp.1-19.

Inghram, M.G. and Hayden, R.J. (1954). A Handbook on Mass Spectrometry. National Academy of Sciences, National Research Council, Washington, D.C. Nuclear Science Report No. 14.

Imamalipour, and MousaviVertical, R. (2017). Vertical Geochemical Zonation in the Masjed Daghi Porphyry Copper-gold Deposit, Northwestern Iran: Implications for Exploration of Blind Mineral Deposits. *Geochemistry: Exploration, Environment, Analysis*. Vol.18, No. 2, pp.120-131.

Isaaks, E. and Srivastava, R. (1989). An Introduction to Applied Geostatistics. Oxford University Press Inc., New York, 580 pp.

IUGS/IAGC Task Group on Global Geochemical Baselines (2015). Annual Report of the Task Group on Global Geochemical Baselines for IUGS and IAGC. http://www.globalgeochemicalbaselines.eu: [Accessed: 13 January 2019].

Jacobs, T.T. (2016). Process Mineralogical Characterisation of the Kansanshi Copper Ore, NW Zambia. Masters Thesis, Departmental of Chemical Engineering, University of Cape Town, 214pp.

Jacobsen, J.B.E. (1967). The Geology of the Artonvilla Mine Messina District , PhD. Thesis (unpublished. Witwaterand University, Johannesburg, 123pp.

Jacobsen, J.B.E., (1974). Structure of the Copper Ore Bodies and Country Rocks at Artonvilla Mine, South Africa. *Transactions of Institution of Mining and Metallurgy, Section B*. Vol. 83, pp. 60-64.

Jacobsen, J.B.E. and McCarthy, T.S. (1976). An Unusual Hydrothermal Copper Deposit at Messina, South Africa. *Economic Geology*, Vol. 71, pp. 117 -130.

Jacobsen, J.B.E., McCarthy, T.S. and Laing, G.F. (1976). The Copper Bearing Pipes of the Messina District, South Africa, *Mineralium, Deposita*, pp. 33-45.

Jafari, A., Karimpour, M.H., Mazaheri, S.A., Shafaroudi, A. M. and Ren, M. (2018). Mineral Chemistry and Thermometry of Chlorites in mineralisation Zones and Metamorphic Rocks from Golgohar Iron Ore Deposit, Sirjan, Kerman. *Ranian Journal of Crystallography and Mineralogy*, Ranian Society of Crystallography and Mineralogy, Vol. 26, No. 4, pp. 45 -59.

Je´brak, M. (1997). Hydrothermal Breccias in Vein-type Deposits: A Review of Mechanisms, Morphology and Size Distribution. *Ore Geology Reviews*, Elsevier, Vol. 12, pp. 111 - 134.

© University of Venda

Jianjum, Y. (2009). A New Scheme for Calculating Mineral End-Members with Reference to Clinopyroxene and Garnet. Abstract. Geological Society of China, China.

John, D.A., Ayuso, R.A., Barton, M.D., Blackely, R.J. Bodnar, R.J., Dilles, J.H., Gray, F., Graybeal, F.T., Mars, J.C., McPhee, D.K., Seal, R.R., Taylor, R.D. and Vikre, P.G. (2010). Porphyry Copper Deposit Model. Chapter B of Mineral Deposit Models for Resource Assessment: *US Geological Survey Scientific Investigation Report* 2010 – 5070 – B, 169 pp.

Joseph, G. (2005). Fundamentals of Remote Sensing. 2nd Ed. New Delhi, Universities Press, 47 pp.

Kalinowski, A. and Oliver, S. (2004). ASTER Mineral Index Processing Manual. Remote Sensing Applications, Geoscience Australia, 37 pp.

Kalyuzhnyi, V. A. (1965). The Homogenization Curves in Mineralogical Thermometry and their Construction. In Roedder, E. Sokooff, V.P. (Eds.): Research on the Nature of Mineral Forming Solutions. New York, Pergamon Press, pp. 565-577.

Kamilli, R.J., Ohmoto, H., (1977). Paragenesis, Zoning, Fluid Inclusion and Isotopic Studies of the Finlandia Vein, Colqui District, Central Peru. *Economic Geology*. Vol. 72, pp. 950–982.

Kariuki, P.C., Woldai, T. and Van der Meer, F. (2004). The Role of Remote Sensing in Mapping Swelling Soils. Asian Journal of Geo-Informatics, Vol. 5. pp. 43-53.

Katongo, C., Koller, F., Kloetzli, U., Koeberl, C., Tembo, F., De Waele, B. (2004). Petrography, Geochemistry, and Geochronology of Granitoid Rocks in the Neoproterozoic- Paleozoic Lufilian-Zambezi Belt, Zambia: Implications for Tectonic Setting and Regional Correlation. *Journal of African Earth Sciences*, Vol. 40, pp. 219– 244.

Keays, R.R., Nickel, E.H., Grovers, D.I. and McGoldrick, P.J. (1982). Iridium and Palladium as Discriminants of Volcanic-exhalative, Hydrothermal, and Magmatic Nickel Sulphide Mineralisation. *Economic Geology*, Vol. 77, pp. 1535-1547.

Kelepertzis, E., Galanos, E. and Mitsis, I. (2013). Origin, Mineral Speciation and Geochemical Baseline Mapping of Ni and Cr in Agricultural Top Soils of Thiva Valley (Crental Greece). *Journal of Geochemical Exploration,* Vol. 125, pp. 56-68.

Kendall, C. (2004). Fundamentals of Stable Isotope Geochemistry: Isotope Tracers Projects - Resource on Isotopes. United States Geological Survey: Science for Changing World. http://wwwrcamnl.wr.usgs.gov/isoig/res/funda.html: [Retrieved 30 May 2016]

Kendall, C. and Caldwell, E. A. (1998). Fundamentals of Isotope Geochemistry. In Kendall, C. and McDonnell, J.J. (Eds.): Isotope Tracers in Catchment Hydrology. Chapter 2, Elsevier Science, Amsterdam, pp. 51 - 86.

© University of Venda

Kendall, C., Sklash, M.G. and Bullen, T.D. (1995). Isotope Tracers of Water and Solute Sources in Catchments. In: Trudgill, S.T. (Ed.). Solute Modelling in Catchment Systems, John Wiley and Sons Ltd., New York, pp. 261-303.

Khalil, A., Hanicha, L., Bannarib, A., Zouhric, L., Pourretc, O. and Hakkoud, R. (2013). Assessment of Soil Contamination around an Abandoned Mine in A Semi-Arid Environment Using Geochemistry and Geostatistics: Pre-Work of Geochemical Process Modeling with Numerical Models. *Journal of Geochemical Exploration*, Vol. 125, pp. 117-129.

Khoza, D.T., Jones, A.G., Muller, M.R. and Webb, S.J. (2011). The Electrical Lithosphere in Archean Cratons: Examples from Southern Africa. American Geophysical Union, Abstract id. DI23C-2101.

Kisters, A.F.M., Kolb, J. and Meyer, F.M. (1998). Gold Mineralisation in High Grade Metamorphism Shear Zones of the Renco Mine, Southern Zimbabwe. *Economic Geology*, Vol. 93, pp. 587-601.

Komeili, S.S., Khalili, M., Haroni, H.A., Bagheri, H. and Ayati, Bagheri. (2017). The Nature of Hydrothermal Fluids in the Kahang Porphory Copper Deposit, Northeast of Isfahan, Based on Mineralography, Fluid Inclusion and Stable Isotopic Data. *Journal of Economic Geology*, Vol. 8, Issue No. 2, pp. 285 -305.

Kowalski, B. and Kissin, S. (2018). A Fluid Inclusion Study of the Brookband Deposit, Northwest Ontario: A transition from Mesothermal to Epithermal Gold Deposition. *Minerals*, MDPI, Vol 8, Issue No. 3.

Kramers, J.D., McCourt, S. and Van Reenen, D.D. (2006). The Limpopo Belt. In Johnson, M.R., Anhaeusser, C.R. and Thomas, R.J. (Eds.). The Geology of South Africa, Geological Society of South Africa, Johannesburg/Council for Geoscience, Pretoria, Chapter 9, pp. 209-236.

Kramers, J.D., McCourt, S., Roaring, C., Smit, C.A. and Van Reenen, D.D. (2011). Origin and Evolution of Precambrian High Grade Gneiss Terranes, with Special Emphasis on the Limpopo Complex of Southern Africa. In Van Reenen, D.D., Kramers, J.D., and McCourt, S. (Eds.). *Geological Society of America Memoirs*, Vol. 207, pp. 31-324.

Kranz, R.L. (1983). Micro-Cracks in Rocks: A Review. *Tectonophysics*. Vol. 100, pp. 449–480.

Krenn, K. and Le Thi-Thu Huong. (2019). Fluid Characteristics from Shallow Magmatic environments: A contribution to Danburite Bearing Luc Yen Pegmatites, Northern Vietnam. Vietnam, *Journal of Earth Sciences,* Vietnam Academy of Scienceand Technology, Vol. 41, No. 1, pp. 1-49.

© University of Venda

Kriti, B. and Rishi, S. (2017). Analysis of Image Enhancement Techniques Used in Remote Sensing Satellite Imagery. *International Journal of Computer Applications*, Vol. 169, No. 10, pp. 1-12.

Kröner, A. (1978). The Namaqua Mobile Belt within the Framework of Precambrian Crustal Evolution in Southren Africa. In Verwoerd, W.J. (ed.): *Mineralisation in Metamorphic Terranes. Geokongress 75*, Stellenbosch, South Africa, Schaik J.L. Limited, Pretoria, Chapter 11, pp.181-188.

Kullerud, G., Yund, R.A. and Moh, G. (1969). Phase Relations in the Cu-Fe-S, Cu-N-S and Fe-Ni-S Systems. *Economic Geology Monograph*, Vol. 4, pp. 323-343.

Kyser, T.K. (1987a). Equilibrium Fractionation Factors for Stable Isotopes. Mineralogical Association of Canada Short Course Handbook, Vol. 13, pp.1 – 84.

Landis, C.A. (1971). Graphitization of Dispersed Carbonaceous Materials in Metamorphic Rocks. *Mineral Petrology*, Vol. 30. Pp. 34-45.

Landon, J. R. (1984). Booker Tropical Soil Manual. New York: Longman Inc.

Levinson, A. A., (1980). Introduction to Exploration Geochemistry. 2nd Edition, Applied Publishing, Wilmette, IL, pp. 615-924.

Li, W. (1995). Automatic Identification of Rocks in Thin-sections using Texture Analysis. *Mathematical Geosciences*, Vol. 27, Issue 7, pp. 847 -865.

Li, Y.B. and Liu, J.M. (2006). Calculation of Sulfur Isotope Fractionation in Sulfides. *Geochim. Cosmochim. Acta* 70, pp. 1789 - 1795.

Li, M., Xi, X., Xiao, G., Cheng, H., Yang, Z., Zhou, G., Ye, J. and Li, Z. (2014). National Multi-purpose Regional Geochemical Survey in China. *Journal of Geochemical Exploration*, Elsevier, Vol. 139, pp. 21 -30.

Li, X., Zhao, X., Zhou, M.F., Chen, W.T. and Chu, Z. (2015). Fluid Inclusion and Isotopic Constraints on the Origin of the Paleoproterozoic Yinachang Fe-Cu-(REE) Deposit, Southwest China. *Economic Geology*, Society of Economic Geologists Inc., Vol. 110, No. 5, pp. 1339 - 1369.

Li, S.N., Ni, P., Bao, T., Li, C.Z., Xiang, H.L., Wang, G.G., Huang, B., Chi, Z., Dai, B.Z. and Ding, J.Y. (2018). Geology, Fluid Inclusion, and Stable Isotope Systematics of the Dongyang Epithermal Gold Deposit, Fujian Province, Southeast China: Implications for Ore Genesis and Mineral Exploration. *Journal of Geochemical Exploration*, Elsevier, Vol. 195, pp. 16 – 30.

Li, W. S., Ni, P., Pan, J.Y. Wang, G.G., Chen, L.L., Yang, Y.L. and Ding, J.Y. (2018). Fluid Inclusion Characteristics as an Indicator for Tungstern Mineralisation in the Mesozoic Yaogangxian Tungsten Deposit, Central Nanling District, South China. *Journal of Geochemical Exploration*, Elsevier, Vol. 192, pp. 1-17.

© University of Venda

Li, S. and Zhang, X. (2019). Ore Genesis at the Jinchang Gold –copper Deposit in Heilongjiang Province, Northern China: Evidence from Geology, Fluid Inclusions, and H-O-S Isotopes. *Minerals*, Vol. 9, Issue No. 2

Limtrakun1 P., Zaw, K., Ryan, C. G. and Mernagh, T. P. (2001). Formation of the Denchai Gem Sapphires, Northern Thailand: Evidence from Mineral Chemistry and Fuid/Melt Inclusion Characteristics. *Mineralogical Magazine*, The Mineralogical Society, Vol. 65, No. 6, pp. 725-735.

Lintz, J. and Simonett, D.S. (1976). Remote Sensing of Environment. 1st Edition, Addison-Wesley Pub. Co., University of Michigan, 694pp.

Liu, W. and Mcphail, D. (2005). Thermodynamic Properties of Copper Chloride Complexes and Copper Transport in Magmatic-hydrothermal Solutions. *Chemical Geology*. Vol. 221, pp. 21-39.

Liu, D. and Xia, F. (2010). Assessing Object-based Classification: Advantages and Limitations. *Remote Sensing Letters*, Vol. 1, No. 4, pp. 187-194.

Liu, Y. Nie, F., Jiang, S., Baga, L., Xiao, W. and Cao, Y. (2016). Geology, geochronology and Sulphur Isotope Geochemistry of the Black Schist-hosted Haoyaerhudong Gold Deposit of Inner Mongolia, China: Implications to Ore Genesis. *Ore Geology Reviews*, Elsevier, Vol. 73, pp. 253-269.

Liu, Y., Zhou, K., Carranza, E.J.M., (2018). Compositional Balance Analysis for Geochemical Pattern Recognition and Anomaly Mapping in the Western Junggar Region, China. *Geochemistry: Exploration, Environment, Analysis*, Vol. 28, pp. 263-76.

Liu, Y., Cheng, Q., Carranza, E.J.M. and Zhou, K. (2019). Assessment of Geochemical Anomaly Uncertainty through Geostatistical Simulation and Singularity Analysis. *Natural Resources Research*, Vol. 28, No, 1, pp. 199 -212.

Lode, J., Piercey, S. J., Layne, G. D., Piercey, G. and Cloutier, J. (2017). Multiple Sulphur and Lead Sources Recorded in Hydrothermal Exhalites Associated with the Lemarchant Volcanogenic Massive Sulphide Deposit, Central Newfoundland, Canada. *Mineralium Deposita*, Vol. 52, Issue 1, pp. 105–128.

Loftus-Hills, G, and Solomon M. (1967). Cobalt, Nickel and Selenium in Sulphides as Indicators of Ore Genesis. *Mineralium Deposita*, Vol. 2, pp. 228–242.

Lombaard, A.F., Ward-Able, N.M. and Bruce, R.W. (1964). The Exploration and Main Geological Features of the Copper Deposit in Carbonatite in Loolekop, Palabora Complex. In Haughton, S.H. (Eds.). *The Geology of Some Ore Deposits of Southern Africa.* Geological Society of South Africa, Vol. 2, pp. 303-314.

Long, J. V. P. (1963). Recent Advances in Electron-probe Analysis. In: Mueller, W. M. and Fay, M. (Eds.). Advances in X-Ray Analysis. *Proceedings of the 11th Annual*

© University of Venda

Conference on Applications of X-ray Analysis, New York, Plenum Press, Vol. 6, pp. 276–90.

Long, J.V.P. and Agrell, S.O. (1965). The Cathodoluminescence of Minerals in Thin Section. *Mineralogical Magazine*, Vol. 34, pp. 318–26.

Longley, P. A., Goodchild, M. F., Maguire, D. J., and Rhind, D. W. (2011). Geographic Information Systems and Science, 3rd Edition.. Hoboken, NJ: John Wiley and Sons. 539pp.

Machel, H.G., Mason, R.A., Mariano, A.N. and Mucci, A. (1991). Causes and Emission of Luminescence in Calcite and Dolomite. In: Barker, C.E. and Kopp, O.C. (Eds.). Luminescence Microscopy and Spectroscopy: Qualitative and Quantitative applications. Society of Sedimentary Geologists, *Special Publication of SEMP*, Short Course, 25, pp. 9 – 25.

Macqueen, R.W. and Thompson, R.I. (1978). Carbonate -hosted Lead-Zinc Occurrence in Northeastern British Columbia with Emphasis on the Robb Lake Deposit. *Canadian Earth Sciences,* Vol. 15, pp. 1737 - 1762.

Maggi, F. and Riley, W. J. (2010). Mathematical Treatment of Isotopologue and Isotopomer Speciation and Fractionation in Biochemical Kinetics. *Geochimica et Cosmochimica Acta*, Elsevier, Vol. 74, Issue 6, pp.1823 -1835.

Manson, D.C., Giustain, L., Garcia-Pintado, J. and Cloke, H.L. (2014). Detection of flooded Urban Areas in high Resolution Synthetic Aperture Radar Images Using Double Scattering Original Research Article. *International Journal of Applied Earth Observation and Geoinformation*, Vol. 28, pp. 150-159.

Marfunin, A.S. (1979). Spectroscopy, Luminescence and Radiation Centers in Minerals. Springer, Berlin Heidelberg New York, 352 pp.

Mason, R. and Loxton, R.F. (1973). The Limpopo Mobile Belt: Sothern Africa. *Phil. Transaction of Royal Society of London*, A273, pp. 463-485.

Marshall, D.J. (1993). The Present Status of Cathodoluminescence Attachments for Optical Microscopes. *Scanning Microscopy*, Vol. 7, pp. 861–74.

Marshall, D.J. (1988). Cathodoluminescence of Geological Materials, Boston, Unwin Hyman, 146 pp.

Martin, A.P., Turnbull, R.E. Ratterberry, M.S., Cohen, D.R., Hoogewerff, J., Rogers, K.M., Baisden, W.T. and Christie, A.B. (2016).The Regional Geochemical Baseline Soil Survey of Southern New Zealand: Design and Initial Interpretation. *Journal of Geochemical Exploration,* Vol.167, pp. 70-82. pp

Martin, H. (1978). The Mineralisation of the Ensialic Damara Orogenic Belt. In Verwoerd, W.J. (ed.): *Mineralisation in Metamorphic Terranes. Geokongress 75*, Stellenbosch, South Africa, Schaik J.L. Limited, Pretoria, Chapter. 26 pp. 405-415.

© University of Venda

Martin, J.D. and Simpson. T.W. (2005). Use of Kriging Models to Approximate Deterministic Computer Models. *The American Institute of Aeronautics and Astronautics (AIAA) Journal*, Vol. 43, No. 4, pp. 853-863.

Mason, R. and Loxton, R.F. (1973). The Limpopo Mobile Belt: Sothern Africa. Phil. *Transaction of Royal Society of London*, A273, pp. 463-485.

Maydagán, L., Franchini, M. Rusk, B., Lentz, D.R. McFarlane, C. Impiccini, A., Ríos, F. J. and Rey, R. (2015). Porphyry to Epithermal Transition in the Altar Cu-(Au-Mo) Deposit, Argentina, Studied by Cathodoluminescence, LA-ICP-MS, and Fluid Inclusion Analysis. *Economic Geology*, Society of Economic Geology, Vol. 110, pp. 889 - 923.

McCarthy, T.S. and Jacobsen, J.B.E. (1976). The Mineralizing Fluid at the Artonvilla copper Deposits: An Example of a Silica-deficient, Alkaline Hydrothermal System. *Economic Geology*, Vol. 71, pp. 131-138.

McCarthy, T.S. and Jacobsen, J.B.E. (1980). Additional Geochemical Data on the Messina Copper Deposits, Transvaal, South Africa- A Discussion. *Economic Geology*, Vol. 75, pp.478-483.

McGowan, R.R., Roberts, S., Foster, R. P., Boyce, A.J. and Coller, D. (2003). Origin of the Copper-Cobalt Deposits of the Zambian Copperbelt: An Epigenetic View from Nchanga. *Geology*, Geological Society of America, Vol. 31, No. 6, pp. 497-500.

McKibben, M.A. and Riciputi, L.R. (1998). Sulfur Isotopes by Ion Microprobe. In Mckibben, M.A., Shanks, W.C. and Ridley, W.I. (eds.): Applications of Micro Analytical Techniques to Understanding Mineralizing Processes. *Reviews in Economic Geology*, Vol. 7, pp. 121 -139.

McMillan, P.F., Dubessy, J., Hemley, R. (1996). Applications in Earth, Planetary and Environmental Sciences. In Turrell, G., and Corset, G. (Eds.): Raman Microscopy. Academic Press, pp. 289 - 351.

Megan, E.E, Ollie, L.R, Lesley, A.I.W. (2002). Potential Applications in Baseline Geochemical Data Integration for Geoscience Australia: A Report of Findings from a Pilot Study. Geoscience Australia, Record 2003/08, pp. 1-3.

Meinert, L.D. (1992). Variability in Skarn Deposits: Guides to Exploration. In Boardman, S.J. (Ed.). Revolution in Earth Sciences, Dubugue, Iowa: Kendall/Hunt, pp. 301-317.

Mendelsohn, F. (1961). The Geology of Northen Rhodesiaan Copperbelt. London:Macdonald and Co., 523pp.

Michael, F. (2008). A Brief History of Data Visualization. In: Chen, C., Härdle, W. and Unwin, A. (Eds.). *Handbook of Computational Statistics: Data Visualization*. Vol. III, Springer-Verlag, Heidelburg. Chapter. II.1, pp. 15-56.

© University of Venda

Mignot, C. (2018). Color (and 3D) for Scanning Electron Microscopy. *Microscopy Today*, Vol. 26, Issue 3, Microscopy Society of America, pp.12-17.

Mihalik, P., Jacobsen, J.B.E. and Hienstra, S.A. (1974). Platinum Groups Minerals from a Hydrothermal Environment. *Economic Geology*, Vol. 69, pp. 257-262.

Miller, D.J., Cervantes, P. (2002). Sulfide Mineral Chemistry and Petrography and Platinum Group Element Composition in Gabbroic Rocks from the Southwest Indian Ridge. In Natland, J.H., Dick, H.J.B., Miller, D.J., and Von Herzen, R.P. (Eds.). *Proceedings of the Ocean Drilling Program*, Scientific Results, Vol.176, pp. 1-29.

Milliken, K.L. and Laubach, S.E. (2000). Brittle Deformation in Sandstone Diagenesis as Revealed by Scanned Cathodoluminescence Imaging with Application to Characterization of Fractured Reservoirs. In: Pagel, M., Barbin, V, Blanc, P. and Ohnenstetter, D. (Eds.). *Cathodoluminescence in Geosciences*, Berlin, Springer-Verlag, pp. 225–243.

Misra, K.C. (2000). Understanding Mineral Deposits. Kluwer Publishers, Netherlands, 843pp.

Misra, K.C. (2012). Introduction to Geochemistry: Principles and Applications. John Wiley and Sons Ltd, UK, 438pp.

Mitchell, C.J. (1993). Industrial Minerals Laboratory Manual: Flake Graphite. Technical Report WG/92/30, *Mineralogy and Petrology Series*. British Geological Survey, UK, pp. 31.

Mokhtari, A.R., Cohen, D.R. and Gatehouse, S.G. (2009). Geochemical Effects of Deeply Buried Cu–Au Mineralization on Transported Regolith in an Arid Terrain. *Geochemistry: Exploration, Environment, Analysis.* Association of Applied Geochemistry and the Geological Society, Vol. 9, No, 3, pp. 227-236.

Moore, W. J. and Nash, T. (1974). Alteration and Fluid Inclusion Studies of the Porphyry Copper Ore Body at Bingham, Utah, *Economic Geology*, Vol. 69, No. 5, pp. 631 - 645.

Mukhopadhyay, T., Chakraborty, S., Dey, S., Adhikari, S. and Chowdhury, R. (2017). A Critical Assessment of Kriging Model Variants for High-Fidelity Uncertainty Quantification in Dynamics of composite Shells. *Achieves of Computational Methods in Engineering*, Springer Netherlands, Vol. 24, No. 3, pp. 495–518.

Müller, A., Seltmann, R. and Behr, H.J. (2000). Application of Cathodoluminescence to Magmatic Quartz in a Tin Granite: Case Study from the Schellerhau Granite Complex, Easyern Erzgebrirge, Germany. *Mineralium Deposita*, Vol. 35, pp.169-189.

Mundalamo, H. R. and Ogola, J.S. (2012). Messina Copper Sulphide Deposits Revisited: Geological and Structural Study of the Deposits. 12th International Multidisciplinary Scientific GeoConference, SGEM2012 Conference Proceedings, Vol. 1, pp. 399-408.

© University of Venda

Nasdala, L., Smith, D.C., Kaindl, R., and Zieman, M.A. (2004). Raman Spectroscopy: Analytical Perspectives in Mineralogical Research. In Beran, A. and Libowitzky, E. (Eds.): Spectroscopic Methods in Mineralogy: EMU Notes in Mineralogy, Vol. 6, pp. 281 - 343.

Nash, J.T. (1976). Fluid-Inclusion Petrology - Data from Porphyry Copper Deposits and Applications to Exploration: A Summary of New and Published Descriptions of Fluid Inclusions from 36 Porphyry Copper Deposits and Discussion of Possible Applications to Exploration for Copper Deposits. Geology and Resources of Copper Deposits, Geological Survey Professional Paper 907-D, Superintendent of Documents, U.S. Government Printing Office Washington, D C, Document No. I19.16:907-D, 26pp.

Nash, J. T. and Theodore, T. G. (1971). Ore Fluids in a Porphyry Copper Deposit at Copper Canyon, Nevada. *Economic Geology*, Vol. 66, pp. 385 - 399.

Ndhlalose, M., Malumbazo, N. and Wagner, N. (2015). Coal Quality and Uranium Distribution Distribution in Uranium Springbok Flats Coalfields Samples, *The Journal of the Southern African Institute of Mining and Metallurgy*, Vol. 115, pp.1167–1174.

Nel, G.P. and Nel, E.J. (2009). Description of the Natural Environment and Biodiversity Impact Assessment of the Planned Vele Colliery, Musina: DUBEL Integrated Environmental Services, 97pp.

Nelson, S.A. (2015). Deformation of Rocks. Retrieved, 30 November 2016 from Tulane University: http://www.tulane.edu/~sanelson/eens1110/deform.htm.

Nesse, W.D., (2012). Introduction to Mineralogy. Oxford University Press Inc, 2nd Edition, New York, pp. 338-358.

Neuser, M.S. (2009). Cathodoluminescence Microscope HC5-LM: User and Service Manual. Lumioc Special Microscopes, Manual No. 1019, Bochum, Germany, 12 pp.

Newton, A.R., Shone, R.W. and Booth, P.W.K. (2006). The Cape Fold Belt. In Johnson, M.R., Anhaeusser, C.R. and Thomas, R.J. (Eds.). *The Geology of South Africa*, Geological Society of South Africa, Johannesburg/Council for Geoscience, Pretoria, Chapter 24, pp. 521-530.

Ngcofe, L., Minnaar, H., Halenyane, K. and Chevallie, I.R. (2013). Multispectral and Hyperspectral Remote Sensing: Target Area Generation for Porphyry Copper Exploration in the Namaqua Metamorphic Province, South Africa. *South African Journal of Geology*, Vol. 116, Number 2, pp. 259-272.

Ngcofe, L., Minnaar, H. and Chevallier, L. (2010). A Comparative Study of Hyperspectral versus Multispectral Mapping near Alexander Bay, Northern Cape, South Africa. *South African Journal of Geology*, Vol.113, No. 2, pp. 141-154.

© University of Venda

Nier, A.O. (1940). Amass Spectrometer for Routine Isotope Abundance Measurements. *Rev. Sci. Instrum.* Vol.11, pp. 212 - 216.

Nier, A.O. (1947). A Mass Spectrometer for Isotope and Gas Analysis. *Rev. Sci. Inst.*, Vo.18, pp. 398 - 411.

Norman, N. and Whitfield, G. (2006). Geological Journeys*: A Traveler's Guide to South Africa's Rocks and Landforms*. Struik Nature, Cape Town, South Africa, 320 pp.

Nxumalo, V. (2013). The Mineral Potential and Geology of the Rosendal Area (Free States Province) with Special Focus on Uranium and Molybdenum Distribution. Technical Report 2013-0089.

Ogola, J.S. (1987). Mineralization in the Migori Greenstone Belt Macalder, Western Kenya. *Geological Journal*, Vol. 22, Thematic Issue, John Wiley and Sons, Ltd., pp. 25-44.

Ogola, J.S. and Mundalamo, H.R. (2011). Investigation of the Origin and Distribution of Heavy Metals around Ebenezer Dam, Limpopo Province, South Africa. Water SA 2567, Vol. 37, No. 2, pp.173-179. ISSN 0378-4738 (Print), ISSN 1816-7950 (On-line).

Ohmoto, H. (1986). Stable Isotope Geochemistry of Ore Deposits. In Valley, J.W., Taylor, Jr. H.P., and O'Neil, J.R. (Eds.): Stable Isotopes in High Temperature Geological Processes. Reviews in Mineralogy, American Mineralogy Society, Blacksburg, Virginia, Chapter 14, Vol. 16, pp. 491 - 560.

Ohmoto, H. and Rye, R.O. (1979). Isotope of Sulur and Carbon. In Barnes, H.I. (ed.): Geochemistry of Hydrothermal Ore Deposits. 2nd Edition. John Wiley and Sons, New York, pp. 517 - 612.

Ohmoto, H. and Goldhaber, M.B. (1997). Sulfur and Carbon Isotopes. In Barnes, H.L. (ed.): Geochemistry of Hydrothermal Ore Deposits. 3rd edition. John Wiley and Sons, pp. 517 - 611.

Ohle, E.L. (1990). A Comparison of the Old Land Belt and the New Belt in Southeast Missouri. *Economic Geology*, Vol. 85, pp.1894 - 1895.

Olea, R (2008). Basic Statistical Concepts and Methods for Earth Scientist. Open -File Report 2008-1017. U.S. *Geological Survey*, Reston, Virginia, 193 pp.

Olson, D.W. (2000). Garnet Industrial: United State. United State Geological Survey Minerals Yearbook, pp. 29.1-29.3.

Ohmoto, H. (1986). Stable Isotope Geochemistry of Ore Deposits. In Valley, J.W., Taylor, Jr. H.P., and O'Neil, J.R. (eds.): Stable Isotopes in High Temperature Geological Processes. Reviews in Mineralogy, *American Mineralogy Society*, Blacksburg, Virginia, Chapter 14, Vol. 16, pp. 491 - 560.

© University of Venda

Ohmoto, H. and Goldhaber, M.B. (1997). Sulfur and Carbon Isotopes. In Barnes, H.L. (ed.): Geochemistry of Hydrothermal Ore Deposits. 3rd edition. John Wiley and Sons, pp. 517 - 611.

O'Neil, J.R. (1986a). Theoretical and Experimental Aspects of Isotopic Fractionation. In Valley, J.W., Taylor, Jr. H.P., and O'Neil, J.R. (eds.): Stable Isotopes in High Temperature Geological Processes. *Reviews in Mineralogy*, American Mineralogy Society, Blacksburg, Virginia, Chapter 1, Vol. 16, pp. 1 - 40.

O'Neil, J.R. (1986b). Terminology and Standards. In Valley, J.W., Taylor, Jr. H.P., and O'Neil, J.R. (eds.): Stable Isotopes in High Temperature Geological Processes. *Reviews in Mineralogy*, American Mineralogy Society, Blacksburg, Virginia, Appendix, Vol. 16, pp. 561 - 570.

Ortiz, J.M., Oz, B. and Deutsch, C.V. (2005). A Step by Step Guide to Bi-Gaussian Disjunctive Kriging. In: Leuangthong, O., Deutsch, C.V. (Eds.). Geostatistics Banff 2004. *Quantitative Geology and Geostatistics*, Springer, Dordrecht, Vol. 14, pp. 1097-1102.

Ossandon, G., Freraut, R., Gustafson, L.B., Lindsay, D.D., and Zentilli, M. (2001). Geology of the Chuquicamata Mine: A Progress Report. *Economic Geology*, Vol. 96, pp. 249–270.

Pagel, M., Barbin, V. Blanc, P. and Ohnenstetter, D. (2000). Cathodoluminescence in Geosciences: An Introduction. In Pagel, M., Barbin, V. Blanc, P. and Ohnenstetter, D. (Eds.). *Cathodoluminescence in Geosciences*. Springer-Verlag, Berlin Heidelberg, New York, Chapter 1, pp.1-22.

Panneerselvan, K., Macfarlane, A.W. and Salters, V.J.M. (2006). Provenance of Ore Metals in Base and Precious Metal Deposits of Central Idaho as Inferred from Lead Isotopes. *Economic Geology*, Vol. 101, pp.1063 - 1078.

Passchier, C.W. and Trouw, R.A.J. (2014). Microtectonics. 2nd Edition. Springer, Heidelberg, Berlin. 366pp.

Pasteris, J.D. (1984). Further Interpretation of the Cu-Fe-Ni Sulfide Mineralization in the Duluth Complex, North-eastern Minnesota. *Canadian Mineralogist*. Vol. 22, No. 1, pp. 39-53.

Paterson, B.A., Riciputi, L.R. and McSween, H.Y. Jr. (1997). A Comparison of Sulfur Isotope Ratio Measurement Using Two Ion Microprobe Techniques and Application to Analysis of Troilite in Ordinary Chondrites. *Geochim Cosmochim Acta*, Vol. 61, pp.601-609.

Park, C.F. and MacDiarmid, R.A. (1975). Ore Deposits. W.H. Freeman and Company Publishers, San Francisco, 529 pp.

Pelletier, R.A. (1964). Mineral Resource of South Central Africa. Oxford University Press, London, 277 pp.

© University of Venda

Peters, S.G. (1993). Nomenclature, Concepts and Classification of Ore-shoots in Vein Deposits. *Ore Geology Reviews*, Elsevier, Vol. 8, Issues 1-2, pp. 3 - 22.

Peters, S. (2008). Ein Vergleich räumlicher Interpolationsverfahren für Ertragswerte im Weinanbau. München: Technische Universität München.

Philpot, W. (2001). CEE 615: Digital Image Processing. Cornell, Cornell University, 21 pp.

Pirajno, F. (2012). Hydrothermal Mineral Deposits: Principles and Fundamental Concepts for the Exploration Geologists. Springer Science and Business Media, 709pp.

Plant, J.A. (1986). Models for Granites and their mineralizing systems in British and Irish Caledonides. In Geology and gneiss of mineral deposits in Ireland. Andrew, C.J. Crowe, R.W.A., Finlay, S., Pennell, W.M. and Pyne, J.F. (Eds.). *Economic Geology*, Dublin Irish Association, pp. 121-156.

Plant J. A., Baldock, J. W. and Smith, B. (1996). The Role of Geochemistry in Environmental and Epidemiological Studies in Developing Countries. In Appleton, J. D., Fuge, R. and McCall, G. J. H. (Eds.): *Environmental Geochemistry and Health*, Geological Society Special Publication No. 113. pp. 7-22.

Podlešáková, E., Němeček, J. and Roth, Z. (1999), Mobility of Trace Elements in Soils. Rostlinna Vyroba, Vol. 45 No. 8, pp. 337-344.

Potter, R.W. (1977). Pressure Corrections for Fluid Inclusion Homogenization Temperatures Based on the Volumetric Properties of the System NaCl–H_2O. *USGS Journal of Research*, Vol. 5, pp. 603 - 607.

Potts, P.J. (1987). A Handbook of Silicate Rock Analysis. Chapman and Hall, 320 pp.

Price, M. and Walsh, K. (2005). Rocks and Minerals: Pocket Nature. Dorling Kindersley Limited, London, 216 pp.

Randive, K.R. (2012). Elements of Geochemistry, Geochemical Exploration and Medical Geology: *Soil Geochemical Survey*. Research Publishing, 330 pp.

Ramírez, L.E., Palacios, C., Townley, B., Parada, M.A., Sial, A.N., Fernandez-Turiel, J.L., Gimeno, D., Garcia-Valles, M. and Lehmann, B. (2006). The Mantos Blancos Copper Deposit: An Upper Jurassic Breccia-style Hydrothermal System in the Coastal Range of Northern Chile. *Mineral Deposita*. Vol. 41, pp. 246 - 258.

Ramsay, J.G. and Huber, M.I. (1987). The Techniques of Mordern Structural Geology: Folds and Fractures, Vol 2. London, Academic Press, 677 pp.

Ray, S.S. (2004). Basics of Remote Sensing. In: Hukum, C. and Kaustav, A. (Eds.). E-book on Techniques of Estimation and Forecasting of Crop Production in India. Chapt. 23, pp. 244 - 250. http://www.iasri.res.in/ebook/TEFCPI_sampling: [Accessed: 17 March 2016].

© University of Venda

Ray, S. S., Sood, A., Das, G., Panigrahy, S., Sharma, P. K. and Parihar, J. S. (2005). Use of GIS and Remote Sensing for Crop Diversification: A Case Study for Punjab State. *Journal of the Indian Society of Remote Sensing*, Vol. 33, No. 2, pp. 181-188.

Reeder, R.J. and Dollase, W.A. (1989). Structural Variation in the Dolomite-Ankerite Solid -solution Series: An X-ray, Mössbauer, and TEM Study. *American Mineralogist*, Vol. 74, pp. 1159-1167.

Rees, C.E. and Holt, B.D. (1991). The Isotopic Analysis of Sulphur and Oxygen. In Krouse, H.R. and Grinenko, V.A. (Eds.): Stable Isotopes: Natural and Anthropogenic Sulphur in the Environment. Scope 43. John Wiley and Sons Ltd., Chichester, UK, Vol. 24, INIS Issue10, 440 pp.

Reif, D., Grasemann, B. and Faber, R.H. (2011). Quantitative Structural Analysis using Remote Sensing Data: Kurdistan, Northeast Iraq. The American Association of Petroleum Geologists, AAPG Bulletin, Vol. 95, No. 6, pp. 941-956.

Reimann, C., and Garret, R. G. (2005). Geochemical Background – Concept and Reality. Science of the Total Environment, 350, 12-27. DOI: 10.1016/j.scitotenv.2005.01.047.

Remond, Gesborn, F., Chapoulie, R., Ohnenstetter, D., Roques-Carmes, C. and Schvoere, M. *et al.* (1992). Remond, G., Cesbron, F., Chapoulie, R., Ohnenstetter, D. Roques-Carmes, C. Schvoerer, M. (1992). Cathodoluminescence Applied to the Micro-characterization of Mineral Materials: A Present Status in Experimentation and Interpretation. *Scanning Microscopy*, Vol. 6, pp. 23–68.

Ren, H. and Chang, C.I. (2000). Target-constrained Interference-minimized Approach to Subpixel Target Detection for Hyperspectral Images. *Optical Engineering*, Vol. 39, No. 12, pp. 3138-3145.

Richards, J.A. (2013). Geometric Processing and Enhancement: Image Domain Techniques. In Richards, J.A. (Ed.): Remote Sensing Digital Image Analysis: An Introduction. Chapt. 5, Springer Berlin Heidelberg, Germany, pp.127 – 159.

Ridley, J.R. (1992). On the Origins and Techtronic Significance of the Charnockite Suit of the Archean Limpopo Belt, Northern Marginal Zone. *Precambrian Research*, Vol. 55, pp. 407-427.

Rigby, M.J., Basson, I.J., Kramers, J.D., Gräser, P. and Mavimbela, P.K. (2011). The Structural, Metamorphic and Temporal Evolution of the Country Rocks Surrounding Venetia Mine, Limpopo Belt, South Africa: Evidence for a Single Palaeoproterozoic Tectono-Metamorphic Event with Implications for a Tectonic Model. *Precambrian Research*, Elsevier, Vol. 186, Issues 1–4, pp. 51-69.

Rivoirard, J. (1994). Introduction to Disjunctive Kriging and Non-Linear Geostatistics: Spatial Information Systems, Published by Oxford University Press, 192pp.

© University of Venda

Roedder, E. (1971). Fluid Inclusion Studies on the Porphyry-type Ore Deposits at Bingham, Utah, Butte, Montana, and Climax, Colorado: *Economic Geology*, Vol. 66, pp. 98 - 120.

Roedder, E. (1972). Composition of Fluid Inclusions. In Fleischer, M. Data of Geochemistry. 6th Edition. U.S. *Geological Survey*, Professional Paper, Chapter JJ-440, 164 pp.

Roeder, E. (1979). Fluid Inclusions as Samples of Ore Fluids. In Geochemistry of the Hydrothermal Ore Deposits. 2nd Edition. Barnes, H.L. (Ed.): New York, John Wiley and Sons, pp. 684 - 737.

Roedder, E. (1984). Fluid Inclusions. In Ribbe, P.H. (Ed.): Reviews in Mineralogy, *Mineralogical Society of America*, Cambridge University Press, New York, Vol. 126, 44pp.

Roedder, E. (2002). Fluid Inclusions. Encyclopaedia of Physical Science and Technology. 3rd Edition, *Academic Press*, US, Vol. 6, pp. 71-77.

Roedder, E. and Bodnar, R.J. (1980). Geologic Pressure Determinations from Fluid Inclusion Studies. *Annual Review of Earth and Planetary Sciences*, Vol. 8, pp. 263 – 30.

Roedder, E. and Bodnar, R.J. (1997). Fluid Inclusion Studies of Hydrothermal Ore Deposits. *Journal of Geochemistry of Hydrothermal Ore Deposits*, John Wiley and Sons, Vol. 3, pp. 657 - 697.

Rollinson, H. R. (1993). Using Geochemical Data: Evaluation, Presentation, and Interpretation. London: Prentice Hall publishers. 352 pp.

Rollinson, H.R. and Bleinkinsop, T. (1989). The Magmatic, Metamorphic and Tectonic Evolution of Northern Marginal Zone of the Limpopo Belt in Zimbabwe. *Journal of Geological Society*, London, Vol. 152, pp. 66-75.

Rose, A. W., Hawkes, H. E. and Webb, J. S. (1979). Geochemistry in Mineral Exploration, 2nd Ed. London: Academic Press, 81 pp.

Rousselot, D. and Weber, C. (1987). Utilization of SPOT for Mineral Exploration, with Special Reference to Western Africa. Advances in Space Research, Vol. 7, No. 3, pp. 95-99.

Rühle, S. (2012). Metadaten. In Kleines Handbuch Metadaten. Kompetenzzentrum Interoperable Metadaten.

Rusk, B.G. (2012). Cathodoluminescence and Trace Elements in Hydrothermal Quartz. In: Gotze, J., Mocke, R. (Eds.). Quartz: Deposits, Mineralogy and Analytics, Springer Berlin, Chapt. 14, pp.307 -329.

Russell, H.D., Hiemstra, S.A. and Groeneveld, D. (1954). The Mineralogy and Petrology of the Carbonatite at Loolekop, Eastern *Transvaal. Transaction of the Geological Society of South Africa,* Vol. 57, pp. 197-208.

© University of Venda

Rye, R.O. and Ohmoto, H. (1974). Sulfur and Carbon Isotopes and Ore Genesis*: A Review. Economic Geology*, Vol. 69, pp. 826 - 842.

Sabins, F.F. (1999). Remote Sensing for Mineral Exploration. *Ore Geology Reviews*, Vol. 14, No. 3, pp. 157-183.

SACS (South African Committee for Stratigraphy), (1980). Stratigraphy of South Africa: Part 1. Handbook of the Geological Survey of South Africa, Vol. 8, pp. 690.

Sadeghi, M., Billay, A. and Carranza, E.J.M. (2015). Analysis and Mapping of Soil Geochemical Anomalies: Implications for Bedrock Mapping and Gold Exploration in Giyani Area, Southn Africa. *Journal of Geochemical Exploration, Elsevier*, Vol. 154, pp. 180 – 193.

SAHRA. (2005). Introduction to Isotopes. Arizona Board of Reagents. Retrieved 08 May 2016, from http://web.sahra.arizona.edu/programs/isotopes/types/index.htm: [Accessed: 17 may 205].

Salati, S., van Ruitenbeek, Frank. van der Meer, Freek and Naimi, B. (2014). Detection of Alteration Induced by Onshore Gas Seeps from ASTER and WorldView-2 Data. Remote Sensing, Vol. 6, pp. 3188-3209.

Salminen, R. (Ed.) (2009). Geochemical Atlas of Northern Europe. Geological Survey of Finland, Espoo. http://weppi.gtk.fi/publ/negatlas: [Achieved: 23 January 2018]

Salminen, R. and Tarvanen, T., (1997). The Problem of Defining Geochemical Baselines. A Case Study of Selected Elements and Geological Materials in Finland. *Journal of Geochemical Exploration*, Vol. 60, pp. 91-98.

Salminen R. and Gregorauskien G. (2000). Considerations Regarding the Definition of Geochemical Baseline in Surficial Materials in Areas Differing in Basic Geology. *Applied Geochemistry.* Vo. 15, pp. 647-653.

Salminen, R., Chekushin, V., Tenhola, M., Bogatiyarev, I. and Zhdanova, L. (2004). Geochemical Atlas of the Eastern Barents Region. Amsterdam: Elsevier Science. *Journal of Geochemical Exploration.* Vol. 83, pp. 526-530.

Santosh, M. and Omori, S. (2008). CO2 Flushing: A Plate Tectonic Perspective. *Gondwana Research*, Vol. 13, pp. 86-102.

Sawkins, F.J. (1977). Fluid Inclusion Studies of the Messina Copper Deposits, Transvaal, South Africa, *Economic Geology*. Vol. 72, pp. 619-631.

Sawkins, F.J. and Rye, R.O. (1979). Additional Geochemical Data on the Messina Copper Deposits, Transvaal, South Africa, *Economic Geology*, pp. 684-688.

Schouwstra, R.P. and Smit, A.J. (2011). Developments in Mineralogical Techniques: What about Mineralogists? *Journal of Minerals Engineering*, Vol. 24, Issue 12, pp. 1224-1228.

© University of Venda

Schowengerdt, R.A. (1983). Techniques for Image Processing and Classification in Remote Sensing. Orlando, New York: Academic Press, 249pp.

Seal II, R.R. (2006). Sulfur Isotope Geochemistry of Sulfide Minerals. In Vaughan, D.J. (Ed.): Sulfide Mineralogy and Geochemistry. *Mineralogical Society of America*, Chapter 12, Vol. 61, pp. 633 - 678.

Seat, Z., Beresford, S.W., Grguric, B.A., Mary Gee, M. A. and Grassineau, N.V. (2009). Reevaluation of the Role of External Sulfur Addition in the Genesis of Ni-Cu-PGE Deposits: Evidence from the Nebo-Babel Ni-Cu-PGE Deposit, West Musgrave, Western Australia. *Economic Geology* , Society of Economic Geologists, Vol. 104, No. 4, pp. 521 - 538.

Seitz, J.C., Pasteris, J.D., Wopenka, B. (1987). Characterization of CO2-CH4-H2O Fluid Inclusions by Microthermometry and Laser Raman Microprobe Spectroscopy: Inferences for Clathrate and Fluid Equilibria. *Geochimica et Cosmochimica Acta*, Vol. 51, pp.1651–1664.

Seo, J.H., Guillong, M. and Heinrich, C. (2009). The Role of Sulphur in the Formation of Magmatic-Hydrothermal Copper-Gold Deposits. *Earth and Planetary Science Letters*. Elsevier, Vol. 282, Issue 1-4, pp. 323-328.

Severson, R. C. and Tidball, R. R. (1979). Spatial Variation in Total Element Concentration in Soil within the Northern Great Plains Coal Region, Vol. 1134, 33 pp.

Seyoum, Z. W. (2006). Environmental Impacts of Gold Mining on Waters and Sediments of Legadembi area. M. Sc. thesis (unpublished.). Ethiopia: Addis Ababa University.

Shand, S.J. (1931). The Granite –syenite –limestone Complex of Palabora, Eastern Transvaal, and its associated Apatite Deposits. *Transaction of Geological Society of South Africa*, Vol.34, pp. 81-105.

Shanks III, W.C.P. and Koski, R.A. (2010). Introduction: In III, W.CP. and Thurston, R. (Eds.). *Volcanogenic Massive Sulphide Occurrence Model*. Scientific Investigation Report 2010-5070-C, US Geological Survey, pp. 1- 21.

Sharp, Z. (2007). Principles of Isotopes Geochemistry. 1st Edition. Pearson Education Inc. Upper Saddle River, USA, 334 pp.

Shelton, K.L. and Rye, D.M. (1982). Sulfur Isotopic Compositions of Ores from Mines Gaspe´ Quebec: An Example of Sulfate-sulfide Isotopic Disequilibria in Ore Forming Fluids with Applications to other Porphyry-type Deposits. *Economic Geology*, Vol. 77, pp. 1688 - 1709.

Sheppard, S.M.F. (1986). Characterization and Isotopic Variations in Natural Waters. In Valley, J.W., Taylor, Jr. H.P., and O'Neil, J.R. (Eds.): Stable Isotopes in High Temperature Geological Processes. *Reviews in Mineralogy, American Mineralogy Society*, Blacksburg, Virginia, Chapter 6, Vol. 16, pp. 165 - 184.

© University of Venda

Shepherd, T.J., Rankin, A.H. and Alderton, D.H.M. (1985). A Practical Guide to Fluid Inclusion Studies. Blackie Sons Ltd., Glasgow, 293pp.

Sheppard, D.S., Christic, A.B., Goff, J. and Carver, R. (2009). Stream Sediment Geochemical Survey in an area of Volcanic-hosted Epithermal. Au-Ag-Zn-Pb-Cu Deposits and Porphyry Cu Prospects, Thames, Coromandel Peninsula, New Zealand. *Geochemistry, Exploration, Environment and Analysis.* Association of Applied Geochemists and the Geological Society, Vol. 9 Part 3, pp. 279-296

Shimazaki, H. (1982).The Sasano Hasting-beARING Copper Skarn Deposit form ed in Aluminous Sediment, at the Yoshioka Mine, Japan. *Economic Geology*, Vol. 77, No. 04, pp. 868 – 876.

Shukla, M. K. and Sharma, A. (2018). A Brief Review on Breccia: It's Contrasting Origin and Diagnostic Signatures. *Journal of Solid Earth Sciences*, Vol. 3, Issue 2, Elsevier, pp. 50-59.

Simmons, G. and Richter, D. (1976). Micro-Cracks in Rock. In: Strens, R.G.J (Ed.): The Physics and Chemistry of Minerals and Rocks. Wiley, New York, pp. 105 -137.

Sittner, J. and Götze, J. (2018). Cathodolumisence (Cl) Characteristics of Quartz from Different Metamorphic Rocks within the Kaoko Belt, Namibia. Special Issue of Mineralogy of Quartz and Silica Minerals, *Minerals*, Vol. 8, Issue 5.

Skoog, D., Holler, J. F. and Crouch, S. R. (2007). Principles of Instrumentals of Analysis. 6th Ed, Belmont, C.A, Thomson. Brooks/Cole, Canada, 238 pp.

Skoog, D. A., Holler, F. J. and Crouch, S. R. (2007). Principles of Instrumental Analysis. Pacific Grove: Brooks Cole. 1039 pp.

Smith, J.V. and Stenstrom, R.C. (1965). Electron-excited Luminescence as a Petrologic Tool. *Journal of Geology*, Vol. 73, No. 4, pp. 627–635.

Smith, M.J., Goodchild, M.F. and Longely, P.A. (2018). Geospatial Analysis: A omprehensive Guide to Principles Techniques and Software Tools. Sixth Edition. Winchelsea Press, 602 pp.

Smirnov, V.I. (1976). Geology of Mineral Deposits. MIR Publishers, Moscow, 520 pp.

So, C.S. and Shelton, K.L. (1983). A Sulfur Isotope and Fluid Inclusion Study of the Cu-W Bearing *Tourmaline Breccia Pipe, Ilkwang Mine, Republic of Korea.* Economic Geology, Vol. 78, pp. 329 - 333.

Söhnge, P.G. (1945). The Geology of the Messina Copper Mines and Surrounding Country. *Geological Survey of South Africa*, Government Printer, Pretoria, M*emoir* No. 40, 272 pp.

Söhnge, A. (1946). The Geology of the Messina Copper Mines and Surrounding Country, Vol. 1. Pretoria, Government Printer, 138 pp.

© University of Venda

Spear, F.S. (2017). Determining The Amount Of Overstepping Required to Nucleate Garnet During Barrovian Regional Metamorphism, Connecticut Valley Synclinorium. *Journal of Metamorphic Geology*, Vol. 36, Issue No. 1, pp. 79-94.

Stenstrom, R.C. and Smith, J.V. (1964). Electron-excited Luminescence as a Petrologic Tool. *Geological Society of America*, Special Paper, Vol. 76, pp. 152 - 158.

Sweeney, M.A., Turner, P. and Vaughan, D.J. (1986). Stable Isotope and Geochemical Studies of the Role of Early Diagenesis in Ore Formation, Konkola Basin, Zambian Copperbelt. *Economic Geology*, Vol. 81, pp. 1836-1852.

Tankard, A., Welsink, H., Aukes, P., Newton, R., and Stettler, E. (2009). Tectonic Evolution of the Cape and Karoo Basins of South Africa. *Marine and Petroleum Geology*, Vol. 26, pp. 1379–1412.

Taylor, H.P. Jr. (1974). The Application of Oxygen and Hydrogen Isotope Studies to Problems of hydrothermal Alteration and Ore Deposition. *Economic Geology*, Vol. 69, pp. 843 - 883.

Taylor, H.P. Jr. (1979). Oxygen and Hydrogen Isotope Relationships in Hydrothermal Mineral Deposits. In Barnes, H.L. (ed.): Geochemistry of Hydrothermal Ore Deposits. 2nd Edition. New York, John Wiley and Sons, pp. 236 - 287.

Taylor, H.P. Jr. (1997). Oxygen and Hydrogen Isotope Relationships in Hydrothermal Mineral Deposits. In Barnes, H.L. (Ed.): Geochemistry of Hydrothermal Ore Deposits. 3rd Edition. New York, John Wiley and Sons, pp. 229 - 302.

Testa, F.J., Zhang, L. and Cooke, D.R. (2018). Physicochemical Conditions of Formation for Bismuth Mineralisation Hosted in a Magmatic –Hydrothermal Breccia Complex: An Example from the Argentine Andes. *Minerals*, Vol. 8, Issue No. 1.

Thenkabail, P.S. (2015). Remote Sensing Handbook: Land Resource Monitoring, *Modelling, and Mapping with Remote Sensing.* Vol. 2: CRC Press, 45 pp.

Theron, J.N. (1969). The Baviaanskloof Range: A South African Nappe. *Transaction of the Geological Society of South Africa*, Vol. 72, pp. 29-40.

Thode, H.G. (1970). Sulfur Isotope Geochemistry and Fractionation between Coexisting Sulfide Minerals. *Mineral Society of America*, Paper 3, pp. 133-140.

Thomson, J. J. (1914). Rays of Positive Electricity. *Proc. Roy. Soc. Lond*. Vol. 89, Series 5, pp.1 - 20.

Toovey, L. (2011). Indicator Minerals, Pathfinder Minerals and Gold Exploration. Gold Article, Gold Report, Gold Investigating News, Western Potash Corporation, pp. 1-8.

Torres, C. (2016). Mineral Exploration Using ASTER Images. www.utsa.edu/lrsg/Teaching/EES505306/project/Mineral%20Exploration%20Using%20ASTER%20Images.pdf: [Accessed: 4 July 2016].

© University of Venda

Toulkeridis, T., Clauer, N., Kröner, A. and Todt, W. (2015). A Mineralogical, Chemical and Isotopic Investigation of Shales from the Barberton Greenstone Belt, South Africa, To Constrain Source Materials and Post-Deposition Evolution. *South African Journal of Geology*. Geological Society of South Africa, Vol.118, No. 4, pp. 389-410.

Touret, J.L.R. (1977). The Significance of Fluid Inclusions in Metamorphic Rocks. In Fraser, D. (ed.): Thermodynamics in Geology. Chapter 12, NATO ASI Series, C. 35, Reidell Pub., Dordrecht, 410 pp.

Touret, J.R.L (2001). Fluids in Metamorphic Rocks. *LITHOS*, Elsevier, Vol. 55, pp. 1 - 25.

Tourtelot, E. and Vine, J.D. (1976). Copper Deposits in Sedimentary and Volcanogenic Rocks. US Department of the Interior, 42pp.

U.S. Geological Survey. (2013). Landsat 1 History. Retrieved, 5 July 2016 from USGS: http://landsat.usgs.gov/about_landsat1.php.

University of Cincinnati. (2016). Centre for Geospatial Information and Environmental Sensor Networks (GIESN). http://giesn.uc.edu/hxliu/teaching/courses/g361/note8.pdf: [Accessed: 30 June 2016].

University of Leicester. (2007). 4 Band Ratios. https://erdas.wordpress.com/2007/12/30/4-band-ratios/: [Accessed: 10 July 2016].

Unwin, A. (2008). Good Graphics? In: Chen, C., Härdle, W. and Unwin, A. (Eds.). Handbook of Computational Statistics: Data Visualization. Vol. III, Springer-Verlag, Heidelburg. Chapter II. 2, pp. 57-78.

Unwin, A., Chen, C. and Härdle, W.K. (2008). Introduction. In: Chen, C., Härdle, W. and Unwin, A. (Eds.). Handbook of Computational Statistics: Data Visualization. Vol. III, Springer-Verlag, Heidelburg. Chapter I, pp.1-14.

Van den Kerkhof, A.M. (1988a). Phase Transitions and Molar Volumes of CO_2–CH_4 - N_2 Inclusions. *Bulletin de Minéralogie*, Vol. 111, pp. 257 - 266.

Van den Kerkhof, A.M. (1988b). The System CO_2–CH_4–N_2 in Fluid Inclusions: Theoretical Modelling and Geological Applications. Ph.D. Thesis, Vrije Universiteit Amsterdam, The Netherlands. 206pp.

Van den Kerkhof, A.M. (1990). Isochoric Phase Diagrams in the System CO_2–CH_4 and CO_2–N_2: Application to Fluid Inclusions. *Geochimica et Cosmochimica Acta* , Vol. 54, pp. 621 - 629.

Van den Kerkhof A.M. (2003) Advancements of Cathodoluminescence Microscopy and Related Techniques with Application to the Study of Fluid-rock Interaction. Göttinger Arb. Geol. Paläont., Sb5, pp. 111-120.

Van den Kerkhof, A.M. and Hein, U.F. (2001). Fluid Inclusion Petrography. *Lithos*, Elsevier, Vol. 55, pp. 27-47.

© University of Venda

Van den Kerkhof, A.M., Simon, K.E., and Kronz, A. (2014). Deciphering Fluid Inclusions in High-grade Rocks. *Geoscience Frontiers*, Vol. 5, pp. 683 - 695.

Van der Meer, F.D., van der Werff, H.M.A., van Ruitenbeek, F.J.A. Hecker, C.A., Bakker, W.H., Noomen, M.F., van der Meijde, M., Carranza, E.J.M., de Smeth, J.B. and Woldai, T. (2012). Multi and Hyperspectral Geologic Remote Sensing: A Review. *International Journal of Applied Earth Observation and Geoinformation*, Elsevier, Vol. 14, Issue 1, pp. 112-128.

Van Graan, S.J. (1964). Geology of the Messina Copper Deposits. In Haughton, S.H. *The Geology of Some Ore Deposits of Southern Africa*. Geological Society of South Africa. Vol. 2, pp. 303-314.

Van Graan, S.J. (1964). Geology of the Messina Copper Deposits. In Haughton, S.H. (Eds.). *The Geology of Some Ore Deposits of Southern Africa.* Geological Society of South Africa. Vol. 2, pp. 303-314.

Van Reenen, D. D., Roering, C., Brandl, G., Smit, C. A. and Barton, J. M. (1990). The Granulite Facies Rocks of the Limpopo Belt, Southern Africa. In Vielzeuf, D. and Vidal, P. (Eds.). *Granulite and Crustal Evolution*, Kluwer, Dordrecht. pp. 255-289.

Van Reenen, D.D., Kramers, J.D., McCourt, S. and Perchuk, L.L. (2011). Origin and Evolution of Precambrian High-Grade Gneiss Terranes, with Special Emphasis on the Limpopo Complex of Southern Africa. *Memoirs: Geological Society of America*, 324 pp.

Van Reenen, D.D., Huizenga, J.M., Smit, C.A., and Roering, C. (2014). Fluid-rock Interaction during High-grade Metamorphism: Instructive Examples from the Southern Marginal Zone of the Limpopo Complex, South Africa. *Precambrian Research*, Vol. 253. pp. 63 - 80.

Vernon-Parry, K.D. (2000). Scanning Electron Microscopy: An Introduction. III-Vs Review, Vol. 13, Issue 4, Elsevier, pp. 40-44.

Verwoerd, W.J. (1966). South African Carbonatites and their Probable Mode of Origin- Ann. Unn. University of Stellenbosch. 4t, Ser. A, No. 2, pp. 145-146.

Vicente-Serrano, S.M., Lasanta, T. and Perez-Cabello, F. (2008). Assessment of Radiometric Correction Techniques in Analyzing Vegetation Variability and Change Using Time Series of Landsat Images. Remote Sensing of Environment, Vol. 112, No. 11, pp. 3916-3934.

Wakefield, J. (1978). Samba: A Deformed Porphyry-type Copper Deposit in the Basement of the Zambian Copperbelt. *Transaction of the Institution of Mining and Metallurgy*, Section B, Vol. 87, pp. 43 -52.

Walker, G. and Burley, S. (1991). Luninescence Petrography and Spectroscopic Studies of Diagenetic Minerals. In Luminescence Microscopy and Spectroscopy: Quantitative and Qualitative Applications, SEPM Short Course 25, pp. 83 -96.

© University of Venda

Walker, R., and Rackham, L. (2010). Metadata Guidelines for Geospatial Data Resources. Association for Geographic Information.

Wang, J. and Zuo, R. (2018). Identification of Geochemical Anomalies through Combined Sequential Gaussian Simulation and Grid-based Local Singularity Analysis. *Computers and Geosciences, 118,* pp. 52–64.

Wanless, R.K. and Thode, H.G. (1953). A New Mass Spectrometer for High Precision Isotope Ratio Determinations. *Journal of Science Institution,* Vol. 30, pp. 395 - 398.

Wasserburg, G.J., Papanastassiou, D., Nerow, E.V. and Bauman, C.A. (1969). A Programmable Magnetic Field Spectrometer with Online Data Processing. *Rev. Sci. Instrum.* Vol. 40, pp. 288 - 295.

Watkeys, M.K. (1979). Explanation of the Geological Map of the Country, West of Beitbridge. Short Report of the Geological Survey of Rhodesia, Vol. 45, 96pp.

Watson, J.S. (1996). Fast, Simple Method of Powder Pellet Preparation for X-Ray Fluorescence Analysis. X-Ray Spectrom. Geostandards Newsletter 25, pp. 173-174.

Weih, R.C. and Riggan, N.D. (2010). Object-based Classification vs Pixel-based Classification: Comparative Importance of Multi-Resolution Imagery. The International Archives of the Photogrammetry, Remote Sensing and Spatial Information Sciences, Vol. 38, No. 4, pp.193-202.

Wen, H., Zhu, C., Zhang, Y., Cloquet, C., Fan, H. and Fu, S. (2016). Zn/Cd Ratio and Cadmium Isotope Evidence for the Classification of Lead Zinc Deposits. *Scientific Reports*, Vol. 6, pp.1- 8.

Wenk, H.R. and Bulakh, A.B. (2008). Minerals: Their Constitution and Origin. Cambridge University Press, Cambridge, UK, 646pp.

West, D. (2003).Ternary Equilibrium Diagram. Second Edition, Springer, New York, 225pp.

White, W.S. (1968). The Native-copper Deposits of Northern Michigan. In Ridge, J.D. (ed.): Ore Deposit of the United States, Am. Inst. Mining, Metal and Petroleum Engineers, Graton-Scale, New York, pp.1933-1967.

White, W. M. (2015). Isotope Geochemistry. John Wiley and Sons Ltd, UK, 496pp.

Wilkinson, J.J. (2001). Fluid Inclusions in Hydrothermal Ore Deposits. *Lithos,* Elsevier, Vol. 55, pp. 229 - 272.

Willis, B. A. (1990). Comminution in the Minerals Industry – An overview. *Minerals Engineering.* Vol. 3, pp. 3–5.

Willis J.P. and Duncan A.R. (2008). Understanding XRF Spectrometry: Quantitative Analysis and Special Sample Preparation and Presentation Methods. Almelo: PANalytical B. Vol. 2, pp.13 -16.

© University of Venda

Wilson, M.G.C. (1998). Copper. In Wilson, M.G.C. and Anhaeusser, (Eds.): *Mineral Resources of South Africa*, 6th Edition, Council for Geoscience, Pretoria, pp. 209-227.

Winter, J.D, (2014). Principles of Igneous and Metamorphic Petrology. Second Edition. Pearson Education Limited, 738 pp.

Worden, R.H. (2005). Geochemical Analysis: Including X-Ray. In Selley, P.C., Cocks, L.R.M and Plimer, I.R. (Eds.): *Encyclopedia of Geology*. Elsevier, United Kingdom, pp. 54-76.

Wynne-Edwards, H.R. (1978). Tectonic Evaluation of Precambrian Metamorphic Terranes for Mineral Exploration. In Verwoerd, W.J. (Ed.): *Mineralisation in Metamorphic Terranes, Geokongress 75*, Stellenbosch, South Africa, Schaik J.L. Limited, Pretoria, Chapter 1, pp. 3-5.

Xu, Y.F., Ni, P., Wang, G.G., Pan, J.Y., Guan, S.J. and Chen, H. (2016). Fluid Inclusion and Stable Isotopes Study of the Huanghan Orogenic Gold Deposit: Implications for Future Exploration along the Jiangshan-Shaoxing Fault Zone, South China. *Journal of Geochemical Exploration*, Vol. 171, pp. 37-54.

Yacobi, C. and Holt, D.B. (1990) Cathodoluminescence Microscopy of Inorganic Solids. *Plenum*, New York, 292 pp.

Yanagisawa, F. and Sakai, H. (1983). Thermal Decomposition of Barium Sulfate-Vanadium Pentoxide-Silica Glass Mixtures for Preparation of Sulfur Dioxide in Sulfur Isotope Ratio Measurements. *Analytical Chemistry*, Vol. 55, pp.985 - 987.

Yang, K. and Bodnar, R.J. (2004). Orthomagmatic Deposit for the Ilkwang Cu-W Breccia Pipe Deposit, Southeastern Kyongsang Basin, South Korea. *Journal of Asian Earth Sciences*, Vol. 24, pp. 259 - 270.

Yang Yang, Fu-Hong Gao, Xiu-Gang Pu, Chang-Wei Chen and Wen-Liang Xu. (2013). Changes to Depositional Palaeoenvironments within the Qikou Depression, Bohaiwan Basin, China. Carbon and Oxygen Isotopes in Lacustrine Carbonates of the Palaeogene Shahejie Formation. *International Geology Review*, Vol. 55, No.15, pp.1909-1921.

Yaylali-abanuz, G. and Tüysüz, N. (2011). Statistical Evaluation of the Geochemical Data from Akoluk Epithermal Gold Area (Ulubey–Ordu), NE Turkey. *Geochemical Journal*, Vol. 45, pp. 209 – 219.

Yoo, B. C., Brown, P.E., and. White, N. C. (2011). Hydrothermal Fluid Characteristics and Genesis of Cu Quartz Veins in the Hwanggangri Metallogenic District, Republic of Korea: Mineralogy, Fluid Inclusion and Stable Isotope Studies. *Journal of Geochemical Exploration*, Elsevier, Vol. 110, pp. 245 - 259.

Zelenika, N.Z., Velic, Malvic, T. and Cvetkovic. (2011). Geological Variables Fitting in Normal Distribution and Application in Indicator Geostatistical Methods.

© University of Venda

Proceedings of the IAMG Conference, Salzburg, Croatia, doi:10.5254/iamg.2011.0230.

Zeh, A., Klemd, R. and Barton, Jr., J.M. (2007). Archaean to Proterozoic Crustal Evolution in the Central Zone of the Limpopo Belt (South Africa-Botswana): Constraints from Combined U-Pb and Lu-Hf Isotope Analyses of Zircon. *Journal of Petrology*, Vol. 48, pp.1605-1639.

Zengeya, T.A., Booth, A.J., Bastos, A.D.S. and Chimimba, C.T. (2011). Trophic Interrelationships between the Exotic Nile Tilapia, Oreochromis Niloticus and Indigenous Tilapiine Cichlids in a Subtropical African River System, Limpopo River, South Africa. *Environmental Biology of Fishes*, Vol. 92, Issue 4, pp. 479-489.

Zhang Ruisi, Zeng Min and Chen Jianping (2011). Study on Geological Structural Interpretation Based on Worldview-2 Remote Sensing Image and its Implementation. 2011 3rd International Conference on Environmental Science and Information Application Technology (ESIAT), Procedia Environmental Sciences, SciVerse ScienceDirect, Elsevier, Direct, Vol. 10, pp. 653 – 659.

Zhang, D., Cheng, Q. and Agterberg, F. (2017). Application of Spatially Weighted Technology for Mapping Intermediate and Felsic Igneous Rocks in Fujian Province, China. *Journal of Geochemical Exploration*, Vol. *178*, pp. 55–66.

Zhong, J., Chen, Y. J., Pirajno, F., Chen, J., Li, J., Qi, J.P. and Li, N. (2014). Geology, Geochronology, Fluid Inclusion and H–O Isotope Geochemistry of the Luoboling Porphyry Cu–Mo Deposit, Zijinshan Orefield, Fujian Province, China. Ore Geology Reviews, Elsevier, Vol. 57, pp. 61 - 77.

Zumsprekel, H. and Prinz, T. (2000). Computer-Enhanced Multispectral Remote Sensing Data: A useful Tool for the Geological Mapping of Archean Terrains in Semi-arid Environments. *Computer and Geosciences*, Vol. 26, pp. 87-100.

Zuo, R. and Wang, J. (2016). Fractal/Multifractal Modelling of Geochemical Data: A Review. Journal of Geochem Exploration, Vol. 164, pp. 33-41.

http://www.nr.gov.nl.ca/nr/mines/prospector/matty_mitchell/ Virtual/Metallic%20mineral%20Deposits%20of%20NL,%20Part%203,%20Sedimentary-Hosted.pdf:[Accessed: 25 March 2018].

https://www.911metallurgist.com/blog/geology-of-porphyry-copper-deposits:[Accessed: 02 March 2019/]

hppt://sprottglobal.com/natural.resource-investing/investment-university/cited:[10 March 2019]

www.csr.utexas.edu/projects/rs/hrs/hyper.html#background: [Accessed: 21 January 2019]

www.desktop.arcgis.com/en/arcmap/10.3/guide: [Accessed: 21 February 2019]

www.desktop.arcgis.com/en/arcmap/latest/extensions/geostatistical-analyst/: [Accessed: 21 February 2019]

© University of Venda

www.desktop.arcgis.com/understanding-ordinary-kriging.htm:[Accessed:21 February 2019]

www.digitalglobe.com/:[Accessed: 20 February 2019]

www.geol-amu.org/notes/m7-1-12.htm: [Accessed: 08 March 2019]

www.infomine.com/investment/metal-prices/copper/5-year/: [Accessed: 19 January 2019]

www.kingston.ac.uk/esg/facilities/fluidinc.pp:[13 March 2019]

www.macrotrends.net/1476/copper-prices-historical-chart-data:[Accessed: 19 January 2019]

www.places.co.za/maps/Limpopo: [Accessed: 23 March 2016]

www.saexplorer.co.za/South Africa/climate/Musinaclimate.asp:[Accessed:19 January 2019]

www.satimagingcorp.com/satellite-sensors/worldview-3: [Accessed: 21 January 2019]

© University of Venda